Table des matières

Introduction

1 Généralités sur le climat

> *"Le réchauffement du système climatique est sans équivoque et, depuis les années 1950, beaucoup de changements observés sont sans précédent depuis des décennies voire des millénaires. L'atmosphère et l'océan se sont réchauffés, la couverture de neige et de glace a diminué, le niveau des mers s'est élevé et les concentrations des gaz à effet de serre ont augmenté."*
>
> – Rapport IPCC 2013, extrait du résumé à l'intention des décideurs

Le Groupe d'experts Intergouvernemental sur l'Evolution du Climat (GIEC) fait état dans ses rapports du réchauffement climatique actuel. Ce groupe a pour but de réaliser régulièrement un état de l'art de nos connaissances sur le climat, une mise à jour des observations de ce changement climatique, ainsi que d'étudier les évolutions possibles grâce à l'utilisation de modèles climatiques. La principale source d'incertitude concernant l'évolution future du climat vient de la complexité du système climatique. En effet, le climat est le résultat d'interactions multiples entre l'atmosphère, les continents, les océans, la biosphère et la cryosphère (figure 1). Ces interactions se font au travers de différents processus chimiques et physiques, à des échelles de temps très disparates pouvant aller de quelques heures à plusieurs milliers d'années. Par exemple, la circulation océanique de grande échelle, qui participe aux échanges d'oxygène entre l'océan et l'atmosphère, possède un temps caractéristique d'environ 1 500 ans. A l'inverse, les réactions chimiques au sein de l'atmosphère se font généralement en quelques heures.

La Terre a connu de nombreux changements climatiques naturels au cours des derniers millions d'années, avec l'alternance de périodes froides, dites périodes **glaciaires**, et périodes chaudes, appelées périodes **interglaciaires** (figure 2). A la différence de ces changements climatiques passés, le réchauffement observé au cours des 50 dernières années est en partie causé par l'homme avec les émissions de gaz à effet de serre (GES). Comme nous avons atteint des concentrations de gaz à effet de serre supérieures à celles enregistrées par les archives climatiques au cours du

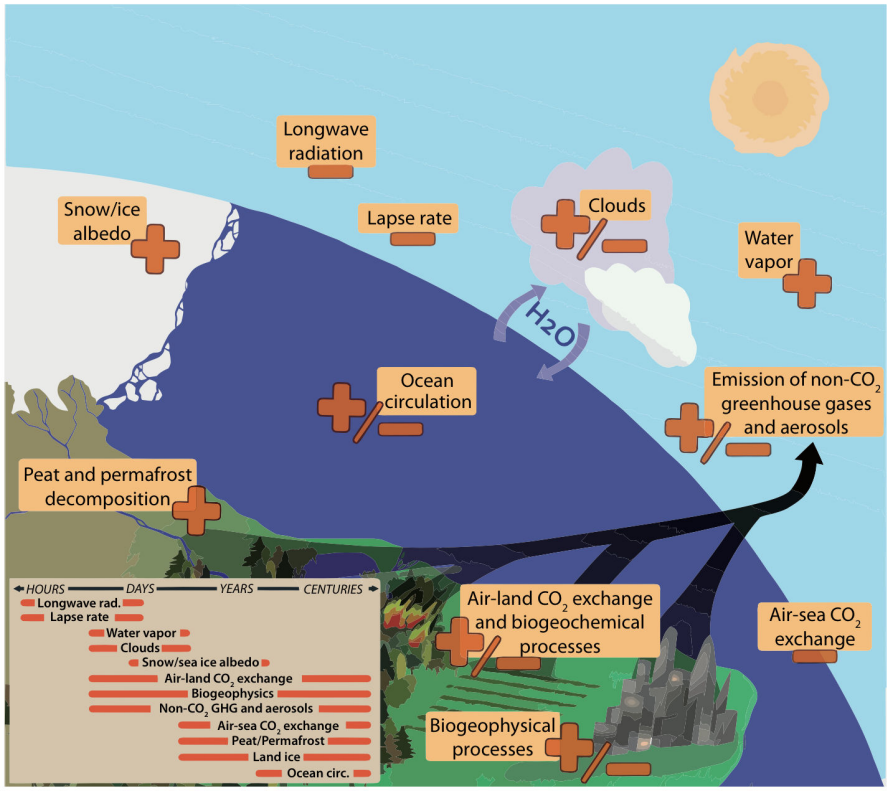

FIGURE 1 – Schéma explicatif des interactions entre les différents réservoirs composant la machinerie climatique. Les signes "–" et "+" illustrent les rétroactions, négatives et positives, qu'engendrent les composants climatiques lors d'une augmentation de la température et de la concentration de CO_2 dans l'atmosphère. L'encadré en bas à gauche fait état des différentes échelles de temps correspondant à ces rétroactions. Extrait du chapitre Introduction de l'IPCC [2013].

dernier million d'années, il nécessaire de quantifier l'influence de cette source anthropique (d'origine humaine) sur le système climatique. Pour cela le GIEC utilise des modèles complexes, reposant sur nos connaissances de la machinerie climatique. Ainsi, dans le but de prévoir l'évolution future du climat, il est nécessaire d'étudier ses variations passées afin d'améliorer notre compréhension du système climatique.

L'étude des paléoclimats peut se faire à partir de différentes archives climatiques : carottes marines, spéléothèmes, carottes lacustres, carottes de glace ; provenant de différents lieux à la surface du globe. Ces archives permettent d'obtenir des informations complémentaires sur le système climatique. Les carottes de glace sont uniques dans le sens où ce sont les seules archives climatiques à renfermer des échantillons d'air passé (figure 3).

2 Les carottes de glace : une archive climatique particulière

Les régions polaires sont des régions clés de la machinerie climatique. Lors d'un réchauffement climatique, la fonte des calottes de glace d'Antarctique et du Groenland peut entraîner une élévation du niveau des mers ou encore un ralentissement de la circulation océanique générale. L'accumulation de neige en surface des calottes permet d'enregistrer les variations du climat local, mais aussi de régions éloignées, sources de certains traceurs mesurés dans les carottes de glace. De plus, l'accumulation de neige à la surface des calottes peut conduire à apporter des informations avec des résolutions temporelles différentes. Par exemple, au Groenland où le taux d'accumulation est important (figure 4), nous avons des enregistrements présentant une résolution saisonnière. Pour les forages effectués en Antarctique de l'Est, les taux d'accumulation sont beaucoup moins importants qu'au Groenland (figure 4), conduisant à une résolution temporelle de l'ordre du siècle. Ainsi, l'analyse d'un même traceur climatique dans les carottes de glace n'apportera pas nécessairement la même information en Antarctique et au Groenland.

Plusieurs traceurs sont mesurés au sein des carottes de glace, que ce soit dans la phase gaz ou glace (cf table 1). Ces traceurs fournissent différentes informations et sont soumis à différentes influences. Par exemple, les isotopes de l'eau (δD et $\delta^{18}O$) sont dépendants des conditions climatiques au site, mais vont aussi dépendre de la région source de l'humidité à l'origine de la précipitation.

Certains traceurs mesurés dans les carottes de glace peuvent être utilisés pour

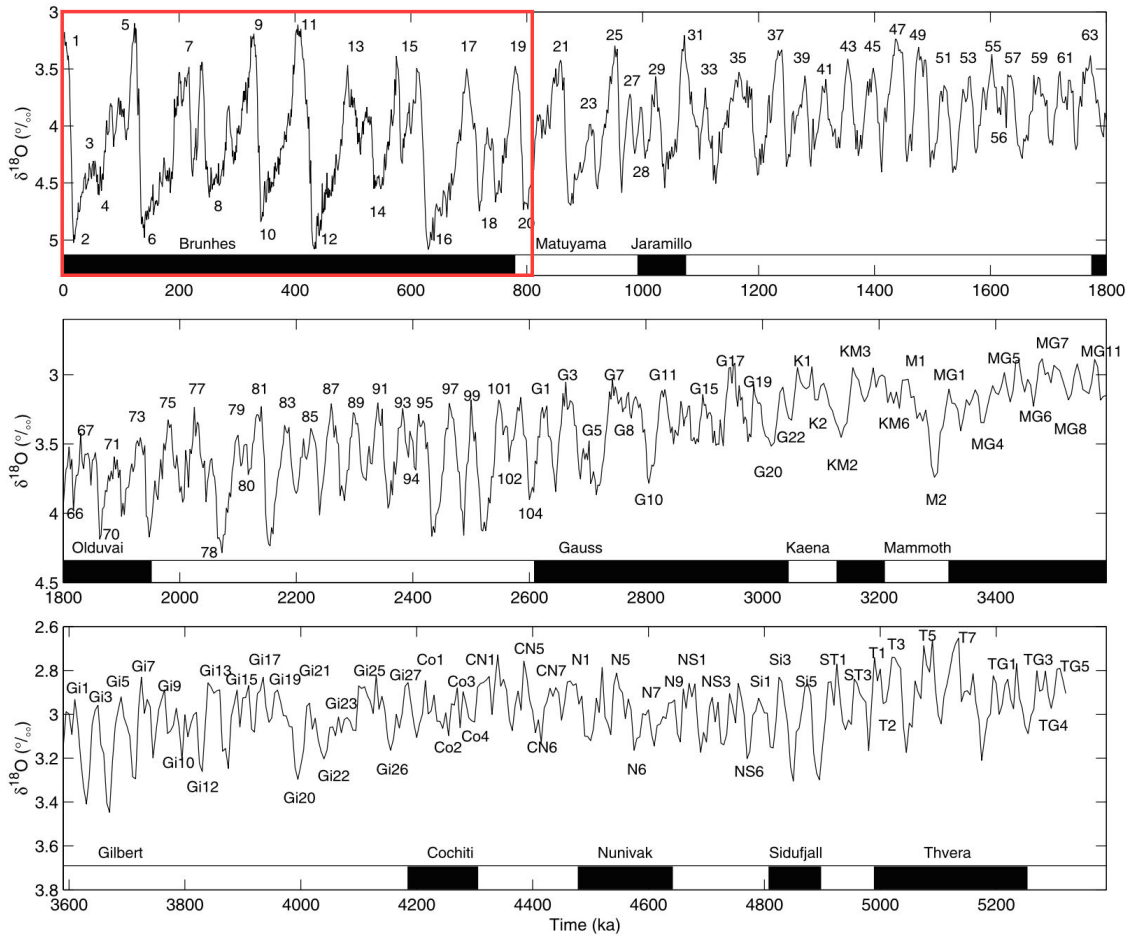

FIGURE 2 – Variations climatiques enregistrées par les carottes marines au cours des derniers 5 millions d'années (1 ka = 1 000 ans). Les numéros correspondent aux "Marine Isotope Stages" (MIS) : les nombres impairs sont associés aux périodes interglaciaires, les numéros pairs aux périodes glaciaires. Les périodes indiquées en bas des courbes par les bandes noires et blanches indiquent les changements de polarité magnétique. Le rectangle rouge met en évidence la période de temps couverte par les carottes de glace. Courbe composite du $\delta^{18}O$ de foraminifères benthiques LR04, extrait de Lisiecki and Raymo [2005].

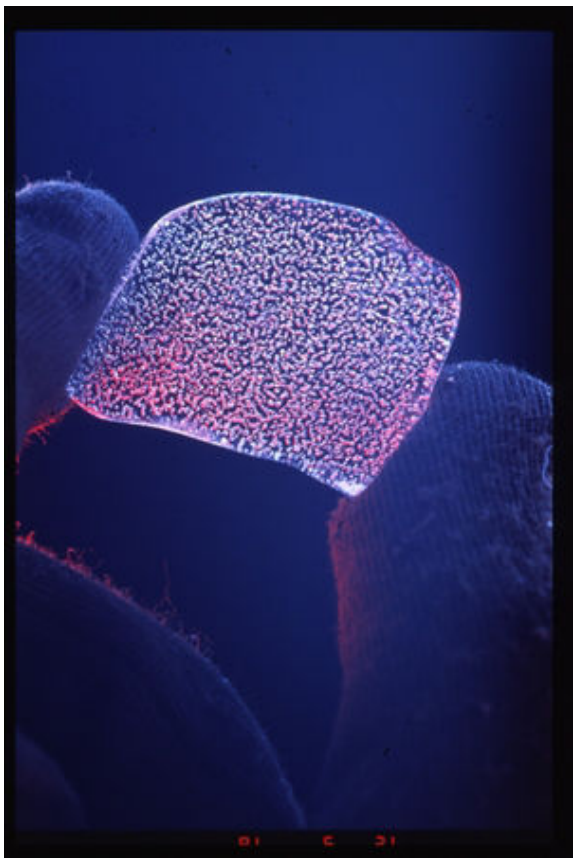

FIGURE 3 – Photographie d'un échantillon de glace renfermant des bulles d'air. ©David Etheridge, David Whillas, CSIRO.

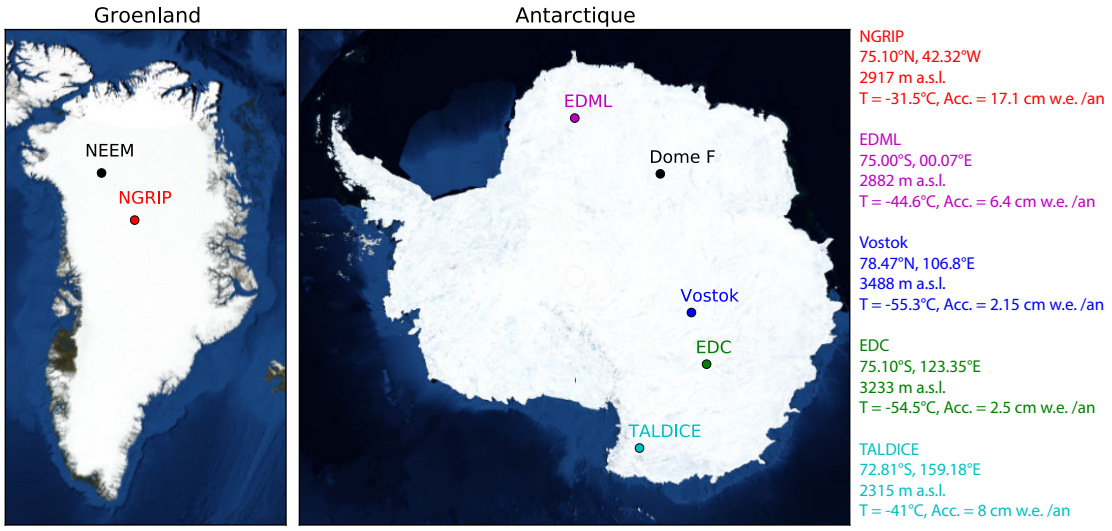

FIGURE 4 – Cartes d'Antarctique et du Groenland indiquant la localisation des carottes de glace discutées dans cette thèse, avec les données d'altitude, de température moyenne annuelle en surface et du taux d'accumulation ("ie" pour équivalent glace et "we" pour équivalent eau) pour les principaux sites [NorthGRIP Community Members, 2004; EPICA Community Members, 2004, 2006; Parrenin et al., 2007a; Stenni et al., 2011; Masson-Delmotte et al., 2011; Capron et al., 2013].

déduire des contraintes chronologiques (indiqués par les "*" dans la table 1). On recense donc des marqueurs dits absolus, comme les téphras ou le comptage des couches annuelles, d'autres qu'on appelle orbitaux, les marqueurs déduits de la synchronisation orbitale du $\delta^{18}O_{atm}$, $\delta O_2/N_2$ et de la teneur en air avec des courbes orbitales, et un dernier type de marqueurs qui permettent de relier les carottes entre elles. La composition isotopique de l'O_2 atmosphérique, $\delta^{18}O_{atm}$, est étroitement liée à la productivité de la biosphère et au cycle hydrologique des basses latitudes. Le $\delta^{18}O_{atm}$, comme le méthane, sont des traceurs dits globaux car ils sont répartis uniformément à la surface de la planète. Il est alors possible d'associer ensemble les variations de ces traceurs enregistrées dans différentes carottes de glace d'Antarctique et du Groenland.

3 La datation des carottes de glace

La datation des carottes de glace est très importante pour bien comprendre les processus liés aux grands changements climatiques. Par exemple, est-ce la concentration des GES qui induit un changement de température, ou bien est-ce l'inverse ? Les carottes de glace sont l'archive climatique appropriée pour ce genre de problématique. En effet, la composition isotopique de la glace est un traceur de la température

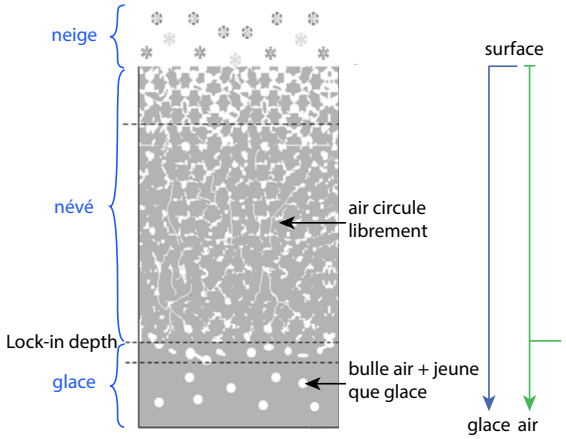

FIGURE 5 – Schéma explicatif du processus de densification de la neige en glace avec le piégeage de l'air à la base du névé (LID).

locale et les bulles d'air renferment des échantillons d'atmosphère passée.

L'air est piégé plusieurs dizaines à centaines de mètres sous la surface de la calotte, à la base du névé. En effet, le processus de densification de la neige en glace se fait progressivement avec la profondeur, jusqu'à ce que les interstices entre les cristaux soient fermés (figure 5). Tant que la porosité, c'est-à-dire l'espace libre entre les cristaux de glace, est ouverte l'air circule librement dans le névé car les pores sont beaucoup plus larges que les molécules d'air. A l'inverse, lorsque les pores deviennent plus petits que les molécules d'air, l'air se retrouve piégé. Cela correspond à la profondeur de piégeage de l'air, généralement appelée "Lock-in Depth" (LID, figure 5). Ainsi, à cette profondeur nous avons de l'air actuel piégé par de la glace plus ancienne. Il est alors nécessaire de calculer une échelle d'âge pour la glace et une autre pour le gaz piégé dans les bulles d'air. Pour ce faire, plusieurs méthodes de datation peuvent être utilisées. Pour les sites où l'accumulation en surface est importante, il est possible de réaliser un comptage des couches annuelles. Pour les sites de plus faible accumulation, on utilise généralement la modélisation inverse, c'est à dire l'utilisation combinée de modèles glaciologiques pour déduire les grandeurs nécessaires à la détermination de l'âge, tout en respectant certaines contraintes chronologiques issues des données. La suite de cette section fait un état de l'art des méthodes de datation utilisées pour construire les chronologies respectives des sites de NorthGRIP (NGRIP), EPICA Dôme C (EDC), EPICA Droning Maud Land (EDML), Vostok et TALos Dome ICE core (TALDICE).

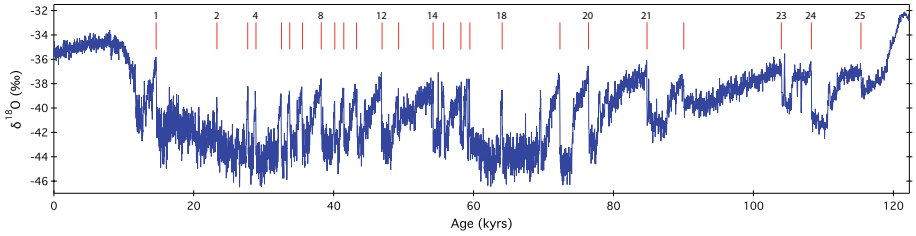

FIGURE 6 – Composition isotopique de la glace de NGRIP au cours des derniers 120 ka. Les traits rouges marquent la position des changements climatiques rapides (évènements de Dansgaard-Oeschger) observés lors de la dernière glaciation.

3.1 NorthGRIP

La carotte de glace de NGRIP a permis pour la première fois d'avoir des enregistrements continus jusqu'à 123 ka, couvrant donc l'entrée en glaciation (figure 6). Cette carotte de glace offre un enregistrement détaillé de la dernière période glaciaire, avec notamment la présence de réchauffements climatiques rapides : les évènements de Dansgaard-Oeschger (DO).

La chronologie de référence pour cette carotte de glace a été obtenue par comptage des couches annuelles sur les derniers 60 ka, puis prolongée jusqu'au fond de la carotte par un modèle d'écoulement [Vinther et al., 2006; Rasmussen et al., 2006; Andersen et al., 2006; Svensson et al., 2008; Wolff et al., 2010]. L'erreur associée à cette chronologie a été obtenue par sommation des couches incertaines. Les couches certaines ont été comptabilisées comme 1 ± 0 année alors que les couches incertaines sont comptées comme 0.5 ± 0.5 année. Cette erreur (Maximum Counting Error, MCE) augmente donc avec la profondeur jusqu'à atteindre 2.6 ka à 60 ka.

3.2 Vostok

La carotte de glace de Vostok a été la première à montrer les variations climatiques passées jusqu'à 400 ka (figure 7). Elle a permis d'établir le lien entre les quatre derniers grands cycles climatiques et les variations des concentrations de CO_2 et de méthane dans l'atmosphère.

La première datation de Vostok a été obtenue par un modèle d'écoulement [GT4, Petit et al., 1999]. La synchronisation orbitale du $\delta^{18}O_{atm}$ mesuré dans l'air piégé dans la glace avec l'insolation de mi–juin aux moyennes latitudes a permis d'estimer l'incertitude associée à cette chronologie, soit ± 5 ka sur les derniers 110 ka et ± 10 ka jusqu'à 400 ka. Plus récemment, Parrenin et al. [2004] a produit une chronologie pour

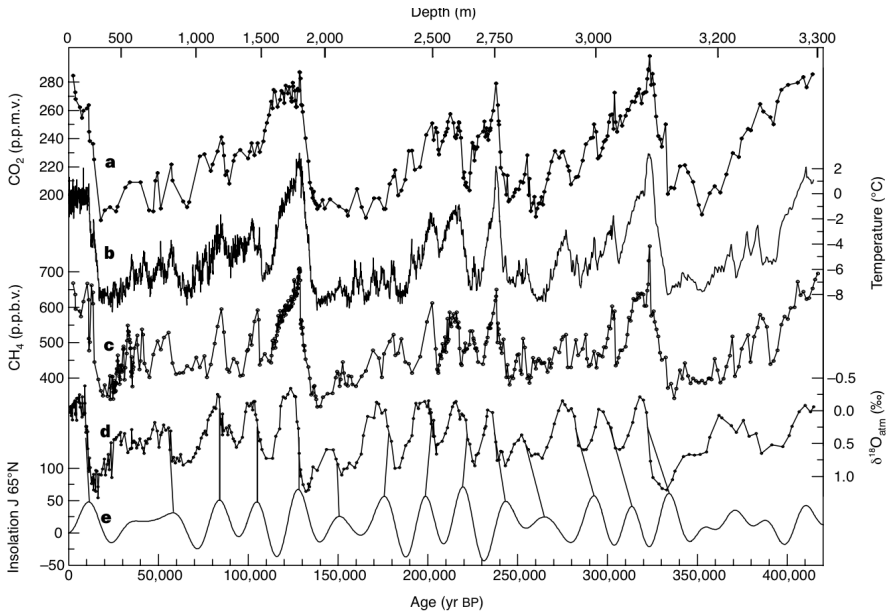

FIGURE 7 – Evolution de différents traceurs mesurés sur la carotte de Vostok : (a) concentration en CO_2, (b) température déduite de la composition isotopique de la glace, (c) concentration en méthane, (d) composition isotopique de l'oxygène atmosphérique et (e) insolation de mi–juin à 65°N. Les traits noirs identifient les points de contrôle ayant été utilisés pour valider la chronologie GT4. Extrait de Petit et al. [1999].

Vostok par modélisation inverse, c'est-à-dire en forçant le modèle d'écoulement à respecter certains horizons datés. La difficulté principale pour dater correctement cette carotte réside dans le fait que celle-ci n'est pas située sur un dôme, il est donc nécessaire de connaître l'écoulement de la glace en amont du site de forage.

3.3 EPICA Dôme C

La carotte d'EDC est celle qui nous permet de remonter le plus loin dans le temps pour les carottes de glace. Elle offre des enregistrements de très bonne qualité sur les derniers 800 ka (figure 8).

La chronologie de référence pour cette carotte est EDC3 [Parrenin et al., 2007a; Dreyfus et al., 2007]. Cette chronologie a été obtenue par modélisation inverse. Dans le but de contraindre au mieux cette chronologie, les auteurs ont utilisé des marqueurs orbitaux issus du $\delta^{18}O_{atm}$ pour contraindre le fond de la carotte. Comme le $\delta^{18}O_{atm}$ est étroitement lié aux basses latitudes, au travers du cycle hydrologique et de la productivité de la biosphère, il est possible d'associer ses variations à celles de la précession des équinoxes. Partant de cela, Dreyfus et al. [2007] ont pu déterminer 38 marqueurs orbitaux entre 398 et 802 ka. Jusqu'à maintenant, cette chronologie a

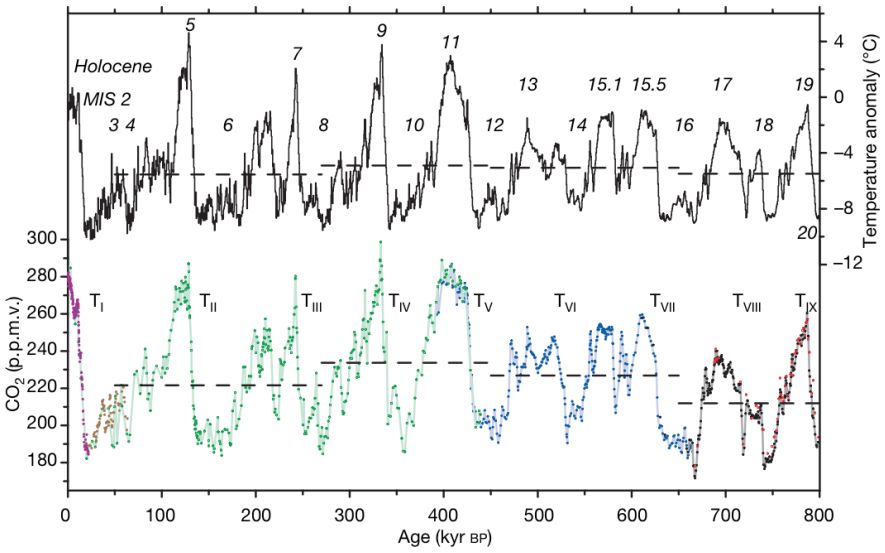

FIGURE 8 – Evolution de la température et de la concentration en CO_2 au cours des derniers 800 ka. Les différentes couleurs dans l'enregistrement de CO_2 sont associées à différentes séries de mesures. Les Marine Isotope Stages (MIS) sont indiqués par les chiffres arabes et les transitions entre périodes glaciaire et interglaciaire sont données par les chiffres romains.Extrait de Lüthi et al. [2008].

été utilisée comme référence pour les carottes de glace.

3.4 EPICA Dronning Maud Land

La particularité de la carotte EDML est qu'elle a été forée dans le secteur en lien avec l'océan Atlantique. Ses enregistrements, couvrant le dernier cycle climatique, permettent d'établir un lien Antarctique–Groenland sur la variabilité millénaire observée lors de la dernière période glaciaire [Capron et al., 2010; Capron, 2010].

La chronologie de référence pour cette carotte est EDML1 [Ruth et al., 2007; Severi et al., 2007]. Cette échelle d'âge a été obtenue par synchronisation volcanique avec la carotte EDC. C'est donc une chronologie relative synchrone à EDC3.

3.5 TALDICE

La carotte de TALDICE est située dans le secteur d'influence de la mer de Ross [Stenni et al., 2011].
La chronologie TALDICE-1a [Buiron et al., 2011; Schüpbach et al., 2011] a été obtenue à l'aide de l'outil de datation Datice [Lemieux-Dudon et al., 2010]. Cet outil, basé sur une statistique bayésienne, offre la possibilité de dater simultanément plu-

sieurs carottes de glace (chapitre 2). Il permet de calculer les âges glace et gaz, avec leurs incertitudes, en réalisant le meilleur compromis entre les datations d'ébauche et les contraintes d'âge appliquées. Pour la production de l'échelle d'âge TALDICE-1a, Datice a été utilisé avec seulement une seule carotte, en couplant une datation d'ébauche purement glaciologique, déduite d'un modèle d'écoulement simple, et des contraintes d'âge gaz et glace transférées depuis NGRIP et EDC.

Une limitation importante pour la comparaison des données des carottes de glace est que chaque carotte possède sa propre échelle d'âge. Ces chronologies sont obtenues à l'aide de méthodes différentes, directement par le comptage des couches annuelles de glace ou bien en mêlant contraintes chronologiques et modélisation. Ces échelles d'âge présentent des incertitudes importantes, de l'ordre de 2.6 ka à 60 ka pour GICC05 et de 6 ka à 800 ka dans le cas d'EDC3. Ces larges barres d'erreur sont induites par le peu de contraintes d'âge absolu disponibles. De plus, les chronologies de différentes carottes de glace peuvent présenter des incohérences entre elles, même lors de l'utilisation de méthodes de datation similaires (voir section 2.1 du chapitre 2). En effet, la variabilité régionale ne peut pas expliquer l'observation d'évènements non synchrones pour deux carottes de glace d'Antarctique.
Ainsi nous manquons de chronologies cohérentes et précises pour les carottes de glace dans le but de comparer correctement les différents traceurs mesurés dans la glace et le gaz des différents forages.

4 Objectif de la thèse

Ce travail de thèse a pour objectif d'améliorer les chronologies des carottes de glace. Il présente deux aspects principaux : la réalisation de nouvelles mesures ainsi que l'utilisation de l'outil de datation "Datice". Je m'intéresse particulièrement aux variations du $\delta^{15}N$, $\delta^{18}O_{atm}$ et $\delta O_2/N_2$ aux échelles de temps orbitales afin de contraindre les chronologies des carottes de glace jusqu'à 800 ka. L'amélioration des chronologies pour les carottes de glace va permettre de mieux appréhender la séquence des évènements de la dernière période glaciaire ainsi que de mieux comprendre les mécanismes prenant place lors des changements climatiques.

Au travers de la réalisation de nouvelles mesures de la composition isotopique de l'air piégé dans la glace de TALDICE et EDC ($\delta^{15}N$, $\delta^{18}O_{atm}$, $\delta O_2/N_2$), nous allons :

— compléter les enregistrements existants de ces trois traceurs dans les parties

profondes de ces deux forages ;
— déduire de nouvelles contraintes chronologiques pour les phases gaz et glace par le calage orbital du $\delta^{18}O_{atm}$ et du $\delta O_2/N_2$ respectivement (marqueurs dit "orbitaux"), ou bien par la synchronisation entre les enregistrements de plusieurs carottes de glace (liens stratigraphiques) ;
— améliorer notre compréhension des paramètres influençant le $\delta^{18}O_{atm}$ et le $\delta O_2/N_2$ au cours des derniers 800 ka.

Le second aspect de cette thèse repose sur l'utilisation et l'amélioration de l'outil de datation "Datice" développé par Lemieux-Dudon [2009] :
— regrouper les contraintes chronologiques pour les sites d'EDC, Vostok, EDML, TALDICE et NGRIP ;
— produire une chronologie cohérente et précise pour ces 5 sites ;
— améliorer la paramétrisation de Datice pour utiliser les contraintes issues du comptage des couches annuelles.

Les mesures de composition isotopique de l'air piégé dans la glace ont été réalisées au Laboratoire des Sciences du Climat et de l'Environnement (LSCE). Ce travail de thèse s'est fait en étroite collaboration avec Bénédicte Lemieux-Dudon pour tout ce qui est en lien avec l'outil de datation Datice.

5 Organisation du manuscrit

Ce manuscrit de thèse s'articule autour de cinq chapitres.

Le chapitre 1 se concentre sur la densification du névé et les fractionnements isotopiques associés. Les différents traceurs mesurés au cours de cette thèse y sont décrits, ainsi que l'état de nos connaissance sur ce qui les contrôle. Le protocole expérimental pour l'extraction de l'air piégé dans la glace et les différentes corrections appliquées suite aux mesures faites à l'aide du spectromètre de masse sont expliqués.

Le chapitre 2 présente la théorie sous-jacente à l'outil de datation Datice et son fonctionnement. Il explique comment sont calculés les âges gaz et glace des carottes de glace considérées ainsi que leurs incertitudes à partir des paramètres d'ébauches, des différentes contraintes d'âge et de leurs erreurs associées. Tout ceci est illustré par la première application réalisée par Lemieux-Dudon et al. [2010] pour quatre carottes de glace sur les derniers 50 ka.

Le chapitre 3 détaille toutes les modifications apportées à Datice depuis la première étude [Lemieux-Dudon et al., 2010] pour produire la nouvelle chronologie de référence pour les carottes de glace AICC2012 (Antarctic Ice Core Chronology 2012). Ce chapitre fait l'inventaire de toutes les données utilisées pour produire cette chronologie (paramètres d'ébauche, marqueurs d'âge, définition des erreurs...) et présente la comparaison de cette dernière avec d'autres échelles d'âge et archives climatiques.

Le chapitre 4 se concentre sur l'amélioration de la méthodologie de Datice. Afin de coller à l'échelle d'âge du Groenland GICC05, la chronologie AICC2012 a été produite en ne respectant pas l'hypothèse de non corrélation entre les contraintes d'âge et les paramètres d'ébauche. Ce chapitre présente l'implémentation des marqueurs de différence d'âge dans Datice et la série de tests associée permettant de forcer les chronologies à respecter le comptage des couches annuelles.

Le dernier chapitre de cette thèse présente les nouvelles données de $\delta O_2/N_2$ et $\delta^{18}O_{atm}$ mesurées sur de la glace bien conservée d'EDC. Ces données permettent d'effectuer une comparaison multi-sites de ces traceurs au cours de la dernière période interglaciaire (MIS 5). L'analyse de l'évolution du $\delta O_2/N_2$ et du $\delta^{18}O_{atm}$ au cours des derniers 800 ka permet de mieux appréhender les paramètres les contrôlant. La dernière section de ce chapitre discute de la complémentarité du $\delta O_2/N_2$ et du $\delta^{18}O_{atm}$ avec la teneur en air, tous trois utilisés comme marqueurs d'âge orbitaux dans Datice, entre 400 et 800 ka.

Au cours de cette thèse j'ai aussi travaillé en collaboration sur la variabilité millénaire de la dernière période glaciaire et sur d'autres applications de Datice. Les articles correspondants sont présentés en annexe.

TABLE 1 – Table récapitulative des différents traceurs mesurés dans les carottes de glace. Les asterisques mettent en évidences les traceurs pouvant être utilisés pour la datation des carottes de glace

Traceur	Information apportées	Source
Isotopes de la glace (δD et $\delta^{18}O$)	Température locale et régions sources	Vimeux et al. [1999]; Jouzel et al. [2007]; Stenni et al. [2011]
Composition chimique de la glace et éléments traces *	Saisonnalité, production primaire marine, éruptions volcaniques, glace de mer, origine des poussières	Andersen et al. [2006]; Svensson et al. [2008]; Rasmussen et al. [2006]; Vinther et al. [2006]; Wolff et al. [2006]
Contenu en poussière	Circulation atmosphérique	Petit et al. [1999]; Lambert et al. [2008]
Conductivité *	Comptage des couches annuelles, volcans	Andersen et al. [2006]; Svensson et al. [2008]; Rasmussen et al. [2006]; Vinther et al. [2006]
Couches de cendres et téphras *	Eruptions volcaniques	Narcisi et al. [2005]; Dunbar et al. [2008]
Isotopes cosmogéniques (^{10}Be) *	Activité solaire et intensité du champ magnétique terrestre	Yiou et al. [1997]; Raisbeck et al. [2007]
GES et leurs isotopes *	Concentrations passées, sources et puits des GES	Petit et al. [1999]; Loulergue et al. [2008]; Lüthi et al. [2008]; Schilt et al. [2010]; Schüpbach et al. [2011]; Baumgartner et al. [2014]
Composition isotopique de l'air ($\delta^{15}N$, $\delta^{18}O_{atm}$ et $\delta O_2/N_2$) *	Névé, biosphère, cycle hydrologique, datation orbitale	Bender et al. [1995]; Petit et al. [1999]; Caillon et al. [2003]; Landais et al. [2006]; Landais et al. [2010, 2012]; Dreyfus et al. [2007]; Severinghaus et al. [2009]; Buiron et al. [2011]
Teneur en air *	Datation orbitale, élévation des calottes polaires	Raynaud et al. [2007]; Lipenkov et al. [2011]

1

L'air dans la glace : processus de piégeage et mesure de sa composition isotopique

Au cours de cette thèse, j'ai mesuré la composition isotopique et la composition élémentaire de l'air piégé dans les carottes de glace de Dôme C et TALDICE. La composition isotopique d'un échantillon revient à comparer sa teneur en isotopes lourds/légers (R_{ech}) à celui d'une référence appelée standard (R_{std}) : $\delta = (R_{ech}/R_{std} - 1) \cdot 1000$ ‰. Les variations de la teneur isotopique d'une espèce chimique sont généralement induites par un changement des conditions climatiques globales et/ou locales. Celles–ci entraînent un fractionnement entre les isotopes lourds et légers, qui est alors enregistré dans la glace et les bulles d'air. Ce fractionnement peut résulter de processus différents et est soumis à différentes influences suivant les espèces chimiques considérées.

Dans le cadre de ma thèse, je me suis concentrée sur les molécules de N_2 et de O_2 de l'air piégé dans la glace. On étudie alors les variations des teneurs $\delta^{15}N$ et $\delta^{18}O$, mais aussi la proportion relative entre les molécules d'O_2 et N_2 ($\delta O_2/N_2$). Le $\delta^{15}N$ de l'atmosphère est resté constant au cours du temps, ainsi, les variations mesurées dans l'air piégé dans la glace vont être dues aux processus prenant place au sein du névé. A l'inverse, le $\delta^{18}O$ et le $\delta O_2/N_2$ de l'atmosphère ont varié par le passé, sur la période couverte par les carottes de glace (800 ka). De ce fait, il est nécessaire de bien comprendre les différents processus affectant ces trois traceurs.

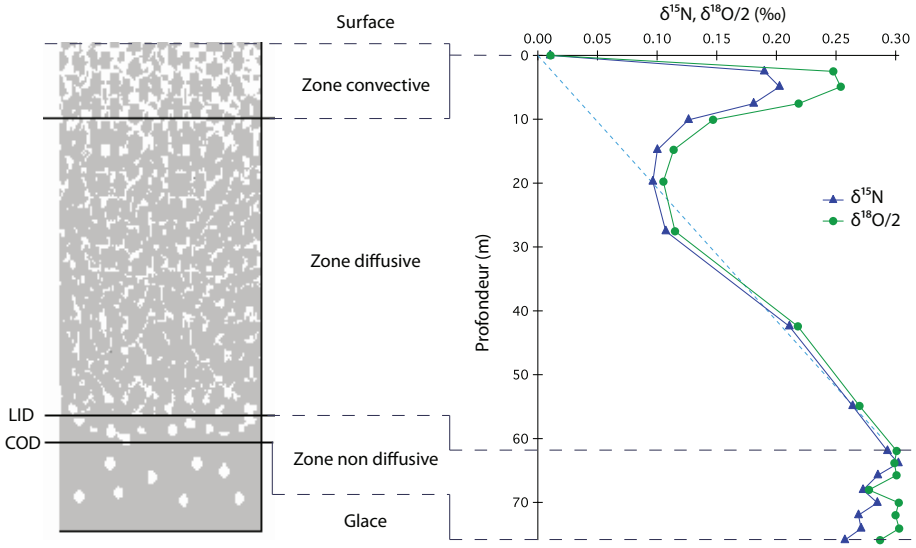

FIGURE 1.1 – Représentation schématique des différentes zones composant le névé et mise en correspondance avec les mesures de $\delta^{15}N$ et $\delta^{18}O/2$ du névé de NEEM. La ligne en bleu tiretée représente la pente du fractionnement gravitationnel (section 1.2). Modifié depuis Guillevic et al. [2013].

1.1 Névé et densification du névé

Le névé constitue la partie poreuse de la calotte de glace (50–120 m), correspondant à la zone de métamorphisme de la neige en glace. Cette transformation se fait par une densification progressive de la neige tombée en surface (de faible densité, d $\sim$ 0.35) en glace (d $\sim$ 0.91 au niveau de la profondeur de fermeture des pores). Sowers et al. [1992] ont permis de décrire simplement la structure du névé (figure 1.1) :

— La **zone convective** est située en dessous de la surface. Elle est soumise à l'effet du vent ainsi qu'à celui des gradients de température et de pression. Ces perturbations génèrent de la convection conduisant à une homogénéisation avec l'air atmosphérique. L'air y possède alors la même composition isotopique que l'air atmosphérique. L'épaisseur de la zone convective dépend des conditions en surface. Pour les sites de forte accumulation comme au Groenland, l'épaisseur de la couche convective est négligeable [inférieure à 2 m pour NorthGRIP et environ 3 m pour NEEM ; Landais et al., 2006; Guillevic et al., 2013]. En Antarctique l'épaisseur de la couche convective varie d'un site à l'autre [environ 13 m à Vostok, 2 m à Dôme C et supérieure à 23 m pour le site Megadunes ; Bender et al., 1994; Landais et al., 2006; Severinghaus et al., 2010].

— La **zone diffusive**, quant à elle, n'est plus soumise aux phénomènes de sur-

face. Au sein de cette couche le transport de l'air se fait par diffusion moléculaire. Cette zone peut représenter jusqu'à 90% du névé. Comme la diffusion moléculaire est lente, l'air est alors affecté par des fractionnements isotopiques. Deux types de fractionnements peuvent être observés : le fractionnement gravitationnel et le fractionnement thermique (section 1.2). La diffusion verticale s'arrête lorsque la taille des interstices entre les cristaux de glace devient inférieure à la taille des molécules d'air. On est alors à la profondeur de piégeage de l'air ("Lock-In Depth", LID, en anglais).

— La **zone non-diffusive** est délimitée par la LID et la profondeur de fermeture des pores ("Close-Off Depth", COD, en anglais). Comme les pores entre les cristaux de glace sont fermés, la diffusion moléculaire est quasi-nulle dans cette zone. A partir de la LID, l'air piégé dans la glace est complètement isolé de l'air ambiant, ce qui fait que sa composition isotopique reste inchangée. Lors de l'enfouissement en profondeur, il est possible que des conditions de pression et température conduisent à la formation de clathrates (cages de molécules d'eau renfermant des molécules de gaz).

D'un point de vue datation, on définit le Δage comme étant la différence d'âge entre la glace et l'air d'une même profondeur. On définit aussi le $\Delta depth$ comme étant la différence de profondeur entre de la glace et du gaz de même âge. Ces Δage et $\Delta depth$ vont donc être fonction des variations de la LID au cours du temps. Ainsi, pour dater correctement la phase gaz dans les carottes de glace il est nécessaire de bien connaître ces trois grandeurs. Les modèles de densification du névé nous permettent d'estimer les variations passées de ces trois paramètres (section 1.3).

1.2 Les fractionnements isotopiques au sein du névé

Le fractionnement isotopique des molécules de N_2 et O_2 se produit dans la zone diffusive. Il a deux origines : gravitationnel et thermique. Sous les conditions climatiques actuelles (c'est-à-dire un climat interglaciaire stable), le fractionnement gravitationnel s'effectue tout le long du névé jusqu'à la LID. A l'inverse, le fractionnement thermique prend place seulement dans la partie supérieure du névé, en réponse aux variations saisonnières de température. Par exemple, la figure 1.1 montre que dans le cas de NEEM le fractionnement thermique se fait sur les 30 premiers mètres (caractérisé par la "bosse" dans les profils isotopiques de $\delta^{15}N$ et

$\delta^{18}O$), et que le fractionnement gravitationnel devient dominant entre 30 et 63 m environ.

Le **fractionnement gravitationnel** est dû à la différence d'attraction gravitationnelle entre les isotopes lourds et légers composant les molécules de gaz. Ce phénomène va entraîner un enrichissement en isotopes lourds à la base de la colonne diffusive. La répartition isotopique suivant la profondeur est alors fonction de la diffusion moléculaire et de la force de gravité. Le fractionnement gravitationnel δ_g est dépendant de la différence de masse entre les deux isotopes (Δm, en $g.mol^{-1}$), mais aussi de la température moyenne (T, en Kelvin) et de l'épaisseur de la couche diffusive (z, en m) ; cette dernière étant fonction des conditions en surface (température et accumulation). L'équation barométrique nous permet d'obtenir l'expression du fractionnement gravitationnel [Sowers et al., 1992] :

$$\delta_g(z) = \left(\exp\left(\frac{\Delta m g z}{RT}\right) - 1\right) \cdot 1000 \simeq \frac{gz}{RT}\Delta m \cdot 1000 \tag{1.1}$$

où g est l'accélération de la pesanteur (9.81 $m.s^{-2}$) et R la constante des gaz parfaits (8.314 $J.mol^{-1}.K^{-1}$). A partir de cette expression, on peut voir que deux espèces présentant la même différence de masse entre leurs isotopes sont alors soumises au même fractionnement gravitationnel.

A partir de cette observation, il est alors possible de retrouver la composition isotopique de l'oxygène d'origine atmosphérique. La différence de masse entre les deux isotopes de l'oxygène (^{16}O et ^{18}O) est deux fois celle entre le ^{14}N et le ^{15}N. Ainsi, en corrigeant les mesures de $\delta^{18}O$ du fractionnement gravitationnel se produisant au sein du névé, à l'aide du $\delta^{15}N$, on en déduit la composition isotopique de l'oxygène atmosphérique ($\delta^{18}O_{atm}$) :

$$\delta^{18}O_{atm} = \delta^{18}O - 2 \cdot \delta^{15}N \tag{1.2}$$

Le **fractionnement thermique** est induit par un gradient de température au sein du névé. Les molécules contenant les isotopes lourds vont alors se diriger préférentiellement vers la région froide du névé, conduisant à un fractionnement. La répartition isotopique au sein du névé est donc fonction de la diffusion moléculaire, de la force de gravité et de celle induite par le gradient de température. Si l'on considère un équilibre des flux entre la diffusion, conduisant à un gradient de concentration des isotopes, et celui induit par le gradient de température, on obtient

une expression simplifiée du fractionnement thermique :

$$\delta_{th} = \left(\frac{R}{R_0} - 1\right) \cdot 1000 \simeq \alpha_T \left(\frac{\Delta T}{T_0}\right) \cdot 1000 \tag{1.3}$$

avec R et R_0 les rapports isotopiques associés aux températures T et T_0, ΔT la différence de température entre le sommet et la base du névé et α_T le coefficient de diffusion thermique ($‰.K^{-1}$).

La différence de température induisant un fractionnement thermique peut avoir plusieurs origines. La variabilité saisonnière entraîne l'apparition d'un gradient de température seulement sur les 20 premiers mètres du névé (cf figure 1.1). Comme cette différence de température n'est pas ressentie jusqu'à la base du névé, cette variabilité n'est pas enregistrée dans les bulles d'air. En revanche, les changements climatiques rapides (évènements de Dansgaard-Oeschger) observés au cours de la dernière période glaciaire ont entraîné l'apparition d'un gradient de température sur l'intégralité de la colonne de névé. Lors d'un tel réchauffement (typiquement 5 à 16°C en quelques $10 - 100$ ans), le fractionnement thermique va conduire à une anomalie positive des teneurs isotopiques de l'air à la base de la zone diffusive du névé. De ce fait, les phases chaudes des événements de Dansgaard-Oeschger sont caractérisées par une composition isotopique de l'air à la base du névé résultant à la fois du fractionnement gravitationnel et du fractionnement thermique.

La différence de température mesurée au sein du névé, induisant le fractionnement thermique, est inférieure à celle observée en surface à cause de la diffusion de la chaleur. C'est pourquoi il n'est pas possible d'inverser directement le problème pour en déduire les variations de température en surface. Pour parvenir à ces grandeurs, il est nécessaire d'utiliser des modèles de densification du névé.

1.3 Les modèles de densification du névé

Les modèles de densification du névé permettent de reconstruire différents paramètres caractéristiques du névé comme la LID, la COD ou encore le Δage, à partir de la connaissance des conditions climatiques en surface.

A partir de l'analyse des profils de densité de plusieurs névés actuels, Herron and Langway [1980] ont développé le premier modèle empirique permettant de déduire le taux de densification à partir des conditions de surface (densité, température et accumulation).

Pimienta [1987] ont développé un second modèle qui a ensuite été repris par

Barnola et al. [1991]. Ce dernier est basé sur les équations d'Herron and Langway [1980] pour la partie haute du névé (d < 0.55) et sur une approche plus physique pour la partie basse.

Arnaud et al. [2000] ont amélioré cette approche en incluant les processus physiques prenant place lors de la densification et la déformation plastique. Cependant ce modèle ne permet pas la prise en compte de variations temporelles du névé (seulement des cas stationnaires), ni la diffusion de la chaleur.

Goujon et al. [2003] ont ensuite repris le modèle d'Arnaud et al. [2000] en y ajoutant la diffusion de la chaleur ainsi que les variations temporelles. Ce modèle permet alors la reconstruction des variations passées de la LID, COD et du Δage, aboutissant à l'obtention d'une chronologie gaz. De plus, par la reproduction des variations passées du $\delta^{15}N$ le modèle de Goujon et al. [2003] est en mesure de reconstruire les variations de température et d'accumulation associées aux évènements de Dansgaard-Oeschger.

C'est ce modèle de densification du névé qui a été utilisé pour produire l'estimation de la LID de NGRIP lors de la construction de AICC2012 (section 3.1.1).

1.4 Les éléments mesurés au cours de cette thèse

1.4.1 $\delta^{15}N$

Les mesures de $\delta^{15}N$ couplées à la modélisation du névé peuvent permettre de reconstruire différents paramètres caractéristiques de ce dernier.

A l'aide du modèle de Goujon et al. [2003], il est possible de reconstruire les variations de $\delta^{15}N$ à l'aide de scénarios plausibles de température et d'accumulation (figure 1.2). L'utilisation de ce modèle a permis de préciser les valeurs d'augmentation de la température associée aux évènements de Dansgaard-Oeschger au Groenland [Huber et al., 2006; Landais et al., 2004; Capron et al., 2010; Guillevic et al., 2013; Kindler et al., 2014].

Le $\delta^{15}N$ mesuré dans les carottes de glace provenant du Groenland présente un autre avantage en plus de la reconstruction des variations de température lors des changements climatiques rapides de la dernière période glaciaire. Lors des réchauffements associés aux évènements de Dansgaard-Oeschger, le $\delta^{15}N$ augmente en même temps que la température. Ainsi, il est possible d'évaluer de manière très précise la différence de profondeur associée à cette augmentation de température, identifiée par un saut dans la composition isotopique de la glace, et par un pic de $\delta^{15}N$ dans

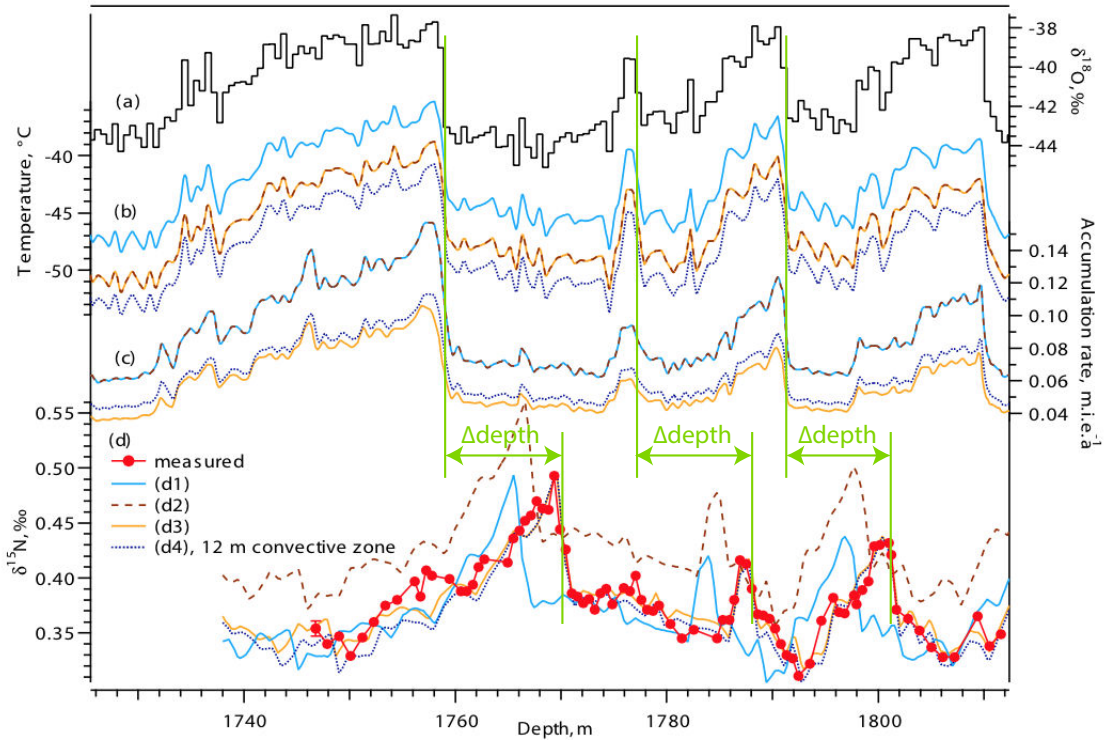

FIGURE 1.2 – Evolution du $\delta^{15}N$ de la carotte de NEEM couvrant les évènements de Dansgaard-Oeschger 8 à 10. (a) composition isotopique de la glace, (b) et (c) scénarios de température et d'accumulation utilisés pour reconstruire le $\delta^{15}N$(d). Les courbes (d1) à (d4) correspondent à différents paramètres du modèle de Goujon et al. [2003]. Extrait de Guillevic et al. [2013].

la phase gaz (figure 1.2). Cette différence de profondeur est communément appelée $\Delta depth$. A partir de la mesure du $\delta^{15}N$ dans les carottes de glace du Groenland, il est alors possible d'utiliser ces contraintes de $\Delta depth$ pour construire les chronologies gaz.

Conjointement, l'utilisation des modèles de densification du névé pour reconstruire les variations du $\delta^{15}N$ mesuré dans les carottes de glace issues du Groenland permet d'obtenir les variations passées de la LID. Comme les modèles de densification utilisés prennent bien en compte les différents fractionnements et sont bien paramétrés pour le Groenland, ils donnent une bonne estimation de la LID [Goujon et al., 2003]. A l'inverse, pour les forages d'Antarctique, qui ne possèdent pas d'analogue pour la période glaciaire, les modèles de densification du névé tendent à prédire un comportement différent des mesures du $\delta^{15}N$ lors des dernières déglaciation et période glaciaire [figure 1.3, Landais et al., 2006; Capron et al., 2013]. En conséquence, les LID issues des modèles de densification conduisent à une mauvaise

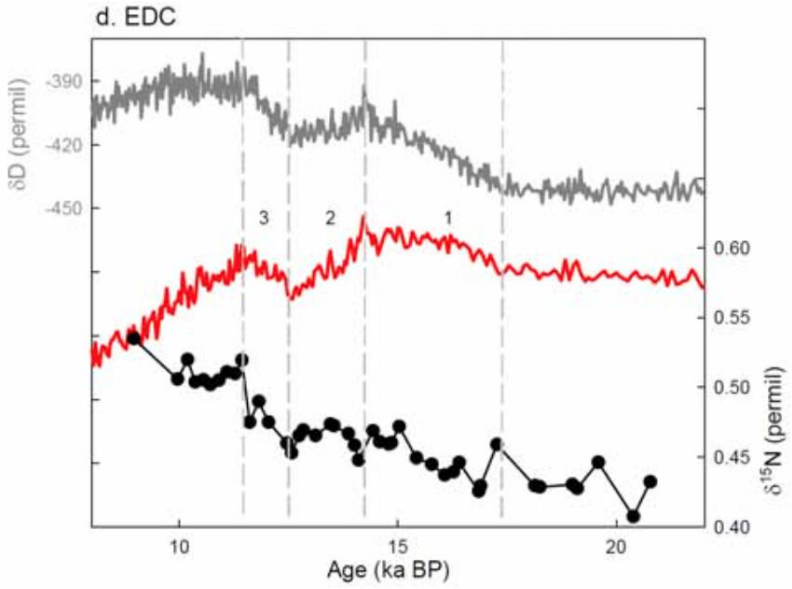

FIGURE 1.3 – Comparaison de la reconstruction du $\delta^{15}N$ par le modèle de Goujon et al. [2003] avec les données mesurées de $\delta^{15}N$ pour EDC au niveau de la Terminaison I. Composition isotopique de la glace (gris), $\delta^{15}N$ mesuré (noir) et $\delta^{15}N$ modélisé (rouge). Extrait de Capron et al. [2013].

estimation du Δage en Antarctique.

Une alternative aux modèles de densification pour reconstruire les LID en Antarctique peut être le $\delta^{15}N$ lui-même [Parrenin et al., 2012a]. En effet, les changements de température en Antarctique se font plus lentement que la diffusion de la chaleur au sein du névé. On peut alors considérer qu'il n'y a pas de fractionnement thermique. En faisant l'hypothèse que le névé ne présente pas de couche convective, il est alors possible de reconstruire la profondeur de la LID en utilisant l'équation barométrique 1.1.

A des fins de datation, nous avons utilisé le $\delta^{15}N$ au cours de cette thèse au travers de contraintes de $\Delta depth$ et comme scénarios d'ébauche pour la construction de la chronologie AICC2012 (chapitre 3).

1.4.2 $\delta^{18}O_{atm}$

Le $\delta^{18}O_{atm}$ correspond à la composition isotopique de l'oxygène d'origine purement atmosphérique. Les variations passées du $\delta^{18}O_{atm}$ sont le résultat d'interactions complexes entre les différents réservoirs du système climatique. En effet, les valeurs du $\delta^{18}O_{atm}$ sont en partie dues aux changements de volume des calottes de glace, influençant la composition isotopique de l'océan ($\delta^{18}O_{sw}$). Le signal du $\delta^{18}O_{atm}$ est

relié au $\delta^{18}O_{sw}$ au travers de la photosynthèse [Guy et al., 1993]. En effet, l'oxygène dans l'atmosphère est intimement lié à la biosphère. La composition isotopique de l'eau présente dans les feuilles va être fonction du $\delta^{18}O_{sw}$. Lors du cycle de l'eau, le $\delta^{18}O_{sw}$ est transmis à l'eau météorique ($\delta^{18}O_{meteoric}$). Cette eau est ensuite consommée par les racines des plantes et entrainée dans les feuilles. Une fois dans la feuille l'évaporation et la photosynthèse vont induire des fractionnements affectant la composition isotopique de cette eau. En plus de ces phénomènes, il faut rappeler que lors de la respiration, les plantes absorbent préférentiellement les molécules d'eau composées d'isotopes légers [Guy et al., 1989].

Le temps de résidence de l'oxygène dans l'atmosphère (∼1200 ans) est largement supérieur au temps de mélange entre les deux hémisphères. De ce fait, le $\delta^{18}O_{atm}$ peut être considéré comme étant un traceur global. Dans le cadre de la datation des carottes de glace, il est alors possible d'utiliser ce type de traceur pour déduire des liens stratigraphiques entre plusieurs carottes de glace (chapitre 3).

Le $\delta^{18}O_{atm}$ présente des variations au cours du temps similaires à celles de la précession. Ainsi, il est possible d'utiliser le $\delta^{18}O_{atm}$ comme outil de datation orbitale par la synchronisation de ses variations avec la courbe de précession [Petit et al., 1999; Suwa and Bender, 2008; Dreyfus et al., 2007].
Comme le $\delta^{18}O_{atm}$ et le $\delta^{18}O_{sw}$ sont tous deux modulés par la précession, il est possible de les combiner pour en déduire l'effet Dole (figure 1.4). De cette façon on s'affranchit des variations de volume des calottes polaires, rendant possible l'étude des autres facteurs influençant le $\delta^{18}O_{atm}$. Ainsi, les variations de l'effet Dole sont étroitement liées aux changements de la productivité de la biosphère et au cycle hydrologique des basses latitudes [Bender et al., 1994; Jouzel et al., 1996; Malaizé et al., 1999; Shackleton et al., 2000; Wang et al., 2008; Landais et al., 2007, 2010; Severinghaus et al., 2009].

Même si le $\delta^{18}O_{atm}$ présente des variations similaires à la precession, l'utilisation de ce traceur comme outil de datation orbitale reste limitée. En effet, l'incertitude associée à ce type de contrainte d'âge reste large (6 ka) du fait de la complexité des facteurs influençant le $\delta^{18}O_{atm}$, ce qui résulte en un retard variable du $\delta^{18}O_{atm}$ par rapport aux variations de la précession. Dans ce travail de thèse nous étudions les variations du retard entre le $\delta^{18}O_{atm}$ et la precession au cours des derniers 800 ka ainsi que ce qui est à l'origine de ces variations (chapitre 5).

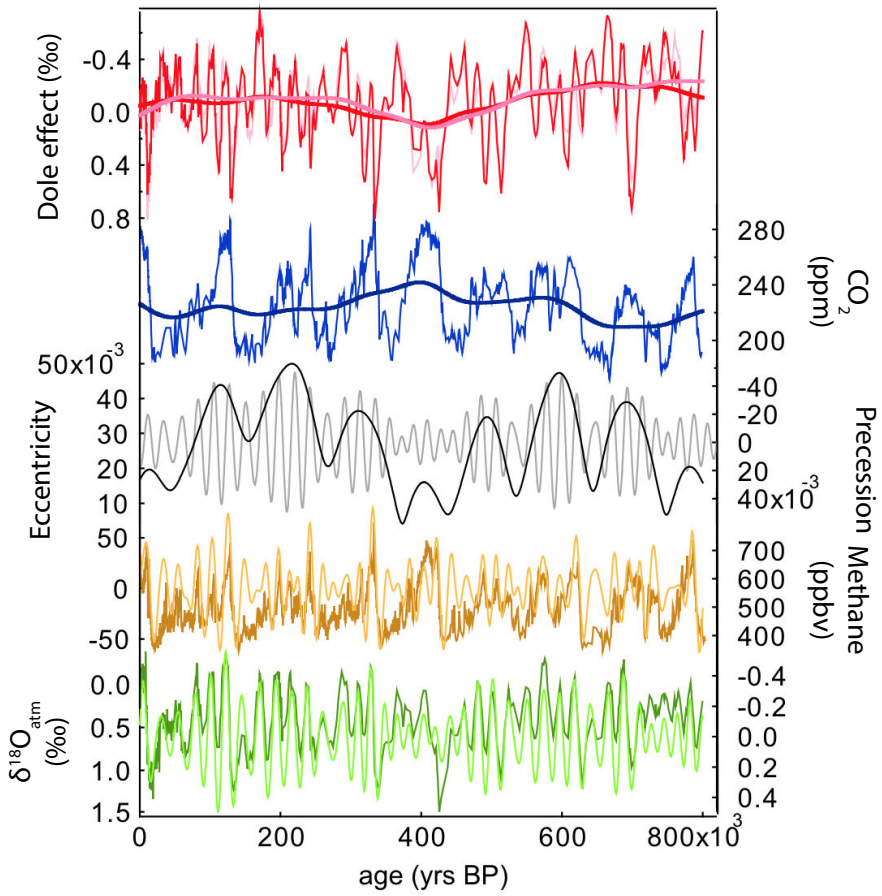

FIGURE 1.4 – Evolution du $\delta^{18}O_{atm}$, de l'effet Dole et de la composition de l'atmosphère au cours des derniers 800 ka. De haut en bas : effet Dole et tendance à long terme ; CO_2 de Vostok et EDC et tendance à long terme ; courbes d'excentricité (noir) et précession (gris) ; Méthane d'EDC ; $\delta^{18}O_{atm}$combiné de Vostok et EDC. Extrait de Landais et al. [2010].

1.4.3 $\delta O_2/N_2$

Le rapport O_2/N_2 des bulles d'air est dépendant des processus physiques au moment de la fermeture des pores dans le névé. La molécule de N_2 est plus grosse que celle de O_2 (2.05 Å pour N_2 contre 2.0 Å pour O_2). Ainsi, la molécule de O_2 est plus mobile et peut encore s'échapper là où le N_2 est déjà piégé au niveau de la profondeur de piégeage de l'air. Le rapport O_2/N_2 est alors fortement soumis aux effets de diffusion et d'exclusion des pores à la base du névé. Il est donc enregistré un appauvrissement en O_2 à la base du névé, causé par la différence de taille moléculaire entre O_2 et N_2 [Battle et al., 1996; Severinghaus and Battle, 2006].

Les mesures du rapport O_2/N_2 de nombreuses carottes de glace montrent un appauvrissement de ce dernier en comparaison à la valeur atmosphérique actuelle. De plus, il a été montré que ce $\delta O_2/N_2$ a varié par le passé [Sowers et al., 1989; Bender et al., 1994; Bender, 2002; Suwa and Bender, 2008; Kawamura et al., 2007; Landais et al., 2012, figure 1.5]. Il est possible d'observer des valeurs positives du $\delta O_2/N_2$ au niveau de la transition bulle/clathrate, où le O_2 et le N_2 se dissolvent sous forme d'hydrates de gaz [Ikeda et al., 1999]. En effet, comme le O_2 se dissout en premier dans la glace, il est moins sujet aux pertes de gaz associés aux processus post-forage que le gaz présent dans les bulles. Nous n'avons pas tenu compte de ces variations de $\delta O_2/N_2$ au niveau de la transition bulle/clathrate pour la suite des discussions. Le $\delta O_2/N_2$ mesuré dans les clathrates présente des variations avec une périodicité de 21 ka.
Bender [2002] a été le premier à relier les variations de $\delta O_2/N_2$ aux variations d'insolation locale au solstice d'été. En effet, l'insolation est un des paramètres influençant le métamorphisme de la neige à la surface de la calotte. Ainsi, l'insolation influence indirectement la structure des cristaux de glace au niveau du piégeage de l'air. Cependant, nos connaissances actuelles sur la densification des névés ne nous permet pas d'expliquer comment ce phénomène en surface se transmet en profondeur jusqu'à la base du névé.

Partant de ce lien entre $\delta O_2/N_2$ et insolation locale au solstice d'été, plusieurs auteurs ont utilisé le $\delta O_2/N_2$ pour construire des échelles d'âge pour la phase glace des carottes de glace de Vostok et Dôme F [Suwa and Bender, 2008; Kawamura et al., 2007]. Le principe utilisé pour produire ces datations dites orbitales est d'associer les variations du $\delta O_2/N_2$ aux variations correspondantes de l'insolation locale. Cependant, il est difficile d'estimer l'incertitude associée à cette méthode de datation car il subsiste de nombreuses inconnues concernant les paramètres influençant le $\delta O_2/N_2$

[conservation du signal d'insolation, processus post-forage, stockage ; Hutterli et al., 2010]. En effet, Bender et al. [1995] ont montré que le $\delta O_2/N_2$ était sensible aux processus post-forage pouvant conduire à la formation de micro-fractures au sein de la glace. Cette diminution de la qualité de la glace engendrerait un fractionnement supplémentaire avec un échappement préférentiel des molécules de O_2 par rapport à celle de N_2 [Bender et al., 1995]. De plus, différentes études, à la fois expérimentales et de modélisation, ont montré que le $\delta O_2/N_2$ est sensible à la durée et à la température de stockage des échantillons de glace [Ikeda-Fukazawa et al., 2005; Kawamura et al., 2007; Landais et al., 2012]. En effet, plus le stockage est long, et plus la teneur en $\delta O_2/N_2$ est appauvrie. De même, des échantillons conservés à une température de -20/-30°C présentent des variations beaucoup plus bruitées que des échantillons conservés à une température de -50°C (figure 5.2 du chapitre 5). Par exemple, Landais et al. [2012] ont combiné des mesures réalisées sur de la glace bien conservée d'EDC (couvrant le MIS 11 et entre 700–800 ka) avec des données issues de glace conservée à -25°C. Pour ce faire, les auteurs ont appliqué une correction déduite des valeurs de $\delta O_2/N_2$ des deux séries de données aux périodes où elles se superposent (figure 1.5). Comme peu de mesures ont été réalisées sur de la glace bien conservée, les auteurs appliquent des corrections sur leurs enregistrements de $\delta O_2/N_2$. Tout cela apporte de l'incertitude aux enregistrements de $\delta O_2/N_2$ et donc à cette méthode de datation orbitale.

C'est pour ces raisons qu'au cours de cette thèse j'ai réalisé des mesures de $\delta O_2/N_2$ sur des échantillons de glace bien conservée provenant d'EDC. Ces nouvelles mesures viennent compléter les données de Landais et al. [2012].

1.5 Extraction de l'air piégé dans la glace

Les mesures de la composition isotopique de l'air piégé dans la glace réalisées au cours de cette thèse ont été faites en plusieurs séries (table 1.1). Ces échantillons correspondent à environ 10 g de glace préalablement découpés et décontaminés en chambre froide (-20°C). En effet, lors de la conservation, il est possible que les surfaces directement en contact avec l'air extérieur échangent avec l'air extérieur. De ce fait, il est nécessaire de rogner 3–5 mm sur toutes les faces de l'échantillon de glace afin de s'affranchir de la contamination par l'air ambiant. Une fois cette étape réalisée, l'extraction de l'air doit être faite dans la journée (pour éviter une nouvelle contamination par l'air ambiant). Deux lignes d'extraction de l'air piégé dans la glace ont été utilisées au cours de cette thèse : la ligne manuelle et la ligne

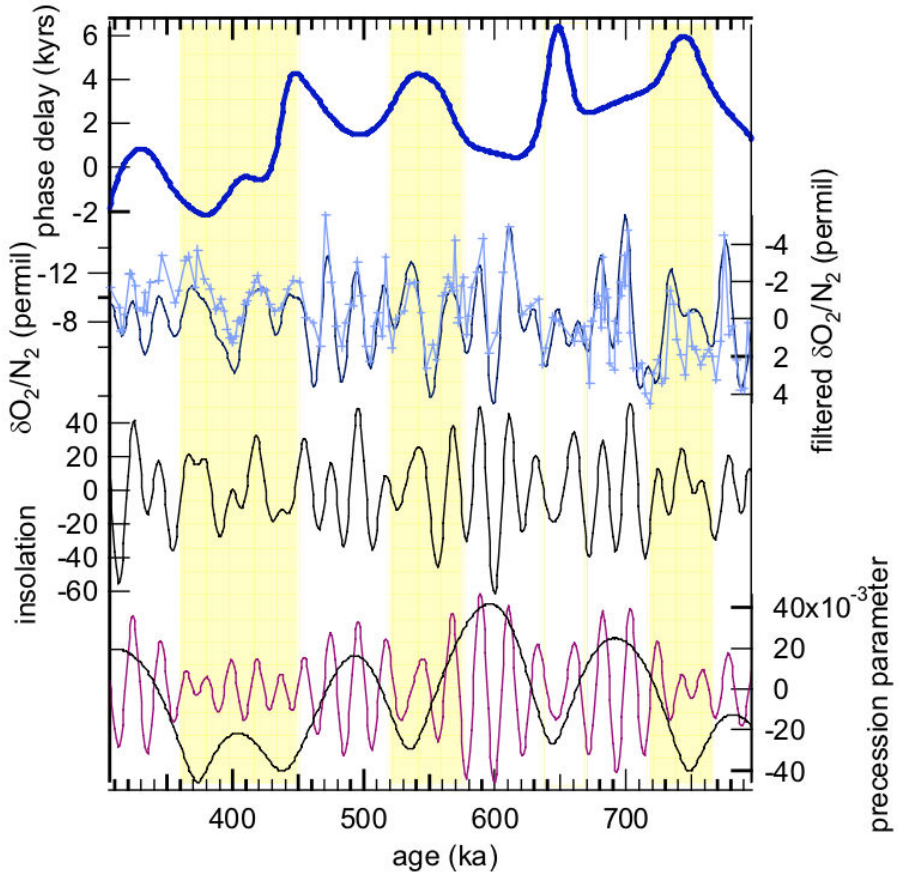

FIGURE 1.5 – Evolution du $\delta O_2/N_2$ mesuré à EDC entre 300 et 800 ka. De bas en haut : courbes de précession et d'excentricité, insolation locale au solstice d'été, courbe composite du $\delta O_2/N_2$ (données corrigées et données mesurées sur la glace à -50°C) et filtrée entre 15–100 ka, retard entre le $\delta O_2/N_2$ et l'insolation locale (filtrés entre 15 et 100 ka). En Jaune sont mises en évidence les périodes où le $\delta O_2/N_2$ ne ressemble pas à l'insolation locale. Extrait de Landais et al. [2012].

semi-automatique (figures 1.6 et 1.7). L'extraction de l'air se fait par fonte et regel des échantillons suivant la méthode développée par Sowers et al. [1989], améliorée ensuite par Landais et al. [2003]. Les protocoles expérimentaux sont quelques peu différents pour les deux lignes d'extraction.

TABLE 1.1 – Table récapitulative des séries de mesures réalisées au cours de cette thèse. "man." pour l'extraction réalisée à l'aide de la ligne manuelle et "s.-auto." pour les échantillons d'air extraits à l'aide de la ligne semi-automatique.

Carotte	Quand	Ligne	Nombre d'échantillons	Périodes couvertes
TALDICE	2011–2012	man.	83 profondeurs (dont 9 répliques)	80–250 ka
EDC	2011	s.-auto.	50 profondeurs (dont 39 répliques)	300–500 ka
EDC (-50°C)	2012–2013	man. et s.-auto.	145 profondeurs (dont 108 répliques)	100–160 ka 380–800 ka

La méthode manuelle permet d'extraire l'air par séries de trois échantillons (2 séries dans une journée). Les morceaux de glace sont introduits dans des ballons qui sont ensuite fixés sur la ligne d'extraction à l'aide d'un système vis-écrous. L'étanchéité est assurée par un joint en cuivre doré. Les ballons sont plongés dans des dewars remplis d'alcool à -20°C afin d'éviter toute fonte pendant la période de pompage (40 min). Ensuite, chaque ballon est isolé de la ligne et laissé à fondre à température ambiante, dégazant ainsi l'air piégé dans l'enceinte du ballon. Lorsque tous les échantillons sont fondus, commence la phase de regel progressif : un pied en cuivre est disposé sous le ballon et trempe (5 cm) dans un dewar rempli d'azote liquide. Un peu d'alcool assure un meilleur contact entre le fond du ballon et le pied en cuivre. Lorsque l'eau est entièrement regelée, le pied en cuivre est alors entièrement trempé dans l'azote liquide pendant environ 15 min. L'air contenu dans le ballon est ensuite transféré par piégeage froid dans un tube en inox plongé dans de l'helium liquide (-269°C) pendant environ 6 min. Le tube contenant l'échantillon d'air est mis en attente pendant 40 min à température ambiante avant de pouvoir être mesuré par spectrométrie de masse.

La méthode d'extraction semi-automatique quant à elle permet de réaliser 2 mesures d'air extérieur, nécessaires à la vérification du bon fonctionnement de la ligne, et 6 échantillons à la fois, en quelques heures seulement. Les 6 flacons contenant les morceaux de glace sont plongés dans un bain d'alcool maintenu à -25°C pendant 40

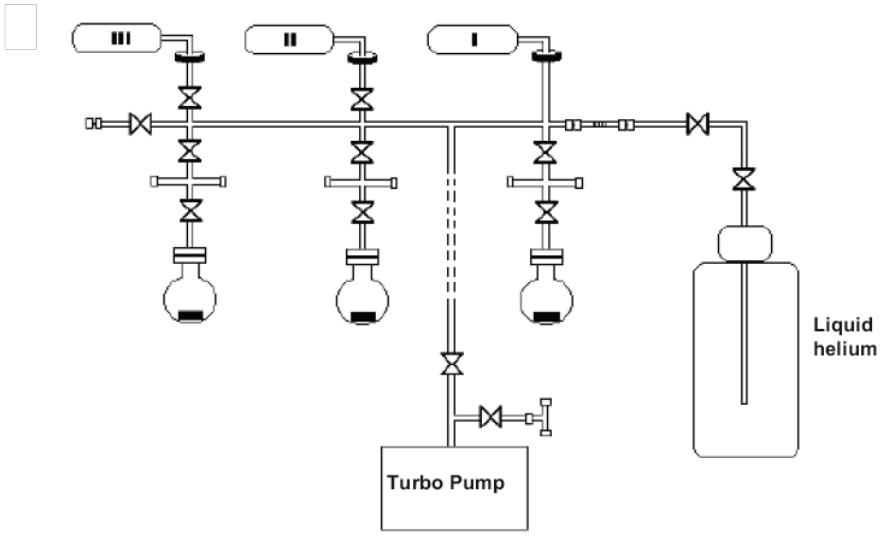

FIGURE 1.6 – Schéma de la ligne manuelle d'extraction de l'air piégé dans la glace.

min le temps du pompage de l'air. Ensuite, les flacons sont isolés de la ligne et mis à fondre à l'aide d'un bain d'eau à température ambiante pendant environ 20 min. Une fois le bain d'eau vidé, les échantillons sont laissés à température ambiante pendant environ 1 heure avant de commencer la séquence de transfert. Les échantillons d'air passent au travers d'un piège de CO_2 et d'un piège à eau avant d'être piégés dans un tube en inox plongé dans de l'hélium liquide. Comme dans le cas de la ligne manuelle, la rosette composée des tubes en inox renfermant les échantillons est laissée pendant environ 40 min à température ambiante avant d'effectuer les mesures au spectromètre de masse.

Les deux méthodes d'extraction de l'air piégé dans la glace donnent les mêmes résultats. On peut alors combiner les séries de mesures réalisées par ces deux méthodes d'extraction sans appliquer de correction.

1.6 Mesures au spectromètre de masse

Le LSCE possède un spectromètre de masse Thermo® Delta V Plus pour effectuer les mesures de composition isotopique de l'air piégé dans la glace. Ce spectromètre contient 10 collecteurs permettant de mesurer simultanément les compositions isotopiques de l'azote (N_2, masses 28, 29 et 30), de l'oxygène (O_2, masses 32, 33, 34), de l'argon (Ar, masses 36, 38 et 40) et du CO_2 (masse 44). Celui-ci est contrôlé par ordinateur à l'aide du système ISODAT. L'introduction simultanée d'un aliquote (1

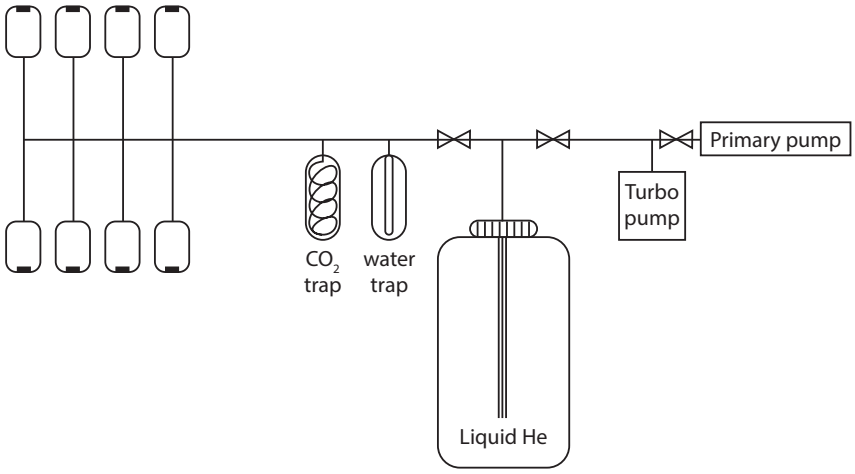

FIGURE 1.7 – Schéma de ligne d'extraction semi-automatique de l'air piégé dans la glace.

cm^3) de standard de laboratoire (air sec atmosphérique prélevé en 2008 et stocké dans un récipient en inox) et de l'échantillon se fait par détente de chacun vers un des volumes variables du spectromètre. Cette introduction identique permet de s'affranchir d'un possible fractionnement lors du transfert de la canne en inox vers le volume variable. Les gaz sont ensuite introduits dans la source, et les volumes sont ajustés pour le standard et l'échantillon. L'acquisition dure environ 45 min et est constituée de deux séquences de 16 mesures du standard en parallèle de 16 mesures de l'échantillon et pour finir une mesure du standard.

Pour les échantillons d'air issus de la ligne semi-automatique, le processus de mesure est le même, mais automatisé par une méthode enregistrée sur ISODAT. Le standard de laboratoire utilisé pour calibrer les échantillons d'air issus de la ligne semi-automatique est de l'air sec sans CO_2.

Il est nécessaire d'apporter des corrections aux résultats bruts afin d'améliorer la reproductibilité des mesures [Severinghaus et al., 2001; Landais et al., 2003] :

— correction de pression : les volumes d'échantillon et de standard introduits sont différents. Les volumes variables du spectromètre sont équilibrés de façon à ce que les pressions soient les mêmes côté échantillon et côté standard ; cependant ils vont avoir des évolutions différentes au cours du cycle. Le gaz va être consommé plus rapidement dans le volume variable le plus comprimé des deux. Ceci entraîne donc une erreur sur les mesures de δ.

— correction d'interférence de masse : les gaz analysés ne sont pas purs, il peut alors y avoir des interférences entre les différentes masses au coeur de la source. Par ce principe, le $\delta^{15}N$ est dépendant de la quantité d'oxygène pré-

sent dans le mélange O_2–N_2, tandis que la teneur en oxygène $\delta^{18}O$ doit elle être corrigée de la proportion d'azote dans le mélange.

— correction de l'interférence du CO^+ sur le rapport 29/28 : Le rapport de masse 29/28 correspond au rapport $^{15}N^{14}N/^{14}N^{14}N$ du diazote. L'ionisation du CO_2 dans la source conduit à la formation de CO^+ de masse 28 et 29. Il peut alors y avoir interférence avec la mesure du $\delta^{15}N$.

Pour finir, les résultats obtenus suite aux mesures par le spectromètre de masse sont calibrés par rapport à l'air extérieur. Pour ce faire, un échantillon d'air extérieur est traité de la même façon que les échantillons de glace (extraction et mesures au spectromètre de masse). Cela permet de corriger les valeurs du standard de laboratoire, et donc de calibrer les mesures par rapport à l'air extérieur. Pour la ligne d'extraction manuelle, un tel calibrage est effectué au moins une fois par série de mesures. Dans le cas de la ligne semi-automatique, la calibration est faite pour chaque journée de mesure grâce aux deux échantillons d'air extérieur traités en même temps que les échantillons.

Ainsi, les teneurs en $\delta^{15}N$, $\delta^{18}O_{atm}$ et $\delta O_2/N_2$ de chaque échantillon sont exprimées par rapport à l'air sec atmosphérique actuel.

2

DATICE

2.1 Introduction

Pour comprendre l'enchainement des séquences d'événements et en particulier le lien entre les forçages (insolation, volcanisme, concentrations des gaz à effet de serre) et le changement climatique, la datation des archives climatiques est un point clé. Dans le cas des carottes de glace nous avons la nécessité de dater à la fois la phase glace et la phase gaz. Jusqu'à récemment, les chronologies des carottes de glace étaient obtenues indépendamment les unes des autres, par différentes méthodes.

Au Groenland, le taux d'accumulation en surface étant conséquent, il est possible de dater précisément les carottes par comptage des couches annuelles jusqu'à 60 ka environ [Vinther et al., 2006; Rasmussen et al., 2006; Andersen et al., 2006; Svensson et al., 2008]. En Antarctique de l'Est, il n'est pas possible d'utiliser cette méthode car l'accumulation en surface est trop faible. On utilise alors la modélisation de l'écoulement de la glace afin de reconstruire les variations passées du taux d'accumulation, de l'amincissement des couches de glace avec la profondeur et de la profondeur de piégeage de l'air en équivalent glace ("Lock-In Depth in Ice Equivalent", LIDIE). Ces paramètres permettent de calculer les âges gaz et glace pour chaque profondeur. Afin de ne pas laisser les modèles glaciologiques s'écarter trop de la réalité, ils sont contraints à respecter des horizons datés (couches de cendre, inversion/excursion du champ géomagnétique, âges orbitaux...), et on leurs impose une certaine forme des paramètres glaciologiques (accumulation déduite de la composition isotopique de la glace, amincissement très contraint en surface) [Parrenin et al., 2004, 2007a].

Cette méthode a été appliquée aux carottes de glace de Dôme C et Vostok afin de produire les chronologies EDC3 et FGT1 [Parrenin et al., 2004, 2007a]. Ces deux sites d'Antarctique de l'Est présentent des conditions climatiques assez proches à

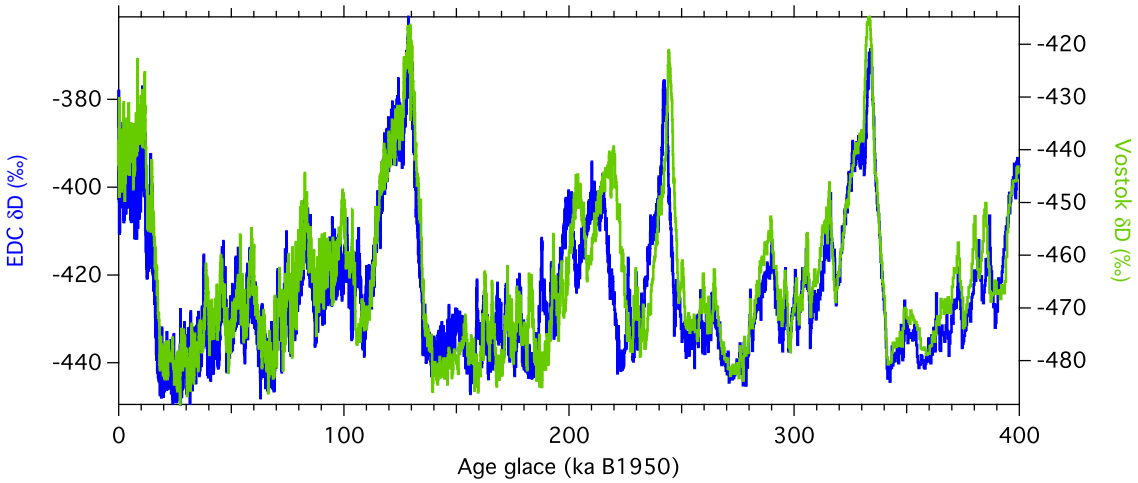

FIGURE 2.1 – Composition isotopique de la glace de Vostok [Petit et al., 1999, vert] et EDC [Jouzel et al., 2007, bleu] présentés sur leurs chronologies respectives FGT1 [Parrenin et al., 2004] et EDC3 [Parrenin et al., 2007a].

l'actuel, ainsi les deux datations devraient être similaires sur les derniers 400 ka. Cependant, sur la figure 2.1 on peut voir que les deux chronologies diffèrent significativement autour de 150–250 ka, c'est-à-dire à des profondeurs assez importantes (2043–2790 m pour Vostok et 1843–2330 m pour EDC). Les deux sites présentent de fortes disparités quant à leur emplacement sur la calotte de glace. Alors que Dôme C est localisé sur un dôme, le site de Vostok lui est situé sur une pente, rendant la modélisation de la fonction d'amincissement particulièrement difficile. Ainsi, même en utilisant la même méthode de datation, il n'est pas nécessairement possible d'obtenir des chronologies cohérentes entre elles.

Il est alors nécessaire d'avoir un outil de datation qui permet de produire des chronologies cohérentes et précises pour plusieurs carottes de glace simultanément. Au cours de cette thèse, j'ai utilisé l'outil de datation Datice, développé par Bénédicte Lemieux-Dudon au cours de sa thèse [Lemieux-Dudon, 2009]. Dans ce chapitre nous allons présenter la théorie sous–jacente à cet outil de datation ainsi que tout ce qui est nécessaire pour le faire fonctionner. Nous allons ensuite présenter brièvement la première application de Datice dans le but de produire une chronologie commune pour les carottes de glace sur les derniers 50 ka .

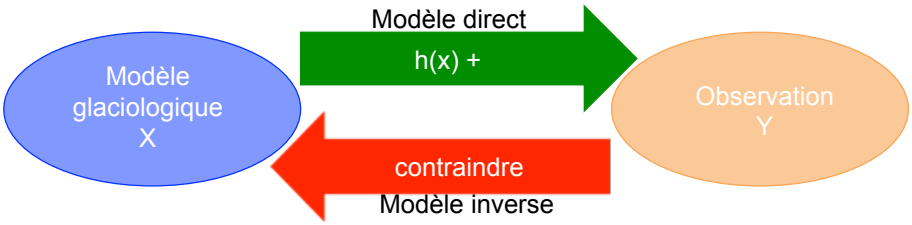

FIGURE 2.2 – Schéma explicatif du principe de la modélisation inverse. Dans le cadre de Datice, cela consiste à déterminer les paramètres glaciologiques (taux d'accumulation, fonction d'amincissement et LIDIE), compte–tenu des contraintes d'âge, dans le but de calculer ensuite les chronologies glace et gaz de chaque carotte de glace.

2.2 L'outil de datation Datice

2.2.1 Formulation du problème inverse

L'approche par modélisation inverse consiste à estimer les paramètres d'un modèle théorique X à partir d'observations Y. Pour cela, on se repose sur l'existence d'un modèle théorique direct qui permet de prédire l'observation Y en connaissant X. On introduit alors la notion d'opérateur d'observation h qui permet de prédire l'observation Y à partir de X. L'écart entre la prédiction et l'observation, noté η, résulte de l'erreur sur l'observation ainsi que de l'incertitude sur le modèle direct (figure 2.2).

Afin d'éviter la multiplicité des solutions, qui est souvent rencontrée en modélisation inverse, Datice est basé sur une approche stochastique dite d'inférence bayésienne. Cela consiste à fournir une ébauche probabiliste qui apporte des informations supplémentaires afin de mieux contraindre les paramètres du modèle et de lever la non–unicité de la solution. Cette ébauche constitue une information *a priori* sur le modèle théorique.

Inférence bayésienne

Lors du développement de Datice, Bénédicte Lemieux-Dudon s'est basée sur l'approche et le vocabulaire introduit par Mosegaard and Tarantola [2002]. Avant d'appliquer le théorème de Bayes à notre problème, il est nécessaire d'introduire différentes définitions.

Tout d'abord, les observations Y et les paramètres du modèle X sont des grandeurs physiques qui peuvent être considérées comme des variables aléatoires et donc définies par une densité de probabilité. On définit une densité de probabilité ho-

mogène (indicé ^{h}) lorsque qu'aucune information *a priori* ne permet d'établir un lien entre les variables aléatoires X et Y. Elle est notée $\mu^h_{X,Y}(X,Y)$. Au couple de variables aléatoires (X,Y) est associé une densité de probabilité jointe $\Theta(X,Y)$ qui décrit les corrélations possibles entre X et Y, ainsi que les incertitudes associées au modèle théorique de façon symétrique [Tarantola, 2005]. Il est possible que les informations *a priori* ne soient pas complètement indépendantes. Il n'est pas exclu qu'une partie des observations Y ait contribué à produire les paramètres d'ébauche X. On introduit alors la densité de probabilité jointe des informations *a priori* : $\rho^b_{X,Y}(X,Y)$ où l'indice ^{b} fait référence à l'ébauche ("background" en anglais).

L'objectif de cette modélisation inverse est de trouver une valeur vraie à X en se basant sur les informations *a priori* à notre disposition. Afin de simplifier l'écriture du théorème de Bayes, nous allons maintenant présenter les hypothèses sur lesquelles repose l'inférence bayésienne :

— Dissymétrie des rôles de X et Y dans le modèle théorique direct. Le qualificatif "direct" signifie que l'on cherche la probabilité d'avoir une mesure Y connaissant la valeur de X $(\rho(Y|X))$. Ceci conduit à la réécriture de la densité de probabilité conditionnelle :

$$\Theta(X,Y) = \rho(Y|X)\mu^h_X(X) \tag{2.1}$$

— Indépendance de l'information *a priori* et des observations. On introduit alors les densités de probabilité associées à l'ébauche $(\rho^b_X(X))$ et aux observations (ρ_Y). Dans ce cas, la densité de probabilité jointe $\rho^b_{X,Y}(X,Y)$ s'écrit :

$$\rho^b_{X,Y}(X,Y) = \rho^b_X(X)\rho_Y \tag{2.2}$$

— La limite homogène de la densité de probabilité jointe. En utilisant la limite homogène de la densité de probabilité jointe (équation 2.2), il est possible de décomposer $\mu^h_{X,Y}(X,Y)$ en deux densités de probabilité homogènes $\mu^h_X(X)$ et $\mu^h_Y(Y)$:

$$\mu^h_{X,Y}(X,Y) = \mu^h_X(X)\mu^h_Y(Y) \tag{2.3}$$

Afin d'obtenir l'état d'information *a posteriori* $\rho^a_{X,Y}(X,Y)$, Mosegaard and Tarantola [2002] s'appuient sur l'opération de conjonction de probabilité simplifiée dans

le cadre de l'inférence bayésienne :

$$\rho^a_{X,Y}(X,Y) = k\frac{\Theta(X,Y)\rho^b_{X,Y}(X,Y)}{\mu^h_{X,Y}(X,Y)} = k\frac{\rho(X|Y)\rho^b_X(X)\rho_Y}{\mu^h_Y(Y)} \tag{2.4}$$

avec k une constante de normalisation.

En intégrant cette équation sur l'espace des observations (D), on obtient l'expression de l'information *a posteriori* sur X :

$$\rho^a_X(X) = \int_D \rho^a_{X,Y}(X,Y)dY = k\rho^b_X(X)\int_D \frac{\rho(X|Y)\rho_Y}{\mu^h_Y(Y)}dY \tag{2.5}$$

Dans le but d'obtenir un contrôle optimal sur X, on introduit la notion de fonction coût, $J(X)$, qui traduit les contraintes du problème imposées à X. Cette fonction coût mesure la distance entre les observations Y et la prédiction du modèle. L'optimalité est obtenue lorsque le critère de maximum de vraisemblance selon Mosegaard and Tarantola [2002] est atteint. Ce critère d'optimalité peut se traduire par la recherche du minimum de la fonction coût :

$$J(X) = -ln\frac{\rho^a_X(X)}{\mu^h_X} \tag{2.6}$$

$$X^a = argmin_X J(X) \tag{2.7}$$

Définition des âges glace et gaz

Les âges glace et gaz en fonction de la profondeur sont déterminés à partir de trois grandeurs glaciologiques :

— le taux d'accumulation $A(z)$,
— la fonction d'amincissement $T(z)$,
— la profondeur de piégeage de l'air en équivalent glace (LIDIE) $C(z)$.

Le taux d'accumulation correspond à la quantité de neige précipitée à la surface de la calotte sur l'année. Il est généralement exprimé en cm/an ou son équivalent en glace cm_{ie}/an. La fonction d'amincissement est définie comme le rapport entre l'épaisseur réelle d'une couche annuelle à la profondeur z et son épaisseur d'origine lors de son dépôt en surface en équivalent glace. La fonction d'amincissement est donc sans unité. On peut directement relier l'épaisseur d'une couche annuelle au taux d'accumulation et à la fonction d'amincissement : $L(z) = A(z) \cdot T(z)$. Ainsi, la relation profondeur–âge d'une carotte de glace correspond à l'intégrale de l'inverse de l'épaisseur de couche annuelle. On définit l'âge glace $\Psi(z)$ comme :

$$\Psi(z) = \int_0^z \frac{D(z')}{L(z')} dz' = \int_0^z \frac{D(z')}{T(z') \cdot A(z')} dz' \tag{2.8}$$

avec $D(z)$ la densité relative du matériau (neige/glace) par rapport à la glace : $D(z) = \rho(z)/\rho_{glace}$.

Pour pouvoir calculer l'âge du gaz, $\chi(z)$, il est nécessaire de connaître la différence de profondeur entre du gaz et de la glace ayant le même âge, appelée $\Delta depth$. Ce $\Delta depth$ va donc correspondre à la profondeur de piégeage de l'air au moment du dépôt, qui a ensuite subi un amincissement lors de son enfouissement jusqu'à la profondeur z (équation 2.9). On en déduit donc l'âge du gaz à la profondeur z comme étant l'âge de la glace à la profondeur $(z - \Delta depth)$ (équation 2.10).

$$\Delta depth(z) = C(z) \cdot T(z) \tag{2.9}$$

$$\chi(z) = \Psi(z - \Delta depth(z)) \tag{2.10}$$

On définit aussi ce qu'on appelle le Δage comme étant la différence d'âge entre la glace et le gaz à une même profondeur :

$$\Delta age(z) = \Psi(z) - \chi(z) \tag{2.11}$$

2.2.2 Formulation du modèle d'inversion

Fonctions de correction

Nous avons vu dans la section 2.2.1 les différents paramètres glaciologiques nécessaires pour le calcul des âges gaz et glace : le taux d'accumulation, la fonction d'amincissement et la LIDIE. L'objectif de Datice est d'améliorer les ébauches de ces paramètres par modélisation inverse. L'inversion se fait simultanément sur N forages où chaque forage k $(\in 1, N)$ possède des ébauches pour le taux d'accumulation $(A^{b,k}(z))$, la fonction d'amincissement $(T^{b,k}(z))$ et la LIDIE $(C^{b,k}(z))$. Datice cherche à obtenir de nouvelles estimations de ces paramètres glaciologiques sous la

forme de corrections des ébauches :

$$A^k(z) = \alpha^k(z) A^{b,k}(z) \tag{2.12}$$

$$T^k(z) = \tau^k(z) T^{b,k}(z) \tag{2.13}$$

$$C^k(z) = \gamma^k(z) C^{b,k}(z) \tag{2.14}$$

où les fonctions $\alpha^k(z)$, $\tau^k(z)$ et $\gamma^k(z)$ sont respectivement les fonctions de correction pour l'accumulation, l'amincissement et la LIDIE. Datice cherche alors à déterminer les fonctions de correction optimales simultanément pour chacun des forages. A partir de cela, l'outil est en mesure de calculer les paramètres glaciologiques optimisés $A^{a,k}(z)$, $T^{a,k}(z)$ et $C^{a,k}(z)$, également appelés grandeurs analysées. Datice peut ensuite en déduire les chronologies gaz et glace optimales pour chacun des forages.

Ainsi, le vecteur X, qui représente les paramètres du modèle, est caractérisé par les fonctions de correction des trois paramètres glaciologiques pour chacun des forages :

$$X^k(z) = \begin{pmatrix} \alpha^k(z) \\ \tau^k(z) \\ \gamma^k(z) \end{pmatrix} \qquad \text{et} \qquad X(z) = \begin{pmatrix} X^1(z) \\ \vdots \\ X^k(z) \\ \vdots \\ X^N(z) \end{pmatrix} \tag{2.15}$$

Le vecteur X est ce qu'on appelle la variable d'état du problème inverse. Par leur nature, et par les définitions 2.8 et 2.10 qui permettent de calculer les âges glace et gaz, le taux d'accumulation, la fonction d'amincissement et la LIDIE ne peuvent prendre que des valeurs strictement positives. De ce fait, les phénomènes tels que l'érosion en surface par le vent, conduisant à une accumulation négative, ou encore le retournement de couches de glace au cours de l'écoulement ne sont pas pris en compte. Ces contraintes sur les grandeurs glaciologiques se propagent aussi sur les fonctions de correction. Ainsi, les composantes du vecteur $X(z)$ sont toutes strictement positives.

Changement de variable

Du fait que les paramètres caractérisant le vecteur X soient strictement positifs, les composantes du vecteur X sont alors mieux décrites par des densités de probabilité lognormales. Les grandeurs $X^{b,k}$ et B^k caractérisant les ébauches sont donc assimilées à la médiane et à une mesure de dispersion. Comme il est plus facile de travailler avec des densités de probabilité gaussiennes, on effectue le changement de

variable suivant :

$$\tilde{X} = \ln X \tag{2.16}$$

$$\tilde{X}^{b,k} = \ln X^{b,k} \tag{2.17}$$

Ainsi, le vecteur d'ébauche $\tilde{X}^{b,k}$ correspond à la moyenne/médiane/mode de la distribution et B^k la matrice de covariance d'erreur d'ébauche.

La variable de contrôle du problème est alors $\tilde{X}$. Le développement de la fonction coût et l'optimisation du problème se font donc à partir de $\tilde{X}$.

2.2.3 Les paramètres d'ébauches

Il nous est possible de déterminer la valeur du vecteur d'ébauche dans l'espace de contrôle, $\tilde{X}^{b,k}$, en nous intéressant au vecteur $X^{b,k}$ puisque ces deux vecteurs sont reliés par la relation 2.17. Au regard de la définition des fonctions de correction, le vecteur $X^{b,k}$ est défini au travers de l'information *a priori* dont on dispose sur les paramètres glaciologiques. Rappelons que ces grandeurs ($A^{b,k}$, $T^{b,k}$ et $C^{b,k}$) sont obtenues à l'aide de modèles glaciologiques et correspondent aux valeurs les plus probables des grandeurs A^k, T^k et C^k *a priori*. En terme de vecteur d'ébauche, ceci se traduit par :

$$X_i^{b,k} = 1 \qquad \text{et} \qquad \tilde{X}_i^{b,k} = 0 \qquad \text{pour } i = 1, .., n^k \tag{2.18}$$

La matrice de covariance d'erreur d'ébauche B^k associée à la carotte de glace k mesure les variances et les covariances d'erreur *a priori* sur le vecteur d'ébauche $\tilde{X}^{b,k}$. Cette matrice est de la forme :

$$B^k = \begin{pmatrix} B_\alpha^k & B_{\alpha\gamma}^k & B_{\alpha\tau}^k \\ B_{\alpha\gamma}^k & B_\gamma^k & B_{\gamma\tau}^k \\ B_{\alpha\tau}^k & B_{\gamma\tau}^k & B_\tau^k \end{pmatrix} \tag{2.19}$$

Les blocs diagonaux correspondent aux covariances d'erreur sur $\tilde{\alpha}^k$, $\tilde{\gamma}^k$ et $\tilde{\tau}^k$. Les blocs non–diagonaux rendent compte des covariances d'erreur croisées entre $\tilde{\alpha}^k - \tilde{\gamma}^k$, $\tilde{\alpha}^k - \tilde{\tau}^k$ et $\tilde{\gamma}^k - \tilde{\tau}^k$. On se restreint aux cas de matrices B^k inversibles en faisant l'hypothèse que la matrice B^k est définie strictement positive.

Dans le cadre des applications présentées dans cette thèse, les hypothèses suivantes ont été considérées :

— pas de corrélation d'erreur entre les scénarios d'ébauche de 2 carottes de glace différentes,

— pas de corrélation d'erreur entre $\tilde{\alpha}^k$, $\tilde{\tau}^k$ et $\tilde{\gamma}^k$ pour une même carotte.

De ce fait, la matrice B est seulement composée des blocs diagonaux B^k associés à chaque forage :

$$B^k = \begin{pmatrix} B_{\alpha^k} & 0 & 0 \\ 0 & B_{\gamma^k} & 0 \\ 0 & 0 & B_{\tau^k} \end{pmatrix} \tag{2.20}$$

avec :

$$[B_{\alpha^k}]_{ij} = [\sigma_\alpha^{b,k}]_i [\sigma_\alpha^{b,k}]_j [\rho_\alpha^{b,k}]_{ij} \tag{2.21}$$

$$[B_{\gamma^k}]_{ij} = [\sigma_\gamma^{b,k}]_i [\sigma_\gamma^{b,k}]_j [\rho_\gamma^{b,k}]_{ij} \tag{2.22}$$

$$[B_{\tau^k}]_{ij} = [\sigma_\tau^{b,k}]_i [\sigma_\tau^{b,k}]_j [\rho_\tau^{b,k}]_{ij} \tag{2.23}$$

Les écart-types $\sigma_\alpha^{b,k}$, $\sigma_\gamma^{b,k}$ et $\sigma_\tau^{b,k}$ sont déduits à partir de l'analyse des erreurs commises sur les paramètres d'ébauche $A^{b,k}$, $C^{b,k}$ et $T^{b,k}$ respectivement. On rappelle que ces paramètres sont généralement obtenus grâce à des modèles glaciologiques (voir Introduction, section 3).

Dans le cas de l'accumulation et la LIDIE, l'hypothèse de non–corrélation d'erreur est discutable. En effet, ces deux grandeurs étant liées, leurs fonctions de correction devraient présenter une corrélation entre elles.

2.2.4 Les observations

Datice peut prendre en compte différents types d'observations pour contraindre les chronologies. On peut les classer en deux groupes :

— les marqueurs d'âge et de grandeurs qui ne contraignent qu'une seule carotte de glace (marqueurs d'âge glace et gaz, marqueurs de $\Delta depth$).

— les liens stratigraphiques définis entre deux carottes de glace (gaz et glace).

Ainsi, il est possible de décomposer le vecteur d'observation sous la forme :

$$Y = \begin{pmatrix} Y^* \\ \Delta Y \end{pmatrix} \tag{2.24}$$

Avec Y^* le vecteur regroupant les contraintes spécifiques à un seul forage, et ΔY celui regroupant les observations se rapportant à un couple de carottes.

Plusieurs hypothèses sont faites quant aux incertitudes associées à ces observations dans le cadre du problème inverse :

— les densités de probabilité des différentes observations sont correctement décrites par des gaussiennes,
— les incertitudes sur les marqueurs d'âge et de grandeurs sont indépendantes entre les forages,
— les incertitudes sur les liens stratigraphiques sont indépendantes entre les forages,
— les incertitudes sur les marqueurs appliqués à un forage et sur un couple de forages sont indépendantes,
— les incertitudes des différents marqueurs sont toutes indépendantes les unes des autres,
— les incertitudes sur les profondeurs des observations sont négligeables devant les incertitudes sur les mesures.

Toutes ces hypothèses permettent de séparer les densités de probabilité de Y^* et ΔY en produit de densités marginales, simplifiant la dérivation de la fonction coût.

Pour la suite, on a besoin de définir l'opérateur d'observation généralisé $h(\tilde{X})$. Ce vecteur permet, étant donnée une valeur pour le vecteur de contrôle $\tilde{X}$, de prédire le vecteur d'observation Y moyennant une erreur :

$$Y = h(\tilde{X}) + \eta \tag{2.25}$$

Du fait de la décomposition faite précédemment du vecteur Y, l'opérateur d'observation s'écrit :

$$h(\tilde{X}) = \begin{pmatrix} h^* \\ \Delta h \end{pmatrix} \qquad \text{et} \qquad \begin{matrix} Y^* = h^*(\tilde{X}) + \eta \\ \Delta Y = \Delta h(\tilde{X}) + \eta' \end{matrix} \tag{2.26}$$

De plus, on fait l'hypothèse que les incertitudes théoriques associées au modèle directe sont négligeables par rapport aux incertitudes de mesure.

Les marqueurs d'âge glace et gaz

Différents traceurs peuvent nous donner des informations sur l'âge de certaines profondeurs. Les marqueurs dits absolus sont associés à des couches de glace datées absolument par des méthodes indépendantes. Ces marqueurs correspondent à des couches de tephra ou cendres volcanique, ou bien à des pics de ^{10}Be associés à des variations du champ magnétique terrestre. Leurs âges peuvent être mesurés directement s'il y a assez de matériel volcanique pour (cas des carottes de glace horizontales). Ils peuvent aussi provenir de datations ^{14}C ou Ar/Ar mesurés sur

des laves issues de différents endroits du globe. Cependant, ces marqueurs sont peu nombreux et ne permettent pas une datation précise des carottes de glace. En conséquence, on déduit des âges par synchronisation orbitale du $\delta^{18}O_{atm}$, $\delta O_2/N_2$ et de la teneur en air. Les variations de ces trois traceurs peuvent être corrélées aux variations de courbes orbitales (précession, insolation locale et insolation locale intégrée respectivement, voir sections 1.4 et 3.1.3).

Comme nous avons défini l'âge comme augmentant avec la profondeur, les marqueurs d'âge sont soumis à la contrainte de positivité. Ils sont donc correctement décrits par des distributions lognormales. Cependant, comme les erreurs commises sur l'âge sont relativement faibles (inférieures à 10 % à 800 ka), les distributions lognormales sont très proches des distributions gaussiennes. On fait alors une hypothèse faible en assimilant ces distributions à des gaussiennes.

A partir de là, il est possible de dériver les opérateurs d'observation pour les âges glace (h_k^{ia}) et gaz (h_k^{ga}), exprimés en fonction de la variable d'état $\tilde{X}$. Pour les marqueurs d'âge glace, l'opérateur d'observation s'écrit :

$$h_k^{ia}(\tilde{X}^k) = \int_{\zeta^k=0}^{\hat{z}^{ia,k}} \frac{\exp[-\tilde{\alpha}^k(\zeta^k)]\exp[-\tilde{\tau}^k(\zeta^k)}{A^{b,k}(\zeta^k)T^{b,k}(\zeta^k)} D^k(\zeta^k)d\zeta^k \tag{2.27}$$

Dans le cas des marqueurs d'âge gaz, l'opérateur d'observation s'écrit :

$$h_k^{ga}(\tilde{X}^k) = \int_{\zeta^k=0}^{\hat{z}^{ga,k}-\Delta depth^k(\hat{z}^{ga,k})} \frac{\exp[-\tilde{\alpha}^k(\zeta^k)]\exp[-\tilde{\tau}^k(\zeta^k)}{A^{b,k}(\zeta^k)T^{b,k}(\zeta^k)} D^k(\zeta^k)d\zeta^k \tag{2.28}$$

avec $\Delta depth^k(\hat{z}^{ga,k}) = C^{b,k}(\hat{z}^{ga,k})\gamma^k(\hat{z}^{ga,k})T^{b,k}(\hat{z}^{ga,k})\tau^k(\hat{z}^{ga,k})$

Les paramètres associés à ces marqueurs sont résumés dans la table 2.1.

TABLE 2.1 – Table récapitulative des grandeurs associées aux marqueurs d'âge glace et gaz.

	Marqueurs d'âge glace	Marqueurs d'âge gaz
Profondeur	$\hat{z}^{ia,k}$	$\hat{z}^{ga,k}$
Age le plus probable	$\hat{Y}^{ia,k}$	$\hat{Y}^{ga,k}$
Matrice d'erreur d'observation	R_k^{ia}	R_k^{ga}
Opérateur d'observation	h_k^{ia}	h_k^{ga}

Les marqueurs de $\Delta depth$

Les seuls marqueurs de grandeur utilisés dans Datice sont les marqueurs de $\Delta depth$. Ces marqueurs sont peu nombreux et peuvent seulement être définis pour les carottes issues du Groenland, lors des évènements de Dansgaard-Oeschger (section

1.4.1). Le $\Delta depth$ est une grandeur qui peut seulement être positive (contrainte de positivité). Ainsi, ces marqueurs sont correctement représentés par des densités de probabilité lognormales. Nous appliquons donc le changement de variable $\tilde{Y}^{dd,k} = \ln Y^{dd,k}$ afin de travailler avec des densités de probabilité gaussiennes. Suite à ce changement de variable, l'opérateur d'observation associé aux marqueurs de $\Delta depth$, h_k^{dd}, s'écrit :

$$h_k^{dd}(\tilde{\tau}^k, \tilde{\gamma}^k) = \ln\left(\tau(\hat{z}^{dd,k})\right) + \ln\left(\gamma(\hat{z}^{dd,k})\right) = \tilde{\tau}^k(\hat{z}^{dd,k}) + \tilde{\gamma}^k(\hat{z}^{dd,k}) \tag{2.29}$$

Les paramètres caractérisant les marqueurs de $\Delta depth$ sont résumés dans la table 2.2.

TABLE 2.2 – Table récapitulative des grandeurs associées aux marqueurs de $\Delta depth$.

	Marqueurs de $\Delta depth$
Profondeur	$\hat{z}^{dd,k}$
Médiane de la lognormale	$\hat{Y}^{dd,k}$
Valeur la plus probable	$\hat{\hat{Y}}^{dd,k}$
Matrice d'erreur d'observation	R_k^{dd}
Opérateur d'observation	h_k^{dd}

Les liens stratigraphiques glace et gaz

Les liens stratigraphiques glace et gaz sont issus de l'identification d'un même évènement dans deux carottes de glace. Ainsi, les liens stratigraphiques sont associés à un couple (J) de forages k_1 et k_2. Ces marqueurs mettent en jeu des profondeurs différentes dans chacun des forages, et donc des âges différents, ce qui implique la connaissance de la différence d'âge entre ces mêmes couches de glace/bulles d'air repérées par ce couple de profondeurs. Comme ces marqueurs sont associés à des âges, ils présentent des densités de probabilité gaussiennes.

L'opérateur d'observation associé aux liens stratigraphiques (glace ou gaz) implique de calculer les âges respectifs pour les forages k_1 et k_2 aux profondeurs $\hat{z}^{is,J,k_1}$ et $\hat{z}^{is,J,k_2}$. Ainsi l'opérateur d'observation associé aux liens stratigraphiques consiste en la différence entre deux opérateurs associés aux âges des deux carottes (équations 2.30 et 2.31).

$$\Delta h^{is,J}(\tilde{X}) = h^{ia,J,K_1}(\tilde{X}^{k_1} - h^{ia,J,K_2}(\tilde{X}^{k_2} \tag{2.30}$$

$$h^{ia,J,K_1}(\tilde{X}^{k_1} = \int_{\zeta^k=0}^{\hat{z}^{is,J,k_1}} \frac{\exp[-\tilde{\alpha}^{k_1}(\zeta^{k_1})]\exp[-\tilde{\tau}^{k_1}(\zeta^{k_1})}{A^{b,k_1}(\zeta^{k_1})T^{b,k_1}(\zeta^{k_1})} D^{k_1}(\zeta^{k_1})d\zeta^{k_1} \tag{2.31}$$

Pour obtenir l'opérateur associé à la carotte k_2 il suffit de remplacer k_1 par k_2 dans l'équation 2.31. Pour les liens stratigraphiques gaz, il faut remplacer ^{ia} par ^{ga} et $\hat{z}^{is,J,k_1}$ par $\hat{z}^{is,J,k_1} - \Delta depth(\hat{z}^{is,J,k_1})$ dans les équations 2.30 et 2.31. Les paramètres caractérisant les liens stratigraphiques glace et gaz sont résumés dans la table 2.3.

TABLE 2.3 – Table récapitulative des grandeurs associées aux liens stratigraphiques glace et gaz.

	Liens stratigraphiques glace	Liens stratigraphiques gaz
Couple de profondeurs	$(\hat{z}^{is,J,k_1}, \hat{z}^{is,J,k_2})$	$(\hat{z}^{gs,J,k_1}, \hat{z}^{gs,J,k_2})$
Différence d'âge la plus probable	$\Delta\hat{Y}^{is,k}$	$\Delta\hat{Y}^{gs,k}$
Matrice d'erreur d'observation	$R^{is,J} = R_k^{is}$	$R^{gs,J} = R_k^{gs}$
Opérateur d'observation	$\Delta h^{is,J} = h_k^{is}$	$\Delta h^{gs,J} = h_k^{gs}$

2.2.5 Fonction coût et minimisation

Fonction coût

Comme chaque forage possède sa propre discrétisation en fonction de la profondeur, le vecteur $\tilde{X}$ peut devenir très grand. En conséquence, il a été choisi que la densité de probabilité *a posteriori* serait déterminée à l'aide du critère d'optimalité de maximum de vraisemblance qui fait intervenir la notion de fonction coût $J(\tilde{X})$.

Sous les hypothèses de l'inversion bayésienne, la fonction coût peut se décomposer en un terme d'ébauche et un terme associé aux observations.

$$J(\tilde{X}) = J^b(\tilde{X}) + J^o(\tilde{X}) \tag{2.32}$$

La fonction coût détaillée pour toutes les observations prises en compte par Datice

s'écrit alors :

$$\begin{aligned}
J(\tilde{X}) = &\sum_{k=1}^{N} \frac{1}{2} \left(\tilde{X}_k - \tilde{X}_k^b\right)^T [\mathbf{B}]^{-1} \left(\tilde{X}_k - \tilde{X}_k^b\right) \\
&+ \sum_{k=1}^{N} \frac{1}{2} \left(Y_k^{dd} - \mathbf{h}_k^{dd}(\tilde{X}_k)\right)^T [\mathbf{R}_k^{dd}]^{-1} \left(Y_k^{dd} - \mathbf{h}_k^{dd}(\tilde{X}_k)\right) \\
&+ \sum_{k=1}^{N} \frac{1}{2} \left(Y_k^{ia} - \mathbf{h}_k^{ia}(\tilde{X}_k)\right)^T [\mathbf{R}_k^{ia}]^{-1} \left(Y_k^{ia} - \mathbf{h}_k^{ia}(\tilde{X}_k)\right) \\
&+ \sum_{k=1}^{N} \frac{1}{2} \left(Y_k^{ga} - \mathbf{h}_k^{ga}(\tilde{X}_k)\right)^T [\mathbf{R}_k^{ga}]^{-1} \left(Y_k^{ga} - \mathbf{h}_k^{ga}(\tilde{X}_k)\right) \\
&+ \sum_{k=1}^{N} \frac{1}{2} \left(Y_k^{is} - \mathbf{h}_k^{is}(\tilde{X}_k)\right)^T [\mathbf{R}_k^{is}]^{-1} \left(Y_k^{is} - \mathbf{h}_k^{is}(\tilde{X}_k)\right) \\
&+ \sum_{k=1}^{N} \frac{1}{2} \left(Y_k^{gs} - \mathbf{h}_k^{gs}(\tilde{X}_k)\right)^T [\mathbf{R}_k^{gs}]^{-1} \left(Y_k^{gs} - \mathbf{h}_k^{gs}(\tilde{X}_k)\right)
\end{aligned} \tag{2.33}$$

Dans l'équation 2.33, le premier terme correspond à l'ébauche, et les 5 autres termes sont associés aux différents types d'observation (^{dd} pour les marqueurs de $\Delta depth$, ^{ia} pour les marqueurs d'âge glace, ^{ga} pour les marqueurs d'âge gaz , ^{is} et ^{gs} pour les liens stratigraphiques glace et gaz respectivement).

Minimisation

Afin d'obtenir le vecteur X^a optimisé, le critère de maximum de vraisemblance impose de trouver le minimum de la fonction coût (équation 2.7). Pour ce faire, l'optimisation repose sur des méthodes numériques dites de descente. On cherche à se diriger vers le minimum de J, par itérations successives suivant un chemin de descente.

Datice utilise le minimiseur m1qn3 [Gilbert and Lemaréchal, 1989]. Il est adapté pour résoudre des problèmes de grande échelle peu contraints. Ce minimiseur repose sur la connaissance de la fonction à minimiser ainsi que son gradient afin de pouvoir approximer son hessien (matrice des dérivées secondes de la fonction). A partir de cela, il est possible de déduire la direction de descente de la minimisation pour la prochaine itération.

La minimisation est arrêtée lorsque le test sur le gradient est satisfait, c'est à dire lorsqu'on atteint une certaine précision définie par l'utilisateur (par exemple, la valeur demandée pour Datice est $\epsilon_g = 10^{-8}$). Ce critère est basé sur la norme du gradient de la fonction coût :

$$\epsilon_i = \frac{|g_i|}{|g_1|} < \epsilon_g$$

avec g_i le gradient de la fonction coût de la $i$ème itération et g_1 celui de la première itération.

2.2.6 Nouvelle chronologie optimisée

Une fois le test du gradient satisfait, ou presque satisfait dans certains cas, Datice détermine le vecteur $\tilde{X}^a$ regroupant les fonctions de correction optimales. En appliquant le changement de variable inverse, on obtient le vecteur X^a regroupant les fonctions de correction $\alpha(z)$, $\tau(z)$ et $\gamma(z)$. L'outil de datation en déduit les grandeurs glaciologiques optimales puis les chronologies correspondantes, gaz et glace, pour chacun des forages. L'atout majeur de cette méthode de datation est qu'elle calcule directement l'incertitude associée aux chronologies.

Erreur *a posteriori* sur $\tilde{X}^a$

Suite à la minimisation, Datice est en mesure de calculer la matrice de covariance d'erreur *a posteriori* sur $\tilde{X}^a$, en faisant l'hypothèse que l'opérateur d'observation généralisé est faiblement non linéaire :

$$P^a \simeq \left(\hat{H}\tilde{R}^{-1}\hat{H} + \tilde{B}^{-1}\right)^{-1} \tag{2.34}$$

où $\hat{H}$ est l'opérateur linéaire tangent associé à l'opérateur d'observation généralisé, $\tilde{B}$ la matrice de covariance d'erreur d'ébauche généralisée (section 2.2.3) et $\tilde{R}$ la matrice de covariance d'erreur d'observation généralisée (section 2.2.4).

Nous pouvons noter que les blocs diagonaux de la matrice P^a donnent les écart–types *a posteriori* sur les composantes de $\tilde{X}^a$:

$$\tilde{\sigma}_i^{a,k} \simeq \sqrt{P_{ii}^{a,k}}$$

avec i et k les indices associés à chaque carotte de glace.

Erreur *a posteriori* sur la chronologie

On rappelle que le changement de variable de X à $\tilde{X}$ a permis de passer de distributions lognormales à gaussiennes. La seule quantité conservée entre ces deux distributions est la médiane. Afin de bien comprendre les étapes successives pour en arriver à l'estimation de l'erreur sur les chronologies analysées, nous allons raisonner sous forme d'intervalle de confiance.

Ainsi, en considérant 1–sigma pour l'erreur *a posteriori* sur $\tilde{X}^a$, cela correspond à un intervalle de confiance à 68% . Si on prend l'exemple des grandeurs associées au

taux d'accumulation, l'optimisation de $\tilde{\alpha}$ pour la carotte de glace k à une profondeur donnée nous permet de dire que l'on fait une erreur de l'ordre de 32 % en affirmant :

$$\tilde{\alpha} \in [\tilde{\alpha}^a - \sigma; \tilde{\alpha}^a + \sigma] \tag{2.35}$$

En appliquant le changement de variable inverse ($\exp \tilde{X} = X$), on en déduit l'intervalle de confiance à 68% sur α :

$$\exp(\tilde{\alpha}) \in [\exp(\tilde{\alpha}^a - \sigma); \exp(\tilde{\alpha}^a + \sigma)] \tag{2.36}$$

$$\alpha \in [\alpha^a \exp(-\sigma); \alpha^a \exp(\sigma)] \tag{2.37}$$

Après conversion en accumulation, en utilisant la relation $A = \alpha A^b$ de la section 2.2.2, cela devient :

$$A = A^b\alpha \in [A^b\alpha^a \exp(-\sigma); A^b\alpha^a \exp(\sigma)] \tag{2.38}$$

$$A \in [A^a \exp(-\sigma); A^a \exp(\sigma)] \tag{2.39}$$

La même démarche s'applique pour la fonction d'amincissement et la LIDIE afin d'en déduire leurs intervalles de confiance à 68% .

L'incertitude sur l'âge est donc fonction de nombreux facteurs. En considérant que tous ces facteurs sont statistiquement indépendants, on peut faire l'hypothèse que les incertitudes sur les chronologies optimales pour chaque site $\Psi^{a,k}$ sont correctement décrites par des gaussiennes.

Le vecteur de l'âge de la glace en fonction de la profondeur pour chaque forage est obtenu à partir de la relation 2.8. On définit la matrice de covariance d'erreur *a posteriori* Q^a associée à la chronologie glace Ψ^a comme :

$$Q^a \simeq \nabla\Psi^{aT} P^a \nabla\Psi^a \tag{2.40}$$

où $\nabla\Psi^a$ est l'opérateur linéaire tangent du modèle d'âge glace. La matrice Q^a est symétrique et ses blocs diagonaux donnent les covariances d'erreur associées à chacun des N forages. L'intervalle de confiance de chacune des chronologies glace optimales est directement donné par les éléments diagonaux de la matrice Q^a. Pour le forage k ayant une grille de profondeur $z_{i\in 1..n}$, l'erreur sur l'âge glace à la profondeur z_i correspond à :

$$\sigma_i^{\Psi,k} = [Q^a_{kk}]^{1/2}_{ii} \tag{2.41}$$

2.3 Première application : Lemieux-Dudon et al. [2010]

La première application de Datice a été présentée par Lemieux-Dudon et al. [2010]. Cet exercice de datation a permis de générer une chronologie commune pour les sites de Vostok, EDC et EDML en Antarctique ainsi que NGRIP au Groenland, à la fois pour la phase glace et la phase gaz sur les derniers 50 ka. Pour ce faire, les auteurs ont utilisé des datations d'ébauche issues de la littérature ainsi que des contraintes d'âge absolues et stratigraphiques pour les différents sites.

2.3.1 Les ébauches et l'estimation de leurs erreurs

Les scénarios d'ébauche pour les paramètres glaciologiques sont tous tirés de la littérature, à l'exception de la LIDIE pour NGRIP. Ils sont généralement basés sur de la modélisation directe ou inverse, ainsi que le comptage des couches annuelles dans le cas de NGRIP.

Vostok

Lemieux-Dudon et al. [2010] a utilisé les grandeurs glaciologiques issues de la datation FGT1 [Parrenin et al., 2001, 2004]. Cette chronologie a été obtenue à l'aide d'un modèle inverse d'écoulement optimisé par la méthode de Monte Carlo. Le taux d'accumulation est déduit à partir de la relation empirique entre le taux de précipitation – la température d'inversion – la température moyenne annuelle – la composition isotopique de la glace. La fonction d'amincissement a été calculée à partir de la chronologie FGT1 et du scénario d'accumulation déduit de la composition isotopique de la glace. Le scénario d'ébauche de la LIDIE a été obtenu à l'aide du modèle de densification du névé de Goujon et al. [2003], parametré avec les températures et taux d'accumulation précédemment obtenus.

EDC

Pour EDC, les scénarios d'ébauche du taux d'accumulation et de la fonction d'amincissement sont issus de la chronologie EDC3 purement glaciologique [Parrenin et al., 2007b]. Cette chronologie a été obtenue à l'aide d'un modèle d'écoulement 1D optimisé par Monte Carlo. Le taux d'accumulation est directement déduit de la composition isotopique de la glace. La fonction d'amincissement a été déduite à l'aide de la chronologie purement glaciologique EDC3 modèle et de ce taux d'accumulation.

La LIDIE est obtenue en forçant le modèle de Goujon et al. [2003] par la température et le taux d'accumulation déduits des isotopes de l'eau [Loulergue et al., 2007].

EDML

Dans le cas d'EDML, la fonction d'amincissement a été obtenue à l'aide du modèle d'écoulement de Huybrechts et al. [2007]. Le taux d'accumulation a été déduit de la composition isotopique de la glace. Comme pour EDC, la LIDIE d'EDML est issue du modèle de Goujon et al. [2003], sur la base de la chronologie EDML1 [Loulergue et al., 2007].

NGRIP

Contrairement aux autres forages où les datations utilisées pour déduire les paramètres glaciologiques sont issues de modèles, dans le cas de NGRIP les auteurs ont utilisé la chronologie de référence GICC05 [Vinther et al., 2006; Rasmussen et al., 2006; Andersen et al., 2006; Svensson et al., 2008]. Cette échelle d'âge a été obtenue par comptage des couches annuelles jusqu'à 60 ka. Par défaut, le comptage des couches annuelles nous donne directement l'épaisseur des couches annuelles *in situ*. A l'aide de la fonction d'amincissement produite par le modèle d'Andersen et al. [2006], utilisé comme ébauche dans cette application, et connaissant l'épaisseur des couches annuelles, les auteurs ont été en mesure de déduire le taux d'accumulation d'ébauche de NGRIP. Comme pour les autres forages, le modèle de densification du névé de Goujon et al. [2003] a été utilisé pour produire le scénario d'ébauche de la LIDIE de NGRIP.

Matrices de covariance d'erreur d'ébauche

Dans le cadre de Lemieux-Dudon et al. [2010], les matrices de covariance d'erreur pour les différentes ébauches (équations 2.21, 2.22 et 2.23) ont été définies de la façon suivante.

Dans les cas de l'accumulation et de la LIDIE, les écart-types ($\sigma_A^{b,k}$ et $\sigma_C^{b,k}$) ont été supposés invariant avec la profondeur et de valeur $\sigma_{A,0}^{b,k}$ propre à chacun des forages. De plus, les auteurs ont défini leurs matrices de corrélation comme étant fonction de la différence d'âge entre les profondeurs i et j. Ceci a été choisi car les variations du taux d'accumulation au sein d'une carotte de glace ne sont pas liées à la profondeur, mais plutôt aux variations climatiques passées. Ainsi, plus on s'écarte des conditions climatiques actuelles, plus il y a d'incertitudes sur les reconstructions du taux d'accumulation et de la LIDIE. Les matrices de corrélation $\rho_A^{b,k}$ et $\rho_C^{b,k}$ sont

alors définies comme des distributions gaussiennes en fonction de l'âge de la glace. Les auteurs ont aussi introduit une longueur de corrélation fixée à 4 ka dans les 2 cas (équations 2.42 et 2.43).

$$[\rho_A^{b,k}]_{ij} = \exp\left[-\frac{1}{2}\left(\frac{\Psi_i^{b,k} - \Psi_j^{b,k}}{L_A^{b,k}}\right)^2\right] \tag{2.42}$$

$$[\rho_C^{b,k}]_{ij} = \exp\left[-\frac{1}{2}\left(\frac{\Psi_i^{b,k} - \Psi_j^{b,k}}{L_C^{b,k}}\right)^2\right] \tag{2.43}$$

Pour le cas de la fonction d'amincissement, l'écart–type a été parametré afin de respecter la condition suivante : plus une particule de glace est enfouie, plus l'erreur modèle est importante. Ainsi, la variance associée à l'amincissement augmente avec la profondeur comme l'inverse de $T^{b,k}$, l'amincissement d'ébauche :

$$[\sigma_T^{b,k}]_i = \sigma_{T,0}^{b,k}\left[\frac{1}{10} + \frac{1}{H}\sum_{j=1}^{i}\frac{dz_j^k}{T_j^{b,k}}\right] \tag{2.44}$$

avec $\sigma_{T,0}^{b,k}$ un paramètre propre à chaque forage et H l'épaisseur totale de glace de la carotte. Cette fois–ci, la matrice de corrélation est définie en fonction d'une différence de profondeur car l'amincissement est lié aux propriétés mécaniques de la glace à chaque profondeur. De même, les auteurs ont introduit une longueur de corrélation fixée ici à 70 m :

$$[\rho_T^{b,k}]_{ij} = \exp\left[-\frac{1}{2}\left(\frac{z_i^{b,k} - z_j^{b,k}}{L_T^{b,k}}\right)^2\right] \tag{2.45}$$

2.3.2 Les marqueurs d'âge

Au total, 1491 marqueurs ont été utilisés pour contraindre la nouvelle chronologie (LD2010), principalement concentrés sur les derniers 50 ka. Lors de cette application, 5 types de marqueurs différents ont été utilisés.

Marqueurs d'âge glace

1034 marqueurs d'âge glace ont été utilisés pour contraindre les chronologies de Vostok (28 marqueurs), EDC (17 marqueurs) et NGRIP (989 marqueurs). Ce sont principalement des marqueurs ayant déjà été utilisés pour produire les chronologies FGT1 [Parrenin et al., 2004] et EDC3 [Parrenin et al., 2007a]. Ces marqueurs sont principalement issus du ^{10}Be, d'éruptions volcaniques bien datées ou encore de la synchronisation orbitale de traceurs (δD pour Vostok et teneur en air pour EDC).

Pour Vostok, ces marqueurs ont été complétés par des marqueurs orbitaux issus de la synchronisation orbitale de la teneur en air et du $\delta O_2/N_2$ avec des courbes d'insolation locale intégrée [données non publiées lors de Lemieux-Dudon et al. [2010] Lipenkov et al., 2011]. Pour NGRIP, les marqueurs ont été déduits de la chronologie GICC05, tous les 60 ans.

Marqueurs d'âge gaz

49 marqueurs d'âge gaz ont servi à contraindre la nouvelle chronologie pour les sites d'EDC et de NGRIP. Pour EDC, 36 marqueurs ont été obtenus par synchronisation orbitale du $\delta^{18}O_{atm}$ avec la précession entre 300 et 800 ka [Dreyfus et al., 2007]. Ces marqueurs ont été utilisés pour construire la chronologie EDC3 [Parrenin et al., 2007a]. A NGRIP, il a été montré que lors des événements de Dansgaard-Oeschger la concentration en méthane et la composition isotopique de la glace augmentent simultanément [Severinghaus et al., 1998]. Ainsi 13 marqueurs ont été déduits afin de contraindre les âges des augmentations de méthane.

Liens stratigraphiques glace

Dans cette étude, des liens stratigraphiques glace ont été incorporés pour les couples Vostok–EDC, EDC–EDML et EDC–NGRIP. Pour ce dernier couple, 2 liens ont été déduits à partir de la structure de l'excursion géomagnétique du Laschamp enregistrée par le ^{10}Be. Pour les deux autres couples de forages, les liens stratigraphiques glace ont été obtenus par identification d'éruptions volcaniques communes aux 2 sites. Celles–ci sont caractérisées par des pics de conductivité ou de sulfate mesurés dans la glace. Ainsi, Lemieux-Dudon et al. [2010] ont utilisé 59 liens pour Vostok–EDC [Udisti et al., 2004; Narcisi et al., 2005] et 270 marqueurs pour le couple EDC–EDML [Severi et al., 2007]. L'incertitude associée à ces marqueurs est fonction de la certitude lors de l'identification des pics volcaniques dans les 2 carottes (variant entre 100 et 300 ans)

Liens stratigraphiques gaz

Comme le méthane est un traceur global, les variations de sa concentration sont enregistrées au même moment à différents endroits du globe. En utilisant ce traceur, il est alors possible de déduire des liens stratigraphiques pour la phase gaz entre les différentes carottes de glace. Pour cette application, Lemieux-Dudon et al. [2010] ont utilisé 50 liens de ce type pour les couples de carottes Vostok–EDC, EDC–EDML et EDML–NGRIP [Loulergue et al., 2007, 2008], avec des incertitudes allant de 100

à 300 ans dans le cas de la synchronisation Vostok–EDC.

Marqueurs de Δdepth

Ce type de marqueur est obtenu par l'identification d'un même événement climatique dans la phase glace, au travers de sa composition isotopique, et dans la phase gaz, grâce au $\delta^{15}N$. Au total, 23 marqueurs de ce type ont été utilisés pour contraindre la nouvelle chronologie [17 pour EDC, 4 pour NGRIP et 2 pour Vostok ; Lemieux-Dudon et al., 2010].

2.3.3 La chronologie LD2010

Grâce à l'outil Datice, Lemieux-Dudon et al. [2010] ont obtenu une nouvelle chronologie commune pour EDC, EDML, Vostok et NGRIP jusqu'à 50 ka. Au regard des courbes de méthane, la nouvelle chronologie permet de réconcilier les enregistrements d'Antarctique et du Groenland lors de la dernière déglaciation (figure 2.3A). Concernant les compositions isotopiques de la glace, la nouvelle chronologie semble indiquer que les chronologies EDC3 et EDML1 étaient trop jeunes au niveau de la dernière déglaciation. Pour la dernière période glaciaire, la nouvelle chronologie commune Antarctique et Groenland est en meilleur accord avec la théorie du see–saw bipolaire que la chronologie Antarctique EDC3/EDML1 (figure 2.3B). Les paramètres glaciologiques obtenus par Datice sont cohérents avec les estimations précédentes des modèles, à l'exception des profondeurs de piégeage de l'air pour les sites froids comme EDC où Datice les estime plus petites que le modèle de densification du névé de Goujon et al. [2003].

Cet outil de datation a prouvé sa robustesse au travers d'une première application pour les carottes de glace sur une courte période. Cependant, plusieurs points restent à améliorer et de futures applications peuvent être envisagées. En effet, l'une des limitations de cette application concerne les paramètres d'ébauche utilisés et leurs erreurs. Dans cette application les erreurs sur les paramètres d'ébauche ont été considérées comme constantes, or cela n'est pas réaliste et nécessite d'être amélioré. Un second point à améliorer, directement lié au principe de datation fédérative des carottes de glace, est la méthode utilisée pour contraindre la chronologie LD2010 à respecter GICC05. Dans le but de respecter au mieux GICC05 Lemieux-Dudon et al. [2010] ont utilisé le taux d'accumulation et des marqueurs d'âge déduits de l'échelle d'âge GICC05, ne respectant pas l'hypothèse de non corrélation entre les contraintes d'âge et les paramètres d'ébauche. Ainsi, il est nécessaire de considérer

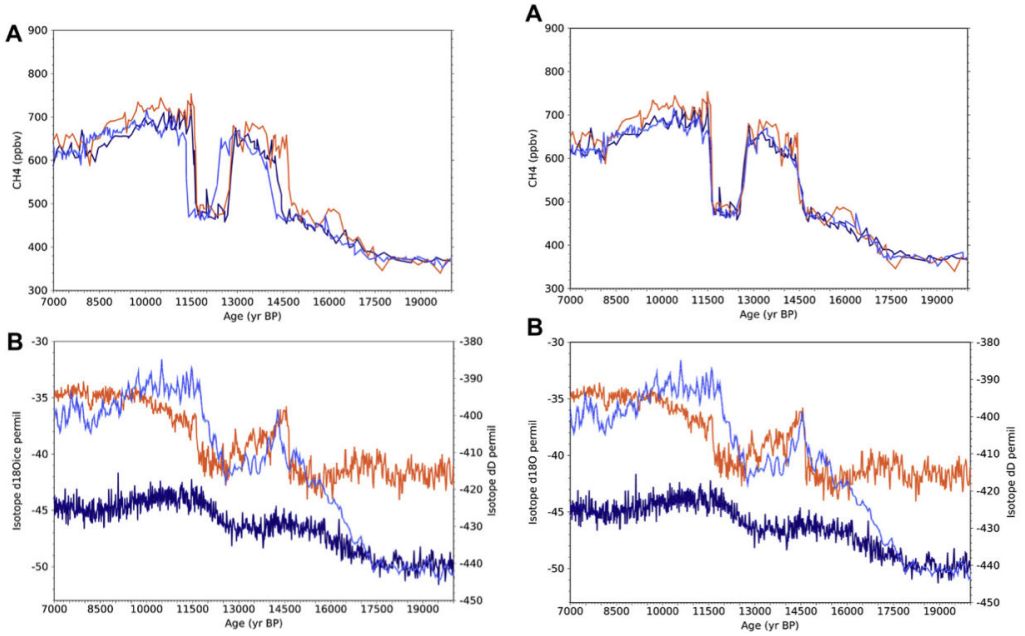

FIGURE 2.3 – Méthane (A) et composition isotopique de la glace (B) pour EDC (bleu clair), EDML (bleu foncé) et NGRIP (orange) entre 7 et 20 ka. Gauche : Les traceurs sont représentés sur les chronologies de référence de chacun des forages : EDC3 pour EDC, EDML1 pour EDML et GICC05 pour NGRIP. Droite : Les mêmes traceurs pour les 3 sites, représentés sur les chronologies gaz et glace obtenues par Lemieux-Dudon et al. [2010]. Figures extraites de Lemieux-Dudon et al. [2010].

une autre méthode pour contraindre la chronologie commune pour les carottes de glace à respecter l'échelle d'âge GICC05. Pour finir, la chronologie LD2010 est commune à quatre carottes de glace et couvre seulement les derniers 50 ka. La prochaine étape est donc d'utiliser Datice pour produire une chronologie commune à plus de forages et couvrant une plus grande période de temps.

Dans les chapitres suivants, nous allons réaliser un exercice de datation à 5 carottes de glace jusqu'à 800 ka et chercher à améliorer l'outil Datice.

3

La nouvelle chronologie de référence carotte de glace : AICC2012

La méthode utilisée pour construire la nouvelle chronologie commune aux carottes de glace ("Antarctic Ice Core Chronology", AICC2012) est une version améliorée de l'outil de datation "Datice" développé par Lemieux-Dudon et al. [2010]. Lors de cet exercice, il a été utilisé afin de produire une chronologie commune pour 4 carottes de glace (EDC, EDML, Vostok et NGRIP) sur les derniers 50 ka. Par la suite Datice a été repris pour construire la chronologie TALDICE-1a de la carotte de Talos Dôme [Buiron et al., 2011]. Comme présenté au chapitre précédent, l'outil Datice a besoin de plusieurs paramètres d'entrée :

- les ébauches du taux d'accumulation, de la fonction d'amincissement et de la LIDIE pour calculer les âges gaz et glace d'ébauche pour toutes les carottes considérées, ainsi que les erreurs associées ;
- différentes contraintes d'âge : soit des marqueurs dit absolus pour une carotte, soit des liens stratigraphiques entre les carottes, ou encore des marqueurs de $\Delta depth$, avec leurs erreurs.

La section 3.1 donne toutes les informations concernant l'adaptation de Datice afin de produire la chronologie pour les carottes de glace AICC2012 commune pour les sites d'EDC, Vostok, EDML, TALDICE et NGRIP, remontant jusqu'à 800 ka. Comparé à Lemieux-Dudon et al. [2010], nous avons revu les paramètres d'ébauche ainsi que la paramétrisation de leurs erreurs et nous avons ajouté un grand nombre de contraintes chronologiques. Lorsque rien n'est précisé, comme par exemple concernant les longueurs de corrélation pour les marqueurs, cela signifie qu'il n'y a eu aucun changement depuis Lemieux-Dudon et al. [2010].

3.1 Améliorations de Datice depuis Lemieux-Dudon et al. [2010]

3.1.1 Les paramètres d'ébauche

Le taux d'accumulation

Pour toutes les carottes de glace d'Antarctique, nous avons suivi l'estimation classique du taux d'accumulation basée sur une relation exponentielle avec les isotopes de l'eau (comme traceurs de la température) [Parrenin et al., 2007b, et références citées dans ce papier]. Ainsi, nous avons conservé les mêmes scénarios que Lemieux-Dudon et al. [2010] et Buiron et al. [2011] pour les quatre sites d'Antarctique. Dans les cas de Vostok et TALDICE, les changements d'élévation de la calotte ont été pris en compte pour corriger les profils de température déduits des isotopes de l'eau. Concernant NGRIP, afin de contraindre AICC2012 à respecter GICC05 sur les derniers 60 ka, le taux d'accumulation a été calculé en combinant l'épaisseur des couches annuelles issues de la chronologie GICC05modelext [Vinther et al., 2006; Rasmussen et al., 2006; Andersen et al., 2006; Svensson et al., 2008; Wolff et al., 2010] avec la fonction d'amincissement obtenue avec le modèle de Dansgaard-Johnsen paramétré pour NGRIP [NorthGRIP Community Members, 2004; Andersen et al., 2006].

La fonction d'amincissement

Les fonctions d'amincissement utilisées pour Vostok et EDC sont les mêmes que celles de Lemieux-Dudon et al. [2010]. Pour Vostok la fonction d'amincissement est déduite à partir de l'accumulation et de la chronologie FGT1 [Parrenin et al., 2004]. Pour EDC, la fonction d'amincissement provient de Parrenin et al. [2007b]. Concernant EDML, la fonction d'amincissement a été obtenu à l'aide du modèle d'écoulement de Huybrechts et al. [2007]. Cette dernière est légèrement différente de celle utilisée par Lemieux-Dudon et al. [2010] en ayant une allure plus lissée autour de 500 m de profondeur. Nous avons utilisé la même fonction d'amincissement que Buiron et al. [2011] pour TALDICE, obtenue à l'aide d'un modèle d'écoulement 1D. La fonction d'amincissement de NGRIP a été obtenue à l'aide du modèle d'écoulement de la glace de Dansgaard-Johnsen [NorthGRIP Community Members, 2004; Andersen et al., 2006].
Afin de vérifier l'influence possible des scénarios d'ébauche de la fonction d'amincissement sur la chronologie finale, nous avons testé cela pour Vostok. Nous avons donc réalisé des simulations avec la fonction d'amincissement utilisée dans AICC2012, ainsi qu'avec une fonction test très simplifiée, appelée "test thinning", obtenue à

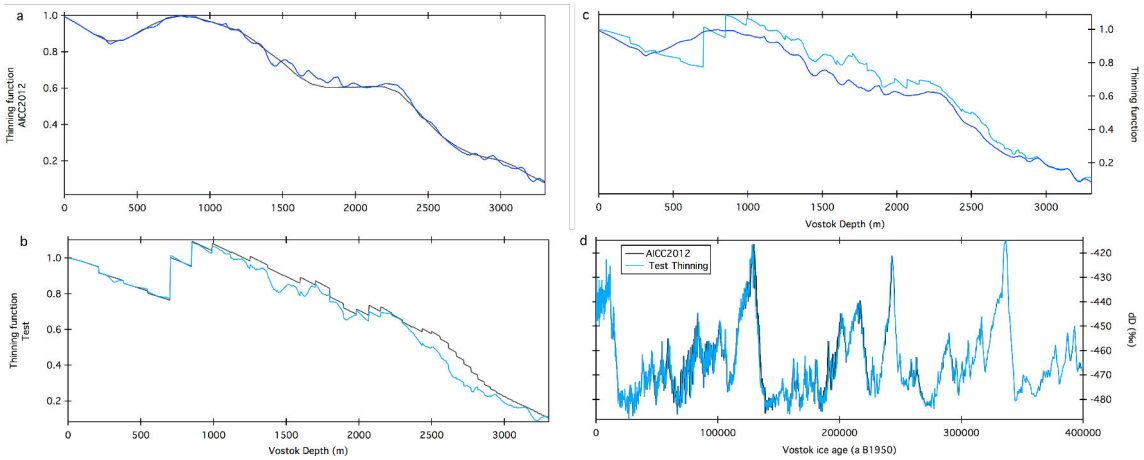

FIGURE 3.1 – Tests sur la fonction d'amincissement de Vostok. Les courbes grises correspondent aux ébauches alors que les courbes bleues représentent les résultats issus de Datice. a : fonction d'amincissement d'AICC2012 ; b : fonction d'amincissement test ; c : comparaison des fonctions d'amincissement en sortie de Datice ; d : composition isotopique de la glace de Vostok en fonction des deux chronologies glace obtenues.

l'aide d'IceChronoModel (F. Parrennin Comm. Pers.). Sur la figure 3.1, nous pouvons voir qu'en utilisant les deux scénarios d'ébauche, Datice tend vers une même fonction d'amincissement en sortie des simulations. De plus, la chronologie résultante ne présente pas de différences significatives en utilisant l'amincissement test comparée à AICC2012.

La LIDIE

Les scénarios d'ébauche pour la LIDIE utilisés par Lemieux-Dudon et al. [2010] et Buiron et al. [2011] ont tous été obtenus en utilisant le modèle de densification du névé de Goujon et al. [2003]. Le modèle a été validé pour le site de NGRIP [Landais et al., 2004; Huber et al., 2006; Guillevic et al., 2013], mais il semble surestimer les LIDIE en période glaciaire pour les carottes de glace d'Antarctique, à l'exception de TALDICE [Landais et al., 2006; Parrenin et al., 2012a; Capron et al., 2013]. Parrenin et al. [2012a] ont suggéré que le $\delta^{15}N$ fournit des contraintes plus réalistes sur la LIDIE pour les sites de faibles taux d'accumulation en Antarctique . Nous avons donc réalisé plusieurs simulations avec Datice en considérant soit la LIDIE obtenue avec le modèle de densification du névé (scénario LIDIE 1), soit une LIDIE inspirée du $\delta^{15}N$ pour tous les sites sauf NGRIP (scénario LIDIE 2). Pour ce deuxième scénario, nous avons fait l'hypothèse que l'épaisseur de la zone convective est invariante dans le temps, avec une valeur de 0 m pour EDML, TALDICE et EDC, et 13 m pour Vostok, comme observé actuellement [Landais et al., 2006]. La LIDIE peut alors

être déduite à partir du $\delta^{15}N$ (équation (3.1)) en l'absence de variations rapides de température à la surface (2°C en 100 ans). Cette hypothèse est valide en Antarctique pour la période de temps considérée.

$$LIDIE = 0.7 \cdot \delta^{15}N \cdot RT/g \tag{3.1}$$

où T est la température moyenne du névé, R la constante des gaz parfaits et g la gravité. Le facteur 0.7 correspond à la densité moyenne du névé. Pour des sites comme Vostok et Dôme C il est nécessaire d'appliquer une correction de 3 m maximum afin de tenir compte du gradient de température au sein du névé affectant la LIDIE en période glaciaire. Cette correction à été effectuée en considérant le gradient de température du névé calculé par le modèle de Goujon et al. [2003]. Pour obtenir les scénarios de LIDIE 2 issus du $\delta^{15}N$, nous avons utilisé les données de Dreyfus et al. [2010] et Landais et al. [2013] pour EDC, Sowers et al. [1992] pour Vostok, et Capron et al. [2013] pour TALDICE et EDML. Comme aucun des profils de $\delta^{15}N$ n'est complet pour les quatre carottes de glace d'Antarctique, nous avons utilisé le lien entre $\delta^{15}N$–δD sur une même échelle d'âge pour compléter les périodes manquantes [Dreyfus et al., 2010; Capron et al., 2013]. Ainsi, nous avons complété les données de $\delta^{15}N$ sur les derniers 300 ka à EDC, à l'exception des terminaisons où le $\delta^{15}N$ a été mesuré par Dreyfus et al. [2010]. Pour ce faire, les périodes de données manquantes ont été complétées par une courbe synthétique de $\delta^{15}N$ déduite à partir de la corrélation entre $\delta^{15}N$–δD lors de la Terminaison I. Pour TALDICE, comme le modèle de densification du névé est en accord avec les données de $\delta^{15}N$ sur la dernière déglaciation [Capron et al., 2013], nous avons donc utilisé ce dernier pour compléter la LIDIE sur les dernières périodes glaciaire et interglaciaire.

Les scénarios d'ébauche de LIDIE sont associés à des variances larges, laissant la possibilité à Datice de fortement les corriger. En conséquence, les LIDIE d'Antarctique en sortie de Datice vont être principalement contraintes par les liens stratigraphiques gaz et glace, surtout lors de la dernière période glaciaire puisque cela correspond à la période présentant le plus grand nombre de marqueurs stratigraphiques (section 3.1.3). Concernant EDC, nous observons un meilleur accord entre la LIDIE de sortie de Datice et le scénario d'ébauche de LIDIE 2, notamment au niveau de la Terminaison I (figure 3.2). Ce résultat est cohérent avec ce qui a été observé par Parrenin et al. [2012a]. Plusieurs explications peuvent être avancées concernant les différences entre les LIDIE en sortie de Datice produites par Lemieux-Dudon et al. [2010] et celles d'AICC2012. Premièrement, AICC2012 présente beaucoup plus de liens stratigraphiques entre les carottes que la première application. Deuxièmement, les scénarios d'ébauche de LIDIE sont différents, avec une LIDIE d'ébauche bien

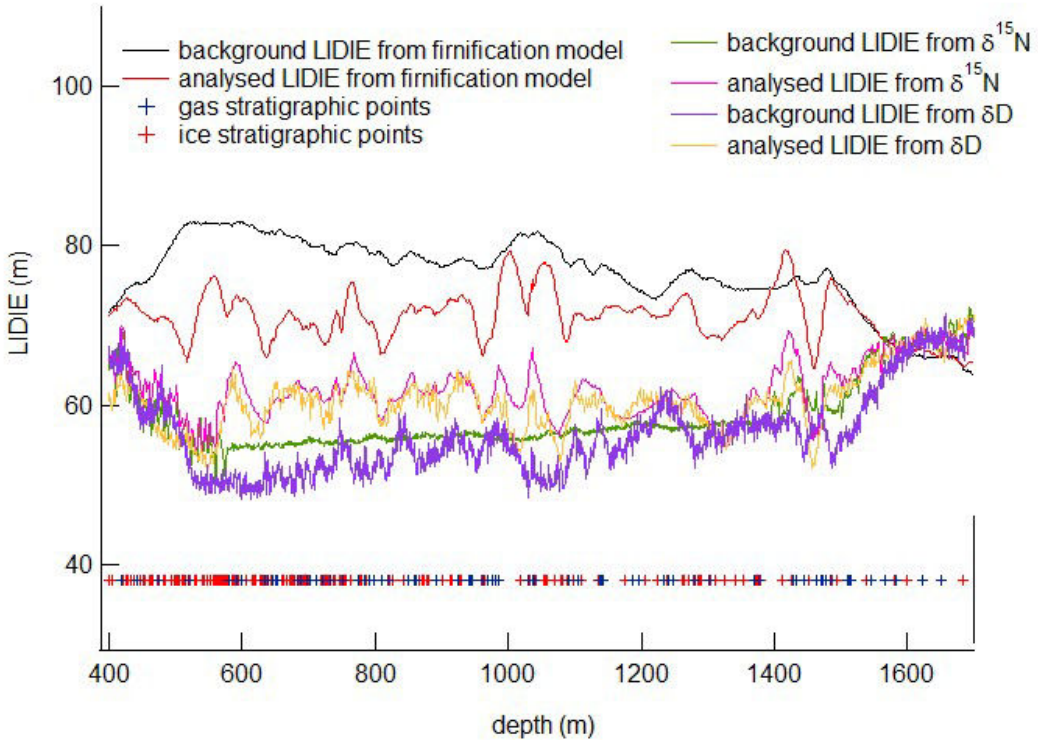

FIGURE 3.2 – Test des scénarios de LIDIE pour EDC. Courbe noir : scénario d'ébauche de la LIDIE issu du modèle de Goujon et al. [2003], courbe rouge : LIDIE de sortie de Datice pour cette ébauche. Courbe verte : scénario d'ébauche de LIDIE tiré des données de $\delta^{15}N$ (Dreyfus et al. [2010] pour la Terminaison III et Landais et al. [2013] pour le MIS 5) ; une interpolation linéaire a été appliquée entre les mesures disponibles au niveau de la dernière déglaciation et de la dernière période glaciaire afin de compléter les données. Le tracé rose correspond à la LIDIE de sortie de Datice obtenue à partir de ce scénario d'ébauche. La courbe violette correspond au scénario d'ébauche obtenu à partir de la relation $\delta^{15}N$–δD ; la courbe jaune correspond à la LIDIE obtenue avec Datice pour ce scénario d'ébauche. Les figurés en bas de la figure représentent la position des différents marqueurs d'âge et liens stratigraphiques pour la carotte EDC.

plus petite dans AICC2012 pour NGRIP (figure 5 de Veres et al. [2013]). Ceci a pour origine une meilleure paramétrisation du modèle de névé afin de respecter les nouvelles données de $\delta^{15}N$ mesurées sur NGRIP [Kindler et al., 2014]. De même, la LIDIE d'ébauche pour EDML est aussi diminuée comparée à l'exercice précédent du fait qu'elle est issues du $\delta^{15}N$ au lieu du modèle de densification du névé. De plus, le scénario d'ébauche de LIDIE pour TALDICE généré avec le modèle de névé est en accord avec les données de $\delta^{15}N$. De ce fait, la combinaison des nombreux liens stratigraphiques ainsi que les nouvelles ébauches de LIDIE pour NGRIP, EDML et TALDICE réduisent la nouvelle LIDIE de Dôme C obtenue pour AICC2012.

Finalement, il est important de noter que le pas d'interpolation de Datice peut être changé. En mode rapide l'interpolation sur les scénarios d'ébauche se fait tout les 2 ou 3 points, alors que le mode lent va considérer le pas d'interpolation originel des scénarios d'ébauche (1 m pour NGRIP, 0.55 m pour EDC, 1 m de 0 à 125 m puis tous les 0.5 m pour EDML, 1 m pour Vostok et 1 m pour TALDICE). La résolution initiale des ébauches ainsi que le pas d'interpolation peuvent avoir une influence sur les chronologies finales. En conséquence, nous avons testé différentes résolutions, mais l'effet sur la chronologie finale reste négligeable comparé à l'effet des incertitudes des marqueurs d'âge et des scénarios d'ébauche.

Table 3.1 – Table récapitulative des scénarios d'ébauche pour les 5 sites.

	Accu.	Amincissement	LIDIE
Vostok	issus isotope	Accu. - FGT1	$\delta^{15}N$– δD
EDC	issus isotope	Accu. - EDC3 modèle	$\delta^{15}N$– δD
EDML	issus isotope	Huybrechts et al. [2007]	$\delta^{15}N$– $\delta^{18}O$
TALDICE	issus isotope	modèle d'écoulement 1D[Buiron et al., 2011]	$\delta^{15}N$–modèle de névé
NGRIP	issusde GICC05	issus de GICC05	modèle de névé

3.1.2 Les profils d'erreur d'ébauche

Chaque scénario d'ébauche est associé à un profil de variance calculé à partir de l'écart-type fourni dans les fichiers d'entrée de Datice. Si la variance est forte, Datice est autorisé à appliquer une correction importante aux paramètres d'ébauche. A l'inverse, lorsque la variance est faible, les paramètres en sortie de Datice seront très proches des ébauches.

Depuis Lemieux-Dudon et al. [2010], nous avons implémenté des profils de variance pour le taux d'accumulation, la fonction d'amincissement et la LIDIE à partir

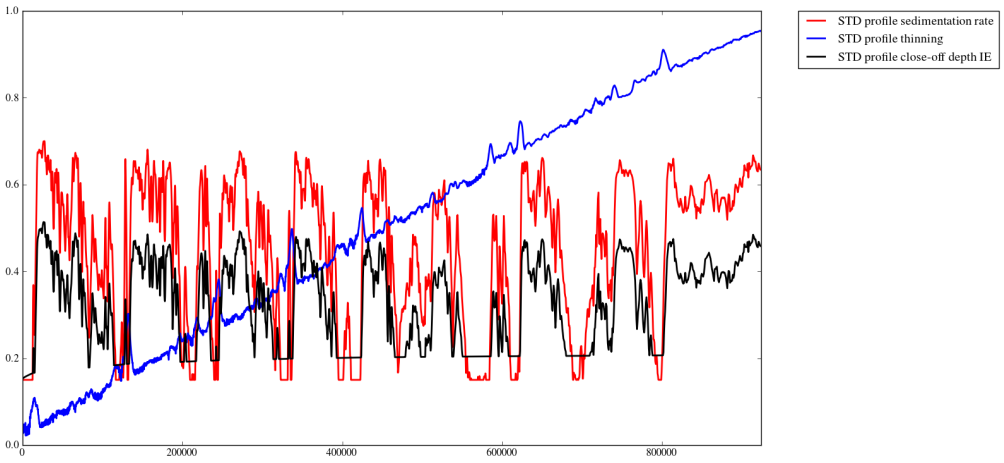

FIGURE 3.3 – Profils des écart-types utilisés pour calculer la variance du taux d'accumulation (rouge), de la fonction d'amincissement (bleu) et de la LIDIE (noir) en fonction de l'âge pour EDC.

de nouvelles formulations de l'écart-type. Ces nouvelles paramétrisations permettent une évolution en fonction de la profondeur, mais aussi une augmentation de la variance lorsque nous nous écartons des conditions interglaciaires actuelles.

La fonction d'amincissement

L'écart-type de la fonction d'amincissement est donné par :

$$\sigma_T(z) = c_{T_1} + c_{T_2} \cdot \int^z \frac{D(z)}{T(z)} dz + c_{T_3} \cdot \frac{\sigma_{A,loc}}{\sigma_{A,loc}^{max}} \tag{3.2}$$

où c_{T_1}, c_{T_2} et c_{T_3} sont des constantes définies par l'utilisateur ($c_{T_2} = c \cdot 0.1/H$ où H est la profondeur maximum du fichier d'ébauche et c une autre constante définie par l'utilisateur), $T(z)$ est la fonction d'amincissement, $D(z)$ la densité relative neige/glace, $\sigma_{A,loc}$ est l'écart-type local (filtré sur 12 ka) de l'accumulation et $\sigma_{A,loc}^{max}$ la valeur maximale. Le dernier terme est implémenté afin d'augmenter la variance de la fonction d'amincissement lors des transitions climatiques comme suggéré par le changement des propriétés mécaniques de la glace à ces périodes [Durand et al., 2007]. Ce dernier terme est cependant du second ordre comparé à la dépendance en fonction de la profondeur (figure 3.3).

Le taux d'accumulation

La formulation pour l'écart-type du taux d'accumulation est la suivante :

$$\sigma_A(z) = \sigma_{b,A} \cdot \frac{\mid A_0 - A \mid}{\mid A_0 - A \mid_{max}} \cdot \left(1 + c_{A_1} \frac{z}{z_{max}}\right) \tag{3.3}$$

avec $\sigma_{b,A}$ étant l'écart-type de référence, A_0 l'accumulation moyenne Holocène, c_{A_1} une constante. Ainsi, la variance associée au taux d'accumulation d'ébauche augmente lorsque nous dévions des valeurs caractéristiques de l'Holocène (figure 3.3). La raison de cette formulation vient du fait que la reconstruction du taux d'accumulation à partir de la composition isotopique de l'eau est une loi exponentielle semi-empirique et son extrapolation à des conditions différentes de l'actuel peut être problématique.
Afin d'éviter des valeurs de variance trop faibles (trop proches de 0), nous avons implémenté une valeur seuil, σ_m, pour chaque carotte. Ainsi, si σ_A est inférieur à σ_m, σ_A est alors défini comme :

$$\sigma_A = \sigma_m \cdot \left(1 + c_{A_1} \frac{z}{z_{max}}\right) \tag{3.4}$$

où σ_m représente la valeur seuil, définie par l'utilisateur.

La LIDIE

L'écart-type associé à la LIDIE d'ébauche est défini comme :

$$\sigma_L(z) = \frac{\sigma_{b,L}}{\sigma_{b,A}} \cdot \frac{\sigma_A(z)}{1 + \frac{m_{A,loc}}{m_{A,loc}^{max}}} \tag{3.5}$$

où $m_{A,loc}$ est une moyenne locale (fenêtre de 12 ka) de l'accumulation et $m_{A,loc}^{max}$ est sa valeur maximale, $\sigma_{b,L}$ correspond à l'écart-type de référence. Dans ce cas, la variance de la LIDIE augmente parallèlement à celle de l'accumulation, soit une variance plus importante en conditions glaciaires. Ceci reflète la non–convergence entre le modèle de densification du névé et les données de $\delta^{15}N$ en Antarctique.

Les écart-types résultant de ces formulations sont présentés sur la figure 3.3. Les valeurs des différents coefficients pour chaque carotte de glace sont résumées dans la table 3.2. Le choix de ces coefficients reste subjectif, mais nous avons appliqué la méthode suivante :

— La dépendance à la profondeur pour l'accumulation et la LIDIE a seulement été considérée pour les sites de forage situés ailleurs que sur un dôme. Par

TABLE 3.2 – Table récapitulant les valeurs des différents coefficients utilisés pour calculer les variances des paramètres d'ébauche.

	Fct. amincissement			Tx accu.		LIDIE
	c_{T_1}	c_{T_2}	c_{T_3}	$\sigma_{b,A}$	c_{A_1}	$\sigma_{b,C}$
Vostok	0.01	0.000084	0.15	0.6	1	0.7
EDC	0.01	0.000030	0.15	0.7	0	0.7
EDML	0.01	0.000078	0.15	0.5	1	0.6
TALDICE	0.01	0.000268	0.15	0.6	0	0.6
NGRIP	0.01	0.000016	0.05	0.6	0	0.6

conséquent le coefficient c_{A_1} a une valeur de 1 pour Vostok et EDML, 0 pour les autres sites.

— Une variance plus grande est considérée pour la LIDIE lorsque le modèle de densification du névé et les données de $\delta^{15}N$ ne sont pas en accord, soit pour Vostok, EDML et EDC.

— Comme Vostok et EDML ne sont pas situés sur un dôme, nous avons choisi de leurs attribuer des variances sur la fonction d'amincissement plus grandes que pour EDC et NGRIP.

— Nous avons ajusté la variance pour l'amincissement de TALDICE par rapport à celle d'EDC afin d'éviter des inconsistances dues au scénario d'ébauche de TALDICE. En effet, les paramètres d'ébauche de TALDICE donnent un modèle d'âge beaucoup trop jeune avec l'optimum du MIS 5 à 110 ka (figure 3.4). Ceci est en contradiction avec les données qui montrent un optimum à environ 130 ka [Waelbroeck et al., 2008] et une incertitude de quelques milliers d'années. En conséquence nous avons augmenté la variance associée à la fonction d'amincissement d'ébauche pour TALDICE (figure 3.5).

— Les variances d'EDC et NGRIP ont été ajustées afin que la nouvelle chronologie donne un âge intermédiaire à EDC3 et NGRIPmodelext pour les MIS 4 et 5. Comme ces chronologies ont toutes deux été obtenues à l'aide de contraintes glaciologiques sur cette période, il n'y a pas de raisons d'avoir plus confiance en l'une ou l'autre.

3.1.3 Les différents marqueurs

Les marqueurs inclus dans Datice pour produire AICC2012 sont communs pour Veres et al. [2013] et Bazin et al. [2013]. La base de données combine des marqueurs absolus et orbitaux gaz et glace, des marqueurs de $\Delta depth$ ainsi que des liens stratigraphiques gaz et glace pour synchroniser les 5 carottes de glace.

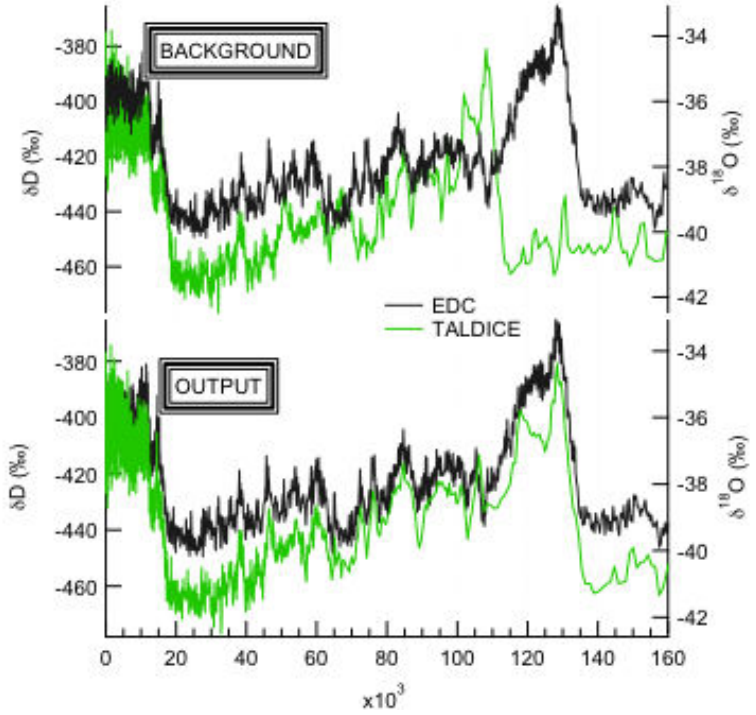

FIGURE 3.4 – Haut : chronologies glace d'ébauche pour EDC (noir) et TALDICE (vert). Bas : Chronologies glace AICC2012 pour EDC (noir) et TALDICE (vert).

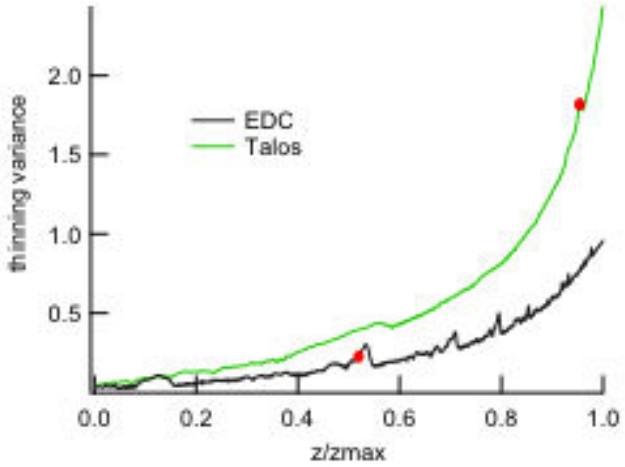

FIGURE 3.5 – Variances de la fonction d'amincissement utilisées pour construire AICC2012 pour EDC (noir) et TALDICE (vert). Les points rouges marquent la position de la Terminaison II sur chacun des profils.

AICC2012 est alors contrainte jusqu'à 800ka, grâce aux marqueurs orbitaux d'EDC, mais seulement commune jusqu'à 350 ka entre EDC et Vostok [Bazin et al., 2013]. En comparaison de la première application de Datice présentée par Lemieux-Dudon et al. [2010], nous avons supprimé les contraintes basées sur des hypothèses de synchronisation climatique et évité les liens stratigraphiques redondant entre les carottes de glace. De ce fait, nous avons retiré ou modifié les marqueurs suivant :

- les marqueurs climatiques dérivés de la synchronisation δD–insolation pour Vostok [Parrenin et al., 2001],
- le marqueur issu des spéléothèmes à 130.1 ka – voir Bazin et al. [2013],
- les marqueurs de teneur en air d'EDC et de Vostok – nous les avons remplacé par de nouveaux points [cf. Bazin et al., 2013],
- tous les points déduits par transfert successif entre les carottes de glace [Parrenin et al., 2007a].

Les marqueurs d'âge absolu

Les marqueurs absolus présentés dans cette section ont tous été datés indépendamment des chronologies carottes de glace. Tous les âges absolus, à l'exception de NGRIP, ont été déterminés par datation Ar/Ar avec le standard de Kuiper et al. [2008] "Fish Canyon sanidine" daté à 28.201 ± 0.046 Ma. Les âges de l'évènement du Laschamp, de l'éruption du Mont Moulton et de l'inversion magnétique Brunhes–Matuyama de cette étude peuvent être légèrement différents des âges publiés à cause du transfert sur le même standard.
Aucun marqueur absolu n'a été appliqué sur les carottes de TALDICE et EDML.

Vostok Les marqueurs absolus de Vostok sont tous déduits des données de ^{10}Be. Un âge de 7.18 ± 0.10 ka pour la profondeur de 178 m a été assigné par comparaison des productions de ^{10}Be et ^{14}C [Parrenin et al., 2001; Raisbeck et al., 1998].
Un second marqueur absolu est associé à l'évènement du Laschamp enregistré à 601 m avec un âge révisé de 40.65 ± 0.95 ka [Raisbeck et al., 1987; Yiou et al., 1997; Singer et al., 2009].

EDC Pour EDC, les marqueurs absolus sont issus du ^{10}Be ainsi que d'une couche de tephra. L'évènement du Laschamp a été enregistré à 740 m et associé au même âge que Vostok [40.65 ± 0.95 ka Raisbeck et al., 2006; Singer et al., 2009]. Le tephra correspondant à l'éruption du Mont Moulton a été observé à 1265.1 m [Narcisi et al., 2006]. Son âge a été déterminé une première fois par Dunbar et al. [2008] avec comme standard le "Fish Canyon Tuff" de Renne et al. [1998]. Nous l'avons donc transféré

sur le standard de [Kuiper et al., 2008] pour être cohérent, et nous avons donc obtenu un âge absolu de 93.2 ± 4.4 ka. Les deux derniers marqueurs absolus d'EDC sont associés à l'inversion magnétique de Brunhes–Matuyama (B–M) et son précurseur, observés à 3165.5 m et 3183.5 m et datés à 780.3 ka et 798.3 ka respectivement [Raisbeck et al., 2006; Dreyfus et al., 2008]. Nous avons décidé d'élargir l'incertitude associée à ces âges (de 3.5 ka à 10 ka) car l'inversion de B–M a été observée à des âges différents à ± 10 ka suivant la littérature. Ces différents âges peuvent s'expliquer par un changement spatial asynchrone de la direction du champ magnétique et/ou par un lissage due à l'incertitude sur la "lock-in depth" dans les sédiments marins [Channell et al., 2010; Camps et al., 2011; Mochizuki et al., 2011; Dreyfus et al., 2008].

NGRIP Comme dans Lemieux-Dudon et al. [2010], la nouvelle chronologie est paramétrée afin de respecter la chronologie GICC05 sur les derniers 60 ka. Pour ce faire, nous avons déduit des marqueurs à partir de cette échelle d'âge tous les 60 ans, jusqu'à 60 ka, soit 990 points. Nous leur avons associé une incertitude artificielle de 50 ans maximum afin de ressembler à la chronologie Groenland à ± 5 ans près (figure 3.6). De plus, nous n'avons pas utilisé les marqueurs absolus gaz de la table 6 de Lemieux-Dudon et al. [2010] car la chronologie gaz de NGRIP est maintenant contrainte par les liens stratigraphiques, mais aussi par des marqueurs de $\Delta depth$. Il est important de noter que la méthode utilisée pour forcer AICC2012 à ressembler à GICC05 ne respecte pas l'hypothèse d'indépendance entre les scénarios d'ébauche et les contraintes d'âge. Cependant c'était la seule façon pratique et efficace pour contraindre la chronologie sur les derniers 60 ka au moment de la construction d'AICC2012.

Les marqueurs d'âge orbitaux

Afin de compléter les marqueurs absolus, peu nombreux et principalement présents sur le dernier cycle glaciaire–interglaciaire, nous avons utilisé des marqueurs orbitaux. Ces marqueurs proviennent de la synchronisation orbitale du $\delta^{18}O_{atm}$, $\delta O_2/N_2$ et de la teneur en air. Cette méthode a déjà été utilisée pour contraindre les chronologies carottes de glace [Suwa and Bender, 2008; Parrenin et al., 2007a; Dreyfus et al., 2007; Kawamura et al., 2007]. Les marqueurs déduits de la teneur en air ont été obtenus après synchronisation de ce traceur avec une courbe d'insolation locale intégrée (ISI) choisie pour posséder les mêmes propriétés spectrales [respect des amplitudes relatives entre les pics correspondant à la précession et à l'obliquité, Raynaud et al., 2007; Lipenkov et al., 2011, plus de détails en section 5.3]. Pour

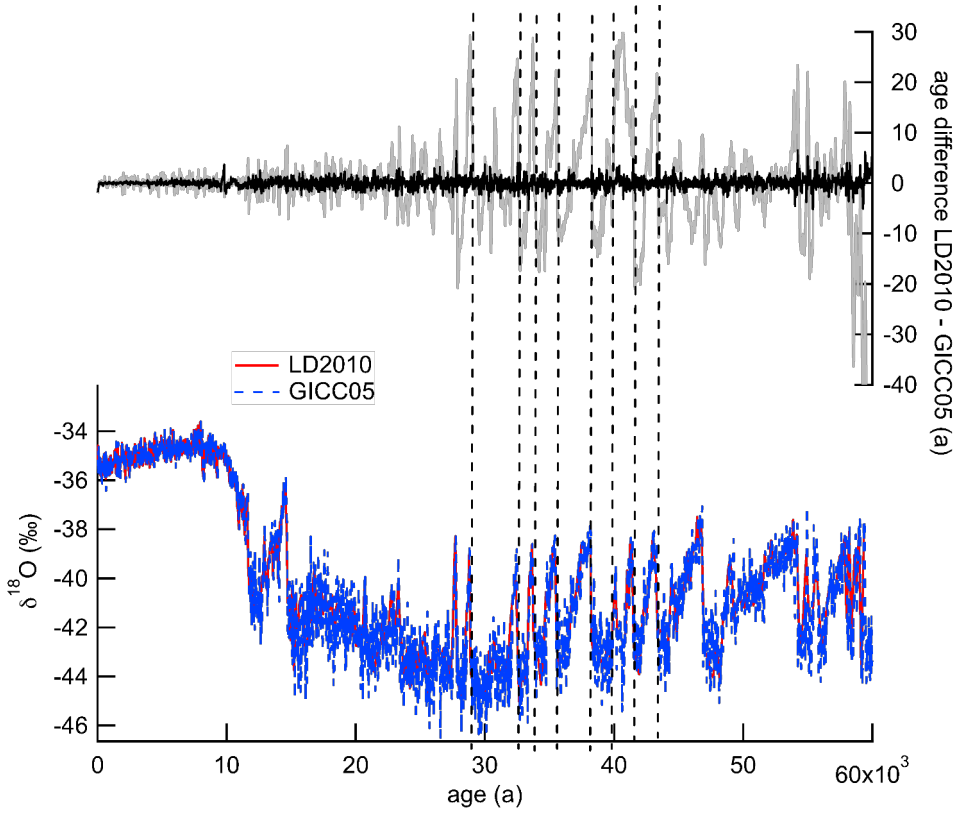

FIGURE 3.6 – Comparaison des chronologies de NGRIP. Haut : différence d'âge glace entre Lemieux-Dudon et al. [2010] et GICC05 (gris) et AICC2012 et GICC05 (noir). Bas : $\delta^{18}O$ de NGRIP sur la chronologie Lemieux-Dudon et al. [2010] (rouge) et AICC2012 (bleu).

ce faire nous avons utilisé les données de teneur en air disponibles pour Vostok et EDC, et associé les mi-pentes des deux signaux. Les marqueurs issus du $\delta O_2/N_2$ ont été repris de Suwa and Bender [2008] pour Vostok, et déduits par association des mi-pentes de la courbe composite de Landais et al. [2012] avec l'insolation locale au solstice d'été pour EDC. Dans le cas des marqueurs provenant du $\delta^{18}O_{atm}$, nous avons repris ceux de Suwa and Bender [2008] pour Vostok, et revu ceux de Dreyfus et al. [2007] pour EDC. La synchronisation orbitale du $\delta^{18}O_{atm}$ a été réalisée par association des mi-pentes de ce traceur avec le signal de precession retardé de 5 ka.

Les marqueurs issus de la teneur en air et du $\delta O_2/N_2$ servent à contraindre la chronologie glace, alors que les marqueurs déduits du $\delta^{18}O_{atm}$sont appliqués à la phase gaz. Plus de détails sur les marqueurs orbitaux utilisés et leurs incertitudes associées sont donnés dans Bazin et al. [2013] (section 3.2). Ici nous justifions seulement le choix de garder ou non certains marqueurs orbitaux présentés dans l'article. Pour la version finale d'AICC2012, nous avons décidé de retirer trois marqueurs orbitaux gaz issus du $\delta^{18}O_{atm}$ autour du MIS 12 à EDC. La figure 3.7 montre la comparaison entre le scénario d'ébauche de la LIDIE, construit à partir de données de $\delta^{15}N$ sur cette période, ainsi que les LIDIE obtenues en sortie de Datice. Nous pouvons voir que l'implémentation de certaines contraintes issues du $\delta^{18}O_{atm}$ entraîne l'apparition de variations rapides de la LIDIE de 10 m en 12 ka vers les MIS 12 et 14. Ces variations ne paraissent pas réalistes. Nous n'observons pas de zone convective dans les conditions actuelles à Dôme C, nous supposons donc qu'aucune zone convective ne devrait affecter la relation $\delta^{15}N$ –LIDIE à ce site sur les derniers 800 ka. De plus, la reconstruction de la LIDIE à partir du $\delta^{15}N$ semble robuste, ce qui nous amène donc à reconsidérer la cohérence de ces marqueurs d'âge. Nous pouvons noter que le retrait de ces trois marqueurs a très peu d'impact sur la chronologie finale, avec des changements bien inférieurs à l'incertitude d'AICC2012 (figure 3.7 bas).

Les fonctions d'amincissement d'EDC issus des chronologies EDC3 et AICC2012 présentent des variations de même amplitude et aux mêmes profondeurs au fond de la carotte [figure 3.8 Parrenin et al., 2007a; Dreyfus et al., 2007]. Nous remarquons ici que ces variations de la fonction d'amincissement sont aussi présentes lorsque seulement les marqueurs de $\delta O_2/N_2$ sont considérés pour le fond de la carotte. Ces résultats montrent que ce comportement de la fonction d'amincissement est robuste.

Les marqueurs de $\Delta depth$

Les marqueurs de $\Delta depth$ sont seulement implémentés pour NGRIP au cours de la dernière période glaciaire. Ces marqueurs sont déduits à partir de l'observation

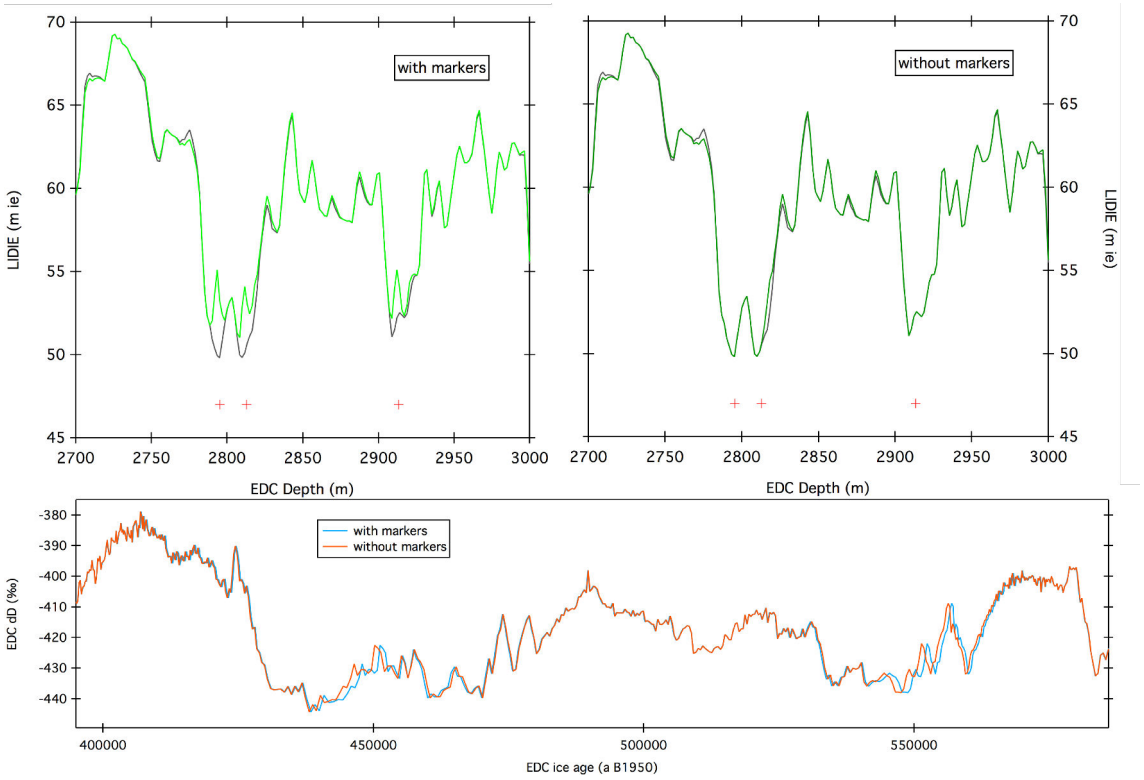

FIGURE 3.7 – Haut : influence des marqueurs de $\delta^{18}O_{atm}$ sur la LIDIE d'EDC vers le MIS 12 (noir : ébauche, vers : sortie de Datice). Les croix rouges indiquent la position des marqueurs de $\delta^{18}O_{atm}$ qui sont inclus (gauche) ou retirés (droite) lors du test de sensibilité. Bas : δDd'EDC sur les chronologies résultantes : avec les points (bleu) et sans les points (orange).

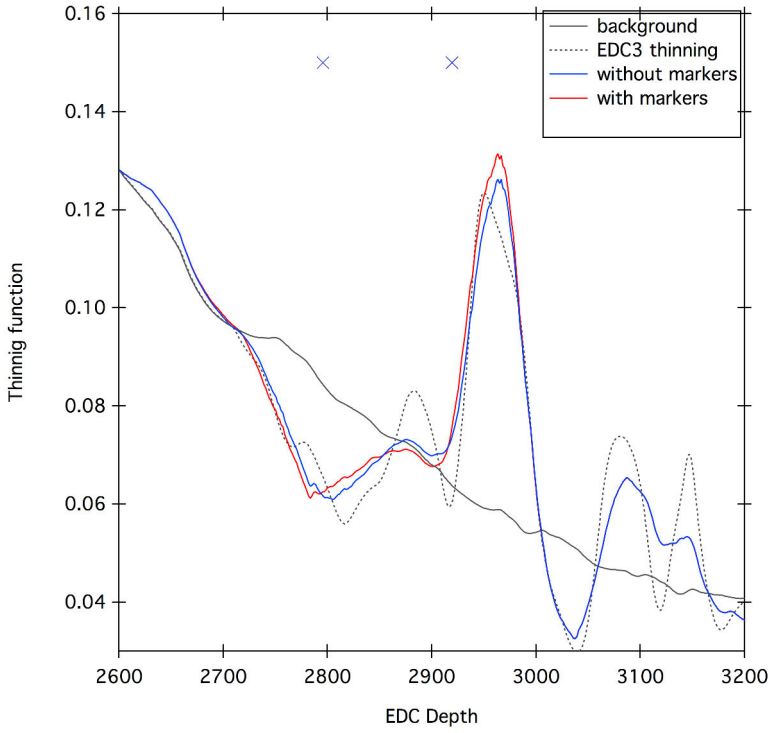

FIGURE 3.8 – Fonction d'amincissement de la carotte EDC entre 540–600 ka. Les croix bleues indiquent la position des marqueurs de $\delta O_2/N_2$. La courbe noir correspond à l'amincissement d'ébauche pour AICC2012, la courbe pointillée est l'amincissement obtenu lors de la construction de la chronologie EDC3, la courbe bleue est obtenue lorsque les 2 marqueurs de $\delta O_2/N_2$ ne sont pas considérés, et la courbe rouge est l'amincissement obtenu pour AICC2012 (qui prend en compte ces points).

TABLE 3.3 – Liste des marqueurs de $\Delta depth$ inclus dans Datice pour AICC2012.

Profondeur (m)	$\Delta depth$	Incertitude (m)
2099.9	16.29	2
2123.6	15.8	2
2157.1	15.56	2
2218.2	15.7	2
2255.6	12.85	2
2345.2	11.74	2
2364.5	12.36	2
2419.31	11.6	2
2465.1	8.85	2
2506.9	8.16	1.5
2577.8	7.66	1.5
2685.1	7.15	2
2890.2	5.54	2
2895.8	4.44	1.5
2936.5	7.8	1.5

d'un même évènement de Dansgaard–Oeschger à une profondeur dans le $\delta^{18}O$ de la glace et à une autre profondeur dans le $\delta^{15}N$ mesuré dans l'air. Les marqueurs de $\Delta depth$ sont définis comme soit les mi–pentes associées du $\delta^{18}O$ de la glace et du $\delta^{15}N$de l'air, soit comme leurs pics respectifs. Nous estimons une incertitude d'environ 1.5–2 m pour ces marqueurs vue la résolution des mesures et la méthode utilisée pour estimer le Δdepth (mi–pente ou pic, table 3.3).

Les liens stratigraphiques gaz

Les liens stratigraphiques gaz sont obtenus par identification de mêmes variations au sein du méthane et du $\delta^{18}O_{atm}$ publiés (table 3.4). Certains liens stratigraphiques de NGRIP ont été déduits à partir des données de $\delta^{15}N$ lors de réchauffements rapides [Capron et al., 2010]. Dans quelques cas les incertitudes associées ont été augmentées à cause d'incohérences avec les scénarios de la fonction d'amincissement, du taux d'accumulation ou de la LIDIE. Quelques points ont dû être retirés pour ces mêmes raisons.

Les liens stratigraphiques glace

Les liens stratigraphiques glace entre les carottes d'Antarctique sont identifiés à partir de la présence de pics de sulfate communs à plusieurs carottes (table 3.5). Ces pics de sulfate sont d'origine volcanique. En effet, lors d'éruptions volcaniques

TABLE 3.4 – Liens stratigraphiques gaz entre les différentes carottes.

Paires	Nb. de points	Sources
Vostok-EDC	67	Lemieux-Dudon et al. [2010] Loulergue [2007] This study
Vostok-TALDICE	8	cette thèse
Vostok-NGRIP	5	Landais et al. [2006]
EDC-EDML	64	Schilt et al. [2010] Loulergue et al. [2007] Loulergue [2007] cette thèse
EDC-TALDICE	22	Buiron et al. [2011] Schüpbach et al. [2011]
EDC-NGRIP	6	Schilt et al. [2010]
EDML-TALDICE	13	Schüpbach et al. [2011]
EDML-NGRIP	45	Lemieux-Dudon et al. [2010] Schilt et al. [2010] Capron et al. [2010]
NGRIP-TALDIC	25	Buiron et al. [2011] (profondeurs NGRIP révisées)

différents produits sont éjectés dans la troposphère et la stratosphère, puis ensuite amenés à la surface de la calotte par dépôt sec ou humide et préservés dans la glace sous forme de couches de tephra ou pics de sulfate. Suivant l'importance des éruptions, il est possible de retrouver des signaux communs entre les différentes carottes de glace. C'est par cette méthode qu'ont été déterminés les liens entre Vostok et EDC, EDC et EDML ainsi que pour EDC et TALDICE. L'erreur associée à ces marqueurs varie en fonction de la confiance accordée à l'identification des pics communs, mais aussi dans certains cas au transfert entre plusieurs carottes d'un même site (exemple d'EDC et Vostok).
Les deux liens présents entre EDC et NGRIP sont issus de l'identification d'un double pic de ^{10}Be au niveau du Laschamp [table 3.5, Loulergue et al., 2007]. Même si les mesures du ^{10}Be ne sont pas encore disponibles pour NGRIP, la synchronisation a été effectuée au travers de GRIP, puis par transfert sur NGRIP grâce à la synchronisation volcanique entre GRIP et NGRIP faite dans le cadre de GICC05 [Rasmussen et al., 2006].

Les sites de NGRIP et EDML sont deux sites présentant de fort taux d'accumulation actuellement. Grâce à cette propriété, il est possible de compter annuellement

les couches de glace sur toute la période Holocène, mais aussi sur des périodes présentant des contraintes chronologiques indépendantes [excursion du Laschamp, éruption du Toba, Vinther et al.; Svensson et al., 2013]. C'est par cette méthode qu'ont été déterminés les liens stratigraphiques glace entre NGRIP et EDML. Nous pouvons noter que cette synchronisation contribue au forçage de la chronologie AICC2012 à respecter l'échelle d'âge GICC05.

TABLE 3.5 – Liens stratigraphiques glace entre les différentes carottes.

Paires	Nb. de points	Sources
Vostok-EDC	104	Udisti et al. [2004] Narcisi et al. [2005] Parrenin et al. [2012b] (profondeurs transférées sur EDC99 et Vostok 5G)
EDC-EDML	273	Ruth et al. [2007] Severi et al. [2007]
EDC-TALDICE	112	Severi et al. [2012]
EDC-NGRIP	2	Loulergue et al. [2007]
EDML-NGRIP	87	Vinther et al. Svensson et al. [2013]

3.2 AICC2012 : Veres et al. [2013]; Bazin et al. [2013]

Clim. Past, 9, 1733–1748, 2013
www.clim-past.net/9/1733/2013/
doi:10.5194/cp-9-1733-2013

Climate of the Past
Open Access

The Antarctic ice core chronology (AICC2012): an optimized multi-parameter and multi-site dating approach for the last 120 thousand years

D. Veres[1,2], L. Bazin[3], A. Landais[3], H. Toyé Mahamadou Kele[4], B. Lemieux-Dudon[4], F. Parrenin[1], P. Martinerie[1], E. Blayo[4], T. Blunier[5], E. Capron[6], J. Chappellaz[1], S. O. Rasmussen[5], M. Severi[7], A. Svensson[5], B. Vinther[5], and E. W. Wolff[6]

[1]UJF – Grenoble 1/CNRS, Laboratoire de Glaciologie et Géophysique de l'Environnement (LGGE), UMR5183, CNRS/INSU – Grenoble, 38041, France
[2]Institute of Speleology, Romanian Academy, 400006 Cluj-Napoca, Romania
[3]Laboratoire des Sciences du Climat et de l'Environnement, UMR8212, CNRS – Gif sur Yvette, France
[4]Laboratoire Jean Kuntzmann, Grenoble, France
[5]Centre for Ice and Climate, Niels Bohr Institute, University of Copenhagen, Copenhagen, Denmark
[6]British Antarctic Survey, Cambridge, UK
[7]Department of Chemistry Ugo Schiff, University of Florence, Florence, Italy

Correspondence to: D. Veres (daniel.veres@lgge.obs.ujf-grenoble.fr, danveres@hasdeu.ubbcluj.ro), L. Bazin (lucie.bazin@lsce.ipsl.fr), and A. Landais (amaelle.landais@lsce.ipsl.fr)

Received: 15 November 2012 – Published in Clim. Past Discuss.: 3 December 2012
Revised: 24 June 2013 – Accepted: 25 June 2013 – Published: 1 August 2013

Abstract. The deep polar ice cores provide reference records commonly employed in global correlation of past climate events. However, temporal divergences reaching up to several thousand years (ka) exist between ice cores over the last climatic cycle. In this context, we are hereby introducing the Antarctic Ice Core Chronology 2012 (AICC2012), a new and coherent timescale developed for four Antarctic ice cores, namely Vostok, EPICA Dome C (EDC), EPICA Dronning Maud Land (EDML) and Talos Dome (TALDICE), alongside the Greenlandic NGRIP record. The AICC2012 timescale has been constructed using the Bayesian tool Datice (Lemieux-Dudon et al., 2010) that combines glaciological inputs and data constraints, including a wide range of relative and absolute gas and ice stratigraphic markers. We focus here on the last 120 ka, whereas the companion paper by Bazin et al. (2013) focuses on the interval 120–800 ka.

Compared to previous timescales, AICC2012 presents an improved timing for the last glacial inception, respecting the glaciological constraints of all analyzed records. Moreover, with the addition of numerous new stratigraphic markers and improved calculation of the lock-in depth (LID) based on δ^{15}N data employed as the Datice background scenario, the AICC2012 presents a slightly improved timing for the bipolar sequence of events over Marine Isotope Stage 3 associated with the seesaw mechanism, with maximum differences of about 600 yr with respect to the previous Datice-derived chronology of Lemieux-Dudon et al. (2010), hereafter denoted LD2010. Our improved scenario confirms the regional differences for the millennial scale variability over the last glacial period: while the EDC isotopic record (events of triangular shape) displays peaks roughly at the same time as the NGRIP abrupt isotopic increases, the EDML isotopic record (events characterized by broader peaks or even extended periods of high isotope values) reached the isotopic maximum several centuries before.

It is expected that the future contribution of both other long ice core records and other types of chronological constraints to the Datice tool will lead to further refinements in the ice core chronologies beyond the AICC2012 chronology. For the time being however, we recommend that AICC2012 be used as the preferred chronology for the Vostok, EDC, EDML and TALDICE ice core records, both over the last glacial cycle

(this study), and beyond (following Bazin et al., 2013). The ages for NGRIP in AICC2012 are virtually identical to those of GICC05 for the last 60.2 ka, whereas the ages beyond are independent of those in GICC05modelext (as in the construction of AICC2012, the GICC05modelext was included only via the background scenarios and not as age markers). As such, where issues of phasing between Antarctic records included in AICC2012 and NGRIP are involved, the NGRIP ages in AICC2012 should therefore be taken to avoid introducing false offsets. However for issues involving only Greenland ice cores, there is not yet a strong basis to recommend superseding GICC05modelext as the recommended age scale for Greenland ice cores.

1 Introduction

The last climatic cycle (last 120 thousand years before present, hereafter ka BP, with present defined as 1950 AD in our study) of the Earth's climate history represents one of the best-studied periods in paleoclimatology, owing to the exceptional insights it provides into several windows of past climate change, all significantly different from each other (Grootes et al., 1993; Masson-Delmotte et al., 2005; Wolff et al., 2010). These include for example the glacial inception and abrupt centennial-to-millennial stadial and interstadial climate variability, the cryosphere expansion that culminated into full glacial climates during Marine Isotope Stages (MIS) 4 and 2, followed by the dynamic environmental changes of the last termination (NGRIP members, 2004; EPICA Community Members, 2004, 2006; Pedro et al., 2011).

From the moment of their discovery decades ago in Greenland ice core records (Dansgaard et al., 1982, 1984), centennial-to-millennial scale climate oscillations, known also as Dansgaard–Oeschger (DO) events, have been the subject of intense research to document their nature, amplitude of change, and links with paleoenvironmental and low-latitude records (e.g. Grootes et al., 1993; NGRIP members, 2004; Landais et al., 2004; Masson-Delmotte et al., 2005; Huber et al., 2006; Loulergue et al., 2008; Wolff et al., 2010). The DO events, most clearly observed in the North Atlantic region, are recorded in Greenland ice cores as abrupt temperature increases of 8–16 °C in a few centuries from cold periods (Greenland stadials, GS) to warm periods (Greenland interstadials, GI) (Severinghaus et al., 1998; Lang et al., 1999; Landais et al., 2004; Huber et al., 2006), while the coolings are more gradual. Associated with the abrupt temperature increases in Greenland, the so-called Antarctic Isotopic Maxima (AIM) have been observed in Antarctic ice core records (e.g. EPICA Community Members, 2006). In the Antarctic records however, the water isotope variability is characterized by more gradual temperature changes (approximately 2 °C per millennium), with Greenland stadials generally corresponding to periods of increasing isotope ratios in Antarctica (Blunier et al., 1998; Blunier and Brook, 2001; Jouzel et al., 2007; Kawamura et al., 2007; Wolff et al., 2009; Barker et al., 2011). In addition to the ice core evidence, a range of proxies in various types of paleoclimate archives host the imprint of these climate oscillations (Voelker, 2002), with the most chronologically significant constraints linked to radiocarbon-dated varved records (e.g. Bronk Ramsey et al., 2012), marine series (Lisiecki and Raymo, 2005 and references therein; Waelbroeck et al., 2008), or absolutely dated cave carbonate records (Drysdale et al., 2007; Wang et al., 2008; Cheng et al., 2009; Fleitmann et al., 2009; Boch et al., 2011).

Still, many questions remain open on the mechanisms and feedbacks within the climate system that were behind the generation and propagation of these events. Such understanding would be greatly facilitated if the regional synchronicity of change and timing of events (Blaauw et al., 2010; Braun et al., 2011; Klauenberg et al., 2011) could be tested with respect to the contrasting thermo-climatic relationship between the polar regions as predicted by the bipolar seesaw hypothesis (Stocker and Johnsen, 2003; Steig et al., 1998; Pedro et al., 2011; Barker et al., 2011; Stenni et al., 2011; Buiron et al., 2012). Advancements in the absolute dating and relative synchronization of records are thus of primary importance for paleoclimatic archives (Blockley et al., 2012 and references therein), including ice cores (Parrenin et al., 2004, 2007, 2012a, 2013; Kawamura et al., 2007; Svensson et al., 2008; Lemieux-Dudon et al., 2010).

A significant issue when dealing with ice cores, however, is that two time-depth relationships must be assessed, one concerning the ice-phase (water isotopes, particulates and chemical impurities, etc.) and one for the gas-phase related proxies (CO_2, CH_4, air isotopes, etc.). This particularity arises from the fact that at any depth, the entrapped air is always younger than the surrounding ice (Sowers et al., 1992 and references therein). This age difference, called Δage, reflects the fact that air is isolated from the atmosphere only at 50–120 m under the ice sheet surface, where firn progressively reaches the density of ice. Knowing the temporal evolution of this lock-in depth (hereafter LID) for each ice core is therefore essential for establishing reliable links between ice and gas chronologies. Classically, estimating LID was based on firn densification models forced by estimates of past accumulation rate and temperature changes (e.g. Schwander et al., 1997; Arnaud et al., 2000; Goujon et al., 2003). However, studies have shown that firn densification models may provide inaccurate constraints that result in overestimating the glacial LID and hence Δage in remote sites of East Antarctica where temperature and accumulation rates, particularly during glacial times, were very low (Loulergue et al., 2007; Parrenin et al., 2012b, 2013). For such settings, the $\delta^{15}N$ of N_2 in the ice-entrapped air, linearly linked to the height of the firn diffusive zone, gives an alternative estimate of LID. Indeed, for remote sites of East Antarctica, the depth of the firn diffusive zone deduced from

$\delta^{15}N$ of N_2 is systematically lower by up to 40 m than the LID deduced from firnification models (Caillon et al., 2003; Dreyfus et al., 2007). By using a compilation of ice and gas stratigraphic markers from three Antarctic ice cores, Parrenin et al. (2012b) have indeed shown that over the last deglaciation at EPICA Dome C (EDC), the $\delta^{15}N$ of N_2 gives a more reliable estimate of LID than firn densification modelling. Following on these arguments, and assuming that the convective zone at the top of the firn did not increase significantly during glacial periods, the $\delta^{15}N$ of N_2 can thus be used alternatively to reconstruct past LID variations, with lower LID and hence Δage over glacial periods than those suggested by firn densification models (Capron et al., 2013; Parrenin et al., 2013).

Here we report on the development of the common timescale AICC2012-Antarctic Ice Core Chronology 2012 over the last glacial period (0–120 ka BP) constructed for four Antarctic, Vostok, EDC, EPICA Dronning Maud Land (EDML) and Talos Dome (TALDICE), and one Greenland (NGRIP) ice cores. New developments over the period 120–800 ka are being treated in the companion paper of Bazin et al. (2013). In the following, we first describe the initial ice core chronologies and associated dating constraints that have been implemented in AICC2012. Then, we discuss the numerous stratigraphic markers included in the inverse modelling analysis, which strongly constrain the relative timing of Greenland and Antarctic records over the last glacial period. Finally, we present some examples of the absolute and relative dating implications of the new chronology over the last glacial inception, and for the bipolar sequence of events associated with the seesaw mechanism over middle MIS 3, respectively. Note that the Supplementary Online Material (SOM) presents common material (methodology and the AICC2012 timescale) for both this work and that of Bazin et al. (2013).

2 The ice core records analyzed

Ice cores recovered from high accumulation settings, such as the Summit Greenland or the coastal Antarctic regions, allow for reliable chronological constraints based on annual or sub-annual layer counting backed by high-resolution glaciochemical and impurity records (Legrand and Mayewski, 1997; Rasmussen et al., 2006; Svensson et al., 2008, 2013). The latter parameters also allow for the identification of common stratigraphic markers that have potential in securely linking records (Zielinski, 2000; Rasmussen et al., 2008; Wolff et al., 2009; Parrenin et al., 2012a), independently of climate modulated proxies such as water isotopes frequently used in data comparison (Grootes et al., 1993; Dahl-Jensen et al., 1998; Masson-Delmotte et al., 2005; Jouzel et al., 2007). The Greenland ice records, although providing exceptional resolution, are limited on a temporal scale and generally do not extend beyond MIS 5 (NGRIP Members, 2004). On the other hand, most Antarctic records, particularly the ones spanning several glacial-interglacial cycles, still rely mainly on glaciological modelling, tuning to orbital parameters, or matching to other dated records for deriving age constraints (Petit et al., 1999; Parrenin et al., 2001, 2004, 2007; Ruth et al., 2007; Kawamura et al., 2007).

We present below a short overview of the original timescales of the ice cores included in the building of the AICC2012 chronology; NGRIP, Vostok, EDC, and EDML have been already synchronized in the LD2010 timescale over the last 50 ka. Subsequently, the TALDICE chronological framework was also built using the Datice tool as discussed in Buiron et al. (2011).

2.1 NGRIP and the composite Greenlandic ice core timescale GICC05

The GICC05 composite timescale provides the most accurate annual chronological constraints for the Greenland ice cores up to 60.2 ka BP. It has been constructed by annual layer counting using water isotopic data from DYE-3, GRIP and NGRIP from present and back to 7.9 ka (Vinther et al., 2006), detailed glaciochemical data from GRIP and NGRIP for the last termination (Rasmussen et al., 2006), and similar parameters aided by visual stratigraphy records back to 60.2 ka BP (Svensson et al., 2008). Because of the cumulative nature of errors when counting annual layers, the relative maximum counting error (at 2σ) of the number of layers are in the order of 2–4 % for late MIS 3 and MIS 2, but exceed 5 % for the early MIS 3 interstadials GI-13 to GI-17, although the GICC05 absolute age uncertainties (at 1σ) remain below 2.2 %.

For NGRIP record we employed the GICC05 composite timescale for the last 60 ka BP, including the accumulation rate estimates derived from layer thickness (Svensson et al., 2008). Beyond 60 ka BP we used constraints from the GICC05modelext timescale that was constructed by patching the ss09sea-modeled age scale shifted to younger ages by 705 yr in order to match it to the end of the annual-layer-counted timescale (Wolff et al., 2010). As for GICC05, the thinning function for the GICC05modelext was taken from the Dansgaard–Johnsen ice flow model adapted to NGRIP, whereas the accumulation rate of GICC05modelext beyond 60 ka BP was calculated from the water isotope data (NGRIP Members, 2004) in the absence of continuous layer counting over that core section.

2.2 Vostok ice core record

The GT4 timescale published by Petit et al. (1999) treated the whole length of the Vostok ice core corresponding to the last 400 ka BP and is based primarily on glaciological modelling with limited point anchoring to selected intervals of a marine $\delta^{18}O$ and magnetic susceptibility records. More recently, Parrenin et al. (2001, 2004) improved the dating of the

Vostok record through inverse dating methods by building an initial thinning function, taking into account the ice origin and a range of anchoring points (^{10}Be alongside six orbital climatic links between insolation peaks and mid-slopes of δD at Termination I with a lag of 3000 yr). These orbital points were also included in the LD2010 timescale, but have been removed in the current AICC2012 chronology (Bazin et al., 2013), whereas the thinning scenario for Vostok initially proposed by Parrenin et al. (2004) has been retained in the AICC2012 background scenario (see SOM).

2.3 EPICA Dome C (EDC) ice core record

The EDC record covers the last 800 ka BP (EPICA Community Members, 2004; Jouzel et al., 2007; Loulergue et al., 2008), and currently, analysis of this ice core relies on the EDC3 chronology proposed by Parrenin et al. (2007) based on ice flow modelling and an inverse method constrained by a limited number of reference age markers. Over the last Termination, the EDC3 age scale used two methane tie points for synchronization with the layer-counted Greenland GICC05 chronology. Other age markers include an absolutely dated ash layer (Dunbar et al., 2008), peaks in cosmogenic isotopes (Raisbeck et al., 2007), and a speleothem-derived absolute age link with the abrupt methane increase at Termination II, and only orbital tuning and a single absolute age marker (the Brunhes–Matuyama reversal recorded in ^{10}Be) beyond (Parrenin et al., 2007). Recently, Parrenin et al. (2013) provided evidence of no-lag between atmospheric CO_2 and surface air temperature during the last deglacial warming at EDC based on revised relative age scale for the EDC record. It has been constructed following improved depth synchronization between the EDC ice cores, improved δ^{15}N-based Δdepth estimates in constraining the gas age, and linear interpolation between selected tie-points.

2.4 EPICA Dronning Maud Land (EDML) ice core record

The EPICA Dronning Maud Land EDML-1 timescale, covering the last 150 ka BP, has been derived directly from the EDC3 timescale (Parrenin et al., 2007) by stratigraphic matching and data synchronization between the two ice records (Ruth et al., 2007). Over the last 128 ka BP, 322 common volcanic stratigraphic horizons were identified in both ice cores. Additional chronological control has been derived from dated volcanic events and the match to the GICC05 timescale via ^{10}Be and methane. The difference between EDML-1 and EDC3 was estimated as less than 450 yr over the last 128 ka BP, and lower than 130 yr over the last 60 ka BP (Ruth et al., 2007).

2.5 Talos Dome (TALDICE) ice core record

The TALDICE ice core record drilled at Talos Dome in East Antarctica covers the last 250 ka BP (Stenni et al., 2011). The TALDICE-1 chronology first published by Buiron et al. (2011) uses stratigraphic (ice and gas) markers to constrain the inverse modelling method of Lemieux-Dudon et al. (2010). This chronology is principally based on methane synchronizations (Spahni et al., 2005; Blunier et al., 2007; Loulergue et al., 2007) with Greenland composite and EDC records. Due to the high accumulation rates in the area, TALDICE provides decadal time resolution during the Holocene and the last deglaciation. The relative uncertainties reported were relatively small, 300 yr for early Holocene and the last deglaciation, 500 yr back to 17.5 ka BP, and up to 1500 yr for the last glacial, but increased significantly for older periods (Buiron et al., 2011).

A chronological refinement for the period 55–112 ka BP and called TALDICE-1a has been proposed by Schüpbach et al. (2011) using high-resolution methane synchronization with the EDC methane record (Loulergue et al., 2007, 2008). Based on this approach, and employing several newly defined tie-points, the uncertainties relative to EDC3 were lowered to less than 1100 yr for this interval.

3 Methodology and approach

3.1 The Datice inverse modelling

The probabilistic inverse modelling employed here is an updated version of the Datice Bayesian inference tool presented in Lemieux-Dudon et al. (2010). The model dynamically constructs parallel chronologies simultaneously for the analyzed ice core records by correcting the associated background information for past accumulation rates, thinning function, and lock-in-depth in ice equivalent (LIDIE), and taking into account independent stratigraphic markers for the ice (based on volcanogenic sulphate, tephra, and ^{10}Be data) and gas (derived from CH_4 and $\delta^{18}O_{atm}$), as well as absolute and orbital age estimates. The optimization of this approach is therefore dependent also on the number, distribution and uncertainties associated with the tie-points (Buiron et al., 2011). The optimization of the system provides analyzed ice and gas chronologies for each ice core as well as modified glaciological quantities (i.e. thinning function, accumulation rate, and LIDIE, respectively).

A detailed description of the model and its application is provided in Lemieux-Dudon et al. (2010), and information on the current constraints and application updates are presented in more detail in the SOM and Bazin et al. (2013).

3.2 Application

3.2.1 Background information

A comprehensive presentation of the background parameters used (initial thinning, accumulation rate, and LID with the associated variances) is given in the SOM. For our application, one aim was to produce an Antarctic chronology that

was tied to GICC05 over the last 60 ka BP, and independent beyond. This decision enables straightforward comparisons between Greenland and Antarctica, without introducing a new Greenland age scale for the last 60 ka BP that based on our observations would very closely follow GICC05. We consider this approach to be justified until significant and validated new absolute age markers in this age interval will be available. As a consequence, the background thinning and accumulation rate profiles for NGRIP are exactly those of GICC05 and GICC05modelext (Svensson et al., 2008; Wolff et al., 2010). For the Antarctic ice cores, the background thinning scenarios were deduced from glaciological models, whilst the accumulation rate was deduced from the water isotopes records through a simple exponential law (details in SOM). The associated variances were adjusted so that: (1) the final thinning function was allowed to deviate more from the background scenario for drilling sites with a complicated ice flow history (e.g. EDML (Huybrechts et al., 2007) and Vostok (Parrenin et al., 2001) on a dome flank; TALDICE (Stenni et al., 2011) with probably increased ice sheet thickness at the Last Glacial Maximum); and (2) the final accumulation rates were allowed to deviate more from the background scenarios when output values deviated far from present-day values based on which the exponential law linking accumulation rate and water isotopes had been calibrated (details in SOM).

Finally, where modelling outputs agreed with constraints from the δ^{15}N-based estimates, the background LIDIE was calculated from firn densification models such as for TALDICE (Capron et al., 2013) or NGRIP (Landais et al., 2004; Huber et al., 2006). At the other sites, a background scenario derived from δ^{15}N was chosen, since it gives more plausible results over the last deglaciation, as for example at EDC (Parrenin et al., 2012b, 2013). This choice of LIDIE background scenario is important since in remote sites of East Antarctica such as Vostok and EDC, the LIDIE is almost 65 % smaller for the glacial period when using the δ^{15}N scenario, assuming no increase of convective zone (during glacial period) compared to the outputs derived from classical firn densification modelling (Schwander et al., 1997; Arnaud et al., 2000; Goujon et al., 2003). Moreover, because there are still questions of what is the best background LIDIE to choose between densification modelling and δ^{15}N, larger variances for LIDIE have been associated for the latter sites, where model and δ^{15}N-derived constraints strongly disagree (see SOM). Finally, both LIDIE scenarios have been tested (SOM), and although none of the LIDIE background scenarios is fully satisfying, it confirms the results of Parrenin et al. (2012b, 2013) that over the last deglaciation at EDC, the LIDIE calculated from δ^{15}N is in much better agreement with the combination of ice and gas stratigraphic markers than the LIDIE calculated by firn densification models alone.

3.2.2 Ice stratigraphic markers

Recently, Parrenin et al. (2012a) refined and extended the synchronization between EDC and Vostok ice cores over the interval 0–145 ka BP through the identification of common volcanic sulphate stratigraphic marker horizons. One hundred four (104) volcanic tie links were proposed following on the previous work of Udisti et al. (2004) that covered only the 0–45 ka BP interval. The synchronization-related uncertainties included in our study were grouped into three ranges, 200 yr for the last 40 ka BP, 150–350 yr between 105–145 ka BP and 500 yr for the glacial period. The relatively large uncertainty reflects the fact that volcanic tie-points are not retrieved from a single core at Vostok but from a combination of ice cores with possible shifts of up to 3 m in-between the individually logged core depths (Parrenin et al., 2012a).

The EDC and EDML ice core records were also synchronized, using mainly volcanic stratigraphic markers identified in the ice phase (Ruth et al., 2007; Severi et al., 2007). We translated the original EDC96 core depths on which these markers were first proposed to the corresponding depths of core EDC99 (following the approach of Parrenin et al., 2012a), and include in our analysis 273 stratigraphic tie links derived from these two records. The majority of the tie points cover the last 120 ka (Fig. 1). Uncertainties attached to these points were 20 yr for "certain" tie points and 100 yr for "probable" tie-points, depending on the proposed confidence levels and our revision (Ruth et al., 2007; Severi et al., 2007).

The work by Severi et al. (2012) reports on the recently accomplished age scale synchronization between the TALDICE and the EDC ice cores, and carried on through the identification of common glaciochemical volcanic signatures. From the range of markers proposed, we employed in our analysis 112 markers (only the "certain" and "probable" ones) stretching over the last 42 ka BP, with attached uncertainties of 20 and 100 yr. Prior to the analysis, the original EDC96 core depths on which these markers were first proposed were translated to the depths of core EDC99 (Fig. 1). Moreover, two stratigraphic tie links with uncertainties of 110 yr tie the EDC and the NGRIP records at the Laschamp geomagnetic excursion (Loulergue et al., 2007).

New records of bipolar volcanic spikes matching between EDML and NGRIP ice cores are currently being proposed following the identification of common glaciochemical stratigraphic features in both records for the Holocene (Vinther et al., 2012), and around 41 ka BP, at the time of the Laschamp geomagnetic excursion (Svensson et al., 2013). The EDML – NGRIP synchronization is further constrained by annual layer counting between the tie points, resulting in a strong interhemispheric link at decadal precision between GI-20 and AIM19/20 at the time of the Toba eruption, around 74 ka BP. From the data points proposed, we used 87 tie links with 50 yr uncertainties for the Holocene and MIS 3, and 100 yr uncertainty for those identified in late MIS 5 (Fig. 1).

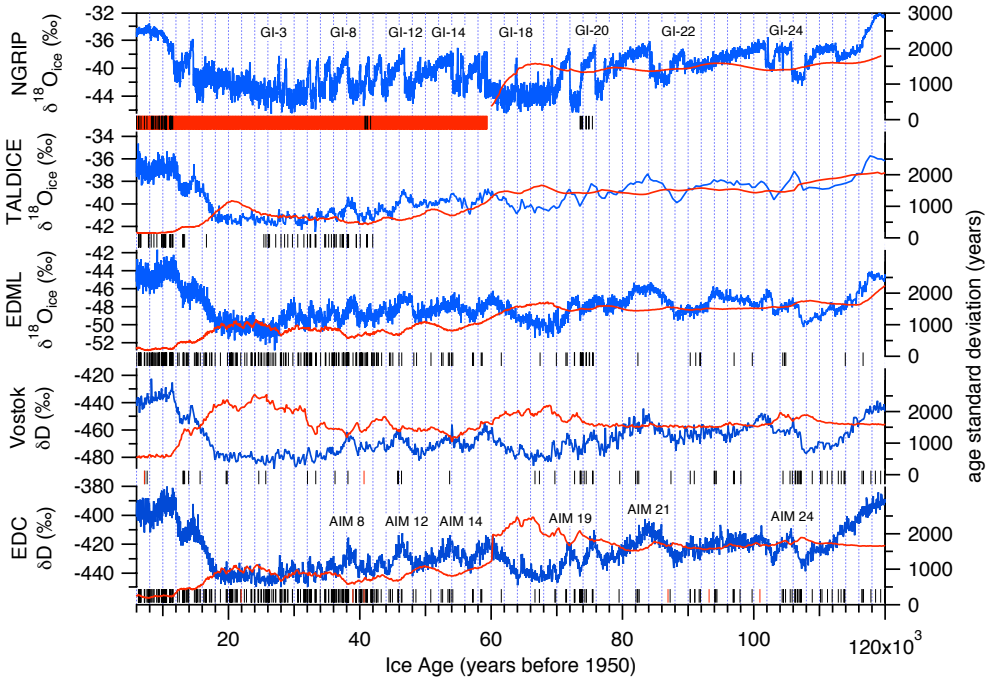

Fig. 1. Water isotopic records from the five ice cores analyzed. From top to bottom: NGRIP (NGRIP members, 2004), TALDICE (Stenni et al., 2011), EDML (EPICA Community Members, 2006), Vostok (Petit et al., 1999), and EDC (Jouzel et al., 2007) on the AICC2012 chronology. Vertical black bars indicate the location of the ice stratigraphic markers and red bars the location of the absolute tie-points in the ice phase. For NGRIP, absolute tie-points are located every meter to closely fit AICC2012 chronology to GICC05 over the last 60 ka. The red lines (right axes) show the ice age standard deviation in years for each of the ice core analyzed. GI- refers to Greenland interstadials and the AIM to selected Antarctic Isotopic Maxima events.

No volcanic stratigraphic ice tie points have been reported between Vostok and EDML, TALDICE or NGRIP, or between TALDICE and EDML.

3.2.3 Gas stratigraphic markers

Methane and the isotopic composition of oxygen ($\delta^{18}O_{atm}$) from air bubbles entrapped in ice provide exceptional tools for synchronizing ice core records (Bender et al., 1994; Blunier et al., 1998; Capron et al., 2010; Köhler, 2010). With a decadal resolution in some ice records, methane shows variations strongly linked to rapid climatic fluctuations such as the centennial-to-millennial climate variability (Chappellaz et al., 1993; Mitchell et al., 2011). The same pattern of change is recorded by both CH_4 and $\delta^{18}O_{atm}$ in Greenland or Antarctic ice core records, even though $\delta^{18}O_{atm}$, driven by precession as well as millennial-scale climate events, shows lower amplitude variations because of the longer O_2 lifetime (Landais et al., 2010).

The gas stratigraphic links employed were derived primarily from literature following established inter-core methane synchronizations, but also from the available $\delta^{18}O_{atm}$ data. Additionally, the $\delta^{15}N$ data are also used as markers of rapid warming in the NGRIP ice core record in sections where methane constraints are not yet available (Capron et al., 2010). More specifically, the methane gas stratigraphic links are derived from the synchronizations performed between EDC and the records of Vostok (Loulergue, 2007; Lemieux-Dudon et al., 2010), EDML (Loulergue, 2007; Loulergue et al., 2007; Schilt et al., 2010), TALDICE (Buiron et al., 2011; Schüpbach et al., 2011; Parrenin et al., 2012b), or NGRIP (Greenland composite: Capron et al., 2010; EPICA Community Members, 2006; Flückiger et al., 2004; Huber et al., 2006; Schilt et al., 2010), respectively. NGRIP is another ice core record that has already been synchronized in the gas phase to all other records analyzed here including Vostok (Landais et al., 2006), EDML (Capron et al., 2010; Lemieux-Dudon et al., 2010; Schilt et al., 2010), or more recently TALDICE (Buiron et al., 2011). Other available gas stratigraphic pairing includes only these between EDML and TALDICE with data derived from Schüpbach et al. (2011) (details in SOM).

3.2.4 Absolute age markers

The imprint of the Laschamp geomagnetic excursion has been detected in the ice cores based on ^{10}Be concentration trends in both Greenland (Yiou et al., 1997) and Antarctic (Raisbeck et al., 2007) records. We use the latest age constraints associated with this event, 40.65 ± 0.95 ka (Singer et

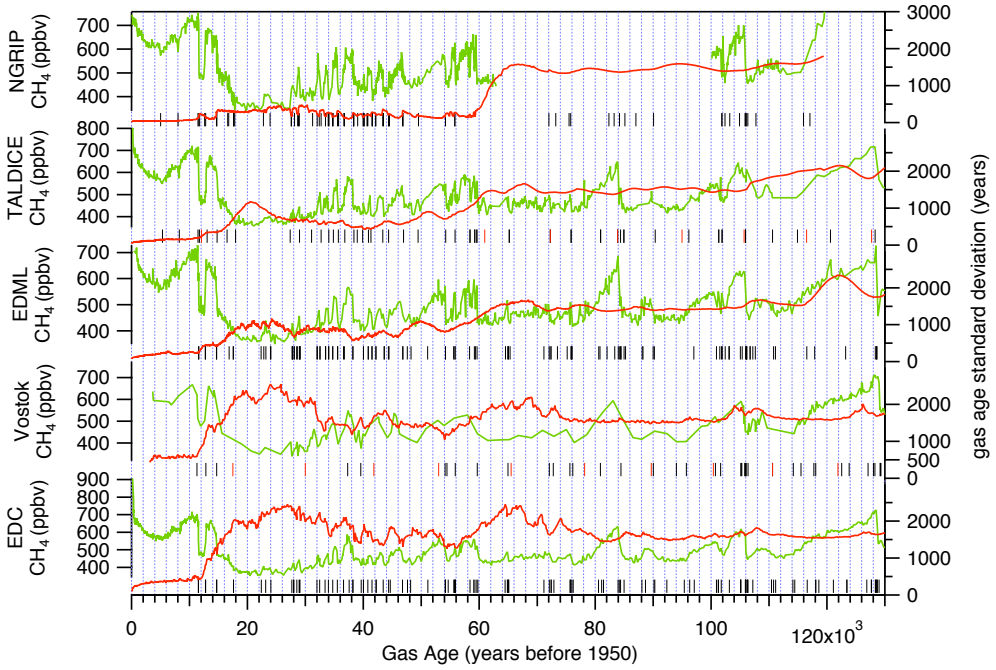

Fig. 2. The methane records of the five ice cores analyzed. From top to bottom: NGRIP (Greenland composite: Flückiger et al., 2004; Huber et al., 2006; EPICA Community Members, 2006; Schilt et al., 2010; Capron et al., 2010), TALDICE (Buiron et al., 2011; Schüpbach et al., 2011), EDML (EPICA Community Members, 2006), Vostok (Caillon et al., 2003; Petit et al., 2009) and EDC (Loulergue et al., 2008) on the AICC2012 gas chronology. Vertical black bars indicate the location of the gas stratigraphic markers and red bars the location of the absolute tie points in the gas phase. The red lines (right axes) show the gas age standard deviation in years for each of the ice core analyzed.

al., 2009) as absolute tie points for EDC and Vostok. Other absolute markers include a Holocene ^{10}Be point for Vostok (Parrenin et al., 2001) and the Mount Moulton tephra layer (Narcisi et al., 2006; Dunbar et al., 2008) for EDC, the latter with an updated ^{40}Ar/^{39}Ar age of 93.2 ± 4.4 ka (see SOM). Absolute age markers have not yet been reported for EDML and TALDICE records. For the NGRIP on the other hand, we used a set of absolute markers from the GICC05 depth-age relationship with artificially small uncertainties to force the model not to deviate from this chronology. Tie points spaced 60 yr apart were used, leading to 990 data points to which we associated uncertainties of maximum 50 yr rather than the reported GICC05 maximum counting errors. In return, the absolute gas age markers employed in LD2010 were not used for this work. For periods older than 120 ka BP, the choice of absolute tie points for all records is discussed in Bazin et al. (2013).

3.2.5 Additional markers

The Δdepth markers given for NGRIP are derived from a depth comparison between $\delta^{18}O_{ice}$ and air $\delta^{15}N$ over a succession of interstadials as detailed in the SOM. The new orbital points are discussed in Bazin et al. (2013).

4 Results and discussion

4.1 The new AICC2012 gas and ice chronologies

As expected from the chronological constraints provided by the numerous gas stratigraphic markers employed, the methane records for all five ice cores display very similar variations over the rapid millennial variability of the last glacial period and last deglaciation, respectively (Fig. 2). The uncertainties attached to the gas and ice stratigraphic tie points as well as uncertainties in the analyzed LIDIE may lead locally to some minor offsets up to a few centuries between the five methane records. In addition, small differences between the records could also reflect a combination of (1) different analytical resolution (e.g. the low resolution in the Vostok record) and precision, (2) the existence of the interhemispheric methane gradient because of possibly stronger proximal methane sources from Northern Hemisphere landmasses (Dällenbach et al., 2000; Schüpbach et al., 2011), and (3) different speeds for the lock-in process that could modulate the trace gases' peak attenuation observed in low accumulation sites (Spahni et al., 2003; Köhler, 2010).

At first order, the water isotopic profiles show consistent similarity between all Antarctic sites, despite the fact that none of the ice stratigraphic tie points are derived from water isotopic data (Fig. 1). This confirms that the AIM succession observed individually on the different Antarctic ice cores

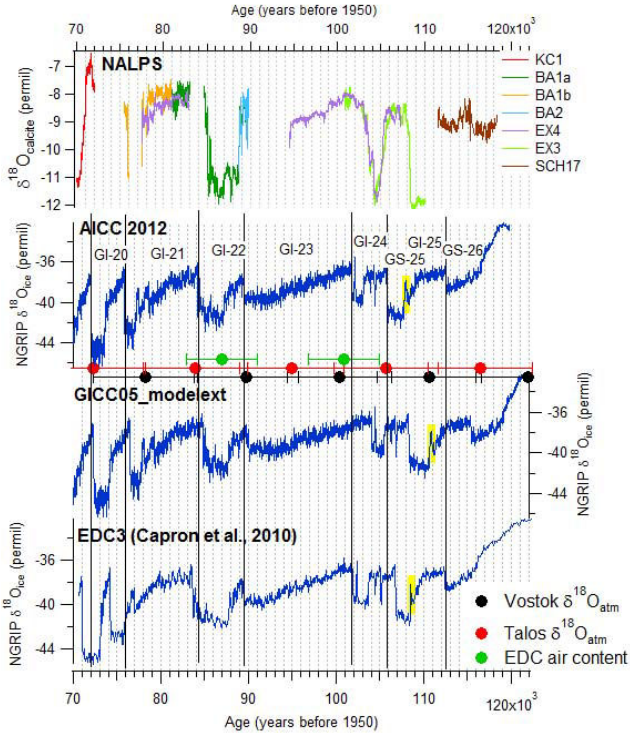

Fig. 3. Comparison of the NGRIP $\delta^{18}O_{ice}$ evolution over the glacial inception on three different time series in use; top panel: AICC2012 (this work); middle panel: GICC05modelext (Wolff et al., 2010); bottom panel: EDC3 (Capron et al., 2010). The yellow highlight shows the location of the rebound event at the end of GI-25. The grey, vertical lines mark the major GS/GI transitions. The circles mark the orbital points with associated error bars ($\delta^{18}O_{atm}$ Vostok in black; $\delta^{18}O_{atm}$ TALDICE in red; air content EDC in green). Note that the $\delta^{18}O_{atm}$ orbital points were taken at mid-slopes for TALDICE (Bazin et al., 2013) and at minima and maxima for Vostok (Suwa and Bender, 2008). The speleothem color-coded composite NALPS $\delta^{18}O_{calcite}$ record (Boch et al., 2011) is also shown for comparison.

(EPICA Community Members, 2006; Jouzel et al., 2007; Wolff et al., 2009; Buiron et al., 2012) is a persistent feature of the Antarctic climate of the last glacial period, even if some differences are clearly visible on the shapes of the AIM for the different ice core records (Fig. 1). The EDML water isotope record shows AIM characterized by broader peaks or even extended periods of high isotope values, whereas the EDC and TALDICE exhibit a more triangular shape over the same AIM events. The temperature maximum over each AIM is thus reached earlier at EDML compared to EDC (see Fig. 4), potentially reflecting that the EDML area picks up a South Atlantic temperature signal that is opposite to the North Atlantic signal, and that according to the bipolar seesaw theory would be expected to increase more rapidly than Antarctic temperatures (Stocker and Johnsen, 2003). The water isotopic record is often of too coarse a resolution in Vostok to clearly see the shape of the AIM.

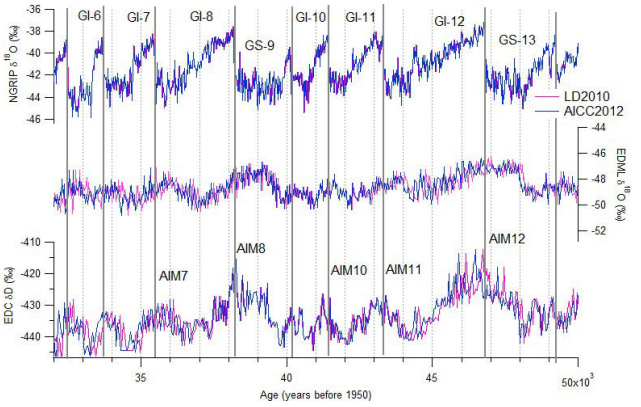

Fig. 4. Water isotopic records of NGRIP (top), EDML (middle), and EDC (bottom), over GI-5 to 12 on the LD2010 timescale in pink, versus the new AICC2012 chronology using additional constraints (this study) in blue. For comparison on the timing of events, the black vertical lines mark the major GS/GI transitions in the NGRIP record.

Within the new coherent chronological scenario, we have chosen to briefly discuss two aspects for the last glacial cycle: first, the dating of the last glacial inception in Greenland; second, the implication for the bipolar sequences of events and the seesaw picture over middle MIS 3.

4.2 Comparison with previous chronological constraints in the 70–120 ka BP period as derived from EDC3 and GICC05modelext

By construction, the AICC2012 chronology closely follows the GICC05 timescale over the last 60 ka with a maximum difference of 5 yr locally. This is due to the high number of absolute ice markers with artificially small uncertainties included for this period, derived from the GICC05 chronology (Fig. 1). For older periods such as MIS 5, a compromise had to be found between data constraints and initial input from glaciological modelling (SOM). Because the initial background scenario for the thinning function for Vostok, EDML, and TALDICE records was associated with quite a large variance over MIS 5, the AICC2012 is mainly constrained by a few orbital markers such as $\delta^{18}O_{atm}$ and air content with large uncertainties of 6000 yr and respectively 4000 yr, and the background age model for EDC (Parrenin et al., 2007) and NGRIP (Wolff et al., 2010) ice cores (see also Bazin et al., 2013).

In Fig. 3 the water isotopic record of NGRIP over the glacial inception and late MIS 5 presented on the AICC2012 chronology is compared with the same record on both the GICC05modelext and EDC3-based timescales, as discussed in Capron et al. (2010). In that study, the EDC3-based chronology was applied to the NGRIP record by using gas stratigraphic links (CH_4 and $\delta^{18}O_{atm}$) between the EDML and NGRIP ice core records, the EDML record being drawn

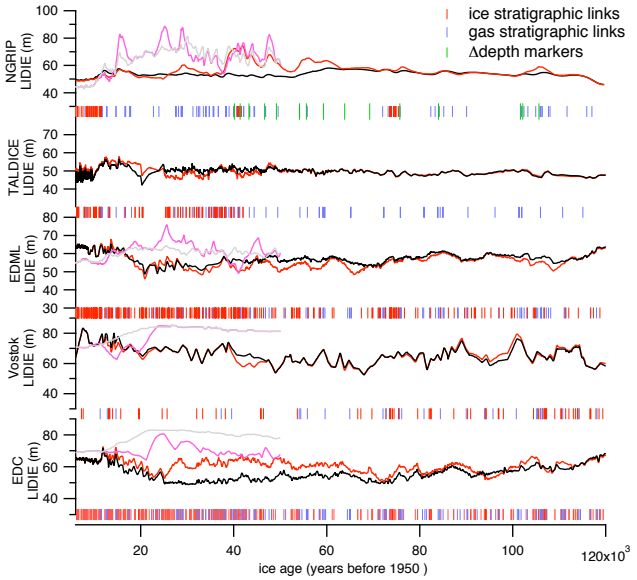

Fig. 5. Evolution of the LIDIE over the last 120 ka for the five ice core records analyzed in this study: background LIDIE scenarios for the LD2010 (grey) and the AICC2012 chronologies (black); Datice-calculated LIDIE for the LD2010 (pink) and the AICC2012 (red) chronologies. The blue, red, and green vertical bars mark the location of ice stratigraphic links, gas stratigraphic links, and Δdepth markers, respectively.

on the EDML-1 timescale (Ruth et al., 2007) initially tuned to the EDC3 chronology (Parrenin et al., 2007) through many volcanic tie points.

Significant differences of several millennia are observed in the timing of the NGRIP glacial inception record between the AICC2012, the GICC05modelext, and the EDC3 chronologies (Fig. 3). The timing of the onsets of GI-25, GI-23, and GI-22 are comparable between the EDC3-based and AICC2012 timescales, but younger than the onset of the same interstadial according to the GICC05modelext. In our view, this difference is likely due to the high uncertainty on the NGRIP thinning function in sectors near the bedrock (NGRIP members, 2004; Wolff et al., 2010), but also because it is mainly the EDC background scenario and the few orbital points (Fig. 3) that are driving the AICC2012 chronology over the interval 85–120 ka BP. The constraint linked to the orbital points is especially important around 100 ka BP, which makes the timing of GI-24 in AICC2012 younger than both GICC05modelext and EDC3 (by ∼2500 and ∼1000 yr, respectively). For the period 60–85 ka BP, the AICC2012 chronology provides a compromise between EDC3 and GICC05modelext with for example the onsets of GI-21 and GI-20 being dated in AICC2012 at intermediate ages between these of corresponding events on the EDC3 and GICC05modelext timescales (Fig. 3).

The duration of events has been strongly modified for the NGRIP $\delta^{18}O_{ice}$ record between the EDC3-based and the AICC2012 chronology. Especially the duration of the $\delta^{18}O_{ice}$ decrease from the climatic optimum of MIS 5.5 and GS-26 is similarly shorter on the GICC05modelext and AICC2012 timescales compared to the EDC3-based chronology (Fig. 3). In addition, the rebound event at the end of GI-25 (yellow hatch on Fig. 3) is much shorter on the EDC3-based chronology of Capron et al. (2010) but has similar duration according to AICC2012 and GICC05modelext.

Table 1 shows a comparison on the duration of selected Greenlandic climate events as constrained by AICC2012, the GICC05modelext (Wolff et al., 2010), and the EDC3-based NGRIP timescale of Capron et al. (2010). As mentioned above, the event durations calculated from AICC2012 are in better agreement with GICC05modelext than with the EDC3-based timescale (Table 1). This is expected from the fact that both GICC05modelext and AICC2012 chronologies use glaciological information, i.e. the glaciological kink model for GICC05modelext (Wolff et al., 2010), and a combination of this same NGRIP kink model with the EDC glaciological model of Parrenin et al. (2007) for the AICC2012 chronology. Still, some differences remain between the AICC2012 and the GICC05modelext chronologies (Fig. 3), as is for example the case for the duration of events GI-20, GS-22, GI-24, or GS-25 (Table 1). Moreover, the DATICE tool has been developed to provide robust uncertainty on the absolute age but not yet for the duration of events. Still, a development is ongoing in integrating the uncertainty on event duration from layer counting information; this methodological update will be provided in a future submission (Lemieux-Dudon et al., 2013).

4.3 Comparison with NALPS in the 70–120 ka BP period

U/Th absolutely dated speleothem isotopic data provide valuable contributions for better constraining the uncertainties associated with ice core dating and assessing leads and lags in the regional response to past climate change (Drysdale et al., 2007; Wang et al., 2008; Cheng et al., 2009; Fleitmann et al., 2009). Although detailed comparison between AICC2012 and other independent and absolutely dated archives will be attempted in the near future (see also discussion in SOM), we briefly compare the AICC2012 chronological constraints over the last glacial inception with the recently published NALPS record (Boch et al., 2011).

The NALPS composite speleothem record extends between 120 and 60 ka BP and provides a precisely dated cave paleoclimate time series from the northern Alpine region. The observed calcite $\delta^{18}O$ variations were interpreted to reflect the North Atlantic type climate variability (Boch et al., 2011). There is good agreement for the timing of GI/GS events 19 to 25 between NALPS and GICC05modelext, but differences such as younger ages for speleothem stadial and interstadial transitions over the period between ca. 106 and 60 ka have also been reported. However, as NALPS is

Table 1. Overview of event durations over the period 70–120 ka BP of the NGRIP $\delta^{18}O_{ice}$ as constrained on three different ice core time series: AICC2012 (this study), GICC05modelext (Wolff et al., 2010) and the EDC-3 (Capron et al., 2010), and the NALPS composite speleothem record (Boch et al., 2011). Stadial-interstadial boundaries have been defined by eye using 20 yr-resolution $\delta^{18}O$ data and Ca^{2+} data from the NGRIP, GRIP, and GISP2 ice cores synchronized to GICC05 following the method described in Rasmussen et al. (2008). The details of this approach will be reported elsewhere (I. Seierstad, personal communication, 2012). The short events within GS-24 and GS-22 ("precursor events") are not included in the GI and GS duration estimates, and the definition of GS-22 follows Vallelonga et al. (2012). As there is no clear evidence of GS-23 in Greenland water isotopic records we give the duration of GI-23 and GS-23 as a whole.

Event	Duration of events (years)			
	AICC2012	GICC05modeltext (Wolff et al., 2010)	EDC3 (Capron et al., 2010)	NALPS (Boch et al., 2011)
GI-20	2166	2340	1067	
GI-21	1340	1320	1716	1720 ± 384
GI-21	7009	7000	7731	7450 ± 475
GI-22	2760	2620	3625	3250 ± 526
GI-22	2467	2440	1839	
GS-23+GI-23	12 512	14 000	12 940	
GI-24	950	920	1220	1040 ± 585
GI-24	2650	2840	3140	3090 ± 636
GI-25	1990	2360	1700	
GI-25	4790	4730	3900	

compiled from several stalagmites that have been affected by growth cessation particularly during stadials, the record is highly discontinuous, and not all DO event boundaries could securely be identified.

The timing of events over the period 70–85 ka is well constrained between AICC2012 and NALPS, particularly for the onsets of GI-19 and GI-20 (Fig. 3). The onset of GI-21 is however around 500 yr younger in AICC2012, and the discrepancy already reported between NALPS and GICC05modelext over the length of GS-22 is also visible in AICC2012. It is likely the cause of this discrepancy resides in the NALPS record, or arises from different expressions of climate variability in the different records.

A significant offset is, however, observed over the early part of the Last Glacial period between NALPS and AICC2012, the speleothem-derived event boundaries being older by $\sim$2000 yr on average compared to AICC2012 over the sequence of GI/GS events 23–25. Over the same interval there is however better agreement between NALPS and GICC05modelext (Fig. 3). Nonetheless, differences exist in the timing and shape of events over GI/GS events 24–25 between NALPS and other well-dated speleothem records such as Corchia, south of the Alps (Drysdale et al., 2007), Sofular, near the Black Sea (Badertscher et al., 2011), or the Sanbao record from China (Wang et al., 2008). A rigorous chronological analysis of various speleothem records is underway (D. Fleitmann, personal communication, 2012). It is expected that it will provide strong constraints for further comparison of such records with the ice core chronological data, including AICC2012. As for the length of events, the error bars associated with the NALPS record make it compatible, at least for some events, with any of the ice core chronologies discussed in Fig. 3.

4.4 Middle MIS 3 – comparison with the LD2010 chronology

One of the strengths of the Datice tool is that it allows for a close assessment of the sequence of events between the different ice cores analyzed. This is particularly relevant for the new AICC2012 chronology that is more carefully constrained with the addition of numerous new gas and ice stratigraphic links between the various ice cores (Figs. 1 and 2). Since we analyzed both Greenland and Antarctic records, the outcome has immediate implications for the timing of the interhemispheric coupling over the last glacial period with respect to the seesaw mechanism (Stocker and Johnsen, 2003; EPICA Community Members, 2006; Barker et al., 2011; Buiron et al., 2012).

A central period for investigating the classical bipolar expression of the millennial variability over the last glacial period is MIS 3 (Blunier and Brook, 2001; EPICA Community Members, 2006; Jouzel et al., 2007; Wolff et al., 2010). With the AICC2012 chronology, the classical pattern where the peaks of AIM correspond with the GI onsets is indeed confirmed (Fig. 4), as already reported in the previous Datice-derived LD2010 chronology (Lemieux-Dudon et al., 2010).

Nevertheless, slight differences were expected between the two chronological frameworks given the improved constraints applied here compared to LD2010. For example, for AIM5, 6, 7 and 12, the AICC2012 age estimates for the Antarctic records are younger by $\sim$500–600 yr compared

to the LD2010 chronology (Fig. 4). However, the slight differences in the AIM timing between the two Datice-derived chronologies do not impact significantly on the understanding of the sequence of events over the last glacial period between Antarctica and Greenland and hence on the seesaw mechanism. As an example, over GS-13/GI-12 there is a very good synchrony between the abrupt increase of $\delta^{18}O_{ice}$ at NGRIP and the $\delta^{18}O_{ice}$ maximum at EDC on the AICC2012 chronology. Using the LD2010 chronology, the isotopic maximum at EDC is lagging the abrupt increase of $\delta^{18}O_{ice}$ at NGRIP by several centuries. Similarly, EDML displays generally younger $\delta^{18}O_{ice}$ maximum over AIM by several centuries in AICC2012 than in LD2010 (Fig. 4).

Despite these small differences, the sequence of events remains in agreement with the seesaw classical pattern (Stocker and Johnsen, 2003; Svensson et al., 2013) within the limitations given by dating as well as the short-term variability of the water isotopic signal and related uncertainties derived from the temporal and analytical constraints employed (see SOM). For example, over the interval corresponding to the onset of GI-8 at EDML, the maximum $\delta^{18}O_{ice}$ at the beginning of the plateau is reached at least 1000 yr – hence significantly more than the 600 yr uncertainty – prior to the abrupt stadial-interstadial transition seen in Greenland. At EDC, for the same event, the maximum of the AIM is synchronous within the 600 yr AICC2012 uncertainty with the abrupt stadial-interstadial transition recorded in Greenland, both for LD2010 and AICC2012.

For GS-13/GI-12, the maximum of $\delta^{18}O_{ice}$ at EDML is reached 1000–1400 yr before the abrupt warming recorded in Greenland, which is significantly larger than the 600 yr AICC2012 uncertainty over this period and the difference between the LD2010 and AICC2012 chronologies. On the opposite, the maximum of $\delta^{18}O_{ice}$ at EDC over AIM12 is synchronous within the AICC2012 uncertainty (i.e. $\pm$600 yr) with the Greenland abrupt warming.

The clear decrease of EDC and EDML $\delta^{18}O_{ice}$ reflecting the Antarctic temperature occurs in-phase within dating uncertainties with the Greenland GS/GI transitions as depicted by the bipolar seesaw hypothesis. The EDML warming rate appears however much faster than the EDC warming rate which strengthen the hypothesis of a shorter response time of the Atlantic sector to an Atlantic Meridional Overturning Circulation weakening in the seesaw pattern (EPICA Community Members, 2006; Stenni et al., 2010; Buiron et al., 2012).

The fact that the Antarctic ice records are systematically younger during glacial periods according to the AICC2012 chronology than the LD2010 chronology is due to the different LIDIE scenarios (Fig. 5). The different LIDIE used for LD2010 relative to the AICC2012 are due to higher density of ice and gas stratigraphic points employed in the latter, as well as differences between the background LIDIE scenarios (SOM). Altogether, this approach had important implications for improving the accuracy of the new timescale. For example, the LD2010 LIDIE background scenarios were all based on firn densification models. On the contrary, for AICC2012 the background LIDIE for EDML, EDC, and Vostok ice core records were deduced from the $\delta^{15}N$ of N_2 in air entrapped in the ice (see Parrenin et al., 2012b; Capron et al., 2013). With this approach, LIDIE are systematically smaller in AICC2012 than in LD2010 (Fig. 5). The main implication is that a smaller LIDIE induces a smaller age difference, Δage, between age of the ice and age of the gas at the same depth. It thus decreases the age of ice when using gas stratigraphic links as CH_4 abruptly increases at each GS/GI transition.

5 Conclusions and outlook

Significant progress has been made recently in synchronizing the long ice core records, and this is an important benchmark in advancing paleoenvironmental research and more carefully assessing both temporal and spatial leads and lags between regions. Here we provided new chronological outputs from a multi-core inverse modelling approach applied to the more recent 120 ka of four Antarctic ice core records, and the NGRIP record, in the frame of the AICC2012 chronology. The development of the new chronology to depict the millennial scale variability of the last glacial period has strongly benefited from the addition of numerous ice and gas stratigraphic tie points as well as a revised expression for the background scenario of LIDIE.

The new AICC2012 chronology provides improved temporal constraints in order to assess the timing of past climate events, and we have shown two such examples in selected time intervals over the last 120 ka BP. First, the dating of the last glacial inception shares many features with the EDC3 chronology developed for the EDC record, but the implementation of new glaciological constraints (revised thinning and accumulation rate) make the duration of events in AICC2012 more reliable than previous estimates. Second, we have shown that the bipolar sequence of events over the succession of GI/GS is slightly modified in AICC2012 compared to the previous LD2010 chronology, with the Antarctic records in general being about 600 yr younger according to the AICC2012.

Several other well-resolved Antarctic ice core records are available for the last climatic cycle and even beyond, with a wealth of dating information including layer counting (Mitchell et al., 2012; Vinther et al., 2012) or orbital markers (Kawamura et al., 2007). Moreover, radiometric age data from well-resolved speleothem profiles could provide absolute chronostratigraphic tie points that can refine the ice core chronologies, providing that the response to climate forcing is proven coeval between regions. It is therefore expected that the future contribution of both other ice cores and other types of chronological constraints to the Datice effort will lead to

further refinements in the ice core chronologies beyond the AICC2012 chronology.

Supplementary material related to this article is available online at: http://www.clim-past.net/9/1733/2013/cp-9-1733-2013-supplement.zip.

Acknowledgements. The authors thank the EDC4 discussion team for stimulating the discussion around the building of AICC2012 and helping to decide on the best parameters to feed the DATICE tool. We are particularly indebted to V. Masson-Delmotte, C. Ritz, H. Fisher, and D. Fleitmann for their constructive suggestions. We further thank the anonymous reviewers and handling editor E. Brook for the critical reviews that improved the manuscript.

This work was financially endorsed mainly by LGGE the CNRS/INSU LEFE program and "Fondation Ars Cuttoli". The research leading to these results has also received funding from the European Union's Seventh Framework programme (FP7/2007-2013) under grant agreement no 243908, "Past4Future. Climate change – Learning from the past climate" and is Past4Future contribution number 47. This is also TALDICE publication no 35. This work is also a contribution to the European Project for Ice Coring in Antarctica (EPICA), a joint European Science Foundation/European Commission scientific programme, funded by the EU and by national contributions from Belgium, Denmark, France, Germany, Italy, the Netherlands, Norway, Sweden, Switzerland and the United Kingdom. The main logistic support was provided by IPEV and PNRA (at Dome C) and AWI (at Dronning Maud Land). This is EPICA publication no. 293.

Edited by: E. Brook

The publication of this article is financed by CNRS-INSU.

References

Arnaud, L., Barnola, J.-M., and Duval, P.: Physical modeling of the densification of snow/firn and ice in the upper part of polar ice sheets, in: Physics of Ice Core Records, edited by: Hondoh, T., Hokkaido University Press, Sapporo, Japan, 285–305, 2000.

Badertscher, S., Fleitmann, D., Cheng, H., Edwards, R. L., Göktürk, O. M., Zumbühl, A., Leuenberger, M., and Tüysüz, O.: Pleistocene water intrusions from the Mediterranean and Caspian seas into the Black Sea, Nat. Geosci., 4, 4–11, 2012.

Barker, S., Knorr, G., Edwards, R. L., Parrenin, F., Putnam, A. E., Skinner, L. C., Wolff, E., and Ziegler, M.: 800,000 years of abrupt climate variability, Science, 334, 347–351, 2011.

Bazin, L., Landais, A., Lemieux-Dudon, B., Toyé Mahamadou Kele, H., Veres, D., Parrenin, F., Martinerie, P., Ritz, C., Capron, E., Lipenkov, V., Loutre, M.-F., Raynaud, D., Vinther, B., Svensson, A., Rasmussen, S. O., Severi, M., Blunier, T., Leuenberger, M., Fischer, H., Masson-Delmotte, V., Chappellaz, J., and Wolff, E.: An optimized multi-proxy, multi-site Antarctic ice and gas orbital chronology (AICC2012): 120–800 ka, Clim. Past, 9, 1715–1731, doi:10.5194/cp-9-1715-2013, 2013.

Bender, M., Sowers, T., and Labeyrie, L. D., The Dole effect and its variation during the last 130,000 years as measured in the Vostok core, Global Biogeochem. Cy., 8, 363–376, 1994.

Blaauw, M., Wohlfarth, B., Christen, J. A., Ampel, L., Veres, D., Hughen, K. A., Preusser, F., and Svensson, A.: Were last glacial climate events simultaneous between Greenland and France? A quantitative comparison using non-tuned chronologies, J. Quaternary Sci., 25, 387–394, 2010.

Blockley, S. P. E., Lane, C. S., Hardiman, M., Rasmussen, S. O., Seierstad, I. K., Steffensen, J. P., Svensson, A., Lotter, A. F., Turney, C. S. M., Bronk Ramsey, C., and INTIMATE members: Synchronisation of palaeoenvironmental records over the last 60,000 years, and an extended INTIMATE event stratigraphy to 48,000 b2k, Quaternary Sci. Rev., 36, 2–10, 2012.

Blunier, T. and Brook, E. J.: Timing of millennial-scale climate change in Antarctica and Greenland during the last glacial period, Science, 291, 109–112, 2001.

Blunier, T., Chappellaz, J., Schwander, J., Dällenbach, A., Stauffer, B., Stocker, T., Raynaud, D., Jouzel, J., Clausen, H., Hammer, C., and Johnsen, S.: Asynchrony of Antarctic and Greenland climate change during the last glacial period, Nature, 394, 739–743, 1998.

Blunier, T., Spahni, R., Barnola, J.-M., Chappellaz, J., Loulergue, L., and Schwander, J.: Synchronization of ice core records via atmospheric gases, Clim. Past, 3, 325–330, doi:10.5194/cp-3-325-2007, 2007.

Boch, R., Cheng, H., Spötl, C., Edwards, R. L., Wang, X., and Häuselmann, Ph.: NALPS: a precisely dated European climate record 120–60 ka, Clim. Past, 7, 1247–1259, doi:10.5194/cp-7-1247-2011, 2011.

Braun, H., Ditlevsen, P., Kurths, J., and Mudelsee, M.: A two-parameter stochastic process for Dansgaard-Oeschger events, Paleoceanography, 26, PA3214, doi:10.1029/2011pa002140, 2011.

Bronk Ramsey, C., Staff, R. A., Bryant, C. L., Brock, F., Kitagawa, H., van der Plicht, J., Schlolaut, G., Marshall, M. H., Brauer, A., Lamb, H. F., Payne, R. L., Tarasov, P. E., Haraguchi, T., Gotanda, K., Yonenobu, H., Yokoyama, Y., Tada, R., and Nakagawa, T. A.: Complete Terrestrial Radiocarbon Record for 11.2 to 52.8 kyr B.P., Science, 338, 370–374, 2012.

Brook, E. J., Sowers, T., and Orchardo, J.: Rapid variations in atmospheric methane concentration during the past 110 000 years, Science, 273, 1087–1091, 1996.

Buiron, D., Chappellaz, J., Stenni, B., Frezzotti, M., Baumgartner, M., Capron, E., Landais, A., Lemieux-Dudon, B., Masson-Delmotte, V., Montagnat, M., Parrenin, F., and Schilt, A.: TALDICE-1 age scale of the Talos Dome deep ice core, East Antarctica, Clim. Past, 7, 1–16, doi:10.5194/cp-7-1-2011, 2011.

Buiron, D., Stenni, B., Chappellaz, J., Landais, A., Baumgartner, M., Bonazza, M., Capron, E., Frezzotti, M. Kageyama, M., Lemieux-Dudon, B., Masson-Delmotte, V., Parrenin, F., Schilt, A., Selmo, E., Severi, M., Swingedouw, D., and Udisti, R.:

Regional imprints of millennial variability during the MIS 3 period around Antarctica, Quaternary Sci. Rev., 48, 99–112, 2012.

Caillon, N., Severinghaus, J. P., Jouzel, J., Barnola, J.-M., Kang, J., and Lipenkov, V. Y.: Timing of atmospheric CO_2 and Antarctic temperature changes across Termination III, Science, 299, 1728–1731, 2003.

Capron, E., Landais, A., Lemieux-Dudon, B., Schilt, A., Masson-Delmotte, V., Buiron, D., Chappellaz, J., Dahl-Jensen, D., Johnsen, S., and Leuenberger, M.: Synchronizing EDML and NorthGRIP ice cores using $\delta^{18}O$ of atmospheric oxygen ($\delta^{18}O_{atm}$) and CH_4 measurements over MIS5 (80–123 kyr), Quaternary Sci. Rev., 29, 222–234, 2010.

Capron, E., Landais, A., Buiron, D., Cauquoin, A., Chappellaz, J., Debret, M., Jouzel, J., Leuenberger, M., Martinerie, P., Masson-Delmotte, V., Mulvaney, R., Parrenin, F., and Prié, F.: Glacial-interglacial dynamics of Antarctic firn columns: comparison between simulations and ice core air-$\delta^{15}N$ measurements, Clim. Past, 9, 983–999, doi:10.5194/cp-9-983-2013, 2013.

Cheng, H., Edwards, R. L., Broecker, W. S., Denton, G. H., Kong, X., Wang, Y., Zhang, R., and Wang, X.: Ice Age Terminations, Science, 326, 248–252, doi:10.1126/science.1177840, 2009.

Chappellaz, J., Blunier, T., Raynaud, D., Barnola, J.-M., Schwander, J., and Stauffer, B.: Synchronous changes in atmospheric CH_4 and Greenland climate between 40 and 8 kyr BP, Nature, 366, 443–445, 1993.

Dahl-Jensen, D., Mosegaard, K., Gundestrup, N., Clow, G. D., Johnsen, S. J., Hansen, A. W., and Balling, N.: Past temperatures directly from the Greenland ice sheet, Science, 282, 268–271, 1998.

Dansgaard, W., Clausen, H. B., Gundestrup, N., He, C. U., Johnsen, S. F., Kristinsdottir, P. M., and Reeh, N.: A new Greenland deep ice core, Science, 218, 1273–1277, 1982.

Dansgaard, W., Johnsen, S., Clausen, H. B., Dahl-Jensen, D., Gundestrup, N., Hammer, C. U., and Oeschger, H.: North Atlantic climatic oscillations revealed by deep Greenland ice cores, in: Climate processes and climate sensitivity, edited by: Hansen, J. E. and Takahashi, T., Am. Geophys. Union, Washington, 288–298, 1984.

Dällenbach, A., Blunier, T., Flückiger, J., Stauffer, B., Chappellaz, J., and Raynaud, D.: Changes in the atmospheric CH_4 gradient between Greenland and Antarctica during the Last Glacial and the transition to the Holocene, Geophys. Res. Lett., 27, 1005–1008, doi:200010.1029/1999GL010873, 2000.

Dreyfus, G. B., Parrenin, F., Lemieux-Dudon, B., Durand, G., Masson-Delmotte, V., Jouzel, J., Barnola, J.-M., Panno, L., Spahni, R., Tisserand, A., Siegenthaler, U., and Leuenberger, M.: Anomalous flow below 2700 m in the EPICA Dome C ice core detected using $\delta^{18}O$ of atmospheric oxygen measurements, Clim. Past, 3, 341–353, doi:10.5194/cp-3-341-2007, 2007.

Drysdale, R. N., Zanchetta, G., Hellstrom, J. C., Fallick, A. E., McDonald, J., and Cartwright, I.: Stalagmite evidence for the precise timing of North Atlantic cold events during the early last glacial, Geology, 35, 77–80, 2007.

Dunbar, N. W., McIntosh, W. C., and Esser, R. P.: Physical setting and tephrochronology of the summit caldera ice record at Mount Moulton, West Antarctica, Geol. Soc. Am. Bull., 120, 796–812, 2008.

EPICA Community Members: Eight glacial cycles from an Antarctic ice core, Nature, 429, 623–628, 2004.

EPICA Community Members: One-to-one coupling of glacial climate variability in Greenland and Antarctica, Nature, 444, 195–198, 2006.

Fleitmann, D., Cheng, H., Badertscher, S., Edwards, R. L., Mudelsee, M., Göktürk, O. M, Fankhauser, A., Pickering, R., Raible, C. C., Matter, A., Kramers, J., and Tüysüz, O.: Timing and climatic impact of Greenland interstadials recorded in stalagmites from northern Turkey, Geophys. Res. Lett., 36, L19707, doi:10.1029/2009GL040050, 2009.

Flückiger, J., Blunier, T., Stauffer, B., Chappellaz, J., Spahni, R., Kawamura, K., Schwander, J., Stocker, T. F., and Dahl-Jensen, D.: N_2O and CH_4 variations during the last glacial epoch: Insight into global processes, Global Biogeochem. Cy., 18, GB1020, doi:10.1029/2003GB002122, 2004.

Goujon, C., Barnola, J. M., and Ritz, C.: Modeling the densification of polar firn including heat diffusion: Application to close-off characteristics and gas isotopic fractionation for Antarctica and Greenland sites, J. Geophys. Res., 108, 101–1018, 2003.

Grootes, P. M., Stuiver, M., White, J. W. C., Johnsen, S. J., and Jouzel, J.: Comparison of the oxygen isotope records from the GISP2 and GRIP Greenland ice cores, Nature, 366, 552–554, 1993.

Huber, C., Leuenberger, M., Spahni, R., Flückiger, J., Schwander, J., Stocker, T., Johnsen, S., Landais, A., and Jouzel, J.: Isotope calibrated Greenland temperature record over Marine Isotope Stage 3 and its relation to CH_4, Earth Planet. Sc. Lett., 243, 504–519, 2006.

Huybrechts, P., Rybak, O., Pattyn, F., Ruth, U., and Steinhage, D.: Ice thinning, upstream advection, and non-climatic biases for the upper 89 % of the EDML ice core from a nested model of the Antarctic ice sheet, Clim. Past, 3, 577–589, doi:10.5194/cp-3-577-2007, 2007.

Jouzel, J., Masson-Delmotte, V., Cattani, O., Dreyfus, G., Falourd, S., Hoffmann, G., Minster, B., Nouet, J., Barnola, J. M., Chappellaz, J., Fischer, H., Gallet, J. C., Johnsen, S., Leuenberger, M., Loulergue, L., Luethi, D., Oerter, H., Parrenin, F., Raisbeck, G., Raynaud, D., Schilt, A., Schwander, J., Selmo, E., Souchez, R., Spahni, R., Stauffer, B., Steffensen, J. P., Stenni, B., Stocker, T. F., Tison, J. L., Werner, M., and Wolff, E. W.: Orbital and Millennial Antarctic climate variability over the past 800,000 years, Science, 317, 793–796, 2007.

Kawamura, K., Parrenin, F., Lisiecki, L., Uemura, R., Vimeux, F., Severinghaus, J. P., Hutterli, M. A., Nakazawa, T., Aoki, S., Jouzel, J., Raymo, M. E., Matsumoto, K., Hisakazu, N., Motoyama, H., Fujita, S., Goto-Azuma, K., Fujii, Y., and Watanabe, O.: Northern Hemisphere forcing of climatic cycles in Antarctica over the past 360 000 years, Nature, 448, 912–916, 2007.

Klauenberg, K., Blackwell, P. G., Buck, C. E., Mulvaney, R., Röthlisberger, R., and Wolff, E. W.: Bayesian Glaciological Modelling to quantify uncertainties in ice core chronologies, Quaternary Sci. Rev., 30, 2961–2975, 2011.

Köhler, P.: Rapid changes in ice core gas records – Part 1: On the accuracy of methane synchronisation of ice cores, Clim. Past Discuss., 6, 1453–1471, doi:10.5194/cpd-6-1453-2010, 2010.

Landais, A., Caillon, N., Goujon, C., Grachev, A. M., Barnola, J. M., Chappellaz, J., Jouzel, J., Masson-Delmotte, V., and Leuenberger, M.: Quantification of rapid temperature change during DO event 12 and phasing with methane inferred from air isotopic measurements, Earth Planet. Sc. Lett., 225, 221–232, 2004.

Landais, A., Barnola, J., Kawamura, K., Caillon, N., Delmotte, M., Ommen, T. V., Dreyfus, G., Jouzel, J., Masson-Delmotte, V., Minster, B., Freitag, J., Leuenberger, M., Schwander, J., Huber, C., Etheridge, D., and Morgan, V.: Firn-air δ^{15}N in modern polar sites and glacial-interglacial ice: a model-data mismatch during glacial periods in Antarctica?, Quaternary Sci. Rev., 25, 49–62, 2006.

Landais, A., Dreyfus, G., Capron, E., Masson-Delmotte, V., Sanchez-Goñi, M. F., Desprat, S., Hoffmann, G., Jouzel, J., Leuenberger, M., and Johnsen, S.: What drives the millennial and orbital variations of $\delta^{18}O_{atm}$?, Quaternary Sci. Rev., 29, 235–246, 2010.

Lang, C., Leuenberger, M., Schwander, J., and Johnsen, S.: 16 °C Rapid temperature variation in Central Greenland 70,000 years ago, Science, 286, 934–937, 1999.

Legrand, M. and Mayewski, P.: Glaciochemistry of polar ice cores: A review, Rev. Geophys., 35, 219–243, doi:10.1029/96RG03527, 1997.

Lemieux-Dudon, B., Blayo, E., Petit, J. R., Waelbroeck, C., Svensson, A., Ritz, C., Barnola, J. M., Narcisi, B. M., and Parrenin, F.: Consistent dating for Antarctic and Greenland ice cores, Quaternary Sci. Rev., 29, 8–20, 2010.

Lisiecki, L. E. and Raymo, M. E.: A Pliocene-Pleistocene stack of 57 globally distributed benthic Δ^{18}O records, Paleoceanography, 20, PA1003, doi:10.1029/2004pa001071, 2005.

Loulergue, L.: Contraintes chronologiques et biogeochimiques grace au methane dans la glace naturelle: une application aux forages du projet EPICA, 2007, Ph.D. thesis, UJF, France, 2007.

Loulergue, L., Parrenin, F., Blunier, T., Barnola, J.-M., Spahni, R., Schilt, A., Raisbeck, G., and Chappellaz, J.: New constraints on the gas age-ice age difference along the EPICA ice cores, 0–50 kyr, Clim. Past, 3, 527–540, doi:10.5194/cp-3-527-2007, 2007.

Loulergue, L., Schilt, A., Spahni, R., Masson-Delmotte, V., Blunier, T., Lemieux, B., Barnola, J. M., Raynaud, D., Stocker, T. F., and Chappellaz, J.: Orbital and millennial-scale features of atmospheric CH_4 over the past 800 000 years, Nature, 453, 383–386, 2008.

Masson-Delmotte, V., Jouzel, J., Landais, A., Stievenard, M., Johnsen, S., White, J. W. C., Werner, M., Sveinbjornsdottir, A., and Fuhrer, K.: Rapid and slow reorganisation of the Northern Hemisphere hydrological cycle during the last glacial period as derived from the GRIP ice core deuterium-excess record, Science, 309, 118–121, 2005.

Mitchell, L. E., Brook, E. J., Sowers, T., McConnell, J. R., and Taylor, K.: Multidecadal variability of atmospheric methane, 1000–1800 C.E., J. Geophys. Res., 116, G02007, doi:10.1029/2010jg001441, 2011.

Narcisi, B., Petit, J. R., and Tiepolo, M.: A volcanic marker (92 ka) for dating deep East Antarctic ice cores, Quaternary Sci. Rev., 25, 2682–2687, 2006.

NGRIP Community Members: High-resolution record of Northern Hemisphere climate extending into the last interglacial period, Nature, 431, 147–151, doi:10.1038/nature02805, 2004.

Parrenin, F., Jouzel, J., Waelbroeck, C., Ritz, C., and Barnola, J.-M.: Dating the Vostok ice core by an inverse method, J. Geophys. Res., 106, 31837–31852, doi:10.1029/2001JD900245, 2001.

Parrenin, F., Remy, F., Ritz, C., Siegert, M. J., and Jouzel, J.: New modeling of the Vostok ice flow line and implication for the glaciological chronology of the Vostok ice core, J. Geophys. Res, 109, 1–14, 2004.

Parrenin, F., Barnola, J.-M., Beer, J., Blunier, T., Castellano, E., Chappellaz, J., Dreyfus, G., Fischer, H., Fujita, S., Jouzel, J., Kawamura, K., Lemieux-Dudon, B., Loulergue, L., Masson-Delmotte, V., Narcisi, B., Petit, J.-R., Raisbeck, G., Raynaud, D., Ruth, U., Schwander, J., Severi, M., Spahni, R., Steffensen, J. P., Svensson, A., Udisti, R., Waelbroeck, C., and Wolff, E.: The EDC3 chronology for the EPICA Dome C ice core, Clim. Past, 3, 485–497, doi:10.5194/cp-3-485-2007, 2007.

Parrenin, F., Petit, J.-R., Masson-Delmotte, V., Wolff, E., Basile-Doelsch, I., Jouzel, J., Lipenkov, V., Rasmussen, S. O., Schwander, J., Severi, M., Udisti, R., Veres, D., and Vinther, B. M.: Volcanic synchronisation between the EPICA Dome C and Vostok ice cores (Antarctica) 0–145 kyr BP, Clim. Past, 8, 1031–1045, doi:10.5194/cp-8-1031-2012, 2012a.

Parrenin, F., Barker, S., Blunier, T., Chappellaz, J., Jouzel, J., Landais, A., Masson-Delmotte, V., Schwander, J., and Veres, D.: On the gas-ice depth difference (Δdepth) along the EPICA Dome C ice core, Clim. Past, 8, 1239–1255, doi:10.5194/cp-8-1239-2012, 2012b.

Parrenin, F., Masson-Delmotte, V., Köhler, P., Raynaud, D., Paillard, D., Schwander, J., Barbante, C., Landais, A., Wegner, A., and Jouzel, J.: Synchronous Change of Atmospheric CO_2 and Antarctic Temperature During the Last Deglacial Warming, Science, 339, 1060–1063, 2013.

Pedro, J. B., van Ommen, T. D., Rasmussen, S. O., Morgan, V. I., Chappellaz, J., Moy, A. D., Masson-Delmotte, V., and Delmotte, M.: The last deglaciation: timing the bipolar seesaw, Clim. Past, 7, 671–683, doi:10.5194/cp-7-671-2011, 2011.

Petit, J. R., Jouzel, J., Raynaud, D., Barkov, N. I., Barnola, J. M., Basile, I., Bender, M., Chappellaz, J., Davis, M., Delaygue, G., Delmotte, M., Kotlyakov, V. M., Legrand, M., Lipenkov, V. Y., Lorius, C., Pépin, L., Ritz, C., Saltzman, E., and Stievenard, M.: Climate and atmospheric history of the past 420 000 years from the Vostok ice core, Antarctica, Nature, 399, 429–436, 1999.

Raisbeck, G. M., Yiou, F., Jouzel, J., and Stocker, T. F.: Direct north-south synchronization of abrupt climate change record in ice cores using Beryllium 10, Clim. Past, 3, 541–547, doi:10.5194/cp-3-541-2007, 2007.

Rasmussen, S. O., Andersen, K. K., Svensson, A. M., Steffensen, J. P., Vinther, B. M., Clausen, H. B., Siggaard-Andersen, M., Johnsen, S. J., Larsen, L. B., Dahl-Jensen, D., Bigler, M., Rothlisberger, R., Fischer, H., Goto-Azuma, K., Hansson, M. E., and Ruth, U.: A new Greenland ice core chronology for the last glacial termination, J. Geophys. Res., 111, D06102, doi:10.1029/2005jd006079, 2006.

Rasmussen, S. O., Seierstad, I. K., Andersen, K. K., Bigler, M., Dahl-Jensen, D., and Johnsen, S. J.: Synchronization of the NGRIP, GRIP, and GISP2 ice cores across MIS 2 and palaeoclimatic implications, Quaternary Sci. Rev., 27, 18–28, 2008.

Ruth, U., Barnola, J.-M., Beer, J., Bigler, M., Blunier, T., Castellano, E., Fischer, H., Fundel, F., Huybrechts, P., Kaufmann, P., Kipfstuhl, S., Lambrecht, A., Morganti, A., Oerter, H., Parrenin, F., Rybak, O., Severi, M., Udisti, R., Wilhelms, F., and Wolff, E.: "EDML1": a chronology for the EPICA deep ice core from Dronning Maud Land, Antarctica, over the last 150 000 years, Clim. Past, 3, 475–484, doi:10.5194/cp-3-475-2007, 2007.

Schilt, A., Baumgartner, M., Blunier, T., Schwander, J., Spahni, R., Fischer, H., and Stocker, T. F.: Glacial-interglacial and millennial-scale variations in the atmospheric nitrous oxide concentration during the last 800,000 years, Quaternary Sci. Rev., 29, 182–192, 2010.

Schüpbach, S., Federer, U., Bigler, M., Fischer, H., and Stocker, T. F.: A refined TALDICE-1a age scale from 55 to 112 ka before present for the Talos Dome ice core based on high-resolution methane measurements, Clim. Past, 7, 1001–1009, doi:10.5194/cp-7-1001-2011, 2011.

Schwander, J., Sowers, T., Barnola, J. M., Blunier, T., Fuchs, A., and Malaizé, B.: Age scale of the air in the summit ice: implication for glacial-interglacial temperature change, J. Geophys. Res., 102, 19483–19493, 1997.

Severi, M., Becagli, S., Castellano, E., Morganti, A., Traversi, R., Udisti, R., Ruth, U., Fischer, H., Huybrechts, P., Wolff, E., Parrenin, F., Kaufmann, P., Lambert, F., and Steffensen, J. P.: Synchronisation of the EDML and EDC ice cores for the last 52 kyr by volcanic signature matching, Clim. Past, 3, 367–374, doi:10.5194/cp-3-367-2007, 2007.

Severi, M., Udisti, R., Becagli, S., Stenni, B., and Traversi, R.: Volcanic synchronisation of the EPICA-DC and TALDICE ice cores for the last 42 kyr BP, Clim. Past, 8, 509–517, doi:10.5194/cp-8-509-2012, 2012.

Severinghaus, J. P., Sowers, T., Brook, E. J., Alley, R. B., and Bender, M. L.: Timing of abrupt climate change at the end of the Younger Dryas interval from thermally fractionated gases in polar ice, Nature, 391, 141–146, 1998.

Singer, B. S., Guillou, H., Jicha, B. R., Laj, C., Kissel, C., Beard, B. L., and Johnson, C. M.: ^{40}Ar/^{39}Ar, K-Ar and ^{230}Th-^{238}U dating of the Laschamp excursion: A radioisotopic tie-point for ice core and climate chronologies, Earth Planet. Sci. Lett., 286, 80–88, 2009.

Sowers, T., Bender, M., Raynaud, D., and Korotkevich, Y. S.: δ^{15}N of N_2 in air trapped in polar ice: a tracer of gas transport in the firn and a possible constraint on ice age-gas age differences, J. Geophys. Res., 97, 15683–15697, 1992.

Spahni, R., Schwander, J., Flückinger, J., Stauffer, B., Chapellaz, J., and Raynaud, D.: The attenuation of fast atmospheric CH_4 variations recorded in polar ice cores, Geophys. Res. Lett., 30, 1571, doi:10.1029/2003GL017093, 2003.

Spahni, R., Chappellaz, J., Stocker, T., Loulergue, L., Hausmmann, G., Kawamura, K., Flückiger, J., Schwander, J., Raynaud, D., Masson-Delmotte, V., and Jouzel, J.: Atmospheric Methane and Nitrous Oxide of the Late Pleistocene from Antarctic Ice Cores, Science, 310, 1317–1321, 2005.

Steig, E. J., Brook, E., White, J., and Sucher, C.: Synchronous Climate Changes in Antarctica and the North Atlantic, Science, 282, 92–95, 1998.

Stenni, B., Buiron, D., Frezzotti, M., Albani, S., Barbante, C., Bard, E., Barnola, J. M., Baroni, M., Baumgartner, M., Bonazza, M., Capron, E., Castellano, E., Chappellaz, J., Delmonte, B., Falourd, S., Genoni, L., Iacumin, P., Jouzel, J., Kipfstuhl, S., Landais, A., Lemieux-Dudon, B., Maggi, V., Masson-Delmotte, V., Mazzola, C., Minster, B., Montagnat, M., Mulvaney, R., Narcisi, B., Oerter, H., Parrenin, F., Petit, J. R., Ritz, C., Scarchilli, C., Schilt, A., Schüpbach, S., Schwander, J., Selmo, E., Severi, M., Stocker, T. F., and Udisti, R.: Expression of the bipolar seesaw in Antarctic climate records during the last deglaciation, Nat. Geosci., 4, 46–49, 2011.

Stocker, T. F. and Johnsen, S. J.: A minimum thermodynamic model for the bipolar seesaw, Paleoceanography, 18, PA000920, doi:10.1029/2003PA000920, 2003.

Suwa, M. and Bender, M. L.: Chronology of the Vostok ice core constrained by O_2/N_2 ratios of occluded air, and its implication for the Vostok climate records, Quaternary Sci. Rev., 27, 1093–1106, 2008.

Svensson, A., Andersen, K. K., Bigler, M., Clausen, H. B., Dahl-Jensen, D., Davies, S. M., Johnsen, S. J., Muscheler, R., Parrenin, F., Rasmussen, S. O., Röthlisberger, R., Seierstad, I., Steffensen, J. P., and Vinther, B. M.: A 60 000 year Greenland stratigraphic ice core chronology, Clim. Past, 4, 47–57, doi:10.5194/cp-4-47-2008, 2008.

Svensson, A., Bigler, M., Blunier, T., Clausen, H. B., Dahl-Jensen, D., Fischer, H., Fujita, S., Goto-Azuma, K., Johnsen, S. J., Kawamura, K., Kipfstuhl, S., Kohno, M., Parrenin, F., Popp, T., Rasmussen, S. O., Schwander, J., Seierstad, I., Severi, M., Steffensen, J. P., Udisti, R., Uemura, R., Vallelonga, P., Vinther, B. M., Wegner, A., Wilhelms, F., and Winstrup, M.: Direct linking of Greenland and Antarctic ice cores at the Toba eruption (74 ka BP), Clim. Past, 9, 749–766, doi:10.5194/cp-9-749-2013, 2013.

Udisti, R., Becagli, S., Castellano, E., Delmonte, B., Jouzel, J., Petit, J.-R., Schwander, J., Stenni, B., and Wolff, E. W.: Stratigraphic correlations between the EPICA-Dome C and Vostok ice cores showing the relative variations of snow accumulation over the past 45 kyr, J. Geophys. Res., 109, D08101, doi:10.1029/2003jd004180, 2004.

Vallelonga, P., Bertagna, G., Blunier, T., Kjær, H. A., Popp, T. J., Rasmussen, S. O., Steffensen, J. P., Stowasser, C., Svensson, A. S., Warming, E., Winstrup, M., Bigler, M., and Kipfstuhl, S.: Duration of Greenland Stadial 22 and ice-gas Δage from counting of annual layers in Greenland NGRIP ice core, Clim. Past, 8, 1839–1847, doi:10.5194/cp-8-1839-2012, 2012.

Voelker, A. H. L.: Global distribution of centennial-scale records for Marine Isotope Stage (MIS) 3: a database, Quaternary Sci. Rev., 21, 1185–1212, 2002.

Vinther, B. M., Clausen, H. B., Johnsen, S. J., Rasmussen, S. O., Andersen, K. K., Buchardt, S. L., Dahl-Jensen, D., Seierstad, I. K., Siggaard-Andersen, M., Steffensen, J. P., Svensson, A., Olsen, J., and Heinemeier, J.: A synchronized dating of three Greenland ice cores throughout the Holocene, J. Geophys. Res., 111, D13102, doi:10.1029/2005jd006921, 2006.

Vinther, B. M., Clausen, H. B., Kipfstuhl, S., Fischer, H., Bigler, M., Oerter, H., Wegner, A., Wilhelms, F., Severi, M., Udisti, R., Beer, J., Steinhilber, F., Muscheler, R., Rasmussen, S. O., and Svensson, A.: An annual layer counted EDML time scale covering the past 16700 years, Geophysical Research Abstracts, 14, EGU2012-13043, 2012.

Waelbroeck, C., Frank, N., Jouzel, J., Parrenin, F., Masson-Delmotte, V., and Genty, D.: Transferring radiometric dating of the last interglacial sea level high stand to marine and ice core records, Earth Planet. Sci. Lett., 265, 183–194, 2008.

Wang, Y. J., Cheng, H., Edwards, R. L., Kong, X., Shao, X., Chen, S., Wu, J., Jiang, X., Wang, X., and An, Z.: Millennial- and orbital-scale changes in the East Asian monsoon over the past 224,000 years, Nature, 451, 1090–1093, 2008.

Wolff, E. W., Fischer, H., and Röthlisberger, R., Glacial terminations as southern warmings without northern control, Nat. Geosci., 2, 206–209, 2009.

Wolff, E. W., Chappellaz, J., Blunier, T., Rasmussen, S. O., and Svensson, A.: Millennial-scale variability during the last glacial: The ice core record, Quaternary. Sci. Rev., 29, 2828–2838, 2010.

Yiou, F., Raisbeck, G. M., Baumgartner, S., Beer, J., Hammer, C., Johnsen, S., Jouzel, J., Kubik, P. W., Lestringuez, J., Stiévenard, M., Suter, M., and Yiou, P.: Beryllium 10 in the Greenland Ice Core Project ice core at Summit, Greenland, J. Geophys. Res., 102, 26783–26794, 1997.

Zielinski, G. A.: Use of paleo-records in determining variability within the volcanism-climate system, Quaternary Sci. Rev., 19, 417–438, 2000.

Clim. Past, 9, 1715–1731, 2013
www.clim-past.net/9/1715/2013/
doi:10.5194/cp-9-1715-2013

Climate of the Past
Open Access

An optimized multi-proxy, multi-site Antarctic ice and gas orbital chronology (AICC2012): 120–800 ka

L. Bazin[1], A. Landais[1], B. Lemieux-Dudon[2], H. Toyé Mahamadou Kele[2], D. Veres[3,4], F. Parrenin[3], P. Martinerie[3], C. Ritz[3], E. Capron[5], V. Lipenkov[6], M.-F. Loutre[7], D. Raynaud[3], B. Vinther[8], A. Svensson[8], S. O. Rasmussen[8], M. Severi[9], T. Blunier[8], M. Leuenberger[10], H. Fischer[10], V. Masson-Delmotte[1], J. Chappellaz[3], and E. Wolff[5]

[1]Laboratoire des Sciences du Climat et de l'Environnement, UMR8212, CNRS – Gif sur Yvette, France
[2]Laboratoire Jean Kuntzmann, Grenoble, France
[3]Laboratoire de Glaciologie et Geophysique de l'Environnement, CNRS-UJF, St. Martin d'Heres, France
[4]Institute of Speleology, Romanian Academy, Cluj-Napoca, Romania
[5]British Antarctic Survey, Cambridge, UK
[6]Arctic and Antarctic Research Institute, St. Petersburg, Russia
[7]Université catholique de Louvain, Earth and Life Institute, Georges Lemaître Center for Earth and Climate Research, Louvain-la-Neuve, Belgium
[8]Centre for Ice and Climate, Niels Bohr Institute, University of Copenhagen, Copenhagen, Denmark
[9]Department of Chemistry Ugo Schiff, University of Florence, Florence, Italy
[10]Climate and Environmental Physics, Physics Institute and Oeschger Center for Climate Change Research, University of Bern, Bern, Switzerland

Correspondence to: L. Bazin (lucie.bazin@lsce.ipsl.fr), A. Landais (alandais@lsce.ipsl.fr)

Received: 14 November 2012 – Published in Clim. Past Discuss.: 30 November 2012
Revised: 24 June 2013 – Accepted: 25 June 2013 – Published:

Abstract. An accurate and coherent chronological framework is essential for the interpretation of climatic and environmental records obtained from deep polar ice cores. Until now, one common ice core age scale had been developed based on an inverse dating method (Datice), combining glaciological modelling with absolute and stratigraphic markers between 4 ice cores covering the last 50 ka (thousands of years before present) (Lemieux-Dudon et al., 2010). In this paper, together with the companion paper of Veres et al. (2013), we present an extension of this work back to 800 ka for the NGRIP, TALDICE, EDML, Vostok and EDC ice cores using an improved version of the Datice tool. The AICC2012 (Antarctic Ice Core Chronology 2012) chronology includes numerous new gas and ice stratigraphic links as well as improved evaluation of background and associated variance scenarios. This paper concentrates on the long timescales between 120–800 ka. In this framework, new measurements of $\delta^{18}O_{atm}$ over Marine Isotope Stage (MIS) 11–12 on EDC and a complete $\delta^{18}O_{atm}$ record of the TALDICE ice cores permit us to derive additional orbital gas age constraints. The coherency of the different orbitally deduced ages (from $\delta^{18}O_{atm}$, $\delta O_2/N_2$ and air content) has been verified before implementation in AICC2012. The new chronology is now independent of other archives and shows only small differences, most of the time within the original uncertainty range calculated by Datice, when compared with the previous ice core reference age scale EDC3, the Dome F chronology, or using a comparison between speleothems and methane. For instance, the largest deviation between AICC2012 and EDC3 (5.4 ka) is obtained around MIS 12. Despite significant modifications of the chronological constraints around MIS 5, now independent of speleothem records in AICC2012, the date of Termination II is very close to the EDC3 one.

1 Introduction

While ice core records offer a wealth of palaeoclimatic and paleoenvironmental information, uncertainties associated with ice core dating limit their contribution to the understanding of past climate dynamics. Age scales in calendar

years have been constructed for Greenland ice cores thanks to layer counting in sites offering sufficient accumulation rates (GRIP, NGRIP) (Rasmussen et al., 2006; Svensson et al., 2006; Svensson et al., 2008), allowing the construction of the GICC05 Greenland age scale currently spanning the past 60 ka (i.e. thousand of years before present, present being year 1950 AD in our study). Layer counting is not possible for deep Antarctic ice cores recovered in low accumulation areas and absolute time markers are generally lacking for these long Antarctic records, now extending to 800 ka. Exceptions are promising studies using $^{40}Ar/^{39}Ar$ and U/Th dating tools (Dunbar et al., 2008; Aciego et al., 2011) as well as links between ^{10}Be peaks and well-dated magnetic events (Raisbeck et al., 2007) but an absolute age scale for the last 800 ka is still missing. As a result, dating of the deepest part of these Antarctic cores is largely based on various approaches combining ice flow modelling with orbital tuning.

Initial orbital dating in ice cores was inspired by orbital dating of marine cores (Imbrie and Imbrie, 1980), assuming that the Milanković theory (1941), linking ice volume and high latitude insolation, is correct. A similar link has been proposed between temperature records from water isotopes and the insolation curves deduced from orbital parameters (obliquity, precession) (Lorius et al., 1985). The imprint of precession in the Vostok ice core record of methane (CH_4) concentration was also investigated (Ruddiman and Raymo, 2003). Such assumptions are, however, not satisfactory when one important question is to identify the insolation–climate phase relationship at orbital timescales. More recently, three different orbital dating approaches have been developed for ice core dating, independent of Antarctic climate or greenhouse gases records.

First, long records of $\delta^{18}O$ of atmospheric O_2 ($\delta^{18}O_{atm}$) have revealed that this parameter is highly correlated with insolation variations in the precession band with a lag of about 5–6 ka (Bender et al., 1994; Petit et al., 1999; Dreyfus et al., 2007). Studies have linked variations in precession to $\delta^{18}O_{atm}$ through changes in the low latitude water cycle and biospheric productivity (Bender et al., 1994; Malaizé et al., 1999; Wang et al., 2008; Severinghaus et al., 2009; Landais et al., 2007, 2010). The significant time delay between changes in precession and changes in $\delta^{18}O_{atm}$ has been attributed to a combination of the 1–2 ka residence time of O_2 in the atmosphere (Bender et al., 1994; Hoffmann et al., 2004) and to the numerous and complex processes linking the isotopic composition of seawater to atmospheric oxygen via the dynamic response of the tropical water cycle to precession forcing and the associated variations in terrestrial and oceanic biospheres (Landais et al., 2010, and references therein). This multiplicity of processes also suggests that lags may vary with time (Jouzel et al., 2002; Leuenberger, 1997). As a consequence, the $\delta^{18}O_{atm}$ record from long ice cores can be used to constrain ice core chronologies, but with a large associated uncertainty (6 ka) (Petit et al., 1999; Dreyfus et al., 2007).

Second, Bender (2002) has proposed that the elemental ratio $\delta O_2/N_2$ in the trapped air could be used as a new orbital tuning tool. Indeed, $\delta O_2/N_2$ measurements in the firn near the pore close-off depth (about 100 m below the ice-sheet surface, i.e. where unconsolidated snow is compressed and lock the air in) have revealed that the air trapping process is associated with a relative loss of O_2 with respect to N_2 (Battle et al., 1996; Severinghaus and Battle, 2006; Huber et al., 2006). Between 160 and 400 ka, the $\delta O_2/N_2$ record of the Vostok ice core displays variations similar to those of the local 21 December insolation (78° S). From these two observations, Bender (2002) formulated the hypothesis that local Antarctic summer insolation influences near-surface snow metamorphism and that this signature is preserved during the firnification process down to the pore close-off depth, where it modulates the loss of O_2. From this hypothesis, he proposed the use of $\delta O_2/N_2$ for dating purposes and this approach was used by Kawamura et al. (2007) and Suwa and Bender (2008) to construct orbital chronologies of the Dome F and Vostok ice cores back to 360 and 400 ka, respectively. Using their high-quality $\delta O_2/N_2$ record on the Dome F ice core and comparison with radiometric dating obtained on speleothem records, Kawamura et al. (2007) estimated the dating uncertainty to be as low as 0.8–2.9 ka. Still, Landais et al. (2012) have suggested that the uncertainty could be higher in some cases because (1) the tuning target is questionable and (2) the match between the $\delta O_2/N_2$ and insolation signal may not always be straightforward in periods characterized by low eccentricity. Moreover, no consistent theory has been put forward that can explain how the insolation signal imprinted in the snow pack survives the densification process.

Third, additional orbital information was derived from local insolation changes imprinted in the record of total air content in polar ice. Raynaud et al. (2007) indeed showed that part of the variance in total air content in the EPICA Dome C (EDC) ice core over the last 440 ka can be explained by the variations of an integrated summer insolation parameter (i.e. summation over the year of the daily insolation exceeding some threshold for a given latitude) that has a dominant obliquity component. This marker was therefore suggested as another tool for orbital dating of ice core records.

When avoiding the use of climate records as orbital targets, three orbital tools ($\delta^{18}O_{atm}$, $\delta O_2/N_2$ and air content) are available for deep ice cores dating. These three tools have different tuning targets and are associated with at least two different mechanisms (local insolation influencing air trapping and precession influencing hydrological cycle and biosphere productivity). They should thus provide independent information and should be used as complementary tools in ice core dating. The full coherency between these orbital age markers still remains to be examined. So far, Suwa and Bender (2008) explored the complementarity of $\delta^{18}O_{atm}$ and $\delta O_2/N_2$ and Lipenkov et al. (2011) the one of $\delta O_2/N_2$ and air content at Vostok between 100 and 400 ka.

The first integrated dating effort for a deep Antarctic ice core combining glaciological modelling and absolute and orbital tuning was conducted for the Vostok ice core (Petit et al., 1999; Parrenin et al., 2001, 2004). Longer ice core climatic and greenhouse gases records have been obtained from the EDC ice core that covers the last 800 ka (Jouzel et al., 2007; Lüthi et al., 2008; Loulergue et al., 2008). The state of the art dating of the EDC ice core (EDC3 chronology) has been described in Parrenin et al. (2007). It is based on ice flow modelling using an inverse method constrained by various age markers. These age markers include reference horizons such as volcanic horizons (Mt. Berlin eruption, Dunbar et al., 2008) and peaks in ^{10}Be flux (i.e. Laschamp event, Yiou et al., 1997; Raisbeck et al., 2007). The EDC3 age scale was synchronized with the layer-counted Greenland GICC05 chronology over the last 6 ka, the deglaciation and the Laschamp event through 5 age constraints. Other tie points are more subject to discussion because they have underlying assumptions that some climatic events are synchronous, for example the abrupt methane increase at Termination II was assumed to be synchronous (within 2 ka) with the abrupt δ^{18}O shift in speleothem calcite recorded in the East Asia (Yuan et al., 2004) and Levantine (Bar-Matthews et al., 2003) regions at around 130.1 ka.

For ice older than the last interglacial period, tie points were mainly derived from orbital tuning. Thirty-eight (38) $\delta^{18}O_{atm}$ tie points with a 6 ka uncertainty were included in EDC3 between 400 and 800 ka as well as 10 air content tie points with a 4 ka uncertainty between 71 and 431 ka. The overall uncertainty attached to the EDC3 timescale was estimated at 6 ka from 130 ka down to the bottom of the record (Parrenin et al., 2007).

The EPICA Dronning Maud Land (EDML) timescale over the past 150 ka has been derived directly from the EDC3 timescale after matching volcanic horizons between the two cores (Ruth et al., 2007). The TALos Dome ICE core (TALDICE) timescale has also been derived from other Antarctic ice cores through synchronization of the CH_4 records (Buiron et al., 2011; Schüpbach et al., 2011), CH_4 being with $\delta^{18}O_{atm}$ a global tracer of the atmosphere, hence of wide use for relative dating of ice cores (e.g. Capron et al., 2010).

Summarizing, each deep ice core has its own chronology which is not necessarily coherent with the other ice core chronologies. Typically, the Vostok GT4 and Dome C EDC3 age scales have been established separately and display significant deviations (Parrenin et al., 2007). Since some proxies are measured on the ice phase, such as water isotopes, dust or chemical species, and other in the gas phase, for example CO_2 and CH_4, ice and gas age scales must be established. The ice and gas timescales are different because air is isolated from the surface at approximately 50–120 m under the ice-sheet surface, at the firn-ice transition, or lock-in depth (LID). In addition to the ice chronology, it is thus essential to have for each ice core a good estimate of the depth evolution of the LID to link gas and ice chronologies. According to firnification models (Herron and Langway, 1980; Schwander et al., 1993; Arnaud et al., 2000; Goujon et al., 2003; Salamatin et al., 2004), the LID evolution can be estimated from past changes in temperature and accumulation rate. The outputs of firnification models have thus classically been used to calculate the LID and provide the gas chronology associated with the ice chronology. However, firnification models have recently been reported to be inaccurate for representing glacial-interglacial changes in LID in Antarctica (Parrenin et al., 2012a; Capron et al., 2013).

Recently, Lemieux-Dudon et al. (2010) developed a method based on an inverse technique to produce coherent ice and gas timescales for 4 different ice cores (Vostok, EDC, EDML, NGRIP). This method aims for the best compromise between individual chronological information for each ice core using glaciological modelling and gas and ice absolute or relative markers. This consistent timescale only covers the last 50 ka (where age markers were compiled and implemented) and does not include all deep ice cores.

In this paper, together with the companion paper of Veres et al. (2013), we aim at producing a coherent ice and gas timescale over the last 800 ka including 5 ice cores (Vostok, EDC, EDML, TALDICE, NGRIP) without any assumption on the synchronism between climatic records and insolation or speleothem-derived tie points. We use the same strategy as the one of Lemieux-Dudon et al. (2010) with some technical and methodological (SOM) improvements. In order to include the TALDICE ice core and extend the timescale prior to 50 ka, we gather a database of age markers and expand $\delta^{18}O_{atm}$ records of TALDICE and EDC. We then discuss the implementation and robustness of orbital points that are key for the long timescales. Finally, we discuss the climatic implications of this new timescales with $\delta^{18}O_{ice}$ and CH_4 records displayed on the new chronology over the last 800 ka with a focus on the last interglacial period (Marine Isotopic Stage, MIS 5).

2 Dating strategy

The Datice tool (Lemieux-Dudon et al., 2010) is a numerical program that permits us to obtain the best compromise between a background chronology (based on modelling of snow accumulation rates, snow densification into ice and ice flow) and observations (absolute ages or certain reference horizons, stratigraphic links between several cores or also orbital ages).

Basically, a background scenario consists of three profiles along the ice core as a function of the depth z: the initial accumulation rate (A), the vertical thinning function (τ) and the Lock-In Depth in Ice Equivalent (LIDIE). Age scales for the ice matrix (ψ) and the gas bubbles (χ), which is assumed to be unique and the same for all species, are deduced using the following equations:

$$\psi(z) = \int_0^z \frac{D(z')}{\tau(z') \cdot A(z')} \mathrm{d}z' \quad (1)$$

$$\Delta\mathrm{depth}(z) \sim \mathrm{LIDIE}(z) \cdot \tau(z) \quad (2)$$

$$\chi(z) = \psi(z - \Delta\mathrm{depth}(z)), \quad (3)$$

where D is the relative density of the snow/ice material.

In the Datice tool, one needs to define how confident we are in the background scenarios, by determining confidence intervals (errors are assumed to be log-normal) on the accumulation, thinning and LIDIE profiles and also correlation lengths for each of these profiles (the errors in between profiles are assumed to be decorrelated). The same is true for the observations (absolute age horizons or stratigraphic links between the cores), which are assumed independent and for which a confidence interval is assigned. The Datice tool then finds the best scenario of accumulation, thinning and LIDIE and the resulting ice and gas chronologies by taking into account the background scenarios and the observations. The Datice methodology relies on the construction of a cost function, which takes into account the full dating information (background scenarios and observations). The best scenario is the one which satisfies more closely all the dating constraints. The search for the best scenario is driven by a quasi-newton algorithm (Gilbert and Lemarechal, 1993), which requires a linearization of the model equations (in order to calculate the gradient of the cost function) at each iteration.

The estimate of the age uncertainty is done exactly the same way as detailed in the SOM of Lemieux-Dudon et al. (2010). In summary, Datice calculates an error covariance matrix denoted **P**, which is an estimate of the errors made on accumulation, thinning and LIDIE at each depth level and for each ice core. The **P** matrix entirely depends on inputs of the dating problem: the **B** matrix storing the covariances of errors of the different background scenarios (accumulation, thinning, LIDIE); the **R** matrix storing the uncertainties associated with each data constraint (absolute, stratigraphic, orbital tie points); and finally the $\boldsymbol{H}$ operator. $\boldsymbol{H}$ is the linearization of the observation operator, denoted h, that predicts the data (absolute, stratigraphic, orbital tie points) from a given scenario of accumulation, thinning and LIDIE. To illustrate this, the observation operator maps a vector $(a_1, \ldots, a_n, t_1, \ldots, t_n, l_1, \ldots, l_n)$ whose components are accumulation, thinning and LIDIE, into an age vector $(h_1, \ldots, h_N)$ that predicts the age at the age markers depths $(z_1, \ldots, z_N)$. Under some assumptions, **P** is expressed as: $\mathbf{P} \simeq (\mathbf{B}^{-1} + \boldsymbol{H}^T \mathbf{R}^{-1} \boldsymbol{H})^{-1}$. The age error covariance matrix, **C**, is expressed as: $\mathbf{C} \simeq \boldsymbol{H}\mathbf{P}\boldsymbol{H}^T$. **C** stores errors propagated from the background and observation variances and covariances. Near an absolute tie point with a small associated uncertainty, the a posteriori error will thus be dominated by the observation error, while near a tie point with a very large associated uncertainty, this error will mainly result from the variances (and covariances) associated with the background scenarios. More details on the age scale uncertainty calculation over different time periods are given in SOM.

After a revision of all the different age markers used in Lemieux-Dudon et al. (2010), we decided to remove the 6 orbital tuning points at Vostok (132.4, 200.6, 246.0, 293.6, 336.2 and 373.8 ka; Parrenin et al., 2001) due to the climatic hypothesis they are based on, the isotopic points between TALDICE and EDC, the tie point at 130.1 ka at EDC from speleothem dating and all points derived by successive transfer from one core to another. The air content data used for the construction of EDC3 (Parrenin et al., 2007) are replaced by new age markers (see Sect. 3).

Few absolute ages (tephra layers, Laschamp event, Brunhes–Matuyama reversal, layer counting) are available for the different ice cores. For tephra layers, we only consider the ones identified in our ice cores directly. As a consequence, we need orbital ages ($\delta^{18}O_{atm}$, $\delta O_2/N_2$ and air content) with coherent uncertainties to constrain the timescale prior to 60 ka when layer counting is not available. We use here available $\delta^{18}O_{atm}$, $\delta O_2/N_2$ and air content profiles on the different ice cores (Dreyfus et al., 2007, 2008; Suwa and Bender, 2008; Landais et al., 2012; Raynaud et al., 2007; Lipenkov et al., 2011) completed by new $\delta^{18}O_{atm}$ data covering the period older than 50 ka on the TALDICE ice core and the period 350–450 ka on the EDC ice core.

The synchronization of the different ice cores is done through CH_4, $\delta^{18}O_{atm}$ measurements in the gas phase (255 tie points) and volcanic tie points in the ice phase (534 tie points) (Udisti et al., 2004; Severi et al., 2007, 2012; Loulergue et al., 2007; Lemieux-Dudon et al., 2010; Landais et al., 2006; Loulergue, 2007; Ruth et al., 2007; Buiron et al., 2011; Schüpbach et al., 2011; Capron et al., 2010; Schilt et al., 2010; Parrenin et al., 2012b; Svensson et al., 2013; Vinther et al., 2013, details in the SOM).

Additional constraints on the depth difference between a concomitant event in the ice and in the gas phases (Δdepth) are available for Greenland ice cores over the millennial scale variability of the last glacial period (Dansgaard–Oeschger events) with the use of $\delta^{15}N$ in the air trapped in the ice. Each rapid warming is indeed recorded as a peak in $\delta^{15}N$ (thermal isotopic fractionation) in the gas phase and as a step in the ice $\delta^{18}O$. The depth difference between the $\delta^{15}N$ peak and the ice $\delta^{18}O$ step has been measured for DO 9–25 on the NorthGRIP ice core (Landais et al., 2004, 2005; Huber et al., 2006; Capron et al., 2010) defining 15 constraints for the Δdepth (Table in SOM).

Finally, it has been suggested that $\delta^{15}N$ in Antarctica can also be used for improving our estimate of LID independently of firnification models (Parrenin et al., 2012a). This is based on the assumption that the firn depth, from surface to the LID, is always equal to the depth of the diffusive zone, which can be inferred from $\delta^{15}N$ data. While this is very often the case for present day firns (Landais et al., 2006), a convective zone of about 20 m may exist during glacial period in remote sites of East Antarctica (Severinghaus et al., 2010).

We thus refrain from imposing any delta-depth constraints from δ^{15}N profiles in Antarctica but use these data for the LIDIE background scenario (details in SOM).

3 Orbital markers

As discussed above, the most critical aspect for the 120–800 ka dating is the availability and use of the orbital markers. In a first sub-section, we will provide new $\delta^{18}O_{atm}$ data for orbital constraints on TALDICE and EDC. In a second sub-section, we review and evaluate dating uncertainties of the available $\delta^{18}O_{atm}$, $\delta O_2/N_2$ and air content series.

3.1 New measurements

All measurements of $\delta^{18}O_{atm}$ of air trapped in the ice cores of EDC and TALDICE were performed at LSCE, using a melt-refreeze method (Sowers et al., 1989; Landais et al., 2003a). The analyses were conducted on a Delta V plus (Thermo Electron Corporation) mass spectrometer and data were corrected for mass interferences (Severinghaus et al., 2001; Landais et al., 2003a). The measurements were calibrated against current dried exterior air. The $\delta^{18}O_{atm}$ is obtained after correction of the $\delta^{18}O$ of O_2 for the gravitational isotopic fractionation in the firn ($\delta^{18}O_{atm}$=$\delta^{18}O-2\delta^{15}N$). The resulting data set has a precision of roughly 0.03 ‰ (1 sigma uncertainty).

3.1.1 $\delta^{18}O_{atm}$ of EDC

The first EDC $\delta^{18}O_{atm}$ record has been produced by Dreyfus et al. (2007, 2008) between 300 and 800 ka with a mean resolution of 1.5 ka. They defined 38 tie points by aligning mid-slope variations of $\delta^{18}O_{atm}$ with their counterparts in the precession parameter (delayed by 5 ka), leading to an uncertainty of 6 ka for each tie point. Still, the period covering 300–410 ka and including MIS 11 shows $\delta^{18}O_{atm}$ variations that cannot unambiguously match the precession curve (Fig. 1). During this period, the low eccentricity damps the variations of the climatic precession parameter, classically expressed as $e\sin(\overline{\omega})$ with e the eccentricity and $\overline{\omega}$ the longitude of perihelion. During periods of low eccentricity, the mid-slope association is thus more difficult. As a consequence, the 6 tie points originally proposed over this period can be challenged.

We have performed $\delta^{18}O_{atm}$ measurements on 92 new ice samples from EDC between 2479 and 2842 m (covering 300 to 500 ka) with a mean resolution of 1 ka.

With our improved resolution of the $\delta^{18}O_{atm}$ signal over this period, we are now able to better constrain the EDC chronology by orbital tuning. To do so, we strictly follow the methodology of Dreyfus et al. (2007) described above. We obtain 7 new orbital tuned ages for the gas phase of EDC ice core, replacing the first 6 points of the Table 1 of Dreyfus et al. (2007). Finally, we end up with 39 $\delta^{18}O_{atm}$ points to be used as orbital constraints in the gas phase for the EDC ice core (Table 1). Note that the $\delta^{18}O_{atm}$ ages are in agreement with the absolute dating of the Brunhes–Matuyama reversal, suggesting that we did not miss any precession cycle (Dreyfus et al., 2008).

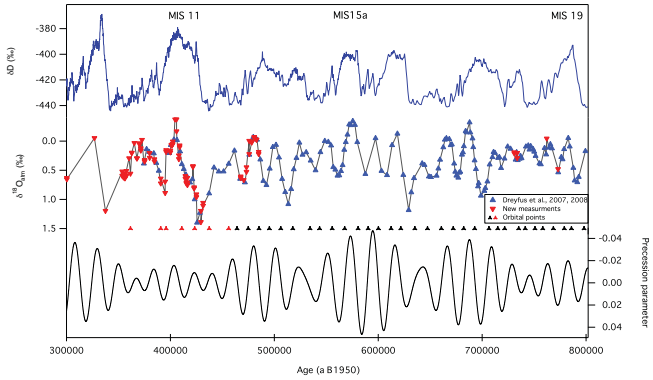

Fig. 1. EDC records between 300 and 800 ka on the EDC3 age scale. Top: water stable isotope (δD) record with labeling of selected interglacial periods (Jouzel et al., 2007). Middle: complete record of $\delta^{18}O_{atm}$, blue triangles from Dreyfus et al. (2007, 2008) and red triangles from this study. Bottom: precession parameter (here on a reverse y axis) obtained with the Analyseries software (Paillard et al., 1996), calculated using the Laskar et al. (2004) solution. Black points indicate the position of tie points between $\delta^{18}O_{atm}$ and precession parameter signals from Dreyfus et al. (2007); the red ones are from this study (Table 1).

3.1.2 $\delta^{18}O_{atm}$ of TALDICE

Buiron et al. (2011) have measured the $\delta^{18}O_{atm}$ of TALDICE between 583 and 1402 m (9.4 and 125.8 ka) and could identify clear precession driven $\delta^{18}O_{atm}$ cycles around 10 and 85 ka. However significant gaps remained at 24–33 ka, 81–110 ka and before 126 ka. With now 83 new depth levels measured in this study, we obtain a complete record of $\delta^{18}O_{atm}$ along the entire core with a mean resolution of 1.5 ka (Fig. 2).

Using the original TALDICE 1a age scale (Buiron et al., 2011; Schüpbach et al., 2011), the full $\delta^{18}O_{atm}$ record displays clear $\sim$ 23 ka cycles corresponding to precession variations back to 200 ka (Fig. 2). Prior to 200 ka, $\delta^{18}O_{atm}$ shows a large variability with much higher frequency variations. This questions the integrity of the record. Spurious variations of $\delta^{18}O_{atm}$ can indeed be used, together with methane, to check the integrity of ice core records especially on their bottom part by comparison with undisturbed records of the same time period (Landais et al., 2003b). A comparison of the methane and $\delta^{18}O_{atm}$ records of Vostok and TALDICE ice cores over the last 300 ka on their respective chronologies (Fig. 3) shows significant differences. Over the last 150 ka, differences are most probably due to the different age scales of the ice cores since the CH_4 and $\delta^{18}O_{atm}$ sequences and amplitudes are similar despite small shifts between the two

Table 1. Orbital ages from $\delta^{18}O_{atm}$ for EDC.

Depth (m)	Gas age (ka)	σ (ka)	Source
2644.44	363.094	6.0	a
2697.23	389.425	6.0	a
2708.24	398.546	6.0	a
2751.13	408.283	6.0	a
2777.54	427.377	6.0	a
2795.31	435.854	6.0	a*
2812.79	454.779	6.0	a*
2819.2	464.557	6.0	b
2829.36	474.756	6.0	b
2841.75	485.293	6.0	b
2856.27	495.921	6.0	b
2872.56	506.642	6.0	b
2890.33	517.602	6.0	b
2913.3	532.027	6.0	b*
2921.99	545.313	6.0	b
2938.24	556.414	6.0	b
2968.08	567.606	6.0	b
2998.96	578.627	6.0	b
3008.93	589.460	6.0	b
3017.25	600.078	6.0	b
3027.54	610.875	6.0	b
3035.41	622.074	6.0	b
3043.01	634.419	6.0	b
3048.51	649.064	6.0	b
3056.77	660.789	6.0	b
3065.93	671.703	6.0	b
3077.74	682.326	6.0	b
3093.51	693.159	6.0	b
3112.43	703.964	6.0	b
3119.57	714.369	6.0	b
3124.27	724.376	6.0	b
3136.18	733.949	6.0	b
3143.2	741.944	6.0	b
3152.25	749.184	6.0	b
3158.91	758.069	6.0	b
3166.87	767.679	6.0	b
3174.81	777.607	6.0	b
3180.6	787.736	6.0	b
3189.83	797.460	6.0	b

a: this study. b: Dreyfus et al. (2007). The asterisks indicate tie points which have been removed (see Sect. 4.1).

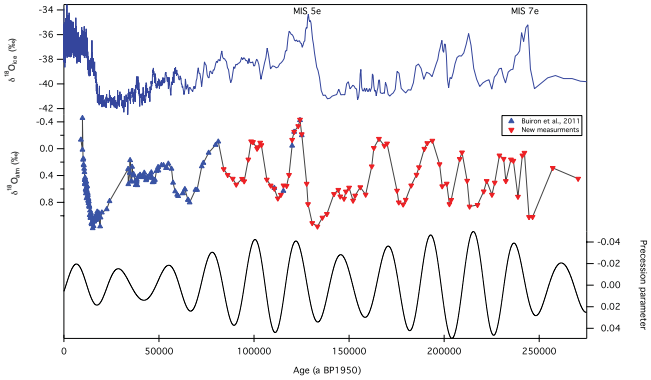

Fig. 2. TALDICE records between 0 and 250 ka on TALDICE 1a age scale. Top: water stable isotope ($\delta^{18}O_{ice}$) record with labeling of selected interglacial periods (Stenni et al., 2011). Middle: complete record of $\delta^{18}O_{atm}$, blue triangles from Buiron et al. (2011) and red triangles from this study. Bottom: precession parameter (same as in Fig. 1).

Table 2. Stratigraphic links between TALDICE and Vostok deduced from $\delta^{18}O_{atm}$.

Depth TALDICE (m)	Depth Vostok (m)	σ (a)
668.93	310.5	1000
1255.55	907	1000
1308.39	1113	1000
1333.37	1244	1000
1357.95	1415	1500
1373.99	1535	1500
1390.4	1672.18	2000
1406.27	1853.15	2000

ice cores. Prior to 150 ka, the methane record has a poor resolution and the two $\delta^{18}O_{atm}$ records show significant differences in amplitude and frequency before 200 ka. We have thus decided to stop analysis and chronologies at 150 ka (corresponding to $\sim$ 1500 m depth) for the TALDICE ice core until new methane and $\delta^{18}O_{atm}$ measurements are performed allowing us to assess the integrity of the stratigraphy. Note that surprisingly large ice crystals have been observed below 1500 m on the TALDICE ice core, which further questions the integrity of the core.

By comparing TALDICE and Vostok $\delta^{18}O_{atm}$ records back to 150 ka, we were able to determine 8 new gas stratigraphic links between these two cores (Fig. 3 and Table 2).

3.2 Orbital points database

In this section, we combine the new orbital tie points derived in the previous section and the orbital tie points already available from previous studies.

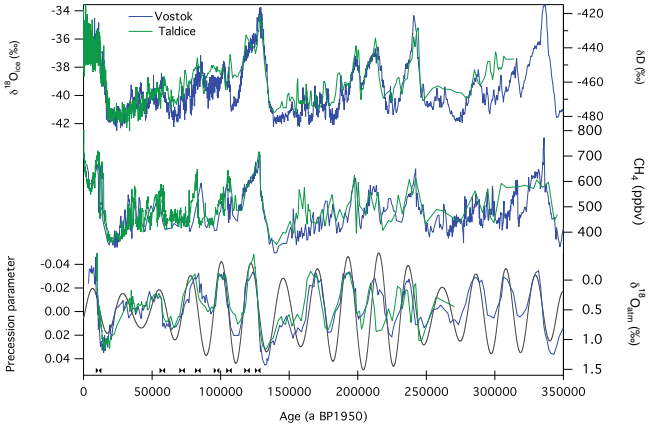

Fig. 3. Comparison between Vostok (blue) and TALDICE (green) ice cores on the $\delta^{18}O_{atm}$ chronology (Bender, 2002) and TALDICE 1a age scale (Buiron et al., 2011; Schüpbach et al., 2011), respectively. Top: water stable isotope records (δD and $\delta^{18}O_{ice}$, respectively) (Petit et al., 1999; Stenni et al., 2011). Middle: methane records, Vostok: Petit et al. (1999); Caillon et al. (2003); Delmotte et al. (2004), TALDICE: Buiron et al. (2011); Schüpbach et al. (2011). Bottom: $\delta^{18}O_{atm}$ records: Vostok: Bender (2002); Suwa and Bender (2008), TALDICE: Buiron et al. (2011) and this study. The grey curve corresponds to the precession parameter. Black markers indicate the position of stratigraphic links between TALDICE and Vostok deduced from $\delta^{18}O_{atm}$ data.

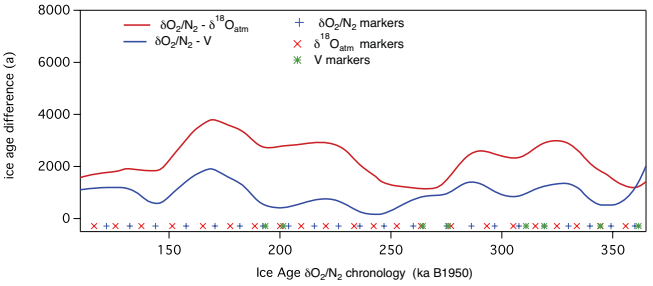

Fig. 4. Ice age difference between the $\delta O_2/N_2$ and air content (V) chronologies (blue) and $\delta O_2/N_2$ and $\delta^{18}O_{atm}$ chronologies (red) on the Vostok ice core. The different markers show the position of the orbital age constraints for each chronology.

3.2.1 $\delta^{18}O_{atm}$

In addition to the EDC $\delta^{18}O_{atm}$ markers discussed above, we also use the markers deduced by Suwa and Bender (2008) for Vostok (Table 2 therein). The tuning is slightly different than the one chosen by Dreyfus et al. (2007) (tuning on the 65° N June insolation curve with a delay of 5.9 ka instead of tuning on the precession signal with a 5 ka delay). A comparison of both tuning strategies has shown that they are equivalent (Dreyfus et al., 2007).

Altogether, we now have a database of $\delta^{18}O_{atm}$ with 39 gas age markers for EDC and 35 for Vostok. The uncertainty associated with all these points is estimated to be a quarter of a precession period (Dreyfus et al., 2007), leading to a value of 6 ka. This relatively large uncertainty accounts for the uncertainty in the choice of the orbital target and for the fact that the shift between $\delta^{18}O_{atm}$ and precession is known to vary with time, especially over terminations (Jouzel et al., 2002; Kawamura et al., 2007).

Table 3. Orbital ages from $\delta O_2/N_2$ for EDC, deduced from Landais et al. (2012).

Depth (m)	Ice age (ka)	σ (ka)
2795.69	449.000	4.0
2808.33	460.000	4.0
2818.15	470.000	4.0
2829.13	480.000	4.0
2841.58	490.000	4.0
2858.78	501.000	4.0
2873.06	512.000	4.0
2888.95	522.000	4.0
2905.88	533.000	4.0
2919.62	551.000	4.0
2936.61	562.000	4.0
2975.52	573.000	4.0
2999.23	583.000	4.0
3009.36	594.000	4.0
3017.73	605.000	4.0
3028.6	616.000	4.0
3065.86	677.000	4.0
3078.05	688.000	4.0
3092.52	698.000	4.0
3109.93	710.000	4.0
3169.32	778.000	6.0
3179.27	788.000	6.0

3.2.2 $\delta O_2/N_2$

For the aim of the AICC2012 chronology, two $\delta O_2/N_2$ records are available: Vostok (100–400 ka, Suwa and Bender, 2008) and EDC (300 to 800 ka, Landais et al., 2012). While Suwa and Bender (2008) already produced 27 $\delta O_2/N_2$ orbital tie points using as target the local December insolation, no tie points were proposed by Landais et al. (2012). Here, we have derived 20 orbital ages from the EDC $\delta O_2/N_2$ record (Table 3). To do this, the $\delta O_2/N_2$ signal is filtered with a band pass between 1/15 ka^{-1} and 1/100 ka^{-1}. Its mid slope variations are then associated with the mid-slopes of the local summer solstice insolation signal. No tie points were attributed in periods with too low $\delta O_2/N_2$ resolution and in periods without a clear correspondence between the $\delta O_2/N_2$ record and the insolation curve.

We have decided to attribute a conservative uncertainty of 4 ka to all of these tie points (both for Vostok and EDC) because of the low quality of the measurements (gas loss) and questions about the phasing of local insolation curve and $\delta O_2/N_2$ curve (Suwa and Bender, 2008; Landais et al.,

Table 4. Orbital ages from air content for EDC, deduced from Raynaud et al. (2007).

depth (m)	ice age (ka)	σ (ka)
501.65	21.950	2.879
693.668	38.950	2.211
1255.93	86.950	3.082
1377.67	100.950	4.031
1790.29	142.950	6.468
2086.69	202.950	6.403
2186.29	216.950	6.316
2307.2	245.950	6.316
2350.1	260.950	6.615
2500.25	306.950	6.652
2510.75	318.950	6.242
2610.8	346.950	7.120
2632.25	359.950	6.576
2783.5	424.950	6.782

2012). Note that choosing a smaller uncertainty for the $\delta O_2/N_2$ tie points does not change the AICC2012 chronology, but mainly leads to an "unrealistically" small uncertainty (i.e. less than 2 ka before 150 ka for Vostok).

3.2.3 Air content

Air content measurements have been published for the Vostok ice core (150–400 ka, Lipenkov et al., 2011) and for the youngest part of the EDC ice core (0–440 ka, Raynaud et al., 2007) but no orbital tie points were provided. To build such tables, we have followed two different approaches, the one proposed by Raynaud et al. (2007) and the one similar to what has been applied for $\delta O_2/N_2$ and $\delta^{18}O_{atm}$.

The method used by Raynaud et al. (2007) and Lipenkov et al. (2011) is to calculate the time delay between air content, filtered in the 1/15 and 1/46 ka^{-1} pass-band, and the integrated local summer insolation (ISI). The ISI curve is obtained by summation of all daily summer insolation above a certain threshold; the threshold being inferred such that the ISI curve has the same spectral properties as the air content. From the cross-correlation between the two filtered signals, they have calculated a time delay, allowing us to associate ages calculated from orbital parameters to mid-slope variations of air content. Using this method, we have determined 14 and 8 orbital ice ages for EDC and Vostok ice cores respectively (Tables 4 and 5). In order to verify the robustness of these points, we also deduced ages by direct matching of the mid-slope variations of the unfiltered air content with the mid-slopes of the ISI target. Age markers obtained with these two methods are consistent within ± 1 ka on average. The uncertainty for each point was calculated as a function of the sampling resolution, the uncertainty of the currently used chronology, the uncertainty of the ISI curves and the age difference with the direct mid-slope method, leading to values from 2.9 to 7.2 ka.

Table 5. Orbital ages from air content for Vostok, deduced from Lipenkov et al. (2011).

depth (m)	ice age (ka)	σ (ka)
2420.28	191.950	6.663
2488.27	202.950	6.600
2848.45	260.950	7.215
2883.02	275.950	6.343
3011	307.950	6.424
3043.04	318.950	6.308
3145.95	346.950	6.527
3185.46	359.950	6.704

3.3 Coherency of orbital markers for the Vostok ice core

In order to evaluate the coherency of the 3 types of orbital markers, we have performed several "chronology tests" using the Datice tool with all the absolute and stratigraphic markers but only one type of orbital markers ($\delta^{18}O_{atm}$, $\delta O_2/N_2$ or air content only). The full comparison between the "$\delta O_2/N_2$ chronology", "$\delta^{18}O_{atm}$ chronology" and the "air content chronology" can only be done when the different orbital marker ages overlap, hence on the Vostok ice core.

When comparing the $\delta O_2/N_2$ and air content chronologies (Fig. 4), the two chronologies seem in good agreement in the period 190–365 ka when markers overlap. The air content markers alone are leading to a chronology younger by 2 ka maximum than the $\delta O_2/N_2$ one during this period. Prior to 365 ka, the comparison cannot be drawn since there is no air content constraint. This coherency of the two dating methods within 2 ka during the period 190–365 ka confirms the conclusion of Lipenkov et al. (2011).

We concentrate now on the comparison of $\delta O_2/N_2 - \delta^{18}O_{atm}$ chronologies in the 110–400 ka period where $\delta O_2/N_2$ and $\delta^{18}O_{atm}$ age markers are homogeneously distributed. We observe differences varying from $\sim$2 to 4 ka. These differences are slightly lower (standard deviation of ± 1.2 ka and difference ranging from -0.005 to 4.1 ka) with Datice than in the similar comparison for Suwa and Bender (2008) (standard deviation of ± 1.9 ka and a range of ± 6 ka). They may result from different links between gas and ice chronologies. In this study we consider the $\delta^{18}O_{atm}$ markers as gas age makers and the link between the gas and ice phases is governed by the LIDIE scenario based on $\delta^{15}N$ measurements and constraints from independent gas and ice stratigraphic links (SOM). In Suwa and Bender (2008), these markers were converted into ice ages and their gas age–ice age equivalence was obtained with a firnification model.

We do not explore in detail here the reasons for the systematic 2 ka offset between the three chronologies. Many reasons can be involved, such as:

- incorrect Δage or LIDIE estimates, since the $\delta O_2/N_2$ and air content markers are ice age markers and the $\delta^{18}O_{atm}$ is a gas age constraint;
- incorrect orbital targets for $\delta O_2/N_2$, air content and $\delta^{18}O_{atm}$. In particular, no definitive quantitative explanation has been given for the 5 ka lag between precession parameter and $\delta^{18}O_{atm}$. Similarly, it is still under discussion if the $\delta O_2/N_2$ curve should be strictly aligned with the summer solstice insolation (Landais et al., 2012; Hutterli et al., 2010).

Moreover, for each orbital tuning, lags between the records and their orbital targets may vary with time (Jouzel et al., 2002).

We conclude that all orbitally tuned chronologies agree well one with each other. This permits us to safely combine the ice and gas orbital ages within their uncertainty range.

4 New chronology

4.1 Chronology construction

When combining all the different observations (absolute ages, stratigraphic links, Δdepth and orbital ages), 3 orbital markers have been removed because they led to anomalous peaks of LIDIE, which are not realistic (10 m variations within 12 ka during MIS 12 and MIS 14, see SOM). The removed points are indicated by a "*" in Table 1: they are all gas age markers from $\delta^{18}O_{atm}$ of the EDC ice core located near eccentricity minima (438 and 534 ka).

300 different Datice simulations were run to optimize the final AICC2012 chronology. In addition to tests of the coherency for the different absolute, orbital and stratigraphic points, it has been found that the background parameters and associated variances have a strong influence on the final chronologies. For example, we had to strongly enlarge the variance of the TALDICE thinning function. Indeed, the background chronology of TALDICE has a much too young Termination II (110 ka), which is unrealistic and should not influence the final AICC2012 chronology.

4.2 The new AICC2012 chronology on orbital timescale

As expected from the numerous stratigraphic markers distributed on the 5 ice cores, the variations imprinted in the methane and water isotopic composition are synchronous within 1.5 ka for our five ice cores on the new AICC2012 chronology over the last 350 ka (Fig. 5). Prior to 350 ka, there is no stratigraphic tie point between EDC and Vostok so that the AICC2012 chronologies are independently established for Vostok and EDC, using their individual $\delta^{18}O_{atm}$, $\delta O_2/N_2$ and air content markers indicated on Fig. 5. New measurements of CH_4 and $\delta^{18}O_{atm}$ are strongly needed to provide stratigraphic links between the two cores back to 400 ka.

Table 6. Comparison of the warm interglacial durations at EDC on the AICC2012 and EDC3 age scales.

Interglacial	EDC EDC3 (ka)		EDC AICC2012 (ka)	
MIS 1	0–12.0	(12.0)	0–12.3	(12.3)
MIS 5.5	116.3–132.5	(16.2)	115.6–132.4	(16.8)
MIS 7.5	239.8–244.7	(4.9)	240.8–245.8	(5.0)
MIS 9.3	323.3–336.8	(13.5)	324.6–338.8	(14.2)
MIS 11.3	395.3–426.1	(30.8)	395.5–426.6	(31.1)

For the EDC ice core, the new AICC2012 chronology is in rather good agreement (within 2–3 ka) with the previous EDC3 timescale (Parrenin et al., 2007) as shown from the water isotope and CH_4 records (Fig. 6). In particular, it does not modify significantly the length of interglacial periods (Table 6). Nevertheless, one period shows significant differences, up to 5.4 ka (shaded zone on Fig. 6), corresponding to MIS 12. Termination V appears similar (within 390 a) in AICC2012 and EDC3, and MIS 11 duration is not significantly changed (Table 6). This period is close to the minimum of eccentricity characterizing MIS 11, which makes the identification of orbital markers difficult by comparison of $\delta O_2/N_2$ and $\delta^{18}O_{atm}$ records with their respective tuning targets. In this study we have improved the resolution of EDC $\delta^{18}O_{atm}$ over MIS 11–12, leading to the determination of new orbital ages replacing those of Dreyfus et al. (2007), used to construct the EDC3 chronology. Consequently, the differences observed over this period between the two chronologies mainly result from the replacement of the $\delta^{18}O_{atm}$ age markers and the addition of ice age markers. Because the identification of orbital age markers remains difficult over this period of low eccentricity, new measurements of $\delta O_2/N_2$ and air content on the EDC ice core are still needed, especially for the small precession peaks at 350–450 ka. The new AICC2012 chronology has also been compared with absolute chronologies established for speleothems. For this purpose, variations of CH_4 in the AICC2012 chronology are compared with variations of the $\delta^{18}O$ of calcite in Chinese speleothems (Wang et al., 2008; Cheng et al., 2009) assuming that both should vary in phase. A strong resemblance and synchronism have indeed been observed between calcite $\delta^{18}O$ and CH_4 variability over Dansgaard–Oeschger events (Fleitmann et al., 2009). The AICC2012 chronology appears in good agreement, within its uncertainty, with the speleothem ages over the considered events (see Table 6 in SOM).

The dating improvements for the AICC2012 chronology concern mainly the last 150 ka, where the numerous new stratigraphic links permit to significantly decrease the dating uncertainties. In the companion paper, Veres et al. (2013) discuss the millennial scale variability of the last 120 ka and we focus here on MIS 5.5. The records are coherent over this period between the 4 Antarctic ice cores (Fig. 7), within

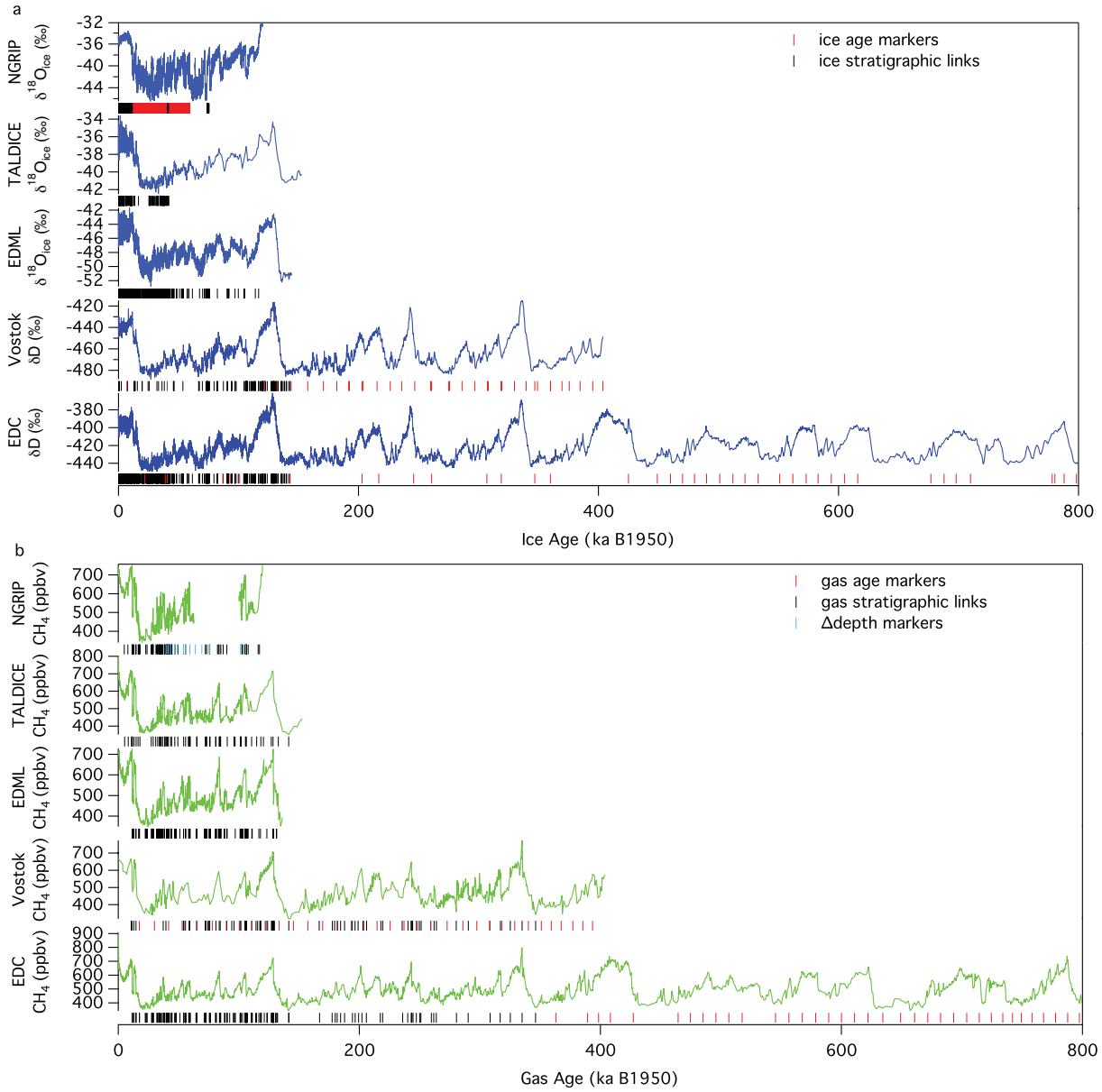

Fig. 5. (a) Water stable isotope records of NGRIP (NorthGRIP Community Members, 2004), TALDICE (Stenni et al., 2011), EDML (EPICA Community Members, 2006, 2010), Vostok (Petit et al., 1999) and EDC (Jouzel et al., 2007) on the AICC2012 age scale. **(b)** Methane records of NGRIP (Greenland composite: Capron et al., 2010; EPICA Community Members, 2006; Flückiger et al., 2004; Huber et al., 2006; Schilt et al., 2010), TALDICE (Buiron et al., 2011; Schüpbach et al., 2011), EDML (EPICA Community Members, 2006), Vostok (Caillon et al., 2003; Delmotte et al., 2004; Petit et al., 1999) and EDC (Loulergue et al., 2008) on the AICC2012 age scale. Stratigraphic links and age marker positions are displayed under each core.

the uncertainty of AICC2012, with the Vostok ice core being slightly older (1 ka) than the other ice cores. The duration of MIS 5.5, defined here by the −403 ‰ threshold of δD on EDC (EPICA Community Members, 2004), is slightly longer in AICC2012 (16.8 ka) compared to its duration in the EDC3 chronology (16.2 ka) and the age of Termination II is not significantly modified compared to its age in EDC3. Still, the reduction of uncertainty associated with the age of Termination II and MIS 5.5 compared to previous ice core chronologies makes it interesting to compare our result with other dated records.

Absolute dating of Termination II has been possible in at least two well-dated speleothems. In China, Cheng et al. (2009) dated a strong decrease of calcite δ^{18}O in the Sanbao cave speleothem at 128.91 ± 0.06 ka. In Italy, Drysdale et al. (2009) obtained a decrease in calcite δ^{18}O on a speleothem of the Corchia cave in two steps: a first 1.5 ‰ decrease between 133 and 131 ka and a second decrease of 1 ‰ between 129

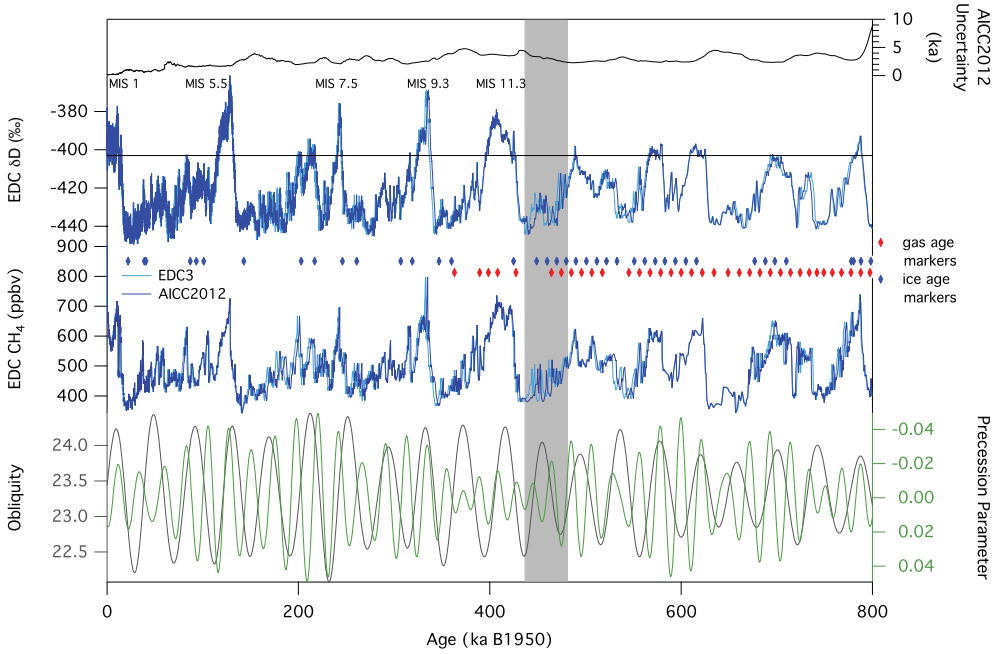

Fig. 6. Top: EDC AICC2012 chronology uncertainty. EDC deuterium records (EPICA Community Members, 2004) over the last 800 ka on the EDC3 (light blue) and AICC2012 (dark blue) age scales. The horizontal line corresponds to −403 ‰ and limits the interglacial periods (EPICA Community Members, 2004). The position of the orbital markers is shown in the gas (red markers) and ice (blue markers). Middle: CH_4 records of EDC (Loulergue et al., 2008) on EDC3 (light blue) and AICC2012 (dark blue). Bottom: obliquity (grey) and precession parameter (green) over the last 800 ka (same as in Fig. 1). The shaded zone highlights the period of significant differences between the two chronologies.

and 128 ka. There is a priori no contradiction between these two dates since calcite $\delta^{18}O$ reflects local or regional intensity of the hydrological cycle in China while the impact of local temperature on meteoric water and then calcite $\delta^{18}O$ is expected to be more pronounced in Italy. The different dates for the calcite $\delta^{18}O$ decrease may thus reflect different regional climatic response during Termination II.

Termination II is well recorded in Antarctic ice cores. At EDC, the main features are: (1) a parallel slow increase of both δD and CO_2 from 135 to 128 ka, (2) an abrupt shift of methane and d-excess occurring during the optimum of δD and CO_2 (Lourantou et al., 2010; Masson-Delmotte et al., 2010a). In the EDC3 timescale, Termination II was constrained with a speleothem-deduced age of 130.1 ± 2.0 ka (Parrenin et al., 2007) synchronized with the methane peak of EDC and converted as an ice depth with an estimated Δdepth. This does not permit to compare independently the ice and speleothem records. As a consequence, in our new chronology, we have removed this tie point from the list of absolute markers and we only use orbital markers ($\delta O_2/N_2$, air content and $\delta^{18}O_{atm}$). Tests performed with the Datice tool with or without the 130.1 ka tie point using the published or an enlarged uncertainty do not change by more than a few centuries the timing of the abrupt increase of CH_4 or maximum of δD observed at 128.51 ka on the EDC AICC2012 timescale (128.79 ka for Vostok)

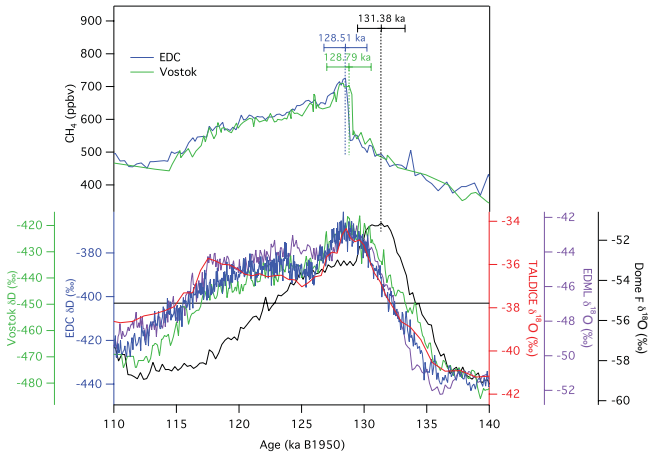

Fig. 7. Bottom: comparison of MIS 5.5 duration in several ice cores. The EDC, Vostok, EDML and TALDICE isotopic records are on AICC2012 age scales. The Dome F $\delta^{18}O$ is on the DFO-2006 chronology (Kawamura et al., 2007). The black horizontal line corresponds to the −403 ‰ interglacial threshold on EDC. Top: methane records of Vostok and EDC. Termination II ages are defined from the timing of the sharp methane rise for EDC (blue) and Vostok (green), and the water stable isotope optima for Dome F (black).

compared to 128.66 ka on the EDC3 timescale (Fig. 7). This result supports the hypothesis of synchronism between CH_4 abrupt increases recorded in ice cores and abrupt calcite $\delta^{18}O$ recorded in East Asiatic caves. However, it should be noted that this is only valid within the uncertainty of our timescale (1.72 ka given by Datice at Termination II, see SOM). We conclude that our AICC2012 chronology appears consistent with the speleothem information.

Even if this dating of Termination II with AICC2012 agrees, within the uncertainties, with the Termination II dating at Dome F, the AICC2012 chronology is 3 ka younger than the DFO-2006 chronology placing the δD optimum at 131.38 ± 1.90 ka (Kawamura et al., 2007). This difference may have different origins. Most importantly, the quality of the $\delta O_2/N_2$ measurements on which both AICC2012 and Dome F chronologies are based is limited by gas loss issues on ice kept at $-20\,^{\circ}C$. Moreover the $\delta^{18}O_{atm}$ variability is at a minimum before the onset of Termination II, making a unique orbital tuning very difficult at that time. New measurements on well-conserved ice should be performed to improve the records.

Finally, the AICC2012 chronology suggests synchronous millennial variations of water stable isotopes at EDC, EDML, and Vostok during the last interglacial, supporting earlier hypotheses (Masson-Delmotte et al., 2011). It also highlights a sharp cooling at 117 ka synchronous in EDML and TALDICE, and distinct from the other more inland records. This behavior is inferred from the stratigraphic links between the Antarctic ice cores and also the $\delta^{18}O_{atm}$ markers of TALDICE around this period. It confirms the different isotope trend at TALDICE and EDC during the last interglacial period, supporting interpretations of this gradient as a glaciological fingerprint of changes in East Antarctic ice sheet topography (Bradley et al., 2013).

5 Conclusions

In this study, together with the companion study of Veres et al. (2013), we have established a new reference chronology for 4 Antarctic ice cores, AICC2012 covering the last 800 ka. An important aspect of the common chronology development has been the compilation of absolute and stratigraphic tie points as well as a careful evaluation of the background scenarios and associated variances for thinning, accumulation rate and LIDIE. These results are available in the Supplement associated with the AICC2012 chronology.

More specifically, we have focused here on the orbital timescale between 120 and 800 ka. First, we have presented new measurements of $\delta^{18}O_{atm}$ of EDC over MIS 11–12 to improve the determination of orbital markers over this period characterized by a low eccentricity. Second, we have provided a complete record of $\delta^{18}O_{atm}$ for the TALDICE ice core prior to 50 ka. This new record has permitted to provide 8 new stratigraphic links with Vostok over the last 150 ka. With this new record, we have also pointed out that the integrity of the TALDICE ice core prior to 150 ka is questionable. Third, we have tested the coherency of the different orbital ages derived from air content, $\delta O_2/N_2$ and $\delta^{18}O_{atm}$ and have concluded that the three markers are coherent at Vostok between 190 and 365 ka, within their respective uncertainties.

The methane and water isotopic records from the 4 Antarctic ice cores are coherent when drawn on the new AICC2012 chronology, supporting earlier interpretations. Small differences between EDC isotopic records drawn on AICC2012 and on the previous EDC3 chronology are evident. Most of the age scale differences between 110 and 800 ka are smaller than 1.5 ka, hence not significant given the uncertainty of AICC2012. The main conclusions on the orbital properties of methane and water stable isotope variations, and their lags with respect to orbital forcing (Jouzel et al., 2007; Loulergue et al., 2008; Masson-Delmotte et al., 2010b) remain robust. Only over MIS 12, the two chronologies differ by up to 5.4 ka, due to our new measurements of $\delta^{18}O_{atm}$ and the addition of new age markers. The timing and duration of MIS 5 in AICC2012 is basically unchanged compared to EDC3. This is an important result since the dating of Termination II in AICC2012 does not rely anymore on the speleothem derived tie point at 130.1 ka which was included in EDC3. It mainly results from ice core orbital markers and numerous new stratigraphic links, with still an influence of the background scenarios.

We have also pointed out the necessity of new measurements. First, higher sampling resolution for ice $\delta^{18}O$, methane and $\delta^{18}O_{atm}$ over the TALDICE ice core are needed prior to 150 ka to assess the integrity of this ice core over its bottom part. Second, new measurements of $\delta O_2/N_2$, air content and $\delta^{18}O_{atm}$ of the EDC ice core on well-conserved ice are strongly required in order to fill the gap of orbital markers over the following periods: 440–800 ka for air content, 0–400 ka for $\delta^{18}O_{atm}$, 0–380 and 480–700 ka for $\delta O_2/N_2$. Third, methodological aspects of the Datice tool also need improvements on the choice of background parameters and associated variances. As an example, new insights of the LID controls should be included in Datice (Freitag et al., 2012; Capron et al., 2013). Information from microstructure and fabric should help to better define the thinning function variance (Durand et al., 2007). Finally, an important added value would be to further extend the Datice tool to include other ice cores such as Dome F, WAIS or also the NEEM ice core in Greenland, all of these ice cores being highly documented with absolute or orbital markers.

Supplementary material related to this article is available online at: http://www.clim-past.net/9/1715/2013/cp-9-1715-2013-supplement.zip.

Acknowledgements. We thank Jeff Severinghaus and the 3 anonymous reviewers for their comments permitting us to improve the clarity of this paper. We thank the EDC4 team for stimulating the discussion around the building of AICC2012 and helping to pick up the best parameters to feed the Datice tool. We address special thanks to Sébastien Nomade and Frédéric Prié for their help in this study. This project was funded by the "Fondation de France Ars Cuttoli", the "ANR Citronnier", INRIA and LEFE funding. The research leading to these results has received funding from the European Union's Seventh Framework programme (FP7/2007-2013) under grant agreement no 243908, "Past4Future. Climate change – Learning from the past climate". This work is a contribution to the European Project for Ice Coring in Antarctica (EPICA), a joint European Science Foundation/European Commission scientific programme, funded by the EU and by national contributions from Belgium, Denmark, France, Germany, Italy, the Netherlands, Norway, Sweden, Switzerland and the United Kingdom. The main logistic support was provided by IPEV and PNRA (at Dome C) and AWI (at Dronning Maud Land). The Talos Dome Ice core Project (TALDICE), a joint European programme, is funded by national contributions from Italy, France, Germany, Switzerland and the United Kingdom. Primary logistical support was provided by PNRA at Talos Dome. This is EPICA publication no. 292. This is Past4Future contribution number 46. This is TALDICE publication no 34. This is LSCE contribution no 4646.

Edited by: E. Brook

The publication of this article is financed by CNRS-INSU.

References

Aciego, S., Bourdon, B., Schwander, J., Baur, H., and Forieri, A.: Toward a radiometric ice clock: uranium ages of the Dome C ice core, Quaternary Sci. Rev., 30, 2389–2397, doi:10.1016/j.quascirev.2011.06.008, 2011.

Arnaud, L., Barnola, J.-M., and Duval, P.: Physical modeling of the densification of snow/firn and ice in the upper part of polar ice sheets, Book: Physics of Ice Core Records, 285–305, edited by: Hondoh, T., Hokkaido Univ. Press, Sapporo, Japan, 2000

Bar-Matthews, M., Ayalon, A., Gilmour, M., Matthews, A., and Hawkesworth, C. J.: Sea-land oxygen isotopic relationships from planktonic foraminifera and speleothems in the Eastern Mediterranean region and their implication for paleorainfall during interglacial intervals, Geochim. Cosmochim. Ac., 67, 3181–3199, doi:10.1016/S0016-7037(02)01031-1, 2003.

Battle, M., Bender, M., Sowers, T., Tans, P. P., Butler, J. H., Elkins, J. W., Ellis, J. T., Conway, T., Zhang, N., Lang, P., and Clarket, A. D.: Atmospheric gas concentrations over the past century measured in air from firn at the South Pole, Nature, 383, 231–235, doi:10.1038/383231a0, 1996.

Bender, M. L.: Orbital tuning chronology for the Vostok climate record supported by trapped gas composition, Earth Planet. Sci. Lett., 204, 275–289, doi:10.1016/S0012-821X(02)00980-9, 2002.

Bender, M., Sowers, T., and Labeyrie, L.: The Dole effect and its variations during the last 130 000 years as measured in the Vostok ice core, Global Biogeochem. Cy., 8, 363–376, doi:10.1029/94GB00724, 1994.

Bradley, S. L., Siddall, M., Milne, G. A., Masson-Delmotte, V., and Wolff, E.: Combining ice core records and ice sheet models to explore the evolution of the East Antarctic Ice sheet during the Last Interglacial period, Global Planet. Change, 100278–100290, doi:10.1016/j.gloplacha.2012.11.002, 2013.

Buiron, D., Chappellaz, J., Stenni, B., Frezzotti, M., Baumgartner, M., Capron, E., Landais, A., Lemieux-Dudon, B., Masson-Delmotte, V., Montagnat, M., Parrenin, F., and Schilt, A.: TALDICE-1 age scale of the Talos Dome deep ice core, East Antarctica, Clim. Past, 7, 1–16, doi:10.5194/cp-7-1-2011, 2011.

Caillon, N., Severinghaus, J. P., Jouzel, J., Barnola, J.-M., Kang, J., and Lipenkov, V. Y.: Timing of atmospheric CO_2 and Antarctic temperature changes across termination III, Science, 299, 1728–1731, doi:10.1126/science.1078758, 2003.

Capron, E., Landais, A., Lemieux-Dudon, B., Schilt, A., Masson-Delmotte, V., Buiron, D., Chappellaz, J., Dahl-Jensen, D., Johnsen, S., Leuenberger, M., Loulergue, L., and Oerter, H.: Synchronising EDML and NorthGRIP ice cores using $\delta^{18}O$ of atmospheric oxygen ($\delta^{18}O_{atm}$) and CH_4 measurements over MIS5 (80–123 kyr), Quaternary Sci. Rev., 29, 222–234, doi:10.1016/j.quascirev.2009.07.014, 2010.

Capron, E., Landais, A., Buiron, D., Cauquoin, A., Chappellaz, J., Debret, M., Jouzel, J., Leuenberger, M., Martinerie, P., Masson-Delmotte, V., Mulvaney, R., Parrenin, F., and Prié, F.: Glacial-interglacial dynamics of Antarctic firns: comparison between simulations and ice core air-d15N measurements, Clim. Past, 9, 983–999, doi:http://dx.doi.org/10.5194/cp-9-983-2013, 2013.

Cheng, H., Edwards, R. L., Broecker, W. S., Denton, G. H., Kong, X., Wang, Y., Zhang, R., and Wang, X.: Ice Age terminations, Science, 326, 248–252, doi:10.1126/science.1177840, 2009.

Delmotte, M., Chappellaz, J., Brook, E., Yiou, P., Barnola, J. M., Goujon, C., Raynaud, D., and Lipenkov, V. I.: Atmospheric methane during the last four glacial-interglacial cycles: rapid changes and their link with Antarctic temperature, J. Geophys. Res.-Atmos, 109, D12104, doi:10.1029/2003JD004417, 2004.

Dreyfus, G. B., Parrenin, F., Lemieux-Dudon, B., Durand, G., Masson-Delmotte, V., Jouzel, J., Barnola, J.-M., Panno, L., Spahni, R., Tisserand, A., Siegenthaler, U., and Leuenberger, M.: Anomalous flow below 2700 m in the EPICA Dome C ice core detected using $\delta^{18}O$ of atmospheric oxygen measurements, Clim. Past, 3, 341–353, doi:10.5194/cp-3-341-2007, 2007.

Dreyfus, G. B., Raisbeck, G. M., Parrenin, F., Jouzel, J., Guyodo, Y., Nomade, S., and Mazaud, A.: An ice core perspective on the age of the Matuyama–Brunhes boundary, Earth Planet. Sci. Lett., 274, 151–156, doi:10.1016/j.epsl.2008.07.008, 2008.

Drysdale, R. N., Hellstrom, J. C., Zanchetta, G., Fallick, A. E., Sanchez Goñi, M. F., Couchoud, I., McDonald, J., Maas, R., Lohmann, G., and Isola, I.: Evidence for obliquity forcing of glacial termination II, Science, 325, 1527–1531, doi:10.1126/science.1170371, 2009.

Dunbar, N. W., McIntosh, W. C., and Esser, R. P.: Physical setting and tephrochronology of the summit caldera ice record at Mount Moulton, West Antarctica, Geol. Soc. Am. Bull., 120, 796–812, doi:10.1130/B26140.1, 2008.

Durand, G., Gillet-Chaulet, F., Svensson, A., Gagliardini, O., Kipfstuhl, S., Meyssonnier, J., Parrenin, F., Duval, P., and Dahl-Jensen, D.: Change in ice rheology during climate variations – implications for ice flow modelling and dating of the EPICA Dome C core, Clim. Past, 3, 155–167, doi:10.5194/cp-3-155-2007, 2007.

EPICA Community Members: Eight glacial cycles from an Antarctic ice core, Nature, 429, 623–628, doi:10.1038/nature02599, 2004.

EPICA Community Members: One-to-one coupling of glacial climate variability in Greenland and Antarctica, Nature, 444, 195–198, doi:10.1038/nature05301, 2006.

EPICA Community Members: Stable oxygen isotopes of ice core EDML, PANGAEA, doi:10.1594/PANGAEA.754444, 2010.

Fleitmann, D., Cheng, H., Badertscher, S., Edwards, R. L., Mudelsee, M., Göktürk, O. M., Fankhauser, A., Pickering, R., Raible, C. C., Matter, A., Kramers, J., and Tüysüz, O.: Timing and climatic impact of Greenland interstadials recorded in stalagmites from Northern Turkey, Geophys. Res. Lett., 36, L19707, doi:10.1029/2009GL040050, 2009.

Flückiger, J., Blunier, T., Stauffer, B., Chappellaz, J., Spahni, R., Kawamura, K., Schwander, J., Stocker, T. F., and Dahl-Jensen, D.: N_2O and CH_4 variations during the last glacial epoch: Insight into global processes, Global Biogeochem. Cy., 18, GB1020, doi:10.1029/2003GB002122, 2004.

Freitag, J., Kipfstuhl, S., Hörhold, M., Wegner, A., Wilhelms, F., and Bigler, M.: Impurity controlled firn densification: a new model approach, in: EGU General Assembly Conference Abstracts, edited by: Abbasi, A. and Giesen, N., vol. 14 of EGU General Assembly Conference Abstracts, 10293, Vienna, Austria, 22–27 April 2012, 2012.

Gilbert, J. and Lemarechal, C.: The modules M1QN3 and N1QN3, Program documentation, INRIA, 1993.

Goujon, C., Barnola, J.-M., and Ritz, C.: Modeling the densification of polar firn including heat diffusion: application to close-off characteristics and gas isotopic fractionation for Antarctica and Greenland sites, J. Geophys. Res.-Atmos., 108, 4792, doi:10.1029/2002JD003319, 2003.

Herron, M. M. and Langway Jr., C. C.: Firn densification: an empirical model, J. Glaciol., 25, 373–385, 1980.

Hoffmann, G., Cuntz, M., Weber, C., Ciais, P., Friedlingstein, P., Heimann, M., Jouzel, J., Kaduk, J., Maier-Reimer, E., Seibt, U., and Six, K.: A model of the Earth's Dole effect, Global Biogeochem. Cy., 18, GB1008, doi:10.1029/2003GB002059, 2004.

Huber, C., Beyerle, U., Leuenberger, M., Schwander, J., Kipfer, R., Spahni, R., Severinghaus, J. P., and Weiler, K.: Evidence for molecular size dependent gas fractionation in firn air derived from noble gases, oxygen, and nitrogen measurements, Earth Planet. Sci. Lett., 243, 61–73, doi:10.1016/j.epsl.2005.12.036, 2006.

Hutterli, M. A., Schneebeli, M., Freitag, J., Kipfstuhl, J., and Rothlisberger, R.: Impact of local insolation on snow metamorphism and ice core records, in: Physics of Ice Core Records II, edited by: Hondoh, T., Hokkaido University Press, 223–232, Sapporo, Japan, 2010.

Imbrie, J. and Imbrie, J. Z.: Modeling the climatic response to orbital variations, Science, 207, 943–953, doi:10.1126/science.207.4434.943, 1980.

Jouzel, J., Hoffmann, G., Parrenin, F., and Waelbroeck, C.: Atmospheric oxygen 18 and sea-level changes, Quaternary Sci. Rev., 21, 307–314, doi:10.1016/S0277-3791(01)00106-8, 2002.

Jouzel, J., Masson-Delmotte, V., Cattani, O., Dreyfus, G., Falourd, S., Hoffmann, G., Minster, B., Nouet, J., Barnola, J. M., Chappellaz, J., Fischer, H., Gallet, J. C., Johnsen, S., Leuenberger, M., Loulergue, L., Luethi, D., Oerter, H., Parrenin, F., Raisbeck, G., Raynaud, D., Schilt, A., Schwander, J., Selmo, E., Souchez, R., Spahni, R., Stauffer, B., Steffensen, J. P., Stenni, B., Stocker, T. F., Tison, J. L., Werner, M., and Wolff, E. W.: Orbital and millennial Antarctic climate variability over the past 800 000 Years, Science, 317, 793–796, doi:10.1126/science.1141038, 2007.

Kawamura, K., Parrenin, F., Lisiecki, L., Uemura, R., Vimeux, F., Severinghaus, J. P., Hutterli, M. A., Nakazawa, T., Aoki, S., Jouzel, J., Raymo, M. E., Matsumoto, K., Nakata, H., Motoyama, H., Fujita, S., Goto-Azuma, K., Fujii, Y., and Watanabe, O.: Northern Hemisphere forcing of climatic cycles in Antarctica over the past 360 000 years, Nature, 448, 912–916, doi:10.1038/nature06015, 2007.

Landais, A., Caillon, N., Severinghaus, J., Jouzel, J., and Masson-Delmotte, V.: Analyses isotopiques à haute précision de l'air piégé dans les glaces polaires pour la quantification des variations rapides de température: méthodes et limites, Notes des activités instrumentales de l'IPSL, Technical Report, 39, 2003a.

Landais, A., Chappellaz, J., Delmotte, M., Jouzel, J., Blunier, T., Bourg, C., Caillon, N., Cherrier, S., Malaizé, B., Masson-Delmotte, V., Raynaud, D., Schwander, J., and Steffensen, J. P.: A tentative reconstruction of the last interglacial and glacial inception in Greenland based on new gas measurements in the Greenland Ice Core Project (GRIP) ice core, J. Geophys. Res.-Atmos., 108, 4563, doi:10.1029/2002JD003147, 2003b.

Landais, A., Barnola, J. M., Masson-Delmotte, V., Jouzel, J., Chappellaz, J., Caillon, N., Huber, C., Leuenberger, M., and Johnsen, S. J.: A continuous record of temperature evolution over a sequence of Dansgaard-Oeschger events during Marine Isotopic Stage 4 (76 to 62 kyr BP), Geophys. Res. Lett., 31, L22211, doi:10.1029/2004GL021193, 2004.

Landais, A., Jouzel, J., Massondelmotte, V., and Caillon, N.: Large temperature variations over rapid climatic events in Greenland: a method based on air isotopic measurements, C. R. Geosci., 337, 947–956, doi:10.1016/j.crte.2005.04.003, 2005.

Landais, A., Waelbroeck, C., and Masson-Delmotte, V.: On the limits of Antarctic and marine climate records synchronization: lag estimates during marine isotopic stages 5d and 5c, Paleoceanography, 21, PA1001, doi::10.1029/2005PA001171, 2006.

Landais, A., Masson-Delmotte, V., Combourieu Nebout, N., Jouzel, J., Blunier, T., Leuenberger, M., Dahl-Jensen, D., and Johnsen, S.: Millenial scale variations of the isotopic composition of atmospheric oxygen over Marine Isotopic Stage 4, Earth Planet. Sci. Lett., 258, 101–113, doi::10.1016/j.epsl.2007.03.027, 2007.

Landais, A., Dreyfus, G., Capron, E., Masson-Delmotte, V., Sanchez-Goñi, M., Desprat, S., Hoffmann, G., Jouzel, J., Leuenberger, M., and Johnsen, S.: What drives the millennial and orbital variations of $\delta^{18}O_{atm}$?, Quaternary Sci. Rev., 29, 235–246,

doi:10.1016/j.quascirev.2009.07.005, 2010.

Landais, A., Dreyfus, G., Capron, E., Pol, K., Loutre, M. F., Raynaud, D., Lipenkov, V. Y., Arnaud, L., Masson-Delmotte, V., Paillard, D., Jouzel, J., and Leuenberger, M.: Towards orbital dating of the EPICA Dome C ice core using $\delta O_2/N_2$, Clim. Past, 8, 191–203, doi:10.5194/cp-8-191-2012, 2012.

Laskar, J., Robutel, P., Joutel, F., Gastineau, M., Correia, A. C. M., and Levrard, B.: A long-term numerical solution for the insolation quantities of the Earth, Astron. Astrophys., 428, 261–285, doi:10.1051/0004-6361:20041335, 2004.

Lemieux-Dudon, B., Blayo, E., Petit, J.-R., Waelbroeck, C., Svensson, A., Ritz, C., Barnola, J.-M., Narcisi, B. M., and Parrenin, F.: Consistent dating for Antarctic and Greenland ice cores, Quat. Sci. Rev., 29, 8–20, doi:10.1016/j.quascirev.2009.11.010, 2010.

Leuenberger, M. C.: Modeling the signal transfer of seawater $\delta^{18}O$ to the $\delta^{18}O$ of atmospheric oxygen using a diagnostic box model for the terrestrial and marine biosphere, J. Geophys. Res., 102, 26841–26850, doi:10.1029/97JC00160, 1997.

Lipenkov, V. Y., Raynaud, D., Loutre, M. F., and Duval, P.: On the potential of coupling air content and O_2/N_2 from trapped air for establishing an ice core chronology tuned on local insolation, Quaternary Sci. Rev., 30, 3280–3289, doi:10.1016/j.quascirev.2011.07.013, 2011.

Lorius, C., Ritz, C., Jouzel, J., Merlivat, L., and Barkov, N. I.: A 150 000-year climatic record from Antarctic ice, Nature, 316, 591–596, doi:10.1038/316591a0, 1985.

Loulergue, L.: Contraintes chronologiques et biogeochimiques grace au methane dans la glace naturelle: une application aux forages du projet EPICA, 2007, Ph. D. thesis, UJF, France, 2007.

Loulergue, L., Parrenin, F., Blunier, T., Barnola, J.-M., Spahni, R., Schilt, A., Raisbeck, G., and Chappellaz, J.: New constraints on the gas age-ice age difference along the EPICA ice cores, 0–50 kyr, Clim. Past, 3, 527–540, doi:10.5194/cp-3-527-2007, 2007.

Loulergue, L., Schilt, A., Spahni, R., Masson-Delmotte, V., Blunier, T., Lemieux, B., Barnola, J.-M., Raynaud, D., Stocker, T. F., and Chappellaz, J.: Orbital and millennial-scale features of atmospheric CH_4 over the past 800 000 years, Nature, 453, 383–386, doi:10.1038/nature06950, 2008.

Lourantou, A., Chappellaz, J., Barnola, J.-M., Masson-Delmotte, V., and Raynaud, D.: Changes in atmospheric CO_2 and its carbon isotopic ratio during the penultimate deglaciation, Quaternary Sci. Rev., 29, 1983–1992, doi:10.1016/j.quascirev.2010.05.002, 2010.

Lüthi, D., Le Floch, M., Bereiter, B., Blunier, T., Barnola, J.-M., Siegenthaler, U., Raynaud, D., Jouzel, J., Fischer, H., Kawamura, K., and Stocker, T. F.: High-resolution carbon dioxide concentration record 650 000–800 000 years before present, Nature, 453, 379–382, doi:10.1038/nature06949, 2008.

Malaizé, B., Paillard, D., Jouzel, J., and Raynaud, D.: The Dole effect over the last two glacial-interglacial cycles, J. Geophys. Res., 104, 14199–14208, doi:10.1029/1999JD900116, 1999.

Masson-Delmotte, V., Stenni, B., Blunier, T., Cattani, O., Chappellaz, J., Cheng, H., Dreyfus, G., Edwards, R. L., Falourd, S., Govin, A., Kawamura, K., Johnsen, S. J., Jouzel, J., Landais, A., Lemieux-Dudon, B., Lourantou, A., Marshall, G., Minster, B., Mudelsee, M., Pol, K., Rothlisberger, R., Selmo, E., and Waelbroeck, C.: Abrupt change of Antarctic moisture origin at the end of Termination II, P. Natl. Acad. Sci. USA, 107, 12091–12094, doi:10.1073/pnas.0914536107, 2010a.

Masson-Delmotte, V., Stenni, B., Pol, K., Braconnot, P., Cattani, O., Falourd, S., Kageyama, M., Jouzel, J., Landais, A., Minster, B., Barnola, J. M., Chappellaz, J., Krinner, G., Johnsen, S., Röthlisberger, R., Hansen, J., Mikolajewicz, U., and Otto-Bliesner, B.: EPICA Dome C record of glacial and interglacial intensities, Quat. Sci. Rev., 29, 113–128, doi:10.1016/j.quascirev.2009.09.030, 2010b.

Masson-Delmotte, V., Buiron, D., Ekaykin, A., Frezzotti, M., Gallée, H., Jouzel, J., Krinner, G., Landais, A., Motoyama, H., Oerter, H., Pol, K., Pollard, D., Ritz, C., Schlosser, E., Sime, L. C., Sodemann, H., Stenni, B., Uemura, R., and Vimeux, F.: A comparison of the present and last interglacial periods in six Antarctic ice cores, Clim. Past, 7, 397–423, doi:10.5194/cp-7-397-2011, 2011.

NorthGRIP Community Members: High-resolution record of Northern Hemisphere climate extending into the last interglacial period, Nature, 431, 147–151, doi:10.1038/nature02805, 2004.

Paillard, D., Labeyrie, L., and Yiou, P.: Macintosh Program performs time-series analysis, EOS Transactions, 77, 379–379, doi:10.1029/96EO00259, 1996.

Parrenin, F., Jouzel, J., Waelbroeck, C., Ritz, C., and Barnola, J.-M.: Dating the Vostok ice core by an inverse method, J. Geophys. Res., 106, 31837–31852, doi:10.1029/2001JD900245, 2001.

Parrenin, F., Rémy, F., Ritz, C., Siegert, M. J., and Jouzel, J.: New modeling of the Vostok ice flow line and implication for the glaciological chronology of the Vostok ice core, J. Geophys. Res.-Atmos., 109, D20102, doi:10.1029/2004JD004561, 2004.

Parrenin, F., Barnola, J.-M., Beer, J., Blunier, T., Castellano, E., Chappellaz, J., Dreyfus, G., Fischer, H., Fujita, S., Jouzel, J., Kawamura, K., Lemieux-Dudon, B., Loulergue, L., Masson-Delmotte, V., Narcisi, B., Petit, J.-R., Raisbeck, G., Raynaud, D., Ruth, U., Schwander, J., Severi, M., Spahni, R., Steffensen, J. P., Svensson, A., Udisti, R., Waelbroeck, C., and Wolff, E.: The EDC3 chronology for the EPICA Dome C ice core, Clim. Past, 3, 485–497, doi:10.5194/cp-3-485-2007, 2007.

Parrenin, F., Barker, S., Blunier, T., Chappellaz, J., Jouzel, J., Landais, A., Masson-Delmotte, V., Schwander, J., and Veres, D.: On the gas-ice depth difference (Δdepth) along the EPICA Dome C ice core, Clim. Past, 8, 1239–1255, doi:10.5194/cp-8-1239-2012, 2012a.

Parrenin, F., Petit, J.-R., Masson-Delmotte, V., Wolff, E., Basile-Doelsch, I., Jouzel, J., Lipenkov, V., Rasmussen, S. O., Schwander, J., Severi, M., Udisti, R., Veres, D., and Vinther, B. M.: Volcanic synchronisation between the EPICA Dome C and Vostok ice cores (Antarctica) 0–145 kyr BP, Clim. Past, 8, 1031–1045, doi:10.5194/cp-8-1031-2012, 2012b.

Petit, J. R., Jouzel, J., Raynaud, D., Barkov, N. I., Barnola, J.-M., Basile, I., Bender, M., Chappellaz, J., Davis, M., Delaygue, G., Delmotte, M., Kotlyakov, V. M., Legrand, M., Lipenkov, V. Y., Lorius, C., Pépin, L., Ritz, C., Saltzman, E., and Stievenard, M.: Climate and atmospheric history of the past 420 000 years from the Vostok ice core, Antarctica, Nature, 399, 429–436, doi:10.1038/20859, 1999.

Raisbeck, G. M., Yiou, F., Jouzel, J., and Stocker, T. F.: Direct north-south synchronization of abrupt climate change record in ice cores using Beryllium 10, Clim. Past, 3, 541–547, doi::10.5194/cp-3-541-2007, 2007.

Rasmussen, S. O., Andersen, K. K., Svensson, A. M., Steffensen, J. P., Vinther, B. M., Clausen, H. B., Siggaard-Andersen, M.-L., Johnsen, S. J., Larsen, L. B., Dahl-Jensen, D., Bigler, M., Röthlisberger, R., Fischer, H., Goto-Azuma, K., Hansson, M. E., and Ruth, U.: A new Greenland ice core chronology for the last glacial termination, J. Geophys. Res.-Atmos., 111, D06102, doi:10.1029/2005JD006079, 2006.

Raynaud, D., Lipenkov, V., Lemieux-Dudon, B., Duval, P., Loutre, M.-F., and Lhomme, N.: The local insolation signature of air content in Antarctic ice. A new step toward an absolute dating of ice records, Earth Planet. Sci. Lett., 261, 337–349, doi:10.1016/j.epsl.2007.06.025, 2007.

Ruddiman, W. and Raymo, M.: A methane-based time scale for Vostok ice, Quat. Sci. Rev., 22, 141–155, doi:10.1016/S0277-3791(02)00082-3, 2003.

Ruth, U., Barnola, J.-M., Beer, J., Bigler, M., Blunier, T., Castellano, E., Fischer, H., Fundel, F., Huybrechts, P., Kaufmann, P., Kipfstuhl, S., Lambrecht, A., Morganti, A., Oerter, H., Parrenin, F., Rybak, O., Severi, M., Udisti, R., Wilhelms, F., and Wolff, E.: "EDML1": a chronology for the EPICA deep ice core from Dronning Maud Land, Antarctica, over the last 150 000 years, Clim. Past, 3, 475–484, doi:10.5194/cp-3-475-2007, 2007.

Salamatin, A. N., Tsyganova, E. A., Lipenkov, V. Y., and Petit, J. R.: Vostok (Antarctica) ice-core time-scale from datings of different origins, Ann. Glaciol., 39, 283–292, doi:10.3189/172756404781814023, 2004.

Schilt, A., Baumgartner, M., Blunier, T., Schwander, J., Spahni, R., Fischer, H., and Stocker, T. F.: Glacial-interglacial and millennial-scale variations in the atmospheric nitrous oxide concentration during the last 800 000 years, Quat. Sci. Rev., 29, 182–192, doi:10.1016/j.quascirev.2009.03.011, 2010.

Schüpbach, S., Federer, U., Bigler, M., Fischer, H., and Stocker, T. F.: A refined TALDICE-1a age scale from 55 to 112 ka before present for the Talos Dome ice core based on high-resolution methane measurements, Clim. Past, 7, 1001–1009, doi:10.5194/cp-7-1001-2011, 2011.

Schwander, J., Barnola, J.-M., Andrie, C., Leuenberger, M., Ludin, A., Raynaud, D., and Stauffer, B.: The age of the air in the firn and the ice at Summit, Greenland, J. Geophys. Res., 98, 2831–2838, doi:10.1029/92JD02383, 1993.

Severi, M., Becagli, S., Castellano, E., Morganti, A., Traversi, R., Udisti, R., Ruth, U., Fischer, H., Huybrechts, P., Wolff, E., Parrenin, F., Kaufmann, P., Lambert, F., and Steffensen, J. P.: Synchronisation of the EDML and EDC ice cores for the last 52 kyr by volcanic signature matching, Clim. Past, 3, 367–374, doi:10.5194/cp-3-367-2007, 2007.

Severi, M., Udisti, R., Becagli, S., Stenni, B., and Traversi, R.: Volcanic synchronisation of the EPICA-DC and TALDICE ice cores for the last 42 kyr BP, Clim. Past, 8, 509–517, doi:10.5194/cp-8-509-2012, 2012.

Severinghaus, J. P. and Battle, M. O.: Fractionation of gases in polar ice during bubble close-off: New constraints from firn air Ne, Kr and Xe observations, Earth Planet. Sci. Lett., 244, 474–500, doi:10.1016/j.epsl.2006.01.032, 2006.

Severinghaus, J. P., Grachev, A., and Battle, M.: Thermal fractionation of air in polar firn by seasonal temperature gradients, Geochem. Geophys. Geosyst., 2, 1048–1024, doi:10.1029/2000GC000146, 2001.

Severinghaus, J. P., Beaudette, R., Headly, M. A., Taylor, K., and Brook, E. J.: Oxygen-18 of O_2 records the impact of abrupt climate change on the terrestrial biosphere, Science, 324, 1431–1434, doi:10.1126/science.1169473, 2009.

Severinghaus, J. P., Albert, M. R., Courville, Z. R., Fahnestock, M. A., Kawamura, K., Montzka, S. A., Mühle, J., Scambos, T. A., Shields, E., Shuman, C. A., Suwa, M., Tans, P., and Weiss, R. F.: Deep air convection in the firn at a zero-accumulation site, central Antarctica, Earth Planet. Sci. Lett., 293, 359–367, doi:10.1016/j.epsl.2010.03.003, 2010.

Sowers, T., Bender, M., and Raynaud, D.: Elemental and isotopic composition of occluded O_2 and N_2 in polar ice, J. Geophys. Res., 94, 5137–5150, doi:10.1029/JD094iD04p05137, 1989.

Stenni, B., Buiron, D., Frezzotti, M., Albani, S., Barbante, C., Bard, E., Barnola, J. M., Baroni, M., Baumgartner, M., Bonazza, M., Capron, E., Castellano, E., Chappellaz, J., Delmonte, B., Falourd, S., Genoni, L., Iacumin, P., Jouzel, J., Kipfstuhl, S., Landais, A., Lemieux-Dudon, B., Maggi, V., Masson-Delmotte, V., Mazzola, C., Minster, B., Montagnat, M., Mulvaney, R., Narcisi, B., Oerter, H., Parrenin, F., Petit, J. R., Ritz, C., Scarchilli, C., Schilt, A., Schüpbach, S., Schwander, J., Selmo, E., Severi, M., Stocker, T. F., and Udisti, R.: Expression of the bipolar see-saw in Antarctic climate records during the last deglaciation, Nat. Geosci., 4, 46–49, doi:10.1038/ngeo1026, 2011.

Suwa, M. and Bender, M. L.: Chronology of the Vostok ice core constrained by O_2/N_2 ratios of occluded air, and its implication for the Vostok climate records, Quaternary Sci. Rev., 27, 1093–1106, doi:10.1016/j.quascirev.2008.02.017, 2008.

Svensson, A., Andersen, K. K., Bigler, M., Clausen, H. B., Dahl-Jensen, D., Davies, S. M., Johnsen, S. J., Muscheler, R., Rasmussen, S. O., Röthlisberger, R., Peder Steffensen, J., and Vinther, B. M.: The Greenland ice core chronology 2005, 15 42 kyr, Part 2: comparison to other records, Quaternary Sci. Rev., 25, 3258–3267, doi::10.1016/j.quascirev.2006.08.003, 2006.

Svensson, A., Andersen, K. K., Bigler, M., Clausen, H. B., Dahl-Jensen, D., Davies, S. M., Johnsen, S. J., Muscheler, R., Parrenin, F., Rasmussen, S. O., Röthlisberger, R., Seierstad, I., Steffensen, J. P., and Vinther, B. M.: A 60 000 year Greenland stratigraphic ice core chronology, Clim. Past, 4, 47–57, doi:10.5194/cp-4-47-2008, 2008.

Svensson, A., Bigler, M., Blunier, T., Clausen, H. B., Dahle-Jensen, D., Fischer, H., Fujita, S., Goto-Azuma, K., Johnsen, S. J., Kawamura, K., Kipfstuhl, S., Kohno, M., Parrenin, F., Popp, T., Rasmussen, S. O., Schwander, J., Seierstad, I., Severi, M., Steffenson, J. P., Udisti, R., Uemura, R., Vallelonga, P., Vinther, B. M., Wegner, A., Wilhelms, F., and Winstrup, M.: Direct linking of Greenland and Antarctic ice cores at the Toba eruption (74 kyr BP), Clim. Past, 9, 749–766, doi:10.5194/cp-9-749-2013, 2013.

Udisti, R., Becagli, S., Castellano, E., Delmonte, B., Jouzel, J., Petit, J. R., Schwander, J., Stenni, B., and Wolff, E. W.: Stratigraphic correlations between the European Project for Ice Coring in Antarctica (EPICA) Dome C and Vostok ice cores showing the relative variations of snow accumulation over the past 45 kyr, J. Geophys. Res.-Atmos., 109, D08101, doi:10.1029/2003JD004180, 2004.

Veres, D., Bazin, L., Landais, A., Toyé Mahamadou Kele, H., Lemieux-Dudon, B., Parrenin, F., Martinerie, P., Blayo, E., Blunier, T., Capron, E., Chappellaz, J., Rasmussen, S. O., Severi, M., Svensson, A., Vinther, B., and Wolff, E. W.: The Antarctic ice core chronology (AICC2012): an optimized multi-parameter and multi-site dating approach for the last 120 thousand years, Clim. Past, 9, 1733–1748, doi:10.5194/cp-9-1733-2013, 2013.

Vinther, B., Clausen, H., Kipfstuhl, S., Fischer, H., Bigler, M., Oerter, H., Wegner, A., Wilhelms, F., Sevri, M., Udisti, R., Beer, J., Steinhilber, F., Adolphi, F., Muschler, R., Rasmussen, S., Steffensen, J., and Svensson, A.: A stratigraphic Antarctic chronology covering the past 16 700 years in the EPICA deep ice core from Dronning Maud Land, in preparation, 2013.

Wang, Y., Cheng, H., Edwards, R. L., Kong, X., Shao, X., Chen, S., Wu, J., Jiang, X., Wang, X., and An, Z.: Millennial- and orbital-scale changes in the East Asian monsoon over the past 224 000 years, Nature, 451, 1090–1093, doi:10.1038/nature06692, 2008.

Yiou, F., Raisbeck, G. M., Baumgartner, S., Beer, J., Hammer, C., Johnsen, S., Jouzel, J., Kubik, P. W., Lestringuez, J., Stiévenard, M., Suter, M., and Yiou, P.: Beryllium 10 in the Greenland Ice Core Project ice core at Summit, Greenland, J. Geophys. Res., 102, 26783–26794, doi:10.1029/97JC01265, 1997.

Yuan, D., Cheng, H., Edwards, R. L., Dykoski, C. A., Kelly, M. J., Zhang, M., Qing, J., Lin, Y., Wang, Y., Wu, J., Dorale, J. A., An, Z., and Cai, Y.: Timing, duration, and transitions of the Last Interglacial Asian Monsoon, Science, 304, 575–578, doi:10.1126/science.1091220, 2004.

3.3 L'incertitude associée à AICC2012

L'incertitude de la chronologie AICC2012 est directement dérivée de la méthode utilisée par Datice, et donnée par les éléments diagonaux de la matrice Q définie dans le chapitre 2.

L'erreur sur la chronologie gaz est définie comme étant la somme de l'erreur sur la chronologie glace et de l'erreur sur le Δdepth. L'erreur est donc surestimée lorsqu'on est en présence de liens stratigraphiques glace. Dans ce cas, l'erreur sur la phase gaz devrait être plus petite que l'erreur sur la phase glace. Nous pouvons noter que les erreurs sur les chronologies gaz et glace sont très proches, avec des différences de quelques centaines d'années seulement. Afin de ne pas sous-estimer l'erreur sur la chronologie glace, ce qui peut être le cas lorsqu'il y a beaucoup de marqueurs sur la phase gaz, nous avons décidé de considérer comme erreur finale sur la chronologie le maximum entre les erreurs glace et gaz pour chaque carotte. Une exception a été faite pour le forage d'EDC sur les dernier 60 ka à cause de la présence de nombreux liens stratigraphiques glace avec EDML. Dans ce cas l'erreur sur la phase glace doit être plus petite que l'erreur sur la phase gaz qui est principalement influencée par la LIDIE. Ainsi, par la présence d'un grand nombre de liens stratigraphiques glace entre EDC et EDML ayant une petite incertitude, l'erreur sur les chronologies glace d'EDML et EDC devrait être semblable. En conséquence, nous avons attribué l'erreur gaz d'EDML à l'erreur sur la chronologie glace d'EDC sur les derniers 60 ka. Nous devons aussi préciser que l'incertitude calculée par Datice pour NGRIP sur les derniers 60 ka n'a aucun sens car la chronologie a été contrainte par des marqueurs issus de GICC05 associés à des incertitudes artificiellement réduites. En conséquence, l'erreur sur les derniers 60 ka pour la chronologie AICC2012 de NGRIP doit être prise comme l'erreur de la chronologie GICC05, c'est-à-dire $1\sigma = 1/2 \cdot MCE$.

La figure 3.9 montre l'erreur sur la chronologie AICC2012 calculée pour chaque forage. On observe que l'erreur croit avec la profondeur (l'âge) pour plusieurs raisons :

— la variance associée aux scénarios d'ébauche augmente avec la profondeur ;
— plus on remonte dans le passé et moins il y a de marqueurs absolus, orbitaux et/ou stratigraphiques ;
— les marqueurs plus anciens présentent des incertitudes plus importantes.

De plus, en présence de nombreux marqueurs d'âge, l'erreur de la chronologie diminue comme $\sigma/\sqrt{N}$ avec N correspondant au nombre de marqueurs. Ceci explique pourquoi l'incertitude finale sur la chronologie est d'environ 4 ka pour des périodes étant seulement contraintes par des marqueurs d'âge possédant une incertitude de 6 ka.

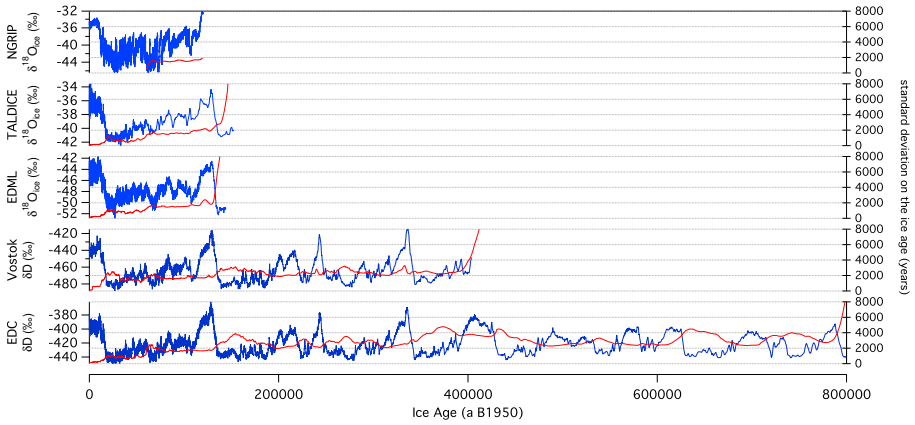

FIGURE 3.9 – Composition isotopique de la glace ($\delta^{18}O_{ice}$ ou δD) pour les 5 forages d'AICC2012 (bleu) et erreur sur la chronologie glace associée pour chaque forage (1σ, rouge).

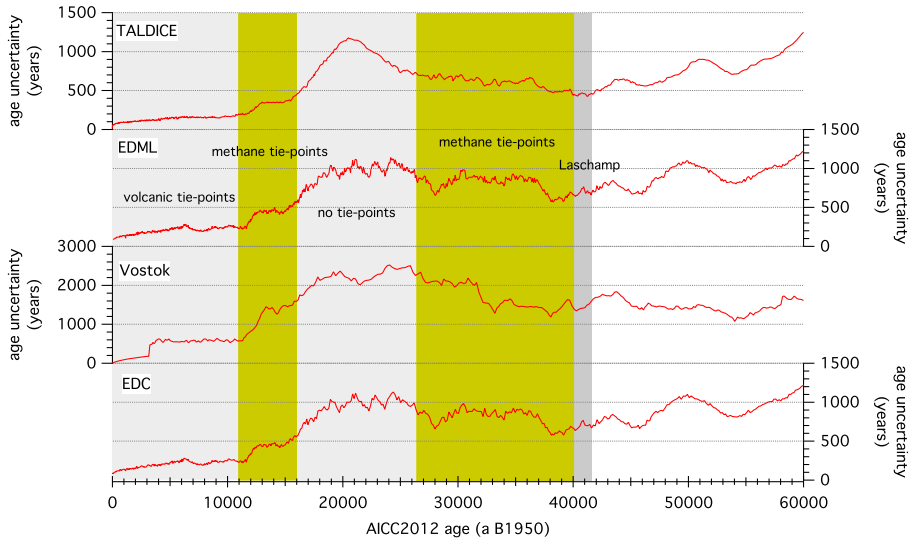

FIGURE 3.10 – Incertitude sur la chronologie AICC2012 pour TALDICE, EDML, Vostok et EDC sur les derniers 60 ka.

Si maintenant on se concentre seulement sur les derniers 60 ka, il est possible d'expliquer l'influence des différents paramètres d'entrée (variance sur les ébauches, présence des différents marqueurs...) sur la variabilité de l'erreur finale de la chronologie AICC2012 (figure 3.10). En l'absence de tout marqueur, l'incertitude sur la chronologie est seulement fonction des variances associées aux scénarios d'ébauche. Par exemple, avec la paramétrisation choisie dans la section 3.1.2 pour les variances des paramètres d'ébauche, l'incertitude est bien plus importante sur la chronologie de TALDICE que sur celle d'EDC (table 3.2). A proximité d'un marqueur d'âge absolu/orbital ou stratigraphique, l'erreur va diminuer en prenant en compte l'erreur associée au marqueur lui-même ainsi que l'erreur sur la chronologie de la seconde carotte dans le cas d'un lien stratigraphique. De ce fait, il est possible de différencier plusieurs phases dans l'evolution de l'erreur sur AICC2012 de la figure 3.10 :

— de 0 à 11 ka, les contraintes sont principalement issues de liens stratigraphiques glace. L'incertitude associée à ces marqueurs est petite, de même que celle associée aux scénarios d'ébauche de l'accumulation et de la fonction d'amincissement (proche des conditions actuelles). L'incertitude la plus petite est observée à EDML, induite par ses liens stratigraphiques avec NGRIP (chronologie forcée à respecter GICC05).
— entre 11–16 ka, nous sommes toujours en présence de quelques liens volcaniques, mais la chronologie est majoritairement contrainte par les liens stratigraphiques gaz issus du méthane avec NGRIP. Les liens déduits du méthane sont associés à des incertitudes plus grandes que les marqueurs volcaniques à cause de la moins bonne résolution des mesures. Ceci entraine donc une augmentation générale de l'incertitude sur les chronologies d'Antarctique.
— La période 16–26 ka, correspondant au MIS 2, a la particularité de ne présenter aucun marqueur pour TALDICE. En conséquence l'erreur de sa chronologie est seulement fonction des variances des paramètres d'ébauche, entraînant une importante augmentation de l'erreur sur AICC2012.
— Entre 26–40 ka, la présence de quelques liens volcaniques et issus du méthane rappelle l'incertitude sur la chronologie au même niveau que lors de la dernière déglaciation.
— L'excursion géomagnétique du Laschamp (∼41 ka) est enregistrée dans les carottes d'EDC et Vostok. Ce marqueur absolu se répercute sur les autres forages au travers des liens stratigraphiques gaz et glace.
— Sur le reste de la période couverte par la figure, on peut voir que l'incertitude associée à AICC2012 augmente. Ceci s'explique par la présence de moins de marqueurs contraignant la chronologie entre 42 et 60 ka.

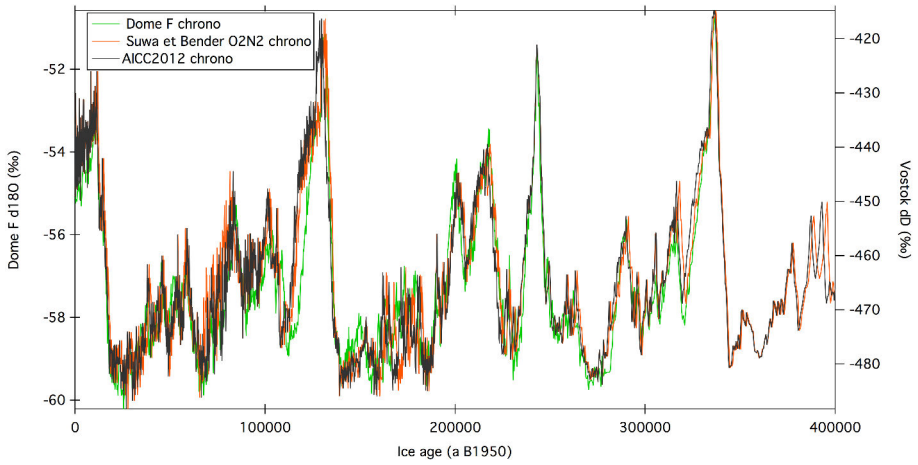

FIGURE 3.11 – Composition isotopique de la glace de Dome F sur la chronologie DFO-2006 ($\delta^{18}O_{ice}$ [Kawamura et al., 2007], vert) et Vostok (δD, Petit et al. [1999]) pour différentes chronologies : Suwa and Bender [2008] (orange) et AICC2012 (noire).

3.4 Comparaison avec d'autres chronologies

La comparaison avec la précédente chronologie carotte de glace de référence EDC3 a été présentée dans Bazin et al. [2013]. Dans cette section nous comparons AICC2012 avec d'autres chronologies carottes de glace ainsi que des spéléothèmes.

3.4.1 AICC2012 .vs. Suwa and Bender [2008]

La chronologie de Vostok construite par Suwa and Bender [2008] couvre les derniers 400 ka. Elle a été déduite à partir de contraintes issues du $\delta O_2/N_2$ et $\delta^{18}O_{atm}$ par synchronisation orbitale. Lors de la construction d'AICC2012 nous avons repris ces mêmes marqueurs d'âge, en conséquence ces deux chronologies devraient être cohérentes entre-elles. En effet, la différence maximale observée (3.5 ka) se situe au niveau de la dernière période glaciaire, et s'explique par les nombreuses contraintes stratigraphiques avec les autres forages présentes dans AICC2012. La deuxième moitié de la dernière période glaciaire est maintenant alignée sur GICC05. Sur le reste de la carotte de Vostok, nous observons des différences inférieures à 2 ka jusqu'à 400 ka (figure 3.11). Notons aussi que la chronologie AICC2012 est seulement contrainte par les marqueurs orbitaux de Vostok entre 100–400 ka et ne possède que peu de marqueurs issus de la teneur en air pour EDC.

3.4.2 AICC2012 .vs. Kawamura et al. [2007]

L'échelle d'âge de référence pour la carotte de glace de Dôme F (DFO-2006) a été construite à partir de contraintes issues du $\delta O_2/N_2$ jusqu'à 360 ka [Kawamura et al., 2007]. La chronologie AICC2012 est cohérente avec la chronologie orbitale de Dôme F à ± 2 ka, sauf lors de la dernière période interglaciaire où nous observons une différence allant jusqu'à 5–6 ka (figure 3.11). Au cours de cette période, la chronologie DFO-2006 est contrainte par 3 marqueurs (à 117 ka, 126 ka et 137ka), alors qu'AICC2012 est dérivée de nombreux liens stratigraphiques glace Vostok–EDC et les marqueurs orbitaux de Vostok (122 ka et 132 ka). Les marqueurs orbitaux de Vostok sont peu précis à cause de la résolution des mesures et l'incertitude associée à ces marqueurs (glace conservée à -20°C). Notons que cette différence significative entre les 2 chronologies était d'ores-et-déjà observée entre la chronologie EDC3 et DFO-2006. De même, AICC2012 ne présente qu'un écart de 1.5 ka avec la chronologie orbitale de Suwa and Bender [2008] sur cette même période. Cette différence pourrait provenir d'une relation différente entre le $\delta O_2/N_2$ et l'insolation locale au cours du MIS 5 aux sites de Vostok et Dôme F (voir chapitre 5). De plus, cette comparaison serait plus complète s'il était possible de discuter les enregistrements de méthane respectifs de ces deux carottes (non publiés pour Dôme F).

3.4.3 AICC2012 .vs. Parrenin et al. [2013]

Parrenin et al. [2013] a récemment publié une nouvelle chronologie gaz et glace pour la Terminaison I à EDC, déduite à partir des données de $\delta^{15}N$ pour contraindre la LIDIE lors de la dernière déglaciation. On ne compare pas les ages absolus entre les deux chronologies, mais seulement les retards relatifs CO_2–température Antarctique observés au cours de cette période sur les deux échelles d'âge (figure 3.12). Ainsi, nous n'observons toujours pas de retard significatifs entre le CO_2 et la température en Antarctique pour le début de la Terminaison I et le Younger–Dryas. Avec la chronologie AICC2012 nous observons néanmoins un retard plus important du CO_2 de 100 à 400 ans au début du Bølling-Allerød et de l'Holocène. Cette différence a probablement pour origine les différentes approches utilisées pour produire la chronologie gaz. Parrenin et al. [2013] utilise seulement le $\delta^{15}N$ d'EDC, alors que dans le cas d'AICC2012 les chronologies gaz sont construites à partir du $\delta^{15}N$ et des LIDIE produites par le modele de Goujon et al. [2003] pour les 5 carottes. De plus, les nombreux liens stratigraphiques glace et gaz présents viennent forcer la chronologie à cette période.

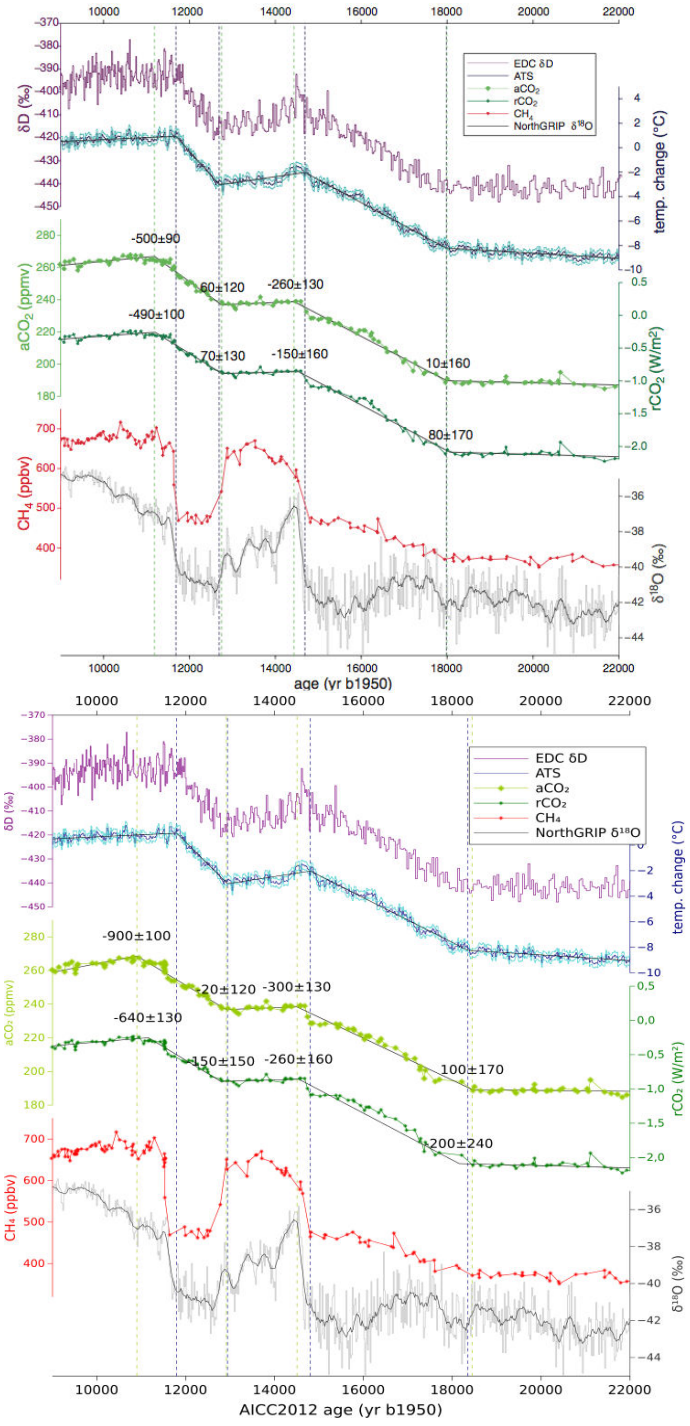

FIGURE 3.12 – Comparaison des résultats de Parrenin et al. [2013] sur sa chronologie dérivée (a) et AICC2012 (b) au niveau de la Terminaison I. De haut en bas : δD d'EDC (violet, Jouzel et al. [2007]), stack de température Antarctique (ATS, bleu foncé, Parrenin et al. [2013]) et son erreur associée (bleu clair),concentration en CO_2 atmosphérique d'EDC (aCO_2, vert clair, Lourantou et al. [2010]), forçage radiatif du CO_2 atmosphérique (rCO_2, vert foncé, Parrenin et al. [2013]), méthane d'EDC (rouge, Loulergue et al. [2008]) et $\delta^{18}O$ de NGRIP sur GICC05 [NorthGRIP Community Members, 2004]. Les meilleures régressions linéaires de l'ATS, aCO_2 et rCO_2 sont représentés en trait plein. Les barres verticales indiquent la position des points de cassure pour la regression linéaire de l'ATS (bleu) et pour l'aCO_2 (vert). Le retard entre aCO_2–ATS est indiqué par les chiffres noirs.

TABLE 3.6 – Comparaison de AICC2012 avec des spéléothèmes.

Evènement	age AICC2012 (ka)	age spéléothème (ka)	
DO-8	38.29	MCL-Hulu	38.32
		MSD-Hulu	38.23
DO-11	43.43	MCL-Hulu	43.81
		MSD-Hulu	44.08
DO-19	72.57	MCL-Hulu	72.17
		SB-22-Sanbao	71.7
DO-22	90.52	SB25-1-Sanbao	91.52
		SB22-Sanbao	90.8
onset MIS 5	128.88	SB25	129.04
		SB11	129.08
onset MIS 7	243.41	B61	243.1
		LZ15	243.6
onset MIS 9	337.2	B61	336.4
		LZ15	337.6
onset MIS 11	426.2	Kesang	426.6
onset MIS 13	492.5	Kesang	492.1

3.4.4 AICC2012 .vs. spéléothèmes

En suivant l'approche de Fleitmann et al. [2009], qui a suggéré que les variations abruptes du méthane lors des évènements de Dansgaard–Oeschger et les changements du $\delta^{18}O$ de la calcite des spéléothèmes sont synchrones, nous avons comparé les variations abruptes de méthane sur AICC2012 avec les changements du $\delta^{18}O$ de la calcite de spéléothèmes chinois [Cheng et al., 2009, 2012; Wang et al., 2001, 2008]. Cet exercice a déjà été proposé afin de valider la chronologie orbitale de Dôme F [Kawamura et al., 2007]. La comparaison a été effectuée sur plusieurs évènements de Dansgaard–Oeschger lors de la dernière période glaciaire, mais aussi étendue aux transitions glaciaire–interglaciaire II à VI [table 3.6, Veres et al., 2013]. La chronologie AICC2012 est en très bon accord avec les âges des spéléothèmes, au regard des incertitudes de AICC2012, ce qui confirme la robustesse de la méthodologie de Datice utilisée pour construire la chronologie.

3.5 Conclusions et perspectives

Dans le but de produire une chronologie la plus précise et cohérente possible, nous avons regroupé de nombreuses contraintes chronologiques pour les sites de NGRIP, TALDICE, EDML, Vostok et EDC. De plus, de nouvelles mesures de $\delta^{18}O_{atm}$ faites sur la carotte d'EDC pour la période MIS 11–12 nous ont permis de réviser/préciser

les marqueurs d'âge proposés par Dreyfus et al. [2007]. De même, de nouvelles mesures de $\delta^{18}O_{atm}$ sur la carotte de TALDICE nous ont permis de compléter l'enregistrement publié par Buiron et al. [2011]. Ces résultats mettent en évidence des différences entre les enregistrements de $\delta^{18}O_{atm}$ de TALDICE et Vostok avant 150 ka, alors que le $\delta^{18}O_{atm}$ est un traceur global et donc synchrone à l'échelle de l'Antarctique. En conséquence, nous avons décidé d'arrêter la chronologie de TALDICE à 150 ka, et nous avons déduit des liens stratigraphiques entre Vostok et TALDICE à partir du $\delta^{18}O_{atm}$ sur les derniers 150 ka. Grâce aux études publiées sur la synchronisation orbitale de la teneur en air avec une courbe intégrée de l'insolation [Lipenkov et al., 2011] ainsi que sur la synchronisation orbitale du $\delta^{18}O_{atm}$ et $\delta O_2/N_2$ à Vostok [Suwa and Bender, 2008], nous avons pu tester la cohérence entre ces 3 marqueurs orbitaux sur les derniers 400 ka. Nous avons observé des différences allant jusqu'à 2 ka entre les chronologies obtenues par le $\delta O_2/N_2$ et la teneur en air, et entre 2 et 4 ka pour la comparaison $\delta^{18}O_{atm}$–$\delta O_2/N_2$. Ces différences ont probablement comme origine les hypothèses de synchronisation orbitale sous-jacentes ainsi que les différences entre phase gaz et glace. Néanmoins, cette comparaison nous a permis de confirmer qu'il est possible de combiner ces différents marqueurs orbitaux en toute sécurité en respectant les incertitudes associées à ces marqueurs (6 ka pour $\delta^{18}O_{atm}$, 4 ka pour $\delta O_2/N_2$ et jusqu'à 7 ka pour la teneur en air).

En combinant tous les marqueurs (âges absolus, orbitaux et liens stratigraphiques) avec les différents scénarios d'ébauche et leurs incertitudes associées dans Datice, nous avons obtenu une chronologie cohérente (AICC2012) pour NGRIP, TALDICE, EDML, Vostok et EDC jusqu'a 350 ka et 800 ka pour EDC. Cette nouvelle échelle d'âge a la particularité de respecter la chronologie groenlandaise GICC05 sur les derniers 60 ka. Grâce à la grande quantité de contraintes introduites sur la dernière période glaciaire, AICC2012 présente une meilleure estimation de la durée des évènements sur cette période. La théorie du see–saw bipolaire reste toujours valable, avec des enregistrements d'Antarctique 600 ans plus jeunes sur AICC2012 que précédemment. L'âge de la Terminaison II observé sur AICC2012 est en accord avec les autres archives climatiques et totalement indépendant. Contrairement à la chronologie EDC3, où cette transition était contrainte par un marqueur provenant de carottes marines [Parrenin et al., 2007a; Waelbroeck et al., 2008], la nouvelle chronologie est seulement contrainte par de nombreux liens stratigraphiques et marqueurs orbitaux sur cette période.

Pour finir, la nouvelle chronologie de référence pour les carottes de glace AICC2012 reste en bon accord avec les autres chronologies d'Antarctique comme Dôme F jusqu'à 360 ka, à l'exception du MIS 5. Une explication possible serait un comportement

différent du $\delta O_2/N_2$ à cette période pour ces 2 sites, conduisant à une synchronisation orbitale sensiblement différente (chapitre 5). Comparé à l'ancienne référence pour les carottes de glace EDC3, AICC2012 présente globalement des différences à $\pm$1.5 ka, exception faite du MIS 12 où AICC2012 est 5.4 ka plus ancienne. Cette différence a pour origine l'implémentation de nouveaux marqueurs issus du $\delta O_2/N_2$ sur cette période dans AICC2012. Cette chronologie, construite à l'aide d'une nouvelle méthode et regroupant un grand nombre de contraintes, ne présente aucun changement significatif sur la durée des périodes interglaciaires et ne remet pas en cause les précédentes interprétations climatiques faites sur EDC3.

Cette nouvelle chronologie représente la première étape vers une nouvelle approche de la datation des archives climatiques. Afin de poursuivre ce travail, plusieurs points restent à améliorer :

- Réaliser de nouvelles mesures de $\delta^{18}O_{atm}$ sur la carotte d'EDC afin d'augmenter la résolution de l'enregistrement actuel, notamment lors des périodes de faible excentricité où la synchronisation orbitale est particulièrement discutable.
- Réaliser de nouvelles mesures de $\delta O_2/N_2$ sur de la glace bien conservée. L'étude de Landais et al. [2012] a montré que les échantillons de glace d'EDC conservés à -50°C ne sont pas soumis à une perte de gaz, contrairement à une conservation à des températures plus élevées. Afin d'avoir un enregistrement non–soumis à de la perte de gaz, de nouvelles mesures sont nécessaires entre 0–380 ka et 420–720 ka. Elles permettront d'affiner la synchronisation orbitale via le $\delta O_2/N_2$ pour EDC.
- Apporter des améliorations à l'outil Datice. Lors de la construction d'AICC2012 nous n'avons pas respecté l'hypothèse de non corrélation entre les scénarios d'ébauche et les marqueurs issus de GICC05 pour NGRIP. Il semble alors nécessaire pour les prochains exercices réalisés avec Datice d'implémenter un nouveau type de marqueurs, mieux adapté aux contraintes issues du comptage de couches annuelles. De plus, les paramétrisations adoptées pour les variances des paramètres d'ébauche lors de la construction d'AICC2012 nécessitent des améliorations. L'augmentation de l'erreur associée à la fonction d'amincissement d'ébauche d'EDC au niveau des transitions glaciaire–interglaciaire a conduit à un comportement étrange de la fonction d'amincissement analysée d'EDC à certaines périodes. L'utilisation des propriétés mécaniques mesurées sur la glace pour mieux définir la variance de la fonction

d'amincissement [Durand et al., 2007], ou encore l'intégration des poussières pouvant influencer la compaction du névé et donc la LIDIE [Freitag et al., 2013] sont des pistes envisageables.

- Etendre la prochaine chronologie commune à d'autres forages d'Antarctique et du Groenland. Il faut néanmoins choisir des sites où il y a assez de données publiées afin de pouvoir effectuer des synchronisation entre les carottes de glace, mais aussi pouvoir générer des paramètres d'ébauche et leurs incertitudes associées. Les sites comme Dome F et WAIS en Antarctique, ou encore NEEM au Groenland permettraient d'apporter des réponses quant aux différences entre Antarctique de l'Ouest et Antarctique de l'Est lors de la dernière transition glaciaire–interglaciaire, ou encore le couplage Nord–Sud lors de la dernière période glaciaire. En effet, ces forages possèdent de nouvelles mesures de bonne qualité qui pourraient permettre de mieux contraindre la datation, notamment grâce au comptage des couches annuelles jusqu'à 30 ka pour la carotte de WAIS.
- Adapter Datice afin de pouvoir intégrer d'autres archives climatiques et de pouvoir discuter des différents temps de réponse observés entre les traceurs des différentes archives lors de changements climatiques. Cela permettrait d'avoir une meilleure connaissance sur les relations prenant place entre les hautes et les basses latitudes lors de tels changements.

4

Vers une prochaine chronologie fédérative : améliorations préliminaires

4.1 Introduction

Lors de la construction d'AICC2012 en utilisant Datice, nous avons forcé cette chronologie à respecter l'échelle d'âge groenlandaise GICC05 obtenue par comptage des couches annuelles [Veres et al., 2013; Vinther et al., 2006; Rasmussen et al., 2006; Andersen et al., 2006; Svensson et al., 2008]. Cette dernière est une chronologie absolue, possédant une incertitude croissante avec la profondeur, jusqu'à 2.6 ka à 60 ka. L'erreur associée à cette échelle d'âge (Maximum Counting Error, MCE) a été obtenue de la façon suivante : les couches incertaines sont comptées comme 0.5 ± 0.5 ans, alors que les couches certaines ont été comptabilisées comme 1 ± 0 ans. Ainsi, Rasmussen et al. [2006] ont estimé que la MCE, qui n'est pas une erreur gaussienne, peut être considérée comme équivalente à 2σ. Ainsi, l'erreur associée à une couche annuelle ne peut être considérée comme indépendante de celle des couches voisines.

Dans le chapitre précédent, nous avons vu que la méthode utilisée pour forcer AICC2012 à respecter GICC05 ne respecte pas les hypothèses sous-jacentes à Datice. En effet, la théorie derrière Datice suppose qu'il n'existe pas de corrélation entre les paramètres d'ébauche de NGRIP et les contraintes d'âge, ce qui n'a pas été le cas pour la construction d'AICC2012 (taux d'accumulation, fonction d'amincissement d'ébauche de NGRIP et marqueurs d'âge tous les 60 ans déduits de GICC05). Afin de limiter les corrections de Datice sur les paramètres d'ébauche, nous avons associé à ces derniers, ainsi qu'aux marqueurs d'âge tirés de GICC05, des erreurs artificiel-

lement petites. De cette façon, nous avons contraint AICC2012 à respecter GICC05 à ± 5 ans.

De nouvelles études ont montré que le taux d'accumulation déduit de GICC05 pouvait être surestimé en période glaciaire [Huber et al., 2006; Guillevic et al., 2013; Kindler et al., 2014]. En effet, en combinant la modélisation du névé avec les données de $\delta^{15}N$ mesurées pour NGRIP et NEEM, ces différents auteurs ont montré qu'il était nécessaire de diminuer le taux d'accumulation de GICC05 ou ss09sea jusqu'à 30–35% pour reconstruire le $\delta^{15}N$ lors de la dernière période glaciaire. De plus, grâce aux récentes données de Kindler et al. [2014], il est maintenant possible de définir de nouveaux marqueurs de $\Delta depth$ pour NGRIP, venant ainsi améliorer l'estimation de la chronologie gaz.

Dans l'article qui suit nous présentons une amélioration de Datice par l'intégration des marqueurs de différence d'âge, mieux adaptés aux contraintes d'âge issues du comptage des couches annuelles. Cet outil de datation offre la possibilité de prendre en compte des corrélations d'erreurs entre les marqueurs d'âge. Ceci est important pour les marqueurs de différence d'âge car les erreurs déduites de la MCE ne peuvent être considérées comme complètement décorrelées, comme c'était le cas pour AICC2012. Différents tests sont présentés afin de contraindre la chronologie commune à respecter GICC05, mais cette fois en utilisant des scenarios d'ébauche indépendants de GICC05 avec des erreurs associées plus cohérentes, tout en intégrant les nouveaux marqueurs de $\Delta depth$ déduits des données de Kindler et al. [2014].

4.2 Optimisation of glaciological parameters for ice core chronology by implementing counted layers between identified depth levels

Cet article a été soumis à Climate of the Past, et est actuellement en cours de révision. Suite aux commentaires des rapporteurs l'article va être retravaillé significativement. Les points clés modifiés suite aux commentaires des rapporteurs sont présentés dans la conclusion de ce chapitre.

Clim. Past Discuss., 10, 3585–3616, 2014
www.clim-past-discuss.net/10/3585/2014/
doi:10.5194/cpd-10-3585-2014

Climate of the Past Discussions

Optimisation of glaciological parameters for ice core chronology by implementing counted layers between identified depth levels

L. Bazin[1], B. Lemieux-Dudon[2], A. Landais[1], M. Guillevic[1,3], P. Kindler[4], F. Parrenin[5], and P. Martinerie[5]

[1]Laboratoire des Sciences du Climat et de l'Environnement, UMR8212, CEA–CNRS–UVSQ, Orme des Merisiers, Gif sur Yvette, France
[2]Laboratoire Jean Kuntzmann, Grenoble, France
[3]Centre for Ice and Climate, Niels Bohr Institute, University of Copenhagen, Copenhagen, Denmark
[4]Climate and Environmental Physics, Physics Institute & Oeschger Center for Climate Change Research, University of Bern, Bern, Switzerland
[5]Laboratoire de Glaciologie et Géophysique de l'Environnement, UMR 5183, Univ. Grenoble Alpes–CNRS, Grenoble, France

Received: 22 July 2014 – Accepted: 5 August 2014 – Published: 28 August 2014

Correspondence to: L. Bazin (lucie.bazin@lsce.ipsl.fr)

Published by Copernicus Publications on behalf of the European Geosciences Union.

Discussion Paper | Discussion Paper | Discussion Paper | Discussion Paper |

Abstract

A recent coherent chronology has been built for 4 Antarctic ice cores and the NorthGRIP (NGRIP) Greenland ice core (Antarctic Ice Core Chronology 2012, AICC2012) using a bayesian approach for ice core dating (Datice). When building the AICC2012 chronology, and in order to prevent any confusion with official ice cores chronology, it has been imposed that the AICC2012 chronology for NGRIP should respect exactly the GICC05 chronology based on layer counting. However, such a strong tuning did not satisfy the hypothesis of independence of background parameters and observations for the NGRIP core as required by Datice. We present here the implementation in Datice of a new type of markers that is better suited to constraints deduced from layer counting: the markers of age-difference. Using this type of markers for NGRIP in a 5 cores dating exercise with Datice, we have performed several sensitivity tests and show that the new ice core chronologies obtained with these new markers do not differ by more than 400 years from AICC2012 for Antarctic ice cores and by more than 130 years from GICC05 for NGRIP over the last 60 000 years. With this new parameterization, the accumulation rate and lock-in depth associated with NGRIP are more coherent with independent estimates than those obtained in AICC2012. While these new chronologies should not be used yet as new ice core chronologies, the improved methodology presented here should be considered in the next coherent ice core dating exercise.

1 Introduction

The reference timescale for Greenland ice cores, GICC05, has been obtained by layer counting back to 60 ka (thousands of years before present, present being year 1950 all along our study; Vinther et al., 2006; Rasmussen et al., 2006; Andersen et al., 2006; Svensson et al., 2008). This chronology is absolute with an increasing associated uncertainty with depth, reaching more than 2.6 ka at 60 ka. Because this chronology is

based on annual layer counting, the duration of events is rather precise, even for old ages, with an uncertainty of about 1–8 years for counting of 20 annual layers. Since the layer counting is not independent from one interval to another, the final uncertainty on the GICC05 chronology cumulates the counting error: uncertain annual layers are counted 0.5 ± 0.5 years, while certain layers are counted as 1 ± 0 years (Rasmussen et al., 2006). The 1-sigma uncertainty of GICC05 is thus expressed as half the Maximum Counting Error (MCE; Rasmussen et al., 2006).

This chronology has been used as a reference for many records of the North Atlantic region (Austin et al., 2012; Walker et al., 2012; Austin and Hibbert, 2012; Davies et al., 2012; Blockley et al., 2012b). It has also been used as a basis over the last 60 ka for the recent construction of the coherent Antarctic Ice Core Chronology (AICC2012) gathering one Greenland ice core (NorthGRIP – NGRIP) and 4 Antarctic ice cores (EPICA Dome C – EDC, EPICA Dronning Maud Land – EDML, Talos Dome ice core – TALDICE and Vostok) (Bazin et al., 2013; Veres et al., 2013). For the construction of AICC2012 with the bayesian tool Datice (Lemieux-Dudon et al., 2010), we have imposed a 1-sigma deviation for NGRIP of 50 years maximum. Even if such a constraint is artificially too strong compared to the true uncertainty of GICC05, it permits to keep a coherency within 5 years between the NGRIP AICC2012 chronology and GICC05.

Still, the strong tie of AICC2012 to GICC05 had raised some technical problems when optimizing the chronology with the bayesian tool Datice. Three glaciological parameters are indeed optimized during this process: accumulation rate, ice thinning and lock-in depth (i.e. the depth at which air is trapped when snow is sufficiently compacted). The bayesian approach imposes to start with first guess (background) scenarios for the three parameters. They are then modified within their imposed variance range so that the final chronology fits the absolute and relative age constraints for each ice core within error bars.

In practice, to force the NGRIP AICC2012 chronology to fit the GICC05 age scale, we had to use the modelled thinning function and accumulation rate adapted to the GICC05 chronology (hereafter DJ–GICC05 scenarios; Vinther et al., 2006; Rasmussen

et al., 2006; Andersen et al., 2006; Svensson et al., 2008) as background thinning and accumulation rate scenarios in Datice. The associated variances were also imposed to be very small to prevent any deviation from the GICC05 timescale as well as absolute markers every 60 years with an artificial maximum uncertainty of 50 years for the NGRIP ice core.

Even if the uncertainty of the GICC05 timescale is well constrained, this is not true for the DJ–GICC05 scenarios of thinning and accumulation. The thinning function is deduced from a simple Dansgaard–Johnsen (DJ) ice flow model (Dansgaard and Johnsen, 1969; Andersen et al., 2006) that has been parameterized to obtain the best match between the modelled and observed depth–age horizons in the ice cores. Then, the thinning function calculated with the DJ model is used together with the observed annual layer thicknesses to produce an accumulation rate history. No uncertainty value is associated with the reconstructions of thinning and accumulation rate in Greenland ice cores but thinning reconstructed from such 1-D ice flow model are generally associated with an uncertainty of 30 % (Cutler et al., 1995).

Recently, studies combining air isotopic measurements (δ^{15}N of N_2) with firnification models have suggested that, both in NGRIP and NEEM, the accumulation rates reconstructed from the GICC05 or ss09sea chronologies, through layer counting and the DJ flow model, were overestimated during the last glacial period (Huber et al., 2006; Guillevic et al., 2013; Kindler et al., 2014). Indeed, δ^{15}N of N_2 of air trapped in an ice core indicates the depth and the amplitude of abrupt temperature changes in the gas phase through thermal fractionation. The depth difference between the same abrupt temperature changes recorded in the ice phase through ice δ^{18}O increase/decrease and in the gas phase through a positive/negative δ^{15}N peak is called delta–depth (Δdepth). Moreover, in the absence of any abrupt temperature change and convection at the top of the firn, the δ^{15}N gives an indication of the past lock-in depth (LID) due to gravitational fractionation. A firnification model including heat diffusion and mainly driven by temperature and accumulation rate can reproduce long term and abrupt δ^{15}N variations with depth for Greenland ice cores. Still, it has been shown that the δ^{15}N profile

is best reproduced when the ss09sea accumulation rate for NGRIP is decreased by ∼ 20 % over the period 20 to 60 ka (Kindler et al., 2014; Huber et al., 2006).

It thus appears that the way NGRIP was implemented in the Datice tool for the AICC2012 chronology is not optimal. In addition to GICC05 chronological uncertainties that were not taken into account by construction, imposing the DJ-GICC05 accumulation rate and thinning scenarios with artificially reduced variances most probably led to incorrect output scenarios for these glaciological parameters.

In this paper, we propose an improvement of Datice to better implement the chronological uncertainties. We incorporate the possibility of integrating markers of age-difference and corresponding uncertainties instead of only absolute ages with artificially small uncertainties. This better respects the construction of the layer counted GICC05 chronology where the uncertainty on age differences is much smaller than on absolute ages. We also relax the strong constraints on thinning and accumulation rate and allow the NGRIP chronology to differ from GICC05 chronology within its error bars.

The outline of the manuscript is the following. In a first methodological section, we present the improvement made on the Datice tool in order to integrate the markers of age-difference with their uncertainties. Then, we show that the relaxation of the constraints on glaciological parameters enables removing some inconsistencies observed in the AICC2012 timescale. Finally, we focus on how this new version of Datice modifies the NGRIP and Antarctic chronologies compared to AICC2012.

2 Construction of the GICC05-free chronology

2.1 Methodology

The purpose of the following section is to describe the modifications implemented in Datice (Lemieux-Dudon et al., 2009, 2010) to take into account an additional type of constraint: the markers of age-difference. This constraint is applied by feeding Datice with the beginning and end depths of the interval, its duration and the duration uncer-

tainty. A last parameter permits to correlate or not this uncertainty with other duration uncertainties at various depth levels. The main modification of the Datice code appears in the expression of the cost function. The minimization of the Datice cost function aims at obtaining the best age model scenario by taking into account the paleo–observations and a background (first guess) age model. The background age model and paleo–observations should be independent from each other. The minimization of the cost function permits to make the best compromise between independent information.

In practice, Datice is applied to N ice cores to calculate coherent chronologies for both the ice and gas phases. For the ice core indexed k, gas and ice chronologies are deduced from the scenarios of the three glaciological parameters optimized in Datice: the total thinning function $T_k(z)$, the accumulation rate $A_k(z)$ and the lock-in depth in ice equivalent (LIDIE) $C_k(z)$ (Appendix A). On the basis of these 3 key parameters, Datice defines the model scenario $\boldsymbol{X}$ as a set of correction functions $\alpha_k(z)$, $\tau_k(z)$ and $\gamma_k(z)$ to be applied as multiplicative factors on prior scenarios for the accumulation, thinning function and LIDIE respectively, for the core k and at each depth level:

$$T_k(z) = \tau_k(z) \cdot T_k^{\mathrm{b}}(z) \tag{1}$$

$$A_k(z) = \alpha_k(z) \cdot A_k^{\mathrm{b}}(z) \tag{2}$$

$$C_k(z) = \gamma_k(z) \cdot C_k^{\mathrm{b}}(z) \tag{3}$$

where the prior (or background) scenarios for the thinning, accumulation and LIDIE are referred to as $T_k^{\mathrm{b}}(z)$, $A_k^{\mathrm{b}}(z)$ and $C_k^{\mathrm{b}}(z)$. In order to run a Datice simulation, background scenarios as well as observations with their respective uncertainties must be provided. Note that a change of variable is applied to all parameters, $\tilde{x} = \log(x)$, since Datice makes the hypothesis of lognormally distributed errors for the background model scenarios $T_k^{\mathrm{b}}(z)$, $A_k^{\mathrm{b}}(z)$ and $C_k^{\mathrm{b}}(z)$. This change of variable enables to transform lognormal into normal probability density functions in the Bayes' theorem (Tarantola, 2005).

Until now, observation $\boldsymbol{Y}$ could be of the following types: ice and gas age markers ($^{\mathrm{ia}}$ and $^{\mathrm{ga}}$), delta-depth markers ($^{\mathrm{dd}}$), or ice and gas stratigraphic links ($^{\mathrm{is}}$ and $^{\mathrm{gs}}$) (Lemieux-

Dudon et al., 2010; Buiron et al., 2011; Veres et al., 2013; Bazin et al., 2013). The application of a supplementary type of observation, named the markers of age-difference ($^{\mathrm{ad}}$), leads to an additional term in the cost function (Eq. 4). This supplementary term (last term in Eq. 4) is added in the original cost function, under the hypothesis of no error correlation between (i) observations of different types, (ii) observation of different cores, or (iii) observation and background model scenarios.

$$\begin{aligned}
J(\tilde{\boldsymbol{X}}) = & \sum_{k=1}^{N} \frac{1}{2} \left(\tilde{\boldsymbol{X}}_k - \tilde{\boldsymbol{X}}_k^{\mathrm{b}}\right)^T [\mathbf{B}]^{-1} \left(\tilde{\boldsymbol{X}}_k - \tilde{\boldsymbol{X}}_k^{\mathrm{b}}\right) \\
& + \sum_{k=1}^{N} \frac{1}{2} \left(\boldsymbol{Y}_k^{\mathrm{dd}} - \mathbf{h}_k^{\mathrm{dd}}(\tilde{\boldsymbol{X}}_k)\right)^T \left[\mathbf{R}_k^{\mathrm{dd}}\right]^{-1} \left(\boldsymbol{Y}_k^{\mathrm{dd}} - \mathbf{h}_k^{\mathrm{dd}}(\tilde{\boldsymbol{X}}_k)\right) \\
& + \sum_{k=1}^{N} \frac{1}{2} \left(\boldsymbol{Y}_k^{\mathrm{ia}} - \mathbf{h}_k^{\mathrm{ia}}(\tilde{\boldsymbol{X}}_k)\right)^T \left[\mathbf{R}_k^{\mathrm{ia}}\right]^{-1} \left(\boldsymbol{Y}_k^{\mathrm{ia}} - \mathbf{h}_k^{\mathrm{ia}}(\tilde{\boldsymbol{X}}_k)\right) \\
& + \sum_{k=1}^{N} \frac{1}{2} \left(\boldsymbol{Y}_k^{\mathrm{ga}} - \mathbf{h}_k^{\mathrm{ga}}(\tilde{\boldsymbol{X}}_k)\right)^T \left[\mathbf{R}_k^{\mathrm{ga}}\right]^{-1} \left(\boldsymbol{Y}_k^{\mathrm{ga}} - \mathbf{h}_k^{\mathrm{ga}}(\tilde{\boldsymbol{X}}_k)\right) \\
& + \sum_{k=1}^{N} \frac{1}{2} \left(\boldsymbol{Y}_k^{\mathrm{is}} - \mathbf{h}_k^{\mathrm{is}}(\tilde{\boldsymbol{X}}_k)\right)^T \left[\mathbf{R}_k^{\mathrm{is}}\right]^{-1} \left(\boldsymbol{Y}_k^{\mathrm{is}} - \mathbf{h}_k^{\mathrm{is}}(\tilde{\boldsymbol{X}}_k)\right) \\
& + \sum_{k=1}^{N} \frac{1}{2} \left(\boldsymbol{Y}_k^{\mathrm{gs}} - \mathbf{h}_k^{\mathrm{gs}}(\tilde{\boldsymbol{X}}_k)\right)^T \left[\mathbf{R}_k^{\mathrm{gs}}\right]^{-1} \left(\boldsymbol{Y}_k^{\mathrm{gs}} - \mathbf{h}_k^{\mathrm{gs}}(\tilde{\boldsymbol{X}}_k)\right) \\
& + \sum_{k=1}^{N} \frac{1}{2} \left(\boldsymbol{Y}_k^{\mathrm{ad}} - \mathbf{h}_k^{\mathrm{ad}}(\tilde{\boldsymbol{X}}_k)\right)^T \left[\mathbf{R}_k^{\mathrm{ad}}\right]^{-1} \left(\boldsymbol{Y}_k^{\mathrm{ad}} - \mathbf{h}_k^{\mathrm{ad}}(\tilde{\boldsymbol{X}}_k)\right)
\end{aligned} \tag{4}$$

In Eq. (4), the first term is related to the background term, while the six following terms are related to the observations. The cost function measures the squared distance

between the background scenarios or observations with the current age model $\tilde{\boldsymbol{X}}$. The observation operators, **h**, have to be introduced to translate the observation value on the current age model at each iteration. All the squared distances are weighted according to the confidence we have in the background model scenarios and in the markers. This is done through the background error covariance matrix **B**, and the observation error covariance matrices **R**. These matrices play a key role since the weights they introduce set the final trade-off between the background and observation constraints in the cost function.

For NGRIP, indexed with k, each marker of age-difference is defined over a depth interval between $z_k^{\mathrm{ad},1}$ and $z_k^{\mathrm{ad},2}$. Such a marker measures the number of years y_k^{ad} counted in between the two depth levels.

Figure 1 shows the result of one Datice simulation, with the optimized ice chronology $\Psi_k^{\mathrm{a}}(z)$ (red line), and the background chronology (grey dotted line). Each marker of age-difference is sketched with a grey rectangle designed to confirm whether the analysed chronology meets the marker constraint or not:

$$\Psi_k^{\mathrm{a}}\left(z_k^{\mathrm{ad},2}\right) - \Psi_k^{\mathrm{a}}\left(z_k^{\mathrm{ad},1}\right) \leq y_k^{\mathrm{ad}} \pm \sigma_k^{\mathrm{ad}} \tag{5}$$

where $\Psi_k^{\mathrm{a}}\left(z_k^{\mathrm{ad},1}\right)$ and $\Psi_k^{\mathrm{a}}\left(z_k^{\mathrm{ad},2}\right)$ are the analysed ice ages at both ends of the depth interval over which $y_k^{\mathrm{ad}} \pm \sigma_k^{\mathrm{ad}}$ years were counted. The analysed ice age curve should therefore be located within the error bars close to the upper right corner of the rectangle.

2.2 Modifications of inputs since AICC2012

An important condition to use Datice properly is to respect the independence between the age constraints and the background scenarios. This was not the case when building AICC2012 for the NGRIP ice core. Here, the new development of Datice allows one to use scenarios for background accumulation rate and thinning function independent from the age constraints deduced from GICC05 for NGRIP. The thinning function is the same as for AICC2012, obtained from the 1-D–DJ glaciological model adapted to NGRIP (Andersen et al., 2006). However, we have largely increased its associated variance to make it comparable to the ones associated with the background thinning function of the other cores implemented in Datice (Appendix A). For the accumulation rate, we use two background scenarios independent from GICC05, i.e. based on variations of water isotopes or $\delta^{15}\mathrm{N}$ of N_2 as detailed in Sect. 3.1. The formulation and coefficients of the variance of NGRIP background accumulation rate are the same as in AICC2012 and comparable to other ice cores. The LIDIE background scenario in AICC2012 was built from a firnification model (Goujon et al., 2003) whose input parameters (temperature and accumulation rate) were roughly adjusted to be coherent with the mean $\delta^{15}\mathrm{N}$ values measured over the NGRIP ice core. It was thus independent from GICC05 and has been kept unchanged for our study.

Concerning the age constraint, the absolute age markers deduced from GICC05 were replaced by markers of age-difference. The markers of age-difference are obtained from the GICC05 chronology at regular time intervals. In the official GICC05 chronology, the markers of age-difference are given every 20 years with the corresponding Maximum Counting Error (MCE), but some adjustments of the periodicity of these age markers were done for this study (Sect. 2.3). In order to constrain the relative gas chronology vs the ice chronology, we use information derived from $\delta^{15}\mathrm{N}$ of air trapped in ice bubbles. New $\delta^{15}\mathrm{N}$ data on the NGRIP ice core have been published since the AICC2012 chronology (Kindler et al., 2014). In particular, these data permit to identify depths of rapid temperature increases associated with the beginning of Greenland Interstadials (GI) 1 to 7 in the gas phase. The depth differences between peaks of $\delta^{18}\mathrm{O_{ice}}$ and $\delta^{15}\mathrm{N}$ of a concomitant event recorded in the ice and the gas phases are thus used as delta-depth (Δdepth) constraints. With the new set of data from Kindler et al. (2014), we were thus able to deduce new Δdepth markers that were not available for the construction of AICC2012 (Table 1). Their uncertainties depend on the resolution of measurements and the difference of Δdepth estimates.

2.3 Incorporation of the markers of age-difference in Datice

The introduction of the markers of age-difference is more appropriate to build a chronology the respecting the original layer counting constraints of the GICC05 chronology. Still, the incorporation of the GICC05 markers of age-difference and associated uncertainties within Datice is not straightforward. The main problems to address are (1) to define the most appropriate time interval for incorporation of the markers of age-difference and (2) to transform an uncertainty expressed as a maximum counting error in GICC05 into an uncertainty expressed as the standard deviation of a Gaussian distribution in Datice.

Different tests, summarized below, were performed to address these two problems and find the best formulation. To address the first problem of the periodicity of age markers, we have initially assumed that the MCE on each interval is completely uncorrelated over the last 60 ka and assigned a 2 MCE uncertainty to markers of age-difference deduced from the GICC05 layer counting. We decide in this paper to treat the error on individual annual layer as normally distributed. On this assumption, one can apply the MCE to age-difference markers as a Gaussian error. The periodicity of markers of age-difference in GICC05 is 20 years with a 1 to 8 years associated uncertainty (Rasmussen et al., 2006). However, as the spatial resolution of Datice is every meter, a too high frequency of the markers of age-difference can create inconsistencies. In particular, 1 m often represents more than 20 years for the NGRIP ice core over the last glacial period. As a consequence, even with an associated interpolation scheme, it is not possible for Datice to properly incorporate these markers and combine them with other dating constraints. This is illustrated on Fig. 2 where we have tested several intervals for the age-difference markers (20, 60, 100 and 200 years) with their corresponding 2 MCE errors. It resulted that markers have to be of 100 years difference or higher for Datice to run correctly without divergence at high depths. We then observe a difference of up to 130 years with the GICC05 chronology between 23–40 ka. We have chosen to retain the chronology built with markers of age-difference

every 100 years in order to keep the strongest possible constraint from the GICC05 chronology.

In this first set of tests, the errors for markers of age-difference were assumed to be completely uncorrelated. This is the reason why even if we have chosen a larger uncertainty than the GICC05 one, the previous chronologies present final uncertainties 4 to 12 times smaller than the half MCE (Fig. 2 bottom). The assumption of uncorrelated errors for markers of age-difference is questionable since the layer counting process may introduce a systematic bias all over the core, or at least on several core sections. The MCE construction takes into account the possible existence of such error correlations by assuming completely correlated errors on individual annual layers. It gives an upper estimate of the error by summing up errors instead of squared errors (and taking the square root of the result). However, no estimate of the error correlation is provided in the GICC05 chronology. In order to test the influence of error correlation between markers of age-difference in our study, we have performed Datice simulations with different values of error correlation between markers of age-difference. For these tests, we have used a 100 years interval between markers of age-difference. We have assigned the value of 1 MCE for the 1-sigma uncertainty of Datice and the error correlation value has been varied between its minimum and maximum possible values. The introduction of the error correlation for markers of age-difference does not lead to strong deviations from the GICC05 chronology. As for the chronology built without correlation, the maximum difference between the new chronologies and GICC05 is of 130 years (Fig. 3). However, the chronologies obtained with or without correlation between errors are not similar: the deviation from GICC05 continuously increases with depth in the case of error correlation while the deviation is maximum for the last glacial maximum and then decreases in the case of no correlation. As expected, when the correlation is increased, the deviation between the new chronology and the first guess increases (Fig. 3 middle).

Even if the deviations from the GICC05 chronology are of the same order of magnitude with or without error correlation, the main difference appears in the final chronol-

ogy uncertainty calculated by Datice (Fig. 3 bottom). Without error correlation, the 1-sigma uncertainty is close to 200 years at 60 ka compared to the double when we consider the error correlation for the markers of age difference. Still, the final error is smaller than the error given for the GICC05 chronology and defined as half the MCE. This result is not unexpected for two reasons. First, there is no direct link between half the MCE and a 1-sigma Gaussian error, even if both errors are symmetric. Second, the 1-sigma uncertainty obtained with Datice is the result of the chronology optimisation for 5 ice cores with many observations. For each depth level, the final uncertainty is then constrained by more precise sources of information than the age-difference markers. This may lead to a smaller final uncertainty than the one obtained with only one ice core and one kind of dating constraints.

Finally, we have tested several values of the correlation between errors within the possible range from 0 (no correlation) to 1 (complete correlation). Note that because of numerical problems linked to matrix inversion, values higher than 0.6 for error correlation led to improper runs of Datice for a 5 core exercise. Still, we have observed that the resulting chronologies showed only very small differences when varying the values of error correlation and especially the uncertainty on the final chronology does not increase significantly for error correlation higher than 0.3 (Fig. 3). This is due to the fact that the final Datice uncertainty does not depend only on the error on the age-difference markers but also on other markers uncertainties and background parameters covariances. In the following sections, we have first imposed the 2 MCE uncertainty and no error correlation; then we present the Datice results for the 0.5 error correlation simulation as comparison/confirmation of the changes compared to AICC2012 (dotted line on figures).

3 Glaciological implications

When we relax the constraints on the background glaciological parameters at NGRIP, Datice produces new optimized profiles for accumulation rate, thinning function and

LIDIE. Because we work on a multi-site frame, the optimization takes into account not only the age-difference constraints from GICC05 but also the influence of the four Antarctic ice core chronologies through stratigraphic links.

3.1 Accumulation rate

Different background accumulation rate scenarios are tested for NGRIP. Two scenarios, independent from the GICC05 chronology, have been chosen. First, we use the accumulation associated with the ss09sea chronology (Johnsen et al., 2001). An accumulation rate scenario is deduced from the water isotope profile corrected for the isotopic composition of seawater, as it was done for Vostok, EDC, EDML and TALDICE (e.g. Lorius et al., 1985; Parrenin et al., 2007; Bazin et al., 2013). Then, the relationship between the accumulation rate and the δ^{18}O profile is adjusted in order for the 1-D–DJ ice flow model to match observed depth–age horizons. The obtained accumulation rate profile (ss09sea, Fig. 4) is fairly close to the DJ–GICC05 accumulation rate scenario over the millennial scale variability of the last glacial period. Nevertheless, the ss09sea accumulation rate is higher by $\sim 20\,\%$ than the DJ–GICC05 one at the end of the Younger Dryas and over the early Holocene. Alternatively, we have used the accumulation rate produced by Kindler et al. (2014), hereafter PK2014. It has been derived from ss09sea and adjusted with a firnification model (Schwander et al., 1997) to reproduce the δ^{15}N data measured over the glacial period. The PK2014 accumulation rate is much lower than the DJ–GICC05 accumulation rate over the last glacial period, by up to 30 %.

When taking ss09sea or PK2014 accumulation rate as background scenario and despite the difference between them, Datice produces very similar accumulation rates (Fig. 4). While the two output accumulation rate scenarios are much alike the DJ–GICC05 scenario over the early Holocene, they show significantly lower values than DJ–GICC05 for the last glacial period. On average, the Datice output accumulation rate for NGRIP is 10 to 15 % lower than the DJ–GICC05 accumulation rate over the

glacial period after 60 ka. The same result is obtained for both the case with no error correlation and the case with error correlation (Fig. 4).

Our study confirms the overestimation of GICC05 accumulation rate already suggested by Guillevic et al. (2013) and Kindler et al. (2014), even if our accumulation rate scenarios for NGRIP are not showing values as low as those suggested by Kindler et al. (2014) on the δ^{15}N basis over the whole glacial period (Fig. 4). This conclusion is mainly valid for the last 60 ka since our study does not bring any improvement for the oldest part of NGRIP. For the following tests in this study, we chose to use the ss09sea accumulation rate as background.

3.2 Lock-in depth in ice equivalent

When building the AICC2012 chronology, we used a background LIDIE obtained from a densification model (Goujon et al., 2003). Indeed, in Greenland the LIDIE produced by the densification model is in agreement with the LIDIE deduced from δ^{15}N measurements (Huber et al., 2006; Guillevic et al., 2013). The background LIDIE scenario for NGRIP in AICC2012 was thus in agreement with the δ^{15}N mean level over the last 120 ka (Landais et al., 2004, 2005; Huber et al., 2006; Kindler et al., 2014). Still, because the δ^{15}N data from Kindler et al. (2014) were not published at that time, we could not implement the Δdepth constraints at the beginning of GI 1 to 7 as done here (Sect. 2.2).

When running Datice as for AICC2012, i.e. with the strong constraints to the GICC05 chronology, thinning function and accumulation rate for NGRIP, and with the addition of the new Δdepth constraints from Kindler et al. (2014), we obtain very large LIDIE levels for NGRIP between 28 and 38 ka (Fig. 5). LIDIE levels are deeper than 100 m, implying a lock-in depth exceeding 140 m. Deepest lock-in depths observed today in Antarctica are about 100–110 m deep (Landais et al., 2006) and NGRIP glacial lock-in depth is not expected to be deeper than 90 m from firnification models (Goujon et al., 2003). These large values were not obtained for AICC2012 in the absence of Δdepth constraints at the onset of GI 1 to 7. The Δdepth constraints from δ^{15}N measurements

cannot be questioned since the δ^{15}N peaks in Greenland air bubbles clearly respond to abrupt surface temperature increases and are thus in phase with the increases in water isotopes (δ^{18}O) recorded in the ice phase. On the opposite, the DJ–GICC05 thinning function is very smooth and could be revised to be more realistic and sensitive to changes in ice properties (Guillevic et al., 2013). Since the LIDIE is simply calculated as Δdepth divided by the thinning function, a too small thinning function will lead to a too high LIDIE.

In our study, the NGRIP thinning function is not tied to the DJ estimate as in AICC2012 and it deviates significantly during the glacial period. As a result, the output LIDIE is not showing very strong values exceeding 100 m, which is more realistic (light blue curve, Fig. 5). We still observe quite large variations of the LIDIE by more than 15 m between 1900 and 2100 m. These variations are much larger than the LIDIE variations deduced from δ^{15}N mean levels over this depth interval (brown curve, Fig. 5). Indeed, except during abrupt warming, the δ^{15}N level in air trapped in ice is only influenced by gravitational fractionation (Severinghaus et al., 1998). In the absence of a deep convective zone at the surface of the firn, the δ^{15}N level can thus be linked directly to the firn depth. To reduce the non realistic short-term variations of LIDIE, we have thus reduced the variance of the background LIDIE ($\sigma_{b,L}$ = 0.6 to 0.3 and minimum value at 0.05, Appendix A, pink curve Fig. 5). The final LIDIE is in better agreement with the one deduced from δ^{15}N measurements. Note that this modification of the LIDIE variance has only a very minor effect on the chronology, thinning function and accumulation rate. Again, both simulations with or without error correlation lead to nearly the same results (Fig. 5).

4 Chronological and climatic implications

As an introduction, we strengthen that the GICC05-free chronologies discussed here should not be taken as new official chronologies but rather as studies of glaciological and climatic implications of reducing some constraints in the chronology construction.

The AICC2012 chronology has the strong advantage of being in exact agreement with the GICC05 chronology and hence to facilitate the multi-archives comparison taking GICC05 as reference as already made in many studies (INTIMATE project: Blockley et al., 2012a). When looking at the NGRIP ice records, the final GICC05-free chronologies do not differ from the GICC05 or AICC2012 chronologies by more than 130 years over the last 60 ka (Fig. 6).

The Antarctic chronologies are not much modified compared to the AICC2012 chronologies. Both EDML and EDC GICC05-free chronologies differ by less than 400 years from AICC2012 (Fig. 6), which is well within the uncertainties of these chronologies (400–1000 years over this period). The small differences between the new GICC05-free and AICC2012 chronologies mean that the relationship between Greenland and Antarctic climate discussed with AICC2012 for the millennial scale variability of the last glacial period stays valid on GICC05-free (Veres et al., 2013). We observe a classical seesaw pattern with Antarctic temperature increasing during the Greenland stadials, with a faster and shorter increase at EDML than at EDC (Fig. 7).

5 Conclusions

The bayesian tool Datice used for the construction of the AICC2012 chronology has been improved and now enables one to consider the duration of events as dating constraints. This development is more coherent with the building of chronologies based on layer counting where the absolute error, defined as the maximum counted error, increases with depth because of a cumulative effect. To account for the fact that the counted errors on each interval are not uncorrelated, we have also introduced a correlation between age-difference errors. This has permitted us to produce coherent Greenland–Antarctica timescales that respect the correlated counting errors of GICC05 without forcing artificially the glaciological background parameters. Compared to the AICC2012 results, the NGRIP glaciological parameters obtained in this study are in better agreement with expected behaviours: (1) the accumulation rate is decreased

in agreement with independent studies based on δ^{15}N measurements; (2) the LIDIE is in agreement with typical firn depth expected in Greenland. The final chronology does not differ by more than 130 years from GICC05 for NGRIP, which is well within the published uncertainty. For Antarctic ice cores, no difference larger than 400 years is observed and the bipolar seesaw pattern is not modified with these new chronologies. As a consequence and to avoid confusion with the reference GICC05 timescale, we do not recommend to use GICC05-free chronologies. However, the improvements performed in this study should be incorporated in the next coherent ice core dating effort. A more specific study on the determination and variation of the error correlation of the layer counted GICC05 chronology, and its translation as age-difference markers in Datice should be performed in the future.

Appendix A: Ages calculation in Datice and background variances definitions

The Datice age models are derived from three key ice core quantities: the total thinning function ($T(z)$), the accumulation rate ($A(z)$) and the LIDIE ($C(z)$). They allow to estimate the ice age chronology ($\Psi(z)$) as follows:

$$\Psi(z) = \int_0^z \frac{D(z')}{T(z') \cdot A(z')} \mathrm{d}z' \quad \text{(A1)}$$

with $D(z)$ being the relative density of the snow/ice material. The gas chronology ($\chi(z)$), is calculated using Δdepth, which measures the in-situ depth difference between ice and gas of the same age. Then the gas age is defined as the ice age of the layer situated at the depth ($z - \Delta\text{depth}$).

$$\Delta\text{depth}(z) = C(z) \cdot T(z) \quad \text{(A2)}$$

$$\chi(z) = \Psi(z - \Delta\text{depth}(z)) \quad \text{(A3)}$$

The background parameters with their associated variances, as well as age constraints and their respective uncertainties are needed to calculate the optimized ages. Depending of the confidence assigned to the background parameters, Datice will be authorized to correct them more or less. Here we remind the formulations used to define the thinning function (Eq. A4) and the LIDIE (Eq. A5) variances, as several coefficients were corrected in this study.

The standard deviation of the thinning function is defined as:

$$\sigma_T(z) = c_{T_1} + c_{T_2} \cdot \int^{z} \frac{D(z)}{T(z)} \mathrm{d}z + c_{T_3} \cdot \frac{\sigma_{A,\mathrm{loc}}}{\sigma_{A,\mathrm{loc}}^{\max}} \quad \text{(A4)}$$

where c_{T_1}, c_{T_2} and c_{T_3} are user defined constant parameters (c_{T_2} equals $c \cdot 0.1/H$ where H is the maximum depth of the input and c a user defined constant), $T(z)$ is the thinning function, $D(z)$ the relative density, $\sigma_{A,\mathrm{loc}}$ the local standard deviation of accumulation and $\sigma_{A,\mathrm{loc}}^{\max}$ the maximum standard deviation of accumulation. The last term was implemented in order to increase the thinning variance during large climatic transitions since it has been suggested that the mechanical properties of ice can be modified in these periods. For the purpose of the tests performed in this study, we have corrected the c_{T_2} value (from 0.000016 to 0.000064) that was used for NGRIP when building AICC2012. This correction permits to have a coherent parameterization of the thinning variance for the 5 ice cores. Moreover, we have reduced the c_{T_1} values from 0.01 to 0.00001 in order to be closer to the 0 variance hypothesis at the surface for all sites. The other coefficients have the same values as used to build AICC2012 (SOM Bazin et al., 2013).

The formulation for the LIDIE standard deviation is:

$$\sigma_L(z) = \frac{\sigma_{\mathrm{b,L}}}{\sigma_{\mathrm{b},A}} \cdot \frac{\sigma_A(z)}{1 + \frac{m_{A,\mathrm{loc}}}{m_{A,\mathrm{loc}}^{\max}}} \quad \text{(A5)}$$

with $m_{A,\mathrm{loc}}$ being the local mean accumulation rate and $m_{A,\mathrm{loc}}^{\max}$ its maximum value over the length of the core, $\sigma_{\mathrm{b,L}}$ is a reference standard deviation. In this case, the variance on the LIDIE increases with the variance on the accumulation rate, i.e. with the deviation from present-day conditions. This is justified by the fact that we do not have a standardized way to link LIDIE to accumulation rate and/or temperature (firnification model or δ^{15}N based estimate). In Sect. 3.2 we have reduced the value of the $\sigma_{\mathrm{b,L}}$ coefficient from 0.6 to 0.3 as well as the minimum value possible (from 0.1 to 0.05) for NGRIP. This means that we have more confidence in our background LIDIE scenario than when building the AICC2012 chronology. The other coefficients have the same values as used to build AICC2012 (SOM Bazin et al., 2013).

Acknowledgements. We thank Eric Wolff for his comments on a preliminary version of this article. This project was funded by the "Fondation de France Ars Cuttoli". This work was supported by Labex L-IPSL which is funded by the ANR (Grant n°ANR-10-LABX-0018). This is LSCE contribution no XX.

References

Andersen, K. K., Svensson, A., Johnsen, S. J., Rasmussen, S. O., Bigler, M., Röthlisberger, R., Ruth, U., Siggaard-Andersen, M.-L., Peder Steffensen, J., Dahl-Jensen, D., Vinther, B. M., and Clausen, H. B.: The Greenland Ice Core Chronology 2005, 15 42 ka. Part 1: constructing the time scale, Quaternary Sci. Rev., 25, 3246–3257, doi:10.1016/j.quascirev.2006.08.002, 2006.

Austin, W. E. and Hibbert, F. D.: Tracing time in the ocean: a brief review of chronological constraints (60–8 kyr) on North Atlantic marine event-based stratigraphies, Quaternary Sci. Rev., 36, 28–37, doi:10.1016/j.quascirev.2012.01.015, 2012.

Austin, W., Hibbert, F., Rasmussen, S., Peters, C., Abbott, P., and Bryant, C.: The synchronization of palaeoclimatic events in the North Atlantic region during Greenland Stadial 3 (ca 27.5 to 23.3 kyr b2k), Quaternary Sci. Rev., 36, 154–163, doi:10.1016/j.quascirev.2010.12.014, 2012.

Bazin, L., Landais, A., Lemieux-Dudon, B., Toyé Mahamadou Kele, H., Veres, D., Parrenin, F., Martinerie, P., Ritz, C., Capron, E., Lipenkov, V., Loutre, M.-F., Raynaud, D., Vinther, B., Svensson, A., Rasmussen, S. O., Severi, M., Blunier, T., Leuenberger, M., Fischer, H., Masson-Delmotte, V., Chappellaz, J., and Wolff, E.: An optimized multi-proxy, multi-site Antarctic ice and gas orbital chronology (AICC2012): 120–800 ka, Clim. Past, 9, 1715–1731, doi:10.5194/cp-9-1715-2013, 2013.

Blockley, S., Lane, C., Turney, C., and Bronk Ramsey, C.: The INTegration of Ice core, MArine and TErrestrial records of the last termination (INTIMATE) 60 000 to 8000 BP, Quaternary Sci. Rev., 36, 2–10, doi:10.1016/j.quascirev.2011.10.001, 2012a.

Blockley, S. P., Lane, C. S., Hardiman, M., Rasmussen, S. O., Seierstad, I. K., Steffensen, J. P., Svensson, A., Lotter, A. F., Turney, C. S., and Bronk Ramsey, C.: Synchronisation of palaeoenvironmental records over the last 60,000 years, and an extended INTIMATE event stratigraphy to 48 000 b2k, Quaternary Sci. Rev., 36, 1, doi:10.1016/j.quascirev.2011.09.017, 2012b.

Buiron, D., Chappellaz, J., Stenni, B., Frezzotti, M., Baumgartner, M., Capron, E., Landais, A., Lemieux-Dudon, B., Masson-Delmotte, V., Montagnat, M., Parrenin, F., and Schilt, A.: TALDICE-1 age scale of the Talos Dome deep ice core, East Antarctica, Clim. Past, 7, 1–16, doi:10.5194/cp-7-1-2011, 2011.

Cutler, N. N., Raymond, C. F., Waddington, E. D., Meese, D. A., and Alley, R. B.: The effect of ice-sheet thickness change on the accumulation history inferred from GISP2 layer thicknesses, Ann. Glaciol., 21, 26–32, 1995.

Dansgaard, W. and Johnsen, S. J.: A flow model and a time scale for the ice core from Camp Century, Greenland, J. Glaciol., 8, 215–223, 1969.

Davies, S. M., Abbott, P. M., Pearce, N. J., Wastegard, S., and Blockley, S. P.: Integrating the INTIMATE records using tephrochronology: rising to the challenge, Quaternary Sci. Rev., 36, 11–27, doi:10.1016/j.quascirev.2011.04.005, 2012.

EPICA Community Members: One-to-one coupling of glacial climate variability in Greenland and Antarctica, Nature, 444, 195–198, doi:10.1038/nature05301, 2006.

EPICA Community Members: Stable oxygen isotopes of ice core EDML, PANGAEA, doi:10.1594/PANGAEA.754444, 2010.

Goujon, C., Barnola, J.-M., and Ritz, C.: Modeling the densification of polar firn including heat diffusion: application to close-off characteristics and gas isotopic fractionation for Antarctica and Greenland sites, J. Geophys. Res.-Atmos., 108, 4792, doi:10.1029/2002JD003319, 2003.

Guillevic, M., Bazin, L., Landais, A., Kindler, P., Orsi, A., Masson-Delmotte, V., Blunier, T., Buchardt, S. L., Capron, E., Leuenberger, M., Martinerie, P., Prié, F., and Vinther, B. M.: Spatial gradients of temperature, accumulation and δ^{18}O-ice in Greenland over a series of Dansgaard–Oeschger events, Clim. Past, 9, 1029–1051, doi:10.5194/cp-9-1029-2013, 2013.

Huber, C., Beyerle, U., Leuenberger, M., Schwander, J., Kipfer, R., Spahni, R., Severinghaus, J. P., and Weiler, K.: Evidence for molecular size dependent gas fractionation in firn air derived from noble gases, oxygen, and nitrogen measurements, Earth Planet. Sc. Lett., 243, 61–73, doi:10.1016/j.epsl.2005.12.036, 2006.

Johnsen, S. J., Dahl-Jensen, D., Gundestrup, N., Steffensen, J. P., Clausen, H. B., Miller, H., Masson-Delmotte, V., Sveinbjornsdottir, A. E., and White, J.: Oxygen isotope and palaeotemperature records from six Greenland ice-core stations: Camp Century, Dye-3, GRIP, GISP2, Renland and NorthGRIP, J. Quaternary Sci., 16, 299–307, doi:10.1002/jqs.622, 2001.

Jouzel, J., Masson-Delmotte, V., Cattani, O., Dreyfus, G., Falourd, S., Hoffmann, G., Minster, B., Nouet, J., Barnola, J. M., Chappellaz, J., Fischer, H., Gallet, J. C., Johnsen, S., Leuenberger, M., Loulergue, L., Luethi, D., Oerter, H., Parrenin, F., Raisbeck, G., Raynaud, D., Schilt, A., Schwander, J., Selmo, E., Souchez, R., Spahni, R., Stauffer, B., Steffensen, J. P., Stenni, B., Stocker, T. F., Tison, J. L., Werner, M., and Wolff, E. W.: Orbital and millennial Antarctic climate variability over the past 800 000 years, Science, 317, 793, doi:10.1126/science.1141038, 2007.

Kindler, P., Guillevic, M., Baumgartner, M., Schwander, J., Landais, A., and Leuenberger, M.: Temperature reconstruction from 10 to 120 kyr b2k from the NGRIP ice core, Clim. Past, 10, 887–902, doi:10.5194/cp-10-887-2014, 2014.

Landais, A., Barnola, J. M., Masson-Delmotte, V., Jouzel, J., Chappellaz, J., Caillon, N., Huber, C., Leuenberger, M., and Johnsen, S. J.: A continuous record of temperature evolution over a sequence of Dansgaard–Oeschger events during Marine Isotopic Stage 4 (76 to 62 kyr BP), Geophys. Res. Lett., 31, L22211, doi:10.1029/2004GL021193, 2004.

Landais, A., Jouzel, J., Masson-Delmotte, V., and Caillon, N.: Large temperature variations over rapid climatic events in Greenland: a method based on air isotopic measurements, C. R. Geosci., 337, 947–956, doi:10.1016/j.crte.2005.04.003, 2005.

Landais, A., Waelbroeck, C., and Masson-Delmotte, V.: On the limits of Antarctic and marine climate records synchronization: lag estimates during marine isotopic stages 5d and 5c, Paleoceanography, 21, PA1001, doi:10.1029/2005PA001171, 2006.

Lemieux-Dudon, B., Parrenin, F., and Blayo, E.: A probabilistic method to construct an optimal ice chronology for ice cores, in: Hondoh, T., Proceedings of the 2nd International Workshop on Physics of Ice Core Records (PICR-2), Institute of Low Temperature Science, Hokkaido University, Sapporo, Japan, 2009.

Lemieux-Dudon, B., Blayo, E., Petit, J.-R., Waelbroeck, C., Svensson, A., Ritz, C., Barnola, J.-M., Narcisi, B. M., and Parrenin, F.: Consistent dating for Antarctic and Greenland ice cores, Quaternary Sci. Rev., 29, 8–20, doi:10.1016/j.quascirev.2009.11.010, 2010.

Lorius, C., Ritz, C., Jouzel, J., Merlivat, L., and Barkov, N. I.: A 150,000-year climatic record from Antarctic ice, Nature, 316, 591–596, doi:10.1038/316591a0, 1985.

NorthGRIP Community Members: High-resolution record of Northern Hemisphere climate extending into the last interglacial period, Nature, 431, 147–151, doi:10.1038/nature02805, 2004.

Parrenin, F., Barnola, J.-M., Beer, J., Blunier, T., Castellano, E., Chappellaz, J., Dreyfus, G., Fischer, H., Fujita, S., Jouzel, J., Kawamura, K., Lemieux-Dudon, B., Loulergue, L., Masson-Delmotte, V., Narcisi, B., Petit, J.-R., Raisbeck, G., Raynaud, D., Ruth, U., Schwander, J., Severi, M., Spahni, R., Steffensen, J. P., Svensson, A., Udisti, R., Waelbroeck, C., and Wolff, E.: The EDC3 chronology for the EPICA Dome C ice core, Clim. Past, 3, 485–497, doi:10.5194/cp-3-485-2007, 2007.

Rasmussen, S. O., Andersen, K. K., Svensson, A. M., Steffensen, J. P., Vinther, B. M., Clausen, H. B., Siggaard-Andersen, M.-L., Johnsen, S. J., Larsen, L. B., Dahl-Jensen, D., Bigler, M., Röthlisberger, R., Fischer, H., Goto-Azuma, K., Hansson, M. E., and Ruth, U.: A new Greenland ice core chronology for the last glacial termination, J. Geophys. Res.-Atmos., 111, D06102, doi:10.1029/2005JD006079, 2006.

Schwander, J., Sowers, T., Barnola, J.-M., Blunier, T., Fuchs, A., and Malaizé, B.: Age scale of the air in the summit ice: Implication for glacial-interglacial temperature change, J. Geophys. Res.-Atmos., 102, 19483–19493, doi:10.1029/97JD01309, 1997.

Severinghaus, J. P., Sowers, T., Brook, E. J., Alley, R. B., and Bender, M. L.: Timing of abrupt climate change at the end of the Younger Dryas interval from thermally fractionated gases in polar ice, Nature, 391, 141–146, doi:10.1038/34346, 1998.

Svensson, A., Andersen, K. K., Bigler, M., Clausen, H. B., Dahl-Jensen, D., Davies, S. M., Johnsen, S. J., Muscheler, R., Parrenin, F., Rasmussen, S. O., Röthlisberger, R., Seierstad, I., Steffensen, J. P., and Vinther, B. M.: A 60 000 year Greenland stratigraphic ice core chronology, Clim. Past, 4, 47–57, doi:10.5194/cp-4-47-2008, 2008.

Tarantola, A.: Inverse Problem Theory and Methods for Model Parameter Estimation, Society for Industrial and Applied Mathematics, doi:10.1137/1.9780898717921, 2005.

Veres, D., Bazin, L., Landais, A., Toyé Mahamadou Kele, H., Lemieux-Dudon, B., Parrenin, F., Martinerie, P., Blayo, E., Blunier, T., Capron, E., Chappellaz, J., Rasmussen, S. O., Severi, M., Svensson, A., Vinther, B., and Wolff, E. W.: The Antarctic ice core chronology (AICC2012): an optimized multi-parameter and multi-site dating approach for the last 120 thousand years, Clim. Past, 9, 1733–1748, doi:10.5194/cp-9-1733-2013, 2013.

Vinther, B. M., Clausen, H. B., Johnsen, S. J., Rasmussen, S. O., Andersen, K. K., Buchardt, S. L., Dahl-Jensen, D., Seierstad, I. K., Siggaard-Andersen, M.-L., Steffensen, J. P., Svensson, A., Olsen, J., and Heinemeier, J.: A synchronized dating of three Greenland ice cores throughout the Holocene, J. Geophys. Res.-Atmos., 111, D13102, doi:10.1029/2005JD006921, 2006.

Walker, M., Lowe, J., Blockley, S. P., Bryant, C., Coombes, P., Davies, S., Hardiman, M., Turney, C. S., and Watson, J.: Late glacial and early Holocene palaeoenvironmental "events" in Sluggan Bog, Northern Ireland: comparisons with the Greenland NGRIP GICC05 event stratigraphy, Quaternary Sci. Rev., 36, 124–138, doi:10.1016/j.quascirev.2011.09.008, 2012.

Table 1. New Δdepth markers of NGRIP deduced from the data of Kindler et al. (2014).

depth (m)	Δdepth (m)	σ (m)
1490.2	25.07	2.5
1520.5	21.84	2.5
1574.4	23.51	2.5
1603.0	26.42	2.5
1792.7	25.07	2.5
1868.1	22.62	2.5
1888.4	21.87	2.5
1950.6	21.32	2
1972.6	20.42	2
2007.8	19.22	2
2099.9	17.77	2

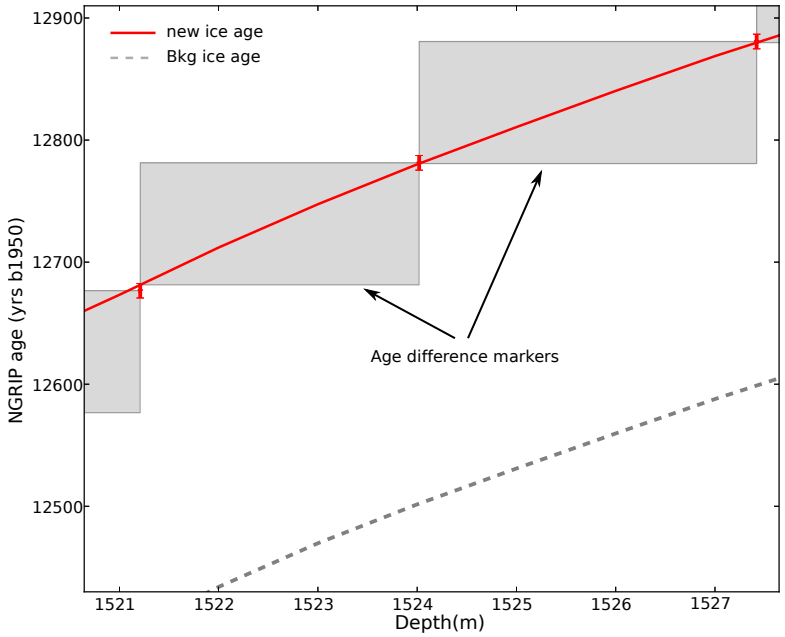

Figure 1. NGRIP ice chronologies centred on two markers of age-difference, over the depth interval 1521–1527 m. The red curve is the analysed ice chronology $\Psi_k^{\mathrm{a}}(z)$, the grey dotted line is the background chronology. The grey rectangles represent the markers of age-difference. The lower left corner of the grey rectangle is attached to the analysed ice chronology, so that its abscissa and ordinate are $\left(z_k^{\mathrm{ad},1}, \Psi_k^{\mathrm{a}}\left(z_k^{\mathrm{ad},1}\right)\right)$. The height of the rectangle equals the counted number of years y_k^{ad}, and the observation error bars $\pm\sigma_k^{\mathrm{ad}}$ (red vertical bars) are centred on the upper right corner.

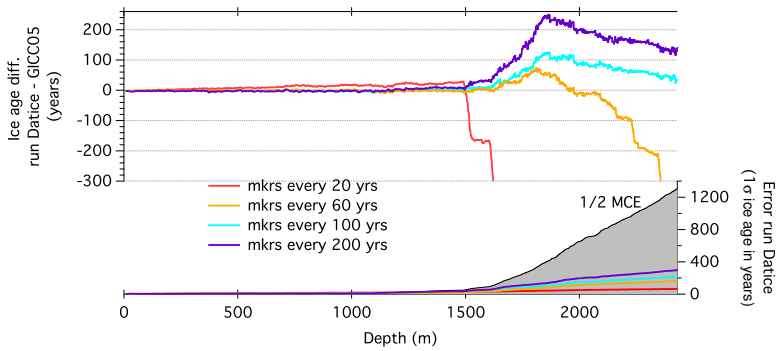

Figure 2. Comparison of age differences with GICC05 chronology for different intervals of age-difference markers over the period covered by layer counting. Top: the difference is calculated for markers every 20 years (red), every 60 years (orange), every 100 years (blue) and every 200 years (purple). Bottom: the corresponding colours represent the final uncertainties calculated by Datice for each frequency of markers. The 1-sigma uncertainty of GICC05 chronology is represented by the grey surface.

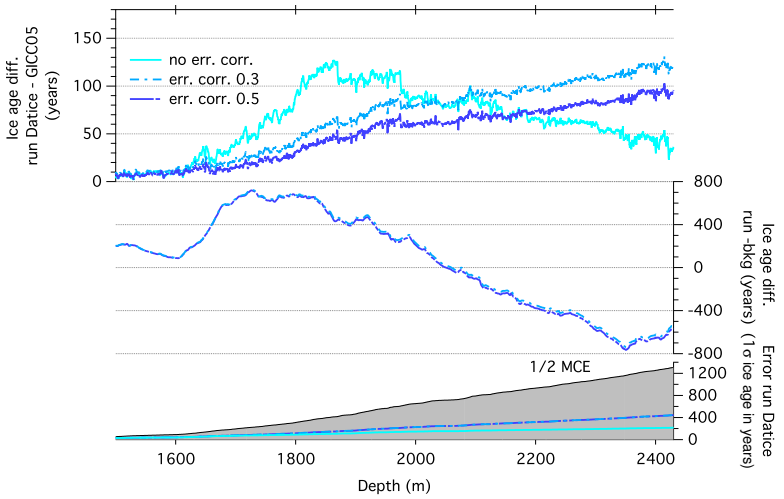

Figure 3. Top: comparison of age differences with GICC05 for Datice simulations when considering markers of age-difference without correlation (light blue line), with low correlation (dashed turquoise line) or moderate correlation (dark blue line). Middle: deviation of the new Datice chronologies from their background estimates for the two simulations considering error correlation. Bottom: 1-sigma error of NGRIP chronologies for GICC05 (grey surface), Datice without error correlation (light blue), with low error correlation (dashed turquoise line) or moderate error correlation (dark blue line) for the markers of age-difference.

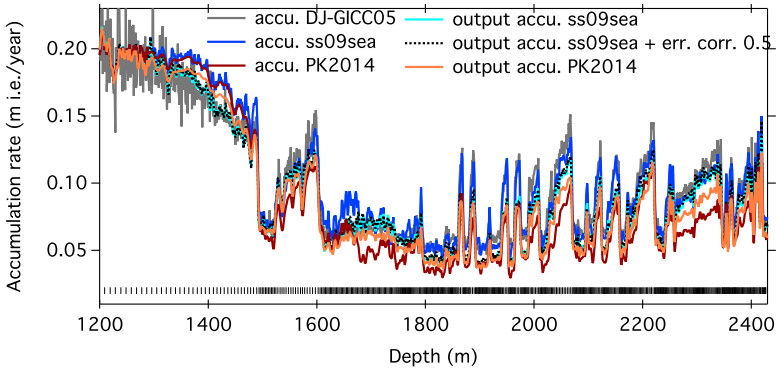

Figure 4. Comparison of accumulation rates for NGRIP over the last 60 ka. The GICC05 accumulation rate (grey) is presented for comparison; the ss09sea (dark blue) and PK2014 (brown) accumulation rates used as background; the Datice output accumulation rates using ss09sea (light blue for the run without error correlation, black dotted line for the run with error correlation) and PK2014 (orange) ones as input. The vertical bars at bottom indicate the positions of the markers of age-difference every 100 years.

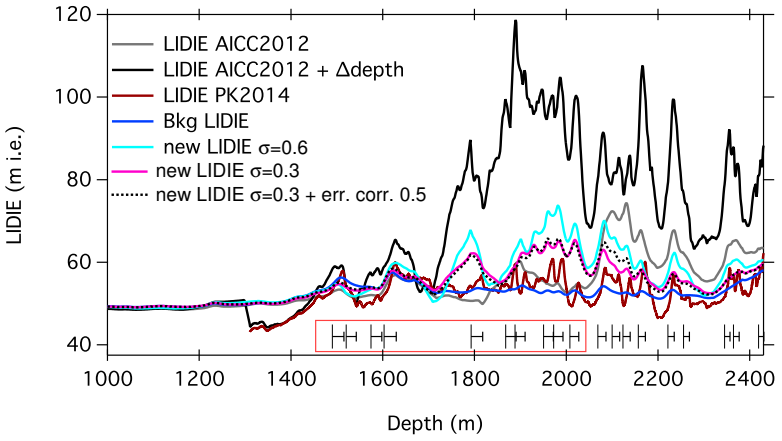

Figure 5. Comparison of NGRIP LIDIE over the glacial period. The LIDIE obtained when building the AICC2012 chronology (grey), the same as AICC2012 + Δdepth markers deduced from Kindler et al. (2014) (black) and the LIDIE obtained from the δ^{15}N data Kindler et al. (2014) are shown for comparison. The background LIDIE used as input is in dark blue. The output LIDIE after running Datice are also presented, in light blue when using the same error as in AICC2012 and in pink/black dotted line when reducing this error. The markers present at the bottom correspond to the Δdepth markers implemented in Datice. The ones in the red box are new Δdepth markers deduced from the data of Kindler et al. (2014).

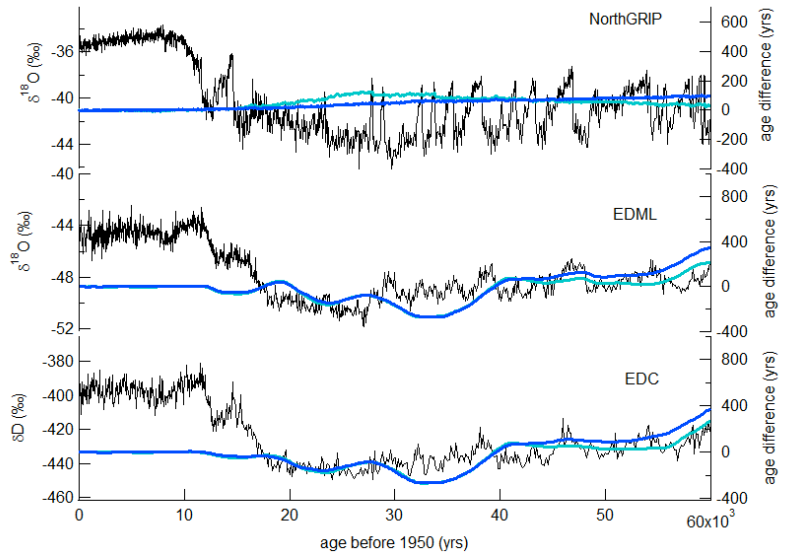

Figure 6. Water isotopic records (black) of NGRIP, EDML and EDC over the last 60 ka on the GICC05-free chronology without error correlation (NorthGRIP Community Members, 2004; EPICA Community Members, 2006, 2010; Jouzel et al., 2007). The blue solid lines indicate the age differences between the GICC05-free and the AICC2012 chronologies (dark blue: run with error correlation; light blue: run without error correlation).

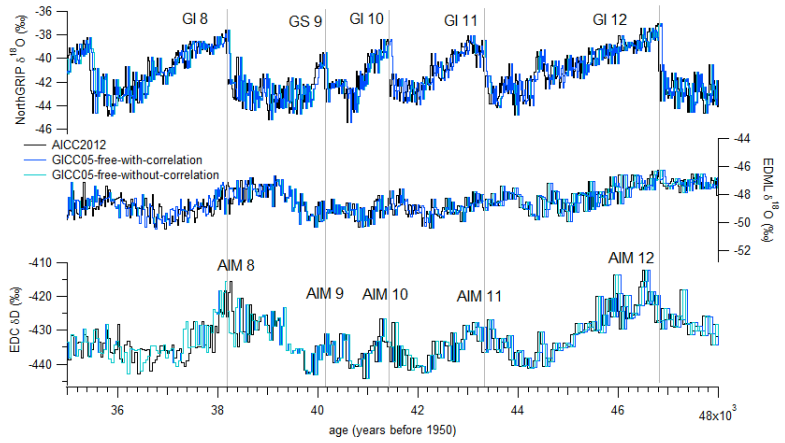

Figure 7. Comparison of NGRIP δ^{18}O (NorthGRIP Community Members, 2004), EDML δ^{18}O (EPICA Community Members, 2006, 2010) and EDC δD (Jouzel et al., 2007) water isotopes on different coherent chronologies (AICC2012 in black, GICC05-free with correlation in dark blue and GICC05-free without correlation in light blue).

4.3 Test pour améliorer la définition de la variance d'ébauche de l'amincissement

L'utilisation des marqueurs de différence d'âge et des corrélations d'erreurs entre les marqueurs représentent une amélioration méthodologique importante de Datice. Ces améliorations permettent maintenant de contraindre la chronologie fédérative des carottes de glace à respecter l'échelle d'âge absolue GICC05 de façon plus appropriée. Ceci vient résoudre le problème lié à la corrélation entre les ébauches et les marqueurs de NGRIP soulevé lors de la construction d'AICC2012. Néanmoins, de nombreux points restent encore à améliorer, notamment sur la formulation des erreurs sur les paramètres d'ébauche.

Dans cette section je présente une piste envisageable pour l'amélioration de la définition de la variance pour la fonction d'amincissement d'ébauche. Je présente seulement le résultat de tests préliminaires, qu'il est nécessaire d'approfondir dans le futur.

Lors de la construction d'AICC2012, nous avons tenté d'exprimer la variance pour la fonction d'amincissement de façon à tenir compte de :

— Une valeur très proche de 0 à la surface. Idéalement ce devrait être 0, mais cela rendrait l'inversion de la matrice de covariance d'erreur d'ébauche impossible pour Datice (chapitre 2) ;
— Une augmentation de l'erreur avec l'enfouissement en profondeur. Plus une couche s'enfonce et plus l'incertitude associée à la fonction d'amincissement reconstruite par les modèles d'écoulement est importante ;
— Une augmentation de l'erreur lors des transitions climatiques, suggérée par le changement des propriétés mécaniques de la glace au cours de ces périodes [Durand et al., 2007].

Cependant, ce dernier point a été paramétré à partir de l'écart-type local de l'accumulation (équation 3.2). Cette formulation a permis d'augmenter la variance associée à la fonction d'amincissement lors des changements glaciaire–interglaciaire, sans pour autant avoir une justification physique. L'analyse de la taille des cristaux de glace (microstructure) et de leurs orientations peuvent nous renseigner directement sur les changements des propriétés mécaniques de la glace lors des transitions climatiques. En effet, des couches de glace présentant des tailles de cristaux différentes ne vont pas se déformer ni s'écouler de la même façon, ce qui va impacter la fonction d'amincissement. L'analyse de la microstructure et de l'orientation des

cristaux de glace permet d'obtenir des informations sur les contraintes subies par la glace au cours de son enfouissement, jusqu'à sa profondeur actuelle. Par exemple, lors de la compression verticale, l'axe *c* des cristaux, défini comme perpendiculaire au plan basal d'un cristal de glace, tend à s'orienter suivant la direction de compression, et les cristaux de glace ont tendance à s'allonger suivant la direction d'extension.

Ainsi, repartant des travaux de G. Durand réalisés au cours de sa thèse, j'ai essayé de voir quelle serait l'influence des changements des propriétés mécaniques de la glace sur la fonction d'amincissement. A partir de la microstructure mesurée sur la glace d'EDC, il est possible de déduire une partie de la déformation subie par les cristaux de glace. Cette dernière est directement reliée à l'amincissement des couches.

Plusieurs paramètres peuvent être déduits de la microstructure mesurée sur les échantillons de glace. On peut alors définir les matrices $\mathbf{M}$ (équation 4.1), le tenseur de texture, et $\mathbf{U}$ (équation 4.2), le tenseur de déformation, à partir de l'identification des joints entre les grains (cristaux de glace), regroupés sous le tenseur $\vec{l} \otimes \vec{l}$ (figure 4.1 gauche), où $\mathbf{M_0}$ est le tenseur de texture isotrope.

$$\mathbf{M} = \langle \vec{l} \otimes \vec{l} \rangle \tag{4.1}$$

$$\mathbf{U} = \frac{log(\mathbf{M}) - log(\mathbf{M_0})}{2} \tag{4.2}$$

Contrairement à ce que supposent les modèles de datation, la déformation n'est pas homogène. Cependant, il est difficile d'interpréter correctement les hétérogénéités de déformation mesurées par la microstructure. De plus, la déformation enregistrée par la microstructure ne reflète pas la déformation réelle ϵ subie par la glace car la microstructure est soumise à de nombreux processus. Comme la plupart des carottes de glace sont situées sur un dôme, ce qui est le cas d'EDC, il est attendu que la composante due au cisaillement ($\mathbf{U_{xz}}$) soit négligeable, et donc que la déformation soit principalement verticale [Durand et al., 2007]. La composante suivant la verticale du tenseur de déformation, $\mathbf{U_{zz}}$, est seulement dépendante de la croissance normale des grains avec la profondeur et de la compression uniaxiale (figure 4.1).

L'amincissement à une certaine profondeur (grandeur macroscopique) peut être reliée à la déformation réelle (déduite des mesures de microstructure, grandeur microscopique) : $\epsilon_{zz}(z) = ln\,(T(z))$. On peut définir les hétérogénéités de déformation comme étant la déviation par rapport à une déformation homogène, correspondant au logarithme de l'amincissement obtenu à l'aide du modèle de datation (équation

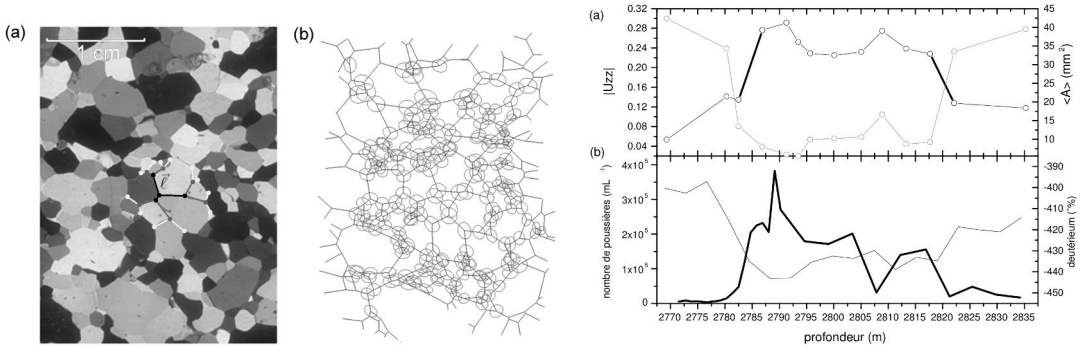

FIGURE 4.1 – Gauche : Section de glace analysée sous lumière polarisée (a) et l'analyse du tenseur de texture correspondant (b). A partir du point noir, il est possible d'identifier 3 vecteurs $\vec{l}$ vers ses plus proches voisins (traits noirs),puis 6 (traits gris) et 12 (traits blancs) par descente en cascade de ses voisins. Le tenseur **M** mesuré à chaque point triple est représenté par une ellipse au point correspondant sur la figure (b). Extrait de Durand et al. [2004]. Droite : (a) Evolution de l'aire des cristaux (<A>) (trait et symboles gris) en fonction de la profondeur entre 2770 et 2835 m à EDC, couvrant la transition V et le MIS 11. L'évolution de $|\mathbf{U_{zz}}|$ est également représentée (trait et symboles noirs), les hétérogénéités significatives ($> 2\sigma$) apparaissent en trait gras. (b) évolution du contenu en particules de poussière (trait gras) et du deutérium pour la même gamme de profondeur (trait fin) [EPICA Community Members, 2004]. Extrait de Durand [2004].

4.3). Si l'on considère deux couches voisines, il est raisonnable de supposer que l'aire moyenne des cristaux de glace de ces deux couches est quasi-inchangée (<10%). Ainsi, il est possible de relier l'hétérogénéité à la déformation enregistrée par la microstructure (équation 4.4). Afin d'éviter de surestimer l'hétérogénéité (cas où le rapport est supérieur à 1), on effectue un lissage par une moyenne glissante sur 5 voisins (équation 4.5). La distribution des hétérogénéités est alors donnée par la distribution des déformations verticales mesurées, représentée sur l'histogramme de la figure 4.2 à gauche dans le cas de la carotte de Dôme C. Cet histogramme est seulement valable pour des variations d'aire des cristaux inférieures à 10%.

$$h = \frac{\epsilon_{zzC_n}}{\epsilon_{zz_{std}}} = \frac{ln\left(T(z)\right)}{ln\left(T_{model}(z)\right)} \tag{4.3}$$

$$\frac{\epsilon_{zzC_n}}{\epsilon_{zz_{std}}} = \frac{\mathbf{U_{zzC_n}}}{\mathbf{U_{zzC_{n+1}}}} \tag{4.4}$$

$$\frac{\epsilon_{zzC_n}}{\epsilon_{zz_{std}}} = \frac{\mathbf{U_{zzC_n}}}{\langle \mathbf{U_{zzC_n}} \rangle_{5v}} \tag{4.5}$$

Afin de prendre en compte l'effet de ces hétérogénéités sur la fonction d'amincissement, j'ai écrit un petit code "python" permettant de générer une fonction

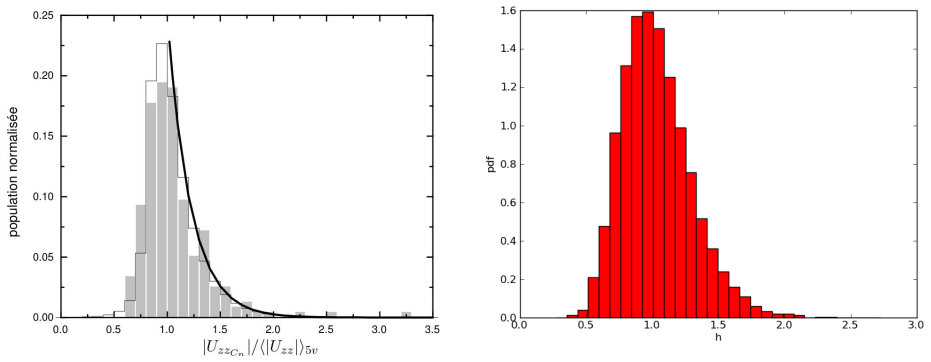

FIGURE 4.2 – Gauche : distribution normalisée du rapport $|\mathbf{U_{zzC_n}}|/\langle|\mathbf{U_{zz}}|\rangle_{5v}$ (histogramme grisé). La partie de la distribution pour laquelle $|\mathbf{U_{zzC_n}}|/\langle|\mathbf{U_{zz}}|\rangle_{5v} > 1$ est bien décrite par une décroissance exponentielle. Droite : histogramme utilisé pour simuler la distribution représentative des hétérogénéités (distribution lognormale de mode 0 et $\sigma = 0.25$).

d'amincissement synthétique perturbée. Pour ce faire, je suis partie de l'équation 4.3. J'ai utilisé la fonction d'amincissement modèle d'EDC [Parrenin et al., 2007b] que j'ai perturbé à l'aide d'une hétérogénéité piochée aléatoirement suivant une distribution similaire à l'histogramme précédent (équation 4.6 et figure 4.2). J'ai utilisé une distribution approchée car nous n'avons pas été en mesure de retrouver les données de microstructure de Gaël Durand (crash de son disque-dur depuis sa thèse). Néanmoins ce test nous permet d'avoir une estimation de l'erreur apportée par les hétérogénéités de déformation sur la fonction d'amincissement.

$$T(z) = T^h_{model}(z) \tag{4.6}$$

Le code permet de générer un amincissement perturbé pour chaque profondeur le long de la carotte de Dôme C (figure 4.3). Par la méthode de Monte-Carlo (10 000 tirs), j'ai été en mesure d'estimer l'erreur due aux hétérogénéités de déformation sur la fonction d'amincissement. Pour ce faire, j'ai analysé les distributions de l'amincissement obtenues pour chaque profondeur et utilisé l'écart-type associé (en se basant sur une distribution gaussienne pour toutes les profondeurs, figure 4.3).

Ce code permet une première estimation de l'incertitude apportée par les hétérogénéités de déformation sur l'amincissement, cependant de futures améliorations sont nécessaires avant de l'intégrer à la définition de la variance sur la fonction d'amincissement dans Datice :

— retrouver les données de microstructure d'EDC, afin de refaire l'histogramme réel de la figure 4.2 (gauche) et pouvoir piocher aléatoirement une hétérogé-

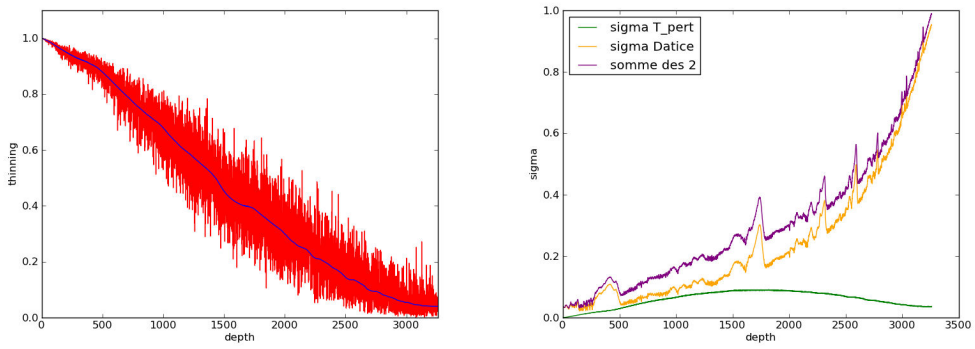

FIGURE 4.3 – Gauche : exemple d'un amincissement perturbé obtenu (rouge). L'amincissement modèle est figuré par la courbe bleue. Droite : écart-type obtenu par la méthode de Monté-Carlo pour ce test (vert), écart-type associé à l'amincissement d'ébauche d'EDC dans Datice (jaune) et la combinaison des deux (violet).

néité suivant cette distribution ;

— paramétrer le code pour que l'amincissement perturbé ne soit créé que dans les cas respectant des différences d'aire entre deux couches voisines de moins de 10% (domaine de validité de l'histogramme). Cette condition est respectée sur la majorité de la carotte, sauf lors de transitions climatiques (comme sur la figure 4.1). La mise en place de ce conditionnement permettrait entre–autre de repérer les transitions glaciaire-interglaciaire, et donc de paramétrer l'erreur sur la fonction d'amincissement en conséquence. Le test réalisé ici a été fait pour toute la carotte et on peut très bien voir que cela n'est pas réaliste sur la figure 4.1, notamment au niveau de transitions climatiques ;

— déduire l'écart-type de chaque profondeur à partir de distributions lognormales et non pas gaussiennes. Ceci s'explique par la formulation de l'amincissement perturbé.

4.4 Conclusions et perspectives

Au travers des améliorations apportées à Datice, nous sommes maintenant en mesure de contraindre la durée des évènements au travers de marqueurs de différence d'âge. Ce type de marqueurs est plus cohérent avec les chronologies basées sur le comptage des couches annuelles. En plus de cela, Datice permet maintenant d'introduire des corrélations d'erreur entre les marqueurs, ce qui permet de prendre en compte le fait que les erreurs associées au comptage des couches annuelles soient corrélées entre elles. Grâce à ces améliorations méthodologiques, il est maintenant possible de produire des chronologies communes à partir de scénarios d'ébauche et

de marqueurs indépendants, pour les contraindre à respecter GICC05. En résultat, les taux d'accumulation et LIDIE de NGRIP produits par Datice sont plus cohérents avec les récentes études basées sur le $\delta^{15}N$.

Les commentaires des trois rapporteurs pour cet article portent principalement sur la présentation des améliorations apportées à la méthodologie et la façon de considérer la MCE dans Datice. Il a été demandé de présenter la validation de la nouvelle approche sur les marqueurs de différence d'âge et la corrélation d'erreur pour un cas plus simple, en ne considérant que NGRIP dans Datice. De plus, Les rapporteurs souhaitent avoir plus d'explications sur comment traduire la MCE en une erreur gaussienne pour Datice. Suite à ces commentaires, nous avons effectué de nouveaux tests et allons modifier l'article de la façon suivante. Nous allons cibler l'introduction sur GICC05 et plus particulièrement sur comment a été calculée la MCE et quels en sont les limites. Nous discuterons ensuite de comment l'intégrer dans Datice et expliquerons pourquoi il est nécessaire de considérer des corrélations entre les erreurs. Nous validerons ces développements méthodologiques de Datice au travers de tests sur un cas simple, ne considérant que la carotte de NGRIP. Les tests présentés porterons sur (1) les différentes formulations possibles de l'erreur associée aux marqueurs de différence d'âge, (2) différentes valeurs de corrélation d'erreur, avec notamment la possibilité d'utiliser des profils de corrélation sur toute la carotte, et comment elles importent sur l'erreur de la chronologie finale (exemple de la figure 4.4) et (3) différentes ébauches des paramètres glaciologiques et l'adaptation de leurs erreurs. Nous comparerons tous les résultats de ces tests avec GICC05 (différence de chronologies, paramètres glaciologiques). Nous finirons par la présentation des résultats d'une expérience à 5 carottes de glace que nous comparerons avec AICC2012.
L'article corrigé aura la référence : "Lemieux-Dudon B., Bazin L., Landais A., Guillevic M., Kindler P., Parrenin F. and Martinerie P. : Implementation of counted layers for cohérent ice core chronology, Climate of the Past" (le titre est susceptible de changer avant la publication finale).

Le test présenté afin de prendre en compte les hétérogénéités de déformation de la glace dans la variance d'ébauche de la fonction d'amincissement n'est qu'un test préliminaire. Comme discuté dans la section 4.3, de nombreuses améliorations sont nécessaires avant de pouvoir avoir une estimation complète de l'influence de ces hétérogénéités sur l'amincissement. Néanmoins, ceci parait une bonne piste pour améliorer la paramétrisation de l'erreur d'ébauche sur la fonction d'amincissement afin d'avoir une définition plus physique.

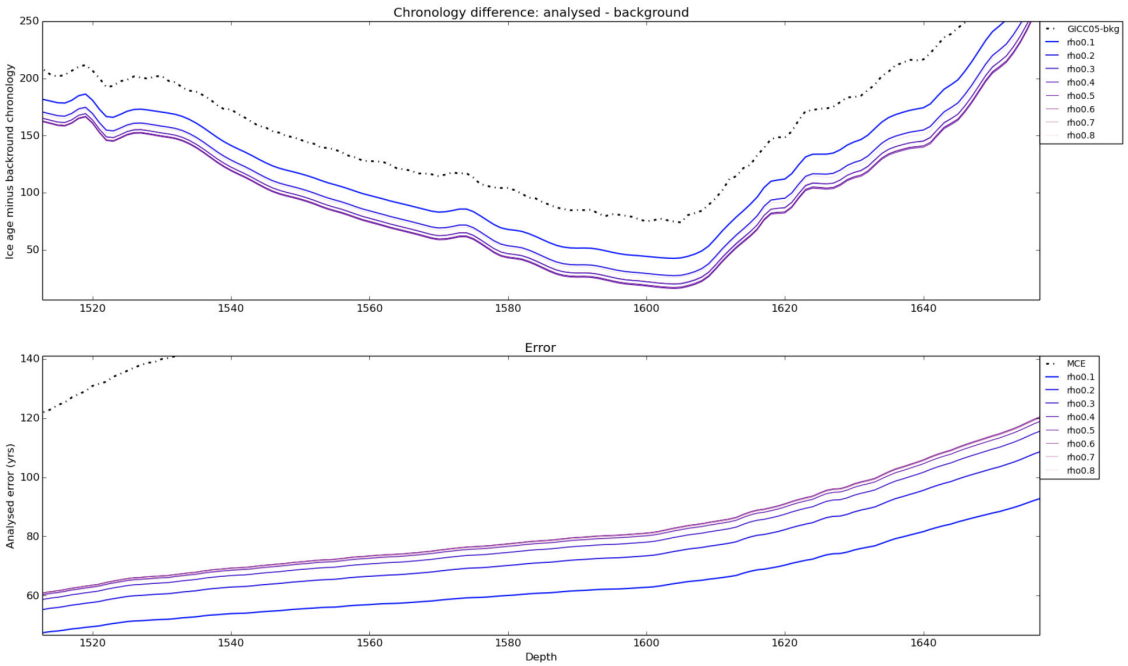

FIGURE 4.4 – Tests réalisés pour étudier l'influence de la corrélation entre les erreurs associées aux marqueurs de différence d'âge (de 0.1 à 0.8) dans le cas simple avec seulement NGRIP. Haut : différence entre les chronologies analysées et d'ébauche. Bas : Erreurs sur les chronologies analysées en sortie de Datice.

Les résultats des différents tests présentés dans ce chapitre associés aux marqueurs de différence d'âge implémentés dans Datice, ainsi que la paramétrisation de l'erreur d'ébauche de la fonction d'amincissement doivent être pris en compte lors de la réalisation de la prochaine chronologie commune officielle pour les carottes de glace.

5

Mesures sur de la glace bien conservée de Dôme C

5.1 Introduction

Lors de la construction d'AICC2012, les enregistrements de $\delta O_2/N_2$ et $\delta^{18}O_{atm}$ ont été utilisés pour déduire des marqueurs d'âge orbitaux servant à contraindre les chronologies glace et gaz, respectivement, des carottes de glace [Bazin et al., 2013]. Comme nous avons pu le voir dans le chapitre 1, le $\delta^{18}O_{atm}$ et le $\delta O_2/N_2$ sont soumis à différentes influences, que l'on rappelle brièvement ici.

Le $\delta^{18}O_{atm}$ est étroitement lié aux variations du cycle hydrologique des basses latitudes ainsi qu'à la productivité de la biosphère. Le temps de résidence de l'oxygène dans l'atmosphère étant d'environ 2 000 ans, le $\delta^{18}O_{atm}$ est réparti uniformément à la surface du globe. Ainsi, il est possible de relier entre eux les enregistrements de $\delta^{18}O_{atm}$ mesurés dans différentes carottes de glace (liens stratigraphiques). Le $\delta^{18}O_{atm}$ présente des variations similaires à la précession et à l'insolation locale des basses latitudes. Lors de la dernière transition glaciaire–interglaciaire, un retard d'environ $\sim$5 ka a été observé entre la précession et le $\delta^{18}O_{atm}$ [figure 5.1, Dreyfus et al., 2007]. De nombreux auteurs ont utilisé la relation entre précession et $\delta^{18}O_{atm}$ pour construire des datations orbitales de carottes de glace [Petit et al., 1999; Suwa and Bender, 2008; Dreyfus et al., 2007]. Cependant, l'incertitude associée à cette méthode reste large (6 ka) du fait du retard variable entre les variations de la précession et du $\delta^{18}O_{atm}$ [Jouzel et al., 2002].

Le $\delta O_2/N_2$ présente des variations similaires à celles de l'insolation locale au solstice d'été. C'est grâce à cette ressemblance qu'il est possible de déduire des marqueurs d'âge orbitaux servant à contraindre les chronologies des carottes de glace [Kawamura et al., 2007; Landais et al., 2012]. Le lien entre ces deux paramètres vient

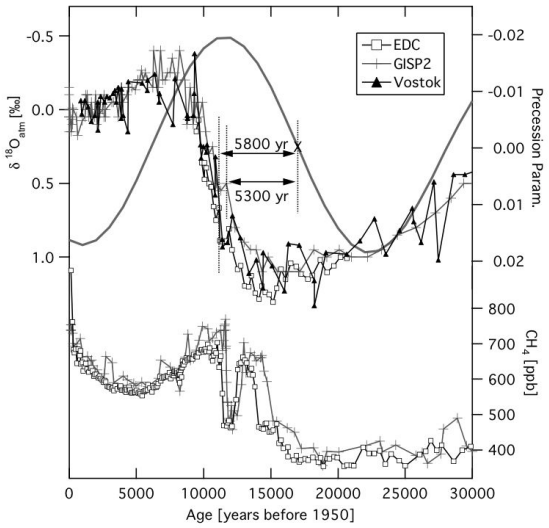

FIGURE 5.1 – Haut : retard entre le $\delta^{18}O_{atm}$ (EDC : carrés blancs, Vostok : triangles noirs et GISP2 : croix grises) et la précession au cours de la Terminaison I. Bas : enregistrements de méthane de ces mêmes carottes. Extrait de Dreyfus et al. [2007].

du fait que l'insolation reçue à la surface va en partie contrôler le métamorphisme des cristaux de neige, pouvant par la suite impacter sur la profondeur de piégeage de l'air. Cependant, nos connaissances actuelles des névés ne nous permettent pas de comprendre comment cette influence en surface se conserve et est transmise au $\delta O_2/N_2$ à la base du névé. De plus, il apparaît que le $\delta O_2/N_2$ est un traceur sensible aux conditions de conservation de la glace. En effet, il a été montré que suivant la température et la durée de stockage des échantillons en chambre froide, il est parfois nécessaire de corriger les valeurs mesurées du $\delta O_2/N_2$ [figure 5.2, Ikeda-Fukazawa et al., 2005; Kawamura et al., 2007; Landais et al., 2012]. Afin d'éviter toute correction, il est nécessaire de mesurer les échantillons de glace rapidement après les avoir rapportés du site de forage et de les conserver à -50°C.

Ainsi, plusieurs points restent à être étudiés concernant le $\delta O_2/N_2$ et le $\delta^{18}O_{atm}$:

— Comment a varié le retard entre $\delta^{18}O_{atm}$ et precession au cours du temps ?
— Quels sont les processus à l'origine de ce retard ?
— Comment le signal d'insolation est transmis au $\delta O_2/N_2$?
— Le $\delta O_2/N_2$ est-il influencé par d'autres paramètres ?
— Quelle incertitude doit-on associer à la synchronisation orbitale de ces deux traceurs ?

La logistique pour rapatrier des échantillons de glace bien conservée reste néan-

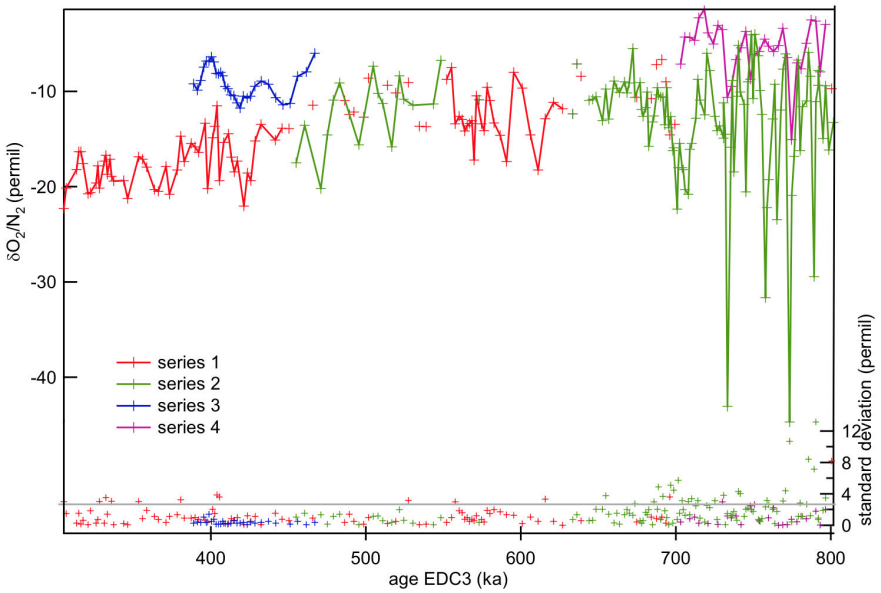

FIGURE 5.2 – Mesures de $\delta O_2/N_2$ d'EDC avec les incertitudes associées. Les séries de mesures 1 (rouge) et 2 (vert) ont été réalisées sur de la glace conservée à -25°C. Les séries de mesures 3 (bleu) et 4 (violet) ont été réalisées sur de la glace conservée à -50°C. Extrait de Landais et al. [2012].

moins compliquée. Les échantillons doivent rester stockés sur le site dans un endroit non soumis à des variations de température. Ensuite, le transport des échantillons du site jusqu'à la côte Antarctique puis jusqu'au laboratoire se fait grâce à des congélateurs froids (-80°C), des eutectiques et de la glace carbonique afin de maintenir une température proche de -50°C.

Dans ce chapitre je vais présenter les résultats associés à de nouvelles mesures de $\delta^{18}O_{atm}$et $\delta O_2/N_2$ effectuées sur de la glace bien conservée d'EDC entre 100–160 ka et 380–800 ka, venant compléter les enregistrements existants (le MIS 5 et 300–800 ka pour le $\delta^{18}O_{atm}$, le MIS 11 et 700–800 ka pour le $\delta O_2/N_2$). Grâce à cela, nous avons été en mesure de proposer la première comparaison entre plusieurs sites d'Antarctique des enregistrements de $\delta O_2/N_2$ et $\delta^{18}O_{atm}$ au cours du MIS 5. Ensuite, le couplage des données entre Vostok et EDC permet de reconstruire les variations de ces deux traceurs sur les derniers 800 ka. Ces deux études ont pour but d'améliorer la compréhension des différents paramètres pouvant influencer le $\delta O_2/N_2$ ainsi qu'à étudier les causes possibles du retard variable entre le $\delta^{18}O_{atm}$ et la précession. La dernière partie de ce chapitre s'intéresse au couplage entre les différents marqueurs orbitaux ($\delta O_2/N_2$, $\delta^{18}O_{atm}$ et teneur en air) sur les derniers 800 ka.

5.2 Phase relationships between orbital forcing and the composition of air trapped in Antarctic ice cores

Article en révision *Climate of the Past*.

Clim. Past Discuss., 11, 1437–1477, 2015
www.clim-past-discuss.net/11/1437/2015/
doi:10.5194/cpd-11-1437-2015

Climate of the Past Discussions

Phase relationships between orbital forcing and the composition of air trapped in Antarctic ice cores

L. Bazin[1], A. Landais[1], V. Masson-Delmotte[1], C. Ritz[2], G. Picard[2], E. Capron[3], J. Jouzel[1], M. Dumont[4], M. Leuenberger[5], and F. Prié[1]

[1]Laboratoire des Sciences du Climat et de l'Environnement, UMR8212, CEA-CNRS-UVSQ, Orme des Merisiers, Gif sur Yvette, France
[2]Laboratoire de Glaciologie et Géophysique de l'Environnement, UMR 5183, Univ. Grenoble Alpes-CNRS, Grenoble, France
[3]British Antarctic Survey, NERC, Cambridge, UK
[4]Météo-France-CNRS, CNRM-GAME UMR 3589, CEN, Grenoble, France
[5]Climate and Environmental Physics, Physics Institute and Oeschger Center for Climate Change Research, University of Bern, Bern, Switzerland

Received: 9 March 2015 – Accepted: 31 March 2015 – Published: 23 April 2015

Correspondence to: L. Bazin (lucie.bazin@lsce.ipsl.fr)

Published by Copernicus Publications on behalf of the European Geosciences Union.

Abstract

Orbital tuning is central for ice core chronologies beyond annual layer counting, available back to 60 ka (i.e. thousand of years before 1950) for Greenland ice cores. While several complementary orbital tuning tools have recently been developed using $\delta^{18}O_{atm}$, $\delta O_2/N_2$ and air content with different orbital targets, quantifying their uncertainties remains a challenge. Indeed, the exact processes linking variations of these parameters, measured in the air trapped in ice, to their orbital targets are not yet fully understood. Here, we provide new series of $\delta O_2/N_2$ and $\delta^{18}O_{atm}$ data encompassing Marine Isotopic Stage (MIS) 5 (between 100–160 ka) and the oldest part (380–800 ka) of the East Antarctic EPICA Dome C (EDC) ice core. For the first time, the measurements over MIS 5 allow an inter-comparison of $\delta O_2/N_2$ and $\delta^{18}O_{atm}$ records from three East Antarctic ice core sites (EDC, Vostok and Dome F). This comparison highlights a site-specific relationship between $\delta O_2/N_2$ and its local summer solstice insolation. Such a relationship increases the uncertainty associated with the use of $\delta O_2/N_2$ as a tool for orbital tuning. Combining records of $\delta^{18}O_{atm}$ and $\delta O_2/N_2$ from Vostok and EDC, we evidence a loss of orbital signature for these two parameters during periods of minimum eccentricity (~ 400, ~ 720–800 ka). Our dataset reveals a time-varying lag between $\delta O_2/N_2$ and $\delta^{18}O_{atm}$ over the last 800 ka that we interpret as variations of the lag between $\delta^{18}O_{atm}$ and precession. Large lags of ~ 5 ka are identified during Terminations I and II, associated with strong Heinrich events. On the opposite, minimal lags (~ 1–2 ka) are identified during four periods characterized by high eccentricity, intermediate ice volume and no Heinrich events (MIS 6–7, the end of MIS 9, MIS 15 and MIS 17). We therefore suggest that the occurrence of Heinrich events influences the response of $\delta^{18}O_{atm}$ to precession.

1 Introduction

Past changes in climate and atmospheric composition are recorded in a variety of ice core proxies. The EPICA Dome C (EDC) ice core has provided the longest available records, and documented glacial–interglacial changes in atmospheric greenhouse gases concentrations (Spahni et al., 2005; Loulergue et al., 2008; Lüthi et al., 2008) and Antarctic temperature (Jouzel et al., 2007) back to 800 ka (thousands of years before present, present being AD 1950). Precise and coherent ice core chronologies are critical to establish the sequence of events and to understand these past changes. A specificity of ice core chronologies lies in the requirement to calculate ice and gas chronologies, due to the fact that air is trapped several tens of meters below the ice sheet surface. The depth at which this trapping process occurs is called the lock-in depth (LID).

Ice core age scales are usually constructed using ice flow models and different age constraints (Parrenin et al., 2001, 2004, 2007; Buiron et al., 2011). Lemieux-Dudon et al. (2010) have developed a new dating tool (Datice) allowing for the first time to produce an optimized and common chronology for several ice cores from Antarctica and Greenland, over the past 50 ka. Using an improved version of this dating tool, as well as an extended set of age constraints, Bazin et al. (2013) and Veres et al. (2013) have established a common chronology (AICC2012 chronology) for four Antarctic ice cores (Vostok; EDC; EPICA Dronning Maud Land, EDML; Talos Dome ice core, TALDICE) and one Greenland ice core (NorthGRIP, NGRIP) extending back to 800 ka for EDC. A key limitation in deep ice core chronologies lies in the lack of absolute age constraints prior to layer counting in NGRIP (for ages older than 60 ka, Svensson et al., 2008). Orbital tuning of several parameters measured in the air trapped in ice cores (air content, $\delta O_2/N_2$ and $\delta^{18}O_{atm}$) has thus played a central role for the construction of the AICC2012 chronology. Orbital tuning permits to attribute ages deduced from the integrated summer insolation, summer insolation or precession variations to their ob-

served counterparts in air content, $\delta O_2/N_2$ or $\delta^{18}O_{atm}$ respectively, with acceptable uncertainties.

Orbital tuning is commonly applied to deep sea cores, using the orbital properties of benthic foraminifera ^{18}O records, themselves related to changes in ice volume (Imbrie and Imbrie, 1980). The most closely related ice core parameter is $\delta^{18}O_{atm}$, ^{18}O of atmospheric O_2. Ice core records of $\delta^{18}O_{atm}$ are strongly correlated with variations of insolation in the precession band, with a lag assumed to be $\sim$ 5–6 ka as established for the last termination (glacial–interglacial transition, Bender et al., 1994; Jouzel et al., 1996; Petit et al., 1999; Shackleton et al., 2000; Dreyfus et al., 2007). The modulation of precession on $\delta^{18}O_{atm}$ operates through the biosphere productivity and changes in low latitude water cycle (Bender et al., 1994; Malaizé et al., 1999; Wang et al., 2008; Severinghaus et al., 2009; Landais et al., 2007, 2010). The significant time delay between precession and $\delta^{18}O_{atm}$ is not straightforward to explain. It partly depends on the 1–2 ka residence time of O_2 in the atmosphere and on the complex response of biosphere productivity and tropical water cycle to precession changes. Caley et al. (2011) have shown lags of several thousand years between the responses of Indian and Asian monsoon systems to orbital forcing over the last 40 ka. Moreover, variations of $\delta^{18}O_{atm}$ are not only affected by the response to orbital forcing, but also by the millennial climate variability (Severinghaus et al., 2009; Landais et al., 2007). During Terminations I and II, $\delta^{18}O_{atm}$ maxima have been linked to Heinrich stadials 1 and 11 (Landais et al., 2013). Because of these complex interactions, the lag between $\delta^{18}O_{atm}$ and precession should vary with time (Leuenberger, 1997; Jouzel et al., 2002). However, for dating purposes, this lag has been assumed to be constant with an uncertainty of a quarter of a precession cycle (6 ka; Parrenin et al., 2007; Dreyfus et al., 2007).

Two other ice core parameters have been used for orbital tuning, but with a completely different underlying mechanism. The air content and $\delta O_2/N_2$ measured in the air trapped in ice cores are controlled by the enclosure process near the close-off depth (depth of closure of ice interstices and formation of air bubbles). At this depth, a depletion of the ratio O_2/N_2 compared to the atmospheric ratio is observed and attributed to

the smaller size of O_2 molecules compared to N_2 ones (Battle et al., 1996; Huber et al., 2006; Severinghaus and Battle, 2006). It is expected that the entrapment process and the associated O_2 effusion effect are linked to the physical properties of snow at this depth. Because snow metamorphism is very strong at the surface of the ice sheet in summer (Town et al., 2008; Picard et al., 2012), snow physical properties are expected to be driven by local summer insolation. Records of $\delta O_2/N_2$ and air content measured at Vostok, Dome F and EDC indeed depict variability at orbital frequencies, which appears in phase with local summer insolation (Bender, 2002; Kawamura et al., 2007; Raynaud et al., 2007; Lipenkov et al., 2011; Landais et al., 2012).

In summary, $\delta^{18}O_{atm}$ provides a relationship between the gas phase age and orbital forcing, due to changes in atmospheric composition driven by changes in low latitude hydrological cycle and biosphere productivity. Air content and $\delta O_2/N_2$ provide a relationship between the ice phase age and local insolation, due to the impact of snow metamorphism on air trapping processes.

$\delta^{18}O_{atm}$ is a well-mixed atmospheric signal, allowing synchronization of different ice core records. It also has a potential to link ice cores with climate records from other latitudes (e.g. global ice volume, low latitude hydrological cycle and biosphere productivity). However, due to the numerous and complex processes affecting the $\delta^{18}O_{atm}$, this orbital dating tool is generally associated with an uncertainty of 6 ka, namely a quarter of a precession cycle. An important challenge to progress on chronological issues is to estimate the variations of the lag between $\delta^{18}O_{atm}$ and precession over the last eight glacial–interglacial cycles.

Contrary to $\delta^{18}O_{atm}$, $\delta O_2/N_2$ and air content are not influenced by remote climatic-driven signals such as low latitude hydrological cycle or Northern Hemisphere land ice volume. However, local climate effects on firn pore structure are not fully understood. If solar radiations impact on $\delta O_2/N_2$ and air content as suspected, it occurs through surface snow metamorphism. Therefore, it depends on the surface energy budget, snow albedo, and upper snow temperature gradients (Picard et al., 2012). However, strong modifications of layering and microstructure are also observed at several tenths

of meters below the surface (Hörhold et al., 2012). It is therefore expected that pore structure at close-off is also affected by changes in dust load (Freitag et al., 2013) and/or accumulation rates (Hutterli et al., 2010). The direct link originally assumed between summer solstice insolation and $\delta O_2/N_2$ variations is therefore complicated by these different influences impacting on firnification.

These different limitations for each parameter have recently motivated a first assessment of the coherency between the different orbital dating tools in ice cores. Indeed, in the framework of the AICC2012 chronology construction (Bazin et al., 2013), we took advantage of available records of $\delta O_2/N_2$, air content and $\delta^{18}O_{atm}$ over the period 100–400 ka from the Vostok ice core (Petit et al., 1999; Bender, 2002; Suwa and Bender, 2008b; Lipenkov et al., 2011). We showed that the final chronology was the same using one or the other orbital markers with uncertainties of up to 7, 4 and 6 ka were attributed to air content, $\delta O_2/N_2$ and $\delta^{18}O_{atm}$, respectively. However, this first assessment was restricted to one single ice core covering only the last 400 ka. The large uncertainties associated with the different orbital markers in this case were partly due to the low resolution of the existing records and to the poor quality of the $\delta O_2/N_2$ data affected by gas loss (Landais et al., 2012). Gas loss, which occurs through micro-cracks during coring and ice core storage at warm temperature (typically freezers at −25 °C), favours the loss of O_2, and alters the original $\delta O_2/N_2$ signal (Kawamura et al., 2007; Bender et al., 1995). In this case, drifts in $\delta O_2/N_2$ have been shown to be related to storage duration (Kawamura et al., 2007) and must be corrected prior to the use of the data.

Our current understanding of these dating tools motivates further comparison of $\delta O_2/N_2$ and $\delta^{18}O_{atm}$ records, obtained (i) at high temporal resolution, (ii) from different East Antarctic ice cores, (iii) under different orbital and climatic contexts and (iv) on ice stored at very cold temperature (−50 °C) to avoid gas loss correction. In order to complement existing records from the Vostok and Dome F ice cores, we have performed new measurements on the long EDC ice core, for which only parts of the

$\delta O_2/N_2$ record were obtained from samples of well-conserved ice (−50 °C) (Landais et al., 2012).

Our goal is to assess the robustness of the use of $\delta O_2/N_2$ and $\delta^{18}O_{atm}$ as combined dating tools over the last 800 ka. For this purpose, we have performed new measurements of $\delta^{18}O_{atm}$ and $\delta O_2/N_2$ on ice stored at −50 °C (i.e. non-affected by gas loss) on the EDC ice core over Marine Isotope Stage (MIS) 5 and between 380–800 ka. Section 2 describes the new measurements from the EDC ice core complementing earlier data (Dreyfus et al., 2007, 2008; Landais et al., 2012, 2013; Bazin et al., 2013). Section 3 is dedicated to the analyses of the datasets, the inter-comparison of Vostok, Dome F and EDC data over MIS 5, as well as an investigation of the lags between $\delta O_2/N_2$ and $\delta^{18}O_{atm}$ during the past 800 ka and their implications for orbital tuning. These records enable us to check the coherency of these parameters for orbital tuning and to provide recommendation for their use in ice core chronologies.

2 Analytical method and measurements

The isotopic composition measurements of air trapped in well-conserved ice from EDC were performed at LSCE. The samples were cut in Antarctica in the archive trench at −40 °C maximum, and then kept at −50 °C during transportation and storage. Measurements were performed only a few months after their transportation from Antarctica. To prevent any contamination from exchanges with ambient air due to micro-cracks, we shave off 3–5 mm of ice on each face, and the air is extracted from a sample of ∼ 10 g of ice. Two different extraction methods have been used, either a manual or a semi-automatic line.

The manual method consists of a melt-refreeze technique (Sowers et al., 1989; Landais et al., 2003) for extracting the air trapped in the ice samples. The sample is placed in a cold flask and then the air in the flask is pumped. The trapped air is extracted by melting and refreezing the sample and is then cryogenically transferred in a stainless-steel tube immersed in liquid helium.

For the semi-automatic extraction line, we proceed with two exterior air samples and three ice samples with duplicates each day. The samples are placed in cold flasks and the air in the flasks is pumped; the air trapped in ice is extracted by melting of the samples and left at room temperature during one hour minimum. The air samples are then transferred one at a time through CO_2 and water vapour traps before being cryogenically trapped into a manifold immersed in liquid helium. An inter-comparison of the two extraction lines has been conducted using air extracted from NGRIP ice samples. No bias is observed in-between the two analytical extraction methods.

After a waiting time of 40 min, allowing the tubes to reach room temperature, measurements are performed with a dual inlet Delta V plus (Thermo Electron Corporation) mass spectrometer. A classical run is composed of 16 measurements of the sample in parallel with 16 measurements of a standard of dried exterior air. We simultaneously measure ^{18}O, $\delta O_2/N_2$ and ^{15}N. The data are then calibrated against the mean exterior air values and corrected for mass interferences following the standard methodologies (Severinghaus et al., 2001; Landais et al., 2003).

We were able to replicate 108 samples over 145 depth levels due to the small size of samples. The $\delta O_2/N_2$ and ^{18}O measurements are corrected for gravitational fractionation using the following equations:

$$\delta^{18}O_{atm} = \delta^{18}O - 2 \cdot \delta^{15}N \quad (1)$$

$$\delta O_2/N_2 = \delta O_2/N_{2raw} - 4 \cdot \delta^{15}N \quad (2)$$

The final precision (pooled SD) for our new set of data is 0.02 ‰ for $\delta^{18}O_{atm}$ and 0.79 ‰ for $\delta O_2/N_2$.

3 Results and discussion

Figure 1 shows the full EDC $\delta^{18}O_{atm}$ dataset, which has a mean temporal resolution of 1.1 ka thanks to our new dataset completing the records of Dreyfus et al. (2007,

2008); Bazin et al. (2013) between 300–800 ka, and Landais et al. (2013) over MIS 5. The data depict variations that coincide with those of precession, together with larger changes associated with glacial terminations. There is an excellent overall agreement between variations in precession and the lagged precession signal in $\delta^{18}O_{atm}$, with two exceptions corresponding to periods of low eccentricity: between 350 and 450 ka (MIS12-11-10) and around 700 to 800 ka. As already observed by Dreyfus et al. (2007), our new results illustrate that precession-driven variations in $\delta^{18}O_{atm}$ are reduced during these periods of low eccentricity. Moreover, with the addition of our new data, the tuning performed by Dreyfus et al. (2007) between 530–550 ka is not as straightforward as previously presented. Still, this stays within the uncertainties associated with $\delta^{18}O_{atm}$ orbital tuning and has no impact on the chronology construction.

Spectral analyses of the $\delta^{18}O_{atm}$ record spanning 300–800 ka (Fig. 2) confirm earlier results obtained by Dreyfus et al. (2007) for EDC, and those obtained for Vostok and Dome F data over the last 400 ka (Petit et al., 1999; Kawamura et al., 2007). The major peaks are observed for periods of 100, 19–23, and 41 ka (by decreasing amplitude) and correspond respectively to the eccentricity and/or glacial–interglacial climatic variations, precession and obliquity bands.

Our new data allow us to establish a record of $\delta O_2/N_2$ from 380 to 800 ka measured on well-conserved ice (Fig. 1). Series A (392–473 ka) and B (706–800 ka) were measured in 2007–2008 (Landais et al., 2012) and are complemented by our new set of data (Series C). The mean temporal resolution of the complete $\delta O_2/N_2$ record is 2.35 ka, with two main gaps (220 between 160–380 ka and 20 between 470–490 ka). The pooled SDs of each dataset vary between 0.3 and 1 ‰ (A: 0.32 ‰, B: 1.03 ‰; C: 0.79 ‰).

When compared with earlier data affected by gas loss (Landais et al., 2012), our data show the same timing of variations of $\delta O_2/N_2$ that coincide with those of local summer solstice insolation at Dome C (Appendix A). However, the relative strengths of minima and maxima of $\delta O_2/N_2$ do not scale with those of summer insolation. Large amplitudes of summer insolation cycles are associated with relatively small amplitudes

of the corresponding cycles in $\delta O_2/N_2$ and vice versa (Fig. 1) and only 13 % of the variance of the raw $\delta O_2/N_2$ data is explained by summer solstice insolation. Finally, the new record reveals an overall decreasing trend of $\delta O_2/N_2$ over the last 800 ka at EDC (0.78 ± 0.08 ‰/100 ka), confirming the observations of Landais et al. (2012) on their composite curve (Appendix A). Moreover, this feature was already identified during the last 400 ka at Vostok (0.56 ± 0.33 ‰/100 ka) and 360 ka at Dome F (0.56 ± 0.28 ‰/100 ka). We conclude that the long term decreasing trend of $\delta O_2/N_2$ with time is not an artifact due to the gas loss correction, but it may still be linked with a different preservation of the air with varying depth in the ice core. Long term changes in the enclosing process or modification in the atmospheric ratio O_2/N_2 can also be evoked.

The spectral analysis of the new EDC $\delta O_2/N_2$ record between 380–800 ka (Fig. 2) depicts peaks associated with the precession and obliquity bands (19–23 and 41 ka), together with a 100 ka periodicity. This 100 ka period was neither observed in $\delta O_2/N_2$ records from other Antarctic ice cores (Bender, 2002; Kawamura et al., 2007) nor in the composite EDC record of Landais et al. (2012).

The 100 ka peak is also absent from the power spectrum of summer solstice insolation, independently of the time window considered (Fig. 2). The 100 ka signal in $\delta O_2/N_2$, most strongly imprinted between 500 and 700 ka, arises from pronounced minima in the $\delta O_2/N_2$ record at 450, 550 and 650 ka. These minima occur during glacial periods characterized by low eccentricity, and therefore coincide with local insolation minima (arrows on Fig. 1). The 100 ka periodicity identified in the EDC $\delta O_2/N_2$ record between 380–800 ka, and absent from records spanning 0–400 ka may thus arise from a reduced influence of precession-driven insolation changes on snow metamorphism during eccentricity minima, similarly to the parallel reduced precession-driven signal in $\delta^{18}O_{atm}$. Such a reduced influence would leave room for other factors to impact EDC $\delta O_2/N_2$, such as local climatic parameters. Indeed, records of local climate (e.g. water stable isotopes and inferred changes in local temperature and accumulation rate, dust) exhibit a strong peak at 100 ka, characteristic of glacial–interglacial cycles (Masson-Delmotte et al., 2010; Lambert et al., 2008). The 100 ka periodicity in

EDC $\delta O_2/N_2$ could therefore arise from an influence of local climate related parameters, which would be more strongly expressed under a low eccentricity context.

3.1 MIS 5 Antarctic inter-comparison

Our EDC $\delta O_2/N_2$ record displays variability in the precession and obliquity ranges, as well as minima and maxima that highlight clear similarities with local summer insolation. However, neither the modulation in amplitude nor the 100 ka signal are related to local summer insolation, pointing to other local influences such as changes in surface energy budget, firn dust content, changes in temperature and accumulation rate, which could affect snow metamorphism and firnification processes. While variations in summer solstice insolation are expected to be very similar in all East Antarctic ice core sites, differences in site characteristics (e.g. snow properties, meteorological situation, mean climate) may cause differences in the $\delta O_2/N_2$ signals from different ice cores, if local processes have a significant influence. This motivates a comparison of $\delta O_2/N_2$ signals from three ice cores drilled in the East Antarctic plateau: Dome F, Vostok and EDC. Present-day conditions at these three dry and particularly cold sites depict differences in the distance to open ocean, elevation (within 577 m), albedo (within 3 %), wind speed (a factor of two), accumulation (within 15 %) and mean annual temperature (within 2.5 °C) (Table 1).

Thanks to our new $\delta O_2/N_2$ data, we now have records of both $\delta O_2/N_2$, $\delta^{18}O_{atm}$ and water isotopes over MIS 5 from EDC, Dome F and Vostok. This MIS 5 period is also of particular interest since it is characterized by large precession parameter variations, together with large glacial-interglacial changes in Antarctic temperature, with warmer-than-present reconstructed interglacial temperatures (Sime et al., 2009; Stenni et al., 2010; Masson-Delmotte et al., 2011; Uemura et al., 2012).

Figure 3 displays the $\delta O_2/N_2$ records from Dome F (on the DFO-2006 time scale), EDC and Vostok (both on their respective AICC2012 chronologies) from 150 to 100 ka. We observe the same orbital scale variations from all three records, i.e. a $\delta O_2/N_2$

maximum at around 126 ka bracketed by 2 minima at 115 and 135 ka. Two major differences are still noticeable:

- A lower $\delta O_2/N_2$ mean value and greater amplitude in variations at Vostok than at Dome F and EDC.
- A site-specific high frequency variability. For instance, between 100–115 ka, EDC and Vostok $\delta O_2/N_2$ records show a double peak that is not observed at Dome F and significantly larger than measurements uncertainties.

The gas loss corrections applied on the Dome F and Vostok $\delta O_2/N_2$ records may explain part of these discrepancies. The resolution of the records (2.3 ka for EDC, 1.5 ka for Vostok and 1.2 ka for Dome F between 100–150 ka) limits the comparison of high frequency variations observed between 100 and 115 and around 126 ka. In the Greenland GISP2 ice core, it has been shown that $\delta O_2/N_2$ can display millennial scale variability, in relationship with glacial climatic variability (Suwa and Bender, 2008a). Only high-resolution measurements conducted on well-conserved ice could allow us to have an objective discussion of high frequency signals in Antarctic ice.

All three $\delta O_2/N_2$ records present variations that occur simultaneously with the ones of the local summer solstice insolation target curves (Fig. 3). This is expected since the different ice core chronologies used in Fig. 3 are based at least partially on the alignment of the $\delta O_2/N_2$ signal on the summer solstice insolation curve. An intriguing feature arises from the comparison of the lags between $\delta O_2/N_2$, $\delta^{18}O_{atm}$ and $\delta^{18}O_{ice}$ within each ice core (Fig. 3). While the $\delta O_2/N_2$ records of the three sites seem aligned, Dome F $\delta^{18}O_{atm}$ and $\delta^{18}O_{ice}$ exhibit a fingerprint of Termination II occurring 2 ka earlier than the ones recorded in Vostok and EDC (as observed on water stable isotope optima, Fig. 3 and Bazin et al., 2013). The same shift between Dome F and EDC/Vostok $\delta^{18}O_{atm}$ and $\delta^{18}O_{ice}$ records is also observed for the glacial inception. This shift of several thousands years between chronologies highlights the limitation of orbital tuning in ice cores, even if the chronologies are also constrained by glaciological modeling (Kawamura et al., 2007; Bazin et al., 2013). It also strengthens the fact that quite large

uncertainties should be associated with $\delta O_2/N_2$ orbital tuning. An objective alignment between $\delta O_2/N_2$ and orbital target is difficult to obtain because of low resolution and scattering of $\delta O_2/N_2$ data.

Still, the $\delta O_2/N_2$ minimum at the timing of Termination II (arrows on Fig. 3) is clearly later at EDC than at Dome F. If only local summer solstice insolation was a direct driver of $\delta O_2/N_2$ changes, one would expect the three $\delta O_2/N_2$ records to be exactly synchronous. We thus look for alternative explanations for a modulation of the lag between summer solstice insolation and $\delta O_2/N_2$.

First, differences between sites may result from a different response of snow metamorphism and therefore $\delta O_2/N_2$ to orbital forcing. One important assumption for the process linking $\delta O_2/N_2$ and orbital forcing is that snow metamorphism is maximum at peak temperature (Kawamura et al., 2007) so that summer solstice insolation curve should be taken as orbital target for $\delta O_2/N_2$ variations. At Dome F, the current seasonal cycle of surface snow temperature measurements shows maximum values at the summer solstice (21 December, Kawamura et al., 2007). At Vostok, the maximum of surface snow temperature is observed about 10 days later, close to 30 December (continuous measurements since 2010, Lefebvre et al., 2012; J.-R. Petit, personal communication, 2013). At Dome C, 3 years continuous measurements of surface snow temperature between 2006–2009 have shown that the maximum of temperature occurs 15–20 days after the summer solstice (Landais et al., 2012, confirmed by the continuous measurements since then). These regional differences highlight the fact that, today, surface snow temperature does not reach its summer maximum in phase with local summer solstice insolation. As a consequence, different insolation target curves for $\delta O_2/N_2$ should be considered for the different sites if the observations performed for present day conditions are also valid for the past. Following this observation, we have tried to use 30 December and 15 January insolation curves as respective orbital targets for EDC and Vostok $\delta O_2/N_2$ records. However, using such orbital targets strengthens the lag between the Dome F and Vostok-EDC age scales over MIS 5.

Second, we explore if inter-site differences in surface albedo could explain differences in the energy input for surface snow metamorphism (Picard et al., 2012). Surface albedo is currently measured over East Antarctica with MODIS multispectral imager on board TERRA and AQUA satellites. Data collected since 2001 enable to compare the albedo of our three sites of interest (Table 1). For this purpose, White Sky broadband albedo data (surface albedo under perfectly diffuse illumination conditions) were extracted from MCD43A3 products (http://www.umb.edu/spectralmass/terra_aqua_modis/v006). Only values for which local solar noon sun zenith angle is less than 65° and high quality flags (QA = 0 in MCD43A2 products) are considered (Schaaf et al., 2011). They show similar values at Vostok and EDC (0.83), and significantly lower values at Dome F (0.80). This implies that, today, about 15 % more incoming solar radiations are absorbed by Dome F surface snow and can act on its metamorphism. However, surface metamorphism is not simply related to surface albedo. This can be investigated using the grain index time series developed by Picard et al. (2012). The amplitude of diurnal cycles and grain size near the surface indicate more metamorphism at Dome C than at Dome F. We note that the largest amplitude of grain growth is observed at South Pole, despite a high local albedo and no diurnal cycle. While present day data provide a hint for possible differences in surface snow metamorphism, further studies are needed to better understand how the surface energy budget controls the surface and subsurface snow metamorphism, and how it can explain the differences in $\delta O_2/N_2$ mean level and phasing between $\delta O_2/N_2$ and insolation forcing at different sites.

Third, we investigate how changes in layering or snow microstructure during the firnification processes can affect $\delta O_2/N_2$. Several indices indeed suggest that $\delta O_2/N_2$ is not only influenced by the energy received at the surface of snow but also by firnification processes, which themselves depend on climatic conditions such as accumulation rate, firn temperature, impurity content of the snow (Hutterli et al., 2010). We have thus searched for local climatic influence on $\delta O_2/N_2$ focusing first on accumulation rates. No significant correlation can be identified between EDC accumulation

rate produced by AICC2012 and $\delta O_2/N_2$ variations (R = 0.107 between 380–800 ka). Moreover, no direct link can be established between the relative values of accumulation rates and $\delta O_2/N_2$ values comparing Dome F, Vostok and EDC over the MIS 5 period (Appendix B). Still, this investigation is limited by the fact that the Vostok and Dome F $\delta O_2/N_2$ records are corrected for gas loss. It is also possible to face different compensating effects of accumulation rate and local temperature that could be site-specific (Bender, 2002; Hutterli et al., 2010).

Finally, changes in dust concentration have been suggested to potentially influence firn density and hence air trapping (Hörhold et al., 2012; Freitag et al., 2013). Records of dust concentration spanning MIS 5 are available for EDC (Lambert et al., 2008) and Vostok (Petit et al., 1999). There is no significant difference between the dust concentration of Vostok and EDC regarding their amplitude and timing of changes, so they should have the same effect at both sites. The lack of published $\delta O_2/N_2$ and dust records from Dome F precludes investigations of the differences between Dome F and Vostok-EDC. Moreover, subsurface processes and reworking of surface snow by the wind are known to have an influence on actual firnification, as a result this should have an impact on the $\delta O_2/N_2$ trapping process (Fujita et al., 2012), even under glacial climatic conditions.

This study provides support for more complex processes affecting the $\delta O_2/N_2$ than just the local summer solstice modulation. We cannot yet explain the origin of such site differences of the $\delta O_2/N_2$ records as we are limited by the lack of available data ($\delta O_2/N_2$ on well-conserved ice for Vostok and Dome F, dust records for Dome F, CH_4 for Dome F) and by our current understanding of firnification processes. However, from the available information we can point to a cautious use of orbital age markers inferred from $\delta O_2/N_2$ with possible differences from one site to another. Based on the inter-site differences, we recommend to use an uncertainty of 3–4 ka, and to combine these data with other dating tools.

3.2 $\delta O_2/N_2$–$\delta^{18}O_{atm}$ lag

A lag of $\delta^{18}O_{atm}$ vs. precession was observed over the last termination at Vostok, EDC and GISP2 with values of 5.8, 5.9 and 5.3 ka on the FGT1, EDC3 and Meese/Sowers chronologies respectively (Dreyfus et al., 2007; Petit et al., 1999; Parrenin et al., 2004, 2007; Bender et al., 1994; Meese et al., 1994). On the new AICC2012 chronology, the lag of $\delta^{18}O_{atm}$ with precession over Termination I is now of 5.6 ka for Vostok and 5.5 ka for EDC.

During Termination II, recently published high-resolution $\delta^{18}O_{atm}$ measurements (Landais et al., 2013) together with the AICC2012 chronology (Bazin et al., 2013) also give a $\sim$ 5 ka phase lag (5.2 ka) between precession and $\delta^{18}O_{atm}$. Bazin et al. (2013) have shown an excelent agreement for the timing of Termination II on a purely orbital ice core chronology (AICC2012 using only ice core orbital age markers over Termination II) and an independent speleothem chronology based on U/Th Dating (Cheng et al., 2009). This comparison rely on the assumption that abrupt variations in CH_4 and calcite $\delta^{18}O$ are synchronous. While this assumption was explicitly used to build the EDC3 chronology (Parrenin et al., 2007; Waelbroeck et al., 2008), this is not the case for AICC2012, which provides high confidence in the accuracy of this chronology for Termination II.

The determination of the lag between $\delta^{18}O_{atm}$ and precession for earlier terminations is more complicated. Indeed, it requires an absolute chronology that is independent from orbital tuning based on $\delta^{18}O_{atm}$. Similarly, determining the phase lag between $\delta O_2/N_2$ and summer solstice insolation is not possible in the absence of an alternative timescale free from $\delta O_2/N_2$ constraints. However, we can still progress on the issue of relative phase lags between $\delta^{18}O_{atm}$, $\delta O_2/N_2$ and orbital targets by studying the relationships between $\delta O_2/N_2$ and $\delta^{18}O_{atm}$. Indeed, even if the orbital targets of both parameters are close and without significant lags between them (less than 500 years over the last 800 ka, Fig. 4), $\delta^{18}O_{atm}$ and $\delta O_2/N_2$ variations are due to very different mechanisms (remote for $\delta^{18}O_{atm}$, local for $\delta O_2/N_2$). As a consequence, it is very un-

likely that variations of $\delta^{18}O_{atm}$ and $\delta O_2/N_2$ lags relative to their orbital targets would occur simultaneously and compensate each other. These changes should then be visible on the lag between $\delta O_2/N_2$ and $\delta^{18}O_{atm}$.

Based on the good agreement of the Vostok and EDC $\delta O_2/N_2$ records over MIS 5, we have combined the full Vostok (0–400 ka) and EDC (380–800 ka) $\delta O_2/N_2$ and $\delta^{18}O_{atm}$ records (Fig. 4). We have re-interpolated the $\delta O_2/N_2$ and the reverse of $\delta^{18}O_{atm}$, in order to account for their negative correlation, every 1 ka. There is a close resemblance of the interpolated and original data. In order to calculate the phase delay, we have then normalized these two interpolated records and filtered them between 15 and 100 ka, using wavelet transform.

During periods of weak eccentricity (e.g. around 400 and before 720 ka), there is no clear correspondence between the variations of $\delta O_2/N_2$ and $\delta^{18}O_{atm}$ on one hand and the variations of their orbital target curves on the other hand, as previously noted (Dreyfus et al., 2007; Landais et al., 2012). During these periods, the variations of insolation in the precession band are probably too small to be imprinted in either $\delta O_2/N_2$ or $\delta^{18}O_{atm}$ records. Moreover, the new $\delta O_2/N_2$ record present missing data between 470–490 ka, so that the phase delay cannot be calculated over this period. Finally, the most recent 100 ka correspond to a period of low eccentricity and the $\delta O_2/N_2$ signal does not display any variability comparable to that of the insolation curve (before the air bubbles/clathrates transition). As a consequence, we disregard these periods for our discussion of the phase delay (not shown on Fig. 4). This also means that the orbital tuning through $\delta^{18}O_{atm}$ and $\delta O_2/N_2$ is much less reliable over these periods. We therefore recommend excluding such orbital tie points during large eccentricity minima, or considering them with larger uncertainties. On Fig. 4, we can see that the $\delta O_2/N_2$ records (original and filtered) do not present the same variability as the local summer solstice insolation during MIS 13. As a result, it is not possible to discuss the phase delay between $\delta O_2/N_2$ and $\delta^{18}O_{atm}$ over this period. The time intervals covered over the following discussion correspond to 100–350 and 530–720 ka.

During the remaining intervals of intermediate to strong eccentricity, the phase delay between $\delta O_2/N_2$ and $\delta^{18}O_{atm}$ varies between −6 and −1 ka. These phase delay values are significant as the re-interpolated and filtered curves present the same variability as the original data (Fig. 4). For Termination II, we obtain a $\delta^{18}O_{atm}$ vs. $\delta O_2/N_2$ phase delay of 4.5 ka, which is in good agreement with the $\delta^{18}O_{atm}$ vs. precession lag observed on raw data and a zero phase between $\delta O_2/N_2$ and summer solstice insolation as displayed on Fig. 3. On Fig. 4, we observe that the phase delay between $\delta O_2/N_2$ and $\delta^{18}O_{atm}$ is minimal during MIS 6–7, the end of MIS 9, MIS 15 and MIS 17, with the minimum value occurring during MIS 15 (−1.1 ka). These periods are marked by high eccentricity levels together with intermediate ice-sheet extents (i.e. neither full glacial conditions nor extremely warm interglacial conditions). On the contrary, local maxima of the $\delta O_2/N_2$–$\delta^{18}O_{atm}$ phase delay are observed for MIS 8 (−5 ka) and MIS 16 (−3 ka).

Part of the variations in the phase delay between $\delta O_2/N_2$ and $\delta^{18}O_{atm}$ may be due to the uncertainty in the age difference between ice and gas ages since $\delta^{18}O_{atm}$ is expressed on a gas timescale while $\delta O_2/N_2$ is on an ice timescale. Such uncertainty is largest during glacial periods, due to the impact of glacial climate conditions on firn processes. This uncertainty always stays below 1 ka, and therefore cannot explain the observed variations in phase delay between $\delta O_2/N_2$ and $\delta^{18}O_{atm}$. We argue that the large variations of the phase delay observed between $\delta O_2/N_2$ and $\delta^{18}O_{atm}$ are mainly due to variations in the phase delay between $\delta^{18}O_{atm}$ and precession, as $\delta O_2/N_2$ is synchronous with local insolation and there is nearly no differences in timing of insolation and precession variations. Indeed, the link between precession and $\delta^{18}O_{atm}$ is not direct and involves global modifications of the low latitude water cycle and biosphere productivity. On the opposite, while the exact mechanism linking $\delta O_2/N_2$ to summer solstice insolation is not yet fully understood, there is no doubt that it involves local firn processes with a faster response time.

Many reasons are invoked to explain the phase lag between precession and $\delta^{18}O_{atm}$. As evidenced over Terminations I and II and over the last 240 ka, $\delta^{18}O_{atm}$ variations are closely related to the dynamic of the low latitude hydrological cycle (Wang et al.,

2008; Severinghaus et al., 2009; Landais et al., 2007, 2010, 2013; Cheng et al., 2009). Monsoons are influenced by orbital forcing, with a strong imprint of precession (Wang et al., 2008; Braconnot et al., 2008), but also by millennial scale variability (Wang et al., 2001; Marzin et al., 2013). The Heinrich event 1 is for instance associated with a weak monsoon interval (e.g. Denton et al., 2010). We note that Termination I and Termination II are associated with large Heinrich events during the first part of the deglaciation, when orbital forcing already acts on sea level and global climate, including Antarctic temperature (Landais et al., 2013).

In order to study the possible link between variations of the $\delta O_2/N_2$–$\delta^{18}O_{atm}$ phase delay and the occurrence of Heinrich events, we confront our results to an Ice Rafted Debris (IRD) proxy (Ca/Sr) from the marine cores U1302/03 and U1308 located within the IRD belt of North Atlantic (Hodell et al., 2008; Channell et al., 2012; Channell and Hodell, 2013). As the two sites are located on the western and eastern borders of the IRD belt respectively, spikes present within both Ca/Sr records indicate the occurrence of Heinrich-like events over the last 800 ka. The Ca/Sr can be considered as an IRD proxy as its spikes correspond to rich detrial carbonate layers, characterizing IRD from the Laurentide ice sheet. At the bottom of Figure 4 are represented the oxygen isotopes and Ca/Sr records of marine cores U1302/03 and U1308 on their respective chronologies. We can see that Ca/Sr spikes recorded in both marine cores occur at the same periods as the local maximum of the $\delta O_2/N_2$–$\delta^{18}O_{atm}$ phase delay (within chronologies uncertainties, red arrows on Fig. 4). On the contrary, periods associated with the smallest lags between $\delta O_2/N_2$ and $\delta^{18}O_{atm}$ present Ca/Sr spikes in the U1302/03 marine core, but not in the U1308. Channell et al. (2012) speculate that these events correspond to debris flows or glacial-lake drainage events caused by changes in hydrological budget or changes in base level. Consequently, the marine data can be interpreted as evidence for the occurrence of Heinrich-like events during MIS 8 and MIS 16. We suggest that, during these two periods, the Heinrich-like events delay the response of monsoons and thus $\delta^{18}O_{atm}$ with respect to precessional forcing. By contrast, where we detect the smallest lags between precession and $\delta^{18}O_{atm}$

(Fig. 4), no Heinrich-like events are observed within both marine cores. We therefore explain the minimum lag between $\delta^{18}O_{atm}$ and precession during MIS 6–7, the end of MIS 9, MIS 15 and MIS 17 by the combination of three factors: minimum effects of ice volume changes (due to intermediate ice sheet extent), strong impact of precession on monsoons (due to high eccentricity), and the absence of Heinrich-like event.

In summary, our datasets suggest that the phase lag between $\delta^{18}O_{atm}$ and precession can vary between 1 to more than 6 ka, with minimum values during periods of strong eccentricity and intermediate ice volume (no Heinrich events). This varying lag results from the complex interplay of orbital and millennial variations affecting changes in sea-water isotopic composition, tropical water cycle, and biosphere productivity. The phase identified over Termination I and II may not apply for earlier transitions without Heinrich events. It implies that the phase lag of Termination I may provide an upper estimation for the associated uncertainty range.

4 Conclusions and perspectives

We have presented new measurements of $\delta O_2/N_2$ and $\delta^{18}O_{atm}$ performed on well-conserved ice from EDC over MIS 5 and between 380–800 ka. As a result, we now have a new reference $\delta O_2/N_2$ curve between 380–800 ka with a mean resolution of 2.35 ka, confirming earlier observations about a decreasing trend over the last 800 ka and timing of orbital scale variations. The spectral analysis of the new $\delta O_2/N_2$ curve between 380–800 ka showed for the first time a significant peak in the periodicity band characterising eccentricity and glacial–interglacial variations, hence suggesting that processes other than local summer insolation do impact $\delta O_2/N_2$ on glacial–interglacial scales. This should motivates further studies to unveil the processes at play both for long term trends and at glacial–interglacial/eccentricity timescales.

Thanks to our comprehensive datasets, we have been able for the first time to compare the sequence of events between water isotopes, $\delta O_2/N_2$ and $\delta^{18}O_{atm}$ for three Antarctic ice cores (EDC, Vostok and Dome F), over MIS 5. Significant differences have

been observed, which cannot be entirely explained by differences in resolution or by the corrections applied on $\delta O_2/N_2$ records of Dome F and Vostok. In particular, we have evidenced that the alignment of $\delta O_2/N_2$ on the summer solstice insolation signal may vary by ~ 2 ka from site to site. This may be due to an influence of local climatic parameters on the $\delta O_2/N_2$. This demonstrates the interest of the multi-proxy, multi-ice cores chronology approach, which is therefore crucial to correctly assess the uncertainties associated with individual age markers. Again the mechanisms responsible for local $\delta O_2/N_2$ variations remain to be understood. This is particularly important over periods of low eccentricity when the insolation variations are not well imprinted in the $\delta O_2/N_2$ records (350–450 and 700–800 ka). The $\delta O_2/N_2$ orbital tuning method should not be used alone during these periods.

Moreover, we have calculated the delay between $\delta O_2/N_2$ and $\delta^{18}O_{atm}$ over the last 800 ka by coupling Vostok and EDC data. This lag has varied from 1 to 6 ka with minimum values during MIS 6–7, the end of MIS 9, MIS 15 and MIS 17, corresponding to periods of high eccentricity and intermediate ice-sheet extent. Based on results observed over MIS 5, we make the assumption that $\delta O_2/N_2$ is synchronous with summer solstice insolation and that this lag is mainly due to variations in the relationship between $\delta^{18}O_{atm}$ and precession. It has been shown over Terminations I and II that the $\delta^{18}O_{atm}$ response to precession can be delayed during Heinrich events, associated with weak monsoon intervals. The small values of the phase delay observed during MIS 6–7, the end of MIS 9, MIS 15 and MIS 17 are therefore attributed to a lack of Heinrich-like event during these periods, combined with high eccentricity and intermediate ice sheet extent.

In order to refine this analysis, new measurements on well-conserved ice of $\delta O_2/N_2$ and $\delta^{18}O_{atm}$ are needed between 160–380 and 470–490 ka for the EDC ice core, and over the last 400 ka for Vostok and Dome F ice cores. Integrating Dome F on the AICC2012 age scale will be crucial to improve the Antarctic chronology. This methodology will then permit to investigate properly the causes of inter-site differences during MIS 5, and assess if similar features arise during other time periods. New measure-

ments on well-conserved ice together with constraints on past changes in dust concentration and accumulation rates should allow us to assess whether there is any robust link between variables that can potentially affect metamorphism such as dust content and accumulation rate. Moreover, further studies are needed on processes affecting surface snow in order to better understand its metamorphism. Finally, it is crucial to better understand how the low latitude water cycle and biosphere productivity influence the $\delta^{18}O_{atm}$ and its lag with precession in order to estimate correctly the uncertainty associated with the $\delta^{18}O_{atm}$ orbital tuning methods. To do so, it is necessary to improve uncertainties associated with ice and marine cores. The development of multi-archives dating tool should permit to synchronize records from different archives and thus discuss in more details how the Heinrich events influence the $\delta^{18}O_{atm}$ lag with precession.

Appendix A: EDC $\delta O_2/N_2$ records

We have compared the $\delta O_2/N_2$ composite curve of Landais et al. (2012), corrected for gas loss, with our new record only measured on well-conserved ice (Fig. A1). We observe nearly the same timing of variations. We conclude that the increased resolution and accuracy of our new dataset do not affect the position of mid-slope variations and therefore orbital tuning. The uncertainty associated with the mid-slope identification is always smaller than the uncertainty associated with $\delta O_2/N_2$ orbital tuning. Note that we have identified an error in the earlier composite curve due to the use of gas age instead of ice age for the time period 400 to 450 ka. This error has been corrected and explains the difference between our new record and the one of Landais et al. (2012). Compared to the Landais et al. (2012) composite curve, the new record presents smaller amplitudes of variations, possibly because of gas loss corrections. Our new data record a long term decrease of $\delta O_2/N_2$ over time of 0.78 ± 0.08 ‰/100 ka, which is very close to the long term decrease of 0.86 ± 0.14 ‰/100 ka, deduced from the Landais et al. (2012) composite curve.

Appendix B: Appendix B: $\delta O_2/N_2$ and accumulation

For East Antarctic ice cores, accumulation rates are usually deduced from water stable isotopes and then adjusted by chronological constraints and ice flow modeling. Here, we use the accumulation rates produced in the AICC2012 chronology. For Dome F, we have transferred the accumulation rate deduced from ice flow modeling (Parrenin et al., 2007, DFGT-2006) on the DFO-2006 chronology. In order to investigate a possible link between $\delta O_2/N_2$ and accumulation rate, we have interpolated them with a 1 ka step between 100–150 ka, and compared their values for EDC, Vostok and Dome F.

Four different time intervals are identified from changes in accumulation rates (Fig. B1):

1. Low accumulation rates during the penultimate glacial period, prior to 140 ka.
2. Accumulation increase during the glacial–interglacial transition.
3. High accumulation rates during the interglacial period and decreasing rates during glacial inception.
4. Last glacial period since 100 ka.

Note that the timing of these 4 phases can differ amongst the three ice core records. Figure B1 shows that no link can be established between accumulation rate and $\delta O_2/N_2$ values. This study is of course limited by the fact that Vostok and Dome F $\delta O_2/N_2$ data are corrected for gas loss, and by the lack of accumulation rate data directly inferred from the DFO-2006 age scale. While no first-order conclusion can be reached, this study should be repeated as soon as data measured on well-conserved ice will be available for Dome F and Vostok over this period.

Acknowledgements. We thank Jean-Robert Petit and Laurent Arnaud for the help with the surface temperature data of Vostok and EDC. We thank James Channel for the marine cores data. The present research project No 902 has been performed at Concordia Station and was supported by the French Polar Institute (IPEV). This project was funded by the "Fondation de France Ars Cuttoli" and the "ANR Citronnier". The research leading to these results has received funding from the European Union's Seventh Framework programme (FP7/2007-2013) under grant agreement no 243908, "Past4Future. Climate change – Learning from the past climate". This is Past4Future contribution number XX. This is LSCE contribution no XX.

References

Battle, M., Bender, M., Sowers, T., Tans, P. P., Butler, J. H., Elkins, J. W., Ellis, J. T., Conway, T., Zhang, N., Lang, P., and Clarket, A. D.: Atmospheric gas concentrations over the past century measured in air from firn at the South Pole, Nature, 383, 231–235, doi:10.1038/383231a0, 1996. 1441

Bazin, L., Landais, A., Lemieux-Dudon, B., Toyé Mahamadou Kele, H., Veres, D., Parrenin, F., Martinerie, P., Ritz, C., Capron, E., Lipenkov, V., Loutre, M.-F., Raynaud, D., Vinther, B., Svensson, A., Rasmussen, S. O., Severi, M., Blunier, T., Leuenberger, M., Fischer, H., Masson-Delmotte, V., Chappellaz, J., and Wolff, E.: An optimized multi-proxy, multi-site Antarctic ice and gas orbital chronology (AICC2012): 120–800 ka, Clim. Past, 9, 1715–1731, doi:10.5194/cp-9-1715-2013, 2013. 1439, 1442, 1443, 1445, 1448, 1452, 1469, 1472

Bender, M.: Orbital tuning chronology for the Vostok climate record supported by trapped gas composition, Earth Planet. Sc. Lett., 204, 275–289, doi:10.1016/S0012-821X(02)00980-9, 2002. 1441, 1442, 1446, 1451

Bender, M., Sowers, T., and Labeyrie, L.: The Dole effect and its variations during the last 130 000 years as measured in the Vostok ice core, Global Biogeochem. Cy., 8, 363–376, doi:10.1029/94GB00724, 1994. 1440, 1452

Bender, M., Sowers, T., and Lipenkov, V.: On the concentrations of O_2, N_2, and Ar in trapped gases from ice cores, J. Geophys. Res.-Atmos., 100, 18651–18660, doi:10.1029/94JD02212, 1995. 1442

Braconnot, P., Marzin, C., Grégoire, L., Mosquet, E., and Marti, O.: Monsoon response to changes in Earth's orbital parameters: comparisons between simulations of the Eemian and of the Holocene, Clim. Past, 4, 281–294, doi:10.5194/cp-4-281-2008, 2008. 1455

Buiron, D., Chappellaz, J., Stenni, B., Frezzotti, M., Baumgartner, M., Capron, E., Landais, A., Lemieux-Dudon, B., Masson-Delmotte, V., Montagnat, M., Parrenin, F., and Schilt, A.:

TALDICE-1 age scale of the Talos Dome deep ice core, East Antarctica, Clim. Past, 7, 1–16, doi:10.5194/cp-7-1-2011, 2011. 1439

Caley, T., Malaizé, B., Revel, M., Ducassou, E., Wainer, K., Ibrahim, M., Shoeaib, D., Migeon, S., and Marieu, V.: Orbital timing of the Indian, East Asian and African boreal monsoons and the concept of a "global monsoon", Quaternary Sci. Rev., 30, 3705–3715, doi:10.1016/j.quascirev.2011.09.015, 2011. 1440

Channell, J., Hodell, D., Romero, O., Hillaire-Marcel, C., de Vernal, A., Stoner, J., Mazaud, A., and Röhl, U.: A 750-kyr detrital-layer stratigraphy for the North Atlantic (IODP Sites U1302–U1303, Orphan Knoll, Labrador Sea), Earth Planet. Sc. Lett., 317–318, 218–230, doi:10.1016/j.epsl.2011.11.029, 2012. 1455

Channell, J. E. T. and Hodell, D. A.: Magnetic signatures of Heinrich-like detrital layers in the Quaternary of the North Atlantic, Earth Planet. Sc. Lett., 369, 260–270, doi:10.1016/j.epsl.2013.03.034, 2013. 1455

Cheng, H., Edwards, R. L., Broecker, W. S., Denton, G. H., Kong, X., Wang, Y., Zhang, R., and Wang, X.: Ice age terminations, Science, 326, 248–252, doi:10.1126/science.1177840, 2009. 1452, 1455

Denton, G. H., Anderson, R. F., Toggweiler, J. R., Edwards, R. L., Schaefer, J. M., and Putnam, A. E.: The last glacial termination, Science, 328, 1652–1656, doi:10.1126/science.1184119, 2010. 1455

Dreyfus, G. B., Parrenin, F., Lemieux-Dudon, B., Durand, G., Masson-Delmotte, V., Jouzel, J., Barnola, J.-M., Panno, L., Spahni, R., Tisserand, A., Siegenthaler, U., and Leuenberger, M.: Anomalous flow below 2700 m in the EPICA Dome C ice core detected using δ^{18}O of atmospheric oxygen measurements, Clim. Past, 3, 341–353, doi:10.5194/cp-3-341-2007, 2007. 1440, 1443, 1444, 1445, 1452, 1453, 1469

Dreyfus, G. B., Raisbeck, G. M., Parrenin, F., Jouzel, J., Guyodo, Y., Nomade, S., and Mazaud, A.: An ice core perspective on the age of the Matuyama-Brunhes boundary, Earth Planet. Sc. Lett., 274, 151–156, doi:10.1016/j.epsl.2008.07.008, 2008. 1443, 1445, 1469

Freitag, J., Kipfstuhl, S., Laepple, T., and Wilhelms, F.: Impurity-controlled densification: a new model for stratified polar firn, J. Glaciol., 59, 1163–1169, doi:10.3189/2013JoG13J042, 2013. 1442, 1451

Fujita, S., Enomoto, H., Fukui, K., Iizuka, Y., Motoyama, H., Nakazawa, F., Sugiyama, S., and Surdyk, S.: Formation and metamorphism of stratified firn at sites located under spatial vari-

ations of accumulation rate and wind speed on the East Antarctic ice divide near Dome Fuji, The Cryosphere Discuss., 6, 1205–1267, doi:10.5194/tcd-6-1205-2012, 2012. 1451

Hodell, D. A., Channell, J. E. T., Curtis, J. H., Romero, O. E., and Röhl, U.: Onset of "Hudson Strait" Heinrich events in the eastern North Atlantic at the end of the middle Pleistocene transition (~640 ka)?, Paleoceanography, 23, 4218, doi:10.1029/2008PA001591, 2008. 1455

Hörhold, M., Laepple, T., Freitag, J., Bigler, M., Fischer, H., and Kipfstuhl, S.: On the impact of impurities on the densification of polar firn, Earth Planet. Sc. Lett., 325–326, 93–99, doi:10.1016/j.epsl.2011.12.022, 2012. 1442, 1451

Huber, C., Beyerle, U., Leuenberger, M., Schwander, J., Kipfer, R., Spahni, R., Severinghaus, J. P., and Weiler, K.: Evidence for molecular size dependent gas fractionation in firn air derived from noble gases, oxygen, and nitrogen measurements, Earth Planet. Sc. Lett., 243, 61–73, doi:10.1016/j.epsl.2005.12.036, 2006. 1441

Hutterli, M. A., Schneebeli, M., Freitag, J., Kipfstuhl, J., and Rothlisberger, R.: Impact of local insolation on snow metamorphism and ice core records, in: Physics of Ice Core Records II, edited by: Hondoh, T., Hokkaido University Press, 223–232, 2010. 1442, 1450, 1451

Imbrie, J. and Imbrie, J. Z.: Modeling the climatic response to orbital variations, Science, 207, 943–953, doi:10.1126/science.207.4434.943, 1980. 1440

Jouzel, J., Waelbroeck, C., Malaize, B., Bender, M., Petit, J., Stievenard, M., Barkov, N., Barnola, J., King, T., Kotlyakov, V., Lipenkov, V., Lorius, C., Raynaud, D., Ritz, C., and Sowers, T.: Climatic interpretation of the recently extended Vostok ice records, Clim. Dynam., 12, 513–521, doi:10.1007/BF00207935, 1996. 1440

Jouzel, J., Hoffmann, G., Parrenin, F., and Waelbroeck, C.: Atmospheric oxygen 18 and sea-level changes, Quaternary Sci. Rev., 21, 307–314, doi:10.1016/S0277-3791(01)00106-8, 2002. 1440

Jouzel, J., Masson-Delmotte, V., Cattani, O., Dreyfus, G., Falourd, S., Hoffmann, G., Minster, B., Nouet, J., Barnola, J. M., Chappellaz, J., Fischer, H., Gallet, J. C., Johnsen, S., Leuenberger, M., Loulergue, L., Luethi, D., Oerter, H., Parrenin, F., Raisbeck, G., Raynaud, D., Schilt, A., Schwander, J., Selmo, E., Souchez, R., Spahni, R., Stauffer, B., Steffensen, J. P., Stenni, B., Stocker, T. F., Tison, J. L., Werner, M., and Wolff, E. W.: Orbital and millennial Antarctic climate variability over the past 800 000 years, Science, 317, 793, doi:10.1126/science.1141038, 2007. 1439, 1469, 1472

Kawamura, K., Parrenin, F., Lisiecki, L., Uemura, R., Vimeux, F., Severinghaus, J. P., Hutterli, M. A., Nakazawa, T., Aoki, S., Jouzel, J., Raymo, M. E., Matsumoto, K., Nakata, H.,

Motoyama, H., Fujita, S., Goto-Azuma, K., Fujii, Y., and Watanabe, O.: Northern Hemisphere forcing of climatic cycles in Antarctica over the past 360 000 years, Nature, 448, 912–916, doi:10.1038/nature06015, 2007. 1441, 1442, 1445, 1446, 1448, 1449, 1468, 1472

Lambert, F., Delmonte, B., Petit, J. R., Bigler, M., Kaufmann, P. R., Hutterli, M. A., Stocker, T. F., Ruth, U., Steffensen, J. P., and Maggi, V.: Dust-climate couplings over the past 800 000 years from the EPICA Dome C ice core, Nature, 452, 616–619, doi:10.1038/nature06763, 2008. 1446, 1451

Landais, A., Caillon, N., Severinghaus, J., Jouzel, J., and Masson- Delmotte, V.: Analyses isotopiques à haute précision de l'air piégé dans les glaces polaires pour la quantification des variations rapides de température: méthodes et limites, Notes des activités instrumentales de l'IPSL, 39, 2003. 1443, 1444

Landais, A., Masson-Delmotte, V., Combourieu Nebout, N., Jouzel, J., Blunier, T., Leuenberger, M., Dahl-Jensen, D., and Johnsen, S.: Millenial scale variations of the isotopic composition of atmospheric oxygen over Marine Isotopic Stage 4, Earth Planet. Sc. Lett., 258, 101–113, doi:10.1016/j.epsl.2007.03.027, 2007. 1440, 1455

Landais, A., Dreyfus, G., Capron, E., Masson-Delmotte, V., Sanchez-Goñi, M., Desprat, S., Hoffmann, G., Jouzel, J., Leuenberger, M., and Johnsen, S.: What drives the millennial and orbital variations of $\delta^{18}O_{atm}$?, Quaternary Sci. Rev., 29, 235–246, doi:10.1016/j.quascirev.2009.07.005, 2010. 1440, 1455

Landais, A., Dreyfus, G., Capron, E., Pol, K., Loutre, M. F., Raynaud, D., Lipenkov, V. Y., Arnaud, L., Masson-Delmotte, V., Paillard, D., Jouzel, J., and Leuenberger, M.: Towards orbital dating of the EPICA Dome C ice core using $\delta O_2/N_2$, Clim. Past, 8, 191–203, doi:10.5194/cp-8-191-2012, 2012. 1441, 1442, 1443, 1445, 1446, 1449, 1453, 1458, 1468, 1469, 1475

Landais, A., Dreyfus, G., Capron, E., Jouzel, J., Masson-Delmotte, V., Roche, D., Prie, F., Caillon, N., Chappellaz, J., Leuenberger, M., Lourantou, A., Parrenin, F., Raynaud, D., and Teste, G.: Two-phase change in CO_2, Antarctic temperature and global climate during Termination II, Nat. Geosci., 6, 1062–1065, doi:10.1038/ngeo1985, 2013. 1440, 1443, 1445, 1452, 1455, 1469, 1472

Laskar, J., Robutel, P., Joutel, F., Gastineau, M., Correia, A. C. M., and Levrard, B.: A long-term numerical solution for the insolation quantities of the Earth, Astron. Astrophys., 428, 261–285, doi:10.1051/0004-6361:20041335, 2004. 1469

Lefebvre, E., Arnaud, L., Ekaykin, A., Lipenkov, V., Picard, G., and Petit, J.-R.: Snow temperature measurements at Vostok station from an autonomous recording system (TAUTO): preliminary results from the first year operation, Ice and Snow, 4, 138–145, 2012. 1449, 1468

Lemieux-Dudon, B., Blayo, E., Petit, J.-R., Waelbroeck, C., Svensson, A., Ritz, C., Barnola, J.-M., Narcisi, B. M., and Parrenin, F.: Consistent dating for Antarctic and Greenland ice cores, Quaternary Sci. Rev., 29, 8–20, doi:10.1016/j.quascirev.2009.11.010, 2010. 1439

Leuenberger, M. C.: Modeling the signal transfer of seawater $\delta^{18}O$ to the $\delta^{18}O$ of atmospheric oxygen using a diagnostic box model for the terrestrial and marine biosphere, J. Geophys. Res., 102, 26841–26850, doi:10.1029/97JC00160, 1997. 1440

Lipenkov, V. Y., Raynaud, D., Loutre, M. F., and Duval, P.: On the potential of coupling air content and O_2/N_2 from trapped air for establishing an ice core chronology tuned on local insolation, Quaternary Sci. Rev., 30, 3280–3289, doi:10.1016/j.quascirev.2011.07.013, 2011. 1441, 1442

Loulergue, L., Schilt, A., Spahni, R., Masson-Delmotte, V., Blunier, T., Lemieux, B., Barnola, J.-M., Raynaud, D., Stocker, T. F., and Chappellaz, J.: Orbital and millennial-scale features of atmospheric CH_4 over the past 800,000 years, Nature, 453, 383–386, doi:10.1038/nature06950, 2008. 1439

Lüthi, D., Le Floch, M., Bereiter, B., Blunier, T., Barnola, J.-M., Siegenthaler, U., Raynaud, D., Jouzel, J., Fischer, H., Kawamura, K., and Stocker, T. F.: High-resolution carbon dioxide concentration record 650 000–800 000 years before present, Nature, 453, 379–382, doi:10.1038/nature06949, 2008. 1439

Malaizé, B., Paillard, D., Jouzel, J., and Raynaud, D.: The Dole effect over the last two glacial-interglacial cycles, J. Geophys. Res., 104, 14199–14208, doi:10.1029/1999JD900116, 1999. 1440

Marzin, C., Kallel, N., Kageyama, M., Duplessy, J.-C., and Braconnot, P.: Glacial fluctuations of the Indian monsoon and their relationship with North Atlantic climate: new data and modelling experiments, Clim. Past, 9, 2135–2151, doi:10.5194/cp-9-2135-2013, 2013. 1455

Masson-Delmotte, V., Stenni, B., Pol, K., Braconnot, P., Cattani, O., Falourd, S., Kageyama, M., Jouzel, J., Landais, A., Minster, B., Barnola, J. M., Chappellaz, J., Krinner, G., Johnsen, S., Röthlisberger, R., Hansen, J., Mikolajewicz, U., and Otto-Bliesner, B.: EPICA Dome C record of glacial and interglacial intensities, Quaternary Sci. Rev., 29, 113–128, doi:10.1016/j.quascirev.2009.09.030, 2010. 1446

Masson-Delmotte, V., Buiron, D., Ekaykin, A., Frezzotti, M., Gallée, H., Jouzel, J., Krinner, G., Landais, A., Motoyama, H., Oerter, H., Pol, K., Pollard, D., Ritz, C., Schlosser, E., Sime, L. C., Sodemann, H., Stenni, B., Uemura, R., and Vimeux, F.: A comparison of the present and last interglacial periods in six Antarctic ice cores, Clim. Past, 7, 397–423, doi:10.5194/cp-7-397-2011, 2011. 1447, 1468

Meese, D. A., Gow, A. J., Grootes, P., Stuiver, M., Mayewski, P. A., Zielinski, G. A., Ram, M., Taylor, K. C., and Waddington, E. D.: The accumulation record from the GISP2 core as an indicator of climate change throughout the Holocene, Science, 266, 1680–1682, doi:10.1126/science.266.5191.1680, 1994. 1452

Paillard, D., Labeyrie, L., and Yiou, P.: Macintosh Program performs time-series analysis, EOS T. Am. Geophys. Un., 77, 379–379, doi:10.1029/96EO00259, 1996. 1469, 1471

Parrenin, F., Jouzel, J., Waelbroeck, C., Ritz, C., and Barnola, J.-M.: Dating the Vostok ice core by an inverse method, J. Geophys. Res., 106, 31837–31852, doi:10.1029/2001JD900245, 2001. 1439

Parrenin, F., Rémy, F., Ritz, C., Siegert, M. J., and Jouzel, J.: New modeling of the Vostok ice flow line and implication for the glaciological chronology of the Vostok ice core, J. Geophys. Res.-Atmos., 109, D20102, doi:10.1029/2004JD004561, 2004. 1439, 1452

Parrenin, F., Barnola, J.-M., Beer, J., Blunier, T., Castellano, E., Chappellaz, J., Dreyfus, G., Fischer, H., Fujita, S., Jouzel, J., Kawamura, K., Lemieux-Dudon, B., Loulergue, L., Masson-Delmotte, V., Narcisi, B., Petit, J.-R., Raisbeck, G., Raynaud, D., Ruth, U., Schwander, J., Severi, M., Spahni, R., Steffensen, J. P., Svensson, A., Udisti, R., Waelbroeck, C., and Wolff, E.: The EDC3 chronology for the EPICA Dome C ice core, Clim. Past, 3, 485–497, doi:10.5194/cp-3-485-2007, 2007. 1439, 1440, 1452, 1459

Petit, J. R., Jouzel, J., Raynaud, D., Barkov, N. I., Barnola, J.-M., Basile, I., Bender, M., Chappellaz, J., Davis, M., Delaygue, G., Delmotte, M., Kotlyakov, V. M., Legrand, M., Lipenkov, V. Y., Lorius, C., Pépin, L., Ritz, C., Saltzman, E., and Stievenard, M.: Climate and atmospheric history of the past 420 000 years from the Vostok ice core, Antarctica, Nature, 399, 429–436, doi:10.1038/20859, 1999. 1440, 1442, 1445, 1451, 1452, 1472

Picard, G., Domine, F., Krinner, G., Arnaud, L., and Lefebvre, E.: Inhibition of the positive snow-albedo feedback by precipitation in interior Antarctica, Nat. Clim. Change, 2, 795–798, doi:10.1038/nclimate1590, 2012. 1441, 1450

Raynaud, D., Lipenkov, V., Lemieux-Dudon, B., Duval, P., Loutre, M.-F., and Lhomme, N.: The local insolation signature of air content in Antarctic ice. A new step toward an absolute dating

of ice records, Earth Planet. Sc. Lett., 261, 337–349, doi:10.1016/j.epsl.2007.06.025, 2007. 1441

Schaaf, C. B., Wang, Z., and Strahler, A. H.: Commentary on Wang and Zender – MODIS snow albedo bias at high solar zenith angles relative to theory and to in situ observations in Greenland, Remote Sens. Environ., 115, 1296–1300, doi:10.1016/j.rse.2011.01.002, 2011. 1450

Severinghaus, J. P. and Battle, M. O.: Fractionation of gases in polar ice during bubble close-off: new constraints from firn air Ne, Kr and Xe observations, Earth Planet. Sc. Lett., 244, 474–500, doi:10.1016/j.epsl.2006.01.032, 2006. 1441

Severinghaus, J. P., Grachev, A., and Battle, M.: Thermal fractionation of air in polar firn by seasonal temperature gradients, Geochem. Geophy. Geosy., 2, 2000GC000146, doi:10.1029/2000GC000146, 2001. 1444

Severinghaus, J. P., Beaudette, R., Headly, M. A., Taylor, K., and Brook, E. J.: Oxygen-18 of O_2 records the impact of abrupt climate change on the terrestrial biosphere, Science, 324, 1431, doi:10.1126/science.1169473, 2009. 1440, 1455

Shackleton, N. J., Hall, M. A., and Vincent, E.: Phase relationships between millennial-scale events 64 000–24 000 years ago, Paleoceanography, 15, 565–569, doi:10.1029/2000PA000513, 2000. 1440

Sime, L. C., Wolff, E. W., Oliver, K. I. C., and Tindall, J. C.: Evidence for warmer interglacials in East Antarctic ice cores, Nature, 462, 342–345, doi:10.1038/nature08564, 2009. 1447

Sowers, T., Bender, M., and Raynaud, D.: Elemental and isotopic composition of occluded O_2 and N_2 in polar ice, J. Geophys. Res., 94, 5137–5150, doi:10.1029/JD094iD04p05137, 1989. 1443

Spahni, R., Chappellaz, J., Stocker, T. F., Loulergue, L., Hausammann, G., Kawamura, K., Flückiger, J., Schwander, J., Raynaud, D., Masson-Delmotte, V., and Jouzel, J.: Atmospheric methane and nitrous oxide of the late pleistocene from Antarctic ice cores, Science, 310, 1317–1321, doi:10.1126/science.1120132, 2005. 1439

Stenni, B., Masson-Delmotte, V., Selmo, E., Oerter, H., Meyer, H., Röthlisberger, R., Jouzel, J., Cattani, O., Falourd, S., Fischer, H., Hoffmann, G., Iacumin, P., Johnsen, S. J., Minster, B., and Udisti, R.: The deuterium excess records of EPICA Dome C and Dronning Maud Land ice cores (East Antarctica), Quaternary Sci. Rev., 29, 146–159, doi:10.1016/j.quascirev.2009.10.009, 2010. 1447

Suwa, M. and Bender, M. L.: O_2/N_2 ratios of occluded air in the GISP2 ice core, J. Geophys. Res.-Atmos., 113, D11119, doi:10.1029/2007JD009589, 2008a. 1448

Suwa, M. and Bender, M. L.: Chronology of the Vostok ice core constrained by O_2/N_2 ratios of occluded air, and its implication for the Vostok climate records, Quaternary Sci. Rev., 27, 1093–1106, doi:10.1016/j.quascirev.2008.02.017, 2008b. 1442, 1472

Svensson, A., Andersen, K. K., Bigler, M., Clausen, H. B., Dahl-Jensen, D., Davies, S. M., Johnsen, S. J., Muscheler, R., Parrenin, F., Rasmussen, S. O., Röthlisberger, R., Seierstad, I., Steffensen, J. P., and Vinther, B. M.: A 60 000 year Greenland stratigraphic ice core chronology, Clim. Past, 4, 47–57, doi:10.5194/cp-4-47-2008, 2008. 1439

Town, M. S., Waddington, E. D., Walden, V. P., and Warren, S. G.: Temperatures, heating rates and vapour pressures in near-surface snow at the South Pole, J. Glaciol., 54, 487–498, doi:10.3189/002214308785837075, 2008. 1441

Uemura, R., Masson-Delmotte, V., Jouzel, J., Landais, A., Motoyama, H., and Stenni, B.: Ranges of moisture-source temperature estimated from Antarctic ice cores stable isotope records over glacial–interglacial cycles, Clim. Past, 8, 1109–1125, doi:10.5194/cp-8-1109-2012, 2012. 1447

Veres, D., Bazin, L., Landais, A., Toyé Mahamadou Kele, H., Lemieux-Dudon, B., Parrenin, F., Martinerie, P., Blayo, E., Blunier, T., Capron, E., Chappellaz, J., Rasmussen, S. O., Severi, M., Svensson, A., Vinther, B., and Wolff, E. W.: The Antarctic ice core chronology (AICC2012): an optimized multi-parameter and multi-site dating approach for the last 120 thousand years, Clim. Past, 9, 1733–1748, doi:10.5194/cp-9-1733-2013, 2013. 1439, 1469, 1472

Waelbroeck, C., Frank, N., Jouzel, J., Parrenin, F., Masson-Delmotte, V., and Genty, D.: Transferring radiometric dating of the last interglacial sea level high stand to marine and ice core records, Earth Planet. Sc. Lett., 265, 183–194, doi:10.1016/j.epsl.2007.10.006, 2008. 1452

Wang, Y., Cheng, H., Edwards, R. L., Kong, X., Shao, X., Chen, S., Wu, J., Jiang, X., Wang, X., and An, Z.: Millennial- and orbital-scale changes in the East Asian monsoon over the past 224 000 years, Nature, 451, 1090–1093, doi:10.1038/nature06692, 2008. 1440, 1454, 1455

Wang, Y. J., Cheng, H., Edwards, R. L., An, Z. S., Wu, J. Y., Shen, C.-C., and Dorale, J. A.: A high-resolution absolute-dated late pleistocene monsoon record from Hulu cave, China, Science, 294, 2345–2348, doi:10.1126/science.1064618, 2001. 1455

Table 1. Summary of present day local conditions at Vostok, Dome F and EDC (Masson-Delmotte et al., 2011; Kawamura et al., 2007; Landais et al., 2012; Lefebvre et al., 2012, this study).

Site	Lat. Long.	Elevation (m a.s.l.)	Nb of days after 21 December for max temp.	Mean albedo	Accu. rate (cm weq yr^{-1})	Mean annual temp. (°C)	10 m wind speed ($m\,s^{-1}$)
Vostok	78°28′ S 106°48′ E	3488	10	0.83	2.15	−55.3	4.2
Dome F	77° 19′ S 39°40′ E	3810	0	0.80	2.3	−57.0	2.9
EDC	75°06′ S 123°21′ E	3233	5–20	0.83	∼ 2.5	−54.5	5.4

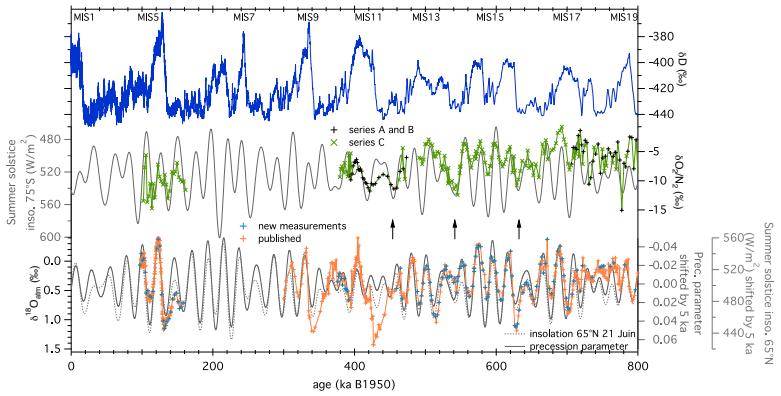

Figure 1. Top: EDC ice core record of water stable isotopes (δD, Jouzel et al., 2007). Middle: EDC record of $\delta O_2/N_2$ (black: Landais et al., 2012, green: this study) and local summer solstice insolation (grey, reversed axis). Bottom: EDC record of $\delta^{18}O_{atm}$ (reversed vertical scale) (orange: Dreyfus et al., 2007, 2008; Landais et al., 2013, blue: this study), precession parameter (grey, reversed axis) and 65° N summer solstice insolation (dashed grey) both shifted by 5 ka. All EDC records are presented on the AICC2012 chronology (Bazin et al., 2013; Veres et al., 2013). The orbital parameters are calculated using the Laskar et al. (2004) solution, with the Analyseries software (Paillard et al., 1996). Arrows mark the position of $\delta O_2/N_2$ minima characterizing the 100 ka periodicity.

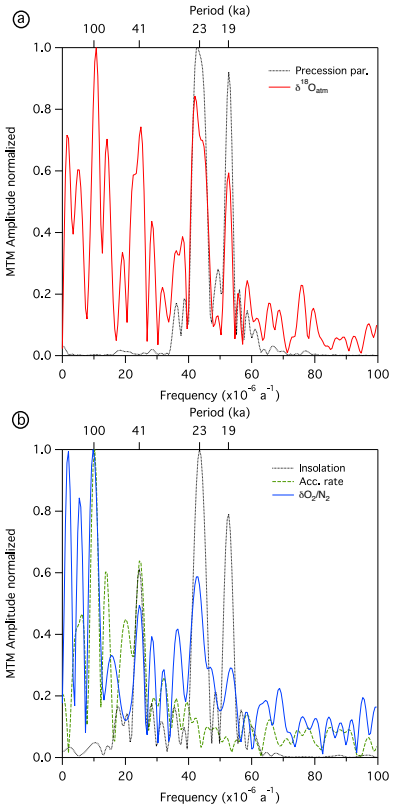

Figure 2. Spectral analysis using the Multi–Taper Method with an interpolation step of 1 ka, obtained with Analyseries (Paillard et al., 1996). Amplitudes are normalized by the maximum value of each serie. **(a)** $\delta^{18}O_{atm}$ between 300–800 ka (red) presented with the precession parameter (grey). **(b)** $\delta O_2/N_2$ between 380–800 ka (blue) presented with local summer solstice insolation (grey) and AICC2012 accumulation rate (dashed green). Periods corresponding to significant peaks (F test > 90 %) are indicated on the upper horizontal axis.

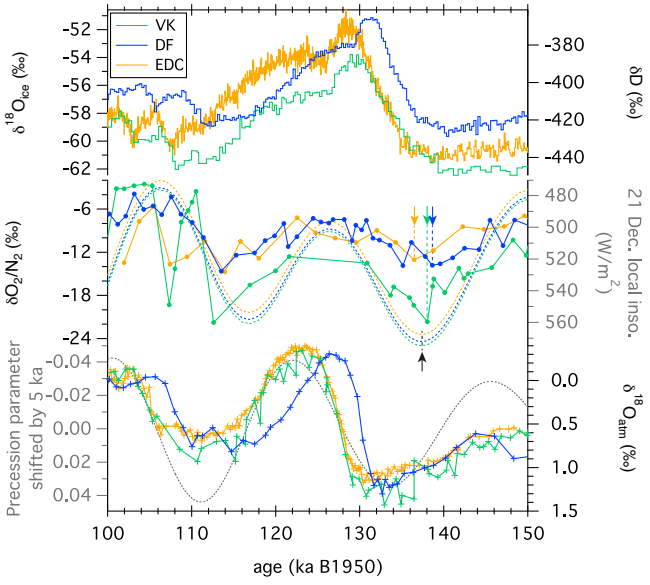

Figure 3. Inter-comparison of Vostok (green), Dome F (blue) and EDC (yellow) data covering MIS 5. Vostok and EDC data are presented on AICC2012 (Bazin et al., 2013; Veres et al., 2013) and Dome F on the DFO-2006 chronology (Kawamura et al., 2007). Top: water isotopic composition (Vostok $\delta^{18}O_{ice}$: Petit et al. (1999), Dome F $\delta^{18}O_{ice}$: Kawamura et al. (2007), EDC δD: Jouzel et al., 2007). Middle: $\delta O_2/N_2$ records and local summer solstice insolation at each site (Suwa and Bender, 2008b; Kawamura et al., 2007, this study). Bottom: $\delta^{18}O_{atm}$ and precession parameter shifted by 5 ka (Suwa and Bender, 2008b; Kawamura et al., 2007; Landais et al., 2013, this study). The arrows mark the different position of insolation maxima (black) and $\delta O_2/N_2$ minima (respective colors) before Termination II.

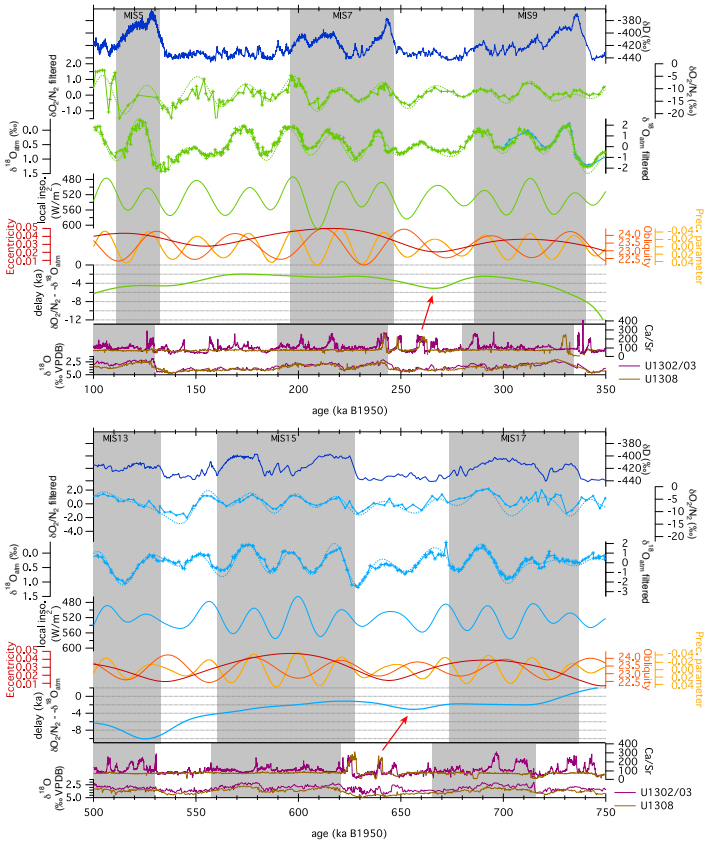

1473

Figure 4. Evolution of the phase delay between $\delta O_2/N_2$ and $\delta^{18}O_{atm}$ between 100–350 ka (top) and 500–750 ka (bottom). The Vostok data are represented in green and EDC data in light blue. The filtered data are first normalized (minus the mean and divided by the SD) and then filtered between 15–100 ka. From top to bottom: δD of EDC, $\delta^{18}O_{atm}$ on reversed axis (line with markers for raw data and dashed line for filtered data), $\delta O_2/N_2$ (line with markers for raw data and dashed line for filtered data), local summer solstice insolation of each sites (reversed axis), orbital parameters: precession (yellow, reversed axis), obliquity (orange) and eccentricity (red), phase delay calculated between $\delta O_2/N_2$ and $\delta^{18}O_{atm}$, Ca/Sr ratio of marine cores U1302/03 (purple) and U1308 (brown), $\delta^{18}O$ planktonic for U1302/03 (purple) and $\delta^{18}O$ benthic for U1308 (brown). Ice cores data are presented on the AICC2012 chronology. Marine data are presented on their respective core chronology. The grey rectangles mark the MIS intervals in both archives. The red arrows show the correspondence between the Heinrich-like events in the Ca/Sr records with the maximum delay of $\delta O_2/N_2$–$\delta^{18}O_{atm}$.

Discussion Paper | Discussion Paper | Discussion Paper | Discussion Paper |

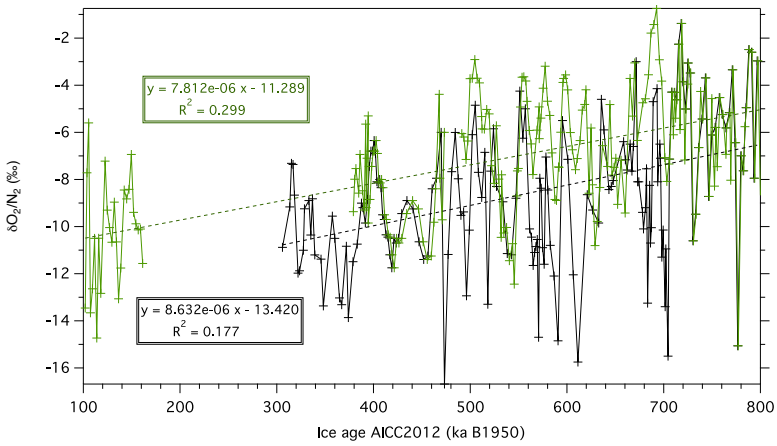

Figure A1. Comparison of the composite $\delta O_2/N_2$ record of Landais et al. (2012) (black) and the new $\delta O_2/N_2$ record measured on well-conserved ice (green). Both are presented on the AICC2012 chronology.

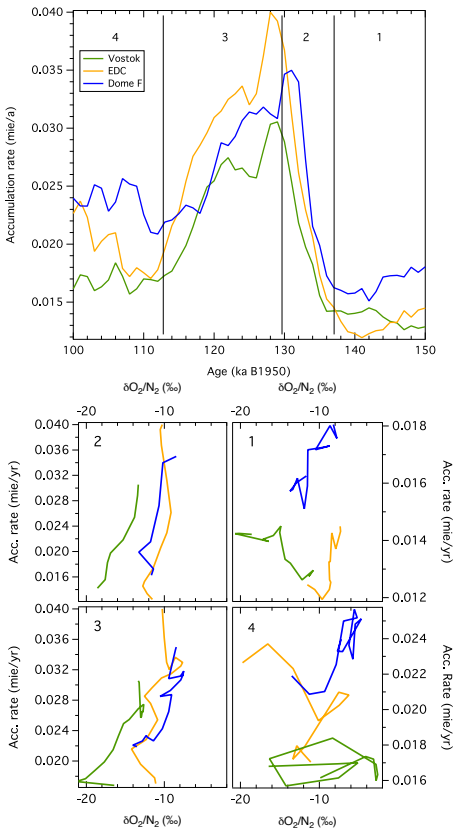

Figure B1. (a) Comparison of accumulation rate of EDC, Vostok and Dome F. Vertical bars and numbers on top delimit approximately the four time intervals (numbered 1 to 4) for which accumulation rates are compared with $\delta O_2/N_2$ values for our three sites. **(b)** Plots of $\delta O_2/N_2$ vs. accumulation rate for the 4 periods delimited on **(a)**.

5.3 Comparaison des différents marqueurs orbitaux sur 800 ka

Les nouvelles mesures de $\delta O_2/N_2$ et $\delta^{18}O_{atm}$ réalisées sur de la glace bien conservée d'EDC ont permis de compléter les enregistrements existants. Nous avons maintenant à disposition un enregistrement de $\delta O_2/N_2$ entre 380–800 ka mesuré sur de la glace conservée à -50°C, présentant des variations plus marquées et mieux identifiables que pour la courbe composite de Landais et al. [2012]. Grâce à cette nouvelle courbe de $\delta O_2/N_2$, nous sommes en mesure de raffiner la synchronisation orbitale effectuée pour contraindre la chronologie AICC2012. Lors de la construction d'AICC2012, trois types de marqueurs orbitaux ($\delta O_2/N_2$, $\delta^{18}O_{atm}$ et teneur en air) ont été utilisés pour contraindre la chronologie avant le dernier cycle glaciaire–interglaciaire. Afin de vérifier la cohérence de ces marqueurs orbitaux, nous avons produit trois chronologies purement orbitales à l'aide de Datice, en ne considérant seulement que le $\delta O_2/N_2$, le $\delta^{18}O_{atm}$ ou la teneur en air. Nous avons comparé ces chronologies pour la carotte de Vostok, seul forage possédant des enregistrements de ces trois traceurs couvrant les derniers 400 ka. Nous avons montré que les chronologies orbitales de chacun des marqueurs présentaient des différences d'âge de l'ordre de 2 ka. Cette différence peut provenir du choix des cibles orbitales, ainsi que de l'estimation de la LIDIE pour les différences entre marqueurs glace et gaz [Bazin et al., 2013]. La comparaison n'a pas pu être effectuée sur EDC car les enregistrements de teneur en air et de $\delta^{18}O_{atm}/\delta O_2/N_2$ disponibles alors ne couvraient pas les mêmes périodes [Raynaud et al., 2007, 0–440 ka pour la teneur en air,].

Depuis cette étude, la teneur en air (V) entre 440 et 800 ka a été mesurée à EDC [Raynaud et al., in prep] et j'ai réalisé les nouvelles mesures de $\delta O_2/N_2$ et $\delta^{18}O_{atm}$ sur de la glace bien conservée d'EDC. Ainsi, il est maintenant possible de réaliser le même test que précédemment sur les derniers 800 ka.

Sur la figure 5.3 sont présentées les nouvelles mesures réalisées au cours de cette thèse sur de la glace bien conservée, ainsi que l'enregistrement complet de teneur en air [Raynaud et al., 2007, in prep]. La teneur en air va être dépendante de la température et la pression au niveau de la profondeur de fermeture des pores. Il a été montré que l'insolation locale était le principal facteur influençant les variations à long terme de la teneur en air mesurées à Vostok et à EDC entre 0–440 ka [Raynaud et al., 2007; Lipenkov et al., 2011]. Raynaud et al. [2007] ont voulu s'inspirer de la méthode de synchronisation orbitale du $\delta O_2/N_2$ pour utiliser la teneur en air comme outil de datation. Cependant, comme la teneur en air présente également un

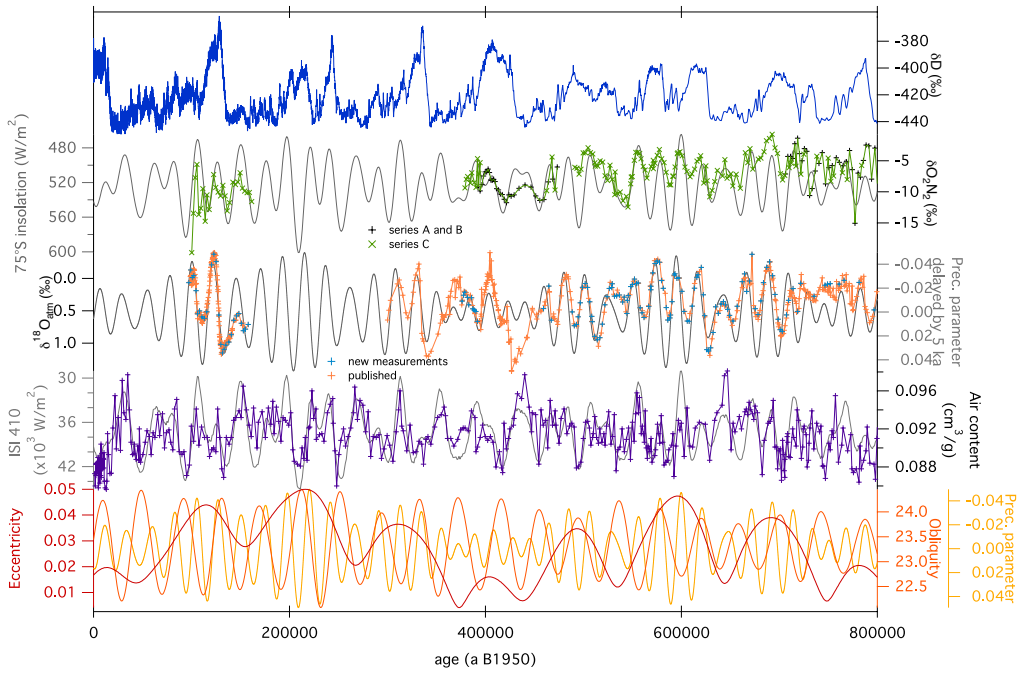

FIGURE 5.3 – Nouvelles mesures de $\delta O_2/N_2$, $\delta^{18}O_{atm}$ et teneur en air (V) pour la carotte d'EDC. De haut en bas : composition isotopique de la glace ; insolation locale au solstice d'été (gris) et $\delta O_2/N_2$: les séries A et B proviennent de Landais et al. [2012], la série C correspond aux mesures réalisées au cours de cette thèse ; précession retardée de 5 ka (gris) et $\delta^{18}O_{atm}$ nouvelles mesures (bleues) et données déjà publiées [Dreyfus et al., 2007, 2008; Bazin et al., 2013; Landais et al., 2013, orange] ; ISI410 (gris) et mesures de teneur en air [Raynaud et al., 2007, in prep, violet] ; paramètres orbitaux : excentricité (rouge), obliquité (orange) et précession (jaune).

fort signal dans la bande spectrale associée à l'obliquité, les auteurs ont avancé l'idée que la teneur en air répondrait à un signal d'insolation intégrée au–delà d'un certain seuil. Dans le but d'utiliser ce traceur à des fins de datations, les auteurs ont donc synchronisé les variations de la teneur en air avec les variations d'une courbe d'insolation locale intégrée (ISI). Les courbes d'ISI sont choisies pour avoir les mêmes propriétés spectrales que la teneur en air (respect de l'amplitude relative entre l'obliquité et la precession). Pour ce faire, ils ont utilisé la méthode des ondelettes afin de calculer un retard entre les courbes d'ISI et de teneur en air filtrées entre 15–46 ka.

Les nouvelles mesures de $\delta^{18}O_{atm}$ ont permis d'améliorer la résolution de l'enregistrement de Dreyfus et al. [2007] entre 300–800 ka et Landais et al. [2013] sur le MIS 5. Il n'y a pas de changements de l'allure de la courbe, j'ai donc conservé les marqueurs de $\delta^{18}O_{atm}$ utilisés pour contraindre AICC2012, avec une incertitude de $\pm$6 ka [Bazin et al., 2013]. Pour le $\delta O_2/N_2$, le nouvel enregistrement, composé seulement des mesures effectuées sur de la glace bien conservée, couvre le MIS 5 et entre 380–800 ka, avec un trou de 20 ka entre 470–490 ka. A partir de ce nouveau profil, j'ai été en mesure de procéder à une nouvelle synchronisation orbitale avec la courbe d'insolation locale au solstice d'été (figure 5.4). Pour ce faire, j'ai associé les mi–pentes des deux enregistrements seulement aux périodes où les variations sont bien marquées. Au fond de la carotte, la synchronisation orbitale peut être multiple (figure 5.5) car les courbes de $\delta O_2/N_2$ et d'insolation ne se ressemblent pas vraiment, rendant plus incertaine cette méthode de datation. Sur l'ensemble de l'enregistrement de $\delta O_2/N_2$ j'ai été en mesure de déduire 19 nouveaux marqueurs d'âge glace, venant remplacer ceux utilisés lors de la construction d'AICC2012 déduits de la courbe composite de Landais et al. [2012], avec une incertitude estimée à $\pm$4 ka. Pour la teneur en air, j'ai déduit les marqueurs à partir de la synchronisation de ses variations (mi-pentes) avec celles de la courbe d'insolation locale d'été intégrée ISI410. Les points ont seulement été considérés au niveau des périodes où les deux enregistrements se ressemblent. En parallèle, j'ai utilisé la méthode de Raynaud et al. [2007], calcul du retard entre les deux enregistrements filtrés entre 15–46 ka, pour estimer l'incertitude sur la détermination de ces marqueurs. Ainsi, j'ai été en mesure de déduire 25 nouvelles contraintes d'âge présentant une incertitude comprise entre 2.2 et 7.3 ka entre 0–800 ka.

Pour réaliser le test de complémentarité, j'ai réalisé 3 expériences en utilisant Datice avec pour chaque cas : tous les liens stratigraphiques et marqueurs d'âge absolus des 5 carottes de glace utilisés pour AICC2012 et toutes les contraintes

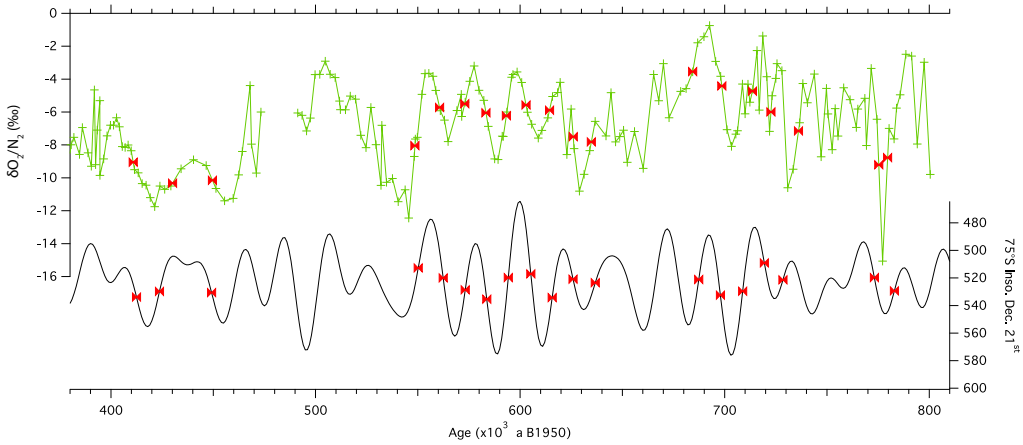

FIGURE 5.4 – Synchronisation du nouvel enregistrement de $\delta O_2/N_2$ avec l'insolation locale au solstice d'été à EDC entre 380 et 800 ka. Les figurés rouges indiquent la position des marqueurs déduits de la synchronisation orbitale.

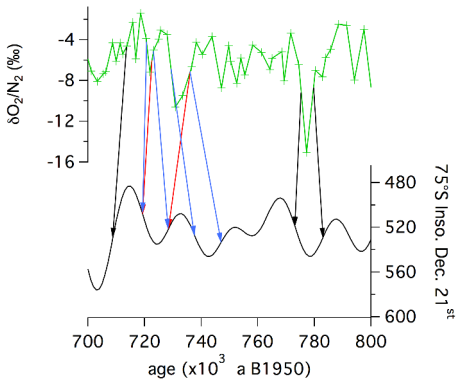

FIGURE 5.5 – Synchronisation du $\delta O_2/N_2$ avec l'insolation locale au solstice d'été à EDC entre 700 et 800 ka. Les flèches noires indiquent les points où l'identification des mi-pentes dans les deux enregistrements est claire. Les flèches rouges et bleues correspondent aux deux possibilités de synchronisation entre les deux courbes. Pour le test présenté dans cette section j'ai retenu la synchronisation associée aux flèches rouges.

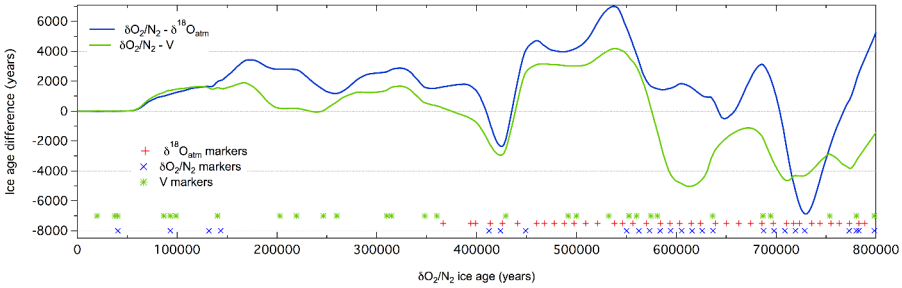

FIGURE 5.6 – Comparaison des différentes chronologies orbitales pour EDC. Différence entre les chronologies glace du $\delta O_2/N_2$ et $\delta^{18}O_{atm}$ (bleu) ainsi que $\delta O_2/N_2$ et teneur en air (vert). Au bas de la figure est indiquée la position des différents marqueurs : les croix bleues pour le $\delta O_2/N_2$, les astérisques vertes pour la teneur en air (V) et les plus rouges pour le $\delta^{18}O_{atm}$.

d'âge déduites à partir de l'un de nos 3 traceurs ($\delta^{18}O_{atm}$, $\delta O_2/N_2$ ou teneur en air) pour Vostok et EDC. J'ai donc obtenu 3 échelles d'âge glace purement orbitales : une à partir du $\delta^{18}O_{atm}$, une basée sur le $\delta O_2/N_2$ et la troisième sur la teneur en air. La comparaison de ces 3 chronologies orbitales est présentée sur la figure 5.6 au travers des différences $\delta O_2/N_2$–$\delta^{18}O_{atm}$ et $\delta O_2/N_2$–V. La comparaison entre les chronologies montre des variations allant jusqu'à ± 7 ka dans le cas de $\delta O_2/N_2$–$\delta^{18}O_{atm}$ et comprises entre $-5/+4$ ka pour $\delta O_2/N_2$–V. Les variations importantes entre les chronologies $\delta O_2/N_2$–$\delta^{18}O_{atm}$ sont observées aux périodes où il n'y a pas de marqueurs de $\delta O_2/N_2$ et entre 700–800 ka. Cette dernière correspond à un minimum d'excentricité et est associée à une synchronisation orbitale plus incertaine à cause de la mauvaise ressemblance entre nos enregistrements et leurs cibles. Pour la différence $\delta O_2/N_2$–V, les variations les plus importantes surviennent lorsque nous sommes en présence de marqueurs de $\delta O_2/N_2$ mais pas de teneur en air. Cela traduit donc un retour vers la datation d'ébauche dans le cas de la chronologie teneur en air.

Les deux courbes de différence ont un comportement similaire jusqu'à 600 ka. Avant cela, les différences s'expliquent par le manque de marqueurs déduits de l'un des traceurs et par la non ressemblance entre ces derniers et leurs cibles orbitales. Ainsi, il apparait raisonnable de combiner les trois types de marqueurs orbitaux ensembles sur les derniers 700 ka, en respectant leurs incertitudes respectives. Avant 700 ka, la datation orbitale reste très incertaine pour les raisons évoquées précédemment (minimum d'excentricité).

5.4 Conclusions et perspectives

Au travers de ce chapitre nous avons présenté les nouvelles mesures de $\delta O_2/N_2$ et $\delta^{18}O_{atm}$ réalisées sur de la glace bien conservée de la carotte EDC au MIS 5 et entre 380–800 ka. Nous avons maintenant à disposition un enregistrement de référence de $\delta O_2/N_2$ entre 380–800 ka présentant une résolution moyenne de 2.35 ka. Cet enregistrement confirme la décroissance du $\delta O_2/N_2$ déjà observée pour la courbe composite de Landais et al. [2012]. L'analyse spectrale du $\delta O_2/N_2$ entre 380–800 ka montre un pic significatif à 100 ka, correspondant à la période caractéristique de l'excentricité et/ou des variations glaciaire–interglaciaire.

Grâce aux mesures couvrant le MIS 5 à EDC, nous avons eu la possibilité de réaliser une comparaison multi-traceurs (composition isotopique de la glace, $\delta O_2/N_2$ et $\delta^{18}O_{atm}$) pour Vostok, Dôme F et EDC. Il apparaît des différences significatives entre les différents sites qui ne peuvent pas être expliquées par les différences de résolution des enregistrements ou bien les corrections appliquées aux $\delta O_2/N_2$ de Vostok et Dôme F. L'explication la plus probable pour ces différences semble être l'influence des paramètres locaux sur le $\delta O_2/N_2$ (figure 5.7). Ceci semble particulièrement important aux périodes de faible excentricité où les variations d'insolation locale ne sont pas clairement retrouvées dans l'enregistrement de $\delta O_2/N_2$. En conséquence, cette méthode de datation orbitale ne devrait pas être utilisée en période de faible excentricité.

L'étude du retard entre le $\delta O_2/N_2$ et le $\delta^{18}O_{atm}$au cours des derniers 800 ka grâce aux données de Vostok et EDC a mis en évidence un retard variable entre le $\delta^{18}O_{atm}$ et la précession. Notamment, les valeurs minimales de ce retard ont été observées au cours des MIS 6–7, la fin du MIS 9, aux MIS 15 et 17. Ces périodes sont associées à une forte excentricité et à un volume de glace intermédiaire. A l'inverse, des retards maximaux ont été observés au MIS 8 et 16. La confrontation de ces résultats avec un traceur des évènements de Heinrich en Atlantique Nord, de même que les observations faites sur les Terminaisons I et II dans la littérature nous ont permis de mettre en évidence que ces périodes étaient associées à des évènements de Heinrich. Ainsi, nous observons un retard plus important entre le $\delta^{18}O_{atm}$ et la précession lorsque nous sommes en présence d'un évènement de Heinrich.

Pour finir, les nouveaux enregistrements de $\delta O_2/N_2$ et $\delta^{18}O_{atm}$ couplés aux mesures de teneur en air à EDC sur les derniers 800 ka nous ont permis de tester la cohérence de ces trois méthodes de datation orbitale. Il apparaît que ces trois marqueurs orbitaux tendent à produire des chronologies cohérentes, mais que leur utilisation est compromise avant 700 ka car la synchronisation orbitale du $\delta O_2/N_2$, du $\delta^{18}O_{atm}$ et de la teneur en air est rendue difficile à cette période. En conséquence,

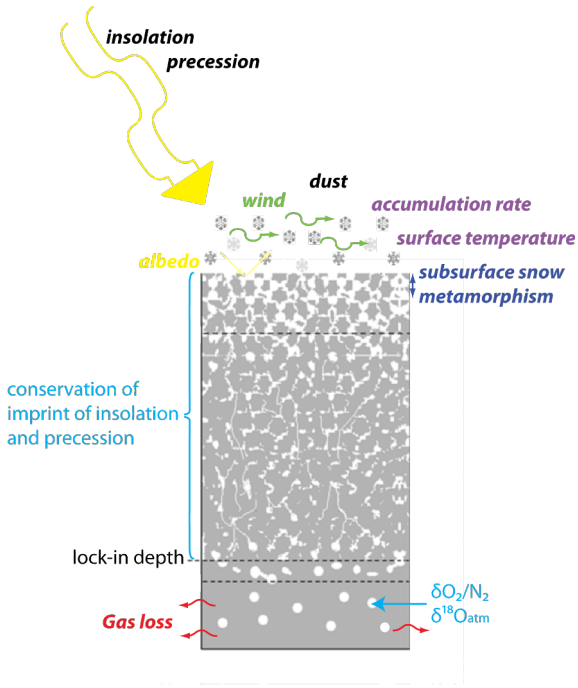

FIGURE 5.7 – Schéma récapitulatif des différentes influences pouvant affecter le $\delta O_2/N_2$ et le $\delta^{18}O_{atm}$mesurés dans l'air piégé dans la glace.

il est possible de combiner les trois types de marqueurs orbitaux lors d'un exercice de datation sur les dernier 700 ka. Avant cela, de nouvelles mesures et études sont nécessaires pour trouver l'origine des différences observées entre nos trois traceurs et leurs cibles orbitales.

Afin de mieux comprendre les différentes influences possibles sur le $\delta O_2/N_2$, il est nécessaire d'améliorer nos connaissances sur les processus de surface affectant le métamorphisme de la neige. De même, la raison pour laquelle l'empreinte de l'insolation sur le $\delta O_2/N_2$ se conserve au cours de la densification du névé reste encore inexpliquée. Pour répondre à ces questions, il est nécessaire de coupler mesures sur le terrain et modélisation du névé. Les profils de $\delta O_2/N_2$ et $\delta^{18}O_{atm}$ restent encore incomplets. Afin de compléter les enregistrements existants, il est nécessaire de mesurer la composition isotopique de l'air piégé dans la glace de la carotte EDC entre 160–380 ka et 470–490 ka. Ces mesures permettraient de définir de nouveaux marqueurs d'âge orbitaux pour EDC dans le but de mieux contraindre ses échelles d'âge gaz et glace. De plus, augmenter la résolution des enregistrements existants au moment des périodes de faible excentricité pourrait permettre de mieux comprendre pourquoi le $\delta O_2/N_2$ et le $\delta^{18}O_{atm}$ ne ressemblent plus à leurs cibles orbitales. Il est nécessaire d'établir un critère objectif afin de déterminer les périodes où la synchro-

nisation orbitale peut être utilisée pour contraindre les chronologies des carottes de glace (par example une valeur seuil pour la corrélation entre les enregistrements). Les résultats présentés dans ce chapitre sont à prendre en compte pour le prochain exercice de datation cohérente carottes de glace.

Conclusions et Perspectives

5.5 Conclusions

Le but de ce travail de thèse était d'améliorer les chronologies pour les carottes de glace. Pour ce faire, j'ai réalisé des nouvelles mesures de la composition isotopique de l'air piégé dans la glace, effectué de nombreux tests et participé à l'amélioration de l'outil Datice.

Le premier résultat important de cette thèse a été la production de la nouvelle chronologie commune d'Antarctique AICC2012. Cette chronologie, commune aux carottes de glace d'EDC, Vostok, EDML, TALDICE et NGRIP a nécessité l'amélioration de plusieurs paramètres comparé à la première application de Datice. Tout d'abord, il a fallu adapter Datice pour ajouter TALDICE. Ensuite, nous avons fait particulièrement attention au choix des paramètres d'ébauche de chaque carotte, ainsi qu'à la définition de leurs variances. En plus de cela, nous avons réalisé une compilation de toutes les contraintes d'âge (marqueurs d'âge absolus, orbitaux et liens stratigraphiques) pour les phases gaz et glace. Grâce aux nouvelles mesures de $\delta^{18}O_{atm}$ réalisées sur la glace de TALDICE, nous avons été en mesure de déduire des liens stratigraphiques gaz avec Vostok sur les derniers 150 ka. Les mesures de $\delta^{18}O_{atm}$ couvrant le MIS 11 de la carotte d'EDC nous ont permis d'augmenter la résolution de l'enregistrement déjà existant ainsi que de revoir les marqueurs de $\delta^{18}O_{atm}$ proposés par Dreyfus et al. [2007] sur cette période. Grâce à Datice, nous avons été en mesure de valider la cohérence des différents marqueurs orbitaux, déduits du $\delta O_2/N_2$, du $\delta^{18}O_{atm}$ et de la teneur en air sur la carotte de Vostok. L'implémentation de toutes ces contraintes nous a permis de produire la chronologie AICC2012. Plus de 300 simulations ont été effectuées avec Datice afin de produire la chronologie AICC2012. Cette nouvelle échelle d'âge respecte la chronologie GICC05 sur les derniers 60 ka. Par la présence de nombreux liens stratigraphiques entre les carottes de glace, AICC2012 présente une meilleure estimation de la durée des évènements lors du dernier cycle glaciaire–interglaciaire. L'âge de la Terminaison II, contraint par

des marqueurs orbitaux principalement, est en accord avec les autres archives climatiques. Contrairement aux méthodes de datation précédemment utilisées, Datice a permis un calcul objectif de l'erreur associée à la chronologie AICC2012. La comparaison d'AICC2012 avec d'autres chronologies carottes de glace a mis en évidence des différences relativement faibles (inférieures à 2 ka). Comparée à l'ancienne référence pour les carottes de glace EDC3, AICC2012 présente une chronologie 5.4 ka plus vieille au niveau du MIS 12. Ceci est expliqué par l'implémentation supplémentaire des marqueurs de $\delta O_2/N_2$ sur cette période. Pour finir, la nouvelle chronologie de référence pour les carottes de glace ne montre pas de changements significatifs sur la durée des périodes interglaciaires et ne remet pas en question les interprétations climatiques réalisées sur l'échelle d'âge EDC3.

Depuis AICC2012, des améliorations ont été apportées à Datice, en collaboration avec Bénédicte Lemieux-Dudon. Nous avons ajouté la possibilité d'utiliser des marqueurs de différence d'âge dans Datice pour pouvoir contraindre les chronologies. Ces marqueurs sont mieux adaptés aux contraintes déduites du comptage des couches annuelles, comme dans le cas de GICC05. En plus de cela, il est maintenant possible d'introduire des corrélations d'erreur entre les marqueurs (soit une valeur constante, soit un profil en fonction de la profondeur). Comme l'erreur associée au comptage des couches annuelles est cumulative, cela permet de prendre en compte le fait que les erreurs associées à cette méthode sont corrélées entre elles. Ces nouvelles implémentations ont permis de réaliser plusieurs exercices de datation en considérant des paramètres d'ébauche et des marqueurs d'âges indépendants les uns des autres, tout en respectant la chronologie GICC05.

Avec pour objectif d'améliorer la définition de l'erreur sur les paramètres glaciologiques d'ébauche, nous avons étudié l'influence des hétérogénéités de déformation sur la fonction d'amincissement en nous basant sur le travail de Durand [2004]. Le modèle réalisé permet de perturber la fonction d'amincissement classiquement produite par les modèles de datation avec des hétérogénéités de déformation. Par la méthode de Monte-Carlo, il est possible d'en déduire l'écart-type pour ensuite l'ajouter à la paramétrisation de l'erreur sur la fonction d'amincissement d'ébauche.

Les nouvelles mesures de $\delta O_2/N_2$ et $\delta^{18}O_{atm}$ réalisées sur de la glace bien conservée d'EDC ont permis de compléter les enregistrements déjà existants. Pour le $\delta^{18}O_{atm}$, les nouvelles mesures ont seulement amélioré la résolution de l'enregistrement existant du MIS 5 et entre 300–800 ka. Concernant le $\delta O_2/N_2$, nous avons maintenant des mesures couvrant le MIS 5 ainsi qu'un enregistrement de référence

entre 380–800 ka. L'analyse spectrale de ce dernier présente un pic correspondant à la période caractéristique de l'excentricité et/ou des variations glaciaire–interglaciaire. La comparaison de la composition isotopique de la glace, du $\delta O_2/N_2$ et du $\delta^{18}O_{atm}$ au MIS 5 pour les carottes de Vostok, Dôme F et EDC a mis en évidence des différences significatives entre les sites. Il apparaît que le $\delta O_2/N_2$ pourrait être influencé par des paramètres climatiques locaux. Ces derniers pourraient avoir de l'importance notamment en période de faible excentricité lorsque les variations d'insolation sont moins bien retrouvées dans le $\delta O_2/N_2$.

Au travers de l'étude de la relation entre le $\delta O_2/N_2$ et le $\delta^{18}O_{atm}$ sur les derniers 800 ka, nous avons suggéré un retard variable entre le $\delta^{18}O_{atm}$ et la précession. Ce retard est maximum aux MIS 8 et 16, et minimum aux MIS 6–7, la fin du MIS 9 et aux MIS 15 et 17. En confrontant ces résultats à un traceur des évènements de Heinrich, nous avons pu montrer que les périodes présentant un retard maximum étaient associées à des évènements de Heinrich. A l'inverse, les périodes où le retard est minimal correspondent à des périodes de forte excentricité, un volume de glace intermédiaire et sans évènements de Heinrich.

Pour finir, lors de la construction d'AICC2012, nous avons montré qu'il était possible de combiner les différents marqueurs issus de la synchronisation orbitale du $\delta O_2/N_2$, du $\delta^{18}O_{atm}$et de la teneur en air, au moins sur les derniers 400 ka à Vostok. Grâce aux nouvelles mesures de ces trois traceurs, nous avons été en mesure d'étendre cette analyse entre 300-800 ka sur la carotte d'EDC. Il apparaît toujours que ces marqueurs sont cohérents, mais aussi qu'il est important de les combiner aux périodes où un des marqueurs n'est pas disponible. Cependant, avant 700 ka, la datation orbitale reste incertaine car nous ne retrouvons pas clairement les variations de l'insolation dans nos enregistrements de $\delta O_2/N_2$, $\delta^{18}O_{atm}$et teneur en air.

Les différents tests, améliorations et mesures présentés dans cette thèse devraient être pris en considération lors de la réalisation du prochain exercice de datation fédérative pour les carottes de glace.

5.6 Perspectives

A la suite de ce travail, plusieurs points restent à améliorer :

— Compléter les mesures de $\delta O_2/N_2$ et $\delta^{18}O_{atm}$ dans le but d'avoir des enregistrements complets entre 100–800 ka provenant de glace bien conservée d'EDC. Ces profils complets permettront de déduire de nouvelles contraintes

chronologiques orbitales et relatives (liens stratigraphiques). Ils permettront d'étendre la comparaison multi–traceurs entre les carottes de Vostok, Dôme F et EDC jusqu'à 400 ka. La courbe de $\delta O_2/N_2$ mesurée sur de la glace bien conservée d'EDC permettra de confirmer la tendance décroissante du $\delta O_2/N_2$ entre 100–400 ka ainsi que de voir si elle a été constante au cours des derniers 800 ka ou si elle a changé au moment du MIS 11. De plus, augmenter la résolution des enregistrements existants aux périodes de minimum d'excentricité pourrait permettre de mieux comprendre pourquoi les variations d'insolation ne sont pas aussi bien marquées qu'aux autres périodes dans le $\delta O_2/N_2$ et le $\delta^{18}O_{atm}$.

— Améliorer nos connaissances sur la densification du névé, depuis le métamorphisme de la neige en surface jusqu'au processus de piégeage de l'air au fond du névé. Le couplage modèle–données sur les névés actuels devrait nous permettre de mieux comprendre comment un forçage en surface peut être conservé sur toute la colonne de névé et se retrouver enregistré par le $\delta O_2/N_2$ et le $\delta^{18}O_{atm}$. Cela nous permettra de mieux comprendre les facteurs influençant ces deux traceurs, et donc de réduire l'incertitude associée à la synchronisation orbitale du $\delta O_2/N_2$ et du $\delta^{18}O_{atm}$.

— Améliorer les paramétrisations de Datice. Notamment, il est nécessaire de retravailler les définitions choisies pour les variances des paramètres d'ébauche. Plusieurs améliorations peuvent être apportées au modèle permettant d'estimer l'influence des hétérogénéités de déformation sur la fonction d'amincissement. Afin de respecter les conditions d'utilisation de l'histogramme en figure 4.2, il est nécessaire d'ajouter la condition sur l'aire. De plus, le paramètre $\mathbf{U_{zz}}$ peut permettre l'identification des couches associées aux transitions glaciaire–interglaciaire et donc de paramétrer l'erreur différemment pour ces périodes. Il est de même nécessaire de retravailler les définitions de la variance pour l'accumulation et la LIDIE afin d'avoir des définitions plus physiques.

— Etendre la prochaine chronologie commune à plus de carottes de glace. De nombreuses informations peuvent être apportées grâce aux données disponibles sur les carottes de l'Antarctique de l'Ouest ainsi que Dôme F en Antarctique, mais aussi la carotte de NEEM au Groenland.

— Adapter l'outil Datice pour réaliser des datations cohérentes multi-archives. Ce travail est d'ores-et-déjà initié. Il est désormais possible d'intégrer des carottes marines dans Datice. Néanmoins il est nécessaire de faire particulièrement attention au choix des paramètres d'ébauche ainsi qu'aux traceurs à utiliser pour réaliser une synchronisation avec les carottes de glace. Amé-

liorer ensuite cet outils de datation pour intégrer encore d'autres archives climatiques permettra d'avoir une chronologie commune plus globale et de mieux comprendre la séquence des évènements prenant place aux différentes latitudes lors des changements climatiques de grande échelle.

— Les datations des archives climatiques sont importantes pour améliorer notre compréhension des changements climatiques passés, que ce soit la variabilité climatique rapide de la dernière période glaciaire (articles en annexe), ou encore les transitions entre périodes glaciaires et interglaciaires. Ainsi, nous aurons la possibilité d'améliorer les modèles climatiques.

Annexes

1 Guillevic et al., 2013

Clim. Past, 9, 1029–1051, 2013
www.clim-past.net/9/1029/2013/
doi:10.5194/cp-9-1029-2013

Climate of the Past
Open Access

Spatial gradients of temperature, accumulation and δ^{18}O-ice in Greenland over a series of Dansgaard–Oeschger events

M. Guillevic[1,2], L. Bazin[1], A. Landais[1], P. Kindler[3], A. Orsi[4], V. Masson-Delmotte[1], T. Blunier[2], S. L. Buchardt[2], E. Capron[5], M. Leuenberger[3], P. Martinerie[6], F. Prié[1], and B. M. Vinther[2]

[1]Laboratoire des Sciences du Climat et de l'Environnement, UMR8212, CEA/CNRS/UVSQ, Gif sur Yvette, France
[2]Centre for Ice and Climate, Niels Bohr Institute, University of Copenhagen, Copenhagen, Denmark
[3]Climate and Environmental Physics, Physics Institute and Oeschger Centre for Climate Change Research, University of Bern, Bern, Switzerland
[4]Scripps Institution of Oceanography, University of California, San Diego, La Jolla, CA, USA
[5]British Antarctic Survey, Cambridge, UK
[6]UJF Grenoble 1/CNRS, Laboratoire de Glaciologie et Géophysique de l'Environnement (LGGE), UMR5183, Grenoble, 38041, France

Correspondence to: M. Guillevic (mgllvc@nbi.ku.dk)

Received: 25 September 2012 – Published in Clim. Past Discuss.: 24 October 2012
Revised: 5 March 2013 – Accepted: 12 March 2013 – Published: 7 May 2013

Abstract. Air and water stable isotope measurements from four Greenland deep ice cores (GRIP, GISP2, NGRIP and NEEM) are investigated over a series of Dansgaard–Oeschger events (DO 8, 9 and 10), which are representative of glacial millennial scale variability. Combined with firn modeling, air isotope data allow us to quantify abrupt temperature increases for each drill site ($1\sigma = 0.6$ °C for NEEM, GRIP and GISP2, 1.5 °C for NGRIP). Our data show that the magnitude of stadial–interstadial temperature increase is up to 2 °C larger in central and North Greenland than in northwest Greenland: i.e., for DO 8, a magnitude of +8.8 °C is inferred, which is significantly smaller than the +11.1 °C inferred at GISP2. The same spatial pattern is seen for accumulation increases. This pattern is coherent with climate simulations in response to reduced sea-ice extent in the Nordic seas. The temporal water isotope (δ^{18}O)–temperature relationship varies between 0.3 and 0.6 (± 0.08) ‰ °C^{-1} and is systematically larger at NEEM, possibly due to limited changes in precipitation seasonality compared to GISP2, GRIP or NGRIP. The gas age−ice age difference of warming events represented in water and air isotopes can only be modeled when assuming a 26 % (NGRIP) to 40 % (GRIP) lower accumulation than that derived from a Dansgaard–Johnsen ice flow model.

1 Introduction

The last glacial period is characterized by rapid climatic instabilities at the millennial timescale occurring in the Northern Hemisphere and recorded both in marine and terrestrial archives (Voelker, 2002; Bond et al., 1993). The NGRIP (North Greenland Ice Core Project) ice core, northern Greenland, offers a high resolution water isotopes record where 25 rapid events were identified and described with a precise timing (NGRIP members, 2004). These events consist of a cold phase or stadial (Greenland stadial, GS), followed by a sharp temperature increase of 9 to 16 °C at the NGRIP site as constrained by gas isotope measurements (Landais et al., 2004a, 2005; Huber et al., 2006). The warm phase is referred as Greenland interstadial (GI). Temperature then gradually cools down, sometimes with a small but abrupt cooling in the end, to the next stadial state. These temperature variations are associated with significant changes in accumulation rate, with annual layer thicknesses varying by a factor of two between GS and GI at NGRIP (Andersen et al., 2006; Svensson et al., 2008).

The identification of ice rafted debris horizons during GS in North Atlantic sediments (Heinrich, 1988; Bond et al., 1993; Elliot et al., 2001), together with proxy records pointing to changes in salinity (Elliot et al., 2001, 2002),

reduced North Atlantic Deep Water formation (Rasmussen and Thomsen, 2004; Kissel et al., 2008) and Atlantic Meridional Overturning Circulation (AMOC) (McManus et al., 1994), had led to the theory that DO (Dansgaard–Oeschger) events are associated with large scale reorganizations in AMOC and interhemispheric heat transport (Blunier and Brook, 2001). The identification of a systematic Antarctic counterpart to each Greenland DO event (EPICA community members, 2006; Capron et al., 2010) supports this theory. This observation can be reproduced with a conceptual see-saw model using the Antarctic ocean as a heat reservoir and the AMOC as the way to exchange heat between Antarctica and Greenland (Stocker and Johnsen, 2003), as well as with climate models (e.g., Roche et al., 2010). Atmospheric teleconnections can also be at play (Chiang et al., 2008) and influence the timing of Antarctic warming with respect to Greenland cooling (Buiron et al., 2012).

Coupled atmosphere–ocean climate models are now able to reproduce the temperature pattern of DO events in Greenland in response to AMOC changes induced by freshwater forcing in the high latitudes of the Atlantic Ocean (Kageyama et al., 2010). However, modeled amplitudes of temperature changes are typically between 5 and 7 °C (Ganopolski and Rahmstorf, 2001; Li et al., 2005, 2010; Otto-Bliesner and Brady, 2010), significantly smaller than the temperature increase of 8–16 °C reconstructed based on ice core data (Landais et al., 2004a; Huber et al., 2006). The correct amplitude of temperature change over the Bølling-Allerød is only reproduced in a fully coupled and high resolution atmosphere–ocean global circulation model (Liu et al., 2009). However, a large part of the simulated warming is due to the simultaneous large changes in insolation (not at play for most DO events) and atmospheric CO_2 concentration. During DO events, limited CO_2 changes (20 ppm) are depicted by existing data (Indermühle et al., 2000; Bereiter et al., 2012; Ahn et al., 2012). This model–data mismatch motivates us to strengthen the description of the magnitude and spatial patterns of DO temperature changes, using different ice core sites. An improved regional description of past changes in Greenland climate will also be needed for the comparison with regional climate models recently equipped with water stable isotopes (Sjolte et al., 2011). So far, no systematic comparison of the signature of DO events in water stable isotopes and temperature (from gas isotopes) has been conducted over an array of drilling sites. This is the main target of this study.

In 2010, bedrock was reached at the North Eemian Ice Core Drilling (NEEM) site, northwest (NW) Greenland. A new deep ice core, 2.5 km long, is now available (Dahl-Jensen et al., 2013). In this paper, we present new data from the NEEM ice core, together with existing and new measurements conducted on the GISP2 (Greenland Ice Sheet Project 2) and NGRIP ice cores on DO events 8 to 10. The location of these drilling sites is depicted in Fig. 1 and their present-day characteristics are summarized in Table 1 (see also Johnsen et al., 2001). At present, the main source of NEEM precipitation is located in the North Atlantic, between 30° N and 50° N (Steen-Larsen et al., 2011). The recent interannual variability of water stable isotopes ($\delta^{18}O$, δD) shows similarities with the variability of the Baffin Bay sea-ice extent. Unlike central Greenland where snow falls year round, NW Greenland precipitation occur predominantly in summer according to snow pit studies (Shuman et al., 1995, 2001) and model simulations (Steen-Larsen et al., 2011; Sjolte et al., 2011; Persson et al., 2011). This specificity of the precipitation seasonality explains the particularly weak fingerprint of the North Atlantic Oscillation in NEEM shallow ice cores (Steen-Larsen et al., 2011) compared to GISP2 (Barlow et al., 1993). These regional peculiarities are of particular interest because past changes in precipitation seasonality are likely to affect water stable isotopes values.

Water isotopes are to a first order markers of local condensation temperature changes at the precipitation site (Dansgaard, 1964). However, they are also affected by evaporation conditions (temperature, relative humidity and wind regime, e.g., Merlivat and Jouzel, 1979; Johnsen et al., 1989), atmospheric transport and distillation, condensation conditions, as well as seasonality of precipitation (Werner et al., 2000; Werner et al., 2001; Masson-Delmotte et al., 2005): they are integrated tracers of the hydrological cycle and quantitative indicators of past site-temperature change, albeit with a time-varying relationship with local surface temperature. This temporal variability of the isotope–temperature relationship has been verified in Greenland thanks to independent constraints on past temperatures, either based on the inversion of borehole temperature data or derived from gas isotopes (e.g., Cuffey and Clow, 1997; Dahl-Jensen et al., 1998; Severinghaus and Brook, 1999; Lang et al., 1999; Johnsen et al., 2001; Landais et al., 2004a; Huber et al., 2006; Vinther et al., 2009).

Using the isotopic composition of nitrogen ($\delta^{15}N$) from N_2 trapped in the ice bubbles allows us to quantify the amplitude of past rapid-temperature changes (e.g., Severinghaus and Brook, 1999; Landais et al., 2004a; Huber et al., 2006; Grachev and Severinghaus, 2005; Kobashi et al., 2011). At the onset of a DO event, the firn surface warms rapidly but its base remains cold because of the slow diffusion of heat in snow and ice. The resulting temperature gradient in the firn leads to thermal fractionation of gases: the heavy nitrogen isotopes migrate towards the cold bottom of the firn, where air is progressively trapped into air bubbles. As a result, a sharp peak in $\delta^{15}N$ is seen in the gas phase as a counterpart to the rapid increase in water stable isotopes in the ice phase. Using $\delta^{15}N$ data and firn modeling, past surface temperature variations can be reconstructed (Schwander et al., 1997; Goujon et al., 2003). This method has already been applied to specific DO events on the NGRIP, GRIP and GISP2 ice

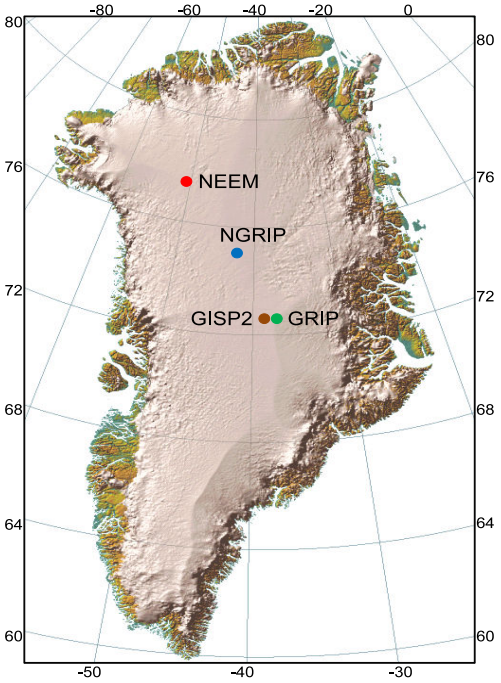

Fig. 1. Greenland map (Simon Ekholm, Danish cadastre) with the ice core sites: NEEM (red), NGRIP (blue), GISP2 (brown) and GRIP (green). Top and bottom numbers indicate longitude (° W), left and right numbers indicate latitude (° N).

cores (Lang et al., 1999; Huber et al., 2006; Landais et al., 2004a, 2005; Goujon et al., 2003; Severinghaus and Brook, 1999; Capron et al., 2010) and will be applied here for the first time to the NEEM ice core.

For this first study of regional variability of temperature changes over DO events, we focus on the series of DO events 8, 9 and 10 during Marine Isotope Stage 3 (MIS3, 28–60 ka b2k, thousand years before 2000 AD). This period is indeed the most widely documented for the millennial scale variability in a variety of natural archives. It is characterized by a large terrestrial ice volume (Bintanja et al., 2005), low atmospheric greenhouse gas concentration (Schilt et al., 2010), decreasing obliquity, low eccentricity and therefore small fluctuations in Northern Hemisphere summer insolation (Laskar et al., 2004). During MIS3, iconic DO events are particularly frequent with short lived interstadials (Capron et al., 2010) and constitute a clear target for model–data comparisons.

In this study, we first present a new δ^{15}N profile covering DO events 8 to 10 on the NEEM ice core. We then produce past temperature and accumulation reconstructions for NEEM and compare them with scenarios obtained with the same method for NGRIP, GISP2 and GRIP, investigating the water isotope–temperature relationships for these four different locations. We finally discuss the implications of our results in terms of regional climate variations.

Table 1. Present-day characteristics of NEEM, NGRIP, GISP2 and GRIP drilling sites (m.i.e., meters ice equivalent).

	NEEM[a]	NGRIP[b]	GISP2	GRIP
Latitude (° N)	77.45	75.10	72.58	72.58
Longitude (° W)	51.06	42.32	38.48	37.64
Elevation (m a.s.l.)	2484	2917	3214	3238
Surface temperature (°C)	∼ −29.0	−31.5	−31.4[c]	−31.7[f]
Accumulation rate (m.i.e.a^{-1})	0.22	0.19	0.25[d]	0.23[g]
δ^{18}O (‰)	∼ −33.0	−35.5	−35.0[e]	−34.9[g]

Sources: [a] Steen-Larsen et al. (2011); accumulation: 1964–2005 average, NEEM07S3 core. [b] NGRIP members (2004). [c] Cuffey et al. (1995). [d] Meese et al. (1994); accumulation: last 200 a average. [e] Average of the top 200 a of B core (1987–1787), Grootes and Stuiver (1997). [f] Gundestrup et al. (1994). [g] Johnsen et al. (1992), 20–220 a b2k average of the GRIP ice core.

2 Method

2.1 Data

2.1.1 Nitrogen isotope data

The isotopic composition of nitrogen (δ^{15}N) was measured on the NEEM core from 1746.8 to 1811.6 m depth at Laboratoire des Sciences du Climat et de l'Environnement (LSCE), France. We have a total of 84 data points with replicates, with an average depth resolution of 77 cm corresponding to an average temporal resolution of ∼ 70 a. On the GRIP ice core, 18 data points covering DO 9 have been measured with an average resolution of 61 cm (equivalent to about 43 a). For these two data sets, we have used a melt–refreeze technique to extract the air from the ice (Sowers et al., 1989; Landais et al., 2004b). The collected air is then measured by dual inlet mass spectrometry (Delta V plus, Thermo Scientific). Data are corrected for mass interferences occurring in the mass spectrometer (Sowers et al., 1989; Bender et al., 1994b). Dry atmospheric air is used as a standard to express the results. The final pooled standard deviation over all duplicate samples is 0.007 ‰.

For the NGRIP core, δ^{15}N was measured at the University of Bern (73 data points from Huber et al. (2006) and 36 new data points on DO 8). A continuous flow method was used for air extraction and mass spectrometry measurement (Huber and Leuenberger, 2004). The associated uncertainty is 0.02 ‰.

For the GISP2 ice core, nitrogen isotopes were measured at Scripps Institution of Oceanography, University of California, using the melt–refreeze technique from Sowers et al. (1989) with a pooled standard deviation of 0.0065 ‰ for the 70 δ^{15}N data points (Orsi et al., 2013). In addition to these data, argon isotopes were also measured using the method from Severinghaus et al. (2003) (46 samples, pooled standard deviation of 0.013 ‰).

2.1.2 δ^{18}O water isotope data

We use the δ^{18}O bag data (one data point corresponds to an average over 55 cm) from the NEEM ice core measured at the Centre for Ice and Climate (CIC), University of Copenhagen, with an analytical accuracy of 0.07 ‰. For the NGRIP and GRIP ice cores, we use the bag data previously measured at CIC, with the same precision (NGRIP members, 2004; Johnsen et al., 1992). The GISP2 δ^{18}O data (Grootes and Stuiver, 1997, 20 cm resolution) are associated with a precision of 0.05 to 0.1 ‰.

2.1.3 Timescale

NEEM, NGRIP, GISP2 and GRIP ice cores are all dated according to the Greenland Ice Core Chronology 2005, GICC05 (Vinther et al., 2006; Rasmussen et al., 2006; Andersen et al., 2006; Svensson et al., 2008). This timescale has been produced based on annual layer counting of several parameters measured continuously on the NGRIP, GRIP and Dye3 ice cores and featuring a clear annual cycle, back to 60 ka b2k. The Maximum Counting Error (MCE), which can be regarded as a 2σ error estimate (Rasmussen et al., 2006) is 1439 a at 38 ka b2k. To transfer this timescale to the NEEM ice core, match points between peaks of electrical conductivity measurements and dielectrical properties, measured continuously on the ice cores, have been used. The obtained timescale for NEEM is called GICC05-NEEM-1 (S. O. Rasmussen, personal communication, 2010). The GISP2 core is matched to NGRIP using the same method as Rasmussen et al. (2008), with match points from I. Seierstad (personal communication, 2012). Using these match points, we scale the Meese et al. (1997) GISP2 timescale, based on annual layer counting, to the GICC05 timescale, in order to keep the information from the annual layer count while producing an age scale consistent with GICC05. The GICC05 age scale gives the age of the ice at each depth, and thus the annual layer thickness at each depth, but not the accumulation rate. This age scale is independent from estimation of thinning and past accumulation rate.

2.1.4 Accumulation rate

Accumulation rate histories for NEEM, NGRIP and GRIP are obtained using a Dansgaard–Johnsen (DJ) ice flow model (Dansgaard and Johnsen, 1969). The ice flow parameters of the model are tuned to obtain the best match between modeled and observed depth-age horizons in the ice cores. The thinning function calculated from the DJ model is then used to correct the observed annual layer thicknesses in the core for the effect of ice flow induced thinning, thereby producing an accumulation rate history. The NEEM version of the DJ model (Buchardt, 2009) is tuned in order to match the GICC05 timescale. For NGRIP, the accumulation rate was first calculated using the ss09sea06bm age scale (Johnsen et al., 2001; Grinsted and Dahl-Jensen, 2002; NGRIP members, 2004). We recalculated that accumulation according to the more accurate GICC05 timescale. We did the same for the GRIP ss09sea-accumulation rate from Johnsen et al. (2001). Note that the ss09sea, ss09sea06bm and the GICC05 timescales agree within the GICC05 uncertainty between 28 and 60 ka b2k. For GISP2, the accumulation rate was first estimated with a 1 m resolution based on the coupled heat and ice flow model from Cuffey and Clow (1997), with the layer counted timescale from Alley et al. (1993), Meese et al. (1994) and Bender et al. (1994b). This timescale has known issues in the vicinity of DO 8 (Orsi et al., 2013; Svensson et al., 2006), which causes the accumulation history derived from it to be also wrong. Orsi et al. (2013) used the layer thickness from the GICC05 timescale to recalculate the accumulation history. Cuffey and Clow (1997) suggested 3 accumulation scenarios and Orsi et al. (2013) use the "200 km margin retreat" scenario adapted to the GICC05 timescale, compatible with the firn thickness and Δage derived from δ^{15}N data. This accumulation scenario has also been proved to best reproduce ice sheet thickness variations (Vinther et al., 2009).

2.1.5 Ice-gas Δdepth data

Figure 2 presents the NEEM δ^{15}N profile over the sequence DO 8–10. The peaks of δ^{15}N at 1769.4, 1787.5, and 1801.0 m are the result of the maximum temperature gradient in the firn corresponding to the abrupt temperature increases of DO 8, 9 and 10. We assume that δ^{15}N peaks and δ^{18}O-ice peaks are synchronous (see Sect. A2) and thus relate the maximum firn temperature gradient to the peaks in δ^{18}O-ice at 1758.1, 1776.8, and 1790.5 m. The depth differences between the temperature increases recorded in the gas and ice phases, named Δdepth, can thus directly be inferred as 11.3, 10.7, and 10.5 m over DO 8, 9, and 10, respectively (Fig. 2, Table 2, points 1, 5, and 7, respectively). We propose another match point between weaker peaks of δ^{15}N and δ^{18}O, see match point 3 in Table 2 and Fig. A3.

δ^{15}N also increases with accumulation increase, which deepens the firn (see Sect. 2.2), and we believe that this effect explains the beginning of δ^{15}N increase at the onset of each DO event. Several abrupt transitions (Bølling-Allerød and DO 8) have been investigated at high resolution (Steffensen et al., 2008; Thomas et al., 2008), also showing that the accumulation increases before the δ^{18}O shifts with a time lead up to decades and ends after the completion of the δ^{18}O increase. We observe the same feature for DO 8, 9, and 10 on the NEEM core. We thus match the onset of the δ^{15}N increase at the beginning of DO events to the onset of accumulation increase, which occurs before the δ^{18}O increase (Table 2 and Fig. A3, match points 2, 6, 8). Finally, match point 4 is a step in accumulation that we relate to the same step seen in δ^{15}N variations.

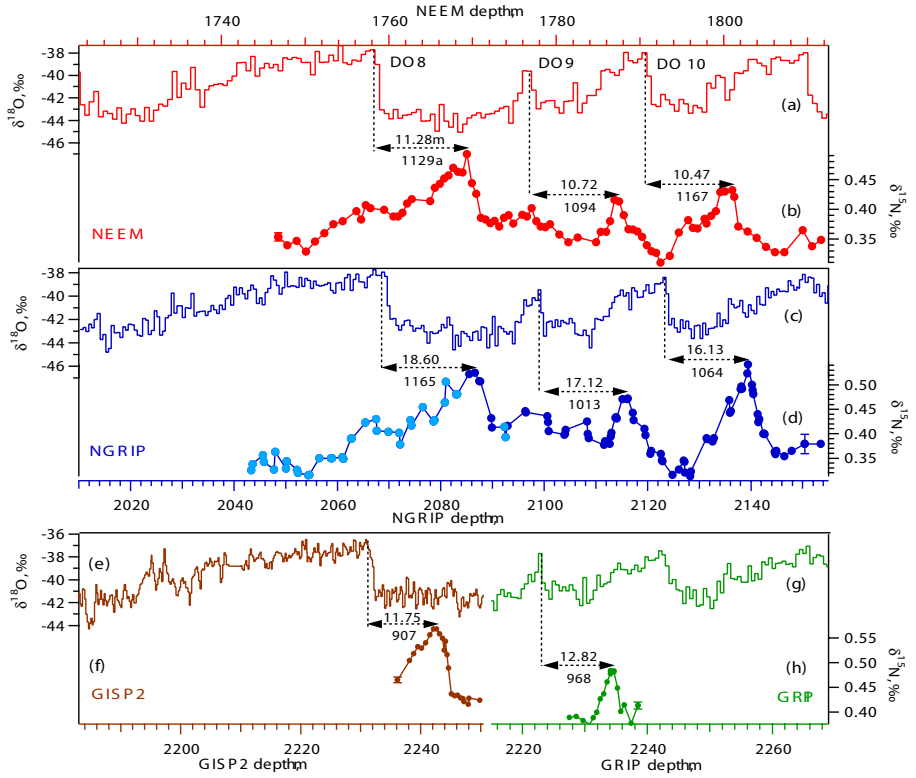

Fig. 2. Water and nitrogen stable isotope data (‰) for NEEM, NGRIP, GISP2 and GRIP. For each δ^{15}N data series the associated uncertainty ($\pm 1\sigma$) is shown. NEEM: **(a)** δ^{18}O bag data (measured along 55 cm samples) measured at CIC, this study; **(b)** δ^{15}N data measured at LSCE, this study. NGRIP: **(c)** δ^{18}O bag data, NGRIP members (2004); **(d)** δ^{15}N data measured at the University of Bern. Dark blue: data points from Huber et al. (2006). Light blue: this study. GISP2: **(e)** δ^{18}O bag data, Grootes and Stuiver (1997); **(f)** δ^{15}N data, Orsi et al. (2013). GRIP: **(g)** δ^{18}O 55 cm bag data, Johnsen et al. (1992); **(h)** δ^{15}N data measured at LSCE, this study.

Table 2. Correspondence between δ^{15}N and δ^{18}O or accumulation for the NEEM and NGRIP cores (see also ig. A3 and D1). δ^{18}O data are averaged over 55 cm (bag data) and we use here the depth at the middle of the 55 cm interval. The age is given according to the GICC05 timescale. The Δdepth (Δage) is obtained by calculating the difference between ice and gas depth (age). The Δage uncertainty is given by the difference between the MCE at the ice depth and the MCE at the gas depth.

Match point	depth (m) for:		Δdepth	age (a b2k) for:		Δage	MCE
	ice	gas		ice	gas		
NEEM							
1, DO 8 δ^{18}O peak	1758.08	1769.35	11.28	38 161	39 290	1129	67
2, DO 8 onset of acc. increase	1759.73	1771.00	11.28	38 274	39 472	1198	79
3, δ^{18}O minor peak	1766.33	1777.05	10.72	38 961	40 119	1158	90
4, acc. step	1775.13	1785.93	10.80	39 953	41 055	1102	51
5, DO 9 δ^{18}O peak	1776.76	1787.50	10.72	40 096	41 190	1094	48
6, DO 9 onset of acc. increase	1778.43	1788.60	10.17	40 254	41 273	1019	43
7, DO 10 δ^{18}O peak	1790.53	1801.00	10.47	41 411	42 559	1167	68
8, DO 10 onset of acc. increase	1791.63	1801.72	10.90	41 499	42 648	1149	69
NGRIP							
1, δ^{18}O minor peak	2028.13	2045.57	17.44	36 657	37 401	744	24
2, DO 8 δ^{18}O peak	2068.00	2086.60	18.60	38 152	39 317	1165	69
3, DO 9 δ^{18}O peak	2099.08	2116.19	17.11	40 131	41 145	1013	46
4, DO 10 δ^{18}O peak	2123.28	2139.41	16.13	41 429	42 493	1064	64

At NGRIP, DO 8, 9 and 10 are seen at 2086.6, 2116.2, and 2139.4 m in the gas phase and at 2068.0, 2099.1, and 2123.3 m in the δ^{18}O from the ice phase (Fig. 2, Table 2 and Fig. D1, match points 2, 3, 4, respectively). For DO 8, δ^{18}O shows a double peak and we use the middle depth for this match point. We propose another match point at the end of DO 8 between weaker peaks of δ^{15}N and δ^{18}O (match point 1). All these Δdepth match points will be used in Sect. 3.1, combined with firn modeling, to reconstruct past surface temperature and accumulation.

2.2 Model description

To reconstruct a surface temperature scenario from the δ^{15}N profiles, we use a classical approach consisting of fitting the output of a firnification and heat diffusion model with the δ^{15}N records (Schwander et al., 1997; Lang et al., 1999; Huber et al., 2006; Goujon et al., 2003; Landais et al., 2004a; Kobashi et al., 2011; Orsi et al., 2013). We use here the semi-empirical firnification model with heat diffusion by Goujon et al. (2003). Adapted to each ice core (see method in Appendix A), this model calculates for each ice age and hence for each corresponding depth level the initial firn depth (defined here as the depth where diffusion of gases stops i.e., lock-in-depth, LID), the age difference between ice and gas at the LID (Δage), and the temperature gradient between the bottom and the top of the firn. It is then possible to calculate the δ^{15}N as the sum of two effects:

- gravitational effect (Craig et al., 1988; Schwander, 1989): the heavy isotopes preferentially migrate towards the bottom of the firn according to the barometric equation:

$$\delta^{15}\mathrm{N}_{\mathrm{grav}} = \exp\left(\frac{\Delta m g z}{R T_{\mathrm{mean}}}\right) - 1 \quad (1)$$

  with Δm being the mass difference between the light and heavy isotope, g the acceleration constant, z the firn depth, R the ideal gas constant, and T_{mean} the mean firn temperature. An increase in accumulation rate increases the firn column depth and therefore increases $\delta^{15}\mathrm{N}_{\mathrm{grav}}$; on the other hand, a high temperature accelerates the densification processes and shallows the LID.

- thermal effect (Severinghaus et al., 1998): the cold part of the firn is enriched in heavy isotopes according to

$$\Delta\delta^{15}\mathrm{N}_{\mathrm{therm}} = \left(\frac{T_{\mathrm{t}}}{T_{\mathrm{b}}}\right)^{\alpha_{\mathrm{T}}} - 1 \cong \Omega \cdot \Delta T \quad (2)$$

  with T_{t} and T_{b} being the temperatures of the top and bottom parcel, respectively, α_{T} the thermal diffusion constant, Ω the thermal diffusion sensitivity (Grachev and Severinghaus, 2003), and ΔT the temperature difference between top and bottom of the firn. A transient temperature increase after a stable cold period will create a transient peak in $\delta^{15}\mathrm{N}_{\mathrm{therm}}$.

The model needs input temperature, accumulation and dating scenarios with a depth-age correspondence. In the standard version of the Goujon model, the temperature scenario is based on a tuned variable relationship between water isotopes and surface firn temperature, with

$$T = \frac{1}{\alpha}(\delta^{18}\mathrm{O} + \beta) \quad (3)$$

where α and β can be variable over time. The reconstructed temperature has thus the shape of the water isotope profile but the temperature change amplitudes are constrained by tuning α and β in order for the modeled δ^{15}N to match the measured δ^{15}N. Several earlier studies have shown that the temporal values of α are lower than the present-day spatial slope for Greenland of 0.80 ‰ °C^{-1} (Sjolte et al., 2011; Masson-Delmotte et al., 2011), which can be used as a maximum value.

3 Results and discussion

3.1 Temperature and accumulation reconstruction

To reconstruct continuous temperature and accumulation scenarios for DO 8 to 10, we run the firnification model from 60 to 30 ka b2k with a time step of one year and try to reproduce the δ^{15}N data as well as the Δdepth match points. Figure 3 shows the comparison between the measured and modeled (scenarios d1 to d3) δ^{15}N over DO 8–10 at NEEM. First we try to reproduce the δ^{15}N data by varying the temperature alone: the measured δ^{15}N amplitudes of DO 8, 9, and 10 can be reproduced with temperature increases at the GS–GI transitions of 8.8, 6.0, and 7.7 °C, respectively (Fig. 3, reconstruction d1). This scenario nicely reproduces both the mean δ^{15}N level and the amplitude of the δ^{15}N peaks. However, the modeled δ^{15}N peaks are systematically at a too shallow depth. To model a larger Δdepth, we systematically lower the temperature scenario used in reconstruction d1 (Fig. 3) by 3.5 °C. This systematically deepens the LID, increasing both Δdepth and δ^{15}N (Fig. 3, reconstruction d2). The modeled Δdepth is therefore closer to the measured one and the amplitude of the δ^{15}N peaks is still correct but the mean δ^{15}N level is systematically too high. From this experiment, we conclude that it is not possible to match both δ^{15}N data and Δdepth by tuning only the temperature scenario.

Several explanations can be proposed to explain the underestimation of the Δdepth by the model:

- the tuning of the Goujon model (LID density, vertical velocity field) is not appropriate for the NEEM site and predicts a too shallow LID. However, we show in Appendix A3 that different tuning strategies have no impact on the modeled LID;

- the Goujon model is not appropriate for the NEEM site. However, this model is valid for present-day at

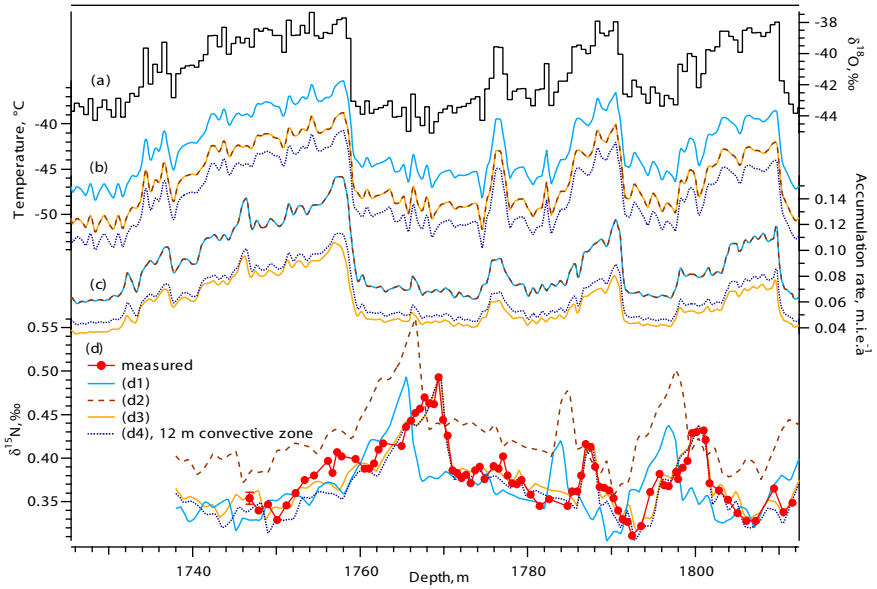

Fig. 3. Measured and modeled δ^{15}N for NEEM on DO 8 to 10, plotted on a depth scale. **(a)** δ^{18}O ice ‰, this study. **(b)** Temperature scenarios and **(c)** accumulation scenarios used to produce the δ^{15}N reconstructions in **(d)** plotted on the same color. Red dots: measured δ^{15}N data. **(d1)** to **(d4)** Modeled δ^{15}N. **(d1)** to **(d3)** using a 2 m convective zone. **(d4)** using a 12 m convective zone.

NEEM (see Appendix A1) and has also been validated for a large range of temperature and accumulation rates covering the expected glacial climatic conditions at NEEM (Arnaud et al., 2000; Goujon et al., 2003; Landais et al., 2006). Moreover, using other firnification models (the Schwander model on NGRIP Huber et al. (2006) and a Herron Langway model on NEEM, see Appendix C) with similar forcings in temperature and accumulation rate does not reproduce the measured Δdepth either;

– fundamental parameters are missing in the description of current firnification models. A recent study has shown that the firn density profile could be strongly influenced by impurities, the density increasing with calcium and dust content in the ice (Hörhold et al., 2012). Calcium and dust in Greenland ice cores are both originating from low-latitude Asian deserts and their content is influenced by source strength and transport conditions (Svensson et al., 2000; Ruth et al., 2007). They covary in Greenland ice cores from seasonal to millennial timescales (Hörhold et al., 2012; Thomas et al., 2008; Steffensen et al., 2008). During cold periods (glacials, stadials), calcium and dust content in Greenland ice cores are strongly enhanced compared to warm periods (interglacials, interstadials) (Mayewski et al., 1997; Ruth et al., 2007; Wolff et al., 2009). Taking this effect into account, the modeled LID during the glacial period should be shallower than the one calculated with the current version of the firnification model calibrated on present-day observations. This would further enhance the disagreement between modeled and observed Δdepth;

– the glacial firn layer at NEEM could be subject to variations in the extent of the convective zone due to katabatic winds and/or low accumulation rate. Considering present-day Antarctic sites as an analogue for the past NEEM firn, a convective zone of 0–3 m (like Dome C, Landais et al., 2005) to 12 m (like Vostok, Bender et al., 1994a) can be considered (Sect. A4 and Fig. A2), event though we suggest that the range 0–3 m is most likely (see discussion in Sect. A4). A convective zone has no direct impact on the Δdepth but it lowers the δ^{15}N level. Accounting for such convective zone in the firn model requires lower temperatures, which increases the Δdepth.

– the forcing in accumulation of the firnification model is not correct. To match the observed Δdepth with a correctly modeled δ^{15}N, we need to significantly decrease the accumulation rate compared to the original DJ estimation.

With a 2 m convective zone, by adjusting changes in accumulation rate and the δ^{18}O–temperature relationship (Fig. 3c, b), we manage to reproduce the δ^{15}N profile as presented in Fig. 3, scenario d3. This best δ^{15}N fit corresponds to a mean accumulation reduction of 34 % (30 to 40 %, depending on the DO event). Because the depth-age correspondence is imposed by the layer counting, this accumulation rate reduction by 34 % directly implies the same 34 % decrease in the ice thinning. If we use this accumulation

scenario as input for the DJ model, with keeping the original DJ accumulation scenario in the remaining ice core sections, the output timescale is just at the limit of the age uncertainty estimated by annual layer counting. With a 12 m convective zone (Fig. 3, d4), the δ^{15}N profile can be reproduced using the temperature scenario d3 systematically lowered by 2 °C and the DJ accumulation rate reduced by 28 %.

For NGRIP, the Goujon model can reproduce the measured δ^{15}N profile with the correct Δdepth when using a convective zone of 2 m and the DJ accumulation rate reduced by 26 % over the whole section (Fig. D1). Alternatively, we can use a 12 m convective zone with a 19 % reduction in accumulation; this impacts the mean temperature level, which has to be lowered by 2 °C (not shown). For GRIP, using a 2 m convective zone, we have to decrease the DJ accumulation rate by 40 %. Note that this reduced GRIP DJ accumulation rate is then very close to the GISP2 accumulation rate for the same period (Fig. 4). We further discuss past changes in accumulation rate in Sect. 3.4.

Based on these calculations, we conclude that reducing the DJ accumulation scenario is necessary to match both δ^{15}N data and Δdepth with a firnification model over the sequence of DO 8–10, even when accounting for uncertainties linked with the presence of a convective zone. This reduction has no impact on the reconstructed rapid temperature variations but requires a lower mean temperature level (Fig. 3, d3, d4). Our 19 to 26 % accumulation reduction for NGRIP supports the findings by Huber et al. (2006) where the original accumulation scenario was reduced by 20 %, without convective zone.

3.2 Uncertainties quantification

Following the same method for the four cores, we estimate the uncertainty (1σ) associated with the temperature increases ΔT at the onset of the DO events to be $\sim$0.6 °C for NEEM, GRIP, and GISP2, and $\sim$ 1.5 °C for NGRIP. For the δ^{18}O increases, $\Delta\delta^{18}$O, the uncertainty is estimated to be $\sim$0.05 ‰ for NEEM, 0.04 ‰ for NGRIP, 0.06 ‰ for GRIP and 0.02 ‰ for GISP2. The thermal sensitivity of δ^{18}O, defined as $\alpha = \Delta\delta^{18}\mathrm{O}/\Delta\mathrm{T}$, is associated with an uncertainty of 0.05, 0.08, 0.04 and 0.02 ‰ °C^{-1} for NEEM, NGRIP, GRIP and GISP2, respectively. The detailed calculations are given in Appendix B. Note that for DO 8, 9 and 10, the GRIP and GISP2 ice cores depict δ^{18}O increases significantly different from each other even though they are geographically very close to each other. Grootes et al. (1993) calculated an 89 % common variance between these two cores for the interval 9–104 ka b2k and suggested local variability to explain the remaining differences.

3.3 Regional δ^{18}O and temperature patterns

Our best guess temperature and accumulation reconstructions for the four Greenland sites are displayed in Fig. 4 as a function of the GICC05 timescale. Our temperature reconstruction for NGRIP is in good agreement with the one from Huber et al. (2006) where a different firnification model was used (see Fig. D1 in Appendix D). For the GISP2 core, the temperature reconstruction for DO 8 follows the same approach (Orsi et al., 2013): temperature and accumulation scenarios are used as inputs to the Goujon firnification model and constrained using δ^{15}N and δ^{40}Ar measurements. Four different accumulation scenarios were used, with a GS to GI increase of 2, 2.5, 3, and 3.5 times. The difference in temperature increase between these four scenarios is very small ($1\sigma = 0.07$ °C). We report in Table 3 the mean temperature increase for these four scenarios.

For a systematic comparison between the different ice core records, we have used a ramp-fitting approach (Mudelsee, 2000) to quantify the start, end and amplitude of DO increases in δ^{18}O, temperature and accumulation: each parameter is assumed to change linearly between GS and GI states. The magnitude of DO increases are then estimated as the difference between the mean GS and GI values (Table 3). The time periods used on each DO event for this statistical analysis are shown in Figs. A3 and D1.

3.3.1 Temperature sensitivity of δ^{18}O for present-day and glacial climate

For all four sites, the temporal sensitivity of water isotopes to temperature varies from 0.34 to 0.63 ‰ °C^{-1}, being therefore systematically smaller than the present-day spatial gradient of 0.80 ‰ °C^{-1} (Table 3 and Sjolte et al., 2011). This reduction can be explained by precipitation intermittency/seasonality effects (Steig et al., 1994; Jouzel et al., 1997): under glacial boundary conditions, atmospheric models depict a shift of Greenland precipitation towards summer; this has been linked to a southward shift of the winter storm tracks due to the position of the Laurentide ice sheet (Werner et al., 2000, 2001; Krinner et al., 1997; Fawcett et al., 1997; Kageyama and Valdes, 2000). During cold periods, summer snow may represent most of the annual accumulation, inducing a bias of the isotopic thermometer towards summer temperature and lowering α compared to the spatial gradient (associated with a classical Rayleigh distillation). So far, seasonality changes have not been systematically investigated in climate model simulations aiming to represent DO events such as driven by freshwater hosing. In reduced sea-ice experiments by Li et al. (2005) using an atmospheric general circulation model, a 7 °C temperature increase and a doubling of the accumulation rate are simulated in GI compared to GS, accompanied with a relatively higher winter snow contribution that could partly explain the low α that we observe here.

Another argument in favor of such seasonality change comes from observations in the NGRIP ice core: records of different ion and dust show synchronous annual peaks during stadials for these species, whereas peaks occur at different periods of the year during interstadials, as for present-day

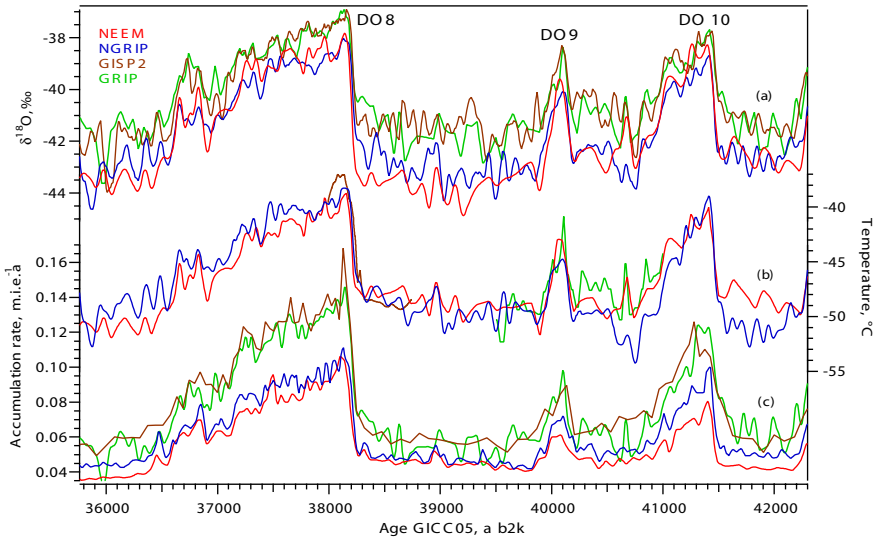

Fig. 4. NEEM (red), NGRIP (blue), GISP2 (brown) and GRIP (green) comparison. **(a)** Water isotopes, 50 yr running average, ‰ vs. VSMOW. NEEM: this study. NGRIP: NGRIP members (2004). GISP2: Grootes et al. (1993). GRIP: Johnsen et al. (1992). **(b)** Temperature reconstruction, °C. **(c)** Accumulation rate reconstruction, m.i.e.a^{-1}.

(Andersen et al., 2006). A first explanation is that during GS the accumulation rate is so low that ion/dust income are dominated by dry deposition all around the year, producing an ion/dust rich layer at the snow surface. This layer is then separated from the one from the following year by the incoming summer snow, resulting in apparent annual synchronous peaks of all species. This supports the hypothesis of a dramatic decrease of winter precipitation during GS at NGRIP. Andersen et al. (2006) also suggested that changes in transport paths may account for the observed pattern. Indeed, the presence of the Laurentide ice sheet (LIS) has been suggested to allow a split jet stream (Andersen et al., 2006). A shift of the path from south to north of the LIS during GI–GS may explain their data. The GS–GI impurities patterns are therefore again in favor of different atmospheric circulation patterns between GS and GI. No such high resolution measurements are yet available for GRIP, GISP2 and NEEM.

In the mean time, studies of the second order parameter deuterium excess suggest that the main source of water vapor is shifted southwards during GS (Johnsen et al., 1989; Masson-Delmotte et al., 2005; Jouzel et al., 2007; Ruth et al., 2003). The enhancement of the source–site temperature gradient enhances isotopic distillation and produces precipitation with lower δ^{18}O levels during cold periods, increasing α. Contradicting earlier assumptions (Boyle, 1997), conceptual distillation models constrained by GRIP deuterium excess data suggest that this effect is most probably secondary (Masson-Delmotte et al., 2005).

3.3.2 Regional differences between the ice cores sites

The magnitude of GS–GI temperature rise is significantly increasing from NW Greenland to Summit for DO 8 and 10: $+8.8 \pm 0.6$ °C at NEEM, $+10.4 \pm 1.5$ °C at NGRIP, and $+11.1 \pm 0.6$ °C at GISP2 for DO 8; for DO 10, ΔT is largest at NGRIP and smallest at NEEM. In the mean time, the amplitude of $\Delta\delta^{18}$O is decreasing from NW to central Greenland: for DO 8, $\Delta\delta^{18}$O is 5.6‰ for NEEM, 4.7‰ for NGRIP, 4.2‰ for GISP2, and 4.6‰ for GRIP (Table 3 and Appendix B for uncertainties estimation). As a result, the α coefficient decreases from NEEM to GISP2 for DO 8 and 10. For DO 9, no significant regional difference can be detected in reconstructed temperatures nor in $\Delta\delta^{18}$O. For this small event, the signal is small compared to the data uncertainties, therefore any spatial gradient becomes difficult to verify. For DO 8 and 10, the larger temporal values of α encountered at NEEM are probably explained by smaller precipitation seasonality effects for this site, which is already biased towards summer at present-day by a factor of 2 to 3.5 (Steen-Larsen et al., 2011; Sjolte et al., 2011; Persson et al., 2011). In other words, because warm periods already undersample the winter snow at NEEM, a winter snow reduction during cold periods at NEEM cannot have an effect as strong as for the NGRIP and the GISP2/GRIP sites, where precipitation are indeed distributed year-round for present-day. We note that α decreases with site elevation (Tables 1 and 3). Interestingly, for DO 8 and 10 the spatial pattern of DO α distribution appears consistent with the spatial patterns of present-day interannual slopes (for summer or winter months), which are also higher in the NW sector (Sjolte et al., 2011). We also note that our spatial patterns of temperature and accumulation increases for DO 8 and 10 are consistent with the pattern obtained by Li et al. (2010). In this study, a 5 °C temperature warming is simulated at

Table 3. DO increase (GI-GS) in δ^{18}O, temperature and accumulation (mm.i.e.a^{-1}) for NEEM, NGRIP, GRIP and GISP2. For $\Delta\delta^{18}$O, ΔT and α, for each given DO event, two numbers written with different colors are significantly different from each other. A number in italic is not significantly different from all other numbers. See text for details and Sect. B for uncertainties quantification.

	DO 8				DO 9				DO 10			
	NEEM	NGRIP	GISP2	GRIP	NEEM	NGRIP	GISP2	GRIP	NEEM	NGRIP	GISP2	GRIP
Stadial δ^{18}O	−43.52	−42.74	−41.32	−41.49	−42.66	−42.62	−40.68	−41.03	−42.65	−42.74	−41.33	−41.43
$\Delta\delta^{18}$O	5.57	4.68	4.21	4.57	3.09	2.59	2.37	3.05	4.32	3.97	3.45	3.66
ΔT	8.85	*10.42*	11.09		*6.02*	*5.50*		*6.21*	7.72	11.56		
α	0.63	*0.45*	0.38		*0.51*	*0.47*		*0.49*	0.56	0.34		
Stadial acc.	47	49	60	59	46	52	64	61	43	51	58	56
Δacc	58	58	82	81	14	18	23	37	36	45	56	55

Summit with an amplitude decreasing from south to north in response to sea-ice reduction in the Nordic seas.

In addition to differences in seasonality/precipitation intermittency, differences in moisture transportation paths may also modulate the spatial gradients of α over DO events. Although this effect cannot fully explain the fact that the slopes are systematically lower than at present, it could contribute to the difference between the slopes at NEEM, NGRIP and GISP2 (see Sect. 3.3.1). Several studies conducted with isotopic atmospheric general circulation models equipped with water tagging have indeed revealed different isotopic depletions related to the fraction of moisture transported from nearby or more distant moisture sources under glacial conditions (Werner et al., 2001; Charles et al., 2001). In particular, changes in storm tracks were simulated in response to the topographic effect of the Laurentide ice sheet, resulting in the advection of very depleted Pacific moisture towards North Greenland. Indeed, systematic offsets between water stable isotope records of GRIP and NGRIP have been documented during the last glacial period (NGRIP members, 2004). So far, we cannot rule out that changes in moisture origin may cause differences in δ^{18}O variations between NEEM, NGRIP, and GISP2. Assessing the importance of source effects will require the combination of deuterium excess and ^{17}O excess data with regional isotopic modeling and remains beyond the scope of this study.

3.4 Past surface accumulation rate reconstruction and glaciological implications

For NEEM, NGRIP and GRIP (reduced DJ-accumulation) as well as GISP2 (original accumulation from Cuffey and Clow, 1997), accumulation variations follow annual layer thickness variations: for each ice core, the smallest accumulation increase is seen for DO 9 and the largest one where the temperature increase is largest (DO 8 for NEEM, DO 8 and 10 for NGRIP). Accumulation shifts therefore scale with temperature variations (Table 3). This is in agreement with the thermodynamic approximation considering the atmospheric vapor content, and thus the amount of precipitation, as an exponential function of the atmospheric temperature. Comparing the four sites, NEEM and NGRIP show similar accumulation rates, whereas the accumulation is clearly higher at GISP2 and GRIP over the whole time period.

One important finding of our study is the requirement for a lower accumulation rate at NEEM, NGRIP and GRIP over DO 8–10, compared to the initial accumulation rate given by the DJ ice flow model. Taking into account the presence of a possible convective zone at NEEM, our reconstruction based on firn modeling needs to reduce the original DJ accumulation rate by 28 % (12 m convective zone) to 35 % (2 m convective zone).

Several lines of evidence point to an overestimation of the glacial accumulation rates given by the DJ model. First, in their temperature reconstruction for DO 9 to 17, Huber et al. (2006), using the firnification model of Schwander et al. (1997), also had to decrease the accumulation rate calculated by the DJ model by 20 % everywhere to fit the observed Δdepth. We found similar results applying the Goujon model to the NGRIP ice core over DO 8–10. For DO 9 on GRIP, we need to reduce the DJ-accumulation rate by 40 %; the resulting accumulation rate is then very similar to that at GISP2 (Fig. 4). For GISP2 on DO 8, Orsi et al. (2013) used the Goujon model and an accumulation rate of 0.059 m.i.e.a^{-1} for the GS preceding DO 8, as calculated by the ice flow model from Cuffey and Clow (1997) adapted to the GICC05 timescale.

It is very unlikely that GISP2 and GRIP have significantly different accumulation histories. Indeed, at present GRIP is located 28 km east of GISP2 and the ice divide is not between them, therefore no foehn effect is expected (Buchardt et al., 2012). A small (8 %) accumulation difference is reported for the last 200 a (Meese et al., 1994; Johnsen et al., 1992). During the glacial period, the expansion of the ice sheet margins is expected to produce a flatter topography in central Greenland, further reducing a possible foehn effect. Therefore, large differences in past accumulation rates between GISP2 and GRIP are not climatically plausible; the observed discrepancy must be an artifact of the different methodologies deployed to estimate accumulation rates. Note that during the glacial inception, Landais et al. (2004a, 2005) were able to reproduce the measured δ^{15}N at NGRIP with the

original timescale (ss09sea06bm, NGRIP members, 2004) and accumulation values from the DJ model. In the climatic context of the glacial inception, marked by higher temperatures compared to DO 8–10, firnification model and DJ ice flow models seem to agree.

Altogether, these results suggest that the DJ model is consistent with firn constraints during interglacials and inceptions, but a mismatch is obvious during DO 8–10, likely representative of glacial conditions. We now summarize three potential causes that could produce an overestimation of glacial accumulation in the DJ model (for a detailed presentation of this model we refer to Dansgaard and Johnsen, 1969).

a. Wrong age scale produced by the DJ model: the DJ model could underestimate the duration between two given depths in the ice core and thus overestimate the accumulation rate. However, for the NEEM ice core from present until 60 ka b2k, the DJ model is tuned in order to produce an age scale in agreement with the GICC05 timescale (Buchardt, 2009). For the NGRIP core, the ss09sea06bm timescale produced by the DJ model together with the accumulation rate has been validated back to 60 ka b2k by comparison to the GICC05 time sale (Svensson et al., 2008). The cumulated uncertainty associated with the GICC05 timescale at 60 ka b2k is 2600 a (Svensson et al., 2008), which could explain 5 % maximum of accumulation reduction, assuming a systematic undercounting of the annual layers. For the glacial inception at NGRIP, Svensson et al. (2011) have counted annual layers on particular sections during DO 25 and the glacial inception and confirm the durations proposed by the ss09sea06bm timescale. We therefore rule out a possible wrong timescale as the main cause for the disagreement on these particular periods.

b. The changing shape of the Greenland ice sheet over time (thickness and margin location) may affect the reconstructed accumulation rate, as suggested by model studies from Cutler et al. (1995) and Cuffey and Clow (1997). The DJ model assumes a constant ice sheet thickness over time for NGRIP (Grinsted and Dahl-Jensen, 2002) and a variable one for NEEM (Buchardt, 2009; Vinther et al., 2009). Concerning the DJ model applied to the NGRIP site, runs with constant ice sheet thickness histories or the one from Vinther et al. (2009) were compared (Buchardt, 2009, Chap. 5, Fig. 5.22) and agree well for MIS3. Using a constant or variable ice sheet thickness in the DJ model should thus not affect much the reconstructed accumulation rate. The DJ model has one spatial dimension and no effect of margin location changes can be assessed. It would be interesting to incorporate a parametrization that could account for this later effect and perform sensitivity tests.

c. The DJ model assumes that the vertical velocity field (v_z) changes only with surface accumulation rate variations, all the other parameters being kept constant (basal sliding, basal melt rate, kink height). The best guess input accumulation rate is a tuned exponential function of δ^{18}O (e.g., Johnsen et al., 1995). Tests with a simple DJ model adapted to the GRIP site show that reducing the input surface accumulation rate also reduces the annual layer thicknesses and the total vertical velocity v_z, integrated from top to bedrock. In the output timescale the modeled ice age at a certain depth is older. To still get a correct timescale in agreement with GICC05, we would need to deepen the kink height. The same effect would apply to all other Greenland sites. The shape of v_z and therefore the kink height is also expected to vary with the ice sheet temperature profile and dust content through changes in ice viscosity (for more details we refer to Cuffey and Paterson, 2010, Chap. 9). During the glacial period, the connection between the Greenland ice sheet and the Ellesmere Island ice could also modify the Greenland ice flow. This effect is expected to affect more the ice flow at NEEM, which is the closest site to Ellesmere Island, than at NGRIP, GRIP and GISP2. In 1969, when creating the DJ model to date the Camp Century ice core, the authors assumed a constant kink height over time due to a lack of information (Dansgaard and Johnsen, 1969). Using a variable kink height will also modify th best guess relationship calculated between input accumulation rate and δ^{18}O.

To conclude, there are huge uncertainties on past accumulation rate reconstructions. Comparing three different reconstructions for Summit (Cutler et al., 1995; Cuffey and Clow, 1997; Johnsen et al., 2001), we suggest that the glacial accumulation rate reconstructed by the DJ model has to be taken as a high boundary, the low boundary being at least 50 % lower. This may apply to NGRIP and NEEM. Our firn-model-based accumulation rates lie in this envelope. We suggest that both thickness and margin location changes should be taken into account in the DJ model. A better agreement between the Cutler et al. (1995) model, the Cuffey and Clow (1997) model and the DJ model may also be found by using a variable kink height in the DJ model.

4 Conclusions and perspectives

Air and water stable isotopes measurements from four Greenland deep ice cores (GISP2, GRIP, NGRIP and NEEM) have been investigated over a series of Dansgaard–Oeschger events (DO 8, 9 and 10), which are representative of glacial millennial scale variability. We have presented the first δ^{15}N data from the NEEM core and combined them with new and previously published δ^{15}N data from NGRIP, GRIP and GISP2. Combined with firn modeling, air isotope data allow us to quantify abrupt temperature increases for each ice core site. For DO 8, the reconstructed temperature increase is 8.8 °C for NEEM, 10.4 °C for NGRIP, and 11.1 °C for

GISP2. Our data show that for DO 8 and 10, the magnitude of GS–GI increase is up to 2 °C larger in central (GISP2) and North Greenland (NGRIP) than in NW Greenland (NEEM). The reconstructed accumulation increases follow the same spatial pattern. These observations are in agreement with a study of spatial Greenland response to reduced sea-ice extent in the Nordic seas (Li et al., 2010). no spatial gradient is detected for the small DO 9 event. The temporal $\delta^{18}O$–temperature relationship varies between 0.3 and 0.6 ‰ $°C^{-1}$ and is systematically larger at NEEM, possibly due to limited changes in precipitation seasonality compared to GISP2 or NGRIP. The relatively high isotope–temperature relationship for NEEM will have implications for climate reconstructions based on NEEM water isotopes data. Further paleotemperature investigations are needed to assess the stability of this relationship over glacial–interglacial variations. In particular, it would be interesting to compare the presented reconstruction with the temperature–water isotopes relationship over the different climatic context of MIS 5. A better understanding of the causes of the regional isotope and temperature gradients in Greenland requires further investigations of possible source effects (using deuterium excess and ^{17}O excess), and an improved characterization of atmospheric circulation patterns. We hope that our results will motivate high resolution simulations of DO type changes with climate models equipped with water stable isotopes, in order to test how models capture regional gradients in temperature, accumulation and isotopes, and to understand the causes of these gradients from sensitivity tests (e.g., associated with changes in ice sheet topography, SST patterns, sea ice extent).

The gas age−ice age difference between abrupt warming in water and air isotopes can only be matched with observations when assuming a 26 % (NGRIP) to 40 % (GRIP) lower accumulation rate than derived from the Dansgaard–Johnsen ice flow model. We question the validity of the DJ model to reconstruct past glacial accumulation rate and recommend on the time interval 42 to 36 ka b2k to use our reduced accumulation scenarios. We also suggest that the DJ ice flow model is too simple to reconstruct a correct accumulation rate all along the ice cores and propose to test the incorporation of variable ice sheet margins location and kink height in this model. Our results call for a systematic evaluation of Greenland temperature and accumulation variations during the last glacial–interglacial cycle, combining continuous $\delta^{15}N$ measurements with firnification modeling. Using a correct accumulation rate is of high importance to reconstruct accurate ice- and gas-age scales and to calculate fluxes based on concentrations of different species in the ice. Moreover, a better estimation of past surface accumulation rates at precise locations in Greenland would help to constrain past changes in ice flow with implications for ice sheet mass balance and dynamics.

Appendix A

The Goujon firnification model: method

The firnification model has only one space dimension and calculates the vertical velocity field along the vertical coordinate and the temperature profile across the entire ice sheet for each time step of one year. In the firn, it calculates the density profile from the surface to the close-off depth. The density profile and the accumulation history allow us to obtain the ice age at LID and, assuming gas age equal to zero at LID, the Δage. The temperature field from surface to bedrock is then used to reconstruct the density profile in the firn, the firn temperature gradient, and from there the $\delta^{15}N$ at LID. We follow Goujon et al. (2003) where the LID is defined as the depth where the ratio closed to total porosity reaches 0.13. The model is adapted to each ice core site in terms of vertical velocity field, basal melt rate, ice sheet thickness, elevation, surface temperature and accumulation scenarios (Table 1). We assume a convective zone of 2 m at the top of the firn.

A1 Validation of the Goujon firnification model for present day at NEEM

We use the present-day characteristics of the firn at NEEM to validate the Goujon firnification model. During the 2008 summer field season, a shallow core was drilled at the S2 site at NEEM. Firn air was sampled at different depths from the surface to 80 m depth in this borehole (for more details see Buizert et al., 2012). From these air samples, $\delta^{15}N$ was measured at LSCE (Fig. A1). The increasing $\delta^{15}N$ with depth reflects the gravitational fractionation. Given the vertical resolution in the data, we do not see a clear convective zone. Below 62 m depth, $\delta^{15}N$ is constant: the nondiffusive zone is reached. We thus have a LID of 62 m at NEEM for present-day according to these $\delta^{15}N$ data only. In Buizert et al. (2012), using measurements of different gases in the firn and several diffusion models, the S2 borehole is described as follows: a convective zone of 3 m, a diffusive zone of 59 m down to 63 m depth (LID), and a nondiffusive zone down to 78.8 m depth (total pore closure depth). Following this description and assuming no thermal effect, we calculated the corresponding gravitational fractionation affecting $\delta^{15}N$ (Fig. A1, blue line). Annual layer counting of the corresponding shallow core and matching with the GICC05 timescale gives an ice age at LID of 190.6 a b2k $\pm$1 a, and 252.5 a at the total pore closure depth. The age of CO_2 is calculated to be 9.6 a at LID and 69.6 a at the total pore closure depth, producing a Δage of 181 a and 183 a, respectively. The best estimate for the true Δage is estimated to be 182 +3/−9 a (Buizert et al., 2012). We observe that from the LID, the Δage becomes constant within uncertainties. Considering the diffusion coefficient to be 1 for CO_2 and using 1.275 for N_2 as in Buizert et al. (2012), the age of N_2 is 7.5 a at the LID, giving a Δage of 183 a.

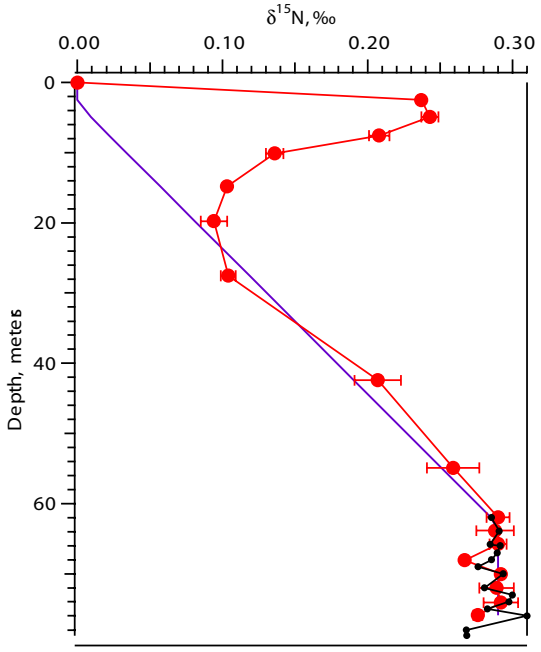

Fig. A1. Present-day firn at NEEM. Red dots: δ^{15}N data measured at LSCE. Blue line: gravitational fractionation for δ^{15}N, assuming a convective zone of 3 m and the LID at 63 m depth (Buizert et al., 2012). Black dots: modeled δ^{15}N with the Goujon firnification model.

We run the Goujon model using the NEEM07S3 shallow core age scale and δ^{18}O for the top 60 m (Steen-Larsen et al., 2011) and the NEEM main core below. The δ^{18}O record is used to reconstruct the past temperature variations using $\alpha = 0.8$ (Sjolte et al., 2011); we use $\beta = 9.8$ in order to obtain the measured average present-day temperature of $-29\,^{\circ}$C (Steen-Larsen et al., 2011). Using the density profile measured along the NEEM07S3 core and the corresponding age scale, the past accumulation history was reconstructed (Steen-Larsen et al., 2011) and used here as input for the firnification model. The firnification model estimates the LID at 61.4 m depth. Modeled δ^{15}N values agree well with the measured ones in this region (Fig. A1). At 63 m depth, the estimated ice age is 189 a (according to the NEEM07S3 core dating, which agrees very well with the S2 core dating). Ignoring the gas age at LID thus results in an overestimation of the Δage by less than 10 yr for present-day.

A2 Reconstruction of the past gas age scale

Simulations with the Goujon model show that at the onset of DO events 8, 9 and 10, the heat diffusion in the firn is slow enough so that the peaks of maximum temperature gradient in the firn are synchronous with the δ^{18}O peaks. We thus consider that the peaks of δ^{15}N occur at the same time as the δ^{18}O peaks. However, the Goujon model has no gas diffusion component and this has two consequences: (a) the gas age at LID, due to the time for air to diffuse in the firn, is assumed to be zero; (b) any broadening of the initial δ^{15}N peak by gas diffusion in the firn is not taken into account. For present-day, the gas age at LID is 9.6 a for CO_2 (Buizert et al., 2012) and we calculate it to be 7.5 a for N_2. The Schwander model calculates a N_2 age up to 20 a at the LID over DO 8 to 10 for NGRIP (Huber et al., 2006). The Goujon model thus systematically overestimates the Δage by 10 to 20 yr in the glacial period, which is within the mean Δage uncertainty of 60 yr (Table 2). For the NGRIP core, our temperature reconstruction with the Goujon model (without gas diffusion) is in agreement with the temperature reconstruction from Huber et al. (2006) where the Schwander model (with gas diffusion) is used (Fig. D1). We thus consider that the lack of gas diffusion in the Goujon model has an impact that stays within the error estimate (Appendix Sect. B).

For DO 8 to 10 at NEEM, we present the measured and modeled δ^{15}N data plotted on an age scale in Fig. A3. The Δage calculated by the model (Fig. A3, subplot d) is used to synchronize the gas record to the ice record. We have also reported here the Δage tie-points from Table 2 and we can see that the modeled Δage reproduces these points, within the error bar.

A3 Sensitivity tests

A3.1 Vertical velocity field

In the firnification model, we used two different parameterizations for the vertical velocity field: the analytical solution from Lliboutry (1979), as in the original model from Goujon et al. (2003), and a Dansgaard–Johnsen type vertical velocity field (Dansgaard and Johnsen, 1969). In the later case, we used the same parametrization as used in the DJ model to calculate past accumulation rates (ice sheet thickness, kink height, fraction of basal sliding, basal melt rate) and then tried different kink heights between 1000 m and 1500 m above bedrock. All these tests produce the same modeled LID and, hence, the same modeled δ^{15}N. The different parameterizations actually produce very similar vertical velocity fields in the firn. Because δ^{15}N is only sensitive to processes occurring in the firn, huge modification of the vertical velocity field deep in the ice (for example by modifying the kink height) has no impact here.

A3.2 Basal temperature

We also varied the basal temperature between $-2.99\,^{\circ}$C as measured at present in the borehole (Simon Sheldon, personal communication, 2012) and $-1.68\,^{\circ}$C, which is the melting temperature as calculated in Ritz (1992) and can be considered as a maximum basal temperature. There is no difference in the modeled LID. Indeed, the relatively high accumulation rate even in the glacial period makes the burial of the snow layers quite fast. As a result, the firn temperature is

mostly influenced by the surface temperature but not by the bedrock temperature.

A4 Effect of a convective zone

The Goujon model is written in a way that there is neither heat diffusion nor densification of the firn in the convective zone. No densification of the top firn may be acceptable on the first 2 m but becomes unrealistic when increasing the convective zone. Alternatively, instead of a "true" convective zone, we can prescribe a nongravitational zone, where heat transfert in ice still occurs. This reduces the diffusive column height (DCH) used to calculate the gravitational enrichment of δ^{15}N but does not modify its thermal fractionation.

A convective zone deeper than 2 m during the glacial period at NEEM is possible, created by strong katabatic winds due to a steep ice sheet flank, like the 14 m convective zone at YM85 site in Antarctica (Fig. A2 and Kawamura et al., 2006). However, during the glacial period, the Greenland ice sheet may have been connected to Ellesmere Island and the lateral margins were extended compared to present. This would create a flatter surface at the NEEM site, possibly also NGRIP, and would not favor the existence of strong katabatic winds. Marshall and Koutnik (2006) modeled the icebergs delivery from the Northern Hemisphere ice sheets over DO events and showed that the ice sheet margins from Greenland and the Canadian Arctic do not particularly respond to DO events, because these regions remain too cold even during GI. This is not in favor of abrupt change in the convective zone due to ice sheet shape changes at the GS–GI transition.

A convective zone may also be created by a low accumulation rate (as observed at Vostok or Dome F, Fig. A2). The deepest known convective zone (23 m) is reported at the zero-accumulation site Megadunes in Antarctica (Severinghaus et al., 2010). However, note that there is no convective zone at Dome C (Landais et al., 2006) where the present-day annual mean accumulation rate is 2.5 cm w.e.a^{-1}, slightly higher than at Vostok and Dome F. Our best guess accumulation rate for NEEM, NGRIP and GRIP during MIS3, using a 2 m convective zone, is always higher than at Dome C today (Fig. A2). This is also true for the GISP2 site (Orsi et al., 2013). All these observations are in favor of no deep convective zone at NEEM, NGRIP, GRIP and GISP2 during MIS3.

The existence of a convective zone would affect the average level of δ^{15}N, through the reduction of the diffusive zone, but not the modeled Δdepth that is a function of the total firn thickness (LID), itself dependant of surface temperature and accumulation. For NEEM, to reproduce both the measured Δdepth and δ^{15}N values, using the original DJ accumulation rate, we need to reduce the temperature scenario d3 by 9 °C everywhere and use a 50 m convective zone (not shown). The obtained system of temperature-accumulation-convective zone is inconsistent with present-day observations

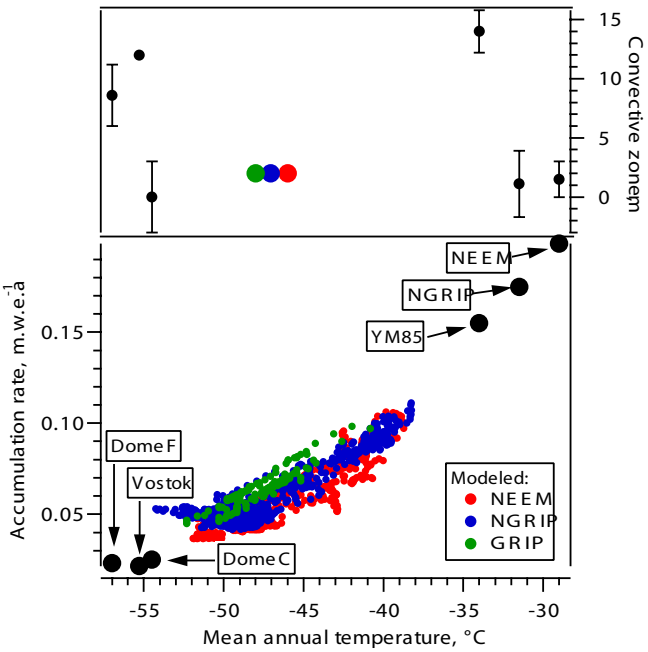

Fig. A2. Bottom: accumulation rate (m.w.e.a^{-1}) vs. temperature (°C). NEEM (red), NGRIP (blue) and GRIP (green), modeled during MIS3. Black dots: measured for different present-day sites. Top: convective zone (m) vs. temperature.

in Greenland and Antarctica (accumulation rate much too large compared to the temperature and convective zone).

As a sensitivity test, we have made simulations with the Goujon model using a constant convective zone of 12 m during MIS3 for NEEM (Fig. 3) and NGRIP (not shown), where we still need to reduce the accumulation rate to match the measured δ^{15}N profile (by 28 % for NEEM and 19 % for NGRIP).

Appendix B

Uncertainties quantification

B1 Temperature increase

The uncertainty associated with temperature reconstruction arises from the contribution of several sources of uncertainties: analytical uncertainties associated with δ^{15}N measurements, uncertainty associated with the estimation of the δ^{15}N temperature sensitivity (Ω parameter), uncertainty related to modeling of firn heat diffusion and firnification. In a simple way, based on Eq. (2), we can write the temperature increase ΔT as

$$\Delta T = \frac{\Delta\delta^{15}\mathrm{N}_{\mathrm{therm}}}{D\Omega}, \tag{B1}$$

where $\Delta\delta^{15}\mathrm{N}_{\mathrm{therm}}$ is the difference in $\delta^{15}\mathrm{N}_{\mathrm{therm}}$ between GS and GI, D is a coefficient for the heat diffusion

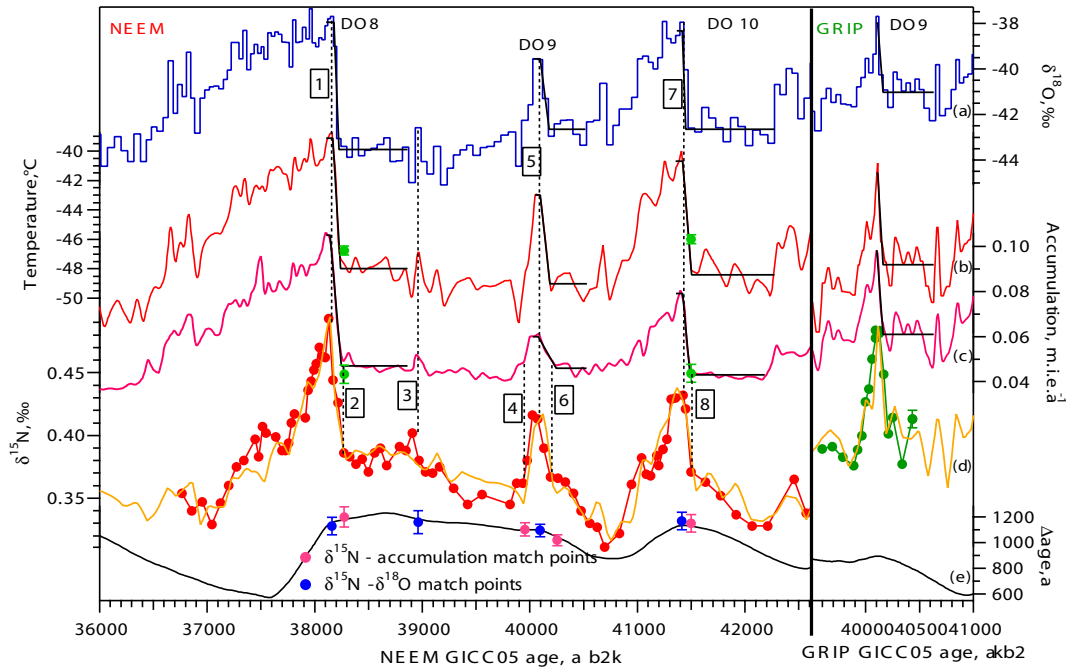

Fig. A3. δ^{15}N reconstruction for NEEM (left) and GRIP (right). **(a)** δ^{18}O profile used to reconstruct the surface temperature profile. **(b)** Surface temperature scenario used in the Goujon model (red line) and in the Herron Langway model (NEEM, 2 green dots). **(c)** Accumulation scenario for the Goujon model (pink line) and the HL model (NEEM, 2 green dots). **(d)** δ^{15}N data measured at LSCE, this study (red (NEEM) and green (GRIP) line and markers) and modeled δ^{15}N by the Goujon model (orange line), using temperature and accumulation scenario shown in **(b)** and **(c)**, plotted on the ice age scale using the Δage produced by the Goujon model (e, black line). Δage tie points are numbered as in Table 2. **(e)** Markers: tie points between δ^{15}N and δ^{18}O (blue markers) or accumulation (pink markers), used to constrain the firnification models. Black line: Δage modeled by the Goujon model. Subplots **(a)**, **(b)** and **(c)**, in black: GS and GI mean states calculated by the rampfit method.

in the ice, and Ω is the thermal diffusion sensitivity (Grachev and Severinghaus, 2003).

To sum the uncertainties we use the general formula (Press et al., 2007):

$$\sigma_x = \sqrt{\sigma_a^2 \left(\frac{\partial x}{\partial a}\right)^2 + \sigma_b^2 \left(\frac{\partial x}{\partial b}\right)^2 + \sigma_c^2 \left(\frac{\partial x}{\partial c}\right)^2} \quad \text{(B2)}$$

where x is a function of a, b, and c associated with, respectively, σ_a, σ_b, and σ_c as standard errors. We can thus sum the uncertainties associated to the temperature increase:

$$\sigma_{\Delta T} = \sqrt{\sigma^2_{\Delta\delta^{15}\mathrm{N_{therm}}} \left(\frac{1}{D\Omega}\right)^2 + \sigma^2_{\Omega} \left(\frac{-\Delta\delta^{15}\mathrm{N_{therm}}}{\Omega^2 D}\right)^2 + \sigma^2_{D} \left(\frac{-\Delta\delta^{15}\mathrm{N_{therm}}}{\Omega D^2}\right)^2} \quad \text{(B3)}$$

$$\text{or } \sigma_{\Delta T} = \sqrt{\sigma^2_{\Delta T,\Delta\delta^{15}\mathrm{N_{therm}}} + \sigma^2_{\Delta T,\Omega} + \sigma^2_{\Delta T,D}}. \quad \text{(B4)}$$

$\sigma_{\Delta T,\Delta\delta^{15}\mathrm{N_{therm}}}$: this uncertainty results from the analytical uncertainty for δ^{15}N measurements and from firnification modeling uncertainty. The pooled standard deviation of our NEEM δ^{15}N measurement is 0.006 ‰. We use n_{GI} points to define the GI value (respectively 1, 2, and 3 points for DO 8, 9, and 10) and n_{GS} points for the GS value (respectively 9, 3, and 6 points). For a GS to GI increase, the $\Delta\delta^{15}$N uncertainty is thus:

$$\sigma_{\Delta\delta^{15}\mathrm{N}} = \sqrt{\frac{\sigma^2_{\delta^{15}\mathrm{N}}}{n_{\mathrm{GS}}} + \frac{\sigma^2_{\delta^{15}\mathrm{N}}}{n_{\mathrm{GI}}}} \quad \text{(B5)}$$

which gives, respectively, 0.006, 0.006, and 0.004 ‰ for DO 8, 9, and 10. We run the firnification model with a modified temperature scenario in order to exceed the δ^{15}N peak value by 0.006 ‰ maximum, for each DO event. The accumulation scenario is kept unchanged. The obtained temperature increase is 0.58 °C larger. If we calculate $\sigma_{\Delta T,\Delta\delta^{15}\mathrm{N}}$ as given by Eq. (B3) we obtain 0.52 °C. We conclude that the maximum associated temperature uncertainty is 0.58 °C. Concerning the validity of the firnification modeling, we have already shown in Sect. 3.1 that numerous tuning tests performed with the Goujon model do not modify the estimated temperature increase. When using different firnification models (Schwander or Goujon) with similar inputs scenarios, the modeled δ^{15}N profiles are similar. Moreover, the duration of temperature increase is well constrained by the GICC05 chronology

and the high resolution δ^{18}O data. The GICC05 dating and the identification of numerous Δage tie points (Table 2) between gas- and ice phases gives strong constrains on the accumulation scenario. We are thus quite confident in the validity of our firnification model to reconstruct past surface temperature and accumulation variations.

$\sigma_{\Delta T,D}$: since the duration of the temperature increase is very well known, the uncertainty on the heat diffusion effect is thus rather small. In our case, it decreases the firn temperature gradient by 1.66 °C with respect to a surface temperature increase of 9.02 °C for DO 8 for NEEM. The major uncertainty in the heat diffusion model is linked to snow/ice conductivity modelisation. For the snow conductivity, we use the formulation from Schwander et al. (1997) where it is a function of the ice conductivity. We have tried different formulations for the ice conductivity (Weller and Schwerdtfeger, 1971; Yen, 1981) and modeled δ^{15}N are very similar.

$\sigma_{\Delta T,\Omega}$: we calculate the uncertainty linked to Ω uncertainty (± 3 %, Grachev and Severinghaus, 2003) to be 0.22, 0.13, and 0.17 °C for DO 8, 9, and 10 respectively for the NEEM core. This uncertainty increases with the estimated temperature increase and is therefore higher for DO 8.

Summing up all these uncertainties, we estimate the error on the reconstructed NEEM temperature increase for each DO event to be ~ 0.6 °C (1σ). Following the same approach, we estimate the uncertainty to be ~ 1.5 °C (1σ) for NGRIP and ~ 0.6 °C for GRIP. For GISP2, we also add an uncertainty of 0.07 °C linked to the amplitude of the accumulation increase (Orsi et al., 2013) and obtain 0.6 °C. The larger uncertainty at NGRIP is mainly caused by the larger analytical uncertainty (0.006 ‰ for NEEM and GRIP δ^{15}N data, 0.02 ‰ for NGRIP δ^{15}N data).

B2 δ^{18}O ice temperature sensitivity

The temperature sensitivity of δ^{18}O measured in the ice is defined by the parameter $\alpha = \Delta\delta^{18}O/\Delta T$. For NEEM, δ^{18}O data are measured with an accuracy of 0.07 ‰. We use 2 δ^{18}O points to estimate the GI value and 12 (DO 8 and 10) or 9 (DO 9) data points to estimate the GS δ^{18}O value. The uncertainty associated with the δ^{18}O increase is

$$\sigma_{\Delta\delta^{18}\mathrm{O}} = \sqrt{\frac{\sigma^2_{\delta^{18}\mathrm{O}}}{n_{\mathrm{GS}}} + \frac{\sigma^2_{\delta^{18}\mathrm{O}}}{n_{\mathrm{GI}}}} \tag{B6}$$

which gives 0.05 ‰ for DO 8, 9, and 10. Following the same approach, we obtain uncertainties for, respectively, DO 8, 9, and 10 of 0.04, 0.05, and 0.04 ‰ for the NGRIP ice core, and 0.04, 0.08, and 0.06 ‰ for the GRIP ice core. We obtain 0.02 ‰ for the GISP2 core.

For NEEM, temperature and δ^{18}O increases uncertainties result in a 0.05 ‰ °C^{-1} uncertainty for α. We obtain 0.08, 0.12, and 0.06 ‰ °C^{-1} for DO 8, 9, and 10 for NGRIP and 0.05 ‰ °C^{-1} for GISP2 and GRIP following the same approach.

B3 Confidence intervals

We propose here two different approaches to determine whether two increases (δ^{18}O or temperature), Δi and Δj, are different from each other.

First approach: for each calculated Δi we have calculated an associated error estimate σ_i (see previous section). Assuming a Gaussian distribution, each Δi can be defined by a Gaussian distribution function centered in Δi:

$$f(x) = \frac{1}{\sigma_i\sqrt{2\pi}} \exp\left(\frac{-(x-\Delta i)^2}{2\sigma_i}\right). \tag{B7}$$

The probability to get a value $x \pm a_i$ for this Δi is the corresponding integral:

$$p_i = \int_{-a_i}^{a_i} f(x) = \mathrm{erf}\left(\frac{x-\Delta i}{\sigma_i\sqrt{2}}\right). \tag{B8}$$

The integral from $-\infty$ to $+\infty$ equals one. For each pair of increases Δi and Δj, we calculate the respective maximum confidence intervals $[-a_i; a_i]$ and $[-a_j; a_j]$ in a way that these two intervals do not overlap and that $\int_{-a_i}^{a_i} f(x) = \int_{-a_j}^{a_j} g(x)$. The integrals $p_i = p_j$ correspond to the probability to have the value $\Delta i \pm a_i$ and $\Delta j \pm a_j$. We consider that if $p_i = p_j \geq 0.9$, the two increases are significantly different from each other.

Second approach: we take a couple of temperatures increases ΔT_i and ΔT_j, assume both to have Gaussian distribution, and calculate the probability of the difference ΔT_i-ΔT_j to have a value X:

$$\Delta T_i - \Delta T_j = X \tag{B9}$$

$$p(X = x) = \int \mathrm{d}\tilde{x}\ p(\Delta T_i = \tilde{x})\ p(\Delta T_j = \tilde{x} - x) \tag{B10}$$

$$p(X = x) = \frac{1}{\sqrt{2\pi}\sqrt{\sigma_i^2 + \sigma_j^2}} \int \exp\left(-\frac{(x - (\Delta T_i - \Delta T_j))^2}{2(\sigma_i^2 + \sigma_j^2)}\right)\mathrm{d}x. \tag{B11}$$

Equation (B11) can then be used to find the probability that $X = 0$, hence that ΔT_i=ΔT_j. The probability that ΔT_i is exactly equal to ΔT_j is nil by definition and we have to define the depth interval over which to integrate Eq. (B11). We will thus calculate the probability that $\Delta T_i = \Delta T_j \pm a$ by assigning the integration range for Eq. (B11) to $[-a; a]$. There is a necessary subjectivity in the choice of this interval. We have chosen to base this estimate of a on the uncertainty

associated with our data so that we take $a = \sqrt{\sigma_i^2 + \sigma_j^2}$:

$$p(-\sqrt{\sigma_i^2+\sigma_j^2} < x < \sqrt{\sigma_i^2+\sigma_j^2}) = \int_{-\sqrt{\sigma_i^2+\sigma_j^2}}^{\sqrt{\sigma_i^2+\sigma_j^2}} p(X=x)\,\mathrm{d}x \quad \text{(B12)}$$

$$= \frac{1}{\sqrt{2\pi}\sqrt{\sigma_i^2+\sigma_j^2}} \int_{-\sqrt{\sigma_i^2+\sigma_j^2}}^{\sqrt{\sigma_i^2+\sigma_j^2}} \exp\left(-\frac{(x-(\Delta T_i - \Delta T_j))^2}{2(\sigma_i^2+\sigma_j^2)}\right)\mathrm{d}x \quad \text{(B13)}$$

$$= \frac{1}{2}\left(\mathrm{erf}\left(\frac{x-(\Delta T_i-\Delta T_j)}{\sqrt{\sigma_i^2+\sigma_j^2}\sqrt{2}}\right) - \mathrm{erf}\left(\frac{-x-(\Delta T_i-\Delta T_j)}{\sqrt{\sigma_i^2+\sigma_j^2}\sqrt{2}}\right)\right). \quad \text{(B14)}$$

Finally, we consider ΔT_i and ΔT_j to be significantly different when $p(-\sqrt{\sigma_i+\sigma_j} < x < \sqrt{\sigma_i+\sigma_j})$ is equal or less than 0.1.

We now apply this probability calculation for DO 8 for the following comparison:

- NEEM vs. NGRIP: $a = 1.6\,^\circ$C, $\Delta\ T_{\mathrm{NEEM}}$-$\Delta\ T_{\mathrm{NGRIP}} = 1.6\,^\circ$C so that the probability that $\Delta\ T_{\mathrm{NEEM}} = \Delta\ T_{\mathrm{NGRIP}} \pm 1.6$ is calculated with Eq. (B14) as $p = 0.48$.
- NGRIP vs. GISP2: $a = 1.6\,^\circ$C, $\Delta\ T_{\mathrm{NGRIP}}$-$\Delta\ T_{\mathrm{GISP2}} = 0.7\,^\circ$C so that the probability that $\Delta\ T_{\mathrm{NGRIP}} = \Delta\ T_{\mathrm{GISP2}} \pm 1.6$ is calculated with Eq. (B14) as $p = 0.62$.
- NEEM vs. GISP2: $a = 0.85\,^\circ$C, $\Delta\ T_{\mathrm{NEEM}}$-$\Delta\ T_{\mathrm{GISP2}} = 2.25\,^\circ$C so that the probability that $\Delta\ T_{\mathrm{NEEM}} = \Delta\ T_{\mathrm{GISP2}} \pm 0.85$ is calculated with Eq. (B14) as $p = 0.05$.

These calculations give the same conclusion as obtained from approach 1: for DO 8, $\Delta\ T_{\mathrm{NEEM}}$ is significantly different from $\Delta\ T_{\mathrm{GISP2}}$ with 94 % confidence (first approach) or, according to approach 2, these two temperature increases are significantly equal with 5 % confidence.

The results are reported in Table 3 in the following way: for each DO event, if two values are written in two different colors, they are significantly different from each other. A value written in italic is not significantly different from all the others.

Appendix C

NEEM firn modelisation with the Herron Langway model

The Herron Langway model (hereafter HL) is an empirical firnification model where the density profile and the ice age in the firn are calculated based on surface temperature and accumulation (Herron and Langway, 1980). We use a surface snow density of $0.350\,\mathrm{g\,cm^{-3}}$, as in the Goujon firnification model. Based on the HL density profile in the firn, we calculate the ratio closed to total porosity along the firn column (Goujon et al., 2003). To allow comparison with the Goujon model, we use the same definition for the LID: the depth where the ratio close to total porosity reaches 0.13. At this depth, the HL model gives us the ice age, that we use as a Δage estimate, and we calculate $\delta^{15}N_{\mathrm{grav}}$ assuming a convective zone of 2 m. This model has no heat diffusion component and we thus use it on periods where the Goujon model shows negligible thermal fractionation for δ^{15}N (within the δ^{15}N measurement uncertainty), meaning where the surface temperature is stable, without temperature gradient in the firn. We thus can use $\delta^{15}N_{\mathrm{grav}}$ as an estimate for $\delta^{15}N_{\mathrm{tot}}$.

Here, we apply this model on the stadial periods at NEEM to investigate the surface temperature and accumulation scenarios that match the right δ^{15}N level and Δage. We use the δ^{15}N and Δage values just preceding the DO events (see Table 2) as target values and tune the surface temperature and accumulation.

For DO 8, we use a target δ^{15}N value of 0.382 ± 0.006 ‰ and Δage value of 1198 ± 79 a (Table 2, NEEM tie point n. 2). The HL model can reproduce these values using a surface temperature of $-46.76 \pm 0.3\,^\circ$C and an accumulation rate of $0.043 \pm 0.004\,\mathrm{m.i.e.a^{-1}}$ (58 % reduction of the one determined by the DJ ice flow model). The LID is at 76 real meters depth (or 52.8 m.i.e. meters ice equivalent).

For DO 10, we use the NEEM tie point n. 9, where $\delta^{15}\mathrm{N} = 0.371 \pm 0.006$ ‰ and $\Delta\mathrm{age} = 1149 \pm 69$ a. These values are reproduced using as surface temperature $-46.0 \pm 0.3\,^\circ$C and as accumulation rate $0.044 \pm 0.004\,\mathrm{m.i.e.a^{-1}}$ (51 % reduction). The LID is at 73.5 real meters depth (51.0 m.i.e.).

Modeled surface temperature and accumulation for the onset of DO 8 and 10 are plotted in Fig. A3 with green dots. For DO 8, the HL and Goujon models produce very similar surface temperature scenarios but the HL accumulation rate is lower. For DO 10, the HL and Goujon accumulation rates are similar but the HL temperature is much higher. It is very likely that the differences are due to the strong assumption of no thermal gradient in the firn for the HL model. In order to fit the measured GS level of δ^{15}N and the Δage at the onset of DO 8 and 10 with the HL model, we need to use a reduced accumulation rate by 58 and 51 %, respectively. We here confirm the finding from the Goujon model: decreasing significantly the accumulation rate estimated by the DJ ice flow model is necessary to match both δ^{15}N and Δage data.

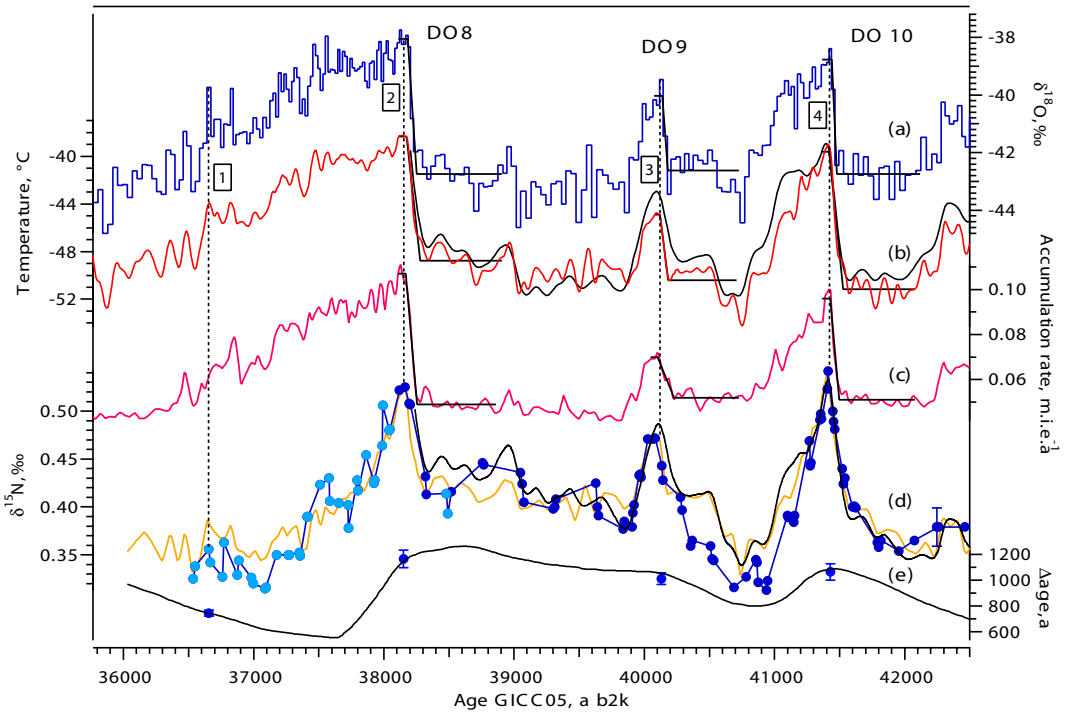

Fig. D1 $\delta^{15}N$ reconstruction for NGRIP. **(a)**, $\delta^{18}O$ profile used to reconstruct the surface temperature profile, NGRIP members (2004). **(b)** Surface temperature scenario used in the Goujon model (red line, this study) and in Huber et al. (2006), black line. Note that the temperature reconstruction covering DO 8 was missing at that time. **(c)** Accumulation scenario for the Goujon model. **(d)** Measured $\delta^{15}N$ data at the University of Bern, Switzerland, with error bar shown on the last point to the right (dark blue dots Huber et al. (2006), new points in light blue dots). Modeled $\delta^{15}N$ by the Goujon model (orange line), using temperature and accumulation scenario shown in **(b)** and **(c)**. Measured and modeled $\delta^{15}N$ are plotted on the ice age scale using the Δage produced by the Goujon model (**e**, black line). Δage tie points are numbered as in Table 2. Black line: modeled $\delta^{15}N$ from Huber et al. (2006) using the temperature scenario in **(b)**, black line. **(e)** Blue markers: tie points between $\delta^{15}N$ and $\delta^{18}O$, used to constrain the firnification models. Black line: Δage modeled by the Goujon model. Subplots **(a)**, **(b)** and **(c)**, in black: stadial and interstatial mean states calculated by the rampfit method.

Appendix D

Reprocessing NGRIP $\delta^{15}N$ data

To allow the comparison between NEEM and NGRIP, we reconstruct here past temperature and accumulation at NGRIP following the same approach as for the NEEM site. We use the Goujon firnification model adapted to the NGRIP site. To constrain the model, we minimize the distance between the measured $\delta^{15}N$ and the modeled one (Fig. D1, c). The corresponding temperature and accumulation scenarios are reported in Fig. D1. For comparison, we also report here the temperature reconstruction from Huber et al. (2006), using the firnification model from Schwander et al. (1997) and the ss09sea06bm timescale. Direct comparison is possible because over DO 8, 9, and 10 (2020 to 2140 m depth), durations proposed by the GICC05 and the ss09sea06bm timescales agree with each other with 5 % difference. Note that the two reconstructions agree well with each other, both for absolute temperature level and temperature variations with time. We use an accumulation rate reduced by 26 % (20 % for Huber et al., 2006) and thus need to reduce the mean temperature level slightly more than Huber et al. (2006) to still match the $\delta^{15}N$ data.

Acknowledgements. We thank Michelle Koutnik, Jesper Sjolte, Aurélien Quiquet and Catherine Ritz for fruitful discussions and furthermore Dan Israel for his great help with statistics. NEEM is directed and organized by the Center for Ice and Climate at the Niels Bohr Institute and US NSF, Office of Polar Programs. It is supported by funding agencies and institutions in 14 countries: Belgium (FNRS-CFB and FWO), Canada (GSC), China (CAS), Denmark (FIST), France (IPEV, CNRS/INSU, CEA and ANR), Germany (AWI), Iceland (RannIs), Japan (NIPR), Korea (KOPRI), The Netherlands (NWO/ALW), Sweden (VR), Switzerland (SNF), UK (NERC) and the USA (US NSF, Office of Polar Programs). LSCE analytical work has been funded by the ANR VMC NEEM project. We also thank the University of Copenhagen and the CNRS/INSU/LEFE program. This is LSCE publication n. 4588

Edited by: F. Parrenin

The publication of this article
is financed by CNRS-INSU.

References

Ahn, J., Brook, E., Schmittner, A., and Kreutz, K.: Abrupt change in atmospheric CO_2 during the last ice age, Geophys. Res. Lett., 39, L18711, doi:10.1029/2012GL053018, 2012.

Alley, R. B., Meese, D. A., Shuman, C. A., Gow, A. J., Taylor, K. C., Grootes, P. M., White, J. W. C., Ram, M., Waddington, E. D., Mayewski, P. A., and Zielinski, G. A.: Abrupt increase in Greenland snow accumulation at the end of the Younger Dryas event, Nature, 362, 527–529, doi:10.1038/362527a0, 1993.

Andersen, K. K., Svensson, A., Johnsen, S. J., Rasmussen, S. O., Bigler, M., Röthlisberger, R., Ruth, U., Siggaard-Andersen, M.-L., Steffensen, J. P., Dahl-Jensen, D., Vinther, B. M., and Clausen, H. B.: The Greenland Ice Core Chronology 2005, 15–42 ka. Part 1: constructing the time scale, Quaternary Sci. Rev., 25, 3246–3257, doi:10.1016/j.quascirev.2006.08.002, 2006.

Arnaud, L., Barnola, J.-M., and Duval, P.: Physical modeling of of the densification of snow/firn and ice in the upper part of polar ice sheets, Hokkaido University Press, Sapporo, Japan, 2000.

Barlow, L. K., White, J. W. C., Barry, R. G., Rogers, J. C., and Grootes, P. M.: The North Atlantic Oscillation signature in deuterium and deuterium excess signals in the Greenland Ice Sheet Project 2 Ice Core, 1840–1970, Geophys. Res. Lett., 20, 2901–2904, doi:10.1029/93GL03305, 1993.

Bender, M., Sowers, T., Barnola, J.-M., and Chappellaz, J.: Changes in the O_2/N_2 ratio of the atmosphere during recent decades reflected in the composition of air in the firn at Vostok Station, Antarctica, Geophys. Res. Lett., 21, 189–192, 1994a.

Bender, M. L., Tans, P. P., Ellis, T., Orchardo, J., and Habfast, K.: A high precision isotope ratio mass spectrometry method for measuring the O_2/N_2 ratio of air, Geochim. Cosmochim. Ac., 58, 4751–4758, 1994b.

Bereiter, B., Lüthi, D., Siegrist, M., Schüpbach, S., Stocker, T. F., and Fischer, H.: Mode change of millennial CO_2 variability during the last glacial cycle associated with a bipolar marine carbon seesaw, Proc. Natl. Acad. Sci. USA, 109, 9755–9760, 2012.

Bintanja, R., van de Wal, R. S. W., and Oerlemans, J.: Modelled atmospheric temperatures and global sea levels over the past million years, Nature, 437, 125–128, doi:10.1038/nature03975, 2005.

Blunier, T. and Brook, E. J.: Timing of Millennial-Scale Climate Change in Antarctica and Greenland During the Last Glacial Period, Science, 291, 109–112, doi:10.1126/science.291.5501.109, 2001.

Bond, G., Broecher, W., Johnsen, S. J., MacManus, J., Laberie, L., Jouzel, J., and Bonani, G.: Correlations between climate records from North Atlantic sediments and Greenland ice, Nature, 365, 143–147, 1993.

Boyle, E. A.: Cool tropical temperatures shift the global δ^{18}O-T relationship: An explanation for the ice core δ^{18}O – borehole thermometry conflict?, Geophys. Res. Lett., 24, 273–276, doi:10.1029/97GL00081, 1997.

Buchardt, S. L.: Basal melting and Eemian ice along the main ice ridge in northern Greenland, Ph.D. Thesis, Niels Bohr Institute, Faculty of Science, University of Copenhagen, 2009.

Buchardt, S. L., Clausen, H. B., Vinther, B. M., and Dahl-Jensen, D.: Investigating the past and recent δ^{18}O-accumulation relationship seen in Greenland ice cores, Clim. Past, 8, 2053–2059, doi:10.5194/cp-8-2053-2012, 2012.

Buiron, D., Stenni, B., Chappellaz, J., Landais, A., Baumgartner, M., Bonazza, M., Capron, E., Frezzotti, M., Kageyama, M., Lemieux-Dudon, B., Masson-Delmotte, V., Parrenin, F., Schilt, A., Selmo, E., Severi, M., Swingedouw, D., and Udisti, R.: Regional imprints of millennial variability during the MIS 3 period around Antarctica, Quaternary Sci. Rev., 48, 99–112, 2012.

Buizert, C., Martinerie, P., Petrenko, V. V., Severinghaus, J. P., Trudinger, C. M., E.Witrant, Rosen, J. L., Orsi, A. J., Rubino, M., Etheridge, D. M., Steele, L. P., Hogan, C., Laube, J. C., Sturges, W. T., Levchenko, V. A., Smith, A. M., Levin, I., Conway, T. J., Dlugokencky, E. J., Lang, P. M., Kawamura, K., Jenk, T. M., White, J. W. C., Sowers, T., Schwander, J., and Blunier, T.: Gas transport in firn: multiple-tracer characterisation and model intercomparison for NEEM, Northern Greenland, Atmos. Chem. Phys., 12, 4259–4277, doi:10.5194/acp-12-4259-2012, 2012.

Capron, E., Landais, A., Chappellaz, J., Schilt, A., Buiron, D., Dahl-Jensen, D., Johnsen, S. J., Jouzel, J., Lemieux-Dudon, B., Loulergue, L., Leuenberger, M., Masson-Delmotte, V., Meyer, H., Oerter, H., and Stenni, B.: Millennial and sub-millennial scale climatic variations recorded in polar ice cores over the last glacial period, Clim. Past, 6, 345–365, doi:10.5194/cp-6-345-2010, 2010.

Charles, C. D., Rind, D., Healy, R., and Webb, R.: Tropical cooling and the isotopic composition of precipitation in general circulation model simulations of the ice age climate, Clim. Dynam., 17, 489–502, 2001.

Chiang, J. C. H., Cheng, W., and Bitz, C. M.: Fast teleconnections to the tropical Atlantic sector from Atlantic thermohaline adjustment, Geophys. Res. Lett., 35, L07704, doi:10.1029/2008GL033292, 2008.

Craig, H., Horibe, Y., and Sowers, T.: Gravitational separation of gases and isotopes in polar ice caps, Science, 242, 1675–1678, 1988.

Cuffey, K. M. and Clow, G. D.: Temperature, accumulation, and ice sheet elevation in central Greenland through the last deglacial transition, J. Geophys. Res., 102, 26383–26396, 1997.

Cuffey, K. M. and Paterson, W. S. B.: The physics of glaciers, Elsevier, 4th Edn., 2010.

Cuffey, K. M., Clow, G. D., Alley, R. B., Stuiver, M., Waddington, E. D., and Saltus, R. W.: Large Arctic Temperature Change at the Wisconsin-Holocene Glacial Transition, Science, 270, 455–458, doi:10.1126/science.270.5235.455, 1995.

Cutler, N., Raymond, C., Waddington, E., Meese, D., and Alley, R.: The effect of ice-sheet thickness change on the accumulation history inferred from GISP2 layer thickness, Ann. Glaciol., 21, 26–32, 1995.

Dahl-Jensen, D., Mosegaard, K., Gundestrup, N., Clow, G. D., Johnsen, S. J., Hansen, A. W., and Balling, N.: Past Temperatures Directly from the Greenland Ice Sheet, Science, 282, 268–271, doi:10.1126/science.282.5387.268, 1998.

Dahl-Jensen, D. and NEEM community members: Eemian interglacial reconstructed from a Greenland folded ice core, Nature,

493, 489–494, 2013.

Dansgaard, W.: Stable isotopes in precipitation, Tellus, 16, 436–468, 1964.

Dansgaard, W. and Johnsen, S. J.: A flow model and a time scale for the ice core from Camp Century, Greenland, J. Glaciol., 8, 215–223, 1969.

Elliot, M., Labeyrie, L., Dokken, T., and Manthé, S.: Coherent patterns of ice rafted debris deposits in the Nordic regions during the last glacial, Earth Planet. Sci. Lett., 194, 151–163, 2001.

Elliot, M., Labeyrie, L., and Duplessy, J.-C.: Changes in North Atlantic deep-water formation associated with the Dansgaard-Oeschger temperature oscillations (60–10 ka), Quaternary Sci. Rev., 21, 1153–1165, 2002.

EPICA community members: One-to-one coupling of glacial climate variability in Greenland and Antarctica, Nature, 444, 195–198, doi:10.1038/nature05301, 2006.

Fawcett, P. J., Agustdóttir, A. M., Alley, R. B., and Shuman, C. A.: The Younger Dryas termination and North Atlantic deepwater formation: insights from climate model simulations and greenland ice data, Paleoceanography, 12, 23–38, doi:10.1029/96PA02711, 1997.

Ganopolski, A. and Rahmstorf, S.: Rapid changes of glacial climate simulated in a coupled climate model, Nature, 409, 153–158, 2001.

Goujon, C., Barnola, J.-M., and Ritz, C.: Modeling the densification of polar firn including heat diffusion: Application to close-off characteristics and gas isotopic fractionation for Antarctica and Greenland sites, J. Geophys. Res., 108, D24, doi:10.1029/2002JD003319, 2003.

Grachev, A. M. and Severinghaus, J. P.: Laboratory determination of thermal diffusion constants for $^{29}N_2/^{28}N_2$ in air at temperatures from -60 to 0 °CC for reconstruction of magnitudes of abrupt climate changes using the ice core fossil-air paleothermometer, Geochim. Cosmochim. Ac., 67, 345–360, 2003.

Grachev, A. M. and Severinghaus, J. P.: A revised +10+/−4 C magnitude of the abrupt change in Greenland temperature at the Younger Dryas termination using published GISP2 gas isotope data and air thermal diffusion constants, Quaternary Sci. Rev., 24, 513–519, 2005.

Grinsted, A. and Dahl-Jensen, D.: A Monte Carlo tuned model of the flow in the NorthGRIP area, J. Glaciol., 35, 527–530, doi:10.3189/172756402781817130, 2002.

Grootes, P. M. and Stuiver, M.: Oxygen 18/16 variability in Greenland snow and ice with 10^{-3} to 10^{5}-year time resolution, J. Geophys. Res., 102, 26455–26470, doi:10.1029/97JC00880, 1997.

Grootes, P. M., Stuiver, M., White, J. W. C., Johnsen, S. J., and Jouzel, J.: Comparison of oxygen isotope records from the GISP2 and GRIP Greenland ice cores, Nature, 366, 552–554, doi:10.1038/366552a0, 1993.

Gundestrup, N., Clausen, H., and Hansen, B.: The UCPH borehole logger in Ice drilling technology, NIPR, Japan, 1994.

Heinrich, H.: Origin and consequences of cyclic ice rafting in the Northeast Atlantic Ocean during the past 130,000 years, Quaternary Res., 29, 142–152, doi:10.1016/0033-5894(88)90057-9, 1988.

Herron, M. M. and Langway, C. C.: Firn densification: an empirical model, J. Glaciol., 25, 373–385, 1980.

Hörhold, M., Laepple, T., Freitag, J., Bigler, M., Fischer, H., and Kipfstuhl, S.: On the impact of impurities on the densification of polar firn, Earth Planet. Sc. Lett., 325–326, 93–99, doi:10.1016/j.epsl.2011.12.022, 2012.

Huber, C. and Leuenberger, M.: Measurements of isotope and elemental ratios of air from polar ice with a new on-line extraction method, Geochem. Geophy. Geosy., 5, 10, doi:10.1029/2004GC000766, 2004.

Huber, C., Leuenberger, M., Spahni, R., Flückiger, J., Schwander, J., Stocker, T. F., Johnsen, S. J., Landais, A., and Jouzel, J.: Isotope calibrated Greenland temperature record over Marine Isotope Stage 3 and its relation to CH_4, Earth Planet. Sci. Lett., 243, 504–519, 2006.

Indermühle, A., Monnin, E., Stauffer, B., Stocker, T., and Wahlen, M.: Atmospheric CO_2 concentration from 60 to 20 kyr BP from the Taylor Dome ice core, Antarctica, Geophys. Res. Lett., 27, 735–738, 2000.

Johnsen, S. J., Dansgaard, W., and White, J. W. C.: The origin of Arctic precipitation under present and glacial climate, Tellus, 41B, 452–468, 1989.

Johnsen, S. J., Clausen, H. B., Dansgaard, W., Fuhrer, K., Gundestrup, N., Hammer, C. U., Iversen, P., Jouzel, J., Stauffer, B., and Steffensen, J. P.: Irregular glacial interstadials recorded in a new Greenland ice core, Nature, 359, 311–313, doi:10.1038/359311a0, 1992.

Johnsen, S., Dahl-Jensen, D., Dansgaard, W., and Gundestrup, N.: Greenland paleotemperatures derived from GRIP borehole temperature and ice core isotope profiles, Tellus, 47B, 624–629, 1995.

Johnsen, S. J., Dahl-Jensen, D., Gundestrup, N., Steffensen, J. P., Clausen, H. B., Miller, H., Masson-Delmotte, V., Sveinbjörnsdóttir, A., and White, J.: Oxygen isotope and palaeotemperature records from six Greenland ice-core stations: Camp Century, Dye-3, GRIP, GISP2, Renland and NorthGRIP, J. Quaternary Sci., 16, 299–307, doi:10.1002/jqs.622, 2001.

Jouzel, J., Alley, R., Cuffey, K., Dansgaard, W., Grootes, P., Hoffmann, G., Johnsen, S., Koster, R., Peel, D., Shuman, C., Stievenard, M., Stuiver, M., and White, J.: Validity of the temperature reconstruction from water isotopes in ice cores, J. Geophys. Res., 102, 21471–26487, 1997.

Jouzel, J., Stiévenard, N., Johnsen, S., Landais, A., Masson-Delmotte, V., Sveinbjörnsdóttir, A., Vimeux, F., von Grafenstein, U., and White, J.: The GRIP deuterium-excess record, Quaternary Sci. Rev., 26, 1–17, 2007.

Kageyama, M. and Valdes, P. J.: Impact of the North American ice-sheet orography on the Last Glacial Maximum eddies and snowfall, Geophys. Res. Lett., 27, 1515–1518, 2000.

Kageyama, M., Paul, A., Roche, D. M., and van Meerbeeck, C. J.: Modelling glacial climatic millennial-scale variability related to changes in the Atlantic meridional overturning circulation: a review, Quaternary Sci. Rev., 29, 2931–2956, doi:10.1016/j.quascirev.2010.05.029, 2010.

Kawamura, K., Severinghaus, J. P., Ishidoya, S., Sugawara, S., Hashida, G., Motoyama, H., Fujii, Y., Aoki, S., and Nakazawa, T.: Convective mixing of air in firn at four polar sites, Earth Planet. Sci. Lett., 244, 672–682, 2006.

Kissel, C., Laj, C., Piotrowski, A., Goldstein, S., and Hemming, S.: Millennial-scale propagation of Atlantic deep waters to the glacial Southern Ocean, Paleoceanography, 23, PA2102, doi:10.1029/2008PA001624, 2008.

Kobashi, T., Kawamura, K., Severinghaus, J. P., Barnola, J.-M., Nakaegawa, T., Vinther, B. M., Johnsen, S. J., and Box, J. E.: High variability of Greenland surface temperature over the past 4000 years estimated from trapped air in an ice core, Geophys. Res. Lett., 38, L21501, doi:10.1029/2011GL049444, 2011.

Krinner, G., Genthon, C., and Jouzel, J.: GCM analysis of local influences on ice core δ signals, Geophys. Res. Lett., 24, 2825–2828, doi:10.1029/97GL52891, 1997.

Landais, A., Barnola, J.-M., Masson-Delmotte, V., Jouzel, J., Chappellaz, J., Caillon, N., Huber, C., Leuenberger, M., and Johnsen, S. J.: A continuous record of temperature evolution over a sequence of Dansgaard-Oeschger events during Marine Isotopic Stage 4 (76 to 62 kyr BP), Geophys. Res. Lett., 31, L22211, doi:10.1029/2004GL021193, 2004a.

Landais, A., Caillon, N., Severinghaus, J., Barnola, J.-M., Goujon, C., Jouzel, J., and Masson-Delmotte, V.: Isotopic measurements of air trapped in ice to quantify temperature changes, CR Geosci., 336, 963–970, 2004b.

Landais, A., Masson-Delmotte, V., Jouzel, J., Raynaud, D., Johnsen, S. J., Huber, C., Leuenberger, M., Schwander, J., and Minster, B.: The glacial inception as recorded in the NorthGRIP Greenland ice core: timing, structure and associated abrupt temperature changes, Clim. Dynam., 26, 273–284, doi:10.1007/s00382-005-0063-y, 2005.

Landais, A., Barnola, J., Kawamura, K., Caillon, N., Delmotte, M., Ommen, T. V., Dreyfus, G., Jouzel, J., Masson-Delmotte, V., Minster, B., Freitag, J., Leuenberger, M., Schwander, J., Huber, C., Etheridge, D., and Morgan, V.: Firn-air $\delta^{15}N$ in modern polar sites and glacial-interglacial ice: a model-data mismatch during glacial periods in Antarctica?, Quaternary Sci. Rev., 25, 49–62, doi:10.1016/j.quascirev.2005.06.007, 2006.

Lang, C., Leuenberger, M., Schwander, J., and Johnsen, S.: 16 °C Rapid Temperature Variation in Central Greenland 70,000 Years Ago, Science, 286, 934–937, doi:10.1126/science.286.5441.934, 1999.

Laskar, J., Robutel, P., Joutel, F., Gastineau, M., Correia, A. C. M., and Levrard, B.: A long-term numerical solution for the insolation quantities of the Earth, Astron. Astrophys., 428, 261–285, doi:10.1051/0004-6361:20041335, 2004.

Li, C., Battisti, D. S., Schrag, D. P., and Tziperman, E.: Abrupt climate shifts in Greenland due to displacements of the sea ice edge, Geophys. Res. Lett., 32, L19702, doi:10.1029/2005GL023492, 2005.

Li, C., Battisti, D., and Bitz, C.: Can North Atlantic sea ice anomalies account for Dansgaard-Oeschger climate signals?, J. Climate, 23, 5457–5475, 2010.

Liu, Z., Otto-Bliesner, B. L., He, F., Brady, E. C., Tomas, R., Clark, P. U., Carlson, A. E., Lynch-Stieglitz, J., Curry, W., Brook, E., Erickson, D., Jacob, R., Kutzbach, J., and Cheng, J.: Transient Simulation of Last Deglaciation with a New Mechanism for Bølling-Allerød Warming, Science, 235, 310–314, doi:10.1126/science.1171041, 2009.

Lliboutry, L.: A critical review of analytical approximate solutions for steady stade velocities and temperature in cold ice-sheets, Z. Gletscherkd. Glazialgeol., 15, 135–148, 1979.

Marshall, S. J. and Koutnik, M. R.: Ice sheet action versus reaction: distinguishing between Heinrich events and Dansgaard-Oeschger cycles in the North Atlantic, Paleoceanography, 21, PA2021, doi:10.1029/2005PA001247, 2006.

Masson-Delmotte, V., Jouzel, J., Landais, A., Stiévenard, M., Johnsen, S. J., White, J. W. C., Werner, M., Sveinbjörnsdóttir, A., and Fuhrer, K.: GRIP Deuterium Excess Reveals Rapid and Orbital-Scale Changes in Greenland Moisture Origin, Science, 309, 118–121, doi:10.1126/science.1108575, 2005.

Masson-Delmotte, V., Braconnot, P., Hoffmann, G., Jouzel, J., Kageyama, M., Landais, A., Lejeune, Q., Risi, C., Sime, L., Sjolte, J., Swingedouw, D., and Vinther, B.: Sensitivity of interglacial Greenland temperature and $\delta^{18}O$: ice core data, orbital and increased CO_2 climate simulations, Clim. Past, 7, 1041–1059, doi:10.5194/cp-7-1041-2011, 2011.

Mayewski, P. A., Meeker, L. D., Twickler, M. S., Whitlow, S., Yang, Q., Lyons, W. B., and Prentice, M.: Major features and forcing of high-latitude northern hemisphere atmospheric circulation using a 110,000-year-long glaciochemical series, J. Geophys. Res., 102, 26345–26366, doi:10.1029/96JC03365, 1997.

McManus, J. F., Bond, G. C., Broecker, W. S., Johnsen, S., Labeyrie, L., and Higgins, S.: High resolution climate records from the North Atlantic during the last interglacial, Nature, 371, 326–329, 1994.

Meese, D. A., Gow, A. J., Grootes, P., Stuiver, M., Mayewski, P. A., Zielinski, G. A., Ram, M., Taylor, K. C., and Waddington, E. D.: The accumulation record from the GISP2 core as an indicator of climate change throughout the Holocene, Science, 266, 1680–1682, doi:10.1126/science.266.5191.1680, 1994.

Meese, D. A., Gow, A. J., Alley, R. B., Zielinski, G. A., Grootes, P. M., Ram, M., Taylor, K. C., Mayewski, P. A., and Bolzan, J. F.: The Greenland Ice Sheet Project 2 depth-age scale: methods and results, J. Geophys. Res., 102, 26411–26423, 1997.

Merlivat, L. and Jouzel, J.: Global climatic interpretation of the deuterium-oxygen 18 relationship for precipitation, J. Geophys. Res., 84, 5029–5033, 1979.

Mudelsee, M.: Ramp function regression: a tool for quantifying climate transitions, Comput. Geosci., 26, 293–307, 2000.

NGRIP members: High-resolution record of Northern Hemisphere climate extending into the last interglacial period, Nature, 431, 147–151, doi:10.1038/nature02805, 2004.

Orsi, A., Cornuelle, B., and Severinghaus, J.: Magnitude and temporal evolution of interstadial 8 abrupt temperature change inferred from nitrogen and argon isotopes in GISP2 ice using a new least-squares inversion, submitted, 2013.

Otto-Bliesner, B. L. and Brady, E. C.: The sensitivity of the climate response to the magnitude and location of freshwater forcing: last glacial maximum experiments, Quaternary Sci. Rev., 29, 56–73, doi:10.1016/j.quascirev.2009.07.004, 2010.

Persson, A., Langen, P. L., Ditlevsen, P., and Vinther, B. M.: The influence of precipitation weighting on interannual variability of stable water isotopes in Greenland, J. Geophys. Res., 116, D20120, doi:10.1029/2010JD015517, 2011.

Press, W. H., Teukolsky, S. A., Wetterling, W. T., and Flannery, B. P.: Numerical recipes: the art of scientific computing, Cambridge University Press, 3rd Edn., 2007.

Rasmussen, S. O., Andersen, K. K., Svensson, A. M., Steffensen, J. P., Vinther, B. M., Clausen, H. B., Siggaard-Andersen, M.-L., Johnsen, S. J., Larsen, L. B., Dahl-Jensen, D., Bigler, M., Röthlisberger, R., Fischer, H., Goto-Azuma, K., Hansson, M. E., and Ruth, U.: A new Greenland ice core chronology for the last glacial termination, J. Geophys. Res., 111, doi:10.1029/2005JD006079, submitted, 2013.

Rasmussen, S. O., Seierstad, I., Andersen, K., Bigler, M., Dahl-Jensen, D., and Johnsen, S.: Synchronization of the NGRIP, GRIP, and GISP2 ice cores across MIS 2 and palaeoclimatic implications, Quaternary Sci. Rev., 27, 18–28, 2008.

Rasmussen, T. L. and Thomsen, E.: The role of the North Atlantic Drift in the millennial timescale glacial climate fluctuations, Palaeogeogr. Palaeocl., 210, 101–116, 2004.

Ritz, C.: Un modèle thermomécanique d'évolution pour le bassin glaciaire antarctique Vostok – Glacier Bird: Sensibilité aux valeurs des paramètres mal connus, Ph.D. Thesis, Université Josepth Fourier, Grenoble, France, 1992.

Roche, D., Wiersma, A., and Renssen, H.: A systematic study of the impact of freshwater pulses with respect to different geographical locations, Clim. Dyn., 34, 997–1013, 2010.

Ruth, U., Wagenbach, D., Steffensen, J. P., and Bigler, M.: Continuous record of microparticle concentration and size distribution in the central Greenland NGRIP ice core during the last glacial period, J. Geophys. Res., 108, D06102, doi:10.1029/2002JD002376, 2003.

Ruth, U., Bigler, M., Röthlisberger, R., Siggaard-Andersen, M.-L., Kipfstuhl, S., Goto-Azuma, K., Hansson, M. E., Johnsen, S. J., Lu, H., and Steffensen, J. P.: Ice core evidence for a very tight link between North Atlantic and east Asian glacial climate, Geophys. Res. Lett., 34, L03706, doi:10.1029/2006GL027876, 2007.

Schilt, A., Baumgartner, M., Blunier, T., Schwander, J., Spahni, R., Fischer, H., and Stocker, T. F.: Glacial-interglacial and millennial-scale variations in the atmospheric nitrous oxide concentration during the last 800,000 years, Quaternary Sci. Rev., 29, 182–192, doi:10.1016/j.quascirev.2009.03.011, 2010.

Schwander, J.: The transformation of snow to ice and the occlusion of gases, New York, 1989.

Schwander, J., Sowers, T., Barnola, J.-M., Blunier, T., Fuchs, A., and Malaizé, B.: Age scale of the air in the Summit ice: Implication for glacial-interglacial temperature change, J. Geophys. Res., 102, 19483–19493, 1997.

Severinghaus, J. P. and Brook, E. J.: Abrupt climate change at the end of the Last Glacial Period inferred from trapped air in polar ice, Science, 286, 930–934, doi:10.1126/science.286.5441.930, 1999.

Severinghaus, J. P., Sowers, T., Brook, E. J., Alley, R. B., and Bender, M. L.: Timing of abrupt climate change at the end of the Younger Dryas interval from thermally fractionated gases in polar ice, Nature, 391, 141–146, 1998.

Severinghaus, J. P., Grachev, A., Luz, B., and Caillon, N.: A method for precise measurement of argon 40/36 and krypton/argon ratios in trapped air in polar ice with applications to past firn thickness and abrupt climate change in Greenland and at Siple Dome, Antarctica, Geochim. Cosmochim. Ac., 67, 325–343, 2003.

Severinghaus, J., Albert, M. R., Courville, Z. R., Fahnestock, M. A., Kawamura, K., Montzka, S. A., Mühle, J., Scambos, T. A., Shields, E., Shuman, C. A., Suwa, M., Tans, P., and Weiss, R. F.: Deep air convection in the firn at a zero-accumulation site, central Antarctica, Earth Planet. Sci. Lett., 293, 359–357, 2010.

Shuman, C., Alley, R., Anandakrishnan, S., White, J., Grootes, P., and Stearns, C.: Temperature and accumulation at the Greenland Summit: comparison of high-resolution isotope profiles and satellite passive microwave brightness temperature trends, J. Geophys. Res., 100, 9165–9177, 1995.

Shuman, C., Bromwich, D., Kipfstuhl, J., and Schwager, M.: Multi-year accumulation and temperature history near the North Greenland Ice Core Project site, north central Greenland, J. Geophys. Res., 106, 33853–33856, 2001.

Sjolte, J., Hoffmann, G., Johnsen, S. J., Vinther, B. M., Masson-Delmotte, V., and Sturm, C.: Modeling the water isotopes in Greenland precipitation 1959–2001 with the meso-scale model REMO-iso, J. Geophys. Res., 116, D18105, doi:10.1029/2010JD015287, 2011.

Sowers, T., Bender, M., and Raynaud, D.: Elemental and isotopic composition of accluded O_2 and N_2 in polar ice, J. Geophys. Res., 94, 5137–5150, doi:10.1029/JD094iD04p05137, 1989.

Steen-Larsen, H. C., Masson-Delmotte, V., Sjolte, J., Johnsen, S. J., Vinther, B. M., Bréon, F.-M., Clausen, H. B., Dahl-Jensen, D., Falourd, S., Fettweis, X., Gallée, H., Jouzel, J., Kageyama, M., Lerche, H., Minster, B., Picard, G., Punge, H. J., Risi, C., Salas, D., Schwander, J., Steffen, K., Sveinbjörnsdóttir, A. E., Svensson, A., and White, J. W. C.: Understanding the climatic signal in the water stable isotope records from the NEEM shallow firn/ice cores in northwest Greenland, J. Geophys. Res., 116, D06108, doi:10.1029/2010JD014311, 2011.

Steffensen, J. P., Andersen, K. K., Bigler, M., Clausen, H. B., Dahl-Jensen, D., Fischer, H., Goto-Azuma, K., Hansson, M., Johnsen, S. J., Jouzel, J., Masson-Delmotte, V., Popp, T., Rasmussen, S. O., Röthlisberger, R., Ruth, U., Stauffer, B., Siggaard-Andersen, M.-L., Sveinbjörnsdóttir, A. E., Svensson, A., and White, J. W. C.: High-Resolution Greenland Ice Core Data Show Abrupt Climate Change Happens in Few Years, Science, 321, 680–684, 2008.

Steig, E., Grootes, P., and Stuiver, M.: Seasonnal precipitation timing and ice core records, Science, 266, 1885–1886, 1994.

Stocker, T. F. and Johnsen, S. J.: A minimum thermodynamic model for the bipolar seesaw, Paleoceanography, 18, 1087, doi:10.1029/2003PA000920, 2003.

Svensson, A., Biscaye, P. E., and Grousset, F. E.: Characterization of late glacial continental dust in the Greenland Ice Core Project ice core, J. Geophys. Res., 105, 4637–4656, 2000.

Svensson, A., Andersen, K., Bigler, M., Clausen, H., Dahl-Jensen, D., Davies, S., Johnsen, S., Muscheler, R., Rasmussen, S., Röthlisberger, R., Steffensen, J., and Vinther, B.: The Greenland Ice Core Chronology 2005, 15–42 ka. Part 2: comparison to other records, Quaternary Sci. Rev., 25, 3258–3267, doi:10.1016/j.quascirev.2006.08.003, 2006.

Svensson, A., Andersen, K. K., Bigler, M., Clausen, H. B., Dahl-Jensen, D., Davies, S. M., Johnsen, S. J., Muscheler, R., Parrenin, F., Rasmussen, S. O., Röthlisberger, R., Seierstad, I., Steffensen, J. P., and Vinther, B. M.: A 60 000 year Greenland stratigraphic ice core chronology, Clim. Past, 4, 47–57, doi:10.5194/cp-4-47-2008, 2008.

Svensson, A., Bigler, M., Kettner, E., Dahl-Jensen, D., Johnsen, S. J., Kipfstuhl, S., Nielsen, M., and Steffensen, J. P.: Annual layering in the NGRIP ice core during the Eemian, Clim. Past, 7, 1427–1437, doi:10.5194/cp-7-1427-2011, 2011.

Thomas, E. R., Wolff, E. W., Mulvaney, R., Johnsen, S. J., Steffensen, J. P., and Arrowsmith, C.: Anatomy of a Dansgaard-Oeschger warming transition: High-resolution analysis of the North Greenland Ice Core Project ice core, J. Geophys. Res., 114, 4098, doi:10.1029/2008JD011215, 2008.

Vinther, B. M., Clausen, H. B., Johnsen, S. J., Rasmussen, S. O., Andersen, K. K., Buchardt, S. L., Dahl-Jensen, D., Seierstad, I. K., Siggaard-Andersen, M.-L., Steffensen, J. P., and Svensson, A.: A synchronized dating of three Greenland ice cores throughout the Holocene, J. Geophys. Res., 11, D13, doi:10.1029/2005JD006921, 2006.

Vinther, B. M., Buchardt, S. L., Clausen, H. B., Dahl-Jensen, D., Johnsen, S. J., Fisher, D. A., Koerner, R. M., Raynaud, D., Lipenkov, V., Andersen, K. K., Blunier, T., Rasmussen, S. O., Steffensen, J. P., and Svensson, A. M.: Holocene thinning of the Greenland ice sheet, Nature, 461, 385–388, doi:10.1038/nature08355, 2009.

Voelker, A. H. L.: Global distribution of centennial-scale records for Marine Isotope Stage (MIS) 3: a database, Quaternary Sci. Rev., 21, 1185–1212, 2002.

Weller, G. E. and Schwerdtfeger, P.: New data on the thermal conductivity of natural snow, J. Glaciol., 10, 309–311, 1971.

Werner, M., Mikolajewicz, U., Heimann, M., and Hoffman, G.: Borehole versus isotope temperatures on Greenland: seasonality does matter, Geophys. Res. Lett., 27, 723–725, 2000.

Werner, M., Heimann, M., and Hoffmann, G.: Isotopic composition and origin of polar precipitation in present and glacial climate simulations, Tellus, 53B, 53–71, 2001.

Wolff, E. W., Chappellaz, J., Blunier, T., Rasmussen, S., and Svensson, A.: Millennial-scale variability during the last glacial: The ice core record, Quaternary Sci. Rev., 29, 2828–2838, doi:10.1016/j.quascirev.2009.10.013, 2009.

Yen, Y.-C.: Review of thermal properties of snow, ice, and sea ice, US Army, Corps of Engineers, Cold Regions Research and Engineering Laboratory, 1981.

2 Guillevic et al., 2014

Clim. Past, 10, 2115–2133, 2014
www.clim-past.net/10/2115/2014/
doi:10.5194/cp-10-2115-2014

Climate of the Past
Open Access

Evidence for a three-phase sequence during Heinrich Stadial 4 using a multiproxy approach based on Greenland ice core records

M. Guillevic[1,2], L. Bazin[1], A. Landais[1], C. Stowasser[2], V. Masson-Delmotte[1], T. Blunier[2], F. Eynaud[3], S. Falourd[1], E. Michel[1], B. Minster[1], T. Popp[2], F. Prié[1], and B. M. Vinther[2]

[1]Laboratoire des Sciences du Climat et de l'environnement, UMR CEA/CNRS/UVSQ 8212, Gif-sur-Yvette, France
[2]Centre for Ice and Climate, Niels Bohr Institute, University of Copenhagen, Copenhagen, Denmark
[3]Laboratoire EPOC, UMR CNRS 5805 EPOC-OASU, Université Bordeaux 1, Talence, France

Correspondence to: M. Guillevic (mgllvc@nbi.ku.dk)

Received: 28 February 2014 – Published in Clim. Past Discuss.: 27 March 2014
Revised: 15 October 2014 – Accepted: 3 November 2014 – Published: 2 December 2014

Abstract. Glacial climate was characterised by two types of abrupt events. Greenland ice cores record Dansgaard–Oeschger events, marked by abrupt warming in-between cold, stadial phases. Six of these stadials appear related to major Heinrich events (HEs), identified from ice-rafted debris (IRD) and large excursions in carbon- and oxygen-stable isotopic ratios in North Atlantic deep sea sediments, documenting major ice sheet collapse events. This finding has led to the paradigm that glacial cold events are induced by the response of the Atlantic Meridional Overturning Circulation to such massive freshwater inputs, supported by sensitivity studies conducted with climate models of various complexities. These models also simulate synchronous Greenland temperature and lower-latitude hydrological changes.

To investigate the sequence of events between climate changes at low latitudes and in Greenland, we provide here the first ^{17}O-excess record from a Greenland ice core during Dansgaard–Oeschger events 7 to 13, encompassing H4 and H5. Combined with other ice core proxy records, our new ^{17}O-excess data set demonstrates that stadials are generally characterised by low ^{17}O-excess levels compared to interstadials. This can be interpreted as synchronous change of high-latitude temperature and lower-latitude hydrological cycle (relative humidity at the oceanic source of evaporation or change in the water mass trajectory/recharge) and/or an influence of local temperature on ^{17}O-excess through kinetic effect at snow formation. As an exception from this general pattern, stadial 9 consists of three phases, characterised first by Greenland cooling during 550 ± 60 years (as shown by markers of Greenland temperature δ^{18}O and δ^{15}N), followed by a specific lower-latitude fingerprint as identified from several proxy records (abrupt decrease in ^{17}O-excess, increase in CO_2 and methane mixing ratio, heavier δD-CH_4 and $\delta^{18}O_{atm}$), lasting 740 ± 60 years, itself ending approximately 390 ± 50 years prior to abrupt Greenland warming. We hypothesise that this lower-latitude signal may be the fingerprint of Heinrich event 4 in Greenland ice cores. The proposed decoupling between stable cold Greenland temperature and low-latitude climate variability identified for stadial 9 provides new targets for benchmarking climate model simulations and testing mechanisms associated with millennial variability.

1 Introduction

Glacial climate is characterised by millennial variability, recorded with specific expressions in different archives and at different latitudes (Voelker, 2002; Clement and Peterson, 2008). Greenland ice core records of ice δ^{18}O, a qualitative proxy of air temperature, unveiled at high resolution the succession of cold phases (Greenland Stadials, GS) and warm phases (Greenland Interstadials, GI) forming the 25 Dansgaard–Oeschger events (DO) of the last glacial period (NGRIP members, 2004). DO events are recorded through climatic and environmental changes in other North Atlantic/European archives such as speleothems (Genty et al., 2010; Boch et al., 2011), pollen and marine bioindicators from North Atlantic marine cores (e.g. Voelker, 2002; Sánchez Goñi and Harrison, 2010), with interstadials being

characterised in Western Europe by warmer and more humid conditions, while stadials are associated with a dry and cold climate. The Tropics also exhibit a fingerprint of DO events as suggested e.g. by (i) variations in monsoon strength (e.g. recorded in speleothem growth rate and calcite $\delta^{18}O$, Wang et al., 2001), (ii) changes in the atmospheric methane concentration (as measured in ice cores, Chappellaz et al., 1993, 2013) with its main source located at low latitudes during glacial periods (e.g. Baumgartner et al., 2012), or (iii) changes in the isotopic composition of atmospheric oxygen $\delta^{18}O_{atm}$ measured in air from ice cores (Landais et al., 2007; Severinghaus et al., 2009), reflecting at this timescale changes in the low-latitude water cycle and global biosphere productivity (Bender et al., 1994b). Such variations in the low-latitude climate are probably due to shifts in the Intertropical Convergence Zone (ITCZ, e.g. Peterson et al., 2000). The bipolar seesaw identified between each Greenland DO event and its Antarctic counterpart (EPICA community members, 2006; Capron et al., 2010) supports a key role of reorganisations of the Atlantic Ocean interhemispheric heat transport (Stocker and Johnsen, 2003), likely associated with strong variations of the Atlantic Meridional Overturning Circulation (AMOC) intensity.

In addition to palaeoclimate records showing this DO succession, a prominent feature identified in North Atlantic marine sediment cores is the occurrence of ice-rafted debris (IRD, Ruddiman, 1977). These IRD are interpreted as the signature of massive iceberg discharges in the North Atlantic Ocean originating from the Laurentide, Icelandic, British–Irish and Fennoscandian ice sheets (e.g. Heinrich, 1988; Bond et al., 1993). Six such Heinrich events (HEs, numbered H1 to H6, Fig. 1) have been unambiguously identified during GS phases of the last glacial period (e.g. Bond et al., 1992; Hemming, 2004). Minor events identified in one or a few cores have additionally been reported – H5a (Rashid et al., 2003), H7a, H7b, H8 to H10 (Rasmussen et al., 2003), see Fig. 1. In addition to the IRD layers, periods of low surface salinity likely due to enhanced freshwater fluxes have been evidenced in a sediment core from the Celtic margin (Fig. 1 blue areas, Eynaud et al., 2012). Studies on the composition of each IRD layer have demonstrated the dominant Laurentide origin of H2, H4 and H5, while H3 and H6 are mainly due to icebergs delivery from European ice sheets (Grousset et al., 1993, 2000; Gwiazdaet al., 1996; Hemming et al., 1998; Snoeckx et al., 1999; Jullien et al., 2006). H1 results from the collapse of several ice sheets (Stanford et al., 2011).

The early proposed synchronicity of HEs in marine cores and GS in Greenland ice cores (e.g. Bond et al., 1993) has led to the paradigm that Greenland stadial/interstadial variability is related to freshwater-induced changes in AMOC. Indeed, the response of climate models of different complexities to freshwater perturbations bears similarities with palaeoclimate observations (e.g. Kageyama et al., 2013). Such GS associated to HEs are also called Heinrich stadials (Barker et al., 2009). Unfortunately, uncertainties associated with marine and ice core chronologies have so far prevented the determination of the exact timing of Heinrich events with respect to GS (Sánchez Goñi and Harrison, 2010; Austin and Hibbert, 2012). In addition, several lines of evidence suggest that HEs are shorter than the corresponding GS (Peters et al., 2008; Roche et al., 2004) and occur after the AMOC entered a weakening trend (Flückiger et al., 2006; Marcott et al., 2011). Therefore the mechanisms relating iceberg discharge, low-latitude climate change and Greenland temperature change during stadials remain debated (Hemming, 2004; Clement and Peterson, 2008; Mulitza et al., 2008).

The impact of HEs is not limited to the North Atlantic but has a signature in mid- to low-latitude palaeoclimate records. For instance speleothem growth rate from South America and Asia and their calcite isotopes indicate a southward displacement of the intertropical convergence zone (ITCZ) during stadials compared to interstadials (e.g. Jo et al., 2014), most pronounced during Heinrich stadials (Kanner et al., 2012; Wang et al., 2007; Mosblech et al., 2012). Model simulations indeed produce in a few years a southward displacement of the ITCZ over the Atlantic Ocean and its margins in response to North Atlantic cooling (e.g. Chiang et al., 2008; Bozbiyik et al., 2011; Cvijanovic and Chiang, 2013). Speleothems from low latitudes have the advantage to provide the best absolute chronology amongst palaeo archives so far, through uranium–thorium dating of the calcite. Associated uncertainties can be as low as $\sim \pm 1\,\%$ (2σ) of the absolute age for the Hulu cave record (Wang et al., 2001). Calcite $\delta^{18}O$ from Southeast Asia speleothems and $\delta^{18}O_{atm}$ variations registered in the air entrapped from ice cores are both mostly controlled by latitudinal shifts of the ITCZ and associated changes in the isotopic composition of tropical precipitation (e.g. Severinghaus et al., 2009). This common driving climatic mechanism therefore offers a direct link between speleothem and ice core archives. However, climate-independent markers have not yet been identified that would allow us to synchronise speleothems to other archives from different latitudes such as marine or ice cores, preventing a precise comparison of the timing of events between high, mid and low latitudes associated with Heinrich events.

In Greenland ice cores, DO events are well dated thanks to annual layer counting. For the GICC05 timescale used here, absolute ages are estimated with $\sim 3\,\%$ uncertainty (2σ) during the glacial period (Svensson et al., 2008, and Appendix A1). A precise synchronisation between marine and ice cores during HEs remains however difficult to establish due to the lack of a direct HE fingerprint within the Greenland ice core records. Neither ice $\delta^{18}O$ (a qualitative proxy of temperature) nor Greenland temperature (reconstructed from $\delta^{15}N$ measurements in the air bubbles based on firn gas gravitational and thermal fractionation) exhibit any additional cooling during Heinrich stadials compared to Greenland stadials (Figs. 1, 4a, b and e.g. Kindler et al., 2014). However, Greenland ice cores do provide proxy records influenced by high-, mid- and low-latitude climate changes. This archive

should thus allow us to explore time leads and lags in between events happening at different latitudes.

The combination of all stable water isotopes has been proposed as a methodology to disentangle local from more remote effects recorded in ice cores (Vimeux et al., 1999; Stenni et al., 2001; Masson-Delmotte et al., 2005; Jouzel et al., 2007; Landais et al., 2012b). δ^{18}O is a qualitative proxy of local Greenland temperature showing the well-known GS–GI pattern. Deuterium excess (d-excess $= \delta D - 8\delta^{18}$O, Dansgaard, 1964) bears a signature of vapour source characteristics (sea surface temperature and relative humidity), but it is also affected by changes in condensation temperature (Masson-Delmotte et al., 2005; Jouzel et al., 2007; Steen-Larsen et al., 2013; Bonne et al., 2014). Temperature influences similarly the fractionation coefficients associated with δ^{17}O and δ^{18}O while the variations of fractionation coefficients associated with δD follow a different link with temperature (Barkan and Luz, 2005; Majoube, 1971; Luz et al., 2009). As a consequence, ^{17}O-excess defined as $\ln(\delta^{17}\mathrm{O}+1) - 0.528\ln(\delta^{18}\mathrm{O}+1)$ is less sensitive than d-excess to the distillation history, hence to local (Greenland) temperature (Masson-Delmotte et al., 2005; Landais et al., 2012b). ^{17}O-excess therefore better reflects the climatic conditions during evaporation or moisture recharge of Greenland vapour source, in particular the relative humidity that controls kinetic fractionation during such processes. At NEEM, a simple water isotopic model tuned on seasonal data has enabled one to show that ^{17}O-excess increases by 1 per meg for a 1 ‰ decrease in relative humidity of the source evaporative region (Landais et al., 2012b).

Still, because kinetic fractionation is also important during snow formation and as already observed for d-excess (Jouzel et al., 2007), the influence of condensation temperature on ^{17}O-excess increases when temperature decreases. While this effect is of second order for Greenland sites or Antarctic sites with a δ^{18}O level higher than -40 ‰ (Winkler et al., 2012; Landais et al., 2012b), it is dominant for colder sites in Antarctica (Landais et al., 2012a; Schoenemann et al., 2014). This is the reason why ^{17}O-excess and d-excess need to be combined with other ice core proxies of the lower latitudes (e.g. $\delta^{18}O_2$ of O_2, CH_4) to faithfully establish the relationship between climate and environmental changes in both polar and lower latitudes.

In this study, we investigate multiple climate proxies registered in the NEEM (North Greenland Eemian Ice Drilling) and NGRIP (North Greenland Ice Core Project) Greenland ice cores (Fig. 2), on the same chronology (Greenland Ice Core Chronology 2005 or GICC05, Appendix A), giving information about the local as well as the remote climate on exactly the same timescale. The aim is to test the synchronicity of climate events at high and low latitudes during Greenland stadials. With this purpose, we present the first ^{17}O-excess record over a sequence of DO events, with a specific focus over GS-9 (following GI-9 and preceding GI-8 according to the INTIMATE labelling scheme that we use in this study (Björck et al., 1998), 38 220–39 900 years before 2000 AD (a b2k) on the GICC05 timescale). GS-9 is characterised by the occurrence of the major H4 IRD event of mostly Laurentide ice sheet (LIS) origin (Hemming, 2004; Jullien et al., 2006). This event occurs during Marine Isotope Stage 3 (MIS3), a period consisting of short-lived and frequent DO events (NGRIP members, 2004). In the following we will argue that the climatic fingerprint of H4 can be identified in multiple proxy records sensitive to climate and environmental changes at high, mid and low latitudes, archived in the ice and air of Greenland ice cores.

2 Measurement method

2.1 ^{17}O-excess

We have performed the first ^{17}O-excess measurements on the NEEM ice core (Dahl-Jensen and NEEM community members, 2013, localisation on Fig. 2), spanning a sequence of 7 DO events during MIS 3, from GI-7 to GI-13. The method for ^{17}O-excess measurements was first described in Luz and Barkan (2005). Two microlitres of water are fluorinated under a helium flow and the resulting oxygen O_2 is purified on a molecular sieve before being trapped in a manifold immersed in liquid helium. O_2 is then measured on a DELTA V isotope ratio mass spectrometer vs. pure oxygen. Dual inlet measurements last 75 min for each converted oxygen sample. Each water sample has been converted and measured at least twice. Every day, we use two in-house water standards in our fluorination line to check the stability of the measurements and to perform calibrations. The resulting pooled standard deviation for ^{17}O-excess measurements is 5 per meg.

For this study with δ^{18}O varying between -43 and -38 ‰, we mainly used three in-house standards at around -32, -40 and -58 ‰. These in-house standards are calibrated vs. V-SMOW (Vienna Standard Mean Ocean Water, $\delta^{18}\mathrm{O} = 0$ ‰; ^{17}O-excess $= 0$ permeg) and SLAP (Standard Light Antarctic Precipitation, $\delta^{18}\mathrm{O} = -55.5$ ‰; ^{17}O-excess $= 0$ permeg, Luz et al., 2009; Schoenemann et al., 2013). The calibration of our raw ^{17}O-excess data can then be performed in two different ways. In a first attempt, we have simply subtracted from all raw ^{17}O-excess data the ^{17}O-excess difference between the measured and the calibrated standard at -40 ‰. In a second attempt, we have used a two-point calibration between measured and accepted values of V-SMOW and SLAP so that the ^{17}O-excess correction increases with the δ^{18}O difference between O_2 obtained from the sample conversion and O_2 obtained from V-SMOW conversion. We show in Fig. 3b the comparison of ^{17}O-excess evolution after these two corrections as well as the raw data. The general evolution of the ^{17}O-excess profile and the particular separation in phases over GS-9 is not affected by the different corrections.

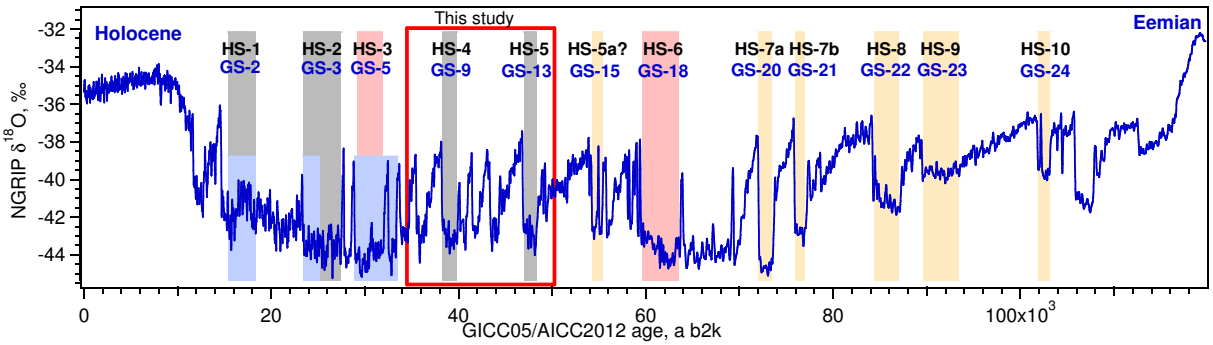

Figure 1. Dansgaard–Oeschger (the warm phases being marked as Greenland Interstadials, GI) and Heinrich Stadials (HSs) during the last glacial period. Blue line: NGRIP δ^{18}O, ‰ (NGRIP members, 2004), on the GICC05 timescale back to 60 ka b2k (Appendix A1) and AICC2012 beyond (Bazin et al., 2013; Veres et al., 2013). Coloured areas: Heinrich Stadials. Grey: HS-1, HS-2, HS-4 and HS-5: occurrence of a major Heinrich event of mainly Laurentide origin. Pink: HS-3 and HS-6, major events of mainly European origin (see text for references). Yellow: HS-5a and HS-7 to HS-10, occurrence of a minor IRD event of Laurentide origin recorded in the West Atlantic (Rashid et al., 2003; Rasmussen et al., 2003). Blue: periods of low salinity corresponding to freshwater input on the Celtic Margin (Eynaud et al., 2012).

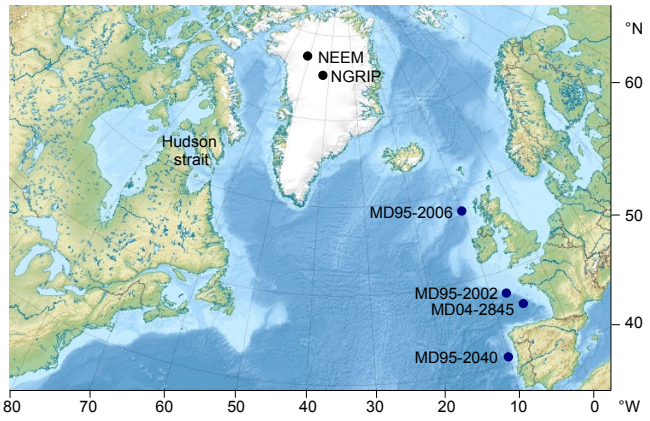

Figure 2. Map of the Northern Hemisphere palaeoclimate archives used in this study. Blue dots: marine cores. Black dots: ice cores. Most of the IRD for H4 and H5 were deposited by icebergs originating from the Laurentide ice sheet and delivered through Hudson Strait (Hemming, 2004). Background map from Uwe Dedering.

Finally, note that the measurements were done in three rounds, with a first series measured in spring 2011, a second one at the beginning of 2012 and a third one in spring 2014. Comparisons of the profiles are displayed in Fig. 3a after correction with the two-point calibration (V-SMOW vs. SLAP). The measurements were not necessarily performed over the same exact depth levels, which makes the inter-comparison less accurate. Both the mean levels and the variability are very coherent between the three ^{17}O-excess profiles.

2.2 $\delta^{18}O_{atm}$

Our new $\delta^{18}O_{atm}$ (δ^{18}O of O_2) data set measured on the NEEM ice core consists of 95 data points with replicates. A melt–refreeze technique has been used to extract the air from the ice samples. Our isotope ratio mass spectrometer is equipped with 10 Faraday cups to measure simultaneously the isotopic ratios δ^{18}O and δ^{15}N as well as the elemental ratios O_2/N_2 (Landais et al., 2010).

To reconstruct the past $\delta^{18}O_{atm}$ signal, δ^{18}O measurements have been first corrected for eventual gas loss during ice storage using the $\delta O_2/N_2$ ratio measured in the same samples (more details can be found in Landais et al., 2010):

$$\delta^{18}O_{\text{gas loss corrected}} = \delta^{18}O_{\text{measured}} + 0.01\,(\delta O_2/N_2 + 10)\,. \quad (1)$$

The obtained data are then corrected for thermal and gravitational fractionation occurring in the firn. To do so, we use the isotopic composition of nitrogen δ^{15}N measured in the very same ice samples as well as firn modelling, to reconstruct the gravitational ($\delta^{15}N_{grav}$) and thermal ($\delta^{15}N_{therm}$) signals contributing to the measured δ^{15}N data (Guillevic et al., 2013; Landais et al., 2010, and references therein). The gravitational effect being proportional to the mass difference in between the two isotopes (Craig et al., 1988; Schwander, 1989), $\delta^{18}O_{grav}$ is therefore twice as large as $\delta^{15}N_{grav}$. Temperature gradients in the firn create thermal fractionation of nitrogen and oxygen isotopes, and this effect is 1.6 times larger for δ^{18}O compared to δ^{15}N due to differences in diffusivity coefficients (Severinghaus et al., 2001). The final $\delta^{18}O_{atm}$ is therefore obtained as follows:

$$\delta^{18}O_{atm} = \delta^{18}O_{\text{gas loss corrected}} - 1.6\,\delta^{15}N_{therm} - 2\,\delta^{15}N_{grav}. \quad (2)$$

The resulting $\delta^{18}O_{atm}$ pooled standard deviation is 0.03 ‰ (Landais et al., 2010). The $\delta^{18}O_{atm}$ data set is reported on the GICC05 timescale (Fig. 4f, black dots) using the NEEM gas age scale from Guillevic et al. (2013). The obtained profile is in agreement with previously published results from Severinghaus et al. (2009) measured on

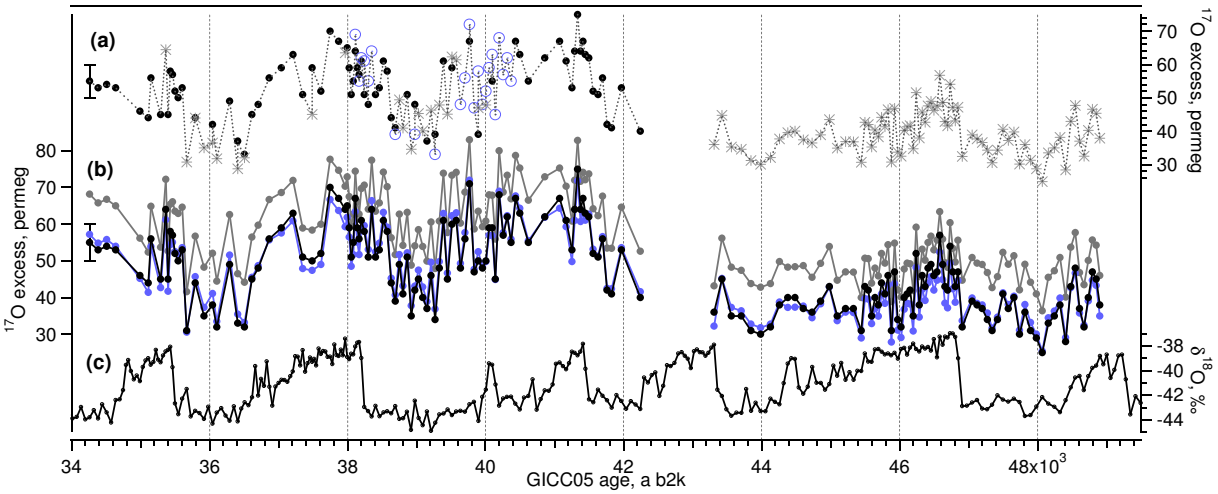

Figure 3. NEEM ^{17}O-excess (per meg) and δ^{18}O (‰) data. **(a)** Comparison of the ^{17}O-excess data measured in spring 2011 (black dots), at the beginning of 2012 (blue circles) and in winter 2013/spring 2014 (grey stars). **(b)** Calibration of the ^{17}O-excess data. Grey dots: measured data; blue dots: one-point calibration; black dots: two-point calibration. **(c)** δ^{18}O, ‰.

the Siple Dome ice core, Antarctica (Fig. 4f, grey dots). The advantage of using the NEEM rather than the Siple Dome $\delta^{18}O_{atm}$ data resides in the smaller NEEM ice–gas synchronisation uncertainty during GS-9 (Appendix A2).

3 Results and discussion

3.1 ^{17}O-excess record

The entire ^{17}O-excess record covering GI-7 to GI-13 (Fig. 4d) shows a general correlation with the δ^{18}O record and an anticorrelation with d-excess, while δ^{18}O and d-excess are themselves well anticorrelated: GI corresponds to high δ^{18}O and ^{17}O-excess levels and low d-excess levels, GS corresponds to low δ^{18}O and ^{17}O-excess levels and high d-excess levels. Following the current understanding of the ^{17}O-excess proxy as given in introduction, such a general correlation with δ^{18}O can be explained by (i) a synchronous change of high-latitude temperature and lower-latitude hydrological cycle (relative humidity at the oceanic source of evaporation or change in the water mass trajectory/recharge) and/or (ii) an influence of local temperature on ^{17}O-excess through kinetic effect at snow formation. In addition to this general correlation with δ^{18}O, the high-resolution ^{17}O-excess record reveals periods where ^{17}O-excess is decoupled from δ^{18}O. The most obvious decoupling between δ^{18}O and ^{17}O-excess is observed during GS-9 (Fig. 4d, green arrows): ^{17}O-excess decreases after the δ^{18}O decrease at the beginning of GS-9 and increases several centuries before the δ^{18}O increase at the beginning of GI-8. In fact, within GS-9 of constantly low δ^{18}O, we can infer three distinct phases from ^{17}O-excess variations (Fig. 4d, Table B1): phase 1 (39 900–39 350 a b2k), corresponding to the beginning of GS-9, is marked by high ^{17}O-excess values (mean = 55 per meg); phase 2 (39 350–38 610 a b2k) corresponds to low ^{17}O-excess values (down to 34 per meg, mean = 42 per meg); finally during phase 3 (38 610–38 220 a b2k) ^{17}O-excess reaches high interstadial levels again (mean = 57 per meg).

The decoupling observed between δ^{18}O and ^{17}O-excess implies that variations of ^{17}O-excess during GS-9 cannot be due to local (Greenland) temperature changes. This conclusion is strengthened by an independent temperature reconstruction based on firn gas fractionation (δ^{15}N, Fig. 4b and Guillevic et al., 2013) confirming a cold and stable temperature over the entire GS-9. The ^{17}O-excess variations during GS-9 thus necessarily reflect changes in the organisation of the hydrological cycle of the lower latitudes, either through their impact on relative humidity at the source of evaporation, or through a change in the recharge of water along transportation towards Greenland. It is counter-intuitive that such changes in the evaporation conditions or moisture source do not affect the d-excess signal. While we do not have a definite explanation for the lack of signal in the d-excess record, we already know that d-excess in Greenland is much more sensitive to local temperature changes than ^{17}O-excess (Winkler et al., 2012; Landais et al., 2012b). Moreover, because of its linear definition, d-excess is not sensitive to mixing of different water masses along the trajectory. A simple mathematical calculation (Risi et al., 2010) shows that the mixing of two water vapour masses with similar d-excess and ^{17}O-excess but different δ^{18}O produces a stable d-excess but a decrease in ^{17}O-excess.

Because of the complexity of processes which may be responsible for the specific ^{17}O-excess signal, it is thus important to confront our finding to other low-latitude proxies registered in Greenland ice cores, to independently confirm

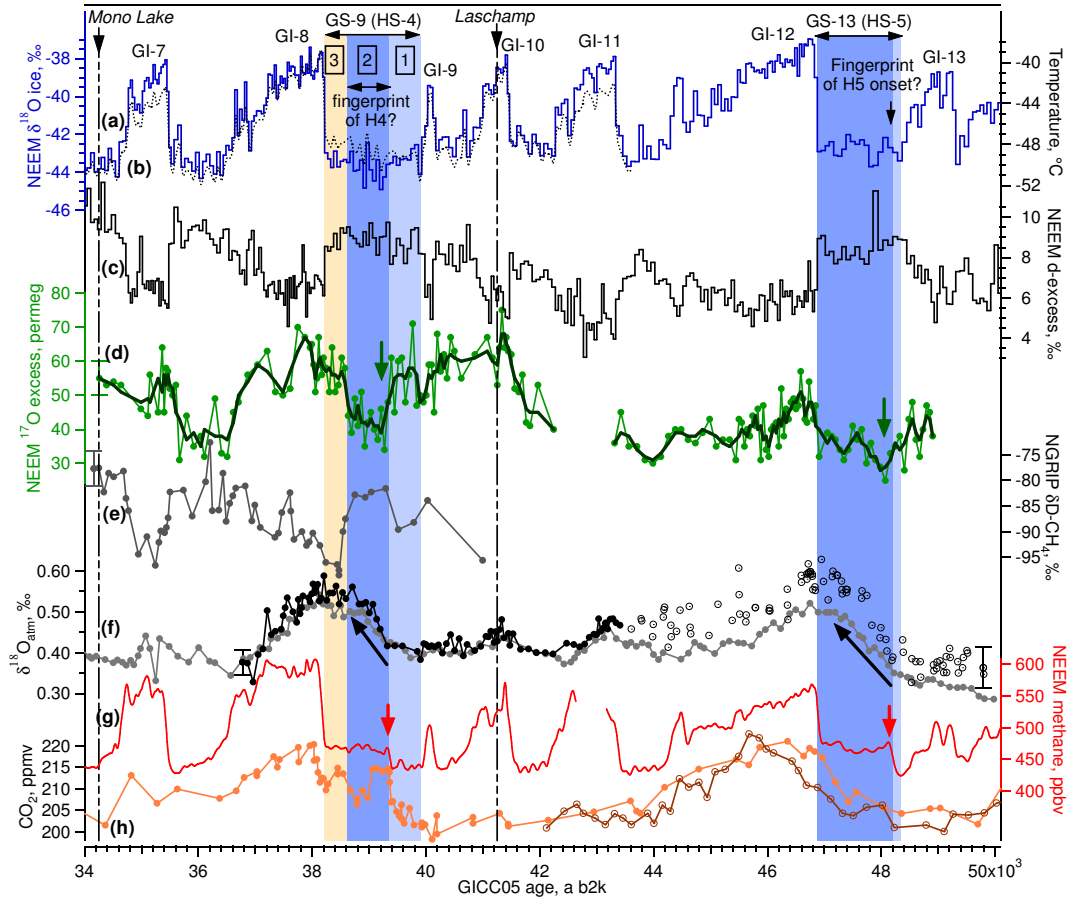

Figure 4. Greenland and Antarctic ice core records surrounding Heinrich events 4 and 5, synchronised to the GICC05 timescale (Appendix A). Position of phase 1 (light blue area), phase 2 (blue area) and phase 3 (yellow area) as given in Table B1. Dashed-dotted vertical lines: position of the geomagnetic excursion events Mono Lake and Laschamp (Svensson et al., 2006, 2008). **(a)** Blue line: NEEM δ^{18}O ice, ‰ (precision: 0.07 ‰) (Guillevic et al., 2013). **(b)** Black dotted line: NEEM temperature reconstructed using δ^{15}N data and firn modelling (Guillevic et al., 2013). **(c)** Black: NEEM deuterium excess, ‰ (±0.7 ‰), this study, measured at LSCE (France). **(d)** Green dots: NEEM ^{17}O-excess, per meg (±5 per meg), this study, measured at LSCE. Each dot corresponds to the average over 55 cm of ice. Green line: three-point running average. **(e)** Dark grey: NGRIP δD-CH$_4$, ‰ (±3.4‰) (Bock et al., 2010). **(f)** Black dots: NEEM δ^{18}O$_{atm}$, ‰ (±0.03 ‰), this study, measured at LSCE. Black circles: NGRIP δ^{18}O$_{atm}$ (Huber et al., 2006). Grey dots: Siple Dome δ^{18}O$_{atm}$ (Severinghaus et al., 2009). **(g)** Red: NEEM methane mixing ratio, ppbv (±5 ppbv), record measured by the CIC instrument (Chappellaz et al., 2013). **(h)** CO$_2$ mixing ratio, ppmv. Orange dots: Byrd ice core, Antarctica (Ahn et al., 2012). Brown open circles: TALDICE ice core, Talos Dome, Antarctica (Bereiter et al., 2012).

the decoupling between Greenland and lower latitudes during GS-9 as highlighted by the ^{17}O-excess record.

3.2 Multi-proxy identification of a three-phase sequence during GS-9 contrasting with the more uniform GS-8, 11 and 12

Our new high-resolution δ^{18}O$_{atm}$ measurements of air entrapped in the NEEM ice core confirm a decoupling between Greenland temperature and lower-latitude water cycle over GS-9. Indeed, earlier studies have shown that millennial δ^{18}O$_{atm}$ variations are global responses to water cycle changes in the northern Tropics (Severinghaus et al., 2009; Landais et al., 2010), where ITCZ shifts drive changes in precipitation isotopic composition (Lewis et al., 2010; Pausata et al., 2011). Our 95 new measurements of δ^{18}O$_{atm}$ depict a stable, low δ^{18}O$_{atm}$ during phase 1, followed by an increase over phase 2 (+0.14 ‰, Fig 4f, black arrow), and finally a stable high plateau during phase 3, in agreement with the Siple Dome record (Fig. 4f). The onsets of changes of δ^{18}O$_{atm}$ and ^{17}O-excess occur synchronously at the beginning of phase 2 (ice–gas synchronisation uncertainty less than ±100 a for the NEEM record, Appendix A2), but the increase of δ^{18}O$_{atm}$ is much slower than the observed changes in ^{17}O-excess; this is expected because of the long residence time of oxygen in the atmosphere (1000–2000 a, Bender et al., 1994a; Hoffmann et al., 2004). Second, in addition to the δ^{18}O$_{atm}$ record, records of NEEM CH$_4$ (Fig. 4g

Chappellaz et al., 2013) and its hydrogen isotopic composition (Fig. 4e, NGRIP $\delta D-CH_4$, Bock et al., 2010) in the air trapped in ice core also exhibit significant variations during GS-9 that are synchronous with the three phases identified from the ^{17}O-excess variations. Phase 1 is characterised by a minimum in methane mixing ratio, whereas the onset of phase 2 is marked by a 20 ppb abrupt increase (Fig. 4g, red arrow) accompanied by a 8 ± 4.8 ‰ increase in $\delta D-CH_4$. At the onset of phase 2, the concomitant changes in CH_4, $\delta D-CH_4$, $\delta^{18}O_{atm}$ and ^{17}O-excess in the absence of any Greenland temperature change can consistently be explained by a low-latitude change in water cycle as induced by a southward shift of the ITCZ.

Concerning the measured increase in $\delta D-CH_4$ at the onset of phase 2, such a shift would also be in agreement with model simulations of the clathrate release signature in ice cores (Bock et al., 2012), and is also supported by the synchronously lighter $\delta^{13}C-CH_4$ anomaly recently measured in the EDML ice core (Möller et al., 2013). We thus cannot exclude a sudden clathrate release at the onset of phase 2 that might be caused by e.g. less dense water masses in the North Atlantic Ocean following e.g. a massive iceberg discharge, as modelled by Flückiger et al. (2006). Higher-resolution methane isotopic data would be necessary to investigate in detail this possibility. However, the long duration of the $\delta D-CH_4$ anomaly (phase 2, 740 a) as well as the stable plateau of methane mixing ratio and $\delta^{13}C-CH_4$ throughout phases 2 and 3 (1130 a) call for an additional mechanism, such as source mix change or/and heavier isotopic composition of tropical precipitation (Möller et al., 2013) at the onset of phase 2. The mixing ratio increase and the following plateau are consistent with the activation of new methane sources in e.g. South America as simulated by Hopcroft et al. (2011), associated with a southward ITCZ shift at the onset of phase 2. Moreover, such a southward ITCZ shift is expected to produce more depleted precipitation in the SH (Southern Hemisphere) Tropics and heavier precipitation in the NH (Northern Hemisphere) Tropics (Pausata et al., 2011; Lewis et al., 2010). The increase in both $\delta D-CH_4$ and $\delta^{18}O_{atm}$ at the onset of phase 2 are consistent with this mechanism, provided that NH Tropics remain the main source of methane and oxygen. A minor part of the $\delta D-CH_4$ increase can be due to oxidation of methane in the troposphere, consuming preferentially the light methane isotopologues, if the mean atmospheric temperature decreases at the onset of phase 2 (Lewis et al., 2010; Bock et al., 2010; Sowers, 2006; Levine et al., 2012).

Finally, two abrupt ~ 20 ppm increases in the atmospheric CO_2 concentration recently unveiled from high-resolution Antarctic ice core records occur at the onsets of phase 2 and phase 3 (Fig. 4h and Ahn et al., 2012). After Antarctic and Greenland gas record synchronisation through CH_4 (Appendix A2), our study evidences that the CO_2 rise at the onset of phase 2 is synchronous (± 100 a) with a southward shift of the ITCZ, as suggested by the other NEEM ice core proxy variations. Different mechanisms are proposed to explain this CO_2 rise, as already discussed in Ahn et al. (2012): most probably upwelling in the Southern Ocean around Antarctica as suggested by increased opal burial rates in marine cores (Anderson et al., 2009), with a potential minor contribution from upwelling off the NW African coast (Jullien et al., 2007; Itambi et al., 2009; Mulitza et al., 2008). The causes of such modifications of the oceanic carbon storage may involve strengthening and/or southward shift of the SH westerlies, and/or AMOC slow down, and therefore remain debated (e.g. Toggweiler et al., 2006; Völker and Köhler, 2013; Menviel et al., 2014).

Altogether, our multi-proxy ice core data set reveals a 740 a long period starting 550 a after the onset of GS-9 (phase 2), which is marked by a southward shift of the ITCZ. The transition to phase 3 is characterised by reversed variations, with ^{17}O-excess and $\delta D-CH_4$ reaching interstadial values 480 ± 50 a prior to the increase in $\delta^{18}O$ marking the onset of GI-8. We explain this pattern by a gradual northward shift of the ITCZ associated with lighter precipitation in the NH Tropics and heavier precipitation in the SH Tropics. The flat methane and $\delta^{18}O_{atm}$ records suggest a globally stable methane budget and biosphere productivity, possibly due to compensating effects at different latitudes.

The sequence of events identified during HS-4 contrasts with the other non-Heinrich stadials where the pattern of changes recorded in Greenland $\delta^{18}O$ and other proxy records mostly depict a GS/GI contrast. These other GS are mostly characterised by low $\delta^{18}O$ and ^{17}O-excess levels, low methane mixing ratio (without any plateau) and slightly increasing $\delta^{18}O_{atm}$ (compared to the strong increase observed during HS-4). We therefore underline that the three-phase sequence identified during HS-4 is really specific and should not be applied to the other stadials studied here.

Some fingerprints of the decoupling between high and low latitudes identified during HS-4 can also be evidenced during HS-5 (or GS-13) even though less proxy data are currently available. We observe synchronous $\delta^{18}O_{atm}$ and methane increases about 140 ± 40 a after the beginning of GS-13, at 48 200 a b2k on the GICC05 chronology, 1340 ± 80 a before the onset of GI-12 (Fig. 4f and g, black and red arrows). This shift is accompanied by a small ^{17}O-excess decrease (Fig. 4d, green arrow). The CO_2 increase that was clear at the onset of phase 2 during GS-9 is however much less pronounced or perhaps even absent at the onset of phase 2 during GS-13 (+5 ppm in TALDICE, less clear in the Byrd CO_2 record, Bereiter et al., 2012; Ahn et al., 2012, and Fig. 4h). Finally, based on the available data we do not observe any decoupling between Greenland and lower latitudes toward the end of GS-13 as was observed over the phase 2 to phase 3 transition during GS-9. However, $\delta D-CH_4$ data are lacking during this time period and we cannot draw any firm conclusion here.

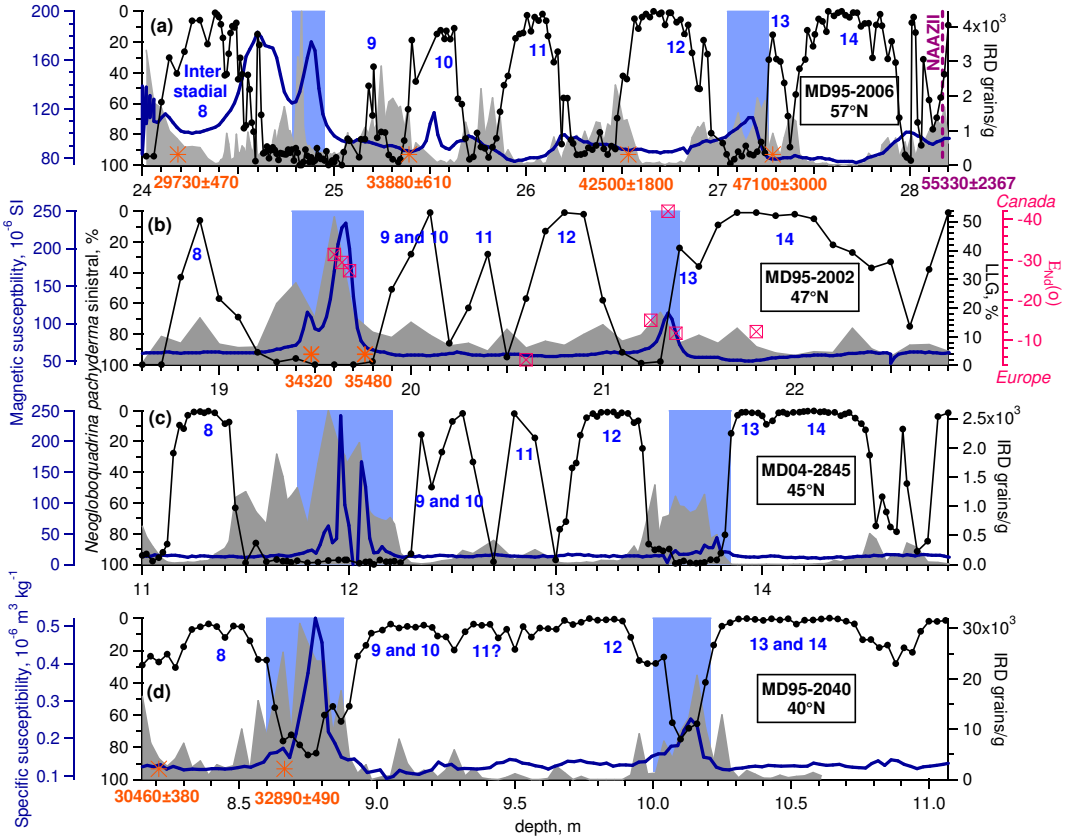

Figure 5. H4 and H5 in marine sediment records from the European margin. Core localisations are shown in Fig. 2. Each core is on its own depth scale. **(a)** Core MD95-2006, Barra Fan, 57°01′82 N, 10°03′48 W (Peters et al., 2008; Dickson et al., 2008). **(b)** Core MD95-2002, Celtic margin, 47°27′12 N, 8°27′03 W (Auffret et al., 2002). **(c)** Core MD04-2845, Bay of Biscay, 45°21′ N, 5°13′ W (Sánchez Goñi et al., 2008). **(d)** Core MD95-2040, Portuguese margin, 40°34′91 N, 9°51′67 W (de Abreu et al., 2003; Eynaud et al., 2009). Orange stars: uncalibrated carbon 14 age measurements (a before 1950 AD) and associated analytical uncertainties. Violet star: NAAZ (North Atlantic Ash Zone) II (Austin et al., 2004) and associated GICC05 age (a before 1950 AD) and MCE (Svensson et al., 2008). Grey shaded area: IRD or LLG (large lithic grains), counted on the > 150 µm fraction. Black line and dots: abundance of the polar foraminifer *N. pachyderma* sinistral, %; a high percentage denotes cold sea surface temperature. Blue line: magnetic susceptibility (**a**, **b**, **c**) and specific susceptibility **(d)**. Pink squares: ϵ neodymium (Nd) of the lithic coarse fraction (> 150 µm). Low values ($\leq$ 40) characterise sediment of Canadian origin, higher values ($\geq$ 15) European origin. Blue shaded areas: possible Laurentide contribution to the IRD/LGG. Origin identification of IRD for core MD95-2006 based on mineral magnetic measurements (for H4 and H5, Peters et al., 2008) and an additional unpublished count of detritial carbonate grains (for H4, W. Austin, personal communication, 2014), on ϵ neodymium and magnetic susceptibility for core MD95-2002 (Auffret et al., 2002) and on magnetic susceptibility (as proposed by Thouveny et al., 2000, for the Iberian Margin) for cores MD04-2845 (Sánchez Goñi et al., 2008) and MD95-2040 (de Abreu et al., 2003).

3.3 Comparison with marine core records from the North Atlantic

Low/mid-latitude palaeoclimate archives have already provided information on climate variations during Greenland stadials and especially over Stadial 9 (e.g. Voelker et al., 2006; Skinner and Elderfield, 2007). In particular, several phases have already been identified in sediment cores off the European margin and especially off Iberia, based on pollen assemblages and charcoal records (Naughton et al., 2009; Daniau et al., 2009): in the first phase, before the IRD layer and until the maximum IRD content is reached, the climate follows a progressively cooler and wetter trend. In the second phase after the IRD peak response, the climate is on the contrary progressively drier, with more frequent fire regime episodes.

Hereafter, we combine North Atlantic marine cores from different latitudes along the European margin, located between 5 to 10° W and 40 to 57° N (Figs. 2 and 5). Note that in Fig. 5, each marine sediment core is on its own depth scale. The available chronological control points are ^{14}C measurements (in orange) and the NAAZ-II (North Atlantic Ash Zone II) tephra layer also identified in the NGRIP ice core (in violet, see figure for references). We have only reported the ^{14}C measurement values and associated analytical uncertainties when available, without reservoir age correction or

calibration to calendar ages. Indeed, for this time period the ^{14}C measurement uncertainties (minimum ±380 years here) and their scarcity already prevent any centennial-scale synchronisation of these marine sediment cores.

We hereafter compare in each core the relative timing of changes in *Neogloboquadrina pachyderma* sinistral percentage (a proxy for sea surface temperature, black dots in Fig. 5) with the potential Laurentide IRD deposition (blue bars in Fig. 5, see Thouveny et al., 2000; Auffret et al., 2002; Peters et al., 2008, for details). As for the multi-proxy study of GS-9 in ice cores, the multi-proxy study of these marine cores in the European margin shows some latitudinal decoupling during stadial 9: (i) prior to the Laurentide IRD delivery, cold conditions are already depicted in the eastern part of the so-called Ruddiman belt (Ruddiman, 1977), at 45–55° N (e.g. Fig. 5a, core MD95–2006, Peters et al., 2008; Dickson et al., 2008), while interstadial conditions persist around the Iberian Peninsula at 35–42° N (e.g. Fig. 5d, core MD95-2040, de Abreu et al., 2003); (ii) the onset of the Laurentide IRD delivery coincides with a possible further cooling at high latitudes, while Iberia enters into cold stadial conditions; (iii) once low Laurentide IRD levels are registered again, mild to interstadial conditions are recorded around the Iberian Peninsula, while cold temperatures persist at 45–55° N. Between 40 and 57° N, cores MD04-2845 and MD95-2002 suggest that the situation might be intermediate, with a slight lag of the Laurentide IRD layer behind the polar species *N. pachyderma* sinistral increase (Fig. 5b, c, Auffret et al., 2002; Sánchez Goñi et al., 2008). Higher-resolution data as well as climate-independent synchronisation tools in between marine cores (such as measurements to detect specific palaeomagnetic events and/or volcanic ash layers) are necessary for a better description.

Over stadial 9, chronological uncertainties prevent us to link ice cores to other archives at a centennial year resolution, due to uncertainties in the GICC05 timescale (±1574 a at 40 000 a b2k, Svensson et al., 2008) and in ^{14}C measurement, reservoir age and calibration curve for marine sediment cores (Fig. 5 and e.g. Reimer et al., 2013). However, we still note that such a southward ITCZ shift can explain both the fingerprints in CH_4, $\delta D-CH_4$, ^{17}O-excess and $\delta^{18}O_{atm}$, as well as the colder conditions registered in the Iberian Peninsula that correspond to the purge of the LIS, i.e. the beginning of H4. Indeed, the H4 iceberg discharge could lead to European cooling as well as southward ITCZ shift, as simulated by climate models (Chiang et al., 2008). With this assumption, the inferred start of H4 would be 39 350 ± 1520 a b2k on the GICC05 chronology.

During phase 3, we note a progressive shift towards interstadial conditions first indicated by lower-latitude ice core proxies (Fig. 4, $\delta D-CH_4$, ^{17}O-excess). This would be consistent with a progressive northwards progression of the climate recovery towards interstadial climate conditions. This is in agreement with marine cores from low/mid-latitudes suggesting the start of a progressive AMOC recovery before full interstadial climate conditions are reached (e.g. Vautravers et al., 2004). The combination of ice and marine core data therefore supports the following sequence of events in phase 3: end of the iceberg delivery in the North Atlantic, northwards shift of the ITCZ and progressive AMOC restart, and finally the abrupt Greenland warming.

Finally, while some common characteristics can be drawn for HS-4 and 5, further studies are needed to assess whether this can be applied to the other Heinrich stadials or not. Considering the different background climate states and origin of the ice sheet collapse for the other HEs (Fig. 1), a different sequence identification in the ice core records can be expected.

3.4 How realistic is a decoupling between Greenland temperature and lower-latitude changes in climate and hydrological cycle?

Our study shows that a change in the mid/low latitudes of the North Atlantic ocean happens after the beginning of GS-9, with a time lag of 550 ± 60 a, i.e. when the North Atlantic region has already entered a cooling trend. Some features of our study suggest that the same may be true for GS-13 with a decoupling between Greenland temperature and lower-latitude climate 140 ± 40 a after the beginning of GS-13. We have hypothesised that this change may be linked to iceberg deliveries, i.e. H4 and H5. This assumption is actually supported by recent studies investigating the triggering mechanisms of HEs. Indeed, it has been suggested that the Northern Atlantic temperature decrease (beginning of GS in our case) is concomitant with the onset of a progressive AMOC slow-down and shoaling accompanied by sea ice extent that isolate the subsurface ocean from the cold atmosphere and produce a subsurface warming (Rasmussen and Thomsen, 2004; Jonkers et al., 2010). In addition, this subsurface warming could lead to a sea-level rise of ∼ 0.5 to 1 m by reorganisation of the North Atlantic dynamic topography and by oceanic thermal expansion (as modelled in Shaffer et al., 2004; Flückiger et al., 2006). Both subsurface warming and sea-level rise then contribute to destabilising ice shelves from the massive Laurentide ice sheet, causing the massive iceberg delivery of Heinrich events occurring several centuries after the onset of the Greenland stadials (Alvarez-Solas et al., 2010; Alvarez-Solas and Ramstein, 2011; Marcott et al., 2011).

The suggestion that HEs 4 and 5 occur after the beginning of Greenland stadials calls for another mechanism to trigger stadial conditions. Recent studies listed hereafter have proposed a local (Arctic) control on DO events, without the need of a freshwater flux into the North Atlantic Ocean. (i) The studies of Norwegian Sea marine sediment cores from Rasmussen and Thomsen (2004) and Dokken et al. (2013) proposed that stadials were induced by progressively increasing winter sea ice cover in the Nordic seas and the formation of a halocline isolating warm subsurface waters from

the North Atlantic drift from the atmosphere. (ii) These studies also showed IRD from the Fennoscandian ice sheet during the warm phases of DO events. The authors proposed that the corresponding freshwater flux helped to establish a halocline and hereby facilitated sea ice formation, inducing a cooling towards a stadial climate. A model study from Roche et al. (2010) has moreover shown that the overturning cell in the Nordic seas is very sensitive to freshwater perturbations, even more than the Ruddiman belt in the North Atlantic. (iii) Finally, a third mechanism (that could be combined with the two previous ones) has been proposed by Petersen et al. (2013): the onset of GI could be induced by the collapse of an ice shelf east of Greenland extending towards Denmark Strait, due to subsurface melt. The slow regrowth together with the expansion of regional sea ice cover would create the progressive cooling towards GS. Moreover, these three mechanisms could explain why the Nordic seas (and Greenland) remain in a stable stadial state, while low/mid-latitudes are gradually shifting towards interstadial conditions (as suggested by the increased ^{17}O excess during phase 3): during stadials, the heat advected along the North Atlantic Drift accumulates in subsurface, below the sea ice in the Nordic seas or below the ice shelf east of Greenland, until the low-density warm subsurface water abruptly reaches the surface, thereby melting the sea ice and/or ice shelf, which results in a rapid warming of the Nordic seas (and Greenland).

These different mechanisms calling for a local Arctic control on DO events are supported by model studies. Indeed, atmospheric simulations (Li et al., 2010) suggest that Greenland temperature is sensitive to changes in sea ice cover anomalies in the Nordic seas because of "a strengthening of the easterly flow over the Nordic seas" impacting Central Greenland. In contrast, in these simulations, NW Atlantic sea ice cover anomalies (supposed to increase during HEs originating from the Laurentide) only affect the western flank of the Icelandic low and the associated atmospheric circulation anomaly does not noticeably impact Central Greenland. Supporting these results, the modelled regional pattern of Greenland warming in response to Nordic seas sea ice retreat is in agreement with regional quantitative reconstruction of Greenland temperature and accumulation rate during MIS3 (Guillevic et al., 2013).

From our data, we found that central Greenland temperature is not sensitive to lower-latitude climate changes during stadials. This is actually not a unique case. Other palaeoclimate archives show the same insensitivity, e.g. no specific sea ice change is depicted during the entire stadial 9 as inferred from deep sea core records obtained from the Irminger Sea and south of the Faroe Islands (Cortijo et al., 2005; Zumaque et al., 2012).

However, bio-indicators in marine cores from the Norwegian Sea robustly record warmer temperature (e.g. based on foraminifers, Rasmussen and Thomsen, 2004; Dokken et al., 2013) and reduced sea ice cover (based on dinocysts, Eynaud et al., 2002) during stadials than during interstadials. To reconcile these conflicting model–data results, Rasmussen and Thomsen (2004) and Dokken et al. (2013) proposed a perennial sea ice cover in the Norwegian Sea during all stadials of MIS3, separated by a halocline from warm subsurface waters in the North Atlantic Drift, to where foraminifers might have moved their depth habitat. Dinocysts on the contrary may have stayed at the surface, and their observed assemblages could be due to productivity anomalies in zones of polynya. According to this scenario, the lack of specific sea ice anomaly in the Nordic seas during GS-9 and GS-13 may explain why no cold anomaly is recorded in Greenland during the same periods.

The proposed decoupling between cold, stable Greenland temperature and lower-latitude climatic changes during stadial 9 has implications for synchronisation of climate archives from different latitudes. For the last glacial period, chronologies of sediment cores from the North Atlantic and Europe are usually constructed by wiggle matching of DO-like variations to the NGRIP δ^{18}O record on its GICC05 chronology. While it has been underlined by several studies that there were no independent chronological support for this hypothesis (Blaauw et al., 2010), the decoupling between ^{17}O excess and δ^{18}O variations during GS-9 suggests that this would actually not be correct for this specific time period. We therefore would like to emphasise the need of high-resolution climate-independent synchronisation tools, such as volcanic ash layers, as already widely encouraged by the INTIMATE working group (e.g. Austin and Hibbert, 2012; Davies et al., 2014; Brendryen et al., 2011).

4 Conclusions and perspectives

Here, we have presented the first ^{17}O-excess record from a Greenland ice core covering a sequence of DO events during the last glacial period, and encompassing two major HEs of Laurentide origin. The ^{17}O-excess profile shows generally high values during GI and low values during GS periods. This can be interpreted as synchronous change of high-latitude temperature and lower-latitude hydrological cycle (relative humidity at the oceanic source of evaporation or change in the water mass trajectory/recharge) and/or an influence of local temperature on ^{17}O-excess through kinetic effect at snow formation. However, especially during GS-9, the ^{17}O-excess record shows additional variability that cannot be identified either in the δ^{18}O or in the d-excess records. The decoupling observed between δ^{18}O and ^{17}O-excess implies that variations of ^{17}O-excess during GS-9 cannot be due to local (Greenland) temperature changes.

Our new multi-proxy record from Greenland ice cores has revealed a three-phase sequence of GS-9, contrasting with the more stable GS-8, 11 and 12. While Greenland temperature remains uniformly cold along GS-9, synchronous changes in ^{17}O-excess, $\delta^{18}O_{atm}$, $\delta D - CH_4$, methane and CO_2 are interpreted as a polar ice core fingerprint of the lower-

latitude climate and hydrological cycle changes, most likely due to a southward shift of the ITCZ delayed by 550 ± 60 a after the beginning of the cold period in Greenland (GS-9). We hypothesise that this lower-latitude change dated at $39\,350 \pm 1\,520$ a b2k on the GICC05 chronology may be associated with the strong Heinrich event 4. This is in agreement with recent data and modelling studies suggesting that the iceberg discharge only occurs several centuries after the cooling of surface ocean in North Atlantic and decrease of AMOC intensity.

The fingerprint of the ITCZ southward shift observed in ice core proxies ends 740 ± 60 a later, when ^{17}O-excess, $\delta^{18}O_{atm}$ and $\delta D - CH_4$ have shifted back to interstadial climate values, 390 ± 50 a before the onset of GI-8. Preliminary investigations on GS-13 encompassing H5 suggest an ITCZ southward shift fingerprint based on the ice core proxies $\delta^{18}O_{atm}$ and CH_4, 140 ± 40 a after the beginning of GS-13. In opposite to what happens during HS-4, the ^{17}O-excess variations are less significant here and we cannot identify three phases for HS-5. Our findings obviously call for systematic and high-resolution investigations of the ice core multi-proxy fingerprints of lower-latitude climate changes in general and HEs in particular.

In contrast to the more stable and uniform non-Heinrich stadials, the decoupling between the constantly cold Greenland temperature during GS-9 and the climate variability associated with H4 at lower latitudes challenges the use of Greenland ice core temperatures as a single target for benchmarking climate simulations focused on HEs. Our multi-proxy study opens new paths for parallel investigations of different marine, terrestrial and ice core climate archives.

Appendix A: Synchronisation of the used ice cores to the GICC05 chronology

A1 Ice age scales

The GICC05 (Greenland Ice Core Chronology 2005) has been constructed for the NGRIP ice core from present back to 60 ka b2k based on annual layer counting in ice cores of parameters featuring seasonal scale variations (Vinther et al., 2006; Andersen et al., 2006; Rasmussen et al., 2006; Svensson et al., 2008). The NEEM ice core (Rasmussen et al., 2013) has been synchronised to NGRIP using match points based on peaks of electrical conductivity and dielectrical properties of the ice. The synchronisation uncertainty between NEEM and NGRIP is estimated to be ~ 10 cm (1σ, Rasmussen et al., 2013), resulting in ~ 10 a synchronisation uncertainty for GS-9. The GICC05 uncertainty is estimated by the maximum counting error in years (Rasmussen et al., 2006), with each uncertain year counted as 0.5 ± 0.5 a. This can be considered as a 2σ uncertainty. We give the duration uncertainty of each of the phases of GS-9 and GS-13 as the sum of the uncertain years counted within each phase.

Table A1. Match points between methane depths from the Byrd ice core (Ahn and Brook, 2008; Ahn et al., 2012), the Siple Dome ice core (Brook et al., 2005; Ahn et al., 2012) and NEEM methane (Chappellaz et al., 2013) gas age according to the GICC05 chronology (Guillevic et al., 2013; Rasmussen et al., 2013).

Event	Byrd depth [m]	Siple Dome depth [m]	NEEM methane gas age, [a b2k]
GI-6	1617.15	795.37	33 716
GI-7	1654.05	809.97	35 435
GI-8, dip	1691.10	818.13	36 901
GI-8	1716.10	825.66	38 125
GS-9, plateau	1743.55	833.81	39 372
GI-9	1759.20	837.90	40 121
GI-10	1780.30	845.97	41 467
GI-11	1807.95	855.28	43 351
		861.20	44 486
GI-12	1863.05	870.43	46 859
GI-13	1898.30	882.41	49 276

A2 Gas age scales

For the NGRIP gas records (δD$-$CH$_4$, $\delta^{18}O_{atm}$), we use the gas age scale from Kindler et al. (2014), initially constructed on the NGRIP ss09sea06bm timescale (NGRIP members, 2004; Wolff et al., 2010), and we transfer it to the GICC05 chronology. We use the NEEM gas age scale from Guillevic et al. (2013) for GS-8 to GS-12, compatible with the later release from Rasmussen et al. (2013), and the one from Rasmussen et al. (2013) for GI-12 to GI-14. The NGRIP and NEEM gas age scale covering GS-9 are well constrained (ice–gas synchronisation uncertainty less than 100 years for NEEM, less than 160 years for NGRIP) thanks to numerous measured δ^{15}N data (Kindler et al., 2014; Guillevic et al., 2013; Rasmussen et al., 2013).

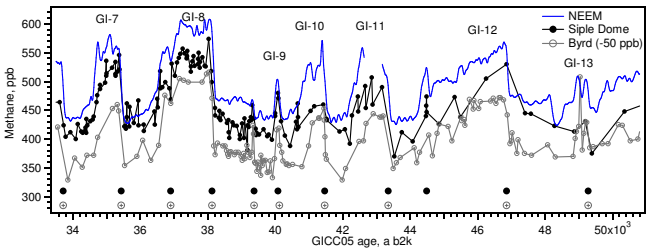

Figure A1. Construction of a gas age scale for the Byrd and Siple Dome ice cores, Antarctica. Blue line: NEEM methane data (Chappellaz et al., 2013) on the NEEM GICC05 gas age scale (Guillevic et al., 2013; Rasmussen et al., 2013). Black line and dots: Siple Dome CH_4 data (Brook et al., 2005; Ahn et al., 2012) after synchronisation. Grey line and open circle: Byrd CH_4 data (Ahn et al., 2012) minus a 50 ppb offset for better clearness, after synchronisation. At the bottom of the figure are indicated the position of the match points listed in Table A1: black circles for NEEM-Siple Dome match points and open grey circles for NEEM-Byrd.

To synchronise the Byrd gas records to the NEEM ice core, we use a traditional approach by matching methane records from both ice cores (Blunier et al., 1998). We first use the high-resolution NEEM methane record on its GICC05 gas age scale (Guillevic et al., 2013). We then match the Byrd methane record (Ahn et al., 2012) to the NEEM methane record, using the mid-slope of each GI onset as match points (Fig. A1 and Table A1). We perform a linear interpolation in between the match points. We then apply the obtain depth-gas age scale for Byrd to the Byrd CO_2 record.

The same method is applied to the Siple Dome methane record in order to place the Siple Dome $\delta^{18}O_{atm}$ record (Severinghaus et al., 2009) on the GICC05 timescale, to compare with the NEEM and NGRIP $\delta^{18}O_{atm}$ record (Fig. A1 and Table A1).

Appendix B: Timing and duration of the phases identified during GS-9 according to the GICC05 timescale

The results are presented in Table B1.

Table B1. Timing and duration of the phases identified during GS-9 in ice core proxies, on the GICC05 timescale. Column 2: onsets of GI and GS are given according to Rasmussen et al. (2014). Column 3: maximum counting error (MCE), reflecting the number of uncertain annual layers compared to year 2000 AD (Rasmussen et al., 2006, and Appendix A1). Column 5: MCE of the phase duration, calculated as the MCE difference between start and end of each phase. Column 6: total duration uncertainty for each phase: MCE of the phase duration, synchronisation uncertainty of the NEEM ice core to the NGRIP GICC05 timescale ($\sim$ 20 a, Rasmussen et al., 2013) and data resolution ($\pm$35 a in average).

	Start time		Duration		
	a b2k	MCE, a	a	MCE, a	uncertainty (2σ), a
GS-13					
Phase 1	48 340	1988	140	7	40
Phases 2 & 3	48 200	1981	1340	69	80
GI-12	46 860	1912			
GS-9					
Phase 1	39 900	1569	550	51	60
Phase 2	39 350	1518	740	47	60
Phase 3	38 610	1471	390	22	50
GI-8	38 220	1449			

The Supplement related to this article is available online at doi:10.5194/cp-10-2115-2014-supplement.

Acknowledgements. We thank S. O. Rasmussen and M. Bock for fruitful discussions and P. Kindler for valuable insights and support. W. Austin kindly provided the data of marine core MD95-2006 and S. Zaragosi the magnetic susceptibility data of core MD04-2845. NEEM is directed and organised by the Centre for Ice and Climate at the Niels Bohr Institute and US NSF, Office of Polar Programs. It is supported by funding agencies and institutions in 14 countries: Belgium (FNRS-CFB and FWO), Canada (GSC), China (CAS), Denmark (FIST), France (IPEV, CNRS/INSU, CEA and ANR), Germany (AWI), Iceland (RannIs), Japan (NIPR), Korea (KOPRI), the Netherlands (NWO/ALW), Sweden (VR), Switzerland (SNF), UK (NERC) and the USA (US NSF, Office of Polar Programs). LSCE analytical work has been funded by the ANR VMC NEEM project. M. Guillevic thanks the University of Copenhagen, Denmark, and the Commissariat à l'Energie Atomique Saclay, France, for funding. The publication of this article is funded by the "Fondation de France Ars Cuttoli".

Edited by: L. Skinner

References

Ahn, J. and Brook, E. J.: Atmospheric CO_2 and climate on millennial time scales during the last glacial period, Science, 322, 83–85, 2008.

Ahn, J., Brook, E., Schmittner, A., and Kreutz, K.: Abrupt change in atmospheric CO_2 during the last ice age, Geophys. Res. Lett., 39, L18771, doi:10.1029/2012GL053018, 2012.

Alvarez-Solas, J. and Ramstein, G.: On the triggering mechanism of Heinrich events, P. Natl. Acad. Sci. USA, 108, E1359–E1360, 2011.

Alvarez-Solas, J., Charbit, S., Ritz, C., Paillard, D., Ramstein, G., and Dumas, C.: Links between ocean temperature and iceberg discharge during Heinrich events, Nat. Geosci., 3, 122–126, 2010.

Andersen, K. K., Svensson, A., Johnsen, S. J., Rasmussen, S. O., Bigler, M., Röthlisberger, R., Ruth, U., Siggaard-Andersen, M.-L., Steffensen, J. P., Dahl-Jensen, D., Vinther, B. M., and Clausen, H. B.: The Greenland Ice Core Chronology 2005, 15–42 ka. Part 1: constructing the time scale, Quaternary Sci. Rev., 25, 3246–3257, 2006.

Anderson, R. F., Ali, S., Bradtmiller, L. I., Nielsen, S. H. H., Fleisher, M. Q., Anderson, B. E., and Burckle, L. H.: Wind-driven upwelling in the Southern Ocean and the deglacial rise in atmospheric CO_2, Science, 323, 1443–1448, 2009.

Auffret, G., Zaragosi, S., Dennielou, B., Cortijo, E., Rooij, D. V., Grousset, F., Pujol, C., Eynaud, F., and Siegert, M.: Terrigenous fluxes at the Celtic margin during the last glacial cycle, Mar. Geol., 188, 79–108, 2002.

Austin, W. E. and Hibbert, F. D.: Tracing time in the ocean: a brief review of chronological constraints (60-8 kyr) on North Atlantic marine event–based stratigraphies, Quaternary Sci. Rev., 36, 28–37, 2012.

Austin, W. E. N., Wilson, L. J., and Hunt, J. B.: The age and chronostratigraphical significance of North Atlantic Ash zone II, J. Quaternary Sci., 19, 137–146, 2004.

Barkan, E. and Luz, B.: High precision measurements of ^{17}O / ^{16}O and ^{18}O / ^{16}O ratios in H_2O, Rapid Commun. Mass Spectrom., 19, 3737–3742, 2005.

Barker, S., Diz, P., Vautravers, M. J., Pike, J., Knorr, G., Hall, I. R., and Broecker, W. S.: Interhemispheric Atlantic seesaw response during the last deglaciation, Nature, 457, 1097–1102, 2009.

Baumgartner, M., Schilt, A., Eicher, O., Schmitt, J., Schwander, J., Spahni, R., Fischer, H., and Stocker, T. F.: High-resolution interpolar difference of atmospheric methane around the Last Glacial Maximum, Biogeosciences, 9, 3961–3977, doi:10.5194/bg-9-3961-2012, 2012.

Bazin, L., Landais, A., Lemieux-Dudon, B., Toyé Mahamadou Kele, H., Veres, D., Parrenin, F., Martinerie, P., Ritz, C., Capron, E., Lipenkov, V., Loutre, M.-F., Raynaud, D., Vinther, B., Svensson, A., Rasmussen, S. O., Severi, M., Blunier, T., Leuenberger, M., Fischer, H., Masson-Delmotte, V., Chappellaz, J., and Wolff, E.: An optimized multi-proxy, multi-site Antarctic ice and gas orbital chronology (AICC2012): 120–800 ka, Clim. Past, 9, 1715–1731, doi:10.5194/cpd-8-5963-2012, 2013.

Bender, M., Sowers, T., Dickinson, M., Orchado, J., Grootes, P., Mayewski, P., and Meese, D.: Climate correlations between Greenland and Antarctica during the past 100 000 years, Nature, 372, 663–666, 1994a.

Bender, M., Sowers, T., and Labeyrie, L.: The Dole effect and its variations during the last 130 000 years as measured in the Vostok ice core, Global Biogeochem. Cy., 8, 363–376, 1994b.

Bereiter, B., Lüthi, D., Siegrist, M., Schüpbach, S., Stocker, T. F., and Fischer, H.: Mode change of millennial CO_2 variability during the last glacial cycle associated with a bipolar marine carbon seesaw, P. Natl. Acad. Sci. USA, 109, 9755–9760, 2012.

Björck, S., Walker, M. J., Cwynar, L. C., Johnsen, S., Knudsen, K.-L., Lowe, J. J., Wohlfarth, B., and Members, I.: An event stratigraphy for the Last Termination in the North Atlantic region based on the Greenland ice-core record: A proposal by the INTIMATE group, J. Quaternary Sci., 13, 283–292, 1998.

Blaauw, M., Wohlfarth, B., Christen, J. A., Ampel, L., Veres, D., Hughen, K. A., Preusser, F., and Svensson, A.: Were last glacial climate events simultaneous between Greenland and France? A quantitative comparison using non-tuned chronologies, J. Quaternary Sci., 25, 387–394, 2010.

Blunier, T., Chappellaz, J., Schwander, J., Dällenbach, A., Stauffer, B., Stocker, T., Raynaud, D., Jouzel, J., Clausen, H., Hammer, C., and Johnsen, S.: Asynchrony of Antarctic and Greenland climate change during the last glacial period, Nature, 394, 739–743, 1998.

Boch, R., Cheng, H., Spötl, C., Edwards, R. L., Wang, X., and Häuselmann, P.: NALPS: a precisely dated European climate record 120–60 ka, Clim. Past, 7, 1247–1259, 2011, http://www.clim-past.net/7/1247/2011/.

Bock, J., Martinerie, P., Witrant, E., and Chappellaz, J.: Atmospheric impacts and ice core imprints of a methane pulse from clathrates, Earth Planet. Sc. Lett., 349/350, 98–108, 2012.

Bock, M., Schmitt, J., Möller, L., Spahni, R., Blunier, T., and Fischer, H.: Hydrogen isotopes preclude marine hydrate CH_4 emis-

sions at the onset of Dansgaard-Oeschger events, Science, 328, 1686–1689, 2010.

Bond, G., Heinrich, H., Broecker, W., Labeyrie, L., McManus, J., Andrews, J., Huon, S., Jantschik, R., Clasen, S., Simet, C., Tedesco, K., Klas, M., Bonani, G., and Ivy, S.: Evidence for massive discharges of icebergs into the North Atlantic ocean during the last glacial period, Nature, 360, 245–249, 1992.

Bond, G., Broecher, W., Johnsen, S. J., MacManus, J., Laberie, L., Jouzel, J., and Bonani, G.: Correlations between climate records from North Atlantic sediments and Greenland ice, Nature, 365, 143–147, 1993.

Bonne, J.-L., Masson-Delmotte, V., Cattani, O., Delmotte, M., Risi, C., Sodemann, H., and Steen-Larsen, H. C.: The isotopic composition of water vapour and precipitation in Ivittuut, southern Greenland, Atmos. Chem. Phys., 14, 4419–4439, 2014, http://www.atmos-chem-phys.net/14/4419/2014/.

Bozbiyik, A., Steinacher, M., Joos, F., Stocker, T. F., and Menviel, L.: Fingerprints of changes in the terrestrial carbon cycle in response to large reorganizations in ocean circulation, Clim. Past, 7, 319–338, doi:10.5194/cp-7-319-2011, 2011.

Brendryen, J., Haflidason, H., and Sejrup, H. P.: Non-synchronous deposition of North Atlantic Ash Zone II in Greenland ice cores, and North Atlantic and Norwegian Sea sediments: an example of complex glacial-stage tephra transport, J. Quaternary Sci., 26, 739–745, 2011.

Brook, E. J., White, J. W., Schilla, A. S., Bender, M. L., Barnett, B., Severinghaus, J. P., Taylor, K. C., Alley, R. B., and Steig, E. J.: Timing of millennial-scale climate change at Siple Dome, West Antarctica, during the last glacial period, Quaternary Sci. Rev., 24, 1333–1343, 2005.

Capron, E., Landais, A., Chappellaz, J., Schilt, A., Buiron, D., Dahl-Jensen, D., Johnsen, S. J., Jouzel, J., Lemieux-Dudon, B., Loulergue, L., Leuenberger, M., Masson-Delmotte, V., Meyer, H., Oerter, H., and Stenni, B.: Millennial and sub-millennial scale climatic variations recorded in polar ice cores over the last glacial period, Clim. Past, 6, 345–365, doi:10.5194/cp-6-345-2010, 2010.

Chappellaz, J., Blunier, T., Raynaud, D., Barnola, J., Schwander, J., and Stauffer, B.: Synchronous changes in atmospheric CH_4 and Greenland climate between 40 and 8 kyr BP, Nature, 366, 443–445, 1993.

Chappellaz, J., Stowasser, C., Blunier, T., Baslev-Clausen, D., Brook, E. J., Dallmayr, R., Faïn, X., Lee, J. E., Mitchell, L. E., Pascual, O., Romanini, D., Rosen, J., and Schüpbach, S.: High-resolution glacial and deglacial record of atmospheric methane by continuous-flow and laser spectrometer analysis along the NEEM ice core, Clim. Past, 9, 2579–2593, doi:10.5194/cp-9-2579-2013, 2013.

Chiang, J. C. H., Cheng, W., and Bitz, C. M.: Fast teleconnections to the tropical Atlantic sector from Atlantic thermohaline adjustment, Geophys. Res. Lett., 35, L07704, doi:10.1029/2008GL033292, 2008.

Clement, A. C. and Peterson, L. C.: Mechanisms of abrupt climate change of the last glacial period, Rev. Geophys., 46, RG4002, doi:10.1029/2006RG000204, 2008.

Cortijo, E., Duplessy, J.-C., Labeyrie, L., Duprat, J., and Paillard, D.: Heinrich events: hydrological impact, CR Geosci., 337, 897–907, 2005.

Craig, H., Horibe, Y., and Sowers, T.: Gravitational separation of gases and isotopes in polar ice caps, Science, 242, 1675–1678, 1988.

Cvijanovic, I. and Chiang, J.: Global energy budget changes to high latitude North Atlantic cooling and the tropical ITCZ response, Climate Dyn., 40, 1435–1452, 2013.

Dahl-Jensen, D. and NEEM community members: Eemian interglacial reconstructed from a Greenland folded ice core, Nature, 493, 489–494, 2013.

Daniau, A.-L., Sánchez Goñi, M. F., and Duprat, J.: Last glacial fire regime variability in western France inferred from microcharcoal preserved in core MD04-2845, Bay of Biscay, Quaternary Res., 71, 385–396, 2009.

Dansgaard, W.: Stable isotopes in precipitation, Tellus, 16, 436–468, 1964.

Davies, S. M., Abbott, P. M., Meara, R. H., Pearce, N. J., Austin, W. E., Chapman, M. R., Svensson, A., Bigler, M., Rasmussen, T. L., Rasmussen, S. O., and Farmer, E. J.: A North Atlantic tephrostratigraphical framework for 130–60 ka b2k: new tephra discoveries, marine-based correlations, and future challenges, Quaternary Sci. Rev., in press, doi:10.1016/j.quascirev.2014.03.024, 2014.

de Abreu, L., Shackleton, N. J., Schönfeld, J., Hall, M., and Chapman, M.: Millennial-scale oceanic climate variability off the Western Iberian margin during the last two glacial periods, Mar. Geol., 196, 1–20, 2003.

Dickson, A. J., Austin, W. E. N., Hall, I. R., Maslin, M. A., and Kucera, M.: Centennial-scale evolution of Dansgaard-Oeschger events in the northeast Atlantic Ocean between 39.5 and 56.5 ka B.P., Paleoceanography, 23, PA3206, doi:10.1029/2008PA001595, 2008.

Dokken, T. M., Nisancioglu, K. H., Li, C., Battisti, D. S., and Kissel, C.: Dansgaard-Oeschger cycles: Interactions between ocean and sea ice intrinsic to the Nordic seas, Paleoceanography, 28, 1–12, 2013.

EPICA community members: One-to-one coupling of glacial climate variability in Greenland and Antarctica, Nature, 444, 195–198, 2006.

Eynaud, F., Turon, J., Matthiessen, J., Kissel, C., Peypouquet, J., de Vernal, A., and Henry, M.: Norwegian sea-surface palaeoenvironments of marine oxygen-isotope stage 3: the paradoxical response of dinoflagellate cysts, J. Quaternary Sci., 17, 349–359, 2002.

Eynaud, F., de Abreu, L., Voelker, A., Schönfeld, J., Salgueiro, E., Turon, J.-L., Penaud, A., Toucanne, S., Naughton, F., Sánchez Goñi, M. F., Malaizé, B., and Cacho, I.: Position of the Polar Front along the western Iberian margin during key cold episodes of the last 45 ka, Geochem. Geophy. Geosy., 10, Q07U05, doi:10.1029/2009GC002398, 2009.

Eynaud, F., Malaizé, B., Zaragosi, S., de Vernal, A., Scourse, J., Pujol, C., Cortijo, E., Grousset, F. E., Penaud, A., Toucanne, S., Turon, J.-L., and Auffret, G.: New constraints on European glacial freshwater releases to the North Atlantic Ocean, Geophys. Res. Lett., 39, L15601, doi:10.1029/2012GL052100, 2012.

Flückiger, J., Knutti, R., and White, J. W. C.: Oceanic processes as potential trigger and amplifying mechanisms for Heinrich events, Paleoceanography, 21, PA2014, doi:10.1029/2005PA001204, 2006.

Genty, D., Combourieu-Nebout, N., Peyron, O., Blamart, D., Wainer, K., Mansuri, F., Ghaleb, B., Isabello, L., Dormoy, I., von Grafenstein, U., Bonelli, S., Landais, A., and Brauer, A.: Isotopic characterization of rapid climatic events during OIS3 and OIS4 in Villars Cave stalagmites (SW-France) and correlation with Atlantic and Mediterranean pollen records, Quaternary Sci. Rev., 29, 2799–2820, 2010.

Grousset, F., Labeyrie, L., Sinko, J., Cremer, M., Bond, G., Duprat, J., Cortijo, E., and Huon, S.: Patterns of ice-rafted detritus in the glacial North Atlantic (40–55N), Paleoceanography, 8, 175–192, 1993.

Grousset, F., Pujol, C., Labeyrie, L., Auffret, G., and Boelaert, A.: Were the North Atlantic Heinrich events triggered by the behavior of the European ice sheets?, Geology, 28, 123–126, doi:10.1130/0091-7613(2000)28<123:WTNAHE>2.0.CO;2, 2000.

Guillevic, M., Bazin, L., Landais, A., Kindler, P., Orsi, A., Masson-Delmotte, V., Blunier, T., Buchardt, S. L., Capron, E., Leuenberger, M., Martinerie, P., Prié, F., and Vinther, B. M.: Spatial gradients of temperature, accumulation and δ^{18}O-ice in Greenland over a series of Dansgaard–Oeschger events, Clim. Past, 9, 1029–1051, doi:10.5194/cp-9-1029-2013, 2013.

Gwiazda, R., Hemming, S., and Broecker, W.: Provenance of icebergs during Heinrich Event 3 and the contrast to their sources during other Heinrich episodes, Paleoceanography, 11, 371–378, doi:10.1029/96PA01022, 1996.

Heinrich, H.: Origin and consequences of cyclic ice rafting in the Northeast Atlantic Ocean during the past 130 000 years, Quaternary Res., 29, 142–152, 1988.

Hemming, S., Broecker, W., Sharp, W., Bond, G., Gwiazda, R., McManus, J., Klas, M., and Hajdas, I.: Provenance of the Heinrich layers in core V28-82, northeastern Atlantic, ^{40}Ar-^{39}Ar ages of ice-rafted hornblende, Pb isotopes in feldspar grains, and Nd-Sr-Pb isotopes in the fine sediment fraction, Earth Planet. Sc. Lett., 164, 317–333, 1998.

Hemming, S. R.: Heinrich events: massive Late Pleistocene detritus layers of the North Atlantic and their global climate imprint, Rev. Geophys., 42, RG1005, doi:10.1029/2003RG000128, 2004.

Hoffmann, G., Cuntz, M., Weber, C., Ciais, P., Friedlingstein, P., Heimann, M., Jouzel, J., Kaduk, J., Maier-Reimer, E., Seibt, U., and Six, K.: A model of the Earth's Dole effect, Global Biogeochem. Cy., 18, GB1008, doi:10.1029/2003GB002059, 2004.

Hopcroft, P. O., Valdes, P. J., and Beerling, D. J.: Simulating idealized Dansgaard-Oeschger events and their potential impacts on the global methane cycle, Quaternary Sci. Rev., 30, 3258–3268, 2011.

Huber, C., Leuenberger, M., Spahni, R., Flückiger, J., Schwander, J., Stocker, T. F., Johnsen, S. J., Landais, A., and Jouzel, J.: Isotope calibrated Greenland temperature record over Marine Isotope Stage 3 and its relation to CH_4, Earth Planet. Sc. Lett., 243, 504–519, 2006.

Itambi, A., von Dobeneck, T., Mulitza, S., Bickert, T., and Heslop, D.: Millennial-scale northwest African droughts related to Heinrich events and Dansgaard-Oeschger cycles: Evidence in marine sediments from offshore Senegal, Paleoceanography, 24, PA1205, doi:10.1029/2007PA001570, 2009.

Jo, K., Woo, K. S., Yi, S., Yang, D. Y., Lim, H. S., Wang, Y., Cheng, H., and Edwards, R. L.: Mid-latitude interhemispheric hydrologic seesaw over the past 550 000 years, Nature, 508, 378–382, doi:10.1038/nature13076, 2014.

Jonkers, L., Moros, M., Prins, M. A., Dokken, T., Dahl, C. A., Dijkstra, N., Perner, K., and Brummer, G.-J. A.: A reconstruction of sea surface warming in the northern North Atlantic during MIS 3 ice-rafting events, Quaternary Sci. Rev., 29, 1791–1800, 2010.

Jouzel, J., Stiévenard, N., Johnsen, S., Landais, A., Masson-Delmotte, V., Sveinbjörnsdóttir, A., Vimeux, F., von Grafenstein, U., and White, J.: The GRIP deuterium-excess record, Quaternary Sci. Rev., 26, 1–17, 2007.

Jullien, E., Grousset, F. E., Hemming, S. R., Peck, V. L., Hall, I. R., Jeantet, C., and Billy, I.: Contrasting conditions preceding MIS3 and MIS2 Heinrich events, Global Planet. Change, 54, 225–238, 2006.

Jullien, E., Grousset, F., Malaizé, B., Duprat, J., Sánchez Goñi, M. F., Eynaud, F., Charlier, K., Schneider, R., Bory, A., Bout, V., and Flores, J. A.: Low-latitude dusty events vs. high-latitude icy Heinrich events, Quaternary Res., 68, 279–386, 2007.

Kageyama, M., Merkel, U., Otto-Bliesner, B., Prange, M., Abe-Ouchi, A., Lohmann, G., Ohgaito, R., Roche, D. M., Singarayer, J., Swingedouw, D., and Zhang, X.: Climatic impacts of fresh water hosing under Last Glacial Maximum conditions: a multi-model study, Clim. Past, 9, 935–953, doi:10.5194/cp-9-935-2013, 2013.

Kanner, L. C., Burns, S. J., Cheng, H., and Edwards, R. L.: High-latitude forcing of the South American summer monsoon during the Last Glacial, Science, 335, 570–573, 2012.

Kindler, P., Guillevic, M., Baumgartner, M., Schwander, J., Landais, A., and Leuenberger, M.: Temperature reconstruction from 10 to 120 kyr b2k from the NGRIP ice core, Clim. Past, 10, 887–902, doi:10.5194/cp-10-887-2014, 2014.

Landais, A., Masson-Delmotte, V., Nebout, N. C., Jouzel, J., Blunier, T., Leuenberger, M., Dahl-Jensen, D., and Johnsen, S.: Millenial scale variations of the isotopic composition of atmospheric oxygen over Marine Isotopic Stage 4, Earth Planet. Sc. Lett., 258, 101–113, 2007.

Landais, A., Dreyfus, G., Capron, E., Masson-Delmotte, V., Sánchez Goñi, M. F., Desprat, S., Hoffmann, G., Jouzel, J., Leuenberger, M., and Johnsen, S.: What drives the millennial and orbital variations of $\delta^{18}O_{atm}$?, Quaternary Sci. Rev., 29, 235–246, 2010.

Landais, A., Ekaykin, A., Barkan, E., Winkler, R., and Luz, B.: Seasonal variations of ^{17}O-excess and d-excess in snow precipitation at the Vostok station (East Antarctica), J. Glaciol., 58, 210, doi:10.3189/2012JoG11J237, 2012a.

Landais, A., Steen-Larsen, H., Guillevic, M., Masson-Delmotte, V., Vinther, B., and Winkler, R.: Triple isotopic composition of oxygen in surface snow and water vapor at NEEM (Greenland), Geochim. Cosmochim. Ac., 77, 304–316, 2012b.

Levine, J. G., Wolff, E. W., Hopcroft, P. O., and Valdes, P. J.: Controls on the tropospheric oxidizing capacity during an idealized Dansgaard-Oeschger event, and their implications for the rapid rises in atmospheric methane during the last glacial period, Geophys. Res. Lett., 39, doi:10.1029/2012GL051866, 2012.

Lewis, S., LeGrande, A. N., Kelley, M., and Schmidt, G. A.: Water vapour source impacts on oxygen isotope variability in tropical precipitation during Heinrich events, Clim. Past, 6, 325–343, doi:10.5194/cp-6-325-2010, 2010.

Li, C., Battisti, D., and Bitz, C.: Can North Atlantic sea ice anomalies account for Dansgaard-Oeschger climate signals?, J. Climate, 23, 5457–5475, 2010.

Luz, B. and Barkan, E.: The isotopic ratios ^{17}O / ^{16}O and $^{18}O/^{16}O$ in molecular oxygen and their significance in biogeochemistry, Geochim. Cosmochim. Ac., 69, 1099–1110, 2005.

Luz, B., Barkan, E., Yam, R., and Shemesh, A.: Fractionation of oxygen and hydrogen isotopes in evaporating water, Geochim. Cosmochim. Ac., 73, 6697–6703, 2009.

Majoube, M.: Fractionnement en oxygène 18 et en deutérium entre l'eau et sa vapeur, J. Clim. Phys., 68, 1423–1436, 1971.

Marcott, S. A., Clark, P. U., Padman, L., Klinkhammer, G. P., Springer, S. R., Liu, Z., Otto-Bliesner, B. L., Carlson, A. E., Ungerer, A., Padman, J., He, F., Cheng, J., and Schmittner, A.: Ice-shelf collapse from subsurface warming as a trigger for Heinrich events, P. Natl. Acad. Sci. USA, 108, 13415–13419, 2011.

Masson-Delmotte, V., Jouzel, J., Landais, A., Stiévenard, M., Johnsen, S. J., White, J. W. C., Werner, M., Sveinbjörnsdóttir, A., and Fuhrer, K.: GRIP deuterium excess reveals rapid and orbital-scale changes in Greenland moisture origin, Science, 309, 118–121, 2005.

Menviel, L., England, M., Meissner, K., Mouchet, A., and Yu, J.: Atlantic-Pacific seesaw and its role in outgassing CO_2 during Heinrich events, Paleoceanography, 29, 1–13, 2014.

Möller, L., Sowers, T., Bock, M., Spahni, R., Behrens, M., Schmitt, J., Miller, H., and Fischer, H.: Independent variations of CH_4 emissions and isotopic composition over the past 160 000 years, Nat. Geosci., 6, 885–890, 2013.

Mosblech, N. A., Bush, M. B., Gosling, W. D., Hodell, D., Thomas, L., van Calsteren, P., Correa-Metrio, A., Valencia, B. G., Curtis, J., and van Woesik, R.: North Atlantic forcing of Amazonian precipitation during the last ice age, Nat. Geosci., 5, 817–820, 2012.

Mulitza, S., Prange, M., Stuut, J.-B., Zabel, M., von Dobeneck, T., Itambi, A. C., Nizou, J., Schulz, M., and Wefer, G.: Sahel megadroughts triggered by glacial slowdowns of Atlantic meridional overturning, Paleoceanography, 23, PA4206, doi:10.1029/2008PA001637, 2008.

Naughton, F., Sánchez Goñi, M. F., Kageyama, M., Bard, E., Duprat, J., Cortijo, E., Desprat, S., Malaizé, B., Joly, C., Rostek, F., and Turon, J.-L.: Wet to dry climatic trend in north-western Iberia within Heinrich events, Earth Planet. Sc. Lett., 284, 329–342, 2009.

NGRIP members: High-resolution record of Northern Hemisphere climate extending into the last interglacial period, Nature, 431, 147–151, 2004.

Pausata, F. S. R., Battisti, D. S., Nisancioglu, K. H., and Bitz, C. M.: Chinese stalagmite $\delta^{18}O$ controlled by changes in the Indian monsoon during a simulated Heinrich event, Nat. Geosci., 4, 474–480, 2011.

Peters, C., Walden, J., and Austin, W. E. N.: Magnetic signature of European margin sediments: Provenance of ice-rafted debris and the climatic response of the British ice sheet during Marine Isotope Stages 2 and 3, J. Geophys. Res.-Earth, 113, F03007, doi:10.1029/2007JF000836, 2008.

Petersen, S. V., Schrag, D. P., and Clark, P. U.: A new mechanism for Dansgaard-Oeschger cycles, Paleoceanography, 28, 24–30, 2013.

Peterson, L. C., Haug, G. H., Hughen, K. A., and Röhl, U.: Rapid changes in the hydrologic cycle of the tropical Atlantic during the Last Glacial, Science, 290, 1947–1951, 2000.

Rashid, H., Hesse, R., and Piper, D.: Evidence for an additional Heinrich event between H5 and H6 in the Labrador Sea, Paleoceanography, 18, 1077, doi:10.1029/2003PA000913, 2003.

Rasmussen, S., Bigler, M., Blockley, S., Blunier, T., Buchardt, S. L., Clausen, H. B., Cvijanovic, I., Dahl-Jensen, D., Johnsen, S. J., Fischer, H., Gkinis, V., Guillevic, M., Hoek, W., Lowe, J. J., Pedro, J., Popp, T., Seierstad, I. E., Steffensen, J., Svensson, A. M., Vallelonga, P., Vinther, B. M., Walker, M. J., Wheatley, J., and Winstrup, M.: A stratigraphic framework for robust naming and correlation of past abrupt climatic changes during the last glacial period based on three synchronized Greenland ice core records, Quaternary Sci. Rev., in press, 2014.

Rasmussen, S. O., Andersen, K. K., Svensson, A. M., Steffensen, J. P., Vinther, B. M., Clausen, H. B., Siggaard-Andersen, M.-L., Johnsen, S. J., Larsen, L. B., Dahl-Jensen, D., Bigler, M., Röthlisberger, R., Fischer, H., Goto-Azuma, K., Hansson, M. E., and Ruth, U.: A new Greenland ice core chronology for the last glacial termination, J. Geophys. Res., 111, D06102, doi:10.1029/2005JD006079, 2006.

Rasmussen, S. O., Abbott, P. M., Blunier, T., Bourne, A. J., Brook, E., Buchardt, S. L., Buizert, C., Chappellaz, J., Clausen, H. B., Cook, E., Dahl-Jensen, D., Davies, S. M., Guillevic, M., Kipfstuhl, S., Laepple, T., Seierstad, I. K., Severinghaus, J. P., Steffensen, J. P., Stowasser, C., Svensson, A., Vallelonga, P., Vinther, B. M., Wilhelms, F., and Winstrup, M.: A first chronology for the North Greenland Eemian Ice Drilling (NEEM) ice core, Clim. Past, 9, 2713–2730, doi:10.5194/cp-9-2713-2013, 2013.

Rasmussen, T., Oppo, D., Thomsen, E., and Lehman, S.: Deep sea records from the southeast Labrador Sea: Ocean circulation changes and ice-rafting events during the last 160 000 years, Paleoceanography, 18, 1018, doi:10.1029/2001PA000736, 2003.

Rasmussen, T. L. and Thomsen, E.: The role of the North Atlantic Drift in the millennial timescale glacial climate fluctuations, Palaeogeogr. Palaeocl., 210, 101–116, 2004.

Reimer, P. J., Bard, E., Bayliss, A., Beck, J. W., Blackwell, P. G., Ramsey, C. B., Buck, C. E., Cheng, H., Edwards, R. L., Friedrich, M., Grootes, P. M., Guilderson, T. P., Haflidason, H., Hajdas, I., Hatté, C., Heaton, T. J., Hoffmann, D. L., Hogg, A. G., Hughen, K. A., Kaiser, K. F., Kromer, B., Manning, S. W., Niu, M., Reimer, R. W., Richards, D. A., Scott, E. M., Southon, J. R., Staff, R. A., Turney, C. S. M., and van der Plicht, J.: IntCal13 and Marine13 radiocarbon age calibration curves 0–50,000 years cal PB, Radiocarbon, 55, 1869–1887, 2013.

Risi, C., Landais, A., Bony, S., Jouzel, J., Masson-Delmotte, V., and Vimeux, F.: Understanding the ^{17}O excess glacial-interglacial variations in Vostok precipitation, J. Geophys. Res.-Atmos., 115, D10112, doi:10.1029/2008JD011535, 2010.

Roche, D., Paillard, D., and Cortijo, E.: Constraints on the duration and freshwater release of Heinrich event 4 through isotope modelling, Nature, 432, 379–382, 2004.

Roche, D., Wiersma, A., and Renssen, H.: A systematic study of the impact of freshwater pulses with respect to different geographical locations, Climate Dyn., 34, 997–1013, 2010.

Ruddiman, W. F.: Late Quaternary deposition of ice-rafted sand in the subpolar North Atlantic (lat 40 to 65N), Geol. Soc. Am. Bull., 88, 1813–1827, 1977.

Sánchez Goñi, M. F. and Harrison, S.: Millennial-scale climate variability and vegetation changes during the Last Glacial: Concepts and terminology, Quaternary Sci. Rev., 29, 2823–2827, 2010.

Sánchez Goñi, M. F., Landais, A., Fletcher, W. J., Naughton, F., Desprat, S., and Duprat, J.: Contrasting impacts of Dansgaard–Oeschger events over a western European latitudinal transect modulated by orbital parameters, Quaternary Sci. Rev., 27, 1136–1151, 2008.

Schoenemann, S. W., Schauer, A. J., and Steig, E. J.: Measurement of SLAP2 and GISP δ^{17}O and proposed VSMOW-SLAP normalization for δ^{17}O and $^{17}O_{excess}$, Rapid Commun. Mass Sp., 27, 582–590, 2013.

Schoenemann, S. W., Steig, E. J., Ding, Q., Markle, B. R., and Schauer, A. J.: Triple water-isotopologue record from WAIS Divide, Antarctica: controls on glacial-interglacial changes in 17Oexcess of precipitation, J. Geophys. Res., 119, doi:10.1002/2014JD021770, 2014.

Schwander, J.: The transformation of snow to ice and the occlusion of gases, J. Wiley and Sons Limited, New York, 1989.

Severinghaus, J., Grachev, A., and Battle, M.: Thermal fractionation of air in polar firn by seasonal temperature gradients, Geochem. Geophy. Geosy., 2,146, doi:10.1029/2000GC000146, 2001.

Severinghaus, J., Beaudette, R., Headly, M. A., Taylor, K., and Brook, E. J.: Oxygen-18 of O_2 records the impact of abrupt climate change on the terrestrial biosphere, Science, 324, 1431–1434, 2009.

Shaffer, G., Olsen, S. M., and Bjerrum, C. J.: Ocean subsurface warming as a mechanism for coupling Dansgaard-Oeschger climate cycles and ice-rafting events, Geophys. Res. Lett., 31, L24202, doi:10.1029/2004GL020968, 2004.

Skinner, L. C. and Elderfield, H.: Rapid fluctuations in the deep North Atlantic heat budget during the last glacial period, Paleoceanography, 22, PA1205, doi:10.1029/2006PA001338, 2007.

Snoeckx, H., Grousset, F., Revel, M., and Boelaert, A.: European contribution of ice-rafted sand to Heinrich layers H3 and H4, Mar. Geol., 158, 197–208, 1999.

Sowers, T.: Late quaternary atmospheric CH_4 isotope record suggests marine clathrates are stable, Science, 311, 838–840, 2006.

Stanford, J., Rohling, E., Bacon, S., Roberts, A., Grousset, F., and Bolshawa, M.: A new concept for the paleoceanographic evolution of Heinrich event 1 in the North Atlantic, Quaternary Sci. Rev., 30, 1047–1066, 2011.

Steen-Larsen, H. C., Johnsen, S. J., Masson-Delmotte, V., Stenni, B., Risi, C., Sodemann, H., Balslev-Clausen, D., Blunier, T., Dahl-Jensen, D., Ellehøj, M. D., Falourd, S., Grindsted, A., Gkinis, V., Jouzel, J., Popp, T., Sheldon, S., Simonsen, S. B., Sjolte, J., Steffensen, J. P., Sperlich, P., Sveinbjörnsdóttir, A. E., Vinther, B. M., and White, J. W. C.: Continuous monitoring of summer surface water vapor isotopic composition above the Greenland Ice Sheet, Atmos. Chem. Phys., 13, 4815–4828, doi:10.5194/acp-13-4815-2013, 2013.

Stenni, B., Masson-Delmotte, V., Johnsen, S., Jouzel, J., Longinelli, A., Monnin, E., Röthlisberger, R., and Selmo, E.: An oceanic cold reversal during the last deglaciation, Science, 293, 2074–2077, 2001.

Stocker, T. F. and Johnsen, S. J.: A minimum thermodynamic model for the bipolar seesaw, Paleoceanography, 18, 1087, doi:10.1029/2003PA000920, 2003.

Svensson, A., Andersen, K., Bigler, M., Clausen, H., Dahl-Jensen, D., Davies, S., Johnsen, S., Muscheler, R., Rasmussen, S., Röthlisberger, R., Steffensen, J., and Vinther, B.: The Greenland Ice Core Chronology 2005, 15-42 ka. Part 2: comparison to other records, Quaternary Sci. Rev., 25, 3258–3267, 2006.

Svensson, A., Andersen, K. K., Bigler, M., Clausen, H. B., Dahl-Jensen, D., Davies, S. M., Johnsen, S. J., Muscheler, R., Parrenin, F., Rasmussen, S. O., Röthlisberger, R., Seierstad, I., Steffensen, J. P., and Vinther, B. M.: A 60 000 year Greenland stratigraphic ice core chronology, Clim. Past, 4, 47–57, doi:10.5194/cp-4-47-2008, 2008.

Thouveny, N., Moreno, E., Delanghe, D., Candon, L., Lancelot, Y., and Shackleton, N.: Rock magnetic detection of distal ice-rafted debries: clue for the identification of Heinrich layers on the Portuguese margin, Earth Planet. Sci. Lett., 180, 61–75, 2000.

Toggweiler, J., Russell, J., and Carson, S.: Midlatitude westerlies, atmospheric CO_2, and climate change during the ice ages, Paleoceanography, 21, PA2005, doi:10.1029/2005PA001154, 2006.

Vautravers, M. J., Shackleton, N. J., Lopez-Martinez, C., and Grimalt, J. O.: Gulf Stream variability during marine isotope stage 3, Paleoceanography, 19, PA2011, doi:10.1029/2003PA000966, 2004.

Veres, D., Bazin, L., Landais, A., Kele, H. T. M., Lemieux-Dudon, B., Parrenin, F., Martinerie, P., Blayo, E., Blunier, T., Capron, E., Chappellaz, J., Rasmussen, S. O., Severi, M., Svensson, A., Vinther, B., , and Wolff, E. W.: The Antarctic ice core chronology (AICC2012): an optimized multi-parameter and multi-site dating approach for the last 120 thousand years, Clim. Past, 9, 1733–1748, doi:10.5194/cp-9-1733-2013, 2013.

Vimeux, F., Masson, V., Jouzel, J., Stievenard, M., and Petit, J.: Glacial-interglacial changes in ocean surface conditions in the Southern Hemisphere, Nature, 398, 410–413, 1999.

Vinther, B. M., Clausen, H. B., Johnsen, S. J., Rasmussen, S. O., Andersen, K. K., Buchardt, S. L., Dahl-Jensen, D., Seierstad, I. K., Siggaard-Andersen, M.-L., Steffensen, J. P., and Svensson, A.: A synchronized dating of three Greenland ice cores throughout the Holocene, J. Geophys. Res., 111, D13102, doi:10.1029/2005JD006921, 2006.

Voelker, A. H., Lebreiro, S., Schönfeld, J., Cacho, I., Erlenkeuser, H., and Abrantes, F.: Mediterranean outflow strengthening during northern hemisphere coolings: A salt source for the glacial Atlantic?, Earth Planet. Sc. Lett., 245, 39–55, 2006.

Voelker, A. H. L.: Global distribution of centennial-scale records for Marine Isotope Stage (MIS) 3: a database, Quaternary Sci. Rev., 21, 1185–1212, 2002.

Völker, C. and Köhler, P.: Responses of ocean circulation and carbon cycle to changes in the position of the Southern Hemisphere westerlies at Last Glacial Maximum, Paleoceanography, 28, 726–739, 2013.

Wang, X., Auler, A. S., Edwards, R. L., Cheng, H., Ito, E., Wang, Y., Kong, X., and Solheid, M.: Millennial-scale precipitation changes in southern Brazil over the past 90 000 years, Geophys. Res. Lett., 34, L23701, doi:10.1029/2007GL031149, 2007.

Wang, Y. J., Cheng, H., Edwards, R. L., An, Z. S., Wu, J. Y., Shen, C. C., and Dorale, J. A.: A high-resolution absolute-dated Late Pleistocene monsoon record from Hulu Cave, China, Science, 294, 2345–2348, 2001.

Winkler, R., Landais, A., Sodemann, H., Dümbgen, L., Prié, F., Masson-Delmotte, V., Stenni, B., and Jouzel, J.: Deglaciation

records of ^{17}O-excess in East Antarctica: reliable reconstruction of oceanic normalized relative humidity from coastal sites, Clim. Past, 8, 1–16, doi:10.5194/cp-8-1-2012, 2012.

Wolff, E. W., Chappellaz, J., Blunier, T., Rasmussen, S. O., and Svensson, A.: Millennial-scale variability during the last glacial: The ice core record, Quaternary Sci. Rev., 29, 2828–2838, 2010.

Zumaque, J., Eynaud, F., Zaragosi, S., Marret, F., Matsuzaki, K. M., Kissel, C., Roche, D. M., Malaizé, B., Michel, E., Billy, I., Richter, T., , and Palis, E.: An ocean–ice coupled response during the last glacial: a view from a marine isotopic stage 3 record south of the Faeroe Shetland Gateway, Clim. Past, 8, 1997–2017, doi:10.5194/cp-8-1997-2012, 2012.

3 Cauquoin et al., 2015

Clim. Past, 11, 355–367, 2015
www.clim-past.net/11/355/2015/
doi:10.5194/cp-11-355-2015

Climate of the Past
Open Access

Comparing past accumulation rate reconstructions in East Antarctic ice cores using ^{10}Be, water isotopes and CMIP5-PMIP3 models

A. Cauquoin[1], A. Landais[1], G. M. Raisbeck[2], J. Jouzel[1], L. Bazin[1], M. Kageyama[1], J.-Y. Peterschmitt[1], M. Werner[3], E. Bard[4], and ASTER Team[4,*]

[1]Laboratoire des Sciences du Climat et de l'Environnement (LSCE/IPSL, CEA-CNRS-UVSQ), CEA Saclay Orme des Merisiers, 91191 Gif-sur-Yvette, France
[2]Centre de Sciences Nucléaires et de Sciences de la Matière (CSNSM), UMR CNRS 8609, Université Paris Sud XI, Bât 108, 91405 Orsay, France
[3]Alfred Wegener Institute for Polar and Marine Research (AWI) Bussestraße 24, 27570 Bremerhaven, Germany
[4]Aix-Marseille Université, CNRS-IRD-Collège de France, UM 34 CEREGE, Technopôle de l'Environnement Arbois-Méditerranée, BP80, 13545 Aix-en-Provence, France
[*]M. Arnold, G. Aumaître, D. L. Bourlès and K. Keddadouche

Correspondence to: A. Cauquoin (alexandre.cauquoin@lmd.jussieu.fr)

Received: 18 July 2014 – Published in Clim. Past Discuss.: 22 August 2014
Revised: 14 January 2015 – Accepted: 2 February 2015 – Published: 5 March 2015

Abstract. Ice cores are exceptional archives which allow us to reconstruct a wealth of climatic parameters as well as past atmospheric composition over the last 800 kyr in Antarctica. Inferring the variations in past accumulation rate in polar regions is essential both for documenting past climate and for ice core chronology. On the East Antarctic Plateau, the accumulation rate is so small that annual layers cannot be identified and accumulation rate is mainly deduced from the water isotopic composition assuming constant temporal relationships between temperature, water isotopic composition and accumulation rate. Such an assumption leads to large uncertainties on the reconstructed past accumulation rate. Here, we use high-resolution beryllium-10 (^{10}Be) as an alternative tool for inferring past accumulation rate for the EPICA Dome C ice core, in East Antarctica. We present a high-resolution ^{10}Be record covering a full climatic cycle over the period 269 to 355 ka from Marine Isotope Stage (MIS) 9 to 10, including a period warmer than pre-industrial (MIS 9.3 optimum). After correcting ^{10}Be for the estimated effect of the palaeomagnetic field, we deduce that the ^{10}Be reconstruction is in reasonably good agreement with EDC3 values for the full cycle except for the period warmer than present. For the latter, the accumulation is up to 13 % larger (4.46 cm ie yr^{-1} instead of 3.95). This result is in agreement with the studies suggesting an underestimation of the deuterium-based accumulation for the optimum of the Holocene (Parrenin et al., 2007a). Using the relationship between accumulation rate and surface temperature from the saturation vapour relationship, the ^{10}Be-based accumulation rate reconstruction suggests that the temperature increase between the MIS 9.3 optimum and present day may be 2.4 K warmer than estimated by the water isotopes reconstruction. We compare these reconstructions to the available model results from CMIP5-PMIP3 for a glacial and an interglacial state, i.e. for the Last Glacial Maximum and pre-industrial climates. While 3 out of 7 models show relatively good agreement with the reconstructions of the accumulation–temperature relationships based on ^{10}Be and water isotopes, the other models either underestimate or overestimate it, resulting in a range of model results much larger than the range of the reconstructions. Indeed, the models can encounter some difficulties in simulating precipitation changes linked with temperature or water isotope content on the East Antarctic Plateau during glacial–interglacial transition and need to be improved in the future.

Published by Copernicus Publications on behalf of the European Geosciences Union.

1 Introduction

Polar ice cores provide reference records for past climatic conditions over the last 130 kyr in Greenland (North Greenland Ice Core Project Members, 2004; NEEM Community Members, 2013) and over the last 800 kyr in Antarctica (EPICA Community Members, 2004). That ice as old as 800 kyr can be retrieved at a depth of 3200 m is due to the very low accumulation rate encountered at this site of the East Antarctic Plateau (2.73 cm ice equivalent (ie) per year today; EPICA Community Members, 2004). Accumulation rate is even smaller during glacial periods as expected from simple thermo-dynamical considerations: cold air holds less moisture than warm air. Still, the quantitative reconstruction of past accumulation rate is not straightforward and large uncertainties ($> 30\,\%$) are often associated with its reconstruction in polar ice cores (Blunier et al., 2007; Guillevic et al., 2013; van Ommen and Morgan, 1997).

Reducing the uncertainties on the reconstruction of past accumulation rate is essential for several reasons. First and most obviously, this will lead to an improved ice core chronology. Second, even if the physical relationship between air moisture content and temperature holds true with time, there is no a priori reason why the link between accumulation rate and temperature should be constant with time in polar regions, at the very end of the water condensation process. Because of the spatial and temporal variations in the origin and trajectories of air masses, some decoupling can be expected between accumulation rate and temperature or water isotopes from which polar temperature is classically retrieved. Finally, the simulation of polar accumulation and of its link with temperature is a weakness for many models, such that an evaluation of the modelled relationship between temperature vs. accumulation against accumulation reconstructions is desirable. There is thus a clear need for estimates of past accumulation changes that are independent of temperature, as well as water isotope.

An alternate way to reconstruct past accumulation rate is the use of beryllium-10 (^{10}Be), a cosmogenic isotope to obtain an independent estimate of past accumulation. After their production in the upper atmosphere (Lal and Peters, 1967), ^{10}Be atoms become fixed to aerosols and fall very quickly (within 1–2 years according to Raisbeck et al., 1981a) on the Antarctic Plateau. A simplistic assumption, namely that the ^{10}Be flux is constant through time, has been applied to estimate accumulation changes along the Vostok ice core, first from a limited set of measurements (Yiou et al., 1985) and then from a more detailed but still low resolution and discontinuous data set covering the last climatic cycle (Jouzel et al., 1989). This assumption was suggested by the anti-correlation observed between ^{10}Be concentrations in ice and accumulation rate derived from oxygen isotopes at the drilling site (Yiou et al., 1985). However, the assumption of a constant ^{10}Be flux is limited by the heliomagnetic and geomagnetic modulations: the higher these fields are, the more primary cosmic ray particles are deflected, which leads to a decrease in cosmogenic isotope production. For example, this problem is important for the last glacial period, which includes the Laschamp excursion, a dramatic short-lived decrease in the Earth's magnetic field intensity occurring at about 41 ka (Singer et al., 2009).

In the present study, we exploit a continuous and very detailed ^{10}Be time series covering a full climatic cycle over a 86 kyr period, from Marine Isotope Stage (MIS) 9 to 10, measured along the Dome C ice core (75°06′ S, 123°21′ E). Two geomagnetic events are mentioned during this time range at 290 ka (the so-called "Portuguese Margin"; Thouveny et al., 2008) and 320 ka (the so-called "Calabrian Ridge 1"; Langereis et al., 1997). This 269–355 ka record has been prepared and measured in the framework of the PhD work of Cauquoin (2013). It completes a high-resolution ^{10}Be record between 170 and 800 ka at EDC that will be published separately. Two advantages of using the period 269–355 ka for this study are that (1) it has the largest glacial–interglacial range of δD and thus estimated temperature and accumulation and (2) it has relatively small geomagnetic variations as compared, for example, to the last climatic cycle (Blake and Laschamp excursions). Thus the sensitivity of ^{10}Be concentration due to accumulation variations compared to those due to production variations should be particularly favourable.

Our manuscript is organized as follows. After reiterating on the classical estimation of past accumulation rates from water isotopes in ice core and a presentation of the procedure, we examine the multidecadal ^{10}Be record and discuss how this ~ 86 kyr long record allows inferences about the associated glacial–interglacial accumulation rate change. In the following section, we discuss the relationship between temperature/δD and accumulation rate changes on the East Antarctic Plateau over deglaciations using constraints both from glaciological data and from 11 modelling outputs inferred from 8 CMIP5-PMIP3 models, plus one simulation (ECHAM5) being equipped with stable water isotope diagnostics for the pre-industrial period (PI) and the Last Glacial Maximum (LGM, 21 ka).

2 Methods

2.1 The classical estimation of past accumulation rates from water isotope data on the East Antarctic Plateau

The physical link between the moisture content of air mass and its temperature has been systematically used to estimate past accumulation in Antarctica and establish ice core chronologies. This approach linking accumulation rate to temperature has been first proposed by Lorius et al. (1985) and Ritz (1992). Using a simple unidimensional model neglecting the possible changes in circulation intensity over the precipitation area, one infers that the precipitation rate at

a time t is given by Eq. 1, where A is the accumulation rate, P_{sat} the saturation pressure over ice, and t_0 refers to present-day values:

$$A(t) = A(t_0) \times \frac{[\partial(P_{\mathrm{sat}}/(T+273))/\partial T]_t}{[\partial(P_{\mathrm{sat}}/(T+273))/\partial T]_{t_0}}. \quad (1)$$

The temperature considered in Eq. (1) is the temperature at condensation, approximated by the inversion temperature, T_{inv}, itself related to surface temperature T_{s} in Antarctica over a range from −15 to −55 °C (Jouzel and Merlivat, 1984) by

$$T_{\mathrm{inv}} = 0.67 \times T_{\mathrm{s}} - 1.2, \quad (2)$$

where T_{s} is the mean near-surface atmospheric temperature either measured at 15 m deep in the firn or deduced from the average of the measured temperatures at 2 m height in weather station. This relation has been confirmed by Connolley (1996) and Ekaykin (2003) for the East Antarctic Plateau.

In Antarctica, past temperature changes are classically retrieved from water isotope records in ice cores (δD or δ^{18}O) assuming that the present-day temperature/isotope spatial slope can be taken as a surrogate for the temporal slope at a given site. Using alternative methods to constrain past temperature in polar regions such as combination of δ^{18}O and d-excess (Vimeux et al., 2002), use of the isotopic composition of inert gases combined with firnification models (Caillon et al., 2001) or borehole temperature inversion (Salamatin et al., 1998), it has been shown that errors associated with this conventional approach are estimated to be of −10 to +30 % over glacial–interglacial transitions (Jouzel et al., 2003). However, a recent modelling experiment has suggested that error on the temperature reconstruction can reach up to 100 % for warmer interglacial periods (Sime et al., 2009).

The classical method for temperature reconstruction applied to sites in East Antarctica like Vostok (Jouzel et al., 1987; Petit et al., 1999), Dome F (Watanabe et al., 2003) and EPICA Dome C (Jouzel et al., 2007) assumes that the temporal variations in δD, $\Delta\delta D$, are proportional to the temporal variations in surface temperature, ΔT_{surf}:

$$\Delta\delta D = 6.04 \times \Delta T_{\mathrm{surf}}. \quad (3)$$

Here the temperatures are expressed in degrees Celcius.

The saturation vapour pressure over ice is linked with temperature and can be approximated in the range −70 °C to 0 °C by the following equation (Wagner and Pruß, 2002):

$$P_{\mathrm{sat}}(T) = A \times 10^{\frac{mT}{T+T_n}}, \quad (4)$$

with $A = 6.114742$, $m = 9.778707$ and $T_n = 273.1466$.

From the numerical solution of Eqs. (1) to (4) over the range of temperature variations observed in East Antarctica ice cores, it appears that the accumulation rate is almost exponentially linked to temperature. Indeed, the Clausius–Clapeyron relation determines that the water-holding capacity of the atmosphere increases by about 7 % for every 1 °C rise in temperature. Keeping this idea of an exponential link, Parrenin et al. (2007a) and Bazin et al. (2013) have formulated the accumulation/isotope relation as

$$A = A_0 \exp(\beta \Delta\delta D), \quad (5)$$

where A_0 is an estimate of the present-day accumulation rate and β an adjustable parameter which is optimized during the chronology construction through chronological control points and an ice flow model (Parrenin et al., 2007b). While the accumulation rate reconstruction should be rather accurate for the upper part of the ice core, the uncertainties increase with depth because fewer chronological constraints are available and ice thinning becomes less predictable.

For the estimate of accumulation rate at Dome C with the EDC3 timescale, Parrenin et al. (2007a, b) used an inverse method in order to get the best fit with a series of age markers (listed in Table 3 of Parrenin et al., 2007a). They have inferred the value of β in Eq. (5) as being equal to 0.0157, a value about 50 % higher than the one (0.0102) corresponding to the saturation vapour assumption (e.g. as derived from Eq. (1) and compared to the EDC3 accumulation rate in Fig. 2a).

More recently, during the construction of the AICC2012 chronology, the imposed relationship between δD and accumulation rate was relaxed. The AICC2012 timescale (Bazin et al., 2013; Veres et al., 2013) was developed for obtaining a coherent chronology between one Greenland ice core (NorthGRIP) and four Antarctic ice cores (EDC, EDML, TALDICE, Vostok) through the intensive use of relative tie points in the ice and gas phases of the different ice cores. In the chronological optimization process of AICC2012 performed by the DATICE Bayesian dating tool (Lemieux-Dudon et al., 2010), the scenarios for both the accumulation rate and the thinning function for the different ice cores are allowed to vary freely, i.e. without an imposed relationship between accumulation rate and water isotopes as for the EDC3 chronology. Although the background scenario for EDC accumulation rate is the one given by Eq. (1), it is associated with a relatively large variance so that it can be easily modified during the chronology optimization process. At the end, the amplitude of glacial–interglacial variations in accumulation rate over Termination IV at Dome C is 5 % smaller in AICC2012 than in EDC3 (Fig. 2b).

2.2 ^{10}Be measurements

The first procedure for measuring ^{10}Be in ice cores was described by Raisbeck et al. (1981b). Since then, efficiency has been greatly improved, both due to improvement of chemical procedures of the samples and AMS (Accelerator Mass Spectrometry) techniques (Raisbeck et al., 1987, 2007; Yiou et al., 1997). The ice from the Dome C ice core available for this study is a continuous series of "bag samples" (each measuring 55 cm) between 2384 and 2627 m deep. Each bag sample was cut into five pieces of 11 cm (weighting ∼ 50 g) in order

to obtain a high-resolution ^{10}Be profile. This corresponds to around 2200 samples. The preparation of the samples was done at the Centre de Sciences Nucléaires et de Sciences de la Matière (CSNSM) in Orsay.

The current chemical procedure is described by Raisbeck et al. (2007). The samples were melted in a centrifuge cone, in the presence of 0.25 mg of ^{9}Be carrier. The $Be(OH)_2$ was then directly precipitated with ammonia (NH_4OH). The precipitate was extracted by centrifugation, then dissolved with 250 µL of nitric acid and 500 µL of highly pure water. The solution was transferred to a ceramic crucible to be dried on a hotplate and then heated to 900 °C for a period of 45 min over an electric furnace in order to transform the precipitate to BeO. The beryllium oxide was mixed with niobium (Nb) powder and pressed into a copper cathode. The ^{10}Be / ^{9}Be measurements were carried out at the ASTER (Accélérateur pour les Sciences de la Terre, Environnement, Risques) AMS facility at the Centre Européen de Recherche et d'Enseignement des Géosciences de l'Environnement (CEREGE) in Aix-en-Provence (Arnold et al., 2010), relative to NIST (National Institute of Standards and Technology) standard reference material SRM (Standard Reference Material) 4325, using the certified ratio of 2.68×10^{-11} ^{10}Be / ^{9}Be. We are aware that many people now use the value of 2.79×10^{-11} given by Nishiizumi et al. (2007) for this standard. We have continued to use the value of 2.68 because it was in excellent agreement with the original home-made standard of the Orsay group (Raisbeck et al., 1978), and has been used for all our previous measurements. If desired, a conversion can be easily made, and it will have no effect on relative values. The isobar ^{10}B is suppressed by use of an absorber foil in the rare isotope path (Klein et al., 2008). The counting statistics lead to an uncertainty of typically 4 % for 1σ standard deviation. The chemical blanks produced with our ^{9}Be carrier used for the ice samples yielded an average process background ^{10}Be / ^{9}Be of $(3.95 \pm 2.35) \times 10^{-15}$. In comparison, the ^{10}Be / ^{9}Be ratios measured for EDC samples were on the order of 3.2×10^{-13}.

2.3 Models

In this study, we also want to test our experimental results by comparing them with the latest climate simulations of the LGM and PI climates, obtained in the framework of the PMIP3 and CMIP5 projects (Braconnot et al., 2012). Both the PI and LGM climate simulations are equilibrium simulations, i.e. obtained by imposing non-evolving boundary conditions and forcings. Compared to the pre-industrial control simulations, LGM climate simulations are obtained by imposing the LGM ice sheet reconstructions (topography, albedo and land–sea mask differences due to sea-level lowering), the LGM atmospheric concentration of the main greenhouse gases as recorded by ice cores and orbital forcing parameters for 21 ka (following Berger, 1978). The experimental setup is described in detail on the PMIP3 website: http://pmip3.lsce.ipsl.fr/. The simulations used in this study are those which were available on the CMIP5 database as of October 2012.

In addition to the CMIP5-PMIP3 atmosphere–ocean coupled simulations we are using pre-industrial and LGM simulation results obtained from the AGCM (Atmospheric General Circulation Model) ECHAM5 (Roeckner et al., 2006) enhanced with stable water isotope diagnostics (Werner et al., 2011). For the LGM climate simulation, PMIP3-conform boundary conditions have been applied. Glacial sea surface temperatures and sea ice coverage have been derived from the GLAMAP Atlantic reconstruction data set (Schäfer-Neth and Paul, 2003). Both the PI and LGM simulation have been performed with a fine T106L31 spectral model resolution (horizontal grid box size of approx. $1.1° \times 1.1°$, 31 vertical levels).

All CMIP5-PMIP3 simulations are summarized in Table 1. From the different simulations we have used the following variables: *tas* (near surface air temperature) and *pr* (precipitation rate). As the sublimation rate was only available for 3 models out of 11 and as its values over the sites of interest were negligible compared to the precipitation rate in these models, we have not included the sublimation rate in the calculation of the accumulation rate changes from LGM to PI. We observe that *tas* is systematically higher than the measured mean atmospheric temperature, which is a typical bias of CMIP5-PMIP3 simulations in polar regions (see Risi et al., 2010). To evaluate the consequences of this bias, we have extracted the modelled inversion temperatures available in the IPSL-CM5A-LR model. These data show that, in the models, the slope of the relationship between *tas* and the modelled inversion temperature is 15 % higher than the one given by Jouzel and Merlivat (1984) (cf. Eq. 2). However, when we use the modelled surface temperature T_{sm} (which is on average 4 °C lower than the simulated *tas* values), we obtain a slope between T_{inv} and T_{sm} very close to the observed value of 0.67 (see Eq. 2). As a consequence, and to artificially compensate for the cold bias of the CMIP5-PMIP3 simulations, we have extracted both *tas* and T_{sm} for the following calculations.

For all the models, the values of the LGM–PI change in near-surface air temperature and precipitation rate are obtained by averaging the values of temperature and precipitation on a box of latitudes 77.6 to 72.6° S and longitudes 120.85 to 125.85° E.

3 From ^{10}Be concentrations to accumulation rate reconstruction

Figure 1a shows the high-resolution profile of ^{10}Be concentrations (available as a supplement). The time resolution for the shown period varies between 20 years for MIS 9.3 and 70 years for MIS 10, the glacial period prior to 340 ka (Fig. 1f). In this study, we will mainly focus on the transition between

the coldest part of the MIS 10 reached just before Termination IV and MIS 9.3. The MIS 10 glacial maximum between 341.77 and 348.41 ka (light-blue area in Fig. 1b) is at the same water isotopic level as the LGM (Jouzel et al., 2007). Then, MIS 9.3 can be decomposed in two phases: (1) a period with a higher isotopic level than PI with an optimum between 332.55 and 334.53 ka (light-red area in Fig. 1b) and (2) a plateau between 325.92 and 330.92 ka at the same isotopic level than PI (light-yellow area in Fig. 1b).

We observe a strong anti-correlation between ^{10}Be concentration (Fig. 1a) and δD or δD-derived accumulation rate (Fig. 1b). This is not unexpected since ^{10}Be reaches the Antarctic Plateau primarily by dry deposition, and so the concentration of ^{10}Be in the ice is reduced for high-accumulation periods. It has thus been proposed that ^{10}Be flux is a more appropriate parameter than concentration for estimating variations in ^{10}Be production (Yiou et al., 1985). This is illustrated in Fig. 1c, showing the ^{10}Be flux $F[^{10}\mathrm{Be}]$ as obtained by multiplying the ^{10}Be concentration $C[^{10}\mathrm{Be}]$ by the accumulation rate A from the EDC3 timescale (Parrenin et al., 2007a, b) and the density of ice ρ as

$$F[^{10}\mathrm{Be}] = C[^{10}\mathrm{Be}] \times A \times \rho. \quad (6)$$

Other potential contributions to ^{10}Be concentration variations are linked to (1) variations in the geomagnetic field intensity over centennial to millennial scales or (2) variations in the solar activity on decadal to centennial timescales. For the influence of the relative changes of geomagnetic field, we can make corrections by using independent estimates of the field intensity obtained by a stacked record of marine sediments (Channell et al., 2009). We assume that our ^{10}Be flux record reflects the globally averaged ^{10}Be production. We have also carried out the calculations using the "polar bias" assumption (polar ^{10}Be flux 20 % less sensitive to geomagnetic field intensity changes (Field et al., 2006), i.e. we multiply the relative variations in the ^{10}Be production according to PISO-1500 by 0.8), with a negligible difference in the resulting accumulation reconstructions. After synchronizing the timescale of the marine record with that of EDC (Cauquoin, 2013), we apply the theoretical estimate of Masarik and Beer (2009) on the relationship between ^{10}Be production and geomagnetic intensity, as shown in Fig. 1d. Then, we divide the ^{10}Be flux at EDC by the relative changes of global ^{10}Be production according to PISO-1500. The main effect of this correction is to remove the long-term decrease in the uncorrected ^{10}Be flux from 270 to 350 ka (Fig. 1e). We have also looked at the theoretical estimate of Kovaltsov and Usoskin (2010) on the relationship between ^{10}Be production and geomagnetic field intensity, with very similar results.

Since we have no independent estimate of the solar variability during the time period being studied, we must assume that the average value of solar activity has been constant during this time. In reality, part of the remaining centennial structure in the ^{10}Be flux of Fig. 1e may be due to variations in solar activity or to centennial geomagnetic variations not recorded by the marine cores. We now use the geomagnetically corrected ^{10}Be flux curve of Fig. 1e to estimate the ice accumulation rate of EDC during our time period using Eq. (6). This procedure assumes that the spatial distribution of geomagnetically corrected ^{10}Be deposition remains constant with time independent of climate and type of deposition. While it is difficult to give a quantitative uncertainty of our constant flux assumption, we can note that the 1σ standard deviation of the smooth corrected flux in Fig. 1e is 8.8 %. Since this is significantly larger than the analytical uncertainty, it essentially must represent the sum of inadequately corrected production variations plus variability in the ^{10}Be deposition. It thus does not seem unreasonable to conclude that this represents an upper limit to the deposition variability.

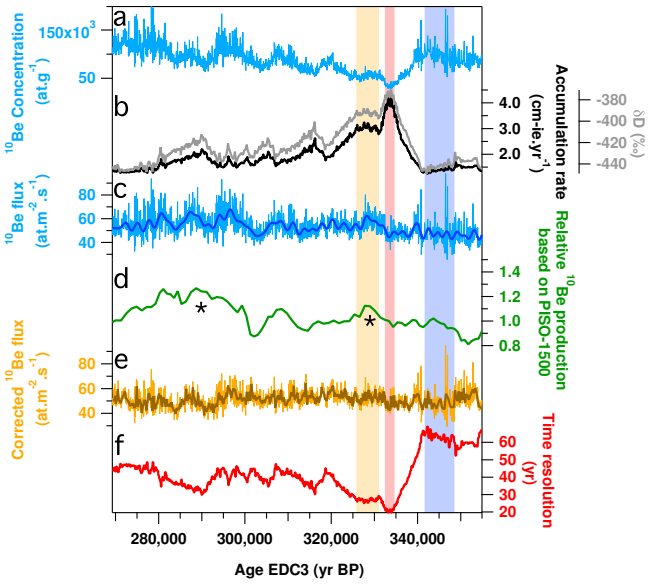

Figure 1. High-resolution ^{10}Be data between 2384 and 2627 m deep (269–355 ka on the EDC3 age scale). **(a)** Raw ^{10}Be concentrations (at g^{-1}). **(b)** In grey, δD profile at EDC including the interglacial period MIS 9.3 (Jouzel et al., 2007). In black, the accumulation rate of the site (cm ie yr^{-1}) (Parrenin et al., 2007b). The light-yellow and light-red areas show the plateau during MIS 9.3 at the same isotopic level than PI and the MIS 9.3 optimum warmer than PI. The light-blue area corresponds to the MIS 10 glacial maximum just before the Termination IV. **(c)** Calculated ^{10}Be flux using EDC3 accumulation rate. The light-blue curve corresponds to raw data, and the bold-blue curve is the low-pass-filtered ^{10}Be flux (1/2000 yr^{-1}). **(d)** ^{10}Be production based on palaeointensity record PISO-1500 (Channell et al., 2009) on the EDC3 age scale and calculated using calculations of Masarik and Beer (2009). The asterisks show the possible correlation with proposed geomagnetic events: the Portuguese Margin ($\sim$ 290 ka) and Calabrian Ridge 1 ($\sim$ 320 ka). **(e)** Raw and 100-year resampled ^{10}Be flux corrected by PISO-1500. **(f)** Time resolution of the ^{10}Be profile (difference between the n and $n+1$ sample ages).

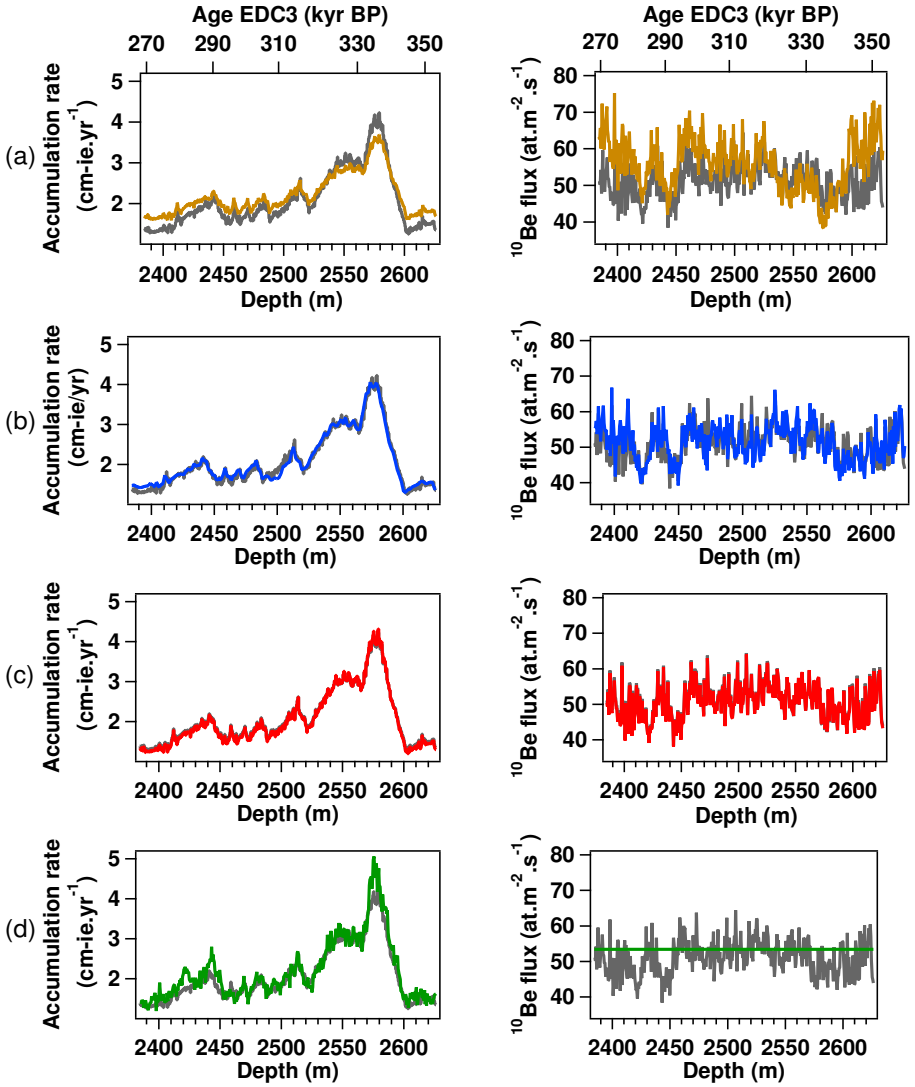

Figure 2. Several accumulation rate reconstructions (left column) and the corresponding ^{10}Be flux corrected by PISO-1500 (right column) discussed in Sect. 3 (coloured curves). The EDC3 reconstruction from Parrenin et al. (2007a, b) is shown in grey for comparison. **(a)** Saturation vapour pressure formulation. **(b)** Application of the AICC2012 chronology on the ^{10}Be record. **(c)** Optimization of the interglacial–glacial amplitude coefficient (β) by minimization of the variance of the ^{10}Be flux corrected for past variations in geomagnetic field intensity (red curves). **(d)** Accumulation rate assuming a constant ^{10}Be flux (fixed at 53.44 at m^{-2} s^{-1} over the whole period).

In a first attempt to use ^{10}Be for such a reconstruction, we have chosen to keep the exponential link between accumulation and δD. Starting from the formulation proposed by Parrenin et al. (2007a), we have tried to adjust β in order to minimize the variance of the ^{10}Be flux signal while keeping consistency with the timescale of EDC3 (Fig. 2c). For this minimization, we have first applied a 100-year resampling to the ^{10}Be record. Using Eqs. (5) and (6), with $A_0 = 2.841$ cm, i.e. yr^{-1}, we have calculated the variance of the ^{10}Be flux (previously corrected for geomagnetic field intensity changes) using different values of β. The variance of the ^{10}Be flux is minimized for a β of 0.0165 (the variance varies by less than 1 % for values of β between 0.0160 and 0.0171). This value is 5 % larger than used by Parrenin et al. (2007a), and corresponds to a larger glacial–interglacial amplitude by the same amount. We also notice a general decrease in the variance by a factor 0.99 which supports this revision of accumulation rate estimate from δD over this glacial–interglacial cycle.

In a second attempt, we have performed a test with the assumption of a strictly constant ^{10}Be flux, after a geomagnetic field intensity correction on the ^{10}Be concentration in the ice. We have deduced the resulting accumulation by dividing the ^{10}Be flux $F[^{10}\mathrm{Be}]$ (53.44 at m^{-2} s^{-1} here) by the ^{10}Be concentration (corrected for radioactive decay and geomagnetic modulation) $C[^{10}\mathrm{Be}]$ times the ice density ρ according to Eq. 6. The inferred accumulation is reported

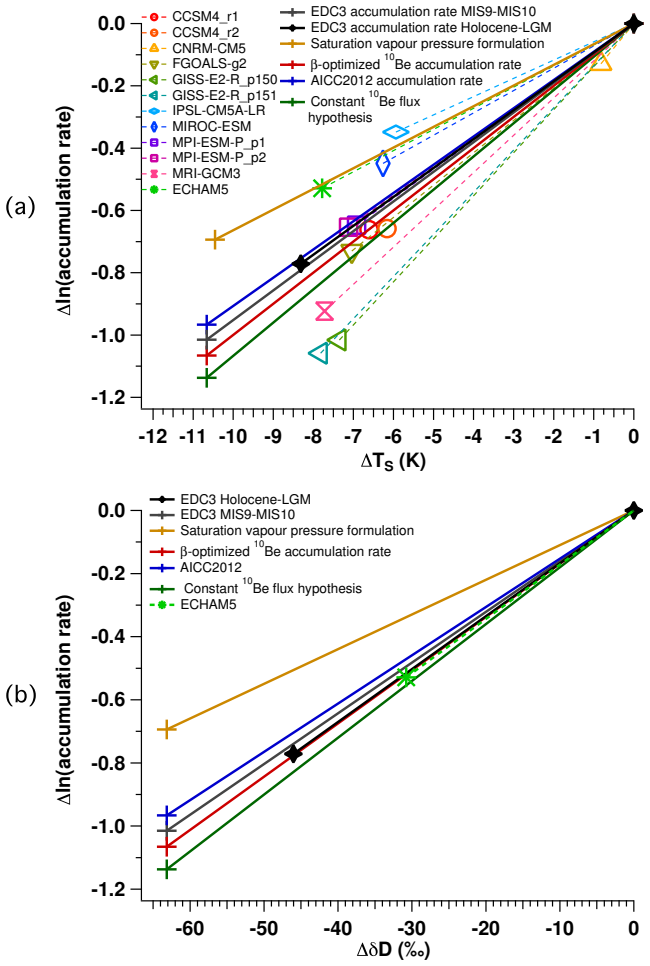

Figure 3. **(a)** Accumulation rate vs. temperature change between the LGM and PI for 12 different simulations and comparison with the relationships from EDC3 (last deglaciation and MIS 9.3) and our reconstructions (average during the glacial and the interglacial period). **(b)** Accumulation rate vs. δD change for both ice core data and ECHAM5 simulation results.

in Fig. 2d. The general shape of the accumulation rate reconstruction follows the evolution of the EDC3 accumulation rate. However, while there is no significant difference in the accumulation reconstruction between the MIS 10 glacial maximum and the plateau of the MIS 9.3 (increase of 1.548 for the ^{10}Be-based accumulation rate reconstruction and of 1.624 cm ie yr^{-1} for EDC3), there is a clear difference for accumulation rate increase between the plateau and the MIS 9.3 optimum (1.364 cm ie yr^{-1} for the ^{10}Be-based reconstruction against 0.920 cm ie yr^{-1} for EDC3). The ^{10}Be-based accumulation rate for the latter is up to 13 % larger than the EDC3 reconstruction (4.46 cm ie yr^{-1} instead of 3.95).

Even if the assumption of a strictly constant ^{10}Be flux is not realistic, we have tested whether the inferred accumulation rate is consistent with chronological constraints (Table 2). For this aim, we have imposed this accumulation rate as a background accumulation rate scenario for EDC in the DATICE tool for chronology optimization with a very small associated variance. The other background scenarios for the four other ice cores (NorthGRIP, EDML, Taldice, Vostok) are kept identical as those of AICC2012 (Bazin et al., 2013; Veres et al., 2013). In this DATICE experiment, we still use the same five ice cores as in AICC2012 for facilitating the comparison with previous chronological studies but for our period of interest, only Vostok goes back until MIS 9/10 and can influence the chronology of EDC. With such a background accumulation rate for EDC, the minimization of DATICE is easily reached with very small modifications of the thinning function, well within the imposed variance, compared to the AICC2012 chronology. We find the same trends on the resulting accumulation rate as for the ^{10}Be-based one.

We conclude that both methods show an underestimation of accumulation deduced from water isotopes for the optimum of MIS 9.3. This is in agreement with the study of Parrenin et al. (2007a), which suggested that the deuterium-based reconstruction underestimates accumulation for the optimum of the Holocene. However the existence of a strong link between past changes in accumulation and temperature is confirmed to first order by our ^{10}Be approach and we next examine how palaeoclimate simulations performed with different GCMs might reveal further insight on this link between accumulation and temperature.

4 Accumulation vs. temperature/δD relationship in East Antarctica

We compare the outputs from the models described in Sect. 2.3, with the accumulation rate reconstruction presented in the previous section.

Figure 3a shows a compilation of accumulation rate and temperature change for the 11 different simulations included in the CMIP5-PMIP3 coupled models plus ECHAM5, between the LGM and the PI. We have chosen to focus only on the relationship between the change in accumulation rate and the change in temperature between the LGM and PI. Indeed, we can hardly discuss absolute levels of temperature and accumulation rate for two reasons. First, the CMIP5-PMIP3 models are known to overestimate temperature on the East Antarctic Plateau. Second, our ^{10}Be data do not cover the last deglaciation as the model simulations do but instead the transition occurring between MIS 10 and the optimum of MIS 9.3, which has larger associated temperature and accumulation rate increases than the last deglaciation (Fig. 3a). Still, the accumulation rate vs. temperature slope reconstructed from water isotopes in the ice core (Eqs. 5 and

Table 1. List of all simulations used in this study (see Fig. 3). The ensemble member (r ⟨*N*⟩ i ⟨*M*⟩ p ⟨*L*⟩) formatted as shown below (e.g. "r3i1p21" with r for "realization", i for "initialization method indicator" and p for "perturbed physics") distinguishes among closely related simulations by a single model (Taylor et al., 2012). The reference given in brackets next to the ensemble number in columns 4 and 5 is the name of the simulation used in Fig. 3.

			CMIP5 experiment Model *ensemble member* used (r⟨*N*⟩i⟨*M*⟩p⟨*L*⟩)	
Institute	Model	Model institution	0k piControl	21k lgm
CNRM-CERFACS	CNRM-CM5	Centre National de Recherches Météorologiques/Centre Européen de Recherche et Formation Avancée en Calcul Scientifique, France	r1i1p1 (CNRM-CM5)	r1i1p1 (CNRM-CM5)
NASA-GISS	GISS-E2-R	NASA Goddard Institute for Space Studies, USA	r1i1p142 (GISS-E2-R_p150) r1i1p142 (GISS-E2-R_p151)	r1i1p150 (GISS-E2-R_p150) r1i1p151 (GISS-E2-R_p151)
IPSL	IPSL-CM5A-LR	Institut Pierre-Simon Laplace, France	r1i1p1 (IPSL-CM5A-LR)	r1i1p1 (IPSL-CM5A-LR)
LASC-CESS	FGOALS-g2	LASG, Institute of Atmospheric Physics, Chinese Academy of Sciences and CESS, Tsinghua University, China	r1i1p1 (FGOALS-g2)	r1i1p1 (FGOALS-g2)
MIROC	MIROC-ESM	Japan Agency for Marine-Earth Science and Technology, Atmosphere and Ocean Research Institute (the University of Tokyo), and National Institute for Environmental Studies, Japan	r1i1p1 (MIROC-ESM)	r1i1p1 (MIROC-ESM)
MPI-M	MPI-ESM-P	Max Planck Institute for Meteorology, Hamburg, Germany	r1i1p1 (MPI-ESM-P_p1) r1i1p1 (MPI-ESM-P_p2)	r1i1p1 (MPI-ESM-P_p1) r1i1p2 (MPI-ESM-P_p1)
MRI	MRI-CGCM3	Meteorological Research Institute, Tsukuba, Japan	r1i1p1 (MRI-CGCM3)	r1i1p1 (MRI-CGCM3)
NCAR	CCSM4	National Center for Atmospheric Research/Dept. of Energy/NSF, USA	r1i1p1 (CCSM4_r1) r2i1p1 (CCSM4_r2)	r1i1p1 (CCSM4_r1) r2i1p1 (CCSM4_2)

3, respectively) is almost the same for the transition between MIS 10 and MIS 9 and the last deglaciation as shown in Fig. 3a. We have also checked that the model results shown in Fig. 3a do not change if we replace the ΔT_s calculation based on the near-surface air temperature (tas) with one based on surface temperature (T_{sm}). Finally, using the IPSL-CM5A-LR model, we have tested the influence of the topography changes on the temperature vs. accumulation rate slope by keeping an identical Antarctic ice cap for the LGM and PI conditions and verifying that the relationship remains the same.

We observe a relatively good agreement between the slope of accumulation vs. temperature over a glacial–interglacial transition of several models (MPI-ESM-P, CCSM4, FGOALS-g2), with an average slope of 0.23 cm ie yr^{-1} °C^{-1} (bold black line in Fig. 3a). Other models are clearly outside the range of the reconstructed accumulation–temperature relationship, either because they overestimate (MRI-GCM3, GISS-E2-R) or underestimate it (IPSL-CM5-LR, MIROC-ESM) or because they simulate very weak changes (CNRM-CM5). Indeed, one can notice a large spread between the different model outputs. The difference in the accumulation rate vs. temperature relationship between different GCM simulations is much larger (100 %) than for the different reconstructions based on ^{10}Be flux and/or chronological constraints. The slope based on the relationship between accumulation rate and saturation pressure over ice is 28 % lower (brown line in Fig. 3a). We conclude that generally the CMIP5-PMIP3 models have more or less difficulties to accurately simulate the temperature–accumulation relationship on the Antarctic Plateau between glacial and interglacial conditions and need to be improved in the future.

To avoid any assumption on the relationship between water isotopes and temperature, we have directly compared the accumulation rate with water isotope variations for both ice core data and model outputs (Fig. 3b). In our study, only one model (ECHAM5) is equipped with water isotopes diagnostics. As it was also observed for the temperature change, the δD increase during the deglaciation is smaller in the ECHAM5 simulations than in ice core records. However the slope of accumulation rate vs. δD given by ECHAM5 compares very well with our different accumulation rate vs. δD slope inferred from both water isotopes and ^{10}Be. Only the slope deduced from the saturation vapour pressure formulation is lower by $\sim$ 30 % compared to EDC3. We observe, however, that the slope of accumulation rate vs. temperature changes of ECHAM5 is smaller than the one reconstructed from water isotopes or ^{10}Be in ice core, and so the modelled Antarctic δD–temperature gradient in ECHAM5 for LGM–PI climate changes at EDC is much lower than the local

Table 2. List of markers used to constrain EDC and Vostok ice cores between 269 and 355 ka for the AICC2012 chronology. References ("Ref."): (1) Suwa and Bender (2008), (2) Lipenkov et al. (2011), (3) Raynaud et al. (2007) and (4) Bazin et al. (2013).

Vostok age markers	Depth	Age	Uncertainty	Type of marker	Ref.
Ice age markers	2882.1	275 200	4000	$\delta O_2/N_2$	1
	2883.02	275 950	6343	air content	2
	2912.1	286 300	4000	$\delta O_2/N_2$	1
	2962.7	296 800	4000	$\delta O_2/N_2$	1
	3005.6	307 700	4000	$\delta O_2/N_2$	1
	3011	307 950	6424	air content	2
	3040.7	319 200	4000	$\delta O_2/N_2$	1
	3043.04	318 950	6308	air content	2
	3080.5	330 000	4000	$\delta O_2/N_2$	1
	3130.6	339 700	4000	$\delta O_2/N_2$	1
	3145.95	346 950	6527	air content	2
	3157.1	349 200	4000	$\delta O_2/N_2$	1
Gas age markers	2887	272 900	6000	$\delta^{18}O_{atm}$	1
	2947.6	285 900	6000	$\delta^{18}O_{atm}$	1
	2990.3	297 500	6000	$\delta^{18}O_{atm}$	1
	3026.9	308 300	6000	$\delta^{18}O_{atm}$	1
	3062.5	318 300	6000	$\delta^{18}O_{atm}$	1
	3101.4	329 000	6000	$\delta^{18}O_{atm}$	1
	3146.2	340 300	6000	$\delta^{18}O_{atm}$	1
	3173.8	351 000	6000	$\delta^{18}O_{atm}$	1
EDC age markers					
Ice age markers	2500.25	306 950	6652	air content	3
	2510.75	318 950	6242	air content	3
	2610.8	346 950	7120	air content	3
Stratigraphic links between EDC and Vostok					
	Depth EDC	Depth Vostok	Uncertainty	Type of marker	Ref.
	2419.34	2911.06	1500	CH_4	4
	2451.33	2954.61	1500	CH_4	4
	2501.4	3018.01	1500	CH_4	4
	2521.2	3051.5	1500	CH_4	4
	2544.83	3079.41	1500	CH_4	4
	2583.9	3123.5	1500	CH_4	4
	2613	3162.8	1500	CH_4	4

geographical gradient as already shown in previous studies (Schmidt et al., 2007; Lee et al., 2008; Sime et al., 2008, 2009). This could imply a problem in the estimation of the surface temperature with measured δD or even indicate that the δD–temperature slope is under-evaluated in the model compared to the hypothesis of the spatial relationship between precipitation isotopic composition and local temperature (Lorius et al., 1969). But given the uncertainties and the lack of models equipped with water isotope diagnostics, it is difficult to conclude on this point. Finally, this implies that the models matching the accumulation vs. temperature relationship of EDC3 for the last glacial–interglacial change would not necessarily accurately reproduce the associated accumulation rate vs. δD slope.

Finally, an important result highlighted in our study is a possible underestimation of accumulation rate during periods warmer than today, as already suggested by Parrenin et al. (2007a) for the optimum of the Holocene. This cannot be tested with the compilation of model outputs displayed here that were only run on colder conditions than the pre-industrial period. Using the relationship between accumulation rate and surface temperature from the saturation vapour formulation, the ^{10}Be-based accumulation rate reconstruction suggests that the temperature increase between the plateau and the MIS 9.3 optimum is underestimated by 2.4 K

with respect to water isotopes reconstruction (5.7 vs. 3.2 K). This is in line with the 3 K underestimation for the peak of the last Antarctic interglacial temperature from the relationship between temperature and surface snow isotopic composition as shown in Sime et al. (2009), suggesting an underestimation of about a factor of 2 for warm interglacials compared to a level similar to present day. Instead, the temporal slope is less affected, for example, by about 30% when comparing the plateau (similar to present day) to MIS 10 glacial maximum (similar to the LGM). Indeed, using the ^{10}Be-based accumulation rate reconstruction and the saturation vapour relationship between accumulation rate and surface temperature leads to an underestimation of the temperature difference between the MIS 10 glacial maximum and the plateau by the water isotopes reconstruction by 25 % only (10.2 vs. 8.2 K). This value is, however, in the upper range of the interval −10 to +30 % estimated from different approaches by Jouzel et al. (2003). We should keep in mind that these estimates rely on a close relationship between the derivative of the saturation vapour pressure and accumulation change, which is subject to large uncertainties.

5 Conclusions

We have produced the first record of ^{10}Be concentration at high resolution in an ice core over a whole climatic cycle (355 to 269 ka), including a period warmer than pre-industrial. After correction for geomagnetic intensity changes, it is generally assumed that the variations in ^{10}Be concentration are mainly linked to variations in the accumulation rate of snow. We have used this property to reconstruct the past accumulation rate at EDC and to compare it with the deuterium-based accumulation rate reconstruction. We have deduced that the ^{10}Be reconstruction is in reasonably good agreement with EDC3 values for the full cycle except the period warmer than present. For the latter, the accumulation is up to 13 % larger (4.46 cm ie yr^{-1} instead of 3.95). This is in agreement with the study of Parrenin et al. (2007a), who suggested that accumulation rate reconstruction from water isotopes underestimates accumulation for the optimum of the Holocene. Using the relationship between accumulation rate and surface temperature from the saturation vapour formulation, the ^{10}Be-based accumulation rate reconstruction suggests that the temperature increase between the MIS 9.3 optimum and present day may be underestimated by 2.4 K with respect to the water isotopes reconstruction. Finally, the relationship between temperature and accumulation rate is comparable when using the different reconstructions and 4 out of 12 (3 out of 7 models) CMIP5-PMIP3 simulations for LGM–PI climate changes. However, we have noticed a large spread in the model outputs. We conclude that the CMIP5-PMIP3 models can encounter some difficulties in simulating precipitation changes linked with temperature or water isotope content on the Antarctic Plateau during large climatic shifts and need to be improved in the future.

The Supplement related to this article is available online at doi:10.5194/cp-11-355-2015-supplement.

Acknowledgements. We acknowledge F. Parrenin, L. Sime and one anonymous referee for their useful comments, which helped to improve this manuscript. This work is a contribution to the European Project for Ice Coring in Antarctica (EPICA), a joint European Science Foundation/European Commission (EC) scientific programme, funded by the EC and by national contributions from Belgium, Denmark, France, Germany, Italy, the Netherlands, Norway, Sweden, Switzerland and the UK. The main logistic support was provided by IPEV and PNRA. We acknowledge the World Climate Research Programme's Working Group on Coupled Modelling, which is responsible for CMIP and the Paleoclimate Modelling Intercomparison Project (PMIP). We thank the climate modelling groups (listed in Table 1 of this paper) for producing and making available their model output. For CMIP, the US Department of Energy's Program for Climate Model Diagnosis and Intercomparison provides coordinating support and led development of software infrastructure in partnership with the Global Organization for Earth System Science Portals. This work was funded by the French ANR project Dome A and through ERC grant COMBINISO (project no. 306045). The ASTER AMS national facility (CEREGE, Aix en Provence) is supported by the INSU/CNRS, and the ANR through the "Projets thématiques d'excellence" programme for the "Equipements d'Excellence" ASTER-CEREGE action, IRD, and CEA.

Edited by: E. Wolff

References

Arnold, M., Merchel, S., Bourlès, D. L., Braucher, R., Benedetti, L., Finkel, R. C., Aumaître, G., Gottdang, A., and Klein, M.: The French accelerator mass spectrometry facility ASTER: improved performance and developments, Nucl. Instrum. Meth. B, 268, 1954–1959, doi:10.1016/j.nimb.2010.02.107, 2010.

Bazin, L., Landais, A., Lemieux-Dudon, B., Toyé Mahamadou Kele, H., Veres, D., Parrenin, F., Martinerie, P., Ritz, C., Capron, E., Lipenkov, V., Loutre, M.-F., Raynaud, D., Vinther, B., Svensson, A., Rasmussen, S. O., Severi, M., Blunier, T., Leuenberger, M., Fischer, H., Masson-Delmotte, V., Chappellaz, J., and Wolff, E.: An optimized multi-proxy, multi-site Antarctic ice and gas orbital chronology (AICC2012): 120–800 ka, Clim. Past, 9, 1715–1731, doi:10.5194/cp-9-1715-2013, 2013.

Berger, A. L.: Long-term variations of daily insolation and quaternary climatic changes, J. Atmos. Sci., 35, 2362–2367, doi:10.1175/1520-0469(1978)035<2362:LTVODI>2.0.CO;2, 1978.

Blunier, T., Spahni, R., Barnola, J.-M., Chappellaz, J., Loulergue, L., and Schwander, J.: Synchronization of ice core records via atmospheric gases, Clim. Past, 3, 325–330, doi:10.5194/cp-3-325-2007, 2007.

Braconnot, P., Harrison, S. P., Kageyama, M., Bartlein, P. J., Masson-Delmotte, V., Abe-Ouchi, A., Otto-Bliesner, B., and Zhao, Y.: Evaluation of climate models using palaeoclimatic data, Nature Climate Change, 2, 417–424, doi:10.1038/nclimate1456, 2012.

Caillon, N., Severinghaus, J. P., Barnola, J.-M., Chappellaz, J., Jouzel, J., and Parrenin, F.: Estimation of temperature change and of gas age-ice age difference, 108 kyr B. P., at Vostok, Antarctica, J. Geophys. Res., 106, 31893, doi:10.1029/2001JD900145, 2001.

Cauquoin, A.: Flux de ^{10}Be en Antarctique durant les 800 000 dernières années et interprétation, Ph.D. thesis, Université Paris-Sud 11, 2013.

Channell, J. E. T., Xuan, C., and Hodell, D. A.: Stacking paleointensity and oxygen isotope data for the last 1.5 Myr (PISO-1500), Earth Planet. Sc. Lett., 283, 14–23, doi:10.1016/j.epsl.2009.03.012, 2009.

Connolley, W. M.: The Antarctic temperature inversion, Int. J. Climatol., 16, 1333–1342, doi:10.1002/(SICI)1097-0088(199612)16:12<1333::AID-JOC96>3.3.CO;2-Y, 1996.

Ekaykin, A.: Meteorological regime of central Antarctica and its role in the formation of isotope composition of snow thickness, Ph.D. thesis, Université Joseph Fourier – Grenoble I, 2003.

EPICA Community Members: Eight glacial cycles from an Antarctic ice core, Nature, 429, 623–628, doi:10.1038/nature02599, 2004.

Field, C. V., Schmidt, G. A., Koch, D., and Salyk, C.: Modeling production and climate-related impacts on ^{10}Be concentration in ice cores, J. Geophys. Res., 111, D15107, doi:10.1029/2005JD006410, 2006.

Guillevic, M., Bazin, L., Landais, A., Kindler, P., Orsi, A., Masson-Delmotte, V., Blunier, T., Buchardt, S. L., Capron, E., Leuenberger, M., Martinerie, P., Prié, F., and Vinther, B. M.: Spatial gradients of temperature, accumulation and δ^{18}O-ice in Greenland over a series of Dansgaard–Oeschger events, Clim. Past, 9, 1029–1051, doi:10.5194/cp-9-1029-2013, 2013.

Jouzel, J. and Merlivat, L.: Deuterium and oxygen 18 in precipitation: modeling of the isotopic effects during snow formation, J. Geophys. Res., 89, 11749, doi:10.1029/JD089iD07p11749, 1984.

Jouzel, J., Genthon, C., Lorius, C., Petit, J. R., and Barkov, N. I.: Vostok ice core – a continuous isotope temperature record over the last climatic cycle (160 000 years), Nature, 329, 403–408, doi:10.1038/329403a0, 1987.

Jouzel, J., Raisbeck, G., Benoist, J. P., Yiou, F., Lorius, C., Raynaud, D., Petit, J. R., Barkov, N. I., Korotkevitch, Y. S., and Kotlyakov, V. M.: A comparison of deep Antarctic ice cores and their implications for climate between 65 000 and 15 000 years ago, Quaternary Res., 31, 135–150, doi:10.1016/0033-5894(89)90003-3, 1989.

Jouzel, J., Vimeux, F., Caillon, N., Delaygue, G., Hoffmann, G., Masson-Delmotte, V., and Parrenin, F.: Magnitude of isotope/temperature scaling for interpretation of central Antarctic ice cores, J. Geophys. Res., 108, 4361, doi:10.1029/2002JD002677, 2003.

Jouzel, J., Masson-Delmotte, V., Cattani, O., Dreyfus, G., Falourd, S., Hoffmann, G., Minster, B., Nouet, J., Barnola, J.-M., Blunier, T., Chappellaz, J., Fischer, H., Gallet, J. C., Johnsen, S., Leuenberger, M., Loulergue, L., Luethi, D., Oerter, H., Parrenin, F., Raisbeck, G., Raynaud, D., Schilt, A., Schwander, J., Delmo, E., Souchez, R., Spahni, R., Stauffer, B., Steffensen, J. P., Stenni, B., Stocker, T. F., Tison, J. L., Werner, M., and Wolff, E.: Orbital and millennial Antarctic climate variability over the past 800 000 years, Science, 317, 793–796, doi:10.1126/science.1141038, 2007.

Klein, M. G., Gottdang, A., Mous, D. J. W., Bourlès, D. L., Arnold, M., Hamelin, B., Aumaitre, G., Braucher, R., Merchel, S., and Chauvet, F.: Performance of the HVE 5 MV AMS system at CEREGE using an absorber foil for isobar suppression, Nucl. Instrum. Meth. B, 266, 1828–1832, doi:10.1016/j.nimb.2007.11.077, 2008.

Kovaltsov, G. A. and Usoskin, I. G.: A new 3D numerical model of cosmogenic nuclide ^{10}Be production in the atmosphere, Earth Planet. Sc. Lett., 291, 182–188, doi:10.1016/j.epsl.2010.01.011, 2010.

Lal, D. and Peters, B.: Cosmic ray produced radioactivity on the Earth, in: Kosmische Strahlung II/Cosmic Rays II, edited by: Sittle, K., vol. 46/2 of Handbuch der Physik, Springer-Verlag, Berlin, doi:10.1007/978-3-642-46079-1_7, 551–612, 1967.

Langereis, C. G., Dekkers, M. J., Lange, G. J., Paterne, M., and Santvoort, P. J. M.: Magnetostratigraphy and astronomical calibration of the last 1.1 Myr from an eastern Mediterranean piston core and dating of short events in the Brunhes, Geophys. J. Int., 129, 75–94, doi:10.1111/j.1365-246X.1997.tb00938.x, 1997.

Lee, J.-E., Fung, I., DePaolo, D. J., and Otto-Bliesner, B.: Water isotopes during the Last Glacial Maximum: New general circulation model calculations, J. Geophys. Res., 113, D19109, doi:10.1029/2008JD009859, 2008.

Lemieux-Dudon, B., Blayo, E., Petit, J.-R., Waelbroeck, C., Svensson, A., Ritz, C., Barnola, J.-M., Narcisi, B. M., and Parrenin, F.: Consistent dating for Antarctic and Greenland ice cores, Quaternary Sci. Rev., 29, 8–20, doi:10.1016/j.quascirev.2009.11.010, 2010.

Lipenkov, V. Y., Raynaud, D., Loutre, M. F., and Duval, P.: On the potential of coupling air content and O_2/N_2 from trapped air for establishing an ice core chronology tuned on local insolation, Quaternary Sci. Rev., 30, 3280–3289, doi:10.1016/j.quascirev.2011.07.013, 2011.

Lorius, C., Merlivat, L., and Hagemann, R.: Variation in the mean deuterium content of precipitations in Antarctica, J. Geophys. Res., 74, 7027–7031, doi:10.1029/JC074i028p07027, 1969.

Lorius, C., Ritz, C., Jouzel, J., Merlivat, L., and Barkov, N. I.: A 150 000-year climatic record from Antarctic ice, Nature, 316, 591–596, doi:10.1038/316591a0, 1985.

Masarik, J. and Beer, J.: An updated simulation of particle fluxes and cosmogenic nuclide production in the Earth's atmosphere, J. Geophys. Res., 114, D11103, doi:10.1029/2008JD010557, 2009.

NEEM Community Members: Eemian interglacial reconstructed from a Greenland folded ice core, Nature, 493, 489–494, doi:10.1038/nature11789, 2013.

Nishiizumi, K., Imamura, M., Caffee, M. W., Southon, J. R., Finkel, R. C., and McAninch, J.: Absolute calibration of ^{10}Be AMS standards, Nucl. Instrum. Meth. B, 258, 403–413, doi:10.1016/j.nimb.2007.01.297, 2007.

North Greenland Ice Core Project Members: High-resolution record of Northern Hemisphere climate extending into the last interglacial period, Nature, 431, 147–151, doi:10.1038/nature02805, 2004.

Parrenin, F., Dreyfus, G., Durand, G., Fujita, S., Gagliardini, O., Gillet, F., Jouzel, J., Kawamura, K., Lhomme, N., Masson-Delmotte, V., Ritz, C., Schwander, J., Shoji, H., Uemura, R., Watanabe, O., and Yoshida, N.: 1-D-ice flow modelling at EPICA Dome C and Dome Fuji, East Antarctica, Clim. Past, 3, 243–259, doi:10.5194/cp-3-243-2007, 2007a.

Parrenin, F., Barnola, J.-M., Beer, J., Blunier, T., Castellano, E., Chappellaz, J., Dreyfus, G., Fischer, H., Fujita, S., Jouzel, J., Kawamura, K., Lemieux-Dudon, B., Loulergue, L., Masson-Delmotte, V., Narcisi, B., Petit, J.-R., Raisbeck, G., Raynaud, D., Ruth, U., Schwander, J., Severi, M., Spahni, R., Steffensen, J. P., Svensson, A., Udisti, R., Waelbroeck, C., and Wolff, E.: The EDC3 chronology for the EPICA Dome C ice core, Clim. Past, 3, 485–497, doi:10.5194/cp-3-485-2007, 2007b.

Petit, J. R., Jouzel, J., Raynaud, D., Barkov, N. I., Barnola, J.-M., Basile, I., Bender, M., Chappellaz, J., Davis, M., Delaygue, G., Delmotte, M., Kotlyakov, V. M., Legrand, M., Lipenkov, V. Y., Lorius, C., Pépin, L., Ritz, C., Saltzman, E., and Stievenard, M.: Climate and atmospheric history of the past 420,000 years from the Vostok ice core, Antarctica, Nature, 399, 429–436, doi:10.1038/20859, 1999.

Raisbeck, G. M., Yiou, F., Fruneau, M., and Loiseaux, J. M.: Beryllium-10 mass spectrometry with a cyclotron, Science, 202, 215–217, doi:10.1126/science.202.4364.215, 1978.

Raisbeck, G. M., Yiou, F., Fruneau, M., Loiseaux, J. M., Lieuvin, M., and Ravel, J. C.: Cosmogenic ^{10}Be/^{7}Be as a probe of atmospheric transport processes, Geophys. Res. Lett., 8, 1015–1018, doi:10.1029/GL008i009p01015, 1981a.

Raisbeck, G. M., Yiou, F., Fruneau, M., Loiseaux, J. M., Lieuvin, M., Ravel, J. C., and Lorius, C.: Cosmogenic ^{10}Be concentrations in Antarctic ice during the past 30,000 years, Nature, 292, 825, doi:10.1038/292825a0, 1981b.

Raisbeck, G. M., Yiou, F., Bourlès, D., Lorius, C., and Jouzel, J.: Evidence for two intervals of enhanced ^{10}Be deposition in Antarctic ice during the last glacial period, Nature, 326, 273–277, doi:10.1038/326273a0, 1987.

Raisbeck, G. M., Yiou, F., Jouzel, J., and Stocker, T. F.: Direct north-south synchronization of abrupt climate change record in ice cores using Beryllium 10, Clim. Past, 3, 541–547, doi:10.5194/cp-3-541-2007, 2007.

Raynaud, D., Lipenkov, V., Lemieux-Dudon, B., Duval, P., Loutre, M.-F., and Lhomme, N.: The local insolation signature of air content in Antarctic ice. A new step toward an absolute dating of ice records, Earth Planet. Sc. Lett., 261, 337–349, doi:10.1016/j.epsl.2007.06.025, 2007.

Risi, C., Bony, S., Vimeux, F., and Jouzel, J.: Water-stable isotopes in the LMDZ4 general circulation model: model evaluation for present-day and past climates and applications to climatic interpretations of tropical isotopic records, J. Geophys. Res., 115, D12118, doi:10.1029/2009JD013255, 2010.

Ritz, C.: Un modèle thermo-mécanique d'évolution pour le bassin glaciaire Antarctique Vostok-Glacier Byrd: Sensibilité aux valeurs des paramètres mal connus, Ph.D. thesis, Université Joseph Fourier – Grenoble I, 1992.

Roeckner, E., Brokopf, R., Esch, M., Giorgetta, M., Hagemann, S., Kornblueh, L., Manzini, E., Schlese, U., and Schulzweida, U.: Sensitivity of simulated climate to horizontal and vertical resolution in the ECHAM5 atmosphere model, J. Climate, 19, 3771, doi:10.1175/JCLI3824.1, 2006.

Salamatin, A. N., Lipenkov, V. Y., Barkov, N. I., Jouzel, J., Petit, J. R., and Raynaud, D.: Ice core age dating and paleothermometer calibration based on isotope and temperature profiles from deep boreholes at Vostok Station (East Antarctica), J. Geophys. Res., 103, 8963–8977, doi:10.1029/97JD02253, 1998.

Schäfer-Neth, C. and Paul, A.: Gridded Global LGM SST and Salinity Reconstruction, IGBP PAGES/World Data Center for Paleoclimatology, Boulder. Data Contribution Series #2003-046., NOAA/NGDC Paleoclimatology Program, Boulder CO, USA, available at: ftp://ftp.ncdc.noaa.gov/pub/data/paleo/contributions_by_author/paul2003, 2003.

Schmidt, G. A., Legrande, A. N., and Hoffmann, G.: Water isotope expressions of intrinsic and forced variability in a coupled ocean-atmosphere model, J. Geophys. Res., 112, D10103, doi:10.1029/2006JD007781, 2007.

Sime, L. C., Tindall, J. C., Wolff, E. W., Connolley, W. M., and Valdes, P. J.: Antarctic isotopic thermometer during a CO_2 forced warming event, J. Geophys. Res., 113, D24119, doi:10.1029/2008JD010395, 2008.

Sime, L. C., Wolff, E. W., Oliver, K. I. C., and Tindall, J. C.: Evidence for warmer interglacials in East Antarctic ice cores, Nature, 462, 342–345, doi:10.1038/nature08564, 2009.

Singer, B. S., Guillou, H., Jicha, B. R., Laj, C., Kissel, C., Beard, B. L., and Johnson, C. M.: ^{40}Ar/^{39}Ar, K-Ar and ^{230}Th – ^{238}U dating of the Laschamp excursion: a radioisotopic tie-point for ice core and climate chronology, Earth Planet. Sc. Lett., 286, 80–88, doi:10.1016/j.epsl.2009.06.030, 2009.

Suwa, M. and Bender, M. L.: Chronology of the Vostok ice core constrained by O_2/N_2 ratios of occluded air, and its implication for the Vostok climate records, Quaternary Sci. Rev., 27, 1093–1106, doi:10.1016/j.quascirev.2008.02.017, 2008.

Taylor, K. E., Balaji, V., Hankin, S., Juckes, M., Lawrence, B., and Pascoe, S.: CMIP5 Data Reference Syntax (DRS) and Controlled Vocabularies, version 1.3.1, available at: http://cmip-pcmdi.llnl.gov/cmip5/docs/cmip5_data_reference_syntax.pdf, 2012.

Thouveny, N., Bourlès, D. L., Saracco, G., Carcaillet, J. T., and Bassinot, F.: Paleoclimatic context of geomagnetic dipole lows and excursions in the Brunhes, clue for an orbital influence on the geodynamo?, Earth Planet. Sc. Lett., 275, 269–284, doi:10.1016/j.epsl.2008.08.020, 2008.

van Ommen, T. D. and Morgan, V.: Calibrating the ice core paleothermometer using seasonality, J. Geophys. Res., 102, 9351–9358, doi:10.1029/96JD04014, 1997.

Veres, D., Bazin, L., Landais, A., Toyé Mahamadou Kele, H., Lemieux-Dudon, B., Parrenin, F., Martinerie, P., Blayo, E., Blunier, T., Capron, E., Chappellaz, J., Rasmussen, S. O., Severi, M., Svensson, A., Vinther, B., and Wolff, E. W.: The Antarctic ice core chronology (AICC2012): an optimized multi-parameter and multi-site dating approach for the last 120 thousand years, Clim. Past, 9, 1733–1748, doi:10.5194/cp-9-1733-2013, 2013.

Vimeux, F., Cuffey, K. M., and Jouzel, J.: New insights into Southern Hemisphere temperature changes from Vostok ice cores using deuterium excess correction, Earth Planet. Sc. Lett., 203, 829–843, doi:10.1016/S0012-821X(02)00950-0, 2002.

Wagner, W. and Pruß, A.: The IAPWS formulation 1995 for the thermodynamic properties of ordinary water substance for general and scientific use, J. Phys. Chem. Ref. Data, 31, 387, doi:10.1063/1.1461829, 2002.

Watanabe, O., Jouzel, J., Johnsen, S., Parrenin, F., Shoji, H., and Yoshida, N.: Homogeneous climate variability across East Antarctica over the past three glacial cycles, Nature, 422, 509–512, doi:10.1038/nature01525, 2003.

Werner, M., Langebroek, P. M., Carlsen, T., Herold, M., and Lohmann, G.: Stable water isotopes in the ECHAM5 general circulation model: Toward high-resolution isotope modeling on a global scale, J. Geophys. Res., 116, D15109, doi:10.1029/2011JD015681, 2011.

Yiou, F., Raisbeck, G. M., Bourles, D., Lorius, C., and Barkov, N. I.: ^{10}Be in ice at Vostok Antarctica during the last climatic cycle, Nature, 316, 616–617, doi:10.1038/316616a0, 1985.

Yiou, F., Raisbeck, G. M., Baumgartner, S., Beer, J., Hammer, C., Johnsen, S., Jouzel, J., Kubik, P. W., Lestringuez, J., Stiévenard, M., Suter, M., and Yiou, P.: Beryllium 10 in the Greenland Ice Core Project ice core at Summit, Greenland, J. Geophys. Res., 102, 26783–26794, doi:10.1029/97JC01265, 1997.

4 Landais et al., 2015

Quaternary Science Reviews 114 (2015) 18–32

Contents lists available at ScienceDirect

Quaternary Science Reviews

journal homepage: www.elsevier.com/locate/quascirev

Invited review

A review of the bipolar see–saw from synchronized and high resolution ice core water stable isotope records from Greenland and East Antarctica

A. Landais [a, *], V. Masson-Delmotte [a], B. Stenni [b, c], E. Selmo [d], D.M. Roche [a, e], J. Jouzel [a], F. Lambert [f], M. Guillevic [a, h], L. Bazin [a], O. Arzel [g], B. Vinther [h], V. Gkinis [h], T. Popp [h]

[a] Laboratoire des Sciences du Climat et de l'Environnement (LSCE), Institut Pierre Simon Laplace (CEA-CNRS-UVSQ UMR 8212), Gif-sur-Yvette, France
[b] Department of Mathematics and Geosciences, University of Trieste, Italy
[c] Department of Environmental Sciences, Informatics and Statistics, Ca' Foscari University of Venice, Italy
[d] Department of Physics and Earth Sciences, University of Parma, Italy
[e] Earth and Climate Cluster, Faculty of Earth and Life Sciences, Vrije Universiteit Amsterdam, Amsterdam, The Netherlands
[f] Center for Climate and Resilience Research, University of Chile, Santiago, Chile
[g] Laboratoire de Physique des Océans, UMR 6523, Université de Bretagne Occidentale, Brest, France
[h] Centre for Ice and Climate, Niels Bohr Institute, University of Copenhagen, Copenhagen, Denmark

ARTICLE INFO

Article history:
Received 23 October 2014
Received in revised form
21 January 2015
Accepted 29 January 2015
Available online 27 February 2015

Keywords:
Ice cores
Bipolar seesaw
Dansgaard Oeschger events
Water isotopes

ABSTRACT

Numerous ice core records are now available that cover the Last Glacial cycle both in Greenland and in Antarctica. Recent developments in coherent ice core chronologies now enable us to depict with a precision of a few centuries the relationship between climate records in Greenland and Antarctica over the millennial scale variability of the Last Glacial period. Stacks of Greenland and Antarctic water isotopic records nicely illustrate a seesaw pattern with the abrupt warming in Greenland being concomitant with the beginning of the cooling in Antarctica at the Antarctic Isotopic Maximum (AIM). In addition, from the precise estimate of chronological error bars and additional high resolution measurements performed on the EDC and TALDICE ice cores, we show that the seesaw pattern does not explain the regional variability in Antarctic records with clear two step structures occurring during the warming phase of AIM 8 and 12. Our Antarctic high resolution data also suggest possible teleconnections between changes in low latitude atmospheric circulation and Antarctic without any Greenland temperature fingerprint.

1. Introduction

This introductory section summarizes the history of the identification of the bipolar seesaw pattern from Greenland and Antarctic ice cores (Section 1.1), and the ongoing debate on its causes and mechanisms, combining information from other natural archives, conceptual models, and a hierarchy of climate models (Section 1.2). From these open questions, it motivates the need for improved chronological constraints and high resolution, synchronized climate records documenting the spatial structure of changes in Greenland and Antarctica. The last Section 1.3 finally explains the structure of this manuscript.

1.1. Identification of the bipolar seesaw pattern from Greenland and Antarctic ice cores

Abrupt events punctuating climate variability of the Last Glacial period have been identified worldwide in highly resolved terrestrial, marine and ice core records (Voelker, 2002; Clement and Peterson, 2008). Since the 1960s, successive deep Greenland ice core records have provided continuous and extremely highly detailed records of climate variability, now encompassing the whole Last Glacial period, from 116 000 to 11 700 years ago recorded in GRIP (Dansgaard et al., 1993), GISP2 (Grootes et al., 1993), NorthGRIP (NorthGRIP Comm. Members, 2004) and NEEM ice cores (NEEM Comm. Members, 2013). During this time interval, 25 rapid events, called "Dansgaard-Oeschger events" (hereafter DO events), have been identified in numerous measurements performed along these Greenland ice cores (NorthGRIP

* Corresponding author. Tel.: +33 (0)169084672; fax: +33 (0)169087716.
E-mail address: amaelle.landais@lsce.ipsl.fr (A. Landais).

http://dx.doi.org/10.1016/j.quascirev.2015.01.031
0277-3791/

Community Members, 2004). Greenland abrupt temperature variations are qualitatively recorded at high resolution in water stable isotopes, while their magnitude is estimated using the thermal fractionation of gases inside the firn with an uncertainty of ~2 °C (Severinghaus and Brook, 1999; Kindler et al., 2014). Lasting a few centuries to a few millennia, DO events are characterized by the succession of a cold phase (Greenland Stadial, GS), an abrupt warming of 5–16 °C in a few years or decades, followed by a warm phase (Greenland Interstadial, GI) marked by a gradual cooling before a relatively abrupt cooling into the next GS, taking place within a few centuries. The widespread extent of DO events is reflected in parallel changes in the atmospheric composition (CH_4 concentration, as well as inflexions in the atmospheric $\delta^{18}O$ of O_2, hereafter $\delta^{18}O_{atm}$) (Chappellaz et al., 1993, 2013; Landais et al., 2007). The strong abrupt temperature and CH_4 increases occur in phase, within 10 years (Severinghaus et al., 1998; Rosen et al., 2014). This abrupt variability in the atmospheric composition, being recorded in the air trapped in Greenland and Antarctic ice cores, has provided a critical tool for the transfer of the accurate Greenland age scales based on annual layer counting towards Antarctic ice core chronologies (Blunier et al., 1998; Schüpbach et al., 2011).

Since the 1970s, East Antarctic ice cores have also depicted millennial climate variability during the Last Glacial period, albeit with limitations in temporal resolution emerging from lower accumulation rates, and less accurate chronologies when annual layer counting is not possible. In Antarctic water stable isotope records, this millennial variability is marked by Antarctic Isotopic Maxima (AIM), initially identified in the central East Antarctic plateau as symmetric gradual isotopic enrichment (warming) and depletion (cooling) trends. Using a first synchronization of the Greenland GRIP and GISP2 ice cores with the Antarctic Vostok ice core through the alignment of $\delta^{18}O_{atm}$, Bender et al. (1994a) evidenced a recurrent relationship between Greenland and Antarctic water stable isotope millennial events for the nine longest GS. This Greenland and Antarctica pattern was also shown in parallel by Jouzel et al. (1994). A refined synchronization of Greenland (GRIP, GISP2) and Antarctic (Byrd) ice core records was built by Blunier et al. (1998) and Blunier and Brook (2001) based on the alignment of CH_4 records over the last 90,000 years. 7 main Antarctic warm events were identified (called A events) as Antarctic counterparts of major Greenland DO events. During each of these 7 events, Antarctic temperatures increased gradually during GS, and the end of Antarctic warming coincided with the onset of rapid warming in Greenland.

Using higher resolution data as well as an improved synchronization, it has been further evidenced that each DO event has an Antarctic Isotopic Maximum counterpart (EPICA Comm Members, 2006; Jouzel et al., 2007), except for the first DO event of the Last Glacial period identified in the NorthGRIP ice core, DO25 (Capron et al., 2012). The same bipolar characteristic was also identified at the sub-millennial scale, during GS precursors of DO, or rebound events at the end of GIS, lasting only a few centuries (Capron et al., 2010a), albeit with the restrictions associated with the accuracy of the chronology, a few hundred years at best.

While there is growing evidence for the recurrence of abrupt climate change with similar characteristics during earlier glacial periods from high resolution Antarctic, terrestrial and deep sea records (e.g. McManus et al., 1999; Loulergue et al., 2007; Martrat et al., 2007; Barker et al., 2011; Lambert et al., 2012), we will focus here on the Last Glacial period for which the bipolar structure of events can be accurately characterized from high resolution and well dated records at both poles.

1.2. Causes and mechanisms of the bipolar seesaw

In parallel to ice core records highlighting millennial scale variability during the Last Glacial period, deep-sea sediments from the North Atlantic have revealed the recurrence of iceberg rafted debris in marine cores during GS, associated with iceberg discharges from glacial ice sheets, changes in sea ice extent, surface temperature and salinity, and reorganizations of the thermohaline circulation (e.g. Heinrich, 1988; Bond et al., 1992; Broecker et al., 1992; Grousset et al., 1993; McManus et al., 1998; Labeyrie et al., 1999; Elliott et al., 2002). Six major iceberg discharge episodes were identified as Heinrich events, corresponding to collapses of the Laurentide and/or European ice sheets (see review by Hemming, 2004). A Heinrich stadial was therefore defined as a Greenland cold phase during which a Heinrich event occurred (Barker et al., 2009; Sanchez-Goñi and Harrison, 2010). This feature led to the hypothesis that cold phases during Heinrich events (and, implicitly, all GS) were caused by changes in large scale Atlantic ocean circulation, driven by massive inflows of freshwater linked with glacial ice sheet collapses (e.g. Broecker, 1991; Paillard and Labeyrie, 1994; Ganopolski and Rahmstorf, 2001).

During the last decade, glacial abrupt events have been investigated using coupled ocean-atmosphere models of varying complexity (e.g. Stouffer et al., 2006; Kageyama et al., 2013). Several aspects of the observed patterns can be captured through the response of the Earth system to imposed freshwater perturbations in the North Atlantic (Ganopolski et al., 2001; Liu et al., 2009; Kageyama et al., 2010; Roche et al., 2010), mimicking Heinrich events. Depending on the background state of the climate (glacial or interglacial, orbital context …), of the simulated Atlantic Meridional Oceanic Circulation (AMOC), and the magnitude of the freshwater forcing, these models can produce a complete shutdown of the AMOC (Heinrich-like state) or a reduction of the strength of the AMOC (GS-like state) (e.g. Menviel et al., 2014). In all models, the injection of freshwater robustly produces a significant cooling of the North Atlantic region. The amplitude of the associated temperature change is probably affected by the simulated change in sea-ice extent and feedbacks between sea-ice and temperature that vary in the different models (Kageyama et al., 2013). These hosing experiments also produce an inter-hemispheric seesaw temperature pattern and impacts on the position of the intertropical convergence zone, hereafter ITCZ (e.g. Dahl et al., 2005; Broccoli et al., 2006; Krebs and Timmermann, 2007; Swingedouw et al., 2009) through changes in meridional heat transport. In response to freshwater forcing, climate models simulate a decrease of the NADW (North Atlantic Deep Water) export and a possible increase of the AABW (Antarctic Bottom Water) export in the Southern Ocean (Rind et al., 2001). The alternation between NADW and AABW formation is supported by paleoceanographic deep circulation tracers (e.g. review by Adkins, 2013), as well as by changes in ^{14}C of CO_2 measurements (Broecker, 1998; Anderson et al., 2009). The different models confirm the robustness of the bipolar seesaw signature of the climate response to AMOC weakening with the South Atlantic systematically warming in response to a freshwater discharge applied in the North Atlantic. There are still regional differences in the simulated Southern Ocean response (Clement and Peterson, 2008; Kageyama et al., 2010; Timmermann et al., 2010). Some models simulate a quasi-uniform warming (e.g. Otto-Bliesner and Brady, 2010) while others show contrasted patterns with a West Pacific cooling associated with the Southern Indian Ocean sector warming.

Conceptual models, paleoceanographic data and climate models of varying complexity all converge to show that DO events are associated with changes in AMOC. However, a number of physical

mechanisms allowing quasi–periodic transitions between different modes of operation of the AMOC have been proposed. Among them one must distinguish between those where abrupt millennial climate shifts result from changes in external forcing (e.g freshwater cycle, solar cycle) from those where either internal instabilities of the large-scale ocean circulation or nonlinear sea ice – ocean – ice sheet interactions play a fundamental role. Recent modeling studies suggest that the relatively weak Atlantic northward heat transport that prevails under cold background conditions is the key to the existence of such instabilities (Arzel et al., 2010; Colin de Verdière and te Raa, 2010; Arzel et al., 2012). In those studies, ice-sheet ocean interactions, atmospheric noise or time-varying external forcing are not essential to the emergence of millennial climate shifts. Glaciological studies have stressed that calving due to internal Laurentide ice sheet instabilities can deliver massive meltwater fluxes albeit with large uncertainties on the exact timing, magnitude and rate of delivery (MacAyeal et al., 1993; Marshall and Clark, 1997). Such calving events and associated meltwater – induced climate variability can be reproduced in climate models of reduced complexity (Ganopolski, 2003; Ganopolski et al., 2010). Whether the iceberg discharge is a cause or a consequence of changes in AMOC is however an open question. Indeed, a reduced AMOC can also trigger subsurface warming and instabilities of ice streams (Shaffer et al., 2004; Alvarez-Solas et al., 2011, 2013; Marcott et al., 2011). Changes in atmospheric circulation in relationship with changes in sea ice extent and/or changes in ice sheet topography may also cause abrupt glacial climate shifts (Wunsch, 2006; Li et al., 2010; Zhang et al., 2014).

The initial trigger of instabilities may not lie within the North Atlantic, which could just act as an amplifier (Cane and Clement, 1999). Several authors have explored the possible role of Antarctic freshwater fluxes on AMOC instabilities. For instance, Weaver et al. (2003) suggested an Antarctic origin of meltwater pulse 1A. This 14–18 m global mean sea level rise occurred during the abrupt Bølling-Allerød warming (Deschamps et al., 2012). While there is evidence for West Antarctic ice retreat coeval with MWP1A (Kilfeather et al., 2011; Smith et al., 2011), the magnitude of the Antarctic contribution remains disputed (Clark et al., 2009; Bentley et al., 2010; Mackintosh et al., 2011; Golledge et al., 2014), as glaciological studies indicate possible large contributions from North America (Carlson and Winsor, 2012; Gregoire et al., 2012). Idealized Southern Ocean hosing simulations do not produce large Greenland warming (Seidov et al., 2005; Stouffer et al., 2007; Swingedouw et al., 2008) and are thus suggesting that Antarctica cannot be the driver of DO events. Intrinsic instabilities of the Southern Ocean stratification have also been found in climate models of intermediate complexity (Meissner et al., 2006). These instabilities generate abrupt multi-millennial oscillations whose mechanism is essentially captured by the Welander (1982) two-box model. Corresponding changes in surface air temperature reach a few degrees in the Southern Ocean with little impact in the Northern Hemisphere.

Finally discriminating the respective role of changes in AMOC with respect to changes in sea ice extent and atmospheric circulation and identifying the trigger for the millennial variability calls for very high resolution paleoclimate records, an accurate identification of the north-south timing of changes, and the characterization of regional patterns of changes.

1.3. Structure of this manuscript

In this manuscript, we focus on the last 60 000 years where our bipolar chronological framework is most accurate, thanks to layer counting for Greenland ice cores and numerous age markers, using the latest available common chronology for Greenland and Antarctic ice core, AICC2012 (Bazin et al., 2013; Veres et al., 2013). The accuracy and limitations of the chronology are specifically addressed in Section 2. The temporal relationships between Antarctic and Greenland temperature over the Last Glacial cycle will be discussed in Section 3 using the AICC2012 chronology. This will include new highly resolved measurements of water stable isotopes from two East Antarctic ice cores (EDC and TALDICE). The comprehensive picture of the see–saw sequence, including regional variability among East Antarctic sites is discussed in Section 4. Finally, Section 5 addresses perspectives to progress in the understanding of mechanisms driving Greenland-Antarctic abrupt climate variability through the use of multiple tracers of climate at lower latitudes, as well as insights expected from earlier glacial periods.

2. The bipolar seesaw using the AICC chronology and age scale uncertainties

2.1. Methods for Greenland and Antarctic age scale synchronization and AICC2012

For a discussion of bipolar seesaw, we concentrate here on the relative uncertainty between Antarctic and Greenland chronologies.

A critical limitation for the description of the sequence of Greenland versus Antarctic climate change is linked to the difficulty of synchronizing different ice cores at high temporal precision. Through time, a collection of absolute and relative ice core dating constraints has been accumulated. For instance, the identification of the Laschamp geomagnetic excursion in the ^{10}Be concentration in different ice cores allows to transfer the absolute age of the excursion, from radiometric dating methods applied on lavas (e.g. Guillou et al., 2004; Singer et al., 2009) to ice core records (Raisbeck et al., 2007). Several parameters provide tools for the synchronization of ice core records. They arise from the global variability of well mixed atmospheric gases and high resolution measurements of CH_4 and $\delta^{18}O$ of O_2 in the gas phase of ice cores (e.g. Capron et al., 2010); or from the occurrence of volcanic events, whose fingerprints can be identified from chemical (major ion concentrations) or physical (electrical conductivity, particles) measurements performed on the ice phase (e.g. Parrenin et al., 2012a).

A specific uncertainty arises from the need to build two different timescales for each ice core, one for the ice phase and one for the gas phase. Age differences between ice and gas at a given depth arise from the firnification processes, when snow is consolidating to ice and the air is trapped inside, at the lock-in depth (LID), about 100 m under the ice-sheet surface. Because firnification processes (and therefore the LID) are affected by changes in temperature, accumulation rate, and possibly by the snow impurity content (Hörhold et al., 2012), the gas age – ice age difference varies through time and space with variations of several thousands years for ice cores of the East Antarctic plateau (EPICA Dome C, Vostok).

During the past 60,000 years, the Greenland ice core GICC05 chronology is based on multi-parameter layer counting and provides a reference ice age scale. The absolute uncertainty of the GICC05 chronology used as a reference for the last 60 ka for AICC2012 has no importance for the bipolar seesaw pattern which is investigated here. On opposite, the gas chronology calculated for NorthGRIP has an impact on the seesaw pattern because of gas stratigraphic links in between ice cores. It therefore needs to be precisely constrained. Due to relatively high accumulation rates, the gas age – ice age difference, Δage, remains small in Greenland (<1000 years) and is very well simulated by firn models. This is verified using markers of abrupt local warming in the gas phase, through abrupt changes in inert gas isotopic composition caused by

firn air thermal fractionation (e.g. Kindler et al., 2014). The depth difference, Δdepth, between the same event (an abrupt warming), recorded in the gas phase (a peak of $\delta^{15}N$) and in the ice phase (an abrupt increase in ice $\delta^{18}O$) enables to constraint the gas chronology vs. the ice chronology in Greenland with minimal uncertainties (Rasmussen et al., 2013).

The transfer of this Greenland gas chronology towards the Antarctic gas chronology relies on the global signals provided by changes in atmospheric composition (in the gas phase). The accuracy of this transfer is only limited by the resolution of the records and the smoothing caused by firn diffusion (Köhler et al., 2011).

A major source of uncertainty for the investigation of the precise temporal sequence between changes in Greenland and Antarctic water stable isotope records (both in the ice phase) arises from the construction of the Antarctic ice age scale from the gas age scale synchronized with that of Greenland. It mostly depends on the ability to accurately estimate the temporal evolution of the LID in Antarctica. Several studies have therefore taken advantage of Antarctic ice cores in the least dry areas (West Antarctica for Byrd or Siple Dome, coastal East Antarctica for Law Dome), where the gas age − ice age difference, Δage, is smallest (several hundreds of years) which limits the associated uncertainty (e.g. Blunier et al., 1998; Pedro et al., 2012). Uncertainties are largest for the dry central East Antarctic sites, where, under glacial conditions, Δage differences can reach several thousand years.

The estimates of past LID based on firnification models are probably associated with an uncertainty of about 20% (Landais et al., 2006; Parrenin et al., 2012b). However, the combination of stratigraphic constraints in both the gas and in the ice phases in different ice cores narrows LID estimates. Moreover, constraints on past LID can also be established using air $\delta^{15}N$ in Antarctic ice cores (Parrenin et al., 2012b). $\delta^{15}N$ is mainly affected by gravitational fractionation in the air circulating in the diffusive zone of the unconsolidated snow. It is therefore directly proportional to the depth of the diffusive column, and therefore to the changes in LID.

While the first Greenland-Antarctic chronologies were manually established from the interpolation of a few age markers, site by site, the AICC2012 timescale has been produced as a community effort for the collection of dating constraints and their integration using a common mathematical framework applied to several deep ice cores. Using a Bayesian tool dedicated to multi-ice cores dating, Lemieux-Dudon (2010), Bazin et al. (2013) and Veres et al. (2013) have built a coherent chronology integrating 5 ice cores from Greenland (NorthGRIP) and Antarctica (EPICA Dome C − EDC -, EPICA Dronning Maud Land − EDML -, TALDICE, Vostok, Fig. 1).

The AICC2012 effort has gathered an unprecedented high number of stratigraphic tie-points between the Greenland NorthGRIP and the 4 Antarctic ice cores and between Antarctic ice cores. The AICC2012 synchronization uncertainty (Fig. 2) mostly arises from (i) the density of gas markers (mainly methane) and their associated uncertainties (Loulergue, 2007; Loulergue et al., 2007; Lemieux-Dudon et al., 2010; Schilt et al., 2010; Capron et al., 2010b; Buiron et al., 2011; Schüpbach et al., 2011; Bazin et al., 2013); (ii) the density of ice markers (volcanic eruption and ^{10}Be peak around the Laschamps event) and their associated uncertainties (Udisti et al., 2004; Loulergue et al., 2007; Ruth et al., 2007; Severi et al., 2007, 2012; Parrenin et al., 2012a; Bazin et al., 2013; Svensson et al., 2013); (iii) the determination of the LID in the different ice cores and their associated uncertainties. Fig. 3 displays the different age markers used in AICC2012 and the associated uncertainties over the last 60 ka (Bazin et al., 2013; Veres et al., 2013). It illustrates how the final relative uncertainties of each Antarctic ice core chronology (relative to NorthGRIP) are strongly linked to these gas and ice markers.

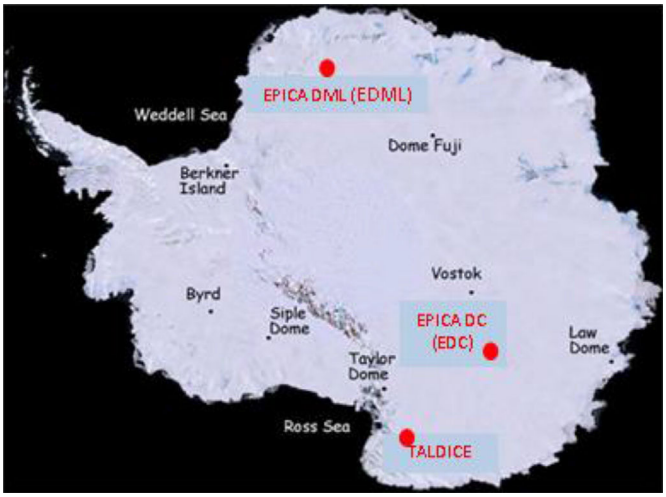

Fig. 1. Location of the Antarctic cores included in the AICC2012 chronology. The red points highlight the sites that are considered in this study.

Between 26 and 17 ka, in the absence of any tie points, chronology uncertainties strongly increase (Fig. 2). Uncertainties of only a few centuries occur when both gas and ice tie points are present. This is the case around the Laschamp event at ~41 ka which concentrates methane tie points for each DO event, numerous volcanic tie points between the Antarctic ice cores, and the ^{10}Be fingerprint of the Laschamp events in Greenland and Antarctic ice cores. Note that we have excluded Vostok from the following discussion because of too weak dating constraints linked to the low resolution of the initial records.

2.2. Uncertainty associated with AICC2012

Here, three issues are discussed with respect to the north-south sequence of events: first, we investigate the uncertainty associated with the estimation of LID at EDC and EDML; second, we revise the estimation of the NorthGRIP LID between DO events which was likely overestimated in AICC2012; third, we discuss the calculation of the AICC2012 uncertainty.

In the construction of AICC2012, the LID background scenarios were driven by the $\delta^{15}N$ profile measured in ice cores. Parrenin et al. (2012b) indeed demonstrated that for EDC, the LID was better estimated from $\delta^{15}N$ than when using a firnification model. Still, $\delta^{15}N$ will not be linearly related to the LID if there are changes in firn convective zone. As a consequence a large variance was associated with the background LID scenario in the building of AICC2012 with DATICE. However, the link between the value of the variance of the background scenario and the final DATICE uncertainty is not straightforward and the chronological uncertainty resulting from the LID uncertainty in Antarctic ice cores may have been overestimated in AICC2012.

The uncertainty associated with the background LID is addressed here by sensitivity tests with DATICE (Fig. 3). Simulations have been performed with different background scenarios for EDC, TALDICE and EDML LID for two extreme cases: either from $\delta^{15}N$ measurements (which leads to the lowest possible value of the LID) or from the firnification model (Goujon et al., 2003, leading to an upper estimate for LID). Using a LID deduced from the firnification model leads to systematically larger glacial Antarctic LID than when using the $\delta^{15}N$ measurements. Antarctic chronologies are therefore systematically older than AICC2012 by up to 500 years around the LGM (red lines, Fig. 3). This chronological change is minor. Indeed, the multiplicity of gas and ice stratigraphic tie-points used in

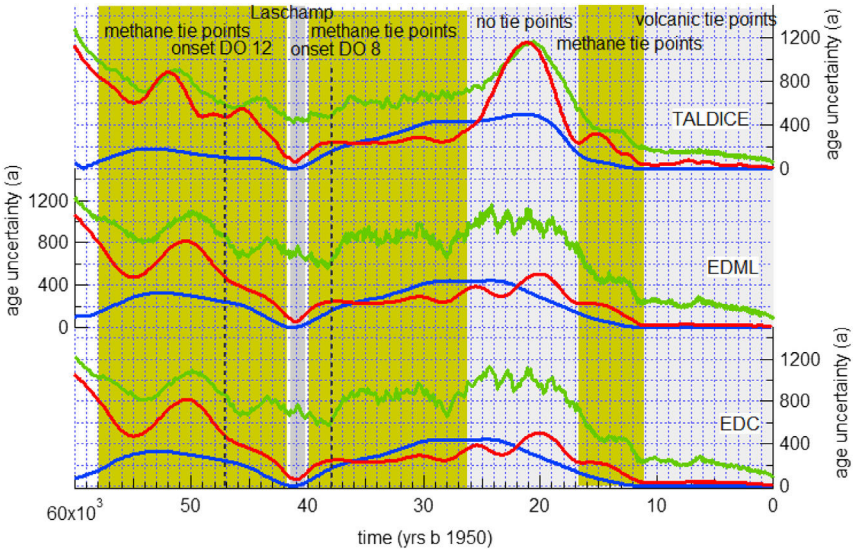

Fig. 2. Illustration of the sources of uncertainty in the AICC2012 chronology: in green the total uncertainty of AICC2012; in blue, the chronology difference induced by different estimates of the background LID (either from firnification model or from $\delta^{15}N$ data); in red, the ice uncertainty calculated by DATICE. The EDC and EDML AICC2012 uncertainties are similar because of the numerous ice tie points between them (see details in SOM of Bazin et al., 2013). Note that this chronology was built with an artificially small uncertainty on the NorthGRIP GICC05 chronology (<20 years over the last 60 ka) so that the displayed uncertainty actually reflects the relative uncertainties of each Antarctic ice core relative to NorthGRIP.

DATICE compensates for the large uncertainty in the background LIDIE scenario. The phasing between Antarctica and Greenland over DO/AIM events is not significantly affected. For DO/AIM 8 (Fig. 3b), the Greenland vs Antarctica phasing is exactly the same for the two different background scenarios of LIDIE because of the proximity of the Laschamp event providing ice stratigraphic tie-points. For DO/AIM 12 (Fig. 3c), the Antarctic records are slightly older by a few centuries, but this does not affect the Greenland vs Antarctica seesaw pattern.

Despite strong and robust constraints at the onset of each DO events from $\delta^{15}N$ measurements (Huber et al., 2006; Kindler et al., 2014), the NorthGRIP LID was not properly estimated between DO events. This is due to the combined effects of two strong constraints imposed on the NorthGRIP chronology in AICC2012 as explained in the following. First, for the onset of each DO event, Δdepth constraints were provided as inputs to DATICE based on the synchronicity of the two temperature-sensitive records ($\delta^{18}O$ increase in ice and $\delta^{15}N$ increase in gas). Then, by construction, AICC2012 was driven by the GICC05 Greenland chronology and with an imposed thinning function for NorthGRIP (NorthGRIP members, 2004). The combination of imposed Δdepth and thinning led DATICE to overestimate NorthGRIP LID by up to 10–20 m, especially around DO 12, compared to the estimate based on $\delta^{15}N$ and firn modeling (Kindler et al., 2014). Bazin et al. (2014) solved this problem by allowing DATICE to modify the NorthGRIP thinning scenario, thus leading to a smaller NorthGRIP LID. The revised Antarctic chronologies produced this way are independent of GICC05 and show small differences with AICC2012 (<400 years). They do not affect significantly the Antarctica vs. Greenland relationship, especially over DO/AIM 12 and DO/AIM 8, this last sequence being particularly well constrained by tie-points around the Laschamp event (Fig. 3b and c).

Antarctic chronologies are mainly based on gas tie points between Greenland and Antarctica, so that the ice chronology is deduced from the gas chronology and thus must incorporate uncertainties associated with the LID estimates. This is however not always the case in DATICE when many ice stratigraphic tie points are present, especially between EDML and EDC (76 ice stratigraphic tie-points over the period 30 to 60 ka). Because a correct reformulation of the error calculation requires significant developments, AICC2012 reported the gas chronological uncertainty, which considers the uncertainty associated with LID, in addition to the uncertainties associated with the ice chronology in DATICE (i.e. stratigraphic and absolute tie points and variance associated with thinning and accumulation rate background scenarios). This formulation is correct when only gas tie points are present, but it is an overestimation of the true uncertainty when mainly ice tie-points are present (Holocene or around the Laschamp event). In this case, the uncertainty attached to the ice chronology should be used for the comparison of water stable isotope records.

Fig. 2 compares two estimates of the ice chronological uncertainty: DATICE uncertainty for the ice chronology (red) and AICC2012 official uncertainty mainly obtained from DATICE uncertainty on the gas chronology (green). As explained above, these uncertainties should be taken as an Antarctica–Greenland synchronization uncertainty. Around the Laschamp event, the difference between the two types of uncertainties is ~400 years at EDML and EDC. We argue that it is overestimated by DATICE in AICC2012. Indeed, for this period, the maximum difference between chronologies obtained with extremely different LID background scenarios is less than 200 years (red and blue lines, Figs. 1, and 2). The relative ice chronological uncertainty between Antarctic (EDC, EDML, TALDICE) and NorthGRIP at the time of DO-AIM 8, very close to the Laschamp event, should therefore be less than 400 years.

For DO 12, the situation is different since there is no ice tie-point common to Greenland and Antarctica (Bazin et al., 2013). There is therefore no reason to challenge the AICC2012 uncertainty of 600–700 years given for the relative chronology between Antarctic and Greenland ice as a correct upper boundary.

3. Water stable isotope records of bipolar seesaw

3.1. Stack Greenland and Antarctic records on AICC2012

In order to extract the common East Antarctic signal, we have combined the water isotopic records for the 4 Antarctic ice cores synchronized on AICC2012 to obtain an East Antarctic isotopic

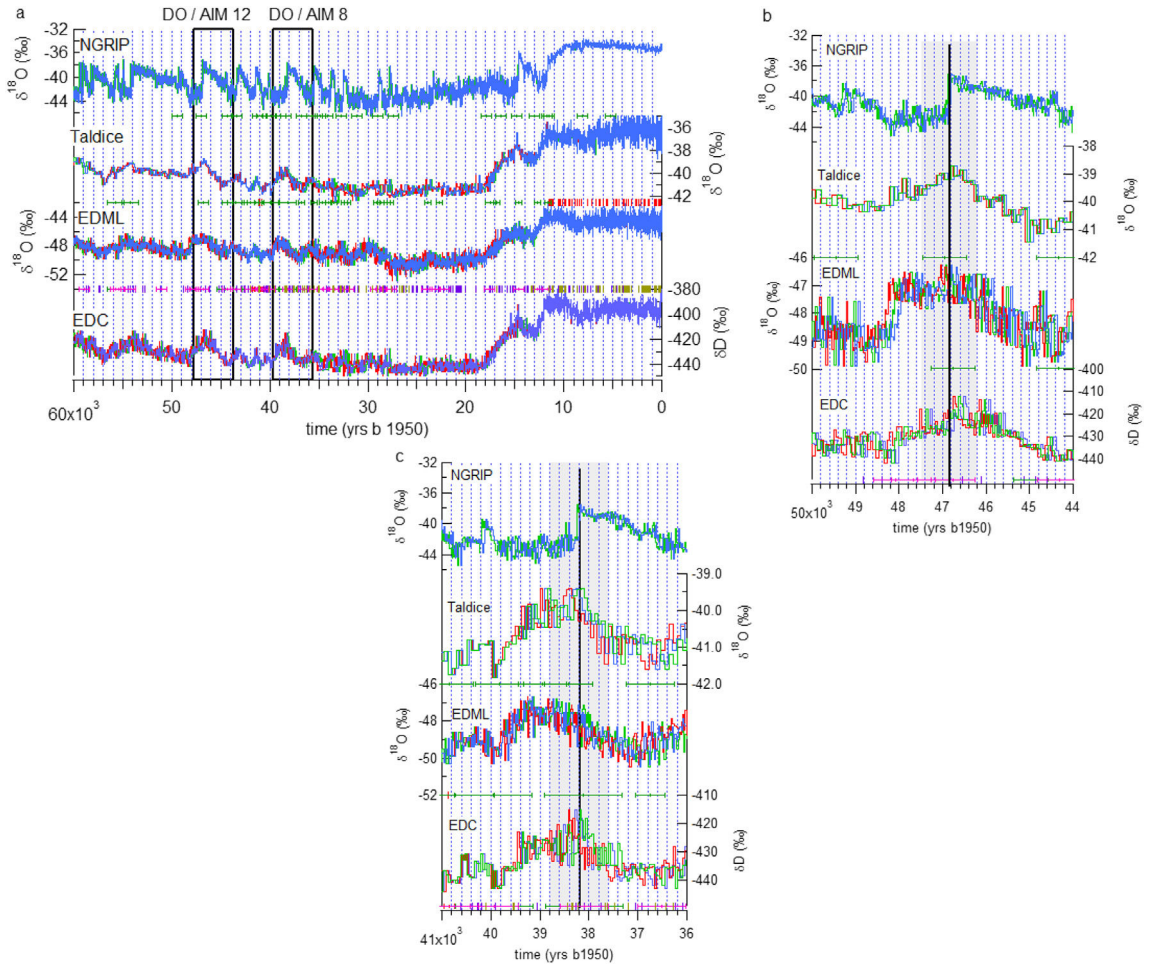

Fig. 3. a) NorthGRIP, Taldice, EDML and EDC $\delta^{18}O$ profiles (55 cm resolution) on AICC2012 (blue) with the identification of the large DO events 8 and 12 (black rectangles). Horizontal markers indicate the position and uncertainties of ice and gas stratigraphic links (green – ice stratigraphic links between EDC and TALDICE; blue – ice stratigraphic links between EDC and EDML; purple – gas stratigraphic links between EDC and EDML). b) Same as (a) but for a zoom on DO 12. c) Same as (a) but for a zoom on DO 8. The red line depicts the results of DATICE calculations when using LID calculations based on firnification model rather than $\delta^{15}N$ data (as in AICC2012). The green line is the output of DATICE without the strong GICC05 constraints (here we show the run with correlation of NorthGRIP markers of age difference from Bazin et al. (2014) which shows the largest difference to AICC2012). The black lines on Fig. 3b and c shows the onset of DO events in Greenland and the gray rectangles the AICC2012 uncertainty of EDML and EDC chronology for this onset.

stack. From the available resolution of individual records, the East Antarctic stack has been produced with a 100 year resolution. For Greenland, we have used the available synchronization of the Greenland ice cores (GRIP, GISP2 and NorthGRIP) performed during the construction of the GICC05 timescale (Svensson et al., 2008 and references herein) to obtain a Greenland isotopic stack on the AICC2012 timescale. These two stacks clearly show the classical bipolar seesaw pattern (Fig. 4), with Antarctic warming during GS, particularly visible for long stadials (e.g. DO 21, 12, 8). During the shortest stadials, the common Antarctic signal is equivocal, due to the noise caused by small chronological shifts, noise and regional differences in water stable isotope patterns (see next section).

The global picture of the bipolar seesaw highlighted in Fig. 4 is in general agreement with the simple modeling of Stocker and

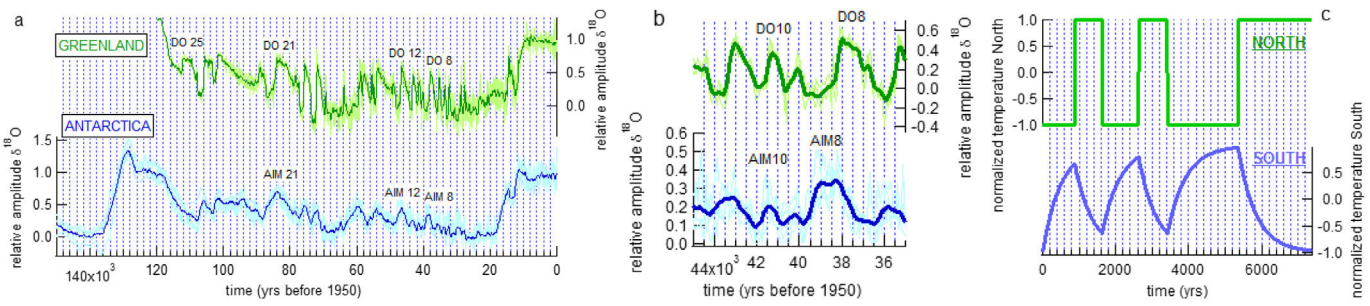

Fig. 4. a) Stack of East Antarctic (Vostok, EDML, EDC and Taldice) $\delta^{18}O$, and Greenland (GRIP, GISP2, NorthGRIP) $\delta^{18}O$ on AICC2012/GICC05 synchronized chronologies, expressed in relative amplitude centered onto the present-day value. The average stack value is depicted with the bold colored lines, while the individual ice core records are shown in light color. b and c) Comparison between the data around DO 8–12 and the results of the thermodynamical model of Stocker and Johnsen (2003).

Johnsen (2003) for the slow thermal response of Antarctic temperature to Greenland abrupt warmings and coolings through a heat reservoir in the southern ocean.

3.2. Regional differences in Greenland and Antarctica

Spatial gradients have already been evidenced in Greenland based on temperature (derived from $\delta^{15}N$), accumulation, and $\delta^{18}O$ records (e.g. Guillevic et al., 2013; Buizert et al., 2014). Using NEEM, NorthGRIP and Summit ice cores during the last deglaciation and over DO event 8, they have shown that, while the magnitude of $\delta^{18}O$ changes is largest at NEEM, the magnitude of abrupt warming is largest in central Greenland (Summit). These studies have confirmed the validity of $\delta^{18}O$ as a qualitative temperature proxy, but revealed that, in Greenland, it is not a reliable indicator of the amplitude of abrupt warming. The pattern of temperature change associated with abrupt warming can be potentially explained with the impacts of changes in Nordic sea ice cover (Li et al., 2005) and the impacts of changes in AMOC on Greenland climate (Buizert et al., 2014).

In Antarctica, no independent paleothermometry method has yet been applied for AIM events, restricting the investigation of the patterns and rates of changes to $\delta^{18}O$ only. Existing simulations performed with isotope enabled atmospheric general circulation models stress the reliability of the isotope–temperature relationship under glacial boundary conditions (e.g. Werner et al., 2001; Jouzel et al., 2013). We will therefore use isotopic rates of changes through time to identify patterns of rates of warming during AIM events.

The new AICC2012 timescale allows investigating regional patterns in Antarctica. Stenni et al. (2010) already stressed a square shape of AIM in the Atlantic sector (EDML), which contrasts with the triangular (symmetric) shape of AIM events in the Indo-Pacific sector (EDC, Vostok, TALDICE, Byrd, WAIS …). During the warming phase of the largest AIM events of the last 50 ka, Buiron et al. (2012) estimated that the rate of warming (isotopic enrichment) was twice smaller at TALDICE and EDC than at EDML. This feature is confirmed using the AICC2012 timescale.

We now focus on EDML, TALDICE and EDC (Fig. 5) for which (i) high resolution water stable isotope records are available (respectively 20, 50 and 70 years for EDML, EDC and TALDICE around AIM 8, at ~38 ka), and (ii) age scale uncertainties are the smallest (Fig. 2). We do not discuss the Vostok ice core which has lower resolution and chronological accuracy. The maximum ice age uncertainty around AIM 8 and AIM 12 estimated through AICC2012 is respectively ±600 years for TALDICE and ±800 years for EDML and EDC. Because of this uncertainty, it is impossible to investigate regional differences during the small and short-lived D/O events of MIS 3.

A clear picture nevertheless emerges for AIM 8 (Fig. 5), where the sharp water stable isotope increase recorded at EDML ends 1200 ± 600 years earlier than the onset of abrupt Greenland warming and hence only 600 years after the preceding Greenland cooling. The first gradual isotopic enrichment recorded at EDC starts in phase with this EDML warming when Greenland is cooling. Because of the numerous ice stratigraphic links between EDML and EDC, their relative ice chronological uncertainty is only ±200 years. This first rapid warming at EDC is followed by a gradual temperature increase along the 1200 years preceding Greenland abrupt warming when EDML $\delta^{18}O$ is on a plateau. Similar patterns are depicted at TALDICE albeit with lower temporal resolution. By contrast, the slow cooling phase following abrupt Greenland warming occurs in phase for all Antarctic ice cores, and in phase with the slow GIS cooling. The same characteristics are also observed during AIM 12: at EDML, a very fast warming ends about 1200 years prior to Greenland abrupt warming, followed by a long lasting plateau; at EDC and TALDICE, the warming phase occurs in two steps (Fig. 5).

Exploring the uncertainties attached to the relative AICC2012 chronologies between EDML, EDC, TALDICE and NorthGRIP ice cores (Fig. 3) confirms the robustness of this sequence of events around AIM 8 and 12. Revised estimates of LID indeed produce older Antarctic ice ages and therefore a longer lag between the first Antarctic warming phase and the onset of Greenland interstadial.

3.3. New high resolution water stable isotope data

To further explore the identified inflexion points in TALDICE and EDC, we report here the additional information provided by new high resolution water stable isotope data for these two sites.

The initial EDC δD and $\delta^{18}O$ profile from EDC were obtained along 55 cm long ice "bag" samples (Jouzel et al., 2007; Stenni et al., 2010). While they document Holocene climate with a resolution of ~20 years (Pol et al., 2011), ice thinning and lower glacial accumulation rates result in a loss of temporal resolution for glacial climate variability (50 year resolution). Higher resolution records have therefore been obtained from more than 8000 new $\delta^{18}O$ measurements performed using 5 sections of 11 cm within each bag sample. These new mass spectrometry measurements have an accuracy of 0.07‰ using a classical method of water/CO_2 equilibration at the Center for Ice and Climate of the University of Copenhagen.

The high resolution data confirm all the details of the low resolution signals available from bag measurements (Jouzel et al., 2007; Stenni et al., 2010). They reveal centennial variability within AIM which was not visible in bag measurements and preferentially occurs during the warm and warming phases of AIM (Fig. 6, red rectangles). These short-lived, sharp events reach a magnitude >2‰ (2.6 °C using the spatial isotope–temperature relationship) in about 20–30 years. AIM 8 and 12 are characterized by a multi peak structure around the maximum $\delta^{18}O$ level of the AIM and one peak during the warming phase, at the inflexion point between the two warming phases at EDC (vertical bar b on Fig. 6b and c). These peaks are also visible through excursions in the calculated 200 years running variance (Fig. 6b and c). In addition, two events occur during the peak and cooling phase of AIM 14, potentially synchronous with sub-event 14-b recorded in NorthGRIP (Rasmussen et al., 2013). Finally, the two events occurring at peak warmth of AIM 16 coincide within chronological uncertainty with the large centennial variability in Greenland (events DO 16.1 and 16.2 as defined by Rasmussen et al., 2013). Similar events may have occurred during AIM 0 (early Holocene optimum) and Last Interglacial early optimum, as recorded in "fine cut" samples δD (Pol et al., 2011, 2014).

We now investigate the patterns of TALDICE $\delta^{18}O$ variability using new measurements. The initial TALDICE $\delta^{18}O$ profile was obtained at 1 m resolution (Stenni et al., 2011; Buiron et al., 2012), leading to 100 years resolution for the Last Glacial period. New high resolution $\delta^{18}O$ measurements spanning AIM 8 and AIM 12 were therefore performed at 10 cm resolution at Parma and Trieste Universities using the classical method of water/CO_2 equilibration. Again, the high resolution $\delta^{18}O$ measurements confirm the details of the initial record (Fig. 6) and clearly depict centennial variability. Both at EDC and TALDICE, the data depict an optimum coinciding with the end of the EDML warming phase. This first optimum is more strongly marked at TALDICE, followed by a "cold-reversal-type" drop, labeled "L" on Fig. 6 and associated with a decrease of the 200 years running variance (Fig. 6b and c). We do not detect the same sharp events as recorded in EDC, questioning the spatial structure of such sharp, short-lived events. Backward trajectory analysis (Scarchilli et al., 2011) suggests that TALDICE is influenced

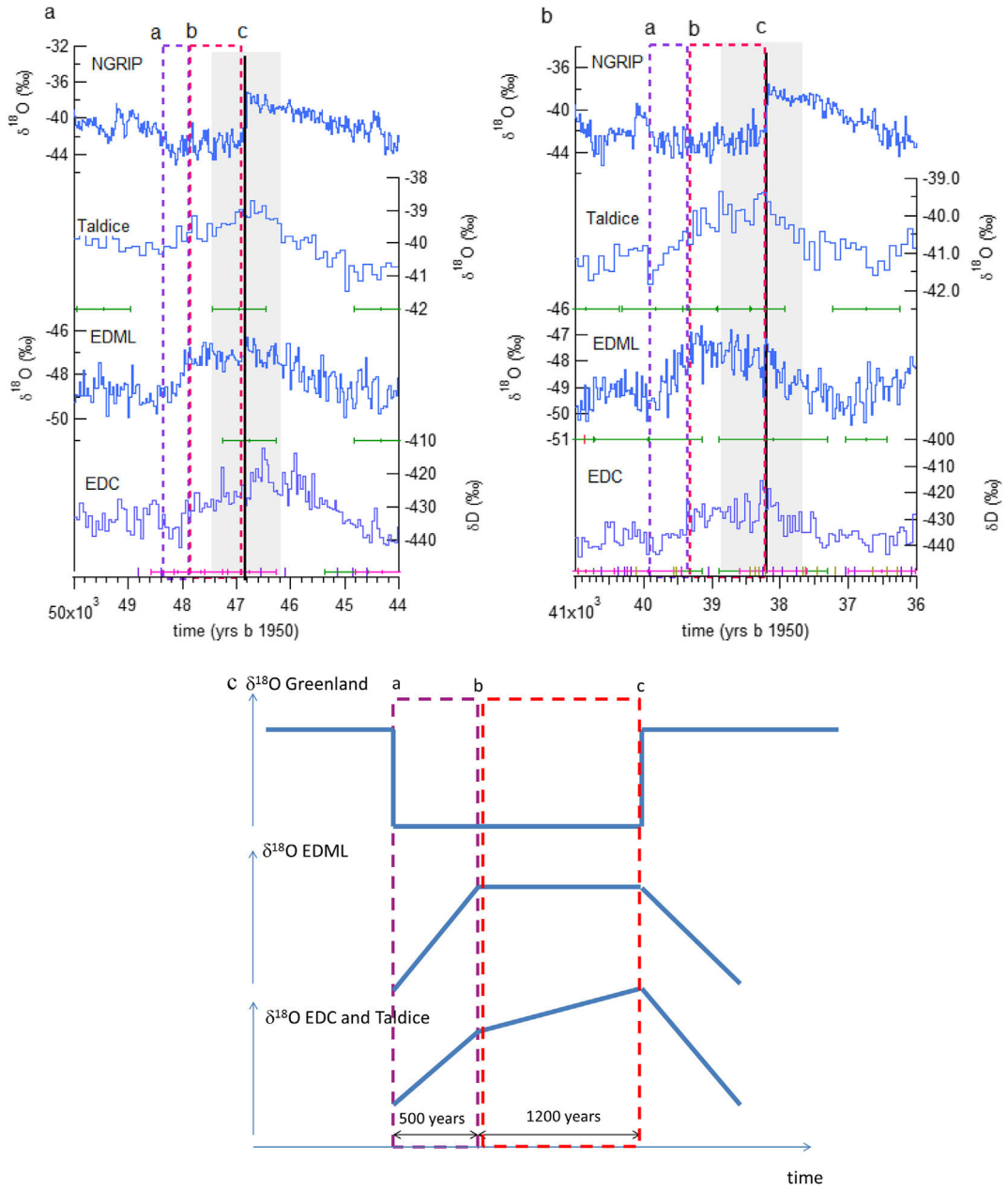

Fig. 5. Focus on DO-AIM 12 (a) and 8 (b). From top to bottom: $\delta^{18}O$ records from NorthGRIP, Taldice, EDML and EDC, on the AICC2012 chronology. Horizontal error bars in panels (a) and (b) stress the position of ice and gas stratigraphic links between EDC, TALDICE and EDML. Panel (c) provides a schematic representation of the structure of $\delta^{18}O$ changes identified during both events. Shaded rectangles highlight the chronological uncertainties for the AIM 12 and 8 in panels a and b. The violet and red rectangles highlight the separation in two phases for the warming of the AIM in each of the 3 panels and the letters a, b and c mark the separation between each phases as used in the following figures.

by moisture originating mainly from the Indian and secondarily from the Pacific sectors of the Southern Ocean, while EDC is mainly influenced by the Indian Ocean. Differences between EDC and TALDICE could thus be linked to different transport paths compared to present day but also to possible differences in their sensitivity to sea-ice variability, mainly due to their different distance to the coast.

We conclude that high resolution data from EDC and TALDICE confirm the three phase structure of AIM8 and 12, with TALDICE showing a marked optimum (followed by a minimum) at the end of the EDML warming phase (vertical bar b on Fig. 6b and c) corresponding to the inflexion between the first and second EDC and EDML warming phases. At EDC, the data depict short-lived, sharp events with a large isotopic anomaly, during the warm phases of AIM events, when Greenland abruptly warms (vertical bar c on Fig. 6b and c). Similar events are seen at the inflexion between the first and second EDC and EDML warming phases (vertical bar b on Fig. 6b and c).

4. Discussion

The structure of Antarctic $\delta^{18}O$ records depicts a variability which does not follow a simple bipolar seesaw scheme, both in the sharp events depicted in high resolution data from EDC and TALDICE, and in the two phase structure observed during major Antarctic warmings (AIM 8 and AIM 12 warming phases). These patterns can therefore not be explained by a simple seesaw mechanism implying a slow response of Antarctic temperature to

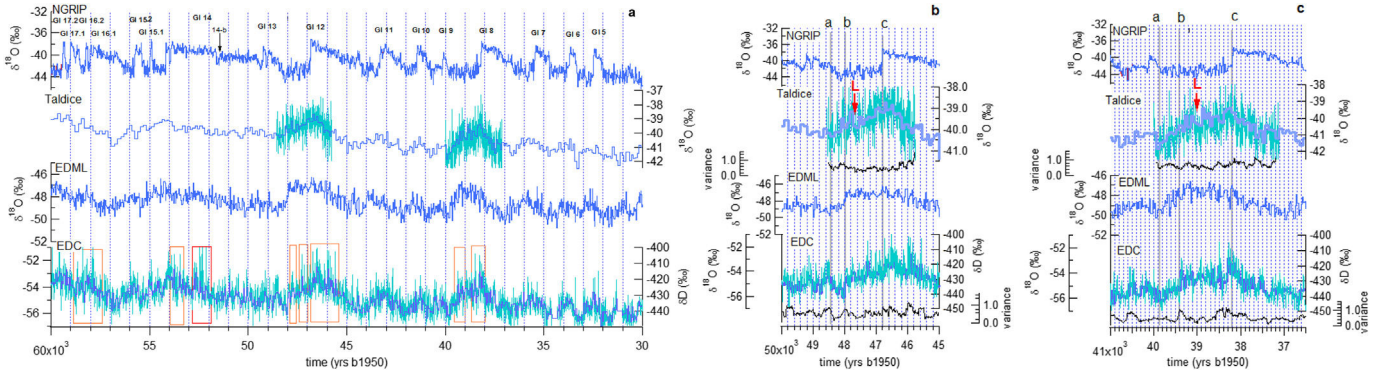

Fig. 6. a) new high resolution water stable isotope measurements from TALDICE and EDC (light blue), superimposed on existing low resolution data (blue) on AICC2012. b) Same as (a) but for a zoom on AIM 12. The 200 year running variance for the Taldice and EDC high resolution data are added. The vertical bars a, b and c respectively indicate the beginning of the GS/AIM, the inflexion point at the end of the EDML $\delta^{18}O$ increase and EDC main $\delta^{18}O$ increase and the abrupt warming in Greenland. c) Same as (b) but for AIM 8.

abrupt North Atlantic climate shifts, modulated by the thermal inertia of the southern ocean. Several hypotheses can be formulated. One option is that this Antarctic variability reflects abrupt changes in atmospheric circulation and/or moisture origin, probably linked to sea ice variability. A second option is that Greenland climate (temperature, accumulation and $\delta^{18}O$) does not reflect changes in North Atlantic ocean circulation. To explore the first option, we compare the Antarctic $\delta^{18}O$ records with aerosol and deuterium excess data (Section 4.1). To explore the second option, we investigate Greenland moisture source, global atmospheric composition, together with our Antarctic records, expanding the work of Guillevic et al. (2014) for multi-proxy Greenland and atmospheric composition records (Section 4.2).

4.1. Antarctic atmospheric circulation: aerosol and d-excess data

Here, we compare our three Antarctic $\delta^{18}O$ records to records of dust aerosols and d-excess in same ice cores. The second order parameter d-excess, expressed as $\delta D - 8^{*}\delta^{18}O$, is linked to evaporation conditions and shifts of moisture sources (e.g. Vimeux et al., 1999; Stenni et al., 2010). The level of high frequency variability (or noise) in d-excess profiles from TALDICE, EDC and EDML is a clear limitation to the detection of climatic signals. The d-excess is generally in anti-phase with $\delta^{18}O$ in EDC and EDML, but in phase at TALDICE (Fig. 7a). This supports the hypothesis that TALDICE has a different moisture source. More abrupt variations are recorded at TALDICE than EDC, while EDML d-excess shows generally smooth variations. Some abrupt shifts in TALDICE and EDC d-excess are detected at the start of the second phase of AIM 8 (plateau of EDML warming), and during Greenland abrupt warming. Similar features are also detected in one or the other core for earlier AIM events.

The signals depicted by the dust and aerosol records are more straightforward. To characterize changes in atmospheric mineral dust deposition (Lambert et al., 2012), we have used the dust flux from EDC and non-sea-salt calcium flux (hereafter $nssCa^{2+}$) from EDML and TALDICE. For EDC, analytical problems rule out the use of continuous flow $nssCa^{2+}$ measurements for AIM 8 (Schüpbach et al., 2013). We therefore report the high resolution dust flux data from Lambert et al. (2012) which are strongly correlated to the flux of $nssCa^{2+}$ in the other parts of EDC. AIM events are clearly recorded through changes in dust fluxes (Lambert et al., 2012; Schüpbach et al., 2013). This implies that AIM are associated with changes in atmospheric dust transport and/or changes in continental dust sources, located primarily in Southern Patagonia for East Antarctic cores during glacial periods (e.g. Basile et al., 1997; Delmonte et al., 2008; Wegner et al., 2012).

During AIM 8, the transition from phase 1 to phase 2 of Antarctic warming (start of the EDML plateau, change in warming rates at TALDICE and EDC) coincides with an abrupt decrease of dust fluxes (red arrows on Fig. 7a), a feature already observed by Ahn et al. (2012). The same pattern is observed in high resolution dust EDC data over AIM 12 but cannot be clearly detected in lower resolution $nssCa^{2+}$ records from EDML and TALDICE. We attribute these abrupt shifts to changes in high latitude atmospheric circulation either reducing the uplift of dust in Patagonia or its atmospheric transport efficiency towards Antarctica. Using the more climatologically representative logarithmic scale to plot the high resolution dust flux of the Dome ice core (Fig. 7b and c), we can also identify some high frequency variations in the dust flux records over the warm phase of the AIM. Due to different resolutions and variability levels, it is not yet possible to detect whether sharp dust changes coincide with those of $\delta^{18}O$. The strong flux reduction occurring on vertical bar b for both AIM 8 and 12, i.e. at the beginning of the $\delta^{18}O$ plateau at EDML, is clearly visible. Moreover, we observe a "cold reversal" like pattern during the warming phases of both AIM 8 and 12 on the dust flux at EDC (marked R between bars b and c on Fig. 7b and c). Within the chronological uncertainties, this corresponds well to the slight cooling identified above on the high resolution profile of TALDICE (marked L between bars b and c on Fig. 7b and c).

Dust records therefore depict changes in atmospheric circulation during the transition from phase 1 to phase 2 of AIM 8 and AIM 12 that support fast atmospheric circulation reorganization taking place in addition to the general bipolar seesaw pattern. This pattern is less clearly imprinted in d-excess, and only visible for some of the d-excess data (EDC, TALDICE), during this transition and abrupt Greenland warming.

4.2. Bipolar climate and global atmospheric composition during AIM8

Here, we use the multi-proxy picture of Greenland and global atmospheric composition changes occurring during AIM 8 (Bock et al., 2010; Ahn et al., 2012; Chappellaz et al., 2013) transferred by Guillevic et al. (2014) on GICC05, together with the synchronized Antarctic records on AICC2012.

In Greenland, we use here the NEEM ice core, where a temperature reconstruction based on $\delta^{15}N$ is available for AIM8. We first stress the same patterns depicted in this temperature reconstruction and ice $\delta^{18}O$: the first long and stable cold phase (stadial) lasts ~1730 years (~39875 ka b 1950 to ~38145 ka b 1950 on the GICC05 – AICC2012 timescale), when an abrupt temperature increase of 10.4 ± 1.5 °C leads to a warm interstadial lasting more

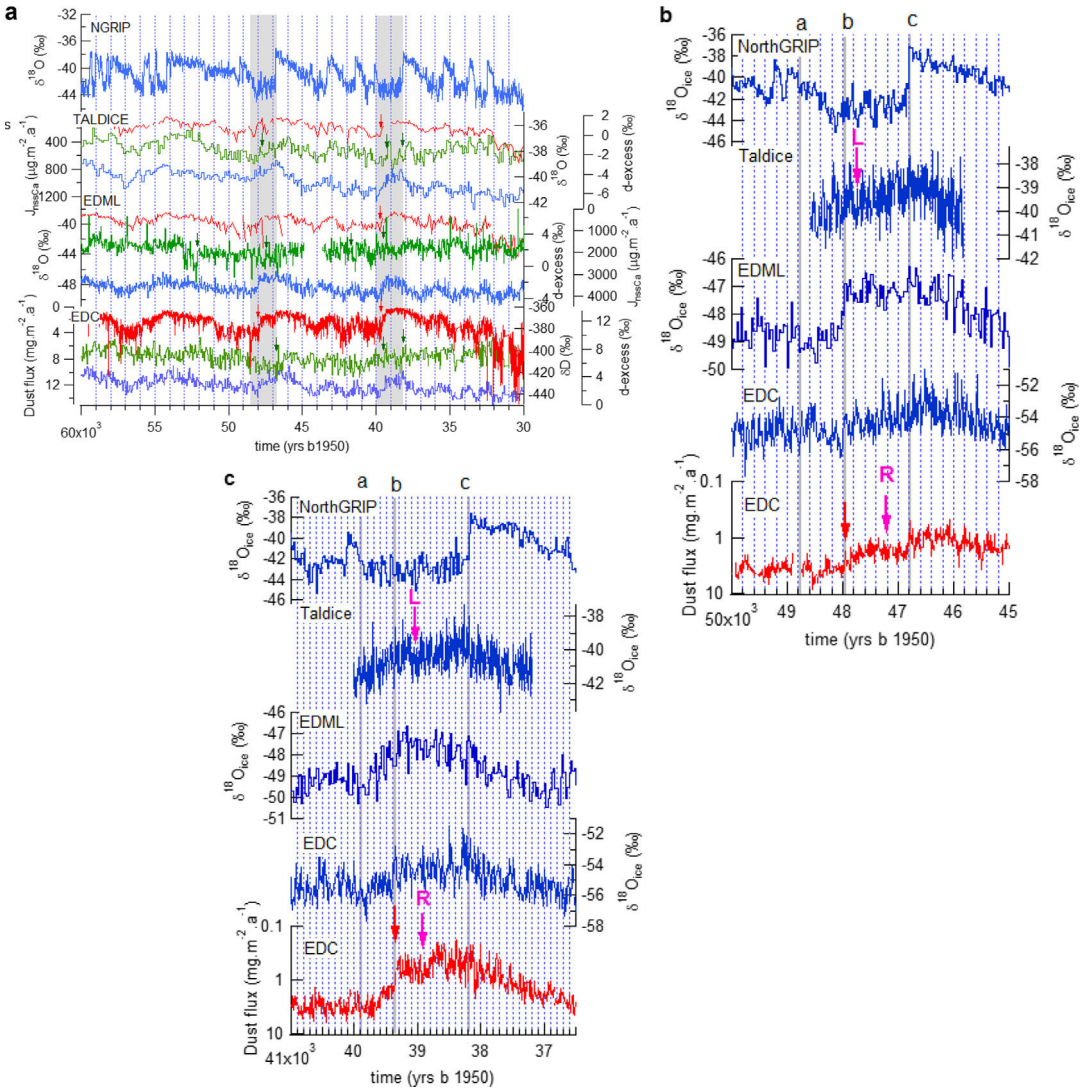

Fig. 7. a) comparison between water stable isotope records ($\delta^{18}O$ or deuterium) (blue), dust (EDC, on reversed axis) or $nssCa^{2+}$ (TALDICE and EDML, on reversed axis) flux records (red) and d-excess records (green). Gray rectangles indicate GS 9 and 13 and red/green arrows the marked changes in dust flux/d-excess records. b) and c) comparison between high resolution water records at TALDICE and EDC with high resolution dust flux (running median of EDC dust flux at 10 cm resolution in logarithmic scale) at EDC for AIM 12 (b) and 8 (c). The red arrows is the same as in 7a and the pink arrows indicate the "cold reversal" like pattern identified in the dust record (R) and in the TALDICE water isotope records (L).

than 1200 years (Guillevic et al., 2013). While no sub-event can be identified during GS 9 in Greenland temperature reconstructions, more information emerges from proxy records which are sensitive to low latitude climate.

Continuous CH_4 measurements performed with a laser analyzer provide an unprecedented high resolution record at NEEM (Chappellaz et al., 2013), which unveils sub-millennial variations in CH_4 without a counter-part in Greenland ice $\delta^{18}O$. Several centuries after the onset of GS 9, at ~39.3 ka b 1950, when Greenland temperature is cold and stable, a small increase in CH_4 is detected and probably caused by changes in low latitude methane production (Dällenbach et al., 2000). Other parameters measured in Greenland ice cores, hence without chronological biases, confirm the occurrence of low latitude climatic shifts, several centuries after the onset of GS 9. Guillevic et al. (2014) show that NEEM ^{17}O-excess and $\delta^{18}O_{atm}$ remain stable over GIS 9 and the first part of GS 9, i.e. until 39.3 ka b 1950 on the AICC2012 timescale. While they do not record any variability at the time of abrupt Greenland cooling (at the beginning of GS 9), ^{17}O-excess ($\delta^{18}O_{atm}$) is showing a significant decrease (increase) at 39.3 ka b 1950, i.e. 600 years after the onset of GS 9. ^{17}O-excess is defined by analogy to d-excess as the deviation of $\delta^{17}O$ from the $\delta^{17}O$ vs $\delta^{18}O$ meteoric water line as ^{17}O-excess $= \ln(\delta^{17}O + 1) - 0.528 * \ln(\delta^{18}O + 1)$. In Greenland ice cores, it reflects changes in the evaporative conditions of the low latitudes oceanic moisture sources (Landais et al., 2012) so that an increase in ^{17}O-excess is directly linked to a decrease of relative humidity at evaporation. This is due to the influence of kinetic fractionation during evaporation of water (the drier the atmosphere, the stronger the kinetic fractionation and the higher the ^{17}O-excess). $\delta^{18}O_{atm}$ is an integrated tracer of changes in biosphere productivity and low latitudes water cycle (Bender et al., 1994b). Modifications of the low latitude hydrological cycle during DO events strongly influence the $\delta^{18}O$ of meteoric water in the low latitudes (Pausata et al., 2011). This signal is transmitted to $\delta^{18}O_{atm}$ through evapotranspiration in plants and photosynthesis. The strong similarities between the $\delta^{18}O_{atm}$ signal and the calcite $\delta^{18}O$ of low latitude speleothems also strongly suggests that $\delta^{18}O_{atm}$ is a direct tracer of low latitude hydrological cycle in the air trapped in ice core.

About 600 years after the onset of GS 9, the concomitant changes recorded in $\delta^{18}O_{atm}$, ^{17}O-excess and CH_4 reflect changes in

low latitude climate and water cycle, probably induced by a southward shift in the ITCZ occurring without fingerprint in Greenland temperature (Guillevic et al., 2014). Similarly, we suggest that a northward ITCZ shift explains the changes recorded at 38.6 ka b 1950, about 400 years before the abrupt Greenland temperature warming marking the end of GS 9. This encompasses an increase of ^{17}O-excess by ~20 ppm and a decrease of the δD of CH_4 by more than 10‰, consistent with changes in the low latitude precipitation isotopic composition (Bock et al., 2010).

A finer structure of changes within GS 9 is further supported by a highly resolved atmospheric CO_2 concentration obtained from the Antarctic Byrd ice (Ahn et al., 2012). The 20 ppm CO_2 increase during GS 9/AIM 8 occurs in two main steps, at ~39.3 ka b 1950 and at ~38.15 ka BP, punctuated by an intermediate smaller step at 38.6 ka b 1950 (Fig. 8).

The evolution of the Antarctic $\delta^{18}O$ records presents synchronicity with the sequence of changes within GS 9/AIM 8 (Fig. 5). The changes in CH_4, CO_2, $\delta^{18}O_{atm}$ and in ^{17}O-excess at 39.3 ka BP occur in phase (within age scale uncertainties) with the AIM 8 phase 1 and the increase to the EDML plateau (between vertical bars a and b, Figs. 6b, c and 8). We therefore identify simultaneous changes in low latitudes and Antarctic climate without any fingerprint in Greenland climate.

As in Guillevic et al. (2014) and as already observed from comparison of Greenland ice cores and lower latitudes marine cores (Sanchez Goni et al., 2008), we therefore conclude that Greenland climate during GS9 is decoupled from climate changes occurring at lower latitudes. During stadials, the onset of the iceberg rafted discharge appears delayed with respect to the collapse of the North Atlantic Deep Water (NADW) formation (Hall et al., 2006; Jonkers et al., 2010), itself often associated with the North Atlantic/Greenland surface temperature cooling. An explanation for this lag has been suggested by Marcott et al. (2011) and Alvarez-Solas et al. (2013). They argue that the collapse of NADW formation, leading to the strong Greenland cooling, induces a slow sub-surface warming in North Atlantic, which would then trigger the iceberg discharge. Delays between abrupt North Atlantic cooling and the Heinrich event are therefore expected to reflect the duration required for sufficient heat accumulation in subsurface to trigger an iceberg discharge. Our structure is consistent with a lag between North Atlantic/Greenland cooling and a strong iceberg discharge which can then affect the atmospheric circulation at lower latitudes. Note that the recent modeling study of Roberts et al. (2014) shows that changes in topography following a strong iceberg discharge could also have a direct impact on North Atlantic climate. This is not obvious from Greenland records where no clear signature of Heinrich event has been detected (e.g. Guillevic et al., 2014).

We now summarize our findings for AIM 8. As predicted by the bipolar seesaw thermodynamical model, we observe (i) that the onset of Antarctic warming coincides with Greenland cooling, and (ii) that Greenland abrupt warming marks the beginning of Antarctic cooling. During GI 8, both Greenland and Antarctica are cooling in parallel. In addition to the seesaw pattern, the inflexion in Antarctic warming that we have identified during AIM8, most strongly recorded in EDML (start of a plateau) occurs in phase (within dating uncertainties) with low latitude climatic changes at 39.3 ka BP affecting sources of Greenland moisture as well as global atmospheric composition (CH_4, CO_2, $\delta^{18}O_{atm}$) and attributed to a southward ITCZ shift. While it has no fingerprint in Greenland temperature, this event marks the end of the first rapid increase in Antarctic temperature during AIM8, as well as rapid large-scale atmospheric circulation reorganizations from low latitudes (ITCZ southward shift) to high southern latitudes (as depicted by Antarctic dust and d-excess). We conclude that low latitudes climatic

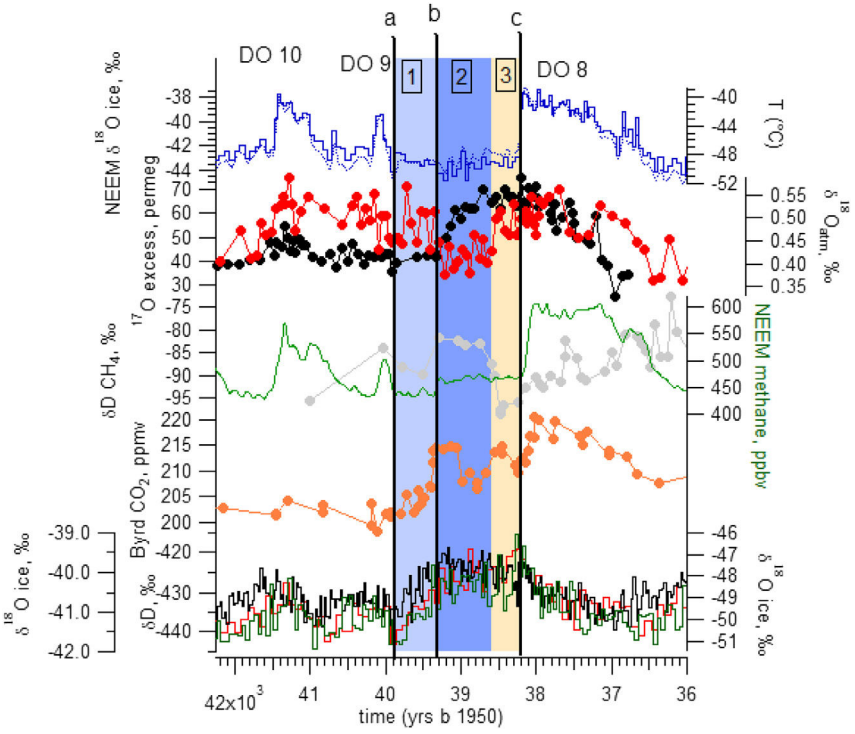

Fig. 8. Expanded from Guillevic et al. (2014). From top to bottom: NEEM $\delta^{18}O$ ice and reconstructed temperature (based on $\delta^{15}N$); NEEM ^{17}O-excess (red) and $\delta^{18}O_{atm}$ (black); NEEM methane concentration (Chappellaz et al., 2013, green) and NorthGRIP δD of CH_4 (Bock et al., 2010, gray), Byrd CO_2 (Ahn et al., 2012, orange) and Antarctic ice core $\delta^{18}O$ (black, EDML; red, TALDICE; green, EDC). All records have been synchronized on AICC2012. The vertical colored rectangles depict three phases within GS 9, identified in the Greenland records. The vertical bars a, b and c refer to the separation between phases of the AIM identified on Figs. 5 and 6.

changes during the course of a Greenland stadial complicate the classical picture of the bipolar seesaw. The decoupling between low and high latitudes during the Greenland stadial may be linked with a delayed iceberg discharge during the stadial due to subsurface warming as explained in the previous paragraph.

Simulations performed with coupled ocean-atmosphere models, forced by freshwater hosing in the North Atlantic in order to depict a millennial scale variability, show some decoupling between Greenland temperature (mostly affected by surface conditions, e.g. sea-ice) and AMOC strength. Otto-Bliesner and Brady (2010) performed an idealized experiment where a massive freshwater flux (1 Sv) is applied during 100 years and obtained a gradual AMOC reduction within 100 years and a slow recovery over the next 500 years. The associated simulated Greenland temperature shows an abrupt cooling of about 6 °C at the beginning of the freshwater flux in response to very fast sea-ice area increase in the North Hemisphere and a slow return to initial conditions following the AMOC response. The simulated temperature response is anti-phased with AMOC in the South Atlantic and more gradual in the Antarctic regions. In another study investigating the role of realistic geographic freshwater forcing in a coupled climate model, Roche et al. (2010) found also a slight decoupling between simulated Greenland temperatures and AMOC strength, the latter being delayed when the AMOC is close to a complete shutdown, while the simulated temperature in Greenland is more sensitive to surface conditions in the Nordic Seas. In particular, they showed that the occurrence of deep convection in the Nordic Seas is a prime control on sea-ice extent, recovery time of the AMOC and Greenland temperature anomalies. Finally Roche et al. (2010) found that the Antarctic warming is weak and delayed with respect to the peak Greenland cooling. Even if the last feature is not obvious in the ice core data, it shows that the modeled climatic evolution in response to freshwater fluxes can thus be different from the simple bipolar seesaw idealized by Stocker and Johnsen (2003).

5. Conclusions and perspectives

Despite uncertainties associated with chronologies of East Antarctic ice cores, the AICC2012 approach provides an accurate framework to investigate the bipolar patterns of glacial climate variability at the millennial time scale, and at the multi-centennial time scale when sufficient stratigraphic links are available, such as for the period close to the Laschamp event.

Common features of Antarctic climate variability are evidenced in a $\delta^{18}O$ stack record. Precise synchronization of the different ice core records reveals regional differences. At EDML, AIM 8 and AIM 12 are marked by a fast $\delta^{18}O$ increase, followed by a plateau, while TALDICE and EDC depict a more gradual increase, with reduced rate of warming when EDML reaches this plateau. High resolution data from EDC and TALDICE further depict an optimum at this inflexion point and sharp warm events at EDC associated with the warm AIM phases and inflexion points during the Antarctic warming.

Large scale features of Antarctic $\delta^{18}O$ variations are consistent with the overall seesaw pattern associated with changes in Atlantic ocean circulation modulated by the inertia of the southern Ocean, such as an overall warming during the Greenland cold phases, ending when Greenland is abruptly warming. However, sub-millennial features of Antarctic variability occur without a Greenland counterpart. This is for instance the case for the two step patterns occurring during the warming phase of AIM 8 and AIM 12. Antarctic ice core data related to dust deposition and moisture origin (d-excess) reveal parallel changes in high latitude atmospheric circulation, with a very clear signal in dust.

During the warming phase of AIM 8, Greenland temperature is cold and stable, while changes in Greenland moisture origin and global atmospheric composition suggest reorganizations of low latitude atmospheric circulation, probably associated with a southward ITCZ shift, in parallel with the inflexion identified in the Antarctic ice cores.

During long stadials, there is no fingerprint of Heinrich events in Greenland temperature but a more complex pattern in the bipolar structure of events than described in the conceptual bipolar seesaw thermodynamical model. We suggest that, during these long cold phases, Greenland temperature is decoupled from changes in AMOC and changes in low latitude atmospheric circulation. Our Antarctic high resolution data suggest fast teleconnections between changes in low latitude atmospheric circulation and Antarctic temperature, consistent with recent observations (Ding et al., 2011). The bipolar seesaw concept therefore does not correctly reflect the complexity of processes at play.

In this study, we thus challenge (i) reconstructions of past Greenland temperature based on the inversion of the bipolar seesaw model using long Antarctic climate records (Barker et al., 2011), and (ii) the use of Greenland ice core records as a reference for the timing of climatic changes in North Atlantic during the Last Glacial period. During cold phases, the wide extent of sea ice around Greenland probably isolates this region from climate changes occurring at lower latitudes.

Acknowledgments

This work is a contribution to the European Project for Ice Coring in Antarctica (EPICA), a joint European Science Foundation/European Commission scientific program, funded by the EU and by national contributions from Belgium, Denmark, France, Germany, Italy, the Netherlands, Norway, Sweden, Switzerland and the United Kingdom. The main logistic support was provided by IPEV and PNRA (at Dome C) and AWI (at Dronning Maud Land). The Talos Dome Ice core Project (TALDICE), a joint European programme, is funded by national contributions from Italy, France, Germany, Switzerland and the UK. Primary logistical support was provided by PNRA at Talos Dome. F. Lambert acknowledges support by Project CONICYT/FONDAP 15110009 and NC120066. This work has benefited from supports from the French ANR (Agence Nationale de Recherche), the foundation Ars et Cuttoli and the ERC program COMBINISO (306045). The authors thank the reviewer for his important inputs that improved the quality of the final manuscript.

References

Adkins, J.F., 2013. The role of deep ocean circulation in setting glacial climates. Paleoceanography 28 (3), 539–561.

Ahn, J., Brook, E., Schmittner, A., Kreutz, K., 2012. Abrupt change in atmospheric CO_2 during the last ice age. Geophys. Res. Lett. 39, L18771. http://dx.doi.org/10.1029/2012GL053018.

Alvarez-Solas, J., Ramstein, G., 2011. On the triggering mechanism of Heinrich events. Proc. Natl. Acad. Sci. U. S. A. 108, E1359–E1360. http://dx.doi.org/10.1073/pnas.1116575108.

Alvarez-Solas, J., Robinson, A., Montoya, M., Ritz, C., 2013. Iceberg discharges of the last glacial period driven by oceanic circulation changes. Proc. Natl. Acad. Sci. U. S. A. http://dx.doi.org/10.1073/pnas.1306622110.

Anderson, R.F., Ali, S., Bradtmiller, L.I., Nielsen, S.H.H., Fleisher, M.Q., Anderson, B.E., Burckle, L.H., 2009. Wind-driven upwelling in the Southern Ocean and the deglacial rise in atmospheric CO_2. Science 323, 1443–1448.

Arzel, O., Colin de Verdière, A., England, M.H., 2010. The role of oceanic heat transport and wind-stress forcing in abrupt millennial-scale climate transitions. J. Clim. 23, 2233–2256.

Arzel, O., England, M.H., Colin de Verdière, A., Huck, T., 2012. Abrupt millennial variability and interdecadal-interstadial oscillations in a global coupled model: sensitivity to the background climate state. Clim. Dyn. 39, 259–275.

Barker, S., Diz, P., Vautravers, M.J., Pike, J., Knorr, G., Hall, I.R., Broecker, W.S., 2009. Interhemispheric Atlantic seesaw response during the last deglaciation. Nature 457, 1097–1102.

Barker, S., Knorr, G., Edwards, R.L., Parrenin, F., Putnam, A.E., Skinner, L.C., Wolff, E., Ziegler, M., 2011. 800,000 years of abrupt climate variability. Science 334 (6054), 347–351.

Basile, I., Grousset, F.E., Revel, M., Petit, J.R., Biscaye, P.E., Barkov, N.I., 1997. Patagonian origin of glacial dust deposited in East Antarctica (Vostok and Dome C) during glacial stages 2, 4 and 6. Earth Planet. Sci. Lett. 146, 573–589. http://dx.doi.org/10.1016/S0012-821X(96)00255-5.

Bazin, L., Landais, A., Lemieux-Dudon, B., Toyé Mahamadou Kele, H., Veres, D., Parrenin, F., Martinerie, P., Ritz, C., Capron, E., Lipenkov, V., Loutre, M.-F., Raynaud, D., Vinther, B., Svensson, A., Rasmussen, S.O., Severi, M., Blunier, T., Leuenberger, M., Fischer, H., Masson-Delmotte, V., Chappellaz, J., Wolff, E., 2013. An optimized multi-proxy, multi-site Antarctic ice and gas orbital chronology (AICC2012): 120–800 ka. Clim. Past 9, 1715–1731. http://dx.doi.org/10.5194/cp-9-1715-2013.

Bazin, L., Lemieux-Dudon, B., Landais, A., Guillevic, M., Kindler, P., Parrenin, F., Martinerie, P., 2014. Optimisation of glaciological parameters for ice core chronology by implementing counted layers between identified depth levels. Clim. Past Discuss. 10, 3585–3616.

Bender, M., Sowers, T., Dickson, M.-L., Orchardo, J., Grootes, P., Mayewski, P., Meese, D., 1994a. Climate connections between Greenland and Antarctica during the last 100,000 years. Nature 372, 663–666.

Bender, M., Sowers, T., Labeyrie, L., 1994b. The Dole effect and its variations during the last 130,000 years as measured in the Vostok ice core. Global Biogeochem. Cycles 8, 363–376. http://dx.doi.org/10.1029/94GB00724.

Bentley, M.J., Fogwill, C.J., Le Brocq, A.M., Hubbard, A.L., Sugden, D.E., Dunai, T., Freeman, S.P.H.T., 2010. Deglacial history of the West Antarctic Ice Sheet in the Weddell Sea embayment: constraints on past ice volume change. Geology 38, 411–414.

Blunier, T., Brook, E.J., 2001. Timing of millennial-scale climate change in Antarctica and Greenland during the last glacial period. Science 291, 109–112.

Blunier, T., Chappellaz, J., Schwander, J., Dällenbach, A., Stauffer, B., Stocker, T.F., Raynaud, D., Jouzel, J., Clausen, H.B., Hammer, C.U., Johnsen, S.J., 1998. Asynchrony of Antarctic and Greenland climate change during the last glacial period. Nature 394, 739–743.

Bock, M., Schmitt, J., Möller, L., Spahni, R., Blunier, T., Fischer, H., 2010. Hydrogen isotopes preclude marine hydrate CH_4 emissions at the onset of Dansgaard-Oeschger events. Science 10 (328), 1686–1689. http://dx.doi.org/10.1126/science.1187651.

Bond, G., Heinrich, H., Broecker, W., Labeyrie, L., Mcmanus, J., Andrews, J., Huon, S., Jantschik, R., Clasen, S., Simet, C., 1992. Evidence for massive discharges of icebergs into the North Atlantic Ocean during the last glacial period. Nature 360, 245–249.

Broccoli, A.J., Dahl, K.A., Stouffer, R.J., 2006. The response of the ITCZ to Northern Hemisphere cooling. Geophys. Res. Lett. 33, L01702. http://dx.doi.org/10.1029/2005GL024546.

Broecker, W.S., 1991. The great ocean conveyor. Oceanography 4, 79–89.

Broecker, W.S., 1998. Paleocean circulation during the last deglaciation: a bipolar seesaw? Paleoceanography 13, 119–121.

Broecker, W.S., Bond, G.C., Klas, M., Clark, E., McManus, J.F., 1992. Origin of the northern Atlantic's Heinrich events. Clim. Dyn. 6, 265–273.

Buiron, D., Chappellaz, J., Stenni, B., Frezzotti, M., Baumgartner, M., Capron, E., Landais, A., Lemieux-Dudon, B., Masson-Delmotte, V., Montagnat, M., Parrenin, F., Schilt, A., 2011. TALDICE-1 age scale of the Talos Dome deep ice core, East Antarctica. Clim. Past 7, 1–16. http://dx.doi.org/10.5194/cp-7-1-2011.

Buiron, D., Stenni, B., Chappellaz, J., Landais, A., Baumgartner, M., Bonazza, M., Capron, E., Frezzotti, M., Kageyama, M., Lemieux-Dudon, B., Masson-Delmotte, V., Parrenin, F., Schilt, A., Selmo, E., Severi, M., Swingedouw, D., Udisti, R., 2012. Regional imprints of millennial variability during the MIS 3 period around Antarctica. Quat. Sci. Rev. 48, 99–112.

Buizert, C., Gkinis, V., Severinghaus, J.P., He, F., Lecavalier, B.S., Kindler, P., Leuenberger, M., Carlson, E., Vinther, B., Masson-Delmotte, V., White, J.W.C., Liu, Z., Otto-Bliesner, B., Brook, E.J., 2014. Greenland temperature response to climate forcing during the Last Deglaciation. Science 345, 1177–1180. http://dx.doi.org/10.1126/science.1254961.

Cane, M., Clement, A.C., 1999. A Role for the Tropical Pacific Coupled Ocean-atmosphere System on Milankovitch and Millennial Timescales. Part I: a Modeling Study of Tropical Pacific Variability, Mechanism of Global Climate Change at Millennial Time Scales. In: Geophysical Monograph, 1 12. American Geophysical Union.

Capron, E., Landais, A., Chappellaz, J., Schilt, A., Buiron, D., Masson-Delmotte, V., Jouzel, J., Lemieux-Dudon, B., Govin, A., Loulergue, L., Leuenberger, M., Mayer, H., Oerter, H., Dahl-Jensen, D., Johnsen, S., Stenni, B., 2010a. Millennial-scale climatic variability over the last glacial period: Greenland-Antarctic sequences of events over Marine Isotopic Stage (MIS) 5 compared to MIS 3. Clim. Past 6, 1–49.

Capron, E., Landais, A., Lemieux, B., Schilt, A., Loulergue, L., Buiron, D., Chappellaz, J., Masson-Delmotte, V., Dahl-Jensen, D., Johnsen, S., Leuenberger, M., Oerter, H., 2010b. Synchronising EDML and NorthGRIP ice cores using δ18O of atmospheric oxygen (δ18Oatm) and CH4 measurements over MIS5 (80-123 kyr). QSR 1–2, 222–234.

Capron, E., Landais, A., Chappellaz, J., Buiron, D., Fischer, H., Johnsen, S., Jouzel, J., Leuenberger, M., Masson-Delmotte, V., Stocker, T.F., 2012. A global picture of the first abrupt climatic event occurring during the last glacial inception. GRL. http://dx.doi.org/10.1029/2012GL052656.

Carlson, A.E., Winsor, K., 2012. Northern Hemisphere ice-sheet responses to past climate warming. Nat. Geosci. 5, 607–613.

Chappellaz, J., Blunier, T., Raynaud, D., Barnola, J., Schwander, J., Stauffer, B., 1993. Synchronous changes in atmospheric CH4 and Greenland climate between 40 and 8 kyr BP. Nature 366, 443–445.

Chappellaz, J., Stowasser, C., Blunier, T., Baslev-Clausen, D., Brook, E.J., Dallmayr, R., Faïn, X., Lee, J.E., Mitchell, L.E., Pascual, O., Romanini, D., Rosen, J., Schüpbach, S., 2013. High-resolution glacial and deglacial record of atmospheric methane by continuous flow and laser spectrometer analysis along the NEEM ice core. Clim. Past 9, 2579–2593. http://dx.doi.org/10.5194/cp-9-2579-2013.

Clark, P.U., Dyke, A.S., Shakun, J.D., Carlson, A.E., Clark, J., Wohlfarth, B., Mitrovica, J.X., Hostetler, S.W., McCabe, A.M., 2009. The Last Glacial Maximum. Science 325, 710–714.

Clement, A.C., Peterson, L.C., 2008. Mechanisms of abrupt climate change of the last glacial period. Rev. Geophys. 46, RG4002. http://dx.doi.org/10.1029/2006RG000204.

Colin de Verdière, A., te Raa, L., 2010. Weak oceanic heat transport as a cause of the instability of glacial climates. Clim. Dyn. 35, 1237–1256.

Dahl, K.D., Oppo, D.W., Eglinton, T.I., Hughen, K.A., Curry, W.B., Sirocko, F., 2005. Terrigenous plant wax inputs to the Arabian sea: implications for the reconstruction of winds associated with the Indian Monsoon. Geochim. Cosmochim. Acta 69, 2547–2558.

Dällenbach, A., Blunier, T., Flückiger, J., Stauffer, B., Chappellaz, J., Raynaud, D., 2000. Changes in the atmospheric CH_4 gradient between Greenland and Antarctica during the Last Glacial and the transition to the Holocene. Geophys. Res. Lett. 27, 1005–1008.

Dansgaard, W., Johnsen, S.J., Clausen, H.B., Dahl-Jensen, D., Gundestrup, N.S., Hammer, C.U., Hvidberg, C.S., Steffensen, J.P., Sveinbjörnsdottir, A.E., Jouzel, J., Bond, G., 1993. Evidence for general instability of past climate from a 250-kyr ice-core record. Nature 364, 218–220.

Delmonte, B., Andersson, P.S., Hansson, M., Schöberg, H., Petit, J.R., Basile-Doelsch, I., Maggi, V., 2008. Aeolian dust in East Antarctica (EPICA-Dome C and Vostok): provenance during glacial ages over the last 800 kyr. Geophys. Res. Lett. 35, 2–7. http://dx.doi.org/10.1029/2008GL033382.

Deschamps, P., Durand, N., Bard, E., Hamelin, B., Camoin, G., Thomas, A.L., Henderson, G.M., Okuno, J., Yokoyama, Y., 2012. Ice-sheet collapse and sea-level rise at the Bolling warming 14,600 years ago. Nature 483, 559–564.

Ding, Q., Steig, E.J., Battisti, D.S., Küttel, M., 2011. Winter warming in West Antarctica caused by central tropical Pacific warming. Nat. Geosci. 4, 398–403. http://dx.doi.org/10.1038/ngeo1129.

Elliot, M., Labeyrie, L., Duplessy, J.C., 2002. Changes in North Atlantic deep-water formation associated with the Dansgaard-Oeschger temperature oscillations (10–60 ka). Quat. Sci. Rev. 21, 1153–1165.

EPICA Community Members, 2006. One-to-one coupling of glacial climate variability in Greenland and Antarctica. Nature 444, 195–198. http://dx.doi.org/10.1038/nature05301.

Ganopolski, A., 2003. Glacial integrative modelling. Philos. Trans. R. Soc. A 361, 1871–1884.

Ganopolski, A., Rahmstorf, S., 2001. Rapid changes of glacial climate simulated in a coupled climate model. Nature 409, 153–158.

Ganopolski, A., Calov, R., Claussen, M., 2010. Simulation of the last glacial cycle with a coupled climate ice-sheet model of intermediate complexity. Clim. Past 6, 229–244. http://dx.doi.org/10.5194/cp-6-229-2010.

Golledge, N.R., Menviel, L., Carter, L., Fogwill, C.J., England, M.H., Cortese, G., Levy, R.H., 2014. Antarctic contribution to meltwater pulse 1A from reduced Southern Ocean overturning. Nat. Commun. 5. Article number: 5107.

Goujon, C., Barnola, J.M., Ritz, C., 2003. Modeling the densification of polar firn including heat diffusion: application to close-off characteristics and gas isotopic fractionation for Antarctica and Greenland sites. J. Geophys. Res. 108, 101–1018.

Gregoire, L.J., Payne, A.J., Valdes, P.J., 2012. Deglacial rapid sea level rises caused by ice-sheet saddle collapses. Nature 487 (7406), 219–222. http://dx.doi.org/10.1038/nature11257.

Grootes, P.M., Stulver, M., White, J.W.C., Johnsen, S., Jouzel, J., 1993. Comparison of oxygen isotope records from the GISP2 and GRIP Greenland ice cores. Nature 366, 552–554.

Grousset, F.E., Labeyrie, L., Sinko, J.A., Cremer, M., Bond, G., Duprat, J., Cortijo, E., Huon, S., 1993. Patterns of ice rafted detritus in the glacial North Atlantic (40–55°N). Paleoceanography 8 (2), 175–192.

Guillevic, M., Bazin, L., Landais, A., Kindler, P., Orsi, A., Masson-Delmotte, V., Blunier, T., Buchardt, S.L., Capron, E., Leuenberger, M., Martinerie, P., Prié, F., Vinther, B.M., 2013. Spatial gradients of temperature, accumulation and d18O-ice in Greenland over a 5 series of Dansgaard–Oeschger events. Clim. Past. 9, 1029–1051. http://dx.doi.org/10.5194/cp-9-1029-2013.

Guillevic, M., Bazin, L., Landais, A., Stowasser, C., Masson-Delmotte, V., Blunier, T., Eynaud, F., Falourd, S., Michel, E., Minster, B., Popp, T., Prié, F., Vinther, B.M., 2014. Multi-proxy fingerprint of Heinrich event 4 in Greenland ice core records. Clim. Past Discuss. 10, 1179–1222. http://dx.doi.org/10.5194/cpd-10-1179-2014.

Guillou, H., Singer, B.S., Laj, C., Kissel, C., Scaillet, S., Jicha, B.R., 2004. On the age of the Laschamp geomagnetic excursion. Earth Planet. Sci. Lett. 227, 331–343.

Hall, I.R., Moran, S.B., Zahn, R., Knutz, P.C., Shen, C.C., Edwards, R.L., 2006. Accelerated drawdown of meridional overturning in the late-glacial Atlantic triggered by transient pre-H event freshwater perturbation. Geophys. Res. Lett. 33, L16616. http://dx.doi.org/10.1029/2006GL026239.

Heinrich, H., 1988. Origin and consequences of cyclic ice rafting in the Northeast Atlantic Ocean during the past 130000 years. Quat. Res. 29, 142–152.

Hemming, S.R., 2004. Heinrich events: massive late Pleistocene detritus layers of the North Atlantic and their global climate imprint. Rev. Geophys. 42, RG1005. http://dx.doi.org/10.1029/2003RG000128.
Hörhold, M.W., Laepple, T., Freitag, J., Bigler, M., Fischer, H., Kipfstuhl, S., 2012. On the impact of impurities on the densification of polar firn. Earth Planet. Sci. Lett. 325–326, 93–99. http://dx.doi.org/10.1016/j.epsl.2011.12.022.
Huber, C., Leuenberger, M., Spahni, R., Flückiger, J., Schwander, J., Stocker, T., Johnsen, S., Landais, A., Jouzel, J., 2006. Isotope calibrated Greenland temperature record over Marine Isotope Stage 3 and its relation to CH_4. Earth Planet. Sci. Lett. 243, 504–519.
Jonkers, L., Moros, M., Prins, M.A., Dokken, T., Dahl, C.A., Dijkstra, N., Perner, K., Brummer, G.-J.A., 2010. A reconstruction of sea surface warming in the northern North Atlantic during MIS 3 ice-rafting events. Quat. Sci. Rev. 29, 1791–1800.
Jouzel, J., Lorius, C., Johnsen, S.J., Grootes, P., 1994. Climate instabilities – Greenland and Antarctic records. C. R. l'acad. Sci. série II 319 (1), 65–77.
Jouzel, J., Masson-Delmotte, V., Cattani, O., Dreyfus, G., Falourd, S., Hoffmann, G., Minster, B., Nouet, J., Barnola, J.-M., Chappellaz, J., Fischer, H., Gallet, J.C., Johnsen, S.J., Leuenberger, M., Loulergue, L., Luethi, D., Oerter, H., Parrenin, F., Raisbeck, G., Raynaud, D., Schilt, A., Schwander, J., Selmo, E., Souchez, R., Spahni, R., Stauffer, B., Steffensen, J.P., Stenni, B., Stocker, T., Tison, J.-L., Werner, M., Wolff, E., 2007. Orbital and millennial Antarctic climate variability over the past 800,000 years. Science 317 (5839), 793–797. http://dx.doi.org/10.1126/science.1141038.
Jouzel, J., Delaygue, G., Landais, A., Masson-Delmotte, V., Risi, C., Vimeux, F., 2013. Water isotopes as tools to document oceanic sources of precipitation. Water Resour. Res. 49 (11), 7469–7486. http://dx.doi.org/10.1002/2013WR013508.
Kageyama, M., Paul, A., Roche, D.M., van Meerbeeck, C.J., 2010. Modelling glacial climatic millennial-scale variability related to changes in the Atlantic meridional overturning circulation: a review. Quat. Sci. Rev. 29, 2931–2956.
Kageyama, M., Merkel, U., Otto-Bliesner, B., Prange, M., Abe-Ouchi, A., Lohmann, G., Ohgaito, R., Roche, D.M., Singarayer, J., Swingedouw, D., Zhang, X., 2013. Climatic impacts of fresh water hosing under Last Glacial Maximum conditions: a multi-model study. Clim. Past 9, 935–953.
Kilfeather, A.A., Cofaigh, C.Ó., Lloyd, J.M., Dowdeswell, J.A., Xu, S., Moreton, G., 2011. Ice-stream retreat and ice-shelf history in Marguerite Trough, Antarctic Peninsula: sedimentological and foraminiferal signatures. Geol. Soc. Am. Bull. 123, 997–1015.
Kindler, P., Guillevic, M., Baumgartner, M., Schwander, J., Landais, A., Leuenberger, M., 2014. Temperature reconstruction from 10 to 120 kyr b2k from the NGRIP ice core. Clim. Past 10, 887–902. http://dx.doi.org/10.5194/cp-10-887-2014.
Köhler, P., Knorr, G., Buiron, D., Lourantou, A., Chappellaz, J., 2011. Abrupt rise in atmospheric CO_2 at the onset of the Bølling/Allerød: in-situ ice core data versus true atmospheric signals. Clim. Past 7, 473–486. http://dx.doi.org/10.5194/cp-7-473-2011.
Krebs, U., Timmermann, A., 2007. Tropical air-sea interactions accelerate the recovery of the Atlantic Meridional overturning circulation after a major shutdown. J. Clim. 20, 4940–4956.
Labeyrie, L., Leclaire, H., Waelbroeck, C., Cortijo, E., Duplessy, J.-C., Vidal, L., Elliot, M., Le Coat, B., Auffret, G., 1999. Temporal variability of the surface and deep waters of the North West Atlantic Ocean at orbital and millennial scales. Mechanisms of Global Climate Change at Millennial Time Scales. In: Clark, P.U., Webb, R.S., Keigwin, D. (Eds.), Geophys. Monogr. Ser., vol. 112. AGU, Washington D. C., pp. 77–98.
Lambert, F., Bigler, M., Steffensen, J.P., Hutterli, M., Fischer, H., 2012. Centennial mineral dust variability in high-resolution ice core data from Dome C, Antarctica. Clim. Past 8, 609–623. http://dx.doi.org/10.5194/cp-8-609-2012.
Landais, A., Barnola, J.M., Kawamura, K., Caillon, N., Delmotte, M., Van Ommen, T., Dreyfus, G., Jouzel, J., Masson-Delmotte, V., Minster, B., Freitag, J., Leuenberger, M., Schwander, J., Huber, C., Etheridge, D., Morgan, V., 2006. Firn-air d15N in modern polar sites and glacial-interglacial ice: a model-data mismatch during glacial periods in Antarctica? Quat. Sci. Rev. 25 (1–2), 49–62.
Landais, A., Dreyfus, G., Capron, E., Masson-Delmotte, V., Sanchez-Goni, M., Desprat, S., Hoffmann, G., Jouzel, J., Leuenberger, M., Johnsen, S., 2007. What drives the millennial and orbital variations of d18Oatm? Quat. Sci. Rev. 29, 235–246. http://dx.doi.org/10.1016/j.quascirev.2009.07.005.
Landais, A., Steen-Larsen, H., Guillevic, M., Masson-Delmotte, V., Vinther, B., Winkler, R., 2012. Triple isotopic composition of oxygen in surface snow and water vapor at NEEM (Greenland). Geochim. Cosmochim. Acta 77, 304–316. http://dx.doi.org/10.1016/j.gca.2011.11.022.
Lemieux-Dudon, B., Blayo, E., Petit, J.R., Waelbroeck, C., Svensson, A., Ritz, C., Barnola, J.M., Narcisi, B.M., Parrenin, F., 2010. Consistent dating for Antarctic and Greenland ice cores. Quat. Sci. Rev. 29, 8–20.
Li, C., Battisti, D.S., Schrag, D.P., Tziperman, E., 2005. Abrupt climate shifts in Greenland due to displacements of the sea ice edge. Geophys. Res. Lett. 32 http://dx.doi.org/10.1029/2005GL023492.
Li, C., Battisti, D.S., Bitz, C.M., 2010. Can North Atlantic sea ice anomalies account for Dansgaard–Oeschger climate signals? J. Clim. 23, 5457–5475.
Liu, Z., Otto-Bliesner, B., He, F., Brady, E., Clark, P., Lynch-Steiglitz, J., Carlson, A., Curry, W., Brook, E., Jacob, R., Erickson, D., Kutzbach, J., Cheng, J., 2009. Transient simulation of Last Deglaciation with a new mechanism for Bolling-Allerod warming. Science 325, 310–314.
Loulergue, L., 2007. Contraintes chronologiques et biogeochimiques grace au methane dans la glace naturelle: une application aux forages du projet EPICA, 2007 (Ph.D. thesis). UJF, France.
Loulergue, L., Parrenin, F., Blunier, T., Barnola, J.-M., Spahni, R., Schilt, A., Raisbeck, G., Chappellaz, J., 2007. New constraints on the gas age-ice age difference along the EPICA ice cores, 0–50 kyr. Clim. Past 3, 527–540. http://dx.doi.org/10.5194/cp-3-527-2007.
MacAyeal, D.R., 1993. Binge/purge oscillations of the Laurentide ice sheet as a cause of the North Atlantic's Heinrich events. Paleoceanography 8 (6), 775–784.
Mackintosh, A., Golledge, N., Domack, E., Dunbar, R., Leventer, A., White, D., Pollard, D., DeConto, R., Fink, D., Zwartz, D., Gore, D., Lavoie, C., 2011. Retreat of the East Antarctic ice sheet during the last glacial termination. Nat. Geosci. 4, 95–202.
Marcott, S.A., Clark, P.U., Padman, L., Klinkhammer, G.P., Springer, S.R., Liu, Z., Otto-Bliesner, B.L., Carlson, A.E., Ungerer, A., Padman, J., He, F., Cheng, J., Schmittner, A., 2011. Ice-shelf collapse from subsurface warming as a trigger for Heinrich events. Proc. Natl. Acad. Sci. U. S. A. 108, 13415–13419. http://dx.doi.org/10.1073/pnas.1104772108.
Marshall, S.J., Clarke, G.K.C., 1997. A continuum mixture model of ice stream thermomechanics in the Laurentide Ice Sheet, 2. Application to the Hudson Strait Ice Stream. J. Geophys. Res. 102, 20,615–20,638.
Martrat, B., Grimalt, J.O., Shackleton, N.J., de Abreu, L., Hutterli, M., Stocker, T., 2007. Four climate cycles of recurring deep and surface water destabilizations on the Iberian margin. Science 317, 502–507.
McManus, J.F., Anderson, R., Broecker, W.S., Fleisher, M.Q., Higgins, S.M., 1998. Radiometrically determined sedimentary fluxes in the sub-polar North Atlantic during the last 140,000 years. Earth Planet. Sci. Lett. 155, 29–43.
McManus, J.F., Oppo, D.W., Cullen, J.L., 1999. A 0.5-million-year record of millennial-scale climate variability in the North Atlantic. Science 283, 971–975.
Meissner, K.J., Eby, M., Weaver, A.J., Saenko, O.A., 2006. CO_2 threshold for millennial-scale oscillations in the climate system: implications for global warming scenarios. Clim. Dyn. 30, 161–174.
Menviel, L., Timmermann, A., Friedrich, T., England, M.H., 2014. Hindcasting the continuum of Dansgaard–Oeschger variability: mechanisms, patterns and timing. Clim. Past 10, 63–77. http://dx.doi.org/10.5194/cp-10-63-2014.
NEEM Community Members, 2013. Eemian interglacial reconstructed from a Greenland folded ice core. Nature 493, 489–494.
North Greenland Ice Core Project Members, 2004. High-resolution record of Northern Hemisphere climate extending into the last interglacial period. Nature 431, 147–151.
Otto-Bliesner, B.L., Brady, E.C., 2010. The sensitivity of the climate response to the magnitude and location of freshwater forcing: last glacial maximum experiments. Quat. Sci. Rev. 29, 56–73. http://dx.doi.org/10.1016/j.quascirev.2009.07.004.
Paillard, D., Labeyrie, L.D., 1994. Role of the thermohaline circulation in the abrupt warming after Heinrich events. Nature 372, 162–164.
Parrenin, F., Petit, J.-R., Masson-Delmotte, V., Wolff, E., Basile-Doelsch, I., Jouzel, J., Lipenkov, V., Rasmussen, S.O., Schwander, J., Severi, M., Udisti, R., Veres, D., Vinther, B.M., 2012a. Volcanic synchronisation between the EPICA Dome C and Vostok ice cores (Antarctica) 0–145 kyr B. Clim. Past 8, 1031–1045.
Parrenin, F., Barker, S., Blunier, T., Chappellaz, J., Jouzel, J., Landais, A., Masson-Delmotte, V., Schwander, J., Veres, D., 2012b. On the gas-ice depth difference (Δdepth) along the EPICA Dome C ice core. Clim. Past 8, 1239–1255. http://dx.doi.org/10.5194/cp-8-1239-2012.
Pausata, F.S.R., Battisti, D.S., Nisancioglu, K.H., Bitz, C.M., 2011. Chinese stalagmite $d^{18}O$ controlled by changes in the Indian monsoon during a simulated Heinrich event. Nat. Geosci. 4, 474–480.
Pedro, J.B., Rasmussen, S.O., van Ommen, T.D., 2012. Tightened constraints on the time-lag between Antarctic temperature and CO_2 during the last deglaciation. Clim. Past 8, 1213–1221. http://dx.doi.org/10.5194/cp-8-1213-2012.
Pol, K., Debret, M., Masson-Delmotte, V., Capron, E., Cattani, O., Dreyfus, G., Falourd, S., Johnsen, S., Jouzel, J., Landais, A., Minster, B., Stenni, B., 2011. Links between MIS 11 millennial to sub-millennial climate variability and long term trends as revealed by new high resolution EPICA Dome C deuterium data – a comparison with the Holocene. Clim. Past 7, 437–450. http://dx.doi.org/10.5194/cp-7-437-2011.
Pol, K., Masson-Delmotte, V., Cattani, O., Debret, M., Falourd, S., Jouzel, J., Landais, A., Minster, B., Mudelsee, M., Schulz, M., Stenni, B., 2014. Climate variability features of the last interglacial in the East Antarctic EPICA Dome C ice core. Geophys. Res. Lett. 41 (11), 4004–4012. http://dx.doi.org/10.1002/2014GL059561.
Raisbeck, G.M., Yiou, F., Jouzel, J., Stocker, T.F., 2007. Direct north-south synchronization of abrupt climate change record in ice cores using Beryllium 10. Clim. Past 3, 541–547. http://dx.doi.org/10.5194/cp-3-541-2007.
Rasmussen, S.O., Abbott, P.M., Blunier, T., Bourne, A.J., Brook, E., Buchardt, S.L., Buizert, C., Chappellaz, J., Clausen, H.B., Cook, E., Dahl-Jensen, D., Davies, S.M., Guillevic, M., Kipfstuhl, S., Laepple, T., Seierstad, I.K., Severinghaus, J.P., Steffensen, J.P., Stowasser, C., Svensson, A., Vallelonga, P., Vinther, B.M., Wilhelms, F., Winstrup, M., 2013. A first chronology for the North Greenland Eemian Ice Drilling (NEEM) ice core. Clim. Past 9, 2713–2730. http://dx.doi.org/10.5194/cp-9-2713-2013.
Rind, D., Russell, G.L., Schmidt, G.A., Sheth, S., Collins, D., Demenocal, P., Teller, J., 2001. Effects of glacial meltwater in the GISS Coupled Atmosphere-Ocean Model: part II: a bi-polar seesaw in Atlantic Deep Water production. J. Geophys. Res. 106, 27355–27366. http://dx.doi.org/10.1029/2001JD000954.
Roberts, W.G.H., Valdes, P.J., Payne, A.J., 2014. Topography's crucial role in Heinrich events. PNAS 111 (47), 16688–16693. http://dx.doi.org/10.1073/pnas.1414882111.

Roche, D.M., Wiersma, A.P., Renssen, H., 2010. A systematic study of the impact of freshwater pulses with respect to different geographical locations. Clim. Dyn. 34, 997–1013.
Rosen, J.L., Brook, E.J., Severinghaus, J.P., Blunier, T., Mitchell, L.E., Lee, J.E., Edwards, J.S., Gkinis, V., 2014. An ice core record of near-synchronous global climate changes at the Bolling transition. Nat. Geosci. 7, 459–463. http://dx.doi.org/10.1038/ngeo2147.
Ruth, U., Barnola, J.-M., Beer, J., Bigler, M., Blunier, T., Castellano, E., Fischer, H., Fundel, F., Huybrechts, P., Kaufmann, P., Kipfstuhl, S., Lambrecht, A., Morganti, A., Oerter, H., Parrenin, F., Rybak, O., Severi, M., Udisti, R., Wilhelms, F., Wolff, E., 2007. "EDML1": a chronology for the EPICA deep ice core from Dronning Maud Land, Antarctica, over the last 150 000 years. Clim. Past 3, 475–484. http://dx.doi.org/10.5194/cp-3-475-2007.
Sanchez Goni, M.F., Landais, A., Fletcher, W.J., Naughton, F., Desprat, S., Duprat, J., 2008. Contrasting impacts of Dansgaard-Oeschger events over a western European latitudinal transect modulated by orbital parameters. Quat. Sci. Rev. 27, 1136–1151.
Sanchez-Goni, M.F., Harrison, S.P., 2010. Millennial-scale climate variability and vegetation changes during the Last Glacial: concepts and terminology. Quat. Sci. Rev. 29, 2823–2827.
Scarchilli, C., Frezzotti, M., Ruti, P.M., 2011. Snow precipitation at four ice core sites in East Antarctica: provenance, seasonality and blocking factors. Clim. Dyn. 37, 2107–2125. http://dx.doi.org/10.1007/s00382-010-0946-4.
Schilt, A., Baumgartner, M., Blunier, T., Schwander, J., Spahni, R., Fischer, H., Stocker, T.F., 2010. Glacial-interglacial and millennial-scale variations in the atmospheric nitrous oxide concentration during the last 800,000 years. Quat. Sci. Rev. 29 (1–2), 182–192.
Schüpbach, S., Federer, U., Bigler, M., Fischer, H., Stocker, T.F., 2011. A refined TALDICE-1a age scale from 55 to 112 ka before present for the Talos Dome ice core based on high-resolution methane measurements. Clim. Past 7, 1001–1009. http://dx.doi.org/10.5194/cp-7-1001-2011.
Schüpbach, S., Federer, U., Kaufmann, P.R., Albani, S., Barbante, C., Stocker, T.F., Fischer, H., 2013. High-resolution mineral dust and sea ice proxy records from the Talos Dome ice core. Clim. Past 9, 2789–2807.
Seidov, D., Stouffer, R.J., Haupt, B.J., 2005. Is there a simple bi-polar ocean seesaw? Global Planet. Change 49, 19–27.
Severi, M., Becagli, S., Castellano, E., Morganti, A., Traversi, R., Udisti, R., Ruth, U., Fischer, H., Huybrechts, P., Wolff, E., Parrenin, F., Kaufmann, P., Lambert, F., Steffensen, J.P., 2007. Synchronisation of the EDML and EDC ice cores for the last 52 kyr by volcanic signature matching. Clim. Past 3, 367–374. http://dx.doi.org/10.5194/cp-3-367-2007.
Severi, M., Udisti, R., Becagli, S., Stenni, B., Traversi, R., 2012. Volcanic synchronisation of the EPICA-DC and TALDICE ice cores for the last 42 kyr BP. Clim. Past 8, 509–517. http://dx.doi.org/10.5194/cp-8-509-2012.
Severinghaus, J.P., Brook, E.J., 1999. Abrupt climate change at the end of the last glacial period inferred from trapped air in polar ice. Science 286, 930–934. http://dx.doi.org/10.1126/science.286.5441.930.
Severinghaus, J.P., Sowers, T., Brook, E.J., Alley, R.B., Bender, M.L., 1998. Timing of abrupt climate change at the end of the Younger Dryas interval from thermally fractionated gases in polar ice. Nature 391, 141–146. http://dx.doi.org/10.1038/34346.
Shaffer, G., Olsen, S.M., Bjerrum, C.J., 2004. Ocean subsurface warming as a mechanism for coupling Dansgaard-Oeschger climate cycles and ice-rafting events. Geophys. Res. Lett. 31, L24202. http://dx.doi.org/10.1029/2004GL020968.
Singer, B.S., Guillou, H., Jicha, B.R., Laj, C., Kissel, C., Beard, B.L., Johnson, C.M., 2009. 40Ar/39Ar, K–Ar and 230Th–238U dating of the Laschamp excursion: a radioisotopic tie-point for ice core and climate chronologies. Earth Planet. Sci. Lett. 286 (1–2), 80–88.
Smith, D.E., Harrison, S., Firth, C.R., Jordan, J.T., 2011. The early Holocene sea level rise. Quat. Sci. Rev. 30, 1846–1860.
Stenni, B., Masson-Delmotte, V., Selmo, E., Oerter, H., Meyer, H., Roethlisberger, R., Jouzel, J., Cattani, O., Falourd, S., Fischer, H., Hoffmann, G., Iacumin, P., Johnsen, S.J., Minster, B., Udisti, R., 2010. The deuterium excess records of EPICA Dome C and Dronning Maud Land ice cores (East Antarctica). Quat. Sci. Rev. 29 (1–2), 146–159.
Stocker, T.F., Johnsen, S.J., 2003. A minimum thermodynamic model for the bipolar seesaw. Paleoceanography 18, 1087. http://dx.doi.org/10.1029/2003PA000920.
Stouffer, R.J., Yin, J., Gregory, J.M., Dixon, K.W., Spelman, M.J., Hurlin, W., Weaver, A.J., Eby, M., Flato, G.M., Hasumi, H., Hu, A., Jungclaus, J.H., Kamenkovich, I.J., Levermann, A., Montoya, M., Murakami, S., Nawrath, S., Oka, A., Peltier, W.R., Robitaille, D.Y., Sokolov, A., Vettoretti, G., Weber, S.L., 2006. Investigating the causes of the response of the thermohaline circulation to past and future climate changes. J. Clim. 19, 1365–1387. http://dx.doi.org/10.1175/JCLI3689.1.
Stouffer, R.J., Seidov, D., Haupt, B.J., 2007. Climate response to external sources of freshwater: North Atlantic versus the Southern Ocean. J. Clim. 20 (3) http://dx.doi.org/10.1175/JCLI4015.1.
Svensson, A., Andersen, K.K., Bigler, M., Clausen, H.B., Dahl-Jensen, D., Davies, S.M., Johnsen, S.J., Muscheler, R., Parrenin, F., Rasmussen, S.O., Röthlisberger, R., Seierstad, I., Steffensen, J.P., Vinther, B.M., 2008. A 60 000 year Greenland stratigraphic ice core chronology. Clim. Past 4, 47–57. http://dx.doi.org/10.5194/cp-4-47-2008.
Svensson, A., Bigler, M., Blunier, T., Clausen, H.B., Dahl-Jensen, D., Fischer, H., Fujita, S., Goto-Azuma, K., Johnsen, S.J., Kawamura, K., Kipfstuhl, S., Kohno, M., Parrenin, F., Popp, T., Rasmussen, S.O., Schwander, J., Seierstad, I., Severi, M., Steffensen, J.P., Udisti, R., Uemura, R., Vallelonga, P., Vinther, B.M., Wegner, A., Wilhelms, F., Winstrup, M., 2013. Direct linking of Greenland and Antarctic ice cores at the Toba eruption (74 ka BP). Clim. Past 9, 749–766. http://dx.doi.org/10.5194/cp-9-749-2013.
Swingedouw, D., Fichefet, T., Huybrechts, P., Driesschaert, M., Goosse, H., Loutre, M.F., 2008. Antarctic ice-sheet melting provides negative feedbacks on future global warming. Geophys. Res. Lett. 35. Art. No L17705.
Swingedouw, D., Mignot, J., Braconnot, P., Mosquet, E., Kageyama, M., Alkama, R., 2009. Impact of freshwater release in the North Atlantic under different climate conditions in an OAGCM. J. Clim. 22, 6377–6403.
Timmermann, A., Menviel, L., Okumura, Y., Schilla, A., Merkel, U., Timm, O., Hu, A., Otto-Bliesner, B., Schulz, M., 2010. Towards a quantitative understanding of millennial-scale Antarctic Warming events. Quat. Sci. Rev. 29, 74–85.
Udisti, R., Becagli, S., Castellano, E., Delmonte, B., Jouzel, J., Petit, J.-R., Schwander, J., Stenni, B., Wolff, E.W., 2004. Stratigraphic correlations between the EPICA-Dome C and Vostok ice cores showing the relative variations of snow accumulation over the past 45 kyr. J. Geophys. Res. 109, D08101. http://dx.doi.org/10.1029/2003jd004180.
Veres, D., Bazin, L., Landais, A., Toyé Mahamadou Kele, H., Lemieux-Dudon, B., Parrenin, F., Martinerie, P., Blayo, E., Blunier, T., Capron, E., Chappellaz, J., Rasmussen, S.O., Severi, M., Svensson, A., Vinther, B., Wolff, E.W., 2013. The Antarctic ice core chronology (AICC2012): an optimized multi-parameter and multi-site dating approach for the last 120 thousand years. Clim. Past 9, 1733–1748. http://dx.doi.org/10.5194/cp-9-1733-2013.
Vimeux, F., Masson, V., Jouzel, J., Stievenard, M., Petit, J.-R., 1999. Glacial-interglacial changes in ocean surface conditions in the Southern Hemisphere. Nature 398, 410–413.
Voelker, A.H.L., 2002. Global distribution of centennial-scale records for Marine Isotope Stage (MIS) 3: a database. Quat. Sci. Rev. 21, 1185–1212.
Weaver, A.J., Saenko, O.A., Clark, P.U., Mitrovica, J.X., 2003. Meltwater pulse 1A from Antarctica as a trigger of the Bølling-Allerød warm interval. Science 299, 1709–1713.
Wegner, A., Gabrielli, P., Wilhelms-Dick, D., Ruth, U., Kriews, M., De Deckker, P., Barbante, C., Cozzi, G., Delmonte, B., Fischer, H., 2012. Change in dust variability in the Atlantic sector of Antarctica at the end of the last deglaciation. Clim. Past 8, 135–147. http://dx.doi.org/10.5194/cp-8-135-2012.
Welander, P., 1982. A simple heat-salt oscillator. Dyn. Atmos. Ocean 6, 233–242.
Werner, M., Heimann, M., Hoffmann, G., 2001. Isotopic composition and origin of polar precipitation in present and glacial climate simulations. Tellus B 53 (1).
Wunsch, C., 2006. Abrupt climate change: an alternative view. Quat. Res. 65, 191–203.
Zhang, X., Lohmann, G., Knorr, G., Purcell, C., 2014. Abrupt glacial climate shifts controlled by ice sheet changes. Nature. http://dx.doi.org/10.1038/nature13592 (online 13 August 2014).

5 Govin et al., soumis QSR

Sequence of events from the onset to the demise of the Last Interglacial (140-100 ka) : how to define chronologies in paleoclimatic archives ?

A. Govin, E. Capron, C. Tzedakis, S. Verheyden, B. Ghaleb, C. Hillaire-Marcel, G. St-Onge, J. Stoner, F. Bassinot, L. Bazin, T. Blunier, A. El Ouahabi, D. Genty, R. Gersonde, P. Jimenez-Amat, A. Landais, B. Martrat, V. Masson-Delmotte, M.-S. Seidenkrantz, D. Veres, C. Waelbroeck, R. Zahn.

Abstract

The Last Interglacial (LIG, 129-116 ka) represents a precious case study to investigate the response of vulnerable components of the Earth system to a warmer than present-day climate. However, the scarcity of precise absolute age constraints (e.g. radiometric dating, tephras, magnetic excursions) in most archives leads to the use of many different reference chronologies and various strategies to align paleoclimatic records. Therefore, the investigation of the climatic sequence of events across the LIG remains limited. Here we review the strengths and limitations of the methods that are commonly used to date or define chronologies in various paleoclimatic archives (corals, speleothems, ice cores, marine and lake/peat sediments) during the penultimate deglaciation, the LIG and the glacial inception (140-100 ka). We pay special attention to the description of the climatic hypotheses currently underlining record alignment strategies and the interpretation of the tracers commonly used. We also provide quantitative estimates of the associated absolute and relative age uncertainties. In addition, we provide recommendations on how to define at best absolute and relative chronologies. Future climate alignments should provide (1) a clear statement of climate hypotheses involved, (2) a detailed understanding of environmental parameters controlling selected tracers and (3) a careful evaluation of the synchronicity of aligned paleoclimatic records. We insist on the need to (1) give systematically quantitative estimates of relative and absolute age uncertainties, (2) assess the coherence of the different chronologies used when comparing records and (3) integrate these uncertainties in paleoclimatic interpretations. Finally, for the first time, we propose a sequence of major climatic events with associated age uncertainties from the onset to the demise of the LIG, which should serve as a benchmark to evaluate transient climate simulations and help disentangle involved climate feedbacks.

6 Raynaud et al., en préparation

The 800-ka air content record of the EPICA-DC (EDC) ice core help to improve long ice core chronologies

D. Raynaud, V. Lipenkov, M.-F. Loutre, L. Bazin, A. Landais, V. Masson-Delmotte and E. Capron.

Abstract

We present here new air content (V) data obtained along the Antarctic EPICA Dome C (EDC) ice core. These data extent the existing record which covered the last 430 ka BP (thousands of years before present) to about 800 ka BP, with a time resolution of 2 ka on average. Spectral properties of the V record are obtained by continuous wavelet transform (CWT) and compared with TMT analysis. The eccentricity component in the 100 ka band is attributed to glacial-interglacial changes in surface elevation, but only 3% or less of the variability of air content data measured along the 800 ka record can be explained by elevation changes. The strength of obliquity (41 ka band) relative to the strength of precession (19-23 band) is clearly dominant in the recent part of the record (0-430 ka BP). In contrast, the obliquity strength decreases in the oldest part. The cross CWT analysis performed between the deuterium and air content profiles strongly suggests that the obliquity and precession signature of air content cannot be attributed to temperature. The EDC record of the last 600 ka shows a remarkable correlation between the air content record filtered in a common precession-obliquity band (15-46 ka) and its specific Integrated Summer Insolation (ISI) target, which supports the use of V as a proxy of local summer insolation and confirms its value as local orbital tuning dating tool. Time delays and tie points matching between filtered V in the 15-46 ka band and its ISI target are used to infer a V-chronology tuned on the EDC local summer insolation, which is compared to the new improved AICC2012 chronology. Departure of AICC2012 from the V-chronology is evaluated to vary between -2.5 and +2 ka. Prior 600 ka BP the record shows a lack of coherency between V and ISI, which may reflect the weaker amplitudes of the obliquity forcing compared to the last 600 ka. Finally we compare the orbitally tuned chronology of the EDC ice core by using air content with the one available on the same core for more specific periods using $\delta O_2/N_2$.

Liste des figures

Liste des tableaux

Bibliographie

K. K. Andersen, A. Svensson, S. J. Johnsen, S. O. Rasmussen, M. Bigler, R. Röthlisberger, U. Ruth, M.-L. Siggaard-Andersen, J. Peder Steffensen, D. Dahl-Jensen, B. M. Vinther, and H. B. Clausen. The Greenland Ice Core Chronology 2005, 15 42 ka. Part 1 : constructing the time scale. *Quaternary Science Reviews*, 25 : 3246–3257, 2006. doi: 10.1016/j.quascirev.2006.08.002.

L. Arnaud, J.-M. Barnola, and P. Duval. Physical modeling of the densification of snow/firn and ice in the upper part of polar ice sheets. *Physics of Ice Core Records*, pages 285–305, 2000.

J.-M. Barnola, P. Pimienta, D. Raynaud, and Y. S. Korotkevich. CO_2-climate relationship as deduced from the Vostok ice core : a re-examination based on new measurements and on a re-evaluation of the air dating. *Tellus Series B Chemical and Physical Meteorology B*, 43 :83, April 1991. doi: 10.1034/j.1600-0889.1991.t01-1-00002.x.

M. Battle, M. Bender, T. Sowers, P. P. Tans, J. H. Butler, J. W. Elkins, J. T. Ellis, T. Conway, N. Zhang, P. Lang, and A. D. Clarket. Atmospheric gas concentrations over the past century measured in air from firn at the South Pole. *Nature*, 383 : 231–235, 1996. doi: 10.1038/383231a0.

M. Baumgartner, P. Kindler, O. Eicher, G. Floch, A. Schilt, J. Schwander, R. Spahni, E. Capron, J. Chappellaz, M. Leuenberger, H. Fischer, and T. F. Stocker. Ngrip ch_4 concentration from 120 to 10 kyr before present and its relation to a îÂ´^{15}n temperature reconstruction from the same ice core. *Climate of the Past*, 10(2) : 903–920, 2014. doi: 10.5194/cp-10-903-2014. URL `http://www.clim-past.net/10/903/2014/`.

L. Bazin, A. Landais, B. Lemieux-Dudon, H. Toyé Mahamadou Kele, D. Veres, F. Parrenin, P. Martinerie, C. Ritz, E. Capron, V. Lipenkov, M.-F. Loutre, D. Raynaud, B. Vinther, A. Svensson, S. Rasmussen, M. Severi, T. Blunier, M. Leuenberger, H. Fischer, V. Masson-Delmotte, J. Chappellaz, and E. Wolff. An optimized

multi-proxies, multi-site Antarctic ice and gas orbital chronology (AICC2012) : 120-800 ka. *Climate of the Past*, 9 :1715–1731, 2013. doi: 10.5194/cp-9-1715-2013.

M. Bender, T. Sowers, and L. Labeyrie. The Dole effect and its variations during the last 130,000 years as measured in the Vostok ice core. *Global Biogeochemical Cycles*, 8 :363–376, 1994. doi: 10.1029/94GB00724.

M. L. Bender. Orbital tuning chronology for the Vostok climate record supported by trapped gas composition. *Earth and Planetary Science Letters*, 204 :275–289, November 2002. doi: 10.1016/S0012-821X(02)00980-9.

M. L. Bender, T. Sowers, J.-M. Barnola, and J. Chappellaz. Changes in the o2/n2 ratio of the atmosphere during recent decades reflected in the composition of air in the firn at vostok station, antarctica. *Geophysical Research Letters*, 21(3) : 189–192, 1994. ISSN 1944-8007. doi: 10.1029/93GL03548. URL `http://dx.doi.org/10.1029/93GL03548`.

Michael Bender, Todd Sowers, and Volodya Lipenkov. On the concentrations of o2, n2, and ar in trapped gases from ice cores. *Journal of Geophysical Research : Atmospheres*, 100(D9) :18651–18660, 1995. ISSN 2156-2202. doi: 10.1029/94JD02212. URL `http://dx.doi.org/10.1029/94JD02212`.

D. Buiron, J. Chappellaz, B. Stenni, M. Frezzotti, M. Baumgartner, E. Capron, A. Landais, B. Lemieux-Dudon, V. Masson-Delmotte, M. Montagnat, F. Parrenin, and A. Schilt. TALDICE-1 age scale of the Talos Dome deep ice core, East Antarctica. *Climate of the Past*, 7 :1–16, 2011. doi: 10.5194/cp-7-1-2011.

N. Caillon, J. P. Severinghaus, J. Jouzel, J.-M. Barnola, J. Kang, and V. Y. Lipenkov. Timing of Atmospheric CO_2 and Antarctic Temperature Changes Across Termination III. *Science*, 299 :1728–1731, 2003. doi: 10.1126/science.1078758.

P. Camps, B. S. Singer, C. Carvallo, A. Goguitchaichvili, G. Fanjat, and B. Allen. The Kamikatsura event and the Matuyama-Brunhes reversal recorded in lavas from Tjörnes Peninsula, northern Iceland. *Earth and Planetary Science Letters*, 310 :33–44, 2011. doi: 10.1016/j.epsl.2011.07.026.

E. Capron. *L'air piégé dans les glaces polaires : contraintes chronologiques et caractérisation de la variabilité climatique rapide*. PhD thesis, Université de Versailles Saint-Quentin, 2010.

E. Capron, A. Landais, B. Lemieux-Dudon, A. Schilt, V. Masson-Delmotte, D. Buiron, J. Chappellaz, D. Dahl-Jensen, S. Johnsen, M. Leuenberger, L. Loulergue,

and H. Oerter. Synchronising EDML and NorthGRIP ice cores using δ^{18}O of atmospheric oxygen ($\delta^{18}O_{atm}$) and CH_4 measurements over MIS5 (80-123 kyr). *Quaternary Science Reviews*, 29 :222–234, 2010. doi: 10.1016/j.quascirev.2009.07.014.

E. Capron, A. Landais, D. Buiron, A. Cauquoin, J. Chappellaz, M. Debret, J. Jouzel, M. Leuenberger, P. Martinerie, V. Masson-Delmotte, R. Mulvaney, F. Parrenin, and F. Prié. Glacial-interglacial dynamics of Antarctic firns : comparison between simulations and ice core air-d15N measurements. *Climate of the Past*, 9 :983–999, 2013. doi: 10.5194/cp-9-983-2013.

J. E. T. Channell, D. A. Hodell, B. S. Singer, and C. Xuan. Reconciling astrochronological and $^{40}Ar/^{39}Ar$ ages for the Matuyama-Brunhes boundary and late Matuyama Chron. *Geochemistry, Geophysics, Geosystems*, 11 :12, 2010. doi: 10.1029/2010GC003203.

H. Cheng, P. Z. Zhang, C. Spötl, R. L. Edwards, Y. J. Cai, D. Z. Zhang, W. C. Sang, M. Tan, and Z. S. An. The climatic cyclicity in semiarid-arid central Asia over the past 500,000 years. *Geophys. Res. Lett.*, 39 :1705, 2012. doi: 10.1029/2011GL050202.

Hai Cheng, R. Lawrence Edwards, Wallace S. Broecker, George H. Denton, Xinggong Kong, Yongjin Wang, Rong Zhang, and Xianfeng Wang. Ice Age Terminations. *Science*, 326(5950) :248–252, 2009. doi: 10.1126/science.1177840.

G. B. Dreyfus, F. Parrenin, B. Lemieux-Dudon, G. Durand, V. Masson-Delmotte, J. Jouzel, J.-M. Barnola, L. Panno, R. Spahni, A. Tisserand, U. Siegenthaler, and M. Leuenberger. Anomalous flow below 2700 m in the EPICA Dome C ice core detected using δ^{18}O of atmospheric oxygen measurements. *Climate of the Past*, 3 :341–353, June 2007. doi: 10.5194/cp-3-341-2007.

G. B. Dreyfus, G. M. Raisbeck, F. Parrenin, J. Jouzel, Y. Guyodo, S. Nomade, and A. Mazaud. An ice core perspective on the age of the Matuyama-Brunhes boundary. *Earth and Planetary Science Letters*, 274 :151–156, September 2008. doi: 10.1016/j.epsl.2008.07.008.

Gabrielle B. Dreyfus, Jean Jouzel, Michael L. Bender, Amaëlle Landais, Valérie Masson-Delmotte, and Markus Leuenberger. Firn processes and $\delta^{15}N$: potential for a gas-phase climate proxy. *Quaternary Science Reviews*, 29 :28 – 42, 2010. ISSN 0277-3791. doi: 10.1016/j.quascirev.2009.10.012.

Nelia W. Dunbar, William C. McIntosh, and Richard P. Esser. Physical setting and tephrochronology of the summit caldera ice record at Mount Moulton, West Antarctica. *Geological Society of America Bulletin*, 120(7-8) :796–812, 2008. doi: 10.1130/B26140.1.

G. Durand. *Microstructure, recristallisation et déformation des glaces polaires de la carotte EPICA, Dôme Concordia, Antarctique*. PhD thesis, Université Joseph Fourier, 2004.

G. Durand, F. Graner, and J. Weiss. Deformation of grain boundaries in polar ice. *EPL (Europhysics Letters)*, 67 :1038–1044, September 2004. doi: 10.1209/epl/i2004-10139-0.

G. Durand, F. Gillet-Chaulet, A. Svensson, O. Gagliardini, S. Kipfstuhl, J. Meyssonnier, F. Parrenin, P. Duval, and D. Dahl-Jensen. Change in ice rheology during climate variations – implications for ice flow modelling and dating of the EPICA Dome C core. *Climate of the Past*, 3(1) :155–167, 2007. doi: 10.5194/cp-3-155-2007.

EPICA Community Members. Eight glacial cycles from an Antarctic ice core. *Nature*, 429 :623–628, June 2004. doi: 10.1038/nature02599.

EPICA Community Members. One-to-one coupling of glacial climate variability in Greenland and Antarctica. *Nature*, 444 :195–198, November 2006. doi: 10.1038/nature05301.

D. Fleitmann, H. Cheng, S. Badertscher, R. L. Edwards, M. Mudelsee, O. M. Göktürk, A. Fankhauser, R. Pickering, C. C. Raible, A. Matter, J. Kramers, and O. Tüysüz. Timing and climatic impact of Greenland interstadials recorded in stalagmites from northern Turkey. *Geophys. Res. Lett.*, 36 :19707, 2009. doi: 10.1029/2009GL040050.

Johannes Freitag, Sepp Kipfstuhl, Thomas Laepple, and Frank Wilhelms. Impurity-controlled densification : a new model for stratified polar firn. *Journal of Glaciology*, 59(218) :1163–1169, 2013. doi: doi:10.3189/2013JoG13J042.

J.-C. Gilbert and C. Lemaréchal. Some numerical experiments with variable-storage quasi-Newton algotithms. *Mathematical Programming*, 45 :407–435, 1989.

C. Goujon, J.-M. Barnola, and C. Ritz. Modeling the densification of polar firn including heat diffusion : Application to close-off characteristics and gas isotopic

fractionation for Antarctica and Greenland sites. *Journal of Geophysical Research (Atmospheres)*, 108 :4792, December 2003. doi: 10.1029/2002JD003319.

M. Guillevic, L. Bazin, A. Landais, V. Masson- Delmotte, T. Blunier, S. L. Buchardt, E. Capron, P. Kindler, M. Leuenberger, B. Minster, A. Orsi, F. Prie, and B. M. Vinther. Spatial gradients of temperature, accumulation and $\delta^{18}O$-ice in Greenland over a series of Dansgaard-Oeschger events. *Climate of the Past*, 9 : 1029–1051, 2013. doi: 10.5194/cp-9-1029-2013.

R. D. Guy, M. L. Fogel, and J. A. Berry. Photosynthetic fractionation of the stable isotopes of oxygen and carbon. *Plant Physiology*, 101(1) :37–47, 1993. doi: 10.1104/pp.101.1.37. URL `http://www.plantphysiol.org/content/101/1/37.abstract`.

RobertD. Guy, JosephA. Berry, MarilynL. Fogel, and ThomasC. Hoering. Differential fractionation of oxygen isotopes by cyanide-resistant and cyanide-sensitive respiration in plants. *Planta*, 177(4) :483–491, 1989. ISSN 0032-0935. doi: 10.1007/BF00392616. URL `http://dx.doi.org/10.1007/BF00392616`.

M. M. Herron and C. C. Langway, Jr. Firn densification : an empirical model. *Journal of Glaciology*, 25 :373–385, 1980.

C. Huber, U. Beyerle, M. Leuenberger, J. Schwander, R. Kipfer, R. Spahni, J. P. Severinghaus, and K. Weiler. Evidence for molecular size dependent gas fractionation in firn air derived from noble gases, oxygen, and nitrogen measurements. *Earth and Planetary Science Letters*, 243 :61–73, March 2006. doi: 10.1016/j.epsl.2005.12.036.

M. A. Hutterli, M. Schneebeli, J. Freitag, J. Kipfstuhl, and R Roth-lisberger. Impact of local insolation on snow metamorphism and ice core records. *Physics of ice core records II*, T. Hondoh, Hokkaido University Press :223–232, 2010.

P. Huybrechts, O. Rybak, F. Pattyn, U. Ruth, and D. Steinhage. Ice thinning, upstream advection, and non-climatic biases for the upper 89% of the EDML ice core from a nested model of the Antarctic ice sheet. *Climate of the Past Discussions*, 3 :693–727, May 2007.

T. Ikeda, H. Fukazawa, S. Mae, L. Pepin, P. Duval, B. Champagnon, V. Y. Lipenkov, and T. Hondoh. Extreme fractionation of gases caused by formation of clathrate hydrates in Vostok Antarctic Ice. *Geophys. Res. Lett.*, 26 :91–94, 1999. doi: 10.1029/1998GL900220.

Tomoko Ikeda-Fukazawa, Kenji Fukumizu, Kenji Kawamura, Shuji Aoki, Takakiyo Nakazawa, and Takeo Hondoh. Effects of molecular diffusion on trapped gas composition in polar ice cores. *Earth and Planetary Science Letters*, 229(3–4) :183 – 192, 2005. ISSN 0012-821X. doi: http://dx.doi.org/10.1016/j.epsl.2004.11.011. URL `http://www.sciencedirect.com/science/article/pii/S0012821X04006843`.

IPCC. *Climate Change 2013 : The Physical Science Basis. Contribution of Working Group I to the Fifth Assessment Report of the Intergovernmental Panel on Climate Change*. Cambridge University Press, Cambridge, United Kingdom and New York, NY, USA, 2013.

J. Jouzel, C. Waelbroeck, B. Malaize, M. Bender, J.R. Petit, M. Stievenard, N.I. Barkov, J.M. Barnola, T. King, V.M. Kotlyakov, V. Lipenkov, C. Lorius, D. Raynaud, C. Ritz, and T. Sowers. Climatic interpretation of the recently extended Vostok ice records. *Climate Dynamics*, 12(8) :513–521, 1996. doi: 10.1007/BF00207935.

J. Jouzel, V. Masson-Delmotte, O. Cattani, G. Dreyfus, S. Falourd, G. Hoffmann, B. Minster, J. Nouet, J. M. Barnola, J. Chappellaz, H. Fischer, J. C. Gallet, S. Johnsen, M. Leuenberger, L. Loulergue, D. Luethi, H. Oerter, F. Parrenin, G. Raisbeck, D. Raynaud, A. Schilt, J. Schwander, E. Selmo, R. Souchez, R. Spahni, B. Stauffer, J. P. Steffensen, B. Stenni, T. F. Stocker, J. L. Tison, M. Werner, and E. W. Wolff. Orbital and Millennial Antarctic Climate Variability over the Past 800,000 Years. *Science*, 317 :793–, August 2007. doi: 10.1126/science.1141038.

Jean Jouzel, Georg Hoffmann, Frédéric Parrenin, and Claire Waelbroeck. Atmospheric oxygen 18 and sea-level changes. *Quaternary Science Reviews*, 21 :307–314, January 2002. doi: 10.1016/S0277-3791(01)00106-8.

K. Kawamura, F. Parrenin, L. Lisiecki, R. Uemura, F. Vimeux, J. P. Severinghaus, M. A. Hutterli, T. Nakazawa, S. Aoki, J. Jouzel, M. E. Raymo, K. Matsumoto, H. Nakata, H. Motoyama, S. Fujita, K. Goto-Azuma, Y. Fujii, and O. Watanabe. Northern Hemisphere forcing of climatic cycles in Antarctica over the past 360,000years. *Nature*, 448 :912–916, August 2007. doi: 10.1038/nature06015.

P. Kindler, M. Guillevic, M. Baumgartner, J. Schwander, A. Landais, M. Leuenberger, R. Spahni, E. Capron, and J. Chappellaz. Temperature reconstruction from 10 to 120 kyr b2k from the NGRIP ice core. *Climate of the Past*, 10 :887–902, April 2014. doi: 10.5194/cp-10-887-2014.

K. F. Kuiper, A. Deino, F. J. Hilgen, W. Krijgsman, P. R. Renne, and J. R. Wijbrans. Synchronizing Rock Clocks of Earth History. *Science*, 320 :500–, April 2008. doi: 10.1126/science.1154339.

F. Lambert, B. Delmonte, J. R. Petit, M. Bigler, P. R. Kaufmann, M. A. Hutterli, T. F. Stocker, U. Ruth, J. P. Steffensen, and V. Maggi. Dust-climate couplings over the past 800,000 years from the EPICA Dome C ice core. *Nature*, 452 : 616–619, April 2008. doi: 10.1038/nature06763.

A. Landais, N. Caillon, J. Severinghaus, J. Jouzel, and V. Masson- Delmotte. Analyses isotopiques à haute précision de l'air piégé dans les glaces polaires pour la quantification des variations rapides de température : méthodes et limites. *Notes des activités instrumentales de l'IPSL*, 39, 2003.

A. Landais, J. M. Barnola, V. Masson-Delmotte, J. Jouzel, J. Chappellaz, N. Caillon, C. Huber, M. Leuenberger, and S. J. Johnsen. A continuous record of temperature evolution over a sequence of Dansgaard-Oeschger events during Marine Isotopic Stage 4 (76 to 62 kyr BP). *Geophys. Res. Lett.*, 31 :L22211, November 2004. doi: 10.1029/2004GL021193.

A. Landais, J. M. Barnola, K. Kawamura, N. Caillon, M. Delmotte, T. Van Ommen, G. Dreyfus, J. Jouzel, V. Masson-Delmotte, B. Minster, Johannes Freitag, M. Leuenberger, J. Schwander, C. Huber, D. Etheridge, and V. Morgan. Firn-air d15n in modern polar sites and glacial-interglacial ice : a model-data mismatch during glacial periods in antarctica ? *Quaternary science reviews*, 25(1) :49–62, 2006. doi: 10.1016/j.quascirev.2005.06.007. URL `http://dx.doi.org/10.1016/j.quascirev.2005.06.007`.

A. Landais, V. Masson-Delmotte, N. Combourieu Nebout, J. Jouzel, T. Blunier, M. Leuenberger, D. Dahl-Jensen, and S. Johnsen. Millenial scale variations of the isotopic composition of atmospheric oxygen over Marine Isotopic Stage 4. *Earth and Planetary Science Letters*, 258 :101–113, June 2007. doi: 10.1016/j.epsl.2007.03.027.

A. Landais, G. Dreyfus, E. Capron, V. Masson-Delmotte, M.F. Sanchez-Goñi, S. Desprat, G. Hoffmann, J. Jouzel, M. Leuenberger, and S. Johnsen. What drives the millennial and orbital variations of $\delta^{18}O_{atm}$? *Quaternary Science Reviews*, 29 : 235–246, 2010. ISSN 0277-3791. doi: 10.1016/j.quascirev.2009.07.005.

A. Landais, G. Dreyfus, E. Capron, K. Pol, M. F. Loutre, D. Raynaud, V. Y. Lipenkov, L. Arnaud, V. Masson-Delmotte, D. Paillard, J. Jouzel, and M. Leuenberger.

Towards orbital dating of the EPICA Dome C ice core using $\delta O_2/N_2$. *Climate of the Past*, 8 :191–203, January 2012. doi: 10.5194/cp-8-191-2012.

A. Landais, G. Dreyfus, E. Capron, J. Jouzel, V. Masson-Delmotte, D. M. Roche, F. Prié, N. Caillon, J. Chappellaz, M. Leuenberger, A. Lourantou, F. Parrenin, D. Raynaud, and G. Teste. Two-phase change in CO_2, Antarctic temperature and global climate during Termination II. *Nature Geoscience*, 6 :1062–1065, December 2013. doi: 10.1038/ngeo1985.

B. Lemieux-Dudon. *Conjonction de données et de modèles pour la datation des forages profonds d'Antarctique et du Groenland*. PhD thesis, UJF, Grenoble, 2009.

B. Lemieux-Dudon, E. Blayo, J.-R. Petit, C. Waelbroeck, A. Svensson, C. Ritz, J.-M. Barnola, B. M. Narcisi, and F. Parrenin. Consistent dating for Antarctic and Greenland ice cores. *Quaternary Science Reviews*, 29 :8–20, January 2010. doi: 10.1016/j.quascirev.2009.11.010.

V. Y. Lipenkov, D. Raynaud, M. F. Loutre, and P. Duval. On the potential of coupling air content and O_2/N_2 from trapped air for establishing an ice core chronology tuned on local insolation. *Quaternary Science Reviews*, 30 :3280–3289, November 2011. doi: 10.1016/j.quascirev.2011.07.013.

L. E. Lisiecki and M. E. Raymo. A Pliocene-Pleistocene stack of 57 globally distributed benthic $\delta^{18}O$ records. *Paleoceanography*, 20 :PA1003, March 2005. doi: 10.1029/2004PA001071.

L. Loulergue. *Contraintes chronologiques et biogeochimiques grace au methane dans la glace naturelle : une application aux forages du projet EPICA, 2007*. PhD thesis, UJF, France, 2007.

L. Loulergue, F. Parrenin, T. Blunier, J.-M. Barnola, R. Spahni, A. Schilt, G. Raisbeck, and J. Chappellaz. New constraints on the gas age-ice age difference along the EPICA ice cores, 0-50 kyr. *Climate of the Past*, 3 :527–540, August 2007.

L. Loulergue, A. Schilt, R. Spahni, V. Masson-Delmotte, T. Blunier, B. Lemieux, J.-M. Barnola, D. Raynaud, T. F. Stocker, and J. Chappellaz. Orbital and millennial-scale features of atmospheric CH_4 over the past 800,000years. *Nature*, 453 :383–386, May 2008. doi: 10.1038/nature06950.

A. Lourantou, J. Chappellaz, J.-M. Barnola, V. Masson-Delmotte, and D. Raynaud. Changes in atmospheric CO_2 and its carbon isotopic ratio during the penultimate

deglaciation. *Quaternary Science Reviews*, 29 :1983–1992, August 2010. doi: 10.1016/j.quascirev.2010.05.002.

D. Lüthi, M. Le Floch, B. Bereiter, T. Blunier, J.-M. Barnola, U. Siegenthaler, D. Raynaud, J. Jouzel, H. Fischer, K. Kawamura, and T. F. Stocker. High-resolution carbon dioxide concentration record 650,000-800,000years before present. *Nature*, 453 :379–382, May 2008. doi: 10.1038/nature06949.

B. Malaizé, D. Paillard, J. Jouzel, and D. Raynaud. The Dole effect over the last two glacial-interglacial cycles. *J. Geophys. Res.*, 104 :14199–14208, 1999. doi: 10.1029/1999JD900116.

V. Masson-Delmotte, D. Buiron, A. Ekaykin, M. Frezzotti, H. Gallée, J. Jouzel, G. Krinner, A. Landais, H. Motoyama, H. Oerter, K. Pol, D. Pollard, C. Ritz, E. Schlosser, L. C. Sime, H. Sodemann, B. Stenni, R. Uemura, and F. Vimeux. A comparison of the present and last interglacial periods in six Antarctic ice cores. *Climate of the Past*, 7 :397–423, April 2011. doi: 10.5194/cp-7-397-2011.

N. Mochizuki, H. Oda, O. Ishizuka, T. Yamazaki, and H. Tsunakawa. Paleointensity variation across the Matuyama-Brunhes polarity transition : Observations from lavas at Punaruu Valley, Tahiti. *Journal of Geophysical Research (Solid Earth)*, 116(B15) :B06103, jun 2011. doi: 10.1029/2010JB008093.

K. Mosegaard and A. Tarantola. *International Handbook of Earthquake and Engineering Seismology (Part A). Chapter : Probabilistic Approach to Inverse Problems*. Academic Press, 2002.

B. Narcisi, J. R. Petit, B. Delmonte, I. Basile-Doelsch, and V. Maggi. Characteristics and sources of tephra layers in the EPICA-Dome C ice record (East Antarctica) : Implications for past atmospheric circulation and ice core stratigraphic correlations [rapid communication]. *Earth and Planetary Science Letters*, 239 :253–265, November 2005. doi: 10.1016/j.epsl.2005.09.005.

B. Narcisi, J. Robert Petit, and M. Tiepolo. A volcanic marker (92 ka) for dating deep east Antarctic ice cores. *Quaternary Science Reviews*, 25 :2682–2687, November 2006. doi: 10.1016/j.quascirev.2006.07.009.

NorthGRIP Community Members. High-resolution record of Northern Hemisphere climate extending into the last interglacial period. *Nature*, 431 :147–151, sept 2004. doi: 10.1038/nature02805.

F. Parrenin, J. Jouzel, C. Waelbroeck, C. Ritz, and J.-M. Barnola. Dating the Vostok ice core by an inverse method. *J. Geophys. Res.*, 106 :31837–31852, December 2001. doi: 10.1029/2001JD900245.

F. Parrenin, F. Rémy, C. Ritz, M. J. Siegert, and J. Jouzel. New modeling of the Vostok ice flow line and implication for the glaciological chronology of the Vostok ice core. *Journal of Geophysical Research (Atmospheres)*, 109(D18) :D20102, October 2004. doi: 10.1029/2004JD004561.

F. Parrenin, J.-M. Barnola, J. Beer, T. Blunier, E. Castellano, J. Chappellaz, G. Dreyfus, H. Fischer, S. Fujita, J. Jouzel, K. Kawamura, B. Lemieux-Dudon, L. Loulergue, V. Masson-Delmotte, B. Narcisi, J.-R. Petit, G. Raisbeck, D. Raynaud, U. Ruth, J. Schwander, M. Severi, R. Spahni, J. P. Steffensen, A. Svensson, R. Udisti, C. Waelbroeck, and E. Wolff. The EDC3 chronology for the EPICA Dome C ice core. *Climate of the Past*, 3 :485–497, August 2007a. doi: 10.5194/cp-3-485-2007.

F. Parrenin, G. Dreyfus, G. Durand, S. Fujita, O. Gagliardini, F. Gillet, J. Jouzel, K. Kawamura, N. Lhomme, V. Masson-Delmotte, C. Ritz, J. Schwander, H. Shoji, R. Uemura, O. Watanabe, and N. Yoshida. 1-D-ice flow modelling at EPICA Dome C and Dome Fuji, East Antarctica. *Climate of the Past*, 3 :243–259, 2007b. doi: 10.5194/cp-3-243-2007.

F. Parrenin, S. Barker, T. Blunier, J. Chappellaz, J. Jouzel, A. Landais, V. Masson-Delmotte, J. Schwander, and D. Veres. On the gas-ice depth difference (Δ depth) along the EPICA Dome C ice core. *Climate of the Past Discussions*, 8(2) :1089–1131, 2012a. doi: 10.5194/cpd-8-1089-2012.

F. Parrenin, J.-R. Petit, V. Masson-Delmotte, E. Wolff, I. Basile-Doelsch, J. Jouzel, V. Lipenkov, S. O. Rasmussen, J. Schwander, M. Severi, R. Udisti, D. Veres, and B. M. Vinther. Volcanic synchronisation between the EPICA Dome C and Vostok ice cores (Antarctica) 0-145 kyr BP. *Climate of the Past*, 8 :1031–1045, June 2012b. doi: 10.5194/cp-8-1031-2012.

F. Parrenin, V. Masson-Delmotte, P. Köhler, D. Raynaud, D. Paillard, J. Schwander, C. Barbante, A. Landais, A. Wegner, and J. Jouzel. Synchronous Change of Atmospheric CO2 and Antarctic Temperature During the Last Deglacial Warming. *Science*, 339(6123) :1060–1063, 2013. doi: 10.1126/science.1226368.

J. R. Petit, J. Jouzel, D. Raynaud, N. I. Barkov, J.-M. Barnola, I. Basile, M. Bender, J. Chappellaz, M. Davis, G. Delaygue, M. Delmotte, V. M. Kotlyakov, M. Legrand,

V. Y. Lipenkov, C. Lorius, L. Pépin, C. Ritz, E. Saltzman, and M. Stievenard. Climate and atmospheric history of the past 420,000 years from the Vostok ice core, Antarctica. *Nature*, 399 :429–436, June 1999. doi: 10.1038/20859.

P. Pimienta. *Etude de comportement mécanique des glaces polycristallines aux faibles contraintes ; application aux glaces de calotte polaire*. PhD thesis, Université Joseph Fourier, 1987.

G. Raisbeck, F. Yiou, E. Bard, D. Dollfus, J. Jouzel, and J. R. Petit. Absolute dating of the last 7000 years of the Vostok ice core using 10^Be. *Mineral. Mag.*, 62A :1228, 1998.

G. M. Raisbeck, F. Yiou, D. Bourles, C. Lorius, and J. Jouzel. Evidence for two intervals of enhanced Be-10 deposition in Antarctic ice during the last glacial period. *Nature*, 326 :273–277, March 1987. doi: 10.1038/326273a0.

G. M. Raisbeck, F. Yiou, O. Cattani, and J. Jouzel. ^{10}Be evidence for the Matuyama-Brunhes geomagnetic reversal in the EPICA Dome C ice core. *Nature*, 444 :82–84, November 2006. doi: 10.1038/nature05266.

G. M. Raisbeck, F. Yiou, J. Jouzel, and T. F. Stocker. Direct north-south synchronization of abrupt climate change record in ice cores using Beryllium 10. *Climate of the Past*, 3 :541–547, September 2007. doi: 10.5194/cp-3-541-2007.

S. O. Rasmussen, K. K. Andersen, A. M. Svensson, J. P. Steffensen, B. M. Vinther, H. B. Clausen, M.-L. Siggaard-Andersen, S. J. Johnsen, L. B. Larsen, D. Dahl-Jensen, M. Bigler, R. Röthlisberger, H. Fischer, K. Goto-Azuma, M. E. Hansson, and U. Ruth. A new Greenland ice core chronology for the last glacial termination. *Journal of Geophysical Research (Atmospheres)*, 111(D10) :D06102, March 2006. doi: 10.1029/2005JD006079.

D. Raynaud, V. Lipenkov, B. Lemieux-Dudon, P. Duval, M.-F. Loutre, and N. Lhomme. The local insolation signature of air content in Antarctic ice. A new step toward an absolute dating of ice records. *Earth and Planetary Science Letters*, 261 :337–349, September 2007. doi: 10.1016/j.epsl.2007.06.025.

D. Raynaud, V. Lipenkov, M.-F. Loutre, L. Bazin, A. Landais, V. Masson-Delmotte, and E. Capron. The 800-ka air content record of the epica-dc (edc) ice core help to improve long ice core chronologies. in prep.

Paul R. Renne, Carl C. Swisher, Alan L. Deino, Daniel B. Karner, Thomas L. Owens, and Donald J. DePaolo. Intercalibration of standards, absolute ages and

uncertainties in 40Ar/39Ar dating. *Chemical Geology*, 145(1–2) :117 – 152, 1998. doi: 10.1016/S0009-2541(97)00159-9.

U. Ruth, J.-M. Barnola, J. Beer, M. Bigler, T. Blunier, E. Castellano, H. Fischer, F. Fundel, P. Huybrechts, P. Kaufmann, S. Kipfstuhl, A. Lambrecht, A. Morganti, H. Oerter, F. Parrenin, O. Rybak, M. Severi, R. Udisti, F. Wilhelms, and E. Wolff. "EDML1" : a chronology for the EPICA deep ice core from Dronning Maud Land, Antarctica, over the last 150 000 years. *Climate of the Past*, 3 :475–484, August 2007. doi: 10.5194/cp-3-475-2007.

A. Schilt, M. Baumgartner, T. Blunier, J. Schwander, R. Spahni, H. Fischer, and T. F. Stocker. Glacial-interglacial and millennial-scale variations in the atmospheric nitrous oxide concentration during the last 800,000 years. *Quaternary Science Reviews*, 29 :182–192, January 2010. doi: 10.1016/j.quascirev.2009.03.011.

S. Schüpbach, U. Federer, M. Bigler, H. Fischer, and T. F. Stocker. A refined TALDICE-1a age scale from 55 to 112 ka before present for the Talos Dome ice core based on high-resolution methane measurements. *Climate of the Past*, 7 : 1001–1009, September 2011. doi: 10.5194/cp-7-1001-2011.

M. Severi, S. Becagli, E. Castellano, A. Morganti, R. Traversi, R. Udisti, U. Ruth, H. Fischer, P. Huybrechts, E. Wolff, F. Parrenin, P. Kaufmann, F. Lambert, and J. P. Steffensen. Synchronisation of the EDML and EDC ice cores for the last 52 kyr by volcanic signature matching. *Climate of the Past*, 3 :367–374, July 2007.

M. Severi, R. Udisti, S. Becagli, B. Stenni, and R. Traversi. Volcanic synchronisation of the EPICA-DC and TALDICE ice cores for the last 42 kyr BP. *Climate of the Past*, 8 :509–517, March 2012. doi: 10.5194/cp-8-509-2012.

J. P. Severinghaus and M. O. Battle. Fractionation of gases in polar ice during bubble close-off : New constraints from firn air Ne, Kr and Xe observations. *Earth and Planetary Science Letters*, 244 :474–500, April 2006. doi: 10.1016/j.epsl.2006.01.032.

J. P. Severinghaus, T. Sowers, E. J. Brook, R. B. Alley, and M. L. Bender. Timing of abrupt climate change at the end of the Younger Dryas interval from thermally fractionated gases in polar ice. *Nature*, 391 :141–146, January 1998. doi: 10.1038/34346.

J. P. Severinghaus, A. Grachev, and M. Battle. Thermal fractionation of air in polar firn by seasonal temperature gradients. *Geochem. Geophys. Geosyst.*, 2, 2001. doi: 10.1029/2000GC000146.

J. P. Severinghaus, R. Beaudette, M. A. Headly, K. Taylor, and E. J. Brook. Oxygen-18 of O_2 Records the Impact of Abrupt Climate Change on the Terrestrial Biosphere. *Science*, 324 :1431–, June 2009. doi: 10.1126/science.1169473.

J. P. Severinghaus, M. R. Albert, Z. R. Courville, M. A. Fahnestock, K. Kawamura, S. A. Montzka, J. Mühle, T. A. Scambos, E. Shields, C. A. Shuman, M. Suwa, P. Tans, and R. F. Weiss. Deep air convection in the firn at a zero-accumulation site, central Antarctica. *Earth and Planetary Science Letters*, 293 :359–367, May 2010. doi: 10.1016/j.epsl.2010.03.003.

N. J. Shackleton, M. A. Hall, and E. Vincent. Phase relationships between millennial-scale events 64,000-24,000 years ago. *Paleoceanography*, 15 :565–569, 2000. doi: 10.1029/2000PA000513.

B. S. Singer, H. Guillou, B. R. Jicha, C. Laj, C. Kissel, B. L. Beard, and C. M. Johnson. $^{40}Ar/^{39}Ar$, K-Ar and ^{230}Th-^{238}U dating of the Laschamp excursion : A radioisotopic tie-point for ice core and climate chronologies. *Earth and Planetary Science Letters*, 286 :80–88, August 2009. doi: 10.1016/j.epsl.2009.06.030.

Todd Sowers, Michael Bender, and Dominique Raynaud. Elemental and isotopic composition of occluded O2 and N2 in polar ice. *J. Geophys. Res.*, 94(D4) : 5137–5150, 1989. doi: 10.1029/JD094iD04p05137.

Todd Sowers, Michael Bender, Dominique Raynaud, and Y. S. Korotkevich. $\delta^{15}N$ of N_2 in Air Trapped in Polar Ice : a Tracer of Gas Transport in the Firn and a Possible Constraint on Ice Age-Gas Age Differences. *J. Geophys. Res.*, 97(D14) : 15683–15697, 1992. doi: 10.1029/92JD01297.

B. Stenni, D. Buiron, M. Frezzotti, S. Albani, C. Barbante, E. Bard, J. M. Barnola, M. Baroni, M. Baumgartner, M. Bonazza, E. Capron, E. Castellano, J. Chappellaz, B. Delmonte, S. Falourd, L. Genoni, P. Iacumin, J. Jouzel, S. Kipfstuhl, A. Landais, B. Lemieux-Dudon, V. Maggi, V. Masson-Delmotte, C. Mazzola, B. Minster, M. Montagnat, R. Mulvaney, B. Narcisi, H. Oerter, F. Parrenin, J. R. Petit, C. Ritz, C. Scarchilli, A. Schilt, S. Schüpbach, J. Schwander, E. Selmo, M. Severi, T. F. Stocker, and R. Udisti. Expression of the bipolar see-saw in Antarctic climate records during the last deglaciation. *Nature Geoscience*, 4 :46–49, January 2011. doi: 10.1038/ngeo1026.

M. Suwa and M. L. Bender. Chronology of the Vostok ice core constrained by O_2/N_2 ratios of occluded air, and its implication for the Vostok cli-

mate records. *Quaternary Science Reviews*, 27 :1093–1106, June 2008. doi: 10.1016/j.quascirev.2008.02.017.

A. Svensson, K. K. Andersen, M. Bigler, H. B. Clausen, D. Dahl-Jensen, S. M. Davies, S. J. Johnsen, R. Muscheler, F. Parrenin, S. O. Rasmussen, R. Röthlisberger, I. Seierstad, J. P. Steffensen, and B. M. Vinther. A 60 000 year Greenland stratigraphic ice core chronology. *Climate of the Past*, 4 :47–57, March 2008. doi: 10.5194/cp-4-47-2008.

A. Svensson, M. Bigler, T. Blunier, H. B. Clausen, D. Dahl-Jensen, H. Fischer, S. Fujita, K. Goto-Azuma, S. J. Johnsen, K. Kawamura, S. Kipfstuhl, M. Kohno, F. Parrenin, T. Popp, S. O. Rasmussen, J. Schwander, I. Seierstad, M. Severi, J. P. Steffensen, R. Udisti, R. Uemura, P. Vallelonga, B. M. Vinther, A. Wegner, F. Wilhelms, and M. Winstrup. Direct linking of Greenland and Antarctic ice cores at the Toba eruption (74 ka BP). *Climate of the Past*, 9 :749–766, 2013. doi: 10.5194/cp-9-749-2013.

Albert Tarantola. *Inverse Problem Theory and Methods for Model Parameter Estimation*. Society for Industrial and Applied Mathematics, 2005. doi: 10.1137/1.9780898717921.

R. Udisti, S. Becagli, E. Castellano, B. Delmonte, J. Jouzel, J. R. Petit, J. Schwander, B. Stenni, and E. W. Wolff. Stratigraphic correlations between the European Project for Ice Coring in Antarctica (EPICA) Dome C and Vostok ice cores showing the relative variations of snow accumulation over the past 45 kyr. *Journal of Geophysical Research (Atmospheres)*, 109(D18) :D08101, April 2004. doi: 10.1029/2003JD004180.

D. Veres, L. Bazin, A. Landais, H. Toye Mahamadou Kele, B. Lemieux-Dudon, F. Parrenin, P. Martinerie, E. Blayo, T. Blunier, E. Capron, J. Chappellaz, S. Rasmussen, M. Severi, A. Svensson, B. Vinther, and E. Wolff. The Antarctic ice core chronology (AICC2012) : an optimized multi-parameter and multi-site dating approach for the last 120 thousand years. *Climate of the Past*, 9 :1733–1748, 2013. doi: 10.5194/cp-9-1733-2013.

F. Vimeux, V. Masson, J. Jouzel, M. Stievenard, and J. R. Petit. Glacial-interglacial changes in ocean surface conditions in the Southern Hemisphere. *Nature*, 398 : 410–413, April 1999. doi: 10.1038/18860.

B. M. Vinther, H. B. Clausen, S. J. Johnsen, S. O. Rasmussen, K. K. Andersen, S. L. Buchardt, D. Dahl-Jensen, I. K. Seierstad, M.-L. Siggaard-Andersen, J. P. Stef-

fensen, A. Svensson, J. Olsen, and J. Heinemeier. A synchronized dating of three Greenland ice cores throughout the Holocene. *Journal of Geophysical Research (Atmospheres)*, 111(D10) :D13102, July 2006. doi: 10.1029/2005JD006921.

B.M. Vinther, H.B. Clausen, S. Kipfstuhl, H. Fischer, M. Bigler, H. Oerter, A. Wegner, F. Wilhelms, M. Sevri, R. Udisti, J. Beer, F. Steinhilber, F. Adolphi, R. Muschler, S.O. Rasmussen, J.P. Steffensen, and A. Svensson. A stratigraphic Antarctic chronology covering the past 16700 years in the EPICA deep ice core from Dronning Maud Land. *In prep.*

C. Waelbroeck, N. Frank, J. Jouzel, F. Parrenin, V. Masson-Delmotte, and D. Genty. Transferring radiometric dating of the last interglacial sea level high stand to marine and ice core records. *Earth and Planetary Science Letters*, 265 :183–194, January 2008. doi: 10.1016/j.epsl.2007.10.006.

Y. Wang, H. Cheng, R. L. Edwards, X. Kong, X. Shao, S. Chen, J. Wu, X. Jiang, X. Wang, and Z. An. Millennial- and orbital-scale changes in the East Asian monsoon over the past 224,000years. *Nature*, 451 :1090–1093, February 2008. doi: 10.1038/nature06692.

Y. J. Wang, H. Cheng, R. L. Edwards, Z. S. An, J. Y. Wu, C.-C. Shen, and J. A. Dorale. A High-Resolution Absolute-Dated Late Pleistocene Monsoon Record from Hulu Cave, China. *Science*, 294 :2345–2348, December 2001. doi: 10.1126/science.1064618.

E. W. Wolff, H. Fischer, F. Fundel, U. Ruth, B. Twarloh, G. C. Littot, R. Mulvaney, R. Röthlisberger, M. de Angelis, C. F. Boutron, M. Hansson, U. Jonsell, M. A. Hutterli, F. Lambert, P. Kaufmann, B. Stauffer, T. F. Stocker, J. P. Steffensen, M. Bigler, M. L. Siggaard-Andersen, R. Udisti, S. Becagli, E. Castellano, M. Severi, D. Wagenbach, C. Barbante, P. Gabrielli, and V. Gaspari. Southern Ocean sea-ice extent, productivity and iron flux over the past eight glacial cycles. *Nature*, 440 :491–496, March 2006. doi: 10.1038/nature04614.

E. W. Wolff, J. Chappellaz, T. Blunier, S. O. Rasmussen, and A. Svensson. Millennial-scale variability during the last glacial : The ice core record. *Quaternary Science Reviews*, 29 :2828–2838, October 2010. doi: 10.1016/j.quascirev.2009.10.013.

F. Yiou, G. M. Raisbeck, S. Baumgartner, J. Beer, C. Hammer, S. Johnsen, J. Jouzel, P. W. Kubik, J. Lestringuez, M. Stiévenard, M. Suter, and P. Yiou. Beryllium 10

in the Greenland Ice Core Project ice core at Summit, Greenland. *J. Geophys. Res.*, 102 :26783–26794, 1997. doi: 10.1029/97JC01265.